SIGGRAPH Asia 2009

Scattering

Course notes

Diego Gutierrez*
Universidad de Zaragoza

Henrik Wann Jensen†
University of California San Diego

Wojciech Jarosz‡
Disney Research, Zurich

Craig Donner§
Columbia University

*diegog@unizar.es
†henrik@cs.ucsd.edu
‡wjarosz@cs.ucsd.edu
§cdonner@cs.columbia.edu

1 About the Lecturers

Diego Gutierrez
Universidad de Zaragoza
http://giga.cps.unizar.es/ diegog

Diego Gutierrez is an Associate Professor at the University of Zaragoza, in Spain, where he received his PhD in Computer Science. His areas of expertise include physically based global illumination (specializing in participating media), perception and novel image processing techniques. He was Chair of the SIGGRAPH Asia Sketches & Posters programme in 2008, and was Papers Chair for ACM Graphite in 2006. He's served on many other programme committees, including SIGGRAPH Asia 2009 and Eurographics 2007.

Henrik Wann Jensen
University of California San Diego
http://graphics.ucsd.edu/ henrik

Henrik Wann Jensen is an Associate Professor at the University of California at San Diego. His contributions to computer graphics include the photon mapping algorithm for global illumination, and the first technique for efficiently simulating subsurface scattering in translucent materials. In 2004, Professor Jensen received an Academy Award (Technical Achievement Award) from the Academy of Motion Picture Arts and Sciences for pioneering research in rendering translucent materials. He also became a Sloan Fellow and he was selected as one of the top 10 scientists in 2004 by Popular Science magazine.

Wojciech Jarosz
Disney Research, Zurich
http://graphics.ucsd.edu/ wjarosz

Wojciech Jarosz is a computer graphics Ph.D. student at UC San Diego. His main research interest is production-quality global illumination techniques, specifically for participating media, and his current list of publications include three SIGGRAPH papers on those topics. He received his B.S. in Computer Science from University of Illinois, Urbana-Champaign and his M.S. in Computer Science from UC San Diego.

Craig Donner
Columbia University
http://www.cs.columbia.edu/ cdonner/

Craig is currently a Postdoctoral Research Scientist at Columbia University. His core research interests are appearance modeling and global illumination in the context of photorealistic image synthesis, as well as the acquisition and modeling of light transport in complex materials. He has served on the international papers committee for the Eurographics Symposium on Rendering for the past two years, and has many publications concerning light scattering, including four SIGGRAPH papers and three journal articles.

2 Course Abstract

Computer graphics deal with acquiring, interpreting and presenting the rich visual world around us. This is an exciting research field with a wide spectrum of applications that can impact our daily lives. However, most of the computer generated imagery today represents scenes with clear atmospheres, neglecting light scattering effects. Nevertheless, scattering is a fundamental aspect of light transport in a wide range of applications, whether simulating it or interpreting it, from medical imaging to driving simulators or underwater imagery. In this course we address the challenges that arise when faced with light scattering in a computer graphics context. The field has seen great advances over the past few years; however, most of the existing algorithms still assume that light emitted by a source or reflected off a surface reaches the sensor unaltered. This is due mainly to the complex interactions that occur and the high computational costs of simulating them. Scattering effects are one fundamental hurdle that must be overcome to significantly extend and enhance current state-of-the-art graphics techniques and achieve successful impact in a wide range of domains. We hope to increase awareness about this area and open up new research directions.

3 Introduction

Our current understanding of the behavior of light relies on a progression of increasingly complete yet complicated models of light. These are (see Figure 1): ray optics, wave optics, electromagnetic optics, and quantum optics saleh07fundamentals. Computer graphics typically relies on the simplest of these models, ray optics (also called geometric optics). This model makes several simplifying assumptions about the behavior of light that limit the types of phenomena that can be simulated. In essence, in this model light can only be emitted, reflected, and transmitted. Additionally, light is assumed to travel in straight lines and at infinite speed. This means that effects explained by the higher-level models cannot (easily) be incorporated into our simulations. In ray optics, effects such as diffraction and interference (wave optics), polarization and dispersion (electromagnetic optics), and fluorescence and phosphorescence (quantum optics) are completely ignored. In spite of these limitations, we are still able to correctly simulate a wide range of physical phenomena.

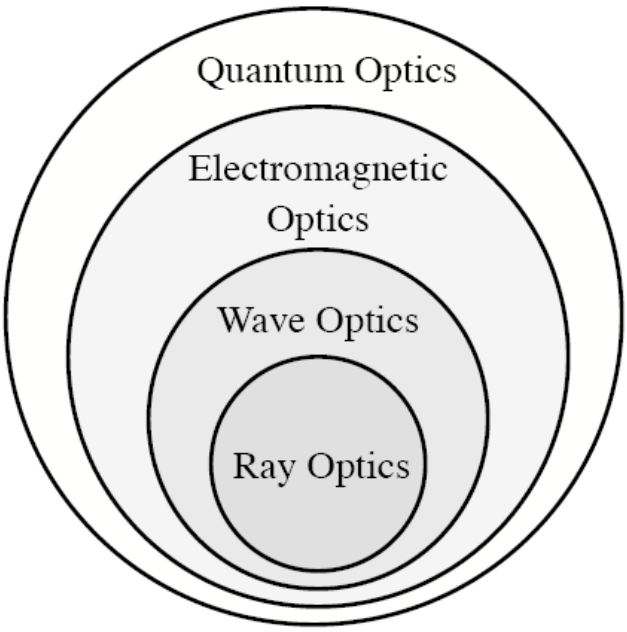

Figure 1: The theory of light is described by a series of increasingly complete optical models, where each successive model is able to account for more optical phenomena. In computer graphics, we often restrict ourselves to the simplest model, ray optics.

In most computer graphics applications, assumptions are made about the properties of the scattering media in order to more easily derive expressions about the behavior of light. In particular, we assume that the participating media can be modeled as a collection of microscopic particles. Since the particles are microscopic and randomly positioned, we do not represent each individual particle in the lighting simulation. Instead, we consider the aggregate probabilistic behavior as light travels through the medium. Moreover, these particles are assumed to be spaced far apart relative to the size of an individual particle. This assumption implies that as a photon travels through the medium and interacts at a particle, this interaction is *statistically independent* from the outcome of subsequent interaction events (Figure 2).

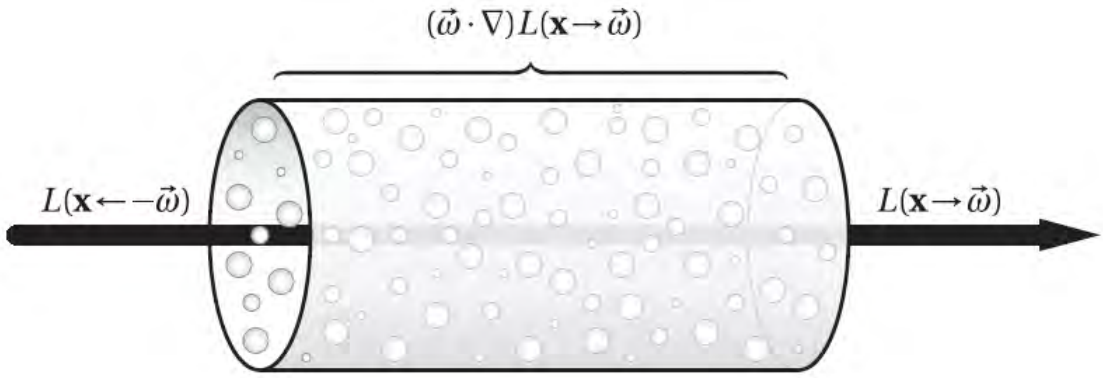

Figure 2: We treat participating media as a collection of microscopic scattering particles. When light travels through the medium, a change of radiance may occur as the photons interact with the particles.

4 Real-time Rendering Techniques for Participating Media

Most of computer generated imagery today in video games, movies, and scientific simulations are of scenes on clear days or nights. Volumetric effects such as the beautiful fog rolling down the hills, the bluish haze of mountains, the eerie night fog or mist reminiscent of Hitchcockian movies, the splendor and brilliance of underwater effects, the light streaming through clouds or the sun rising over the ocean provide pure artistic and entertainment value. They are used in movies and paintings to portray different moods, used in photographs to provide realism, and used even for training in safety and hazardous situations. In the absence of such effects, current attempts at renderings appear unnatural and cartoonish. Thus, it becomes critical to render these effects accurately for achieving photo-realism.

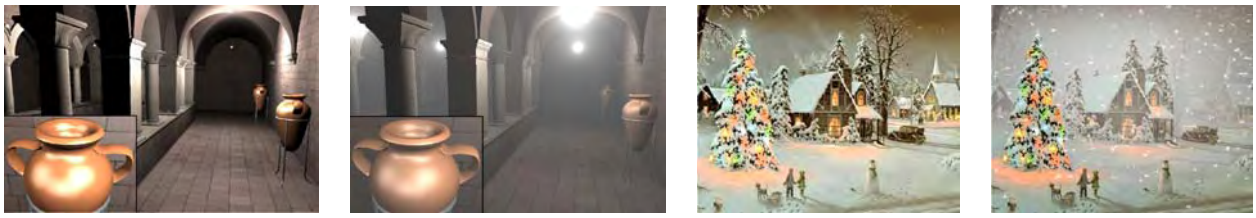

(a) (b) (c) (d)

Figure 3: **Real time rendering of participating media:**. (a)-(b) Real time rendering of homogenous media using an analytic single-scattering model of light transport. (a) Clear scene. (b) Scene with fog added. (c)-(d) Fast rendering of smooth, non-homogenous and dynamic media. (c) Clear day scene. (d) Scene with fog added.

Rendering of participating media requires solving complex light transport equations. Brute-force simulations of light transport based on Monte Carlo and finite element simulation can be prohibitively slow (taking CPU-days or even weeks). However, a variety of applications spanning entertainment (video games), medicine (surgery) and autonomous navigation require real-time or interactive performance. Thus, a recent research thrust has been to make smoothness assumptions, either on the media [4, 12] or the lighting [11] in order to achieve interactive rates. Sun et al [12] have implemented their model in modern programmable graphics hardware using a few small numerical lookup tables stored as texture maps, and achieved truly real time performance. Gupta et al [4] present a technique for fast rendering of non-homogenous, as well as dynamic media, by representing the density and intensity fields in a low-dimensional basis. Sloan et al [11]

use the concept of *pre-computed radiance transfer* to allow for real-time changes in the environment lighting. Snapshots from a couple of representative papers are shown in Figure 3.

5 Measuring Scattering Properties of Participating Media

The appearance of participating media is governed by their optical properties, which must be input to a rendering algorithm to generate realistic images. Even with the most accurate rendering algorithms, the image quality is often limited by the accuracy of these input parameters. Narasimhan et al presented a simple device and technique [10] for robustly estimating the scattering properties of a broad class of participating media such as juices, beverages, sugar/salt crystals, and suspended impurities (ocean water) from a single HDR photograph. They measured the scattering parameters of forty commonly found materials. The results are compiled into a freely available database which can be immediately used by the computer graphics community to render realistic images of arbitrary concentrations of the material with multiple scattering (Figure 4), as well as create realistic images of combinations of the original materials. This technique can be used to design portable devices as well, that can be used for in-situ measurements of impurity levels in natural water bodies (oceans, lakes, rivers) for environmental monitoring.

(a) (b) (c)

Figure 4: **Measuring scattering properties of participating media:** Renderings of a scene with four liquids in their diluted states (b) and their natural high density states (c). The corresponding input HDR images are shown in (a).

Debevec et al presented a technique [7] for capturing time-varying volumetric data of participating media. In their technique, a laser sheet is swept repeatedly through the volume, and the scattered light is imaged using a high-speed camera. Each sweep of the laser provides a near-simultaneous volume of density values. They demonstrated rendered animations under changing viewpoint and illumination, making use of measured values for the scattering phase function and albedo. An example rendering is shown in Figure 5.

6 Inelastic scattering

To simulate inelastic scattering, all frequency changes at higher and lower energy values must be taken into account, based on the spectral quantum efficiency function of the medium. Well-known effects such as

(a) (b)

Figure 5: **Measuring scattering properties of dynamic participating media:**. Measured media can be rendered under a variety of lighting conditions. (a) A captured smoke volume rendered with two spotlights of different colors. (c) A smoke volume rendered with environmental illumination. Images taken from [7].

fluorescence or phosphorescence are due to this phenomenon. This part of the course will explain inelastic scattering and review some of the most relevant works, covering both surface and volume inelastic scattering.

A full solution will be presented in the context of underwater imagery. Simulating the in-water ocean light field is a daunting task. Ocean waters are one of the richest participating media, where light interacts not only with water molecules, but with suspended particles and organic matter as well. The concentration of each constituent greatly affects these interactions, resulting in very different hues. Inelastic scattering events such as fluorescence or Raman scattering imply energy transfers that are usually neglected in the simulations. A bio-optical model of ocean waters is presented in [6], along with a method to obtain the in-water light field based on radiative transfer theory. The bio-optical model of the ocean uses published data from oceanography studies. The method builds on [5], and provides a link between the *inherent optical properties* that define the medium and its *apparent optical properties*, which describe how it looks. Areas of application for this research span from underwater imagery to remote sensing; the resolution method is general enough to be usable in any type of participating medium simulation. Figure 6 shows some results varying the concentration of some of the components of the model: chlorophyll, minerals and detritus and yellow matter.

7 Efficient Rendering of Highly Scattering Materials

Highly scattering, or translucent, materials are all around us. For example, milk, leaves, skin, paper, paint, and marble are all highly scattering materials. These make up the foods and liquids we eat and drink, and the materials that compose everyday objects such as plastics and paper. They make up our environment, and even the various tissues of our own bodies. Translucent materials often have a soft, diffuse appearance when viewed under direct lighting, and sometimes have a "glow" when backlit.

To efficiently render highly scattering materials, the diffusion dipole model, composed of a positive and negative point source, gives a good approximation [8], under the assumption that the material is homogeneous and semi-infinite in depth. The main limitations of the dipole model are its restriction to semi-infinite geometry and homogeneous materials. This is resolved by using arrays of multiple dipoles (a multipole) and convolutions of layer profiles [1]. These extra sources take boundary conditions at the interfaces of thin slabs, and between the boundaries of scattering layers to produce reflectance and transmittance profiles for each layer. Convolving these profiles together allows the rendering of layered materials like leaves, paint,

Figure 6: Resulting pictures varying the chlorophyll concentration C, the minerals and detritus turbidity α_d at 400nm and the CDOM turbidity α_y at 440nm.

and skin (see Figure 7), while these profiles by themselves can be used to render thin materials like paper.

Determining parameters for the above models, however, is a difficult task. Direct acquisition of the properties of translucent materials is time-consuming and expensive, and can even be inaccurate, due to the high orders of light scattering [9]. Instead, parameters can be estimated by fitting to a model, as done in the case of faces [13]. Here, the dipole model allowed the fitting of optical properties and albedo maps for a large database of human faces, and allowed the analysis of facial traits, along with novel facial renderings.

More specific material models give more intuitive and finer controls over appearance. For example, the multipole model provides a basis for a spectral model of human skin's appearance based on skin's chemical and structural composition [2]. Using only four parameters (two types of melanin, hemoglobin, and oiliness) based on real physical properties of skin, this model produces realistic images of many skin types (see Figure 8, top). It allows the intuitive description of appearance through these parameters, and compares well with actual measured reflectance of real skin samples.

Unfortunately, this skin model requires the use of albedo textures to modulate the layered-homogeneous translucent reflectance predicted by the multipole model. Fully controllable spatially varying properties are controllable using a heterogeneous skin model [3]. In addition, using a simple acquisition setup (see Figure 8, middle), the properties of multi-layered skin are recovered through an inverse rendering process. This heterogeneous model allows the synthesis of dynamic changes in skin, and other effects such as inserting artificial pigment (e.g. a tattoo) between skin layers (see Figure 8, bottom).

Figure 7: Renderings of thin and layered materials. In reading order: paper, leaves, skin and paint

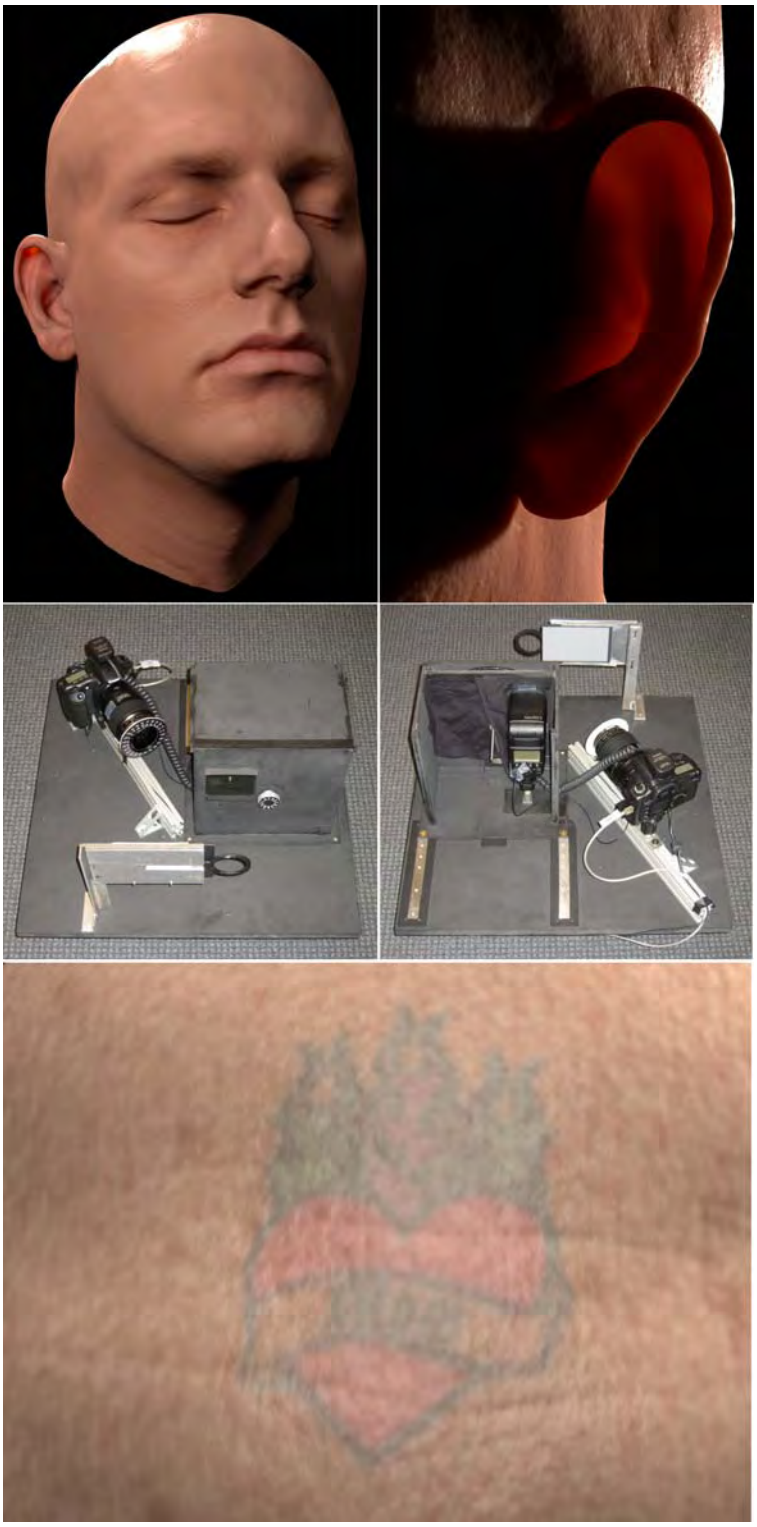

Figure 8: Top: Realistic spectral renderings of human skin. Middle: A device for acquiring the spatially varying spectral properties of skin. Bottom: Inserting a tattoo between skin layers, rendered using a heterogeneous skin model

References

[1] Donner, C., and Jensen, H. W. Light diffusion in multi-layered translucent materials. *24*, 3 (2005), 1032–1039.

[2] Donner, C., and Jensen, H. W. A spectral BSSRDF for shading human skin. In *Rendering Techniques* (2006), pp. 409–417.

[3] Donner, C., Weyrich, T., d'Eon, E., Ramamoorthi, R., and Rusinkiewicz, S. A layered, heterogeneous reflectance model for acquiring and rendering human skin. *27*, 5 (2008), 1–12.

[4] Gupta, M., and Narasimhan, S. G. Legendre fluids: A unified framework for analytic reduced space modeling and rendering of participating media. In *Eurographics/ ACM SIGGRAPH Symposium on Computer Animation (2007)* (August 2007).

[5] Gutierrez, D., Munoz, A., Anson, O., and Seron, F. Non-linear volume photon mapping. *Rendering Techniques (Eurographics Symposium on Rendering)* (2005), 291–300.

[6] Gutierrez, D., Seron, F., Anson, O., and Munoz, A. Visualizing underwater ocean optics. *Computer Graphics Forum (EUROGRAPHICS 2008) 27*, 2 (2008), 547–556.

[7] Hawkins, T., Einarsson, P., and Debevec, P. Acquisition of time-varying participating media. *ACM Transactions on Graphics (SIGGRAPH 2005) 24*, 3 (2005).

[8] Jensen, H. W., Marschner, S. R., Levoy, M., and Hanrahan, P. A practical model for subsurface light transport. In *Proceedings of SIGGRAPH 2001* (2001), pp. 511–518.

[9] Joshi, N., Donner, C., and Jensen, H. W. Noninvasive measurement of scattering anisotropy in turbid materials by nonnormal incident illumination. *31* (2006), 936–938.

[10] Narasimhan, S. G., Gupta, M., Donner, C., Ramamoorthi, R., Nayar, S. K., and Jensen, H. W. Acquiring scattering properties of participating media by dilution. *ACM Transactions on Graphics (SIGGRAPH 2006) 25*, 3 (2006).

[11] Sloan, P.-P., Kautz, J., and Snyder, J. Precomputed radiance transfer for real-time rendering in dynamic, low-frequency lighting environments. *ACM Transactions on Graphics (SIGGRAPH 2002) 21*, 3 (2002).

[12] Sun, B., Ramamoorthi, R., Narasimhan, S. G., and Nayar, S. K. A practical analytic single scattering model for real-time rendering. *ACM Transactions on Graphics (SIGGRAPH 2005)* (August 2005).

[13] Weyrich, T., Matusik, W., Pfister, H., Bickel, B., Donner, C., Tu, C., McAndless, J., Lee, J., Ngan, A., Jensen, H. W., and Gross, M. Analysis of human faces using a measurement-based skin reflectance model. *25* (2006), 1013–1024.

Rendering Participating Media

Wojciech Jarosz
Disney Research, Zürich

SIGGRAPH 2009 Course: Scattering
Thursday, August 6th, 12:45 - 16:30, Room 265-266

Fog

Clouds & Crespucular rays

Aerial (Atmospheric) Perspective

Leonardo da Vinci (1480)

"Thus, if one is to be five times as distant, make it five times bluer."
—*Treatise on Painting*, Leonardo Da Vinci, pp 295, circa 1480.

Nebula

T.A.Rector (NOAO/AURA/NSF) and the Hubble Heritage Team (STScI/AURA/NASA)

Outline

- Theoretical background
- Methods for rendering participating media

Radiance

- The main quantity we are interested in for rendering is radiance:

$$L(\mathbf{x} \rightarrow \vec{\omega}),\ L(\mathbf{x}, \vec{\omega}):\ \text{radiance, or “light”}$$

Participating Media

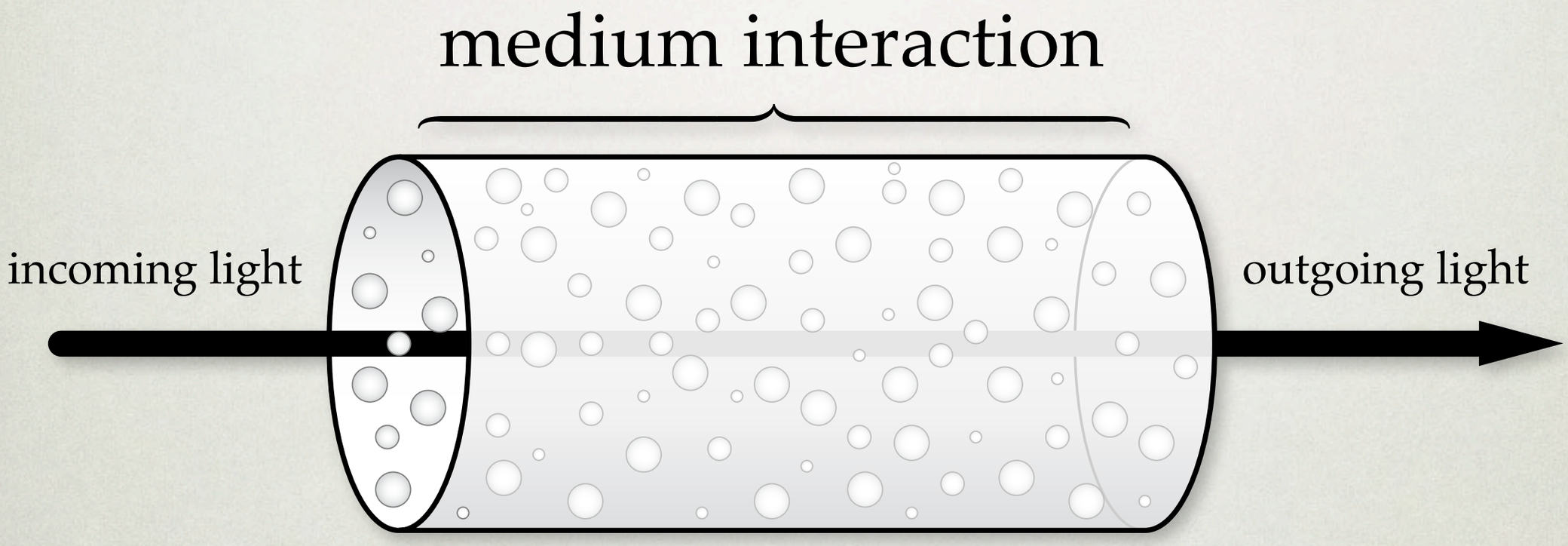

Absorption

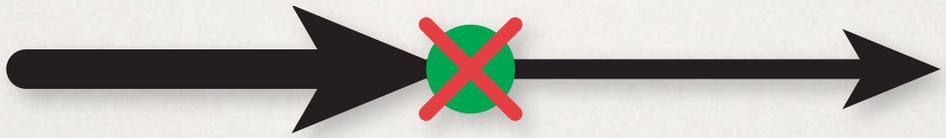

$$(\vec{\omega} \cdot \nabla_a)\, L(\mathbf{x} \rightarrow \vec{\omega}) = -\sigma_a(\mathbf{x})\, L(\mathbf{x} \rightarrow \vec{\omega})$$

$\sigma_a(\mathbf{x})$: absorption coefficient $[1/\mathrm{m}]$

Emission

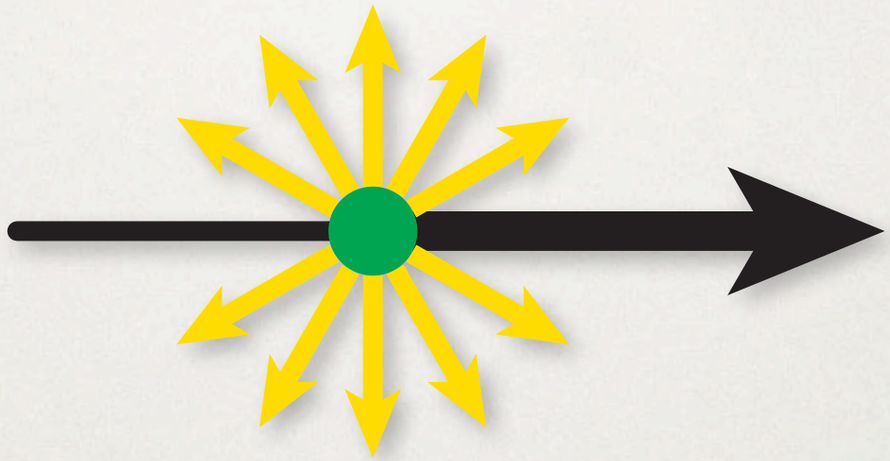

$$(\vec{\omega} \cdot \nabla_e) L(\mathbf{x} \rightarrow \vec{\omega}) = \sigma_a(\mathbf{x}) L_e(\mathbf{x} \rightarrow \vec{\omega})$$

$\sigma_a(\mathbf{x})$: absorption coefficient $[1/\mathrm{m}]$

Out-Scattering

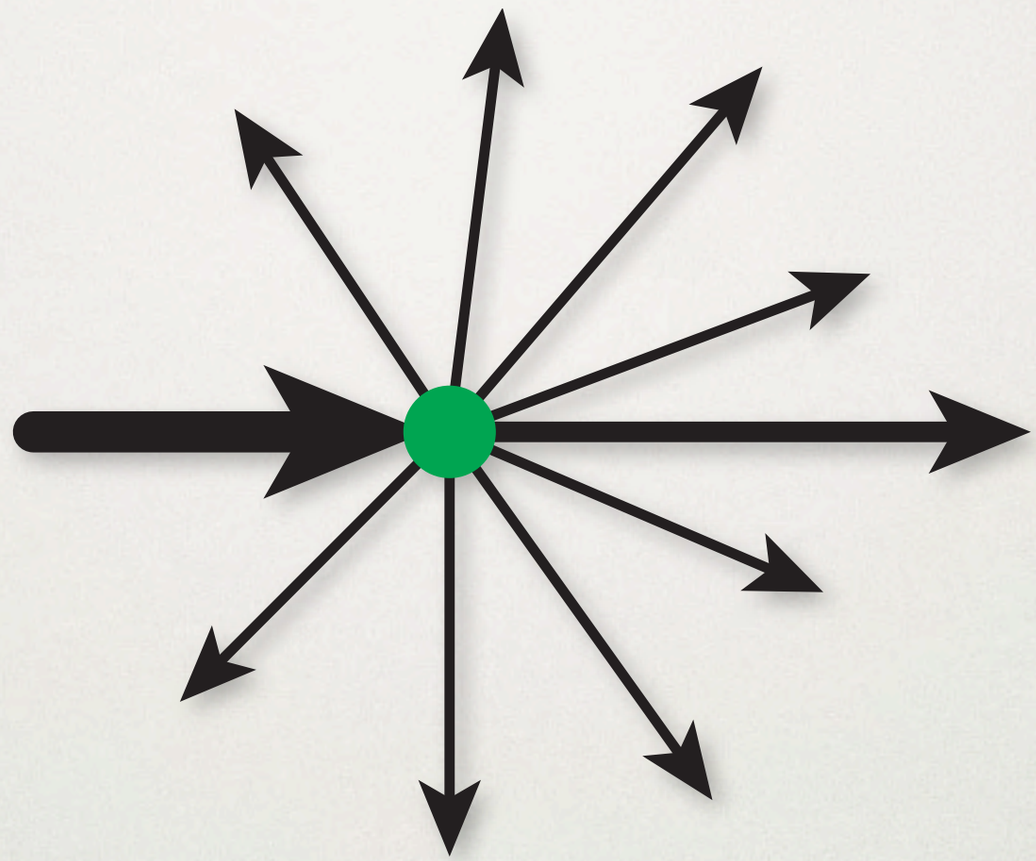

$$(\vec{\omega} \cdot \nabla_o) L(\mathbf{x} \rightarrow \vec{\omega}) = -\sigma_s(\mathbf{x})\, L(\mathbf{x} \rightarrow \vec{\omega})$$

$\sigma_s(\mathbf{x})$: scattering coefficient $[1/\mathrm{m}]$

In-Scattering

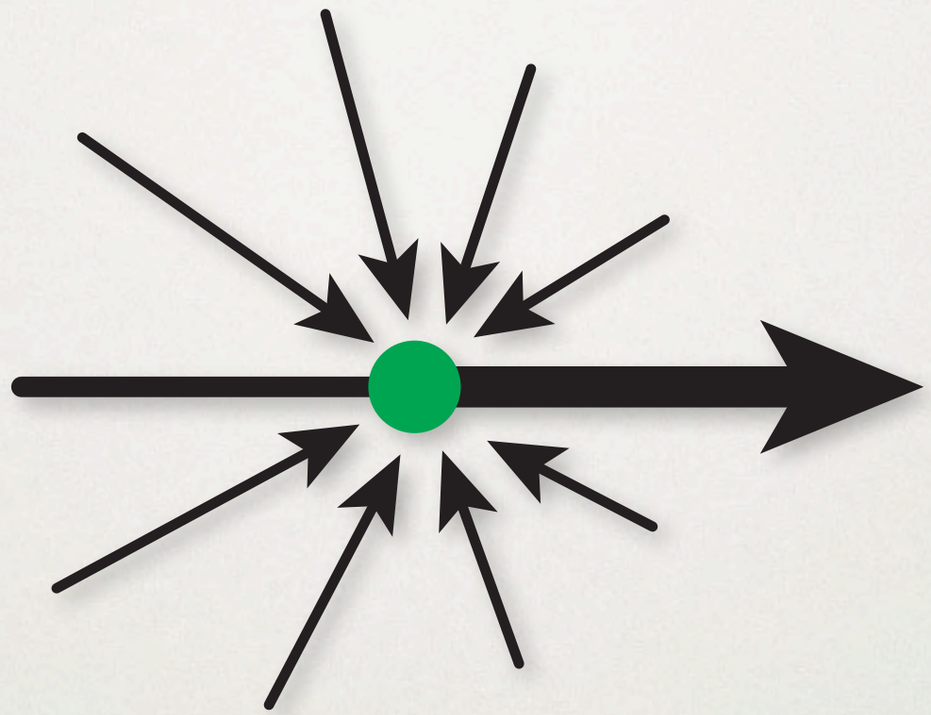

$$(\vec{\omega} \cdot \nabla_i) L(\mathbf{x} \rightarrow \vec{\omega}) = \sigma_s(\mathbf{x})\, L_i(\mathbf{x} \rightarrow \vec{\omega})$$

$\sigma_s(\mathbf{x})$: scattering coefficient $[1/\mathrm{m}]$

In-Scattering

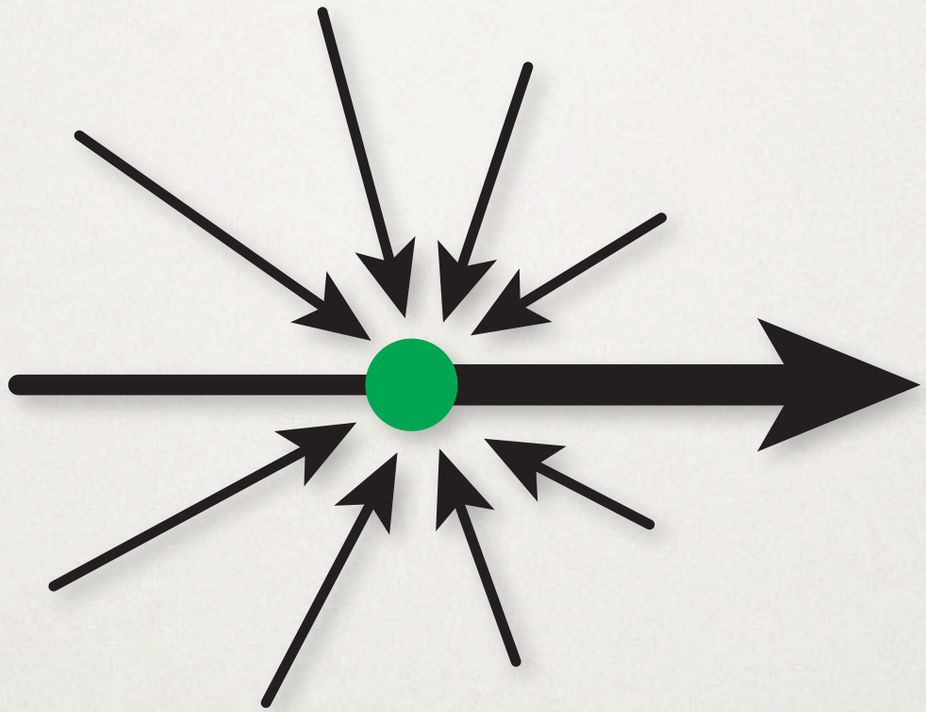

$$(\vec{\omega} \cdot \nabla_i) L(\mathbf{x} \rightarrow \vec{\omega}) = \sigma_s(\mathbf{x})\, L_i(\mathbf{x} \rightarrow \vec{\omega})$$

$$L_i(\mathbf{x} \rightarrow \vec{\omega}) = \int_{\Omega_{4\pi}} p(\mathbf{x}, \vec{\omega}', \vec{\omega})\, L(\mathbf{x} \leftarrow \vec{\omega}')\, d\vec{\omega}'$$

The Phase Function

$$p(\mathbf{x}, \vec{\omega}' \rightarrow \vec{\omega})$$

or

$$p(\mathbf{x}, \vec{\omega}', \vec{\omega})$$

- Local, directional distribution of scattering
- Integrates to 1 over all directions:

$$\int_{\Omega_{4\pi}} p(\mathbf{x}, \vec{\omega}', \vec{\omega})\, d\vec{\omega}' = 1$$

The Phase Function

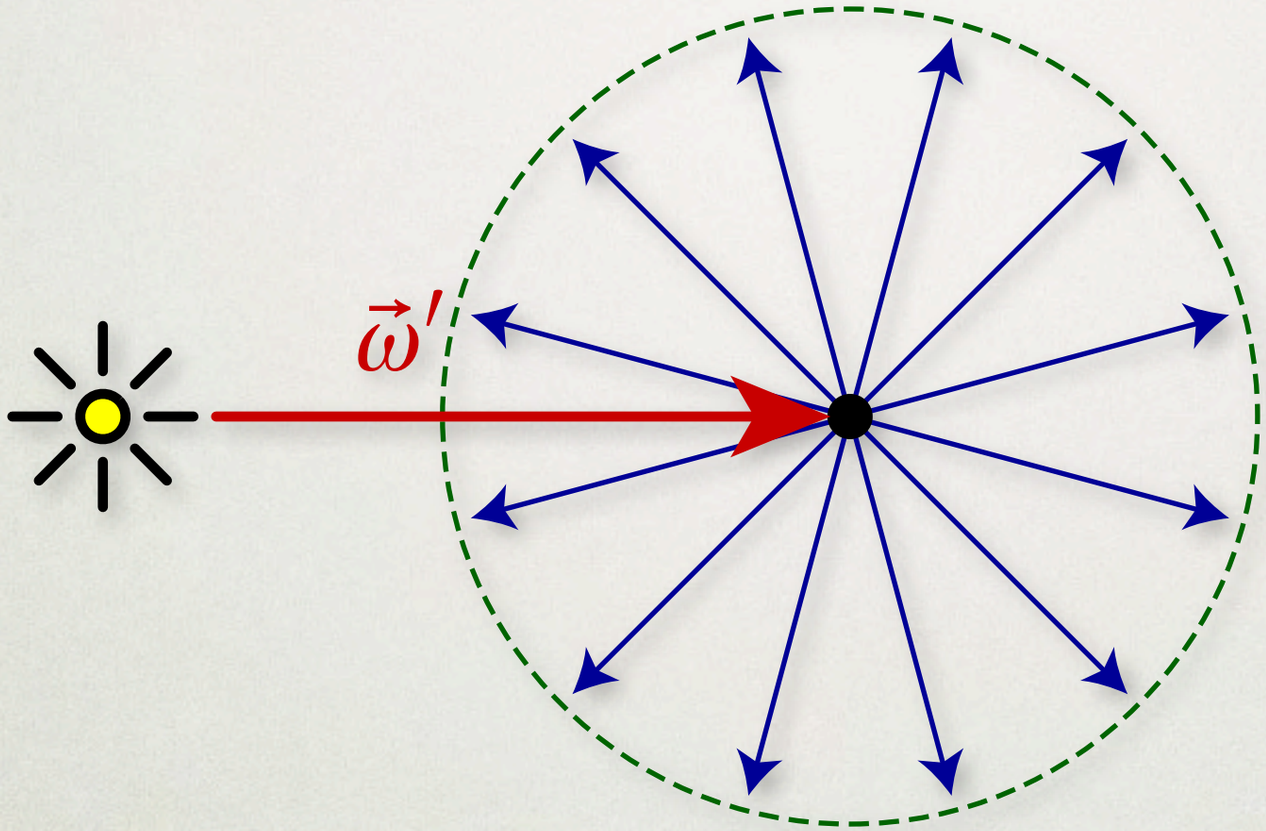

isotropic scattering

$$p(\mathbf{x}, \vec{\omega}', \vec{\omega}) = \frac{1}{4\pi}$$

Anisotropic Scattering

- Anisotropy parameter g (average cosine):

$$g = \int_{\Omega_{4\pi}} p(\mathbf{x}, \vec{\omega}', \vec{\omega}) \cos(\theta) d\vec{\omega}'$$

where,

$$\cos(\theta) = \vec{\omega} \cdot \vec{\omega}'$$

Anisotropic Scattering

- Anisotropy parameter g (average cosine):

$$g = \int_{\Omega_{4\pi}} p(\mathbf{x}, \vec{\omega}', \vec{\omega}) \cos(\theta) d\vec{\omega}'$$

where,

$$\cos(\theta) = \vec{\omega} \cdot \vec{\omega}'$$

- g=0: isotropic scattering

The Phase Function

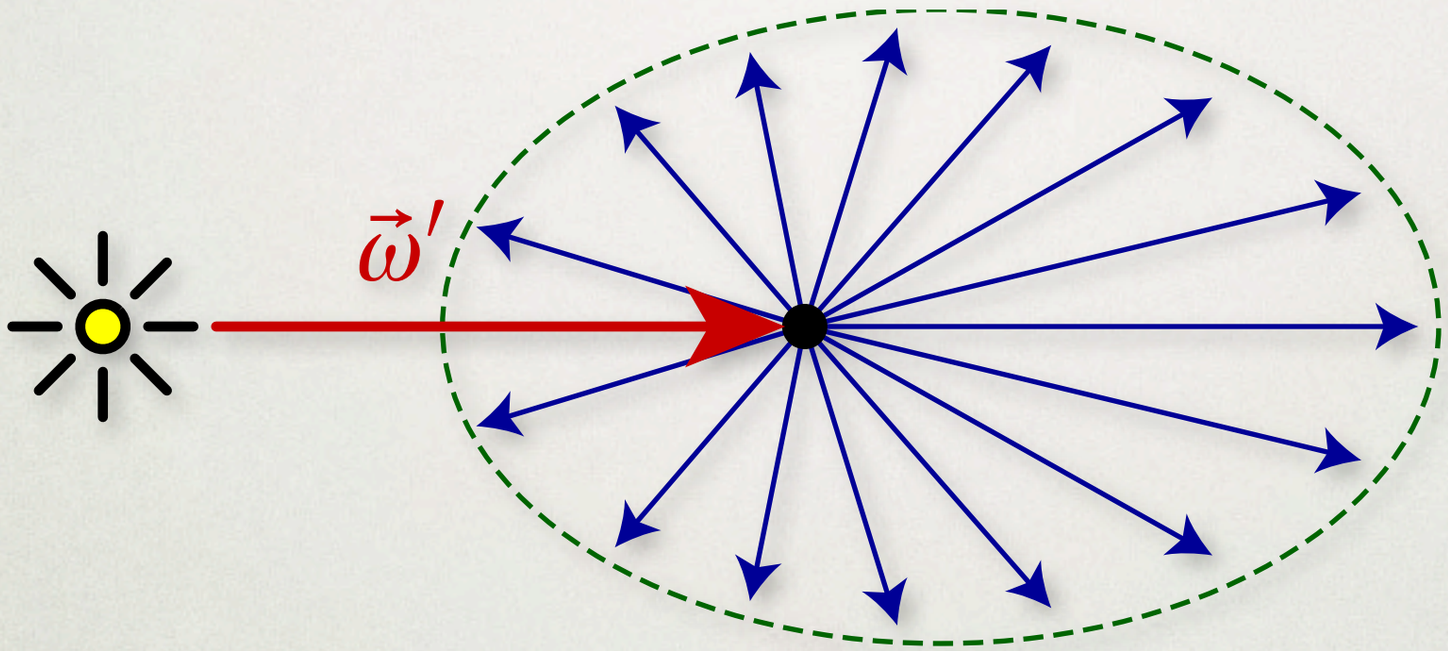

g > 0: forward scattering

The Phase Function

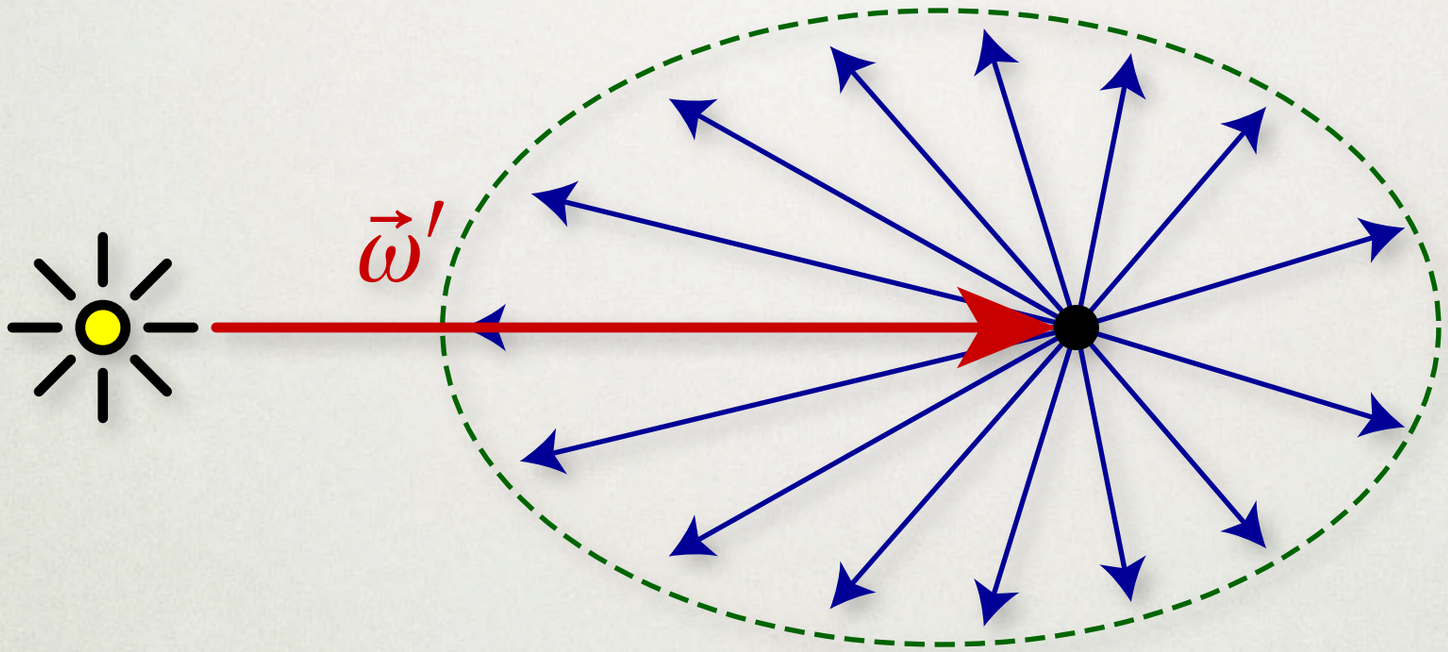

$g < 0$: backward scattering

The 4 Scattering Events

Absorption

$(\vec{\omega} \cdot \nabla_a) L(\mathbf{x} \rightarrow \vec{\omega})$

Emission

$(\vec{\omega} \cdot \nabla_e) L(\mathbf{x} \rightarrow \vec{\omega})$

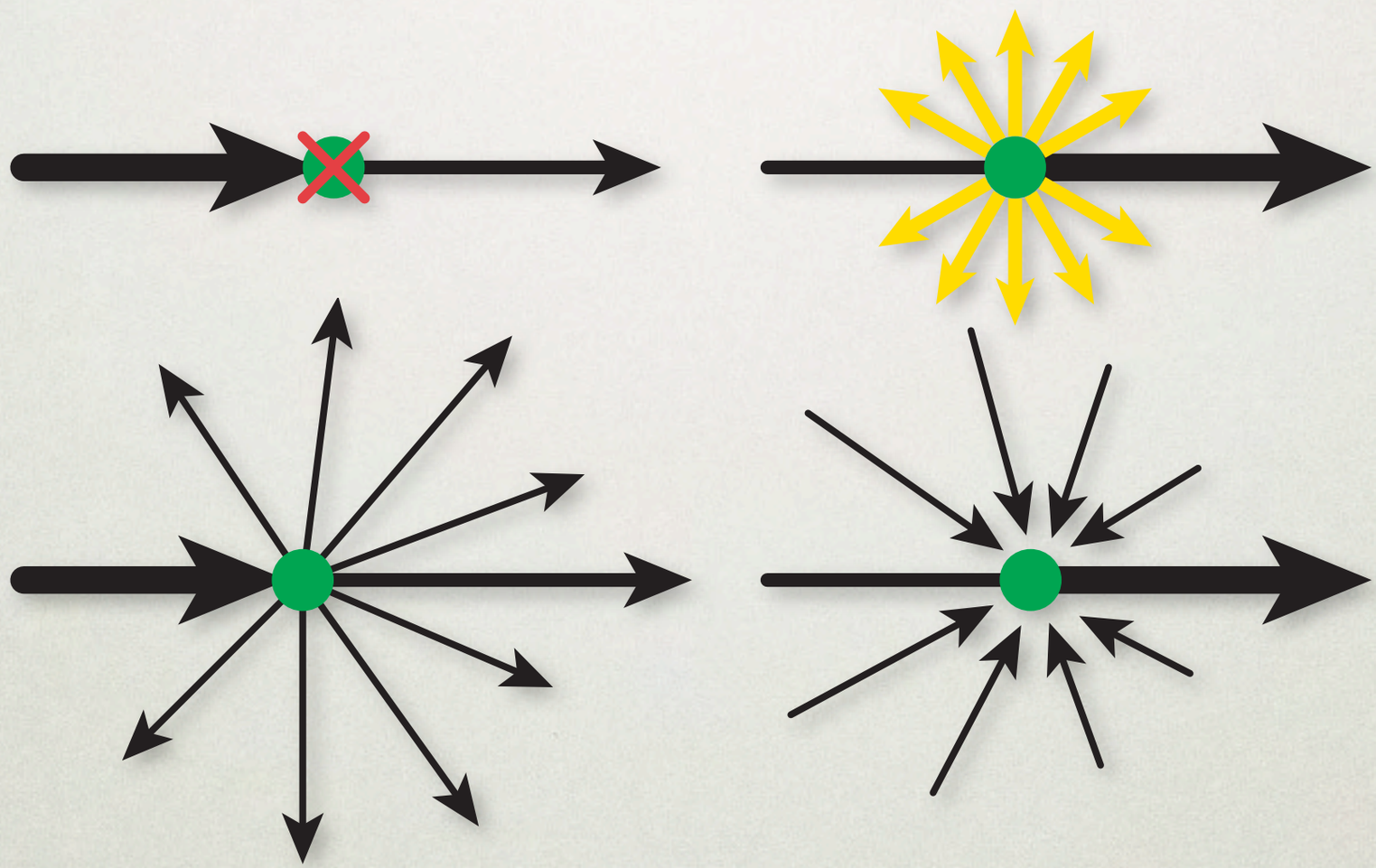

Out-scattering

$(\vec{\omega} \cdot \nabla_o) L(\mathbf{x} \rightarrow \vec{\omega})$

In-scattering

$(\vec{\omega} \cdot \nabla_i) L(\mathbf{x} \rightarrow \vec{\omega})$

Radiative Transport Eqn

$$(\vec{\omega} \cdot \nabla) L(\mathbf{x} \rightarrow \vec{\omega}) = -\underbrace{\sigma_a(\mathbf{x}) L(\mathbf{x} \rightarrow \vec{\omega})}_{\text{absorption}}$$

Radiative Transport Eqn

$$(\vec{\omega} \cdot \nabla) L(\mathbf{x} \rightarrow \vec{\omega}) = -\underbrace{\sigma_a(\mathbf{x}) L(\mathbf{x} \rightarrow \vec{\omega})}_{\text{absorption}} - \underbrace{\sigma_s(\mathbf{x})\, L(\mathbf{x} \rightarrow \vec{\omega})}_{\text{out-scattering}}$$

Radiative Transport Eqn

$$(\vec{\omega} \cdot \nabla) L(\mathbf{x} \rightarrow \vec{\omega}) = -\underbrace{\underbrace{\sigma_a(\mathbf{x}) L(\mathbf{x} \rightarrow \vec{\omega})}_{\text{absorption}} - \underbrace{\sigma_s(\mathbf{x})\, L(\mathbf{x} \rightarrow \vec{\omega})}_{\text{out-scattering}}}_{\text{extinction}}$$

Radiative Transport Eqn

$$(\vec{\omega}\cdot\nabla)L(\mathbf{x}\rightarrow\vec{\omega}) = -\underbrace{\underbrace{\sigma_a(\mathbf{x})L(\mathbf{x}\rightarrow\vec{\omega})}_{\text{absorption}} - \underbrace{\sigma_s(\mathbf{x})\,L(\mathbf{x}\rightarrow\vec{\omega})}_{\text{out-scattering}}}_{\text{extinction}} + \underbrace{\sigma_a(\mathbf{x})\,L_e(\mathbf{x}\rightarrow\vec{\omega})}_{\text{emission}}$$

Radiative Transport Eqn

$$(\vec{\omega}\cdot\nabla)L(\mathbf{x}\rightarrow\vec{\omega}) = -\underbrace{\underbrace{\sigma_a(\mathbf{x})L(\mathbf{x}\rightarrow\vec{\omega})}_{\text{absorption}} - \underbrace{\sigma_s(\mathbf{x})\,L(\mathbf{x}\rightarrow\vec{\omega})}_{\text{out-scattering}}}_{\text{extinction}} + \underbrace{\sigma_a(\mathbf{x})\,L_e(\mathbf{x}\rightarrow\vec{\omega})}_{\text{emission}} + \underbrace{\sigma_s(\mathbf{x})\,L_i(\mathbf{x}\rightarrow\vec{\omega})}_{\text{in-scattering}}$$

Radiative Transport Eqn

$$(\vec{\omega} \cdot \nabla) L(\mathbf{x} \rightarrow \vec{\omega}) = -\underbrace{\sigma_t(\mathbf{x}) L(\mathbf{x} \rightarrow \vec{\omega})}_{\text{extinction}} +$$

$$\underbrace{\sigma_a(\mathbf{x})\, L_e(\mathbf{x} \rightarrow \vec{\omega})}_{\text{emission}} + \underbrace{\sigma_s(\mathbf{x})\, L_i(\mathbf{x} \rightarrow \vec{\omega})}_{\text{in-scattering}}$$

Radiative Transport Eqn

$$(\vec{\omega} \cdot \nabla) L(\mathbf{x} \rightarrow \vec{\omega}) = -\underbrace{\sigma_t(\mathbf{x}) L(\mathbf{x} \rightarrow \vec{\omega})}_{\text{extinction}} +$$

$$\underbrace{\sigma_a(\mathbf{x})\, L_e(\mathbf{x} \rightarrow \vec{\omega})}_{\text{emission}} + \underbrace{\sigma_s(\mathbf{x})\, L_i(\mathbf{x} \rightarrow \vec{\omega})}_{\text{in-scattering}}$$

$$\sigma_t(\mathbf{x}) = \sigma_a(\mathbf{x}) + \sigma_s(\mathbf{x})$$

extinction coefficient

Volume Rendering Eqn

$$L(\mathbf{x} \leftarrow \vec{\omega}) = \underbrace{T_r(\mathbf{x} \leftrightarrow \mathbf{x}_s)\, L(\mathbf{x}_s \rightarrow -\vec{\omega})}_{\text{reduced surface radiance}} +$$

$$\underbrace{\int_0^s T_r(\mathbf{x} \leftrightarrow \mathbf{x}_t)\, \sigma_a(\mathbf{x})\, L_e(\mathbf{x} \rightarrow -\vec{\omega})\, dt}_{\text{accumulated emitted radiance}} +$$

$$\underbrace{\int_0^s T_r(\mathbf{x} \leftrightarrow \mathbf{x}_t)\, \sigma_s(\mathbf{x}_t)\, L_i(\mathbf{x}_t \rightarrow -\vec{\omega})\, dt}_{\text{accumulated in-scattered radiance}}$$

Volume Rendering Eqn

$$L(\mathbf{x} \leftarrow \vec{\omega}) = \underbrace{T_r(\mathbf{x} \leftrightarrow \mathbf{x}_s)\, L(\mathbf{x}_s \rightarrow -\vec{\omega})}_{\text{reduced surface radiance}} +$$

$$\underbrace{\int_0^s T_r(\mathbf{x} \leftrightarrow \mathbf{x}_t)\, \sigma_s(\mathbf{x}_t)\, L_i(\mathbf{x}_t \rightarrow -\vec{\omega})\, dt}_{\text{accumulated in-scattered radiance}}$$

Volume Rendering Eqn

$$L(\mathbf{x} \leftarrow \vec{\omega}) = \underbrace{T_r(\mathbf{x} \leftrightarrow \mathbf{x}_s)\, L(\mathbf{x}_s \rightarrow -\vec{\omega})}_{\text{reduced surface radiance}} + \underbrace{\int_0^s T_r(\mathbf{x} \leftrightarrow \mathbf{x}_t)\, \sigma_s(\mathbf{x}_t)\, L_i(\mathbf{x}_t \rightarrow -\vec{\omega})\, dt}_{\text{accumulated in-scattered radiance}}$$

Scene with Medium

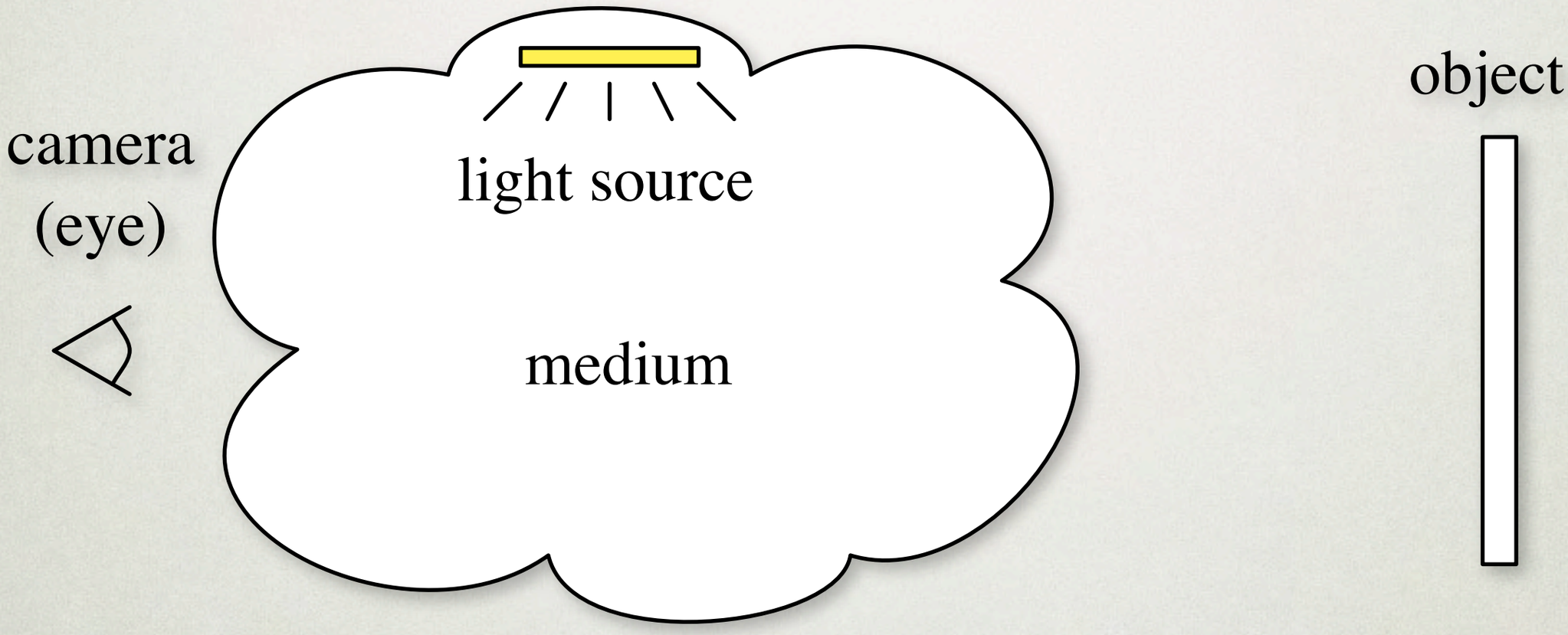

Volume Rendering Eqn

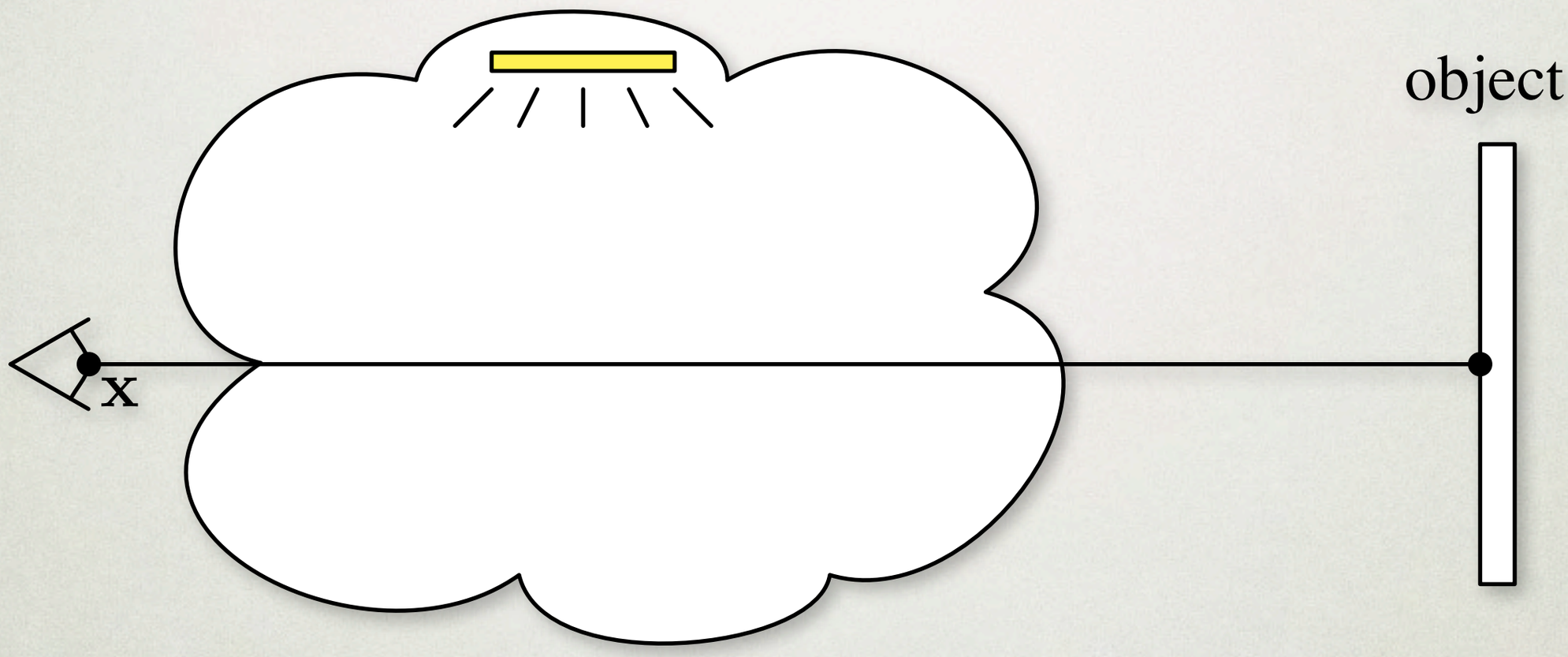

$$L(\mathbf{x}, \vec{\omega}) = \int_0^s T_r(\mathbf{x} \leftrightarrow \mathbf{x}_t)\sigma_s(\mathbf{x}_t)L_i(\mathbf{x}_t, \vec{\omega})\ dt + T_r(\mathbf{x} \leftrightarrow \mathbf{x}_s)L(\mathbf{x}_s, \vec{\omega})$$

Volume Rendering Eqn

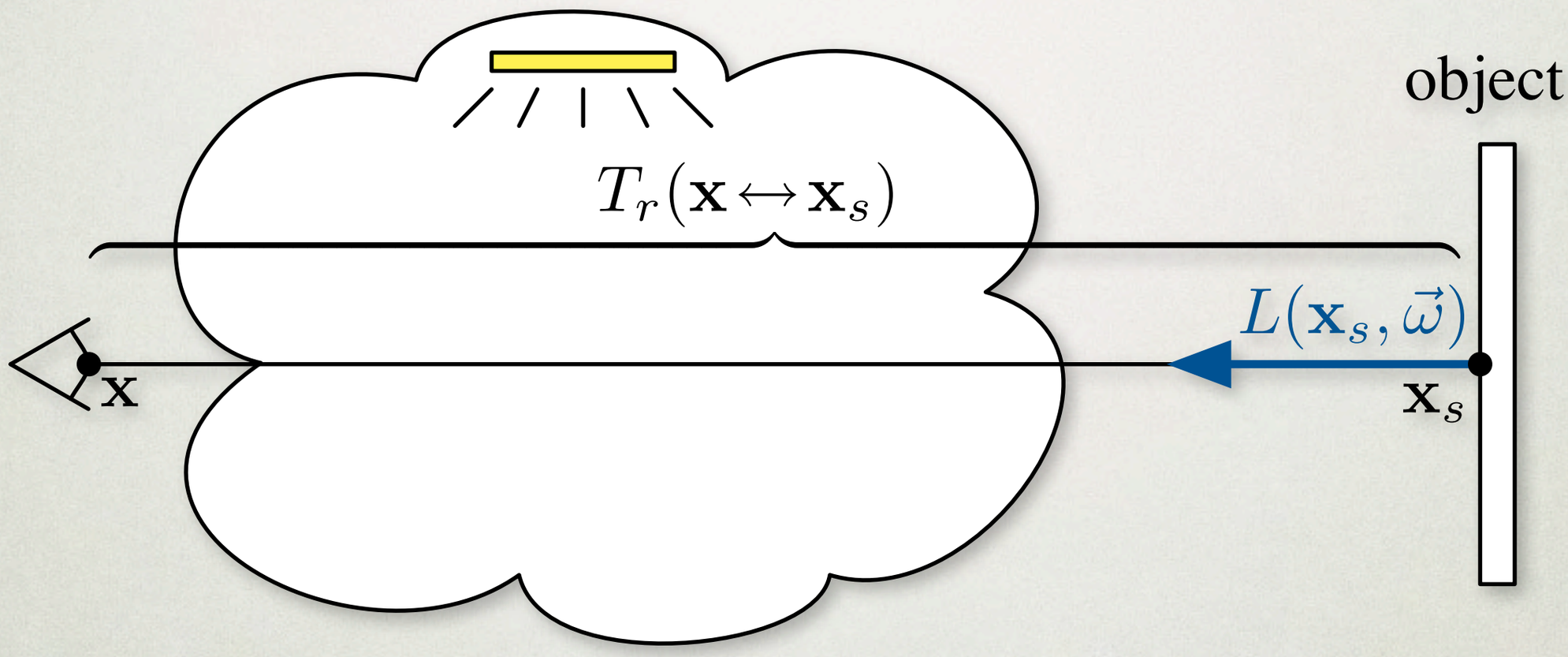

$$L(\mathbf{x}, \vec{\omega}) = \int_0^s T_r(\mathbf{x} \leftrightarrow \mathbf{x}_t)\sigma_s(\mathbf{x}_t)L_i(\mathbf{x}_t, \vec{\omega})\, dt + \boxed{T_r(\mathbf{x} \leftrightarrow \mathbf{x}_s)L(\mathbf{x}_s, \vec{\omega})}$$

Transmittance: $T_r(\mathbf{x} \leftrightarrow \mathbf{x}_s) = \exp\left(-\int_0^s \sigma_t(\mathbf{x} + t\vec{\omega})\, dt\right)$

Volume Rendering Eqn

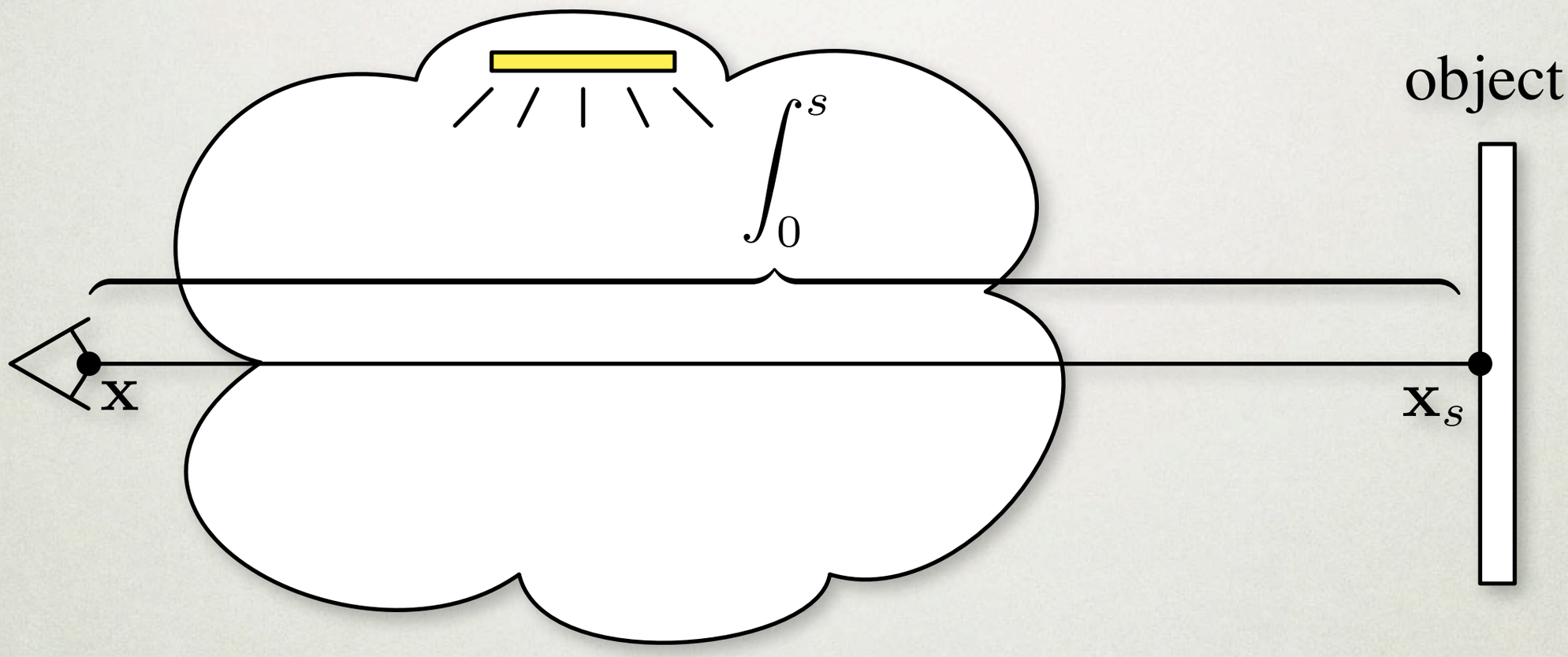

$$L(\mathbf{x}, \vec{\omega}) = \boxed{\int_0^s T_r(\mathbf{x} \leftrightarrow \mathbf{x}_t)\sigma_s(\mathbf{x}_t)L_i(\mathbf{x}_t, \vec{\omega})\ dt} + T_r(\mathbf{x} \leftrightarrow \mathbf{x}_s)L(\mathbf{x}_s, \vec{\omega})$$

Volume Rendering Eqn

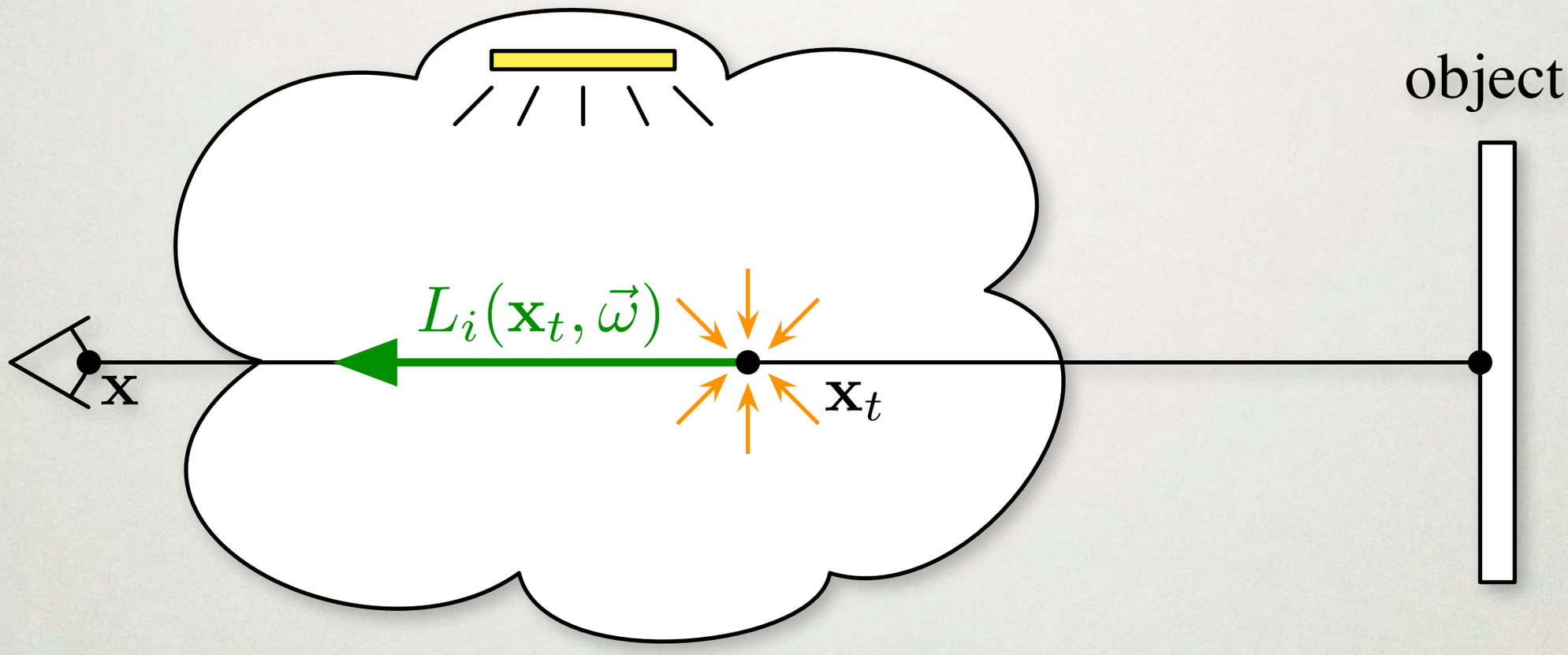

$$L(\mathbf{x}, \vec{\omega}) = \int_0^s T_r(\mathbf{x} \leftrightarrow \mathbf{x}_t)\sigma_s(\mathbf{x}_t)\boxed{L_i(\mathbf{x}_t, \vec{\omega})}\,dt + T_r(\mathbf{x} \leftrightarrow \mathbf{x}_s)L(\mathbf{x}_s, \vec{\omega})$$

$$L_i(\mathbf{x}_t, \vec{\omega}) = \int_{\Omega_{4\pi}} p(\mathbf{x}_t, \vec{\omega}_t, \vec{\omega})L(\mathbf{x}_t, \vec{\omega}_t)\ d\omega_t$$

Volume Rendering Eqn

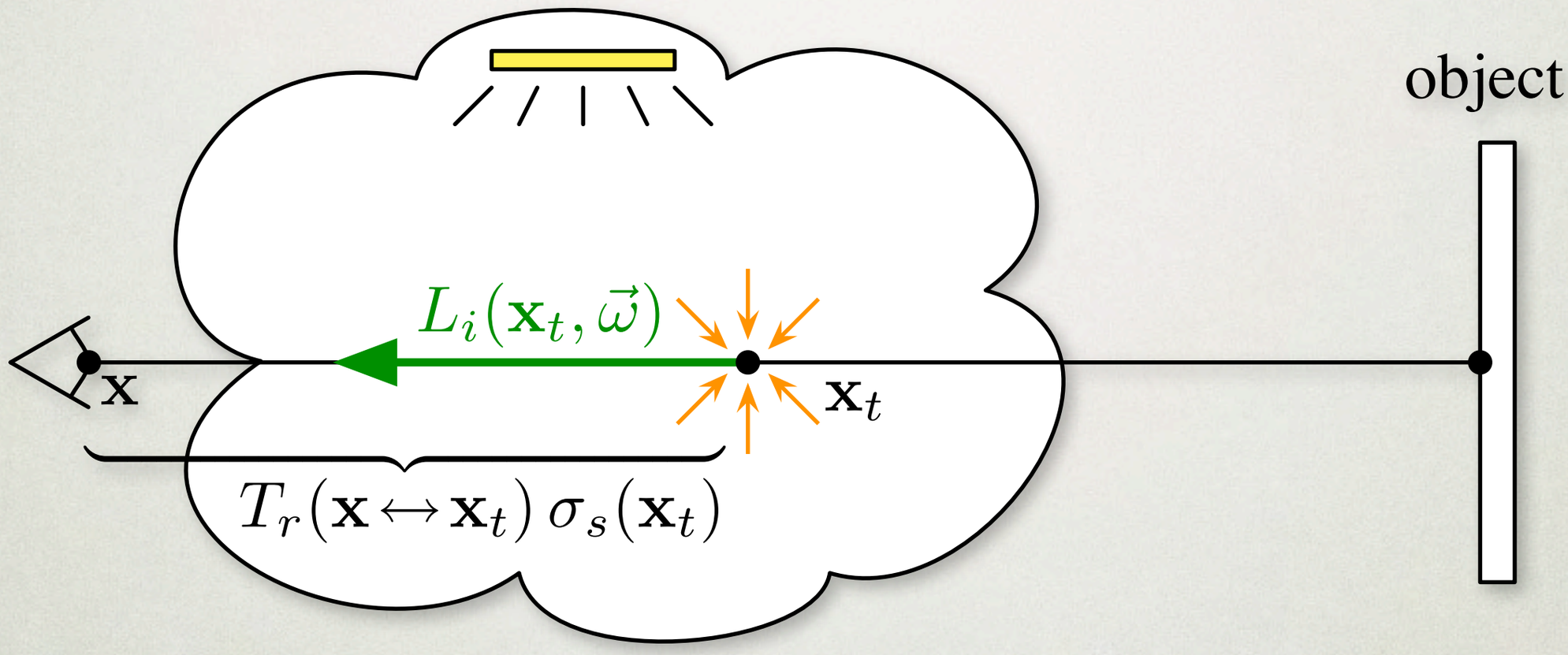

$$L(\mathbf{x}, \vec{\omega}) = \int_0^s \boxed{T_r(\mathbf{x} \leftrightarrow \mathbf{x}_t)\sigma_s(\mathbf{x}_t)} L_i(\mathbf{x}_t, \vec{\omega})\ dt + T_r(\mathbf{x} \leftrightarrow \mathbf{x}_s) L(\mathbf{x}_s, \vec{\omega})$$

Media Properties

$\sigma_s(\mathbf{x})$: scattering coefficient $[1/m]$

$\sigma_a(\mathbf{x})$: absorption coefficient $[1/m]$

$p(\mathbf{x}, \vec{\omega}', \vec{\omega})$: phase function $[1/sr]$

Media Properties

$\sigma_s(\mathbf{x})$: scattering coefficient $[1/m]$

$\sigma_a(\mathbf{x})$: absorption coefficient $[1/m]$

$p(\mathbf{x}, \vec{\omega}', \vec{\omega})$: phase function $[1/sr]$

Homogeneous
spatially constant

Heterogeneous
spatially varying

Media Properties

$\sigma_s(\mathbf{x})$: scattering coefficient $[1/m]$

$\sigma_a(\mathbf{x})$: absorption coefficient $[1/m]$

$p(\mathbf{x}, \vec{\omega}', \vec{\omega})$: phase function $[1/sr]$

Homogeneous
spatially constant

Heterogeneous
spatially varying

Isotropic
directionally constant

Anisotropic
directionally varying

Derived Properties

$\sigma_t(\mathbf{x}) = \sigma_s(\mathbf{x}) + \sigma_a(\mathbf{x})$: extinction coefficient $[1/m]$

Derived Properties

$\sigma_t(\mathbf{x}) = \sigma_s(\mathbf{x}) + \sigma_a(\mathbf{x})$: extinction coefficient $[1/m]$

$\frac{1}{\sigma_t}$: mean-free path $[m]$

Derived Properties

$\sigma_t(\mathbf{x}) = \sigma_s(\mathbf{x}) + \sigma_a(\mathbf{x})$: extinction coefficient $[1/m]$

$\frac{1}{\sigma_t}$: mean-free path $[m]$

$\frac{\sigma_s}{\sigma_t}$: scattering albedo $[none]$

Derived Properties

$\sigma_t(\mathbf{x}) = \sigma_s(\mathbf{x}) + \sigma_a(\mathbf{x})$: extinction coefficient $[1/m]$

$\frac{1}{\sigma_t}$: mean-free path $[m]$

$\frac{\sigma_s}{\sigma_t}$: scattering albedo $[none]$

$T_r(\mathbf{x}' \leftrightarrow \mathbf{x})$: transmittance $[none]$

$$\exp\left(-\int_0^d \sigma_t(\mathbf{x} + t\vec{\omega})\, dt\right)$$

Outline

- Theoretical background
- Methods for rendering participating media

Available Techniques

Rendering Participating Media

- "Ray Tracing Volume Densities." Kajiya and Herzen. 1984.
- "The Rendering Equation." Kajiya. 1986.
- "The Zonal Method for Calculating Light Intensities in the Presence of a Participating Medium." Rushmeier and Torrance. 1987.
- "Efficient Light Propagation for Multiple Anisotropic Volume Scattering." Max. 1994.
- "Multiple Scattering as a Diffusion Process." Stam. 1995.
- "Rendering Participating Media with Bidirectional Path Tracing." Lafortune and Willems. 1996.
- "Efficient Simulation of Light Transport in Scenes with Participating Media using Photon Maps." Jensen and Christensen. 1998.
- "Metropolis Light Transport for Participating Media." Pauly et al. 2000.
- "Practical Rendering of Multiple Scattering Effects in Participating Media." Premože et al. 2004.
- "Multidimensional Lightcuts." Walter et al. 2006.
- "Radiance Caching for Participating Media." Jarosz et al. 2008.
- "The Beam Radiance Estimate for Volumetric Photon Mapping." Jarosz et al. 2008.

Available Techniques

Rendering Participating Media

- Path tracing
- Ray marching
- Metropolis
- Finite element methods (Radiosity)
- Diffusion
- Interpolation methods (Radiance caching)
- Density estimation methods (Photon mapping)
- VPL methods (Lightcut, Instant radiosity)

Available Techniques

Rendering Participating Media

- Path tracing
- Ray marching
- Metropolis
- Finite element methods (Radiosity)
- Diffusion
- Interpolation methods (Radiance caching)
- Density estimation methods (Photon mapping)
- VPL methods (Lightcut, Instant radiosity)

Available Techniques

Rendering Participating Media

- Path tracing
- Ray marching
- Metropolis
- Finite element methods (Radiosity)
- Diffusion
- Interpolation methods (Radiance caching)
- Density estimation methods (Photon mapping)
- VPL methods (Lightcut, Instant radiosity)

Available Techniques

Rendering Participating Media

- Path tracing
- Ray marching
- Metropolis
- Finite element methods (Radiosity)
- Diffusion
- Interpolation methods (Radiance caching)
- Density estimation methods (Photon mapping)
- VPL methods (Lightcut, Instant radiosity)

Ray Marching

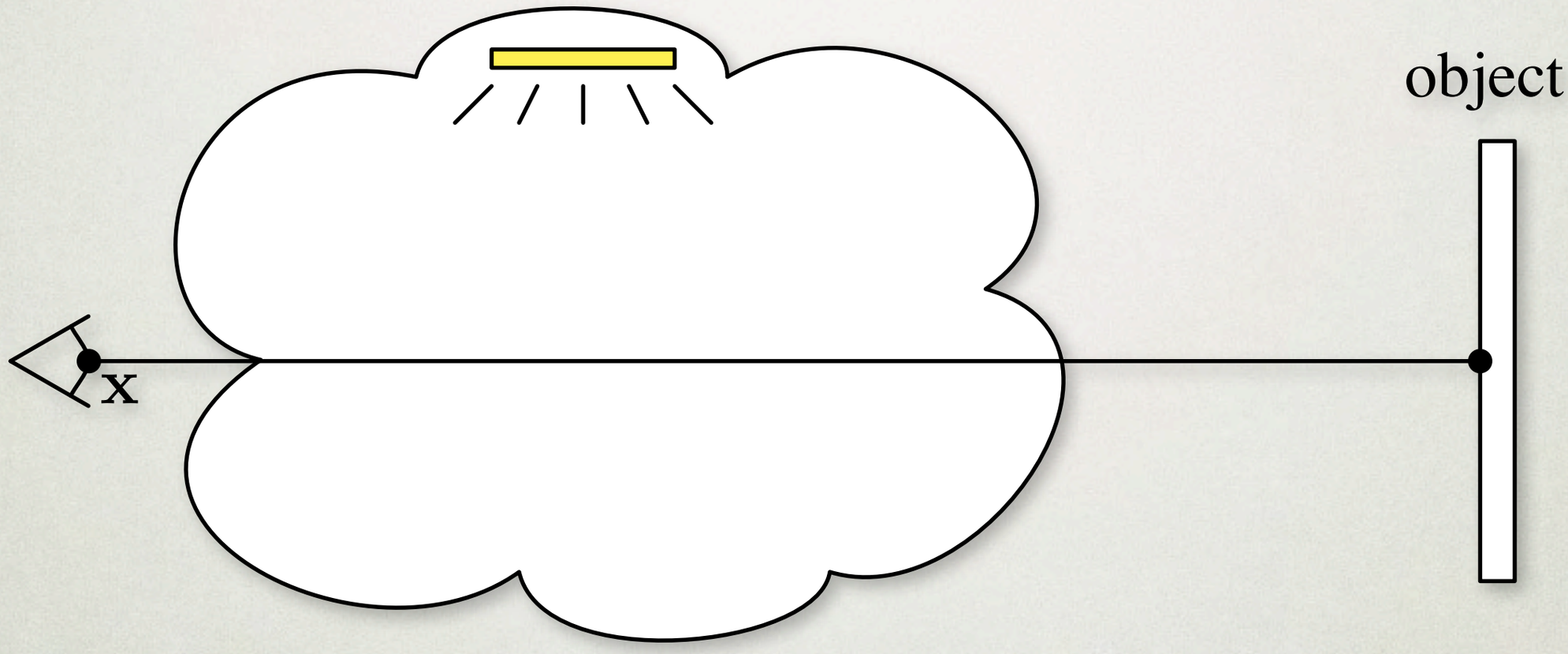

$$L(\mathbf{x}, \vec{\omega}) = \int_0^s T_r(\mathbf{x} \leftrightarrow \mathbf{x}_t)\sigma_s(\mathbf{x}_t)L_i(\mathbf{x}_t, \vec{\omega})\ dt + T_r(\mathbf{x} \leftrightarrow \mathbf{x}_s)L(\mathbf{x}_s, \vec{\omega})$$

Ray Marching

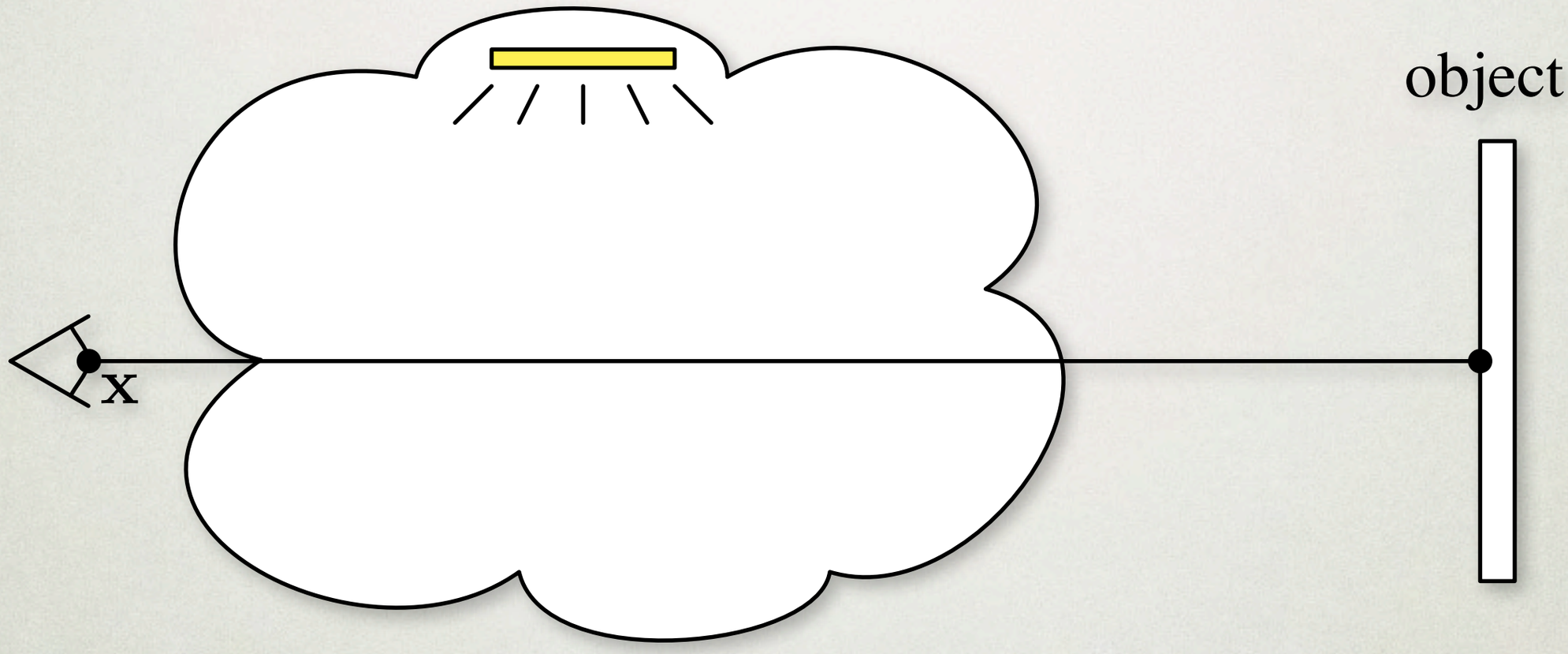

$$L(\mathbf{x}, \vec{\omega}) = \boxed{\int_0^s} T_r(\mathbf{x} \leftrightarrow \mathbf{x}_t)\sigma_s(\mathbf{x}_t)L_i(\mathbf{x}_t, \vec{\omega})\boxed{dt} + T_r(\mathbf{x} \leftrightarrow \mathbf{x}_s)L(\mathbf{x}_s, \vec{\omega})$$

- approximate / compute using Riemann sum

Ray Marching

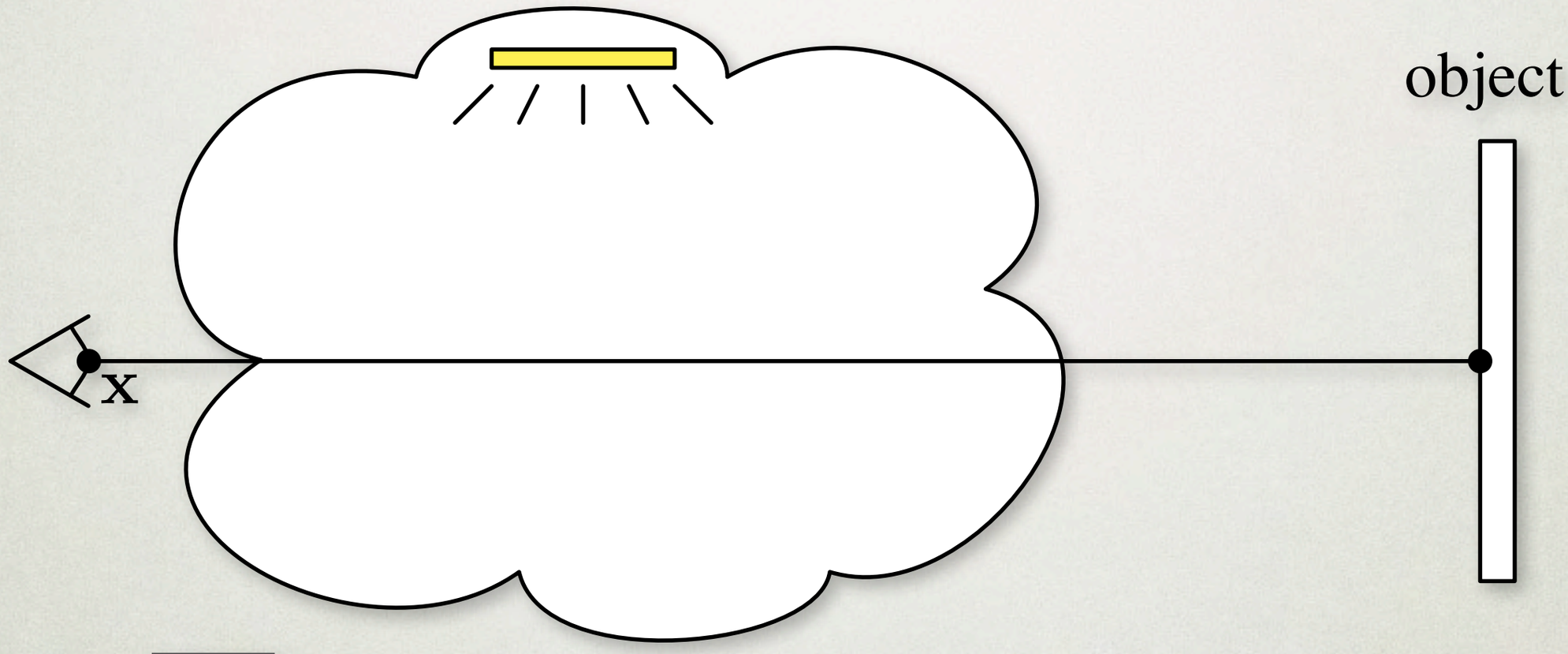

$$L(\mathbf{x}, \vec{\omega}) \approx \boxed{\sum_{t=0}^{S-1}} T_r(\mathbf{x} \leftrightarrow \mathbf{x}_t)\sigma_s(\mathbf{x}_t)L_i(\mathbf{x}_t, \vec{\omega})\boxed{\Delta_t} + T_r(\mathbf{x} \leftrightarrow \mathbf{x}_s)L(\mathbf{x}_s, \vec{\omega})$$

Ray Marching

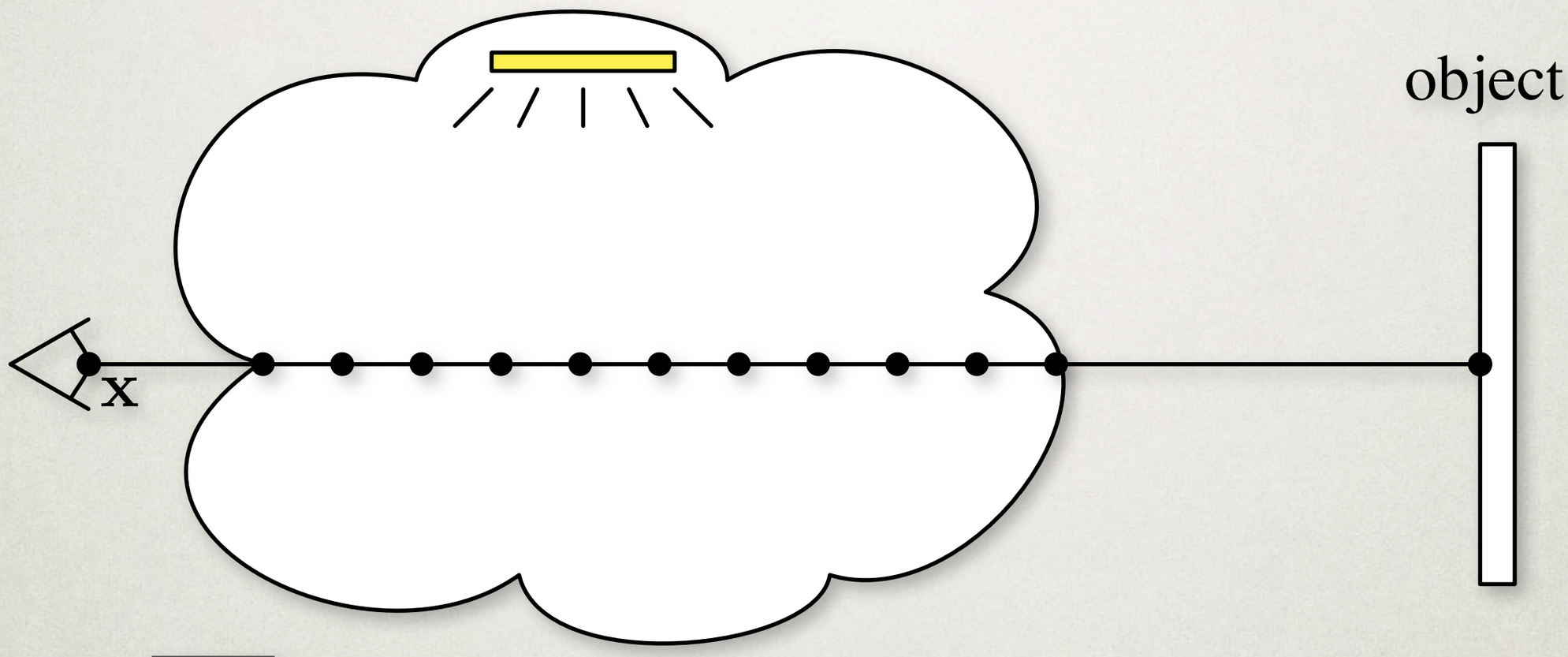

$$L(\mathbf{x},\vec{\omega}) \approx \boxed{\sum_{t=0}^{S-1}} T_r(\mathbf{x}\leftrightarrow\mathbf{x}_t)\sigma_s(\mathbf{x}_t)L_i(\mathbf{x}_t,\vec{\omega})\boxed{\Delta_t} + T_r(\mathbf{x}\leftrightarrow\mathbf{x}_s)L(\mathbf{x}_s,\vec{\omega})$$

Computing T_R

- In general:

$$T_r(\mathbf{x}' \leftrightarrow \mathbf{x}) = \exp\left(-\int_0^d \sigma_t(\mathbf{x} + t\vec{\omega})\, dt\right)$$

- In homogeneous medium:
  - $T_r(\mathbf{x}' \leftrightarrow \mathbf{x}) = e^{\|\mathbf{x}' - \mathbf{x}\| \sigma_t}$

Ray Marching (Homogeneous Media)

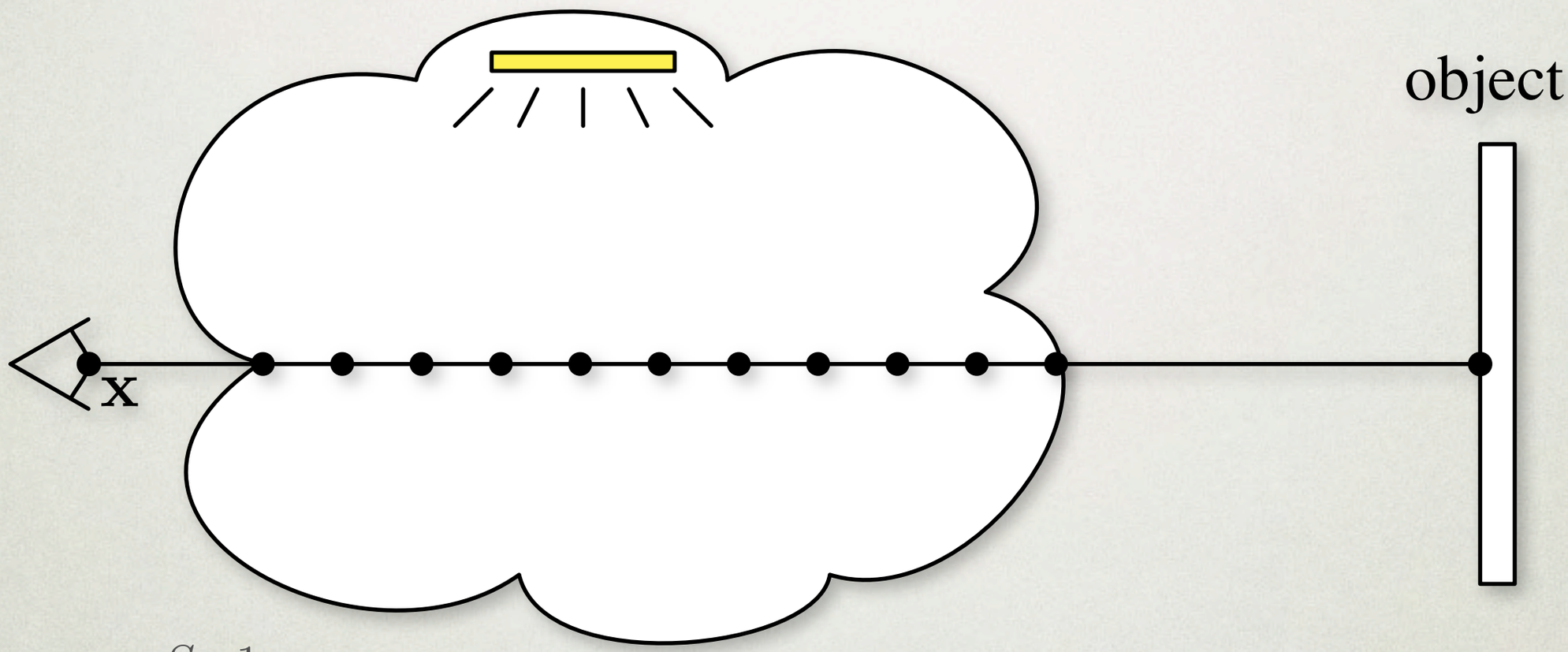

$$L(\mathbf{x}, \vec{\omega}) \approx \sum_{t=0}^{S-1} T_r(\mathbf{x} \leftrightarrow \mathbf{x}_t)\sigma_s(\mathbf{x}_t)L_i(\mathbf{x}_t, \vec{\omega})\Delta_t + T_r(\mathbf{x} \leftrightarrow \mathbf{x}_s)L(\mathbf{x}_s, \vec{\omega})$$

Ray Marching (Homogeneous Media)

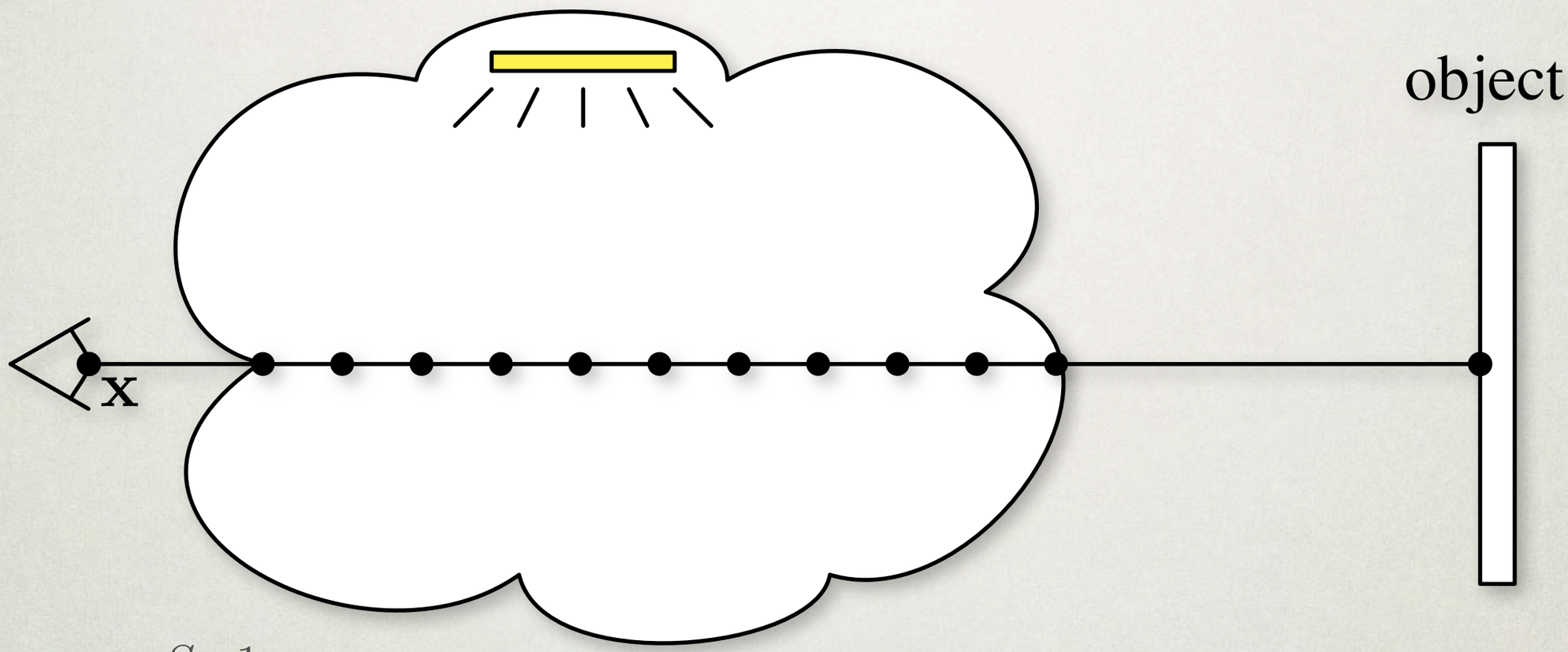

$$L(\mathbf{x},\vec{\omega}) \approx \sum_{t=0}^{S-1} T_r(\mathbf{x} \leftrightarrow \mathbf{x}_t)\sigma_s(\mathbf{x}_t)L_i(\mathbf{x}_t,\vec{\omega})\Delta_t + T_r(\mathbf{x} \leftrightarrow \mathbf{x}_s)L(\mathbf{x}_s,\vec{\omega})$$

$$\downarrow$$

$$L(\mathbf{x},\vec{\omega}) \approx \sum_{t=0}^{S-1} e^{\|\mathbf{x}_t-\mathbf{x}\|\sigma_t}\sigma_s L_i(\mathbf{x}_t,\vec{\omega})\Delta_t + e^{\|\mathbf{x}_s-\mathbf{x}\|\sigma_t}L(\mathbf{x}_s,\vec{\omega})$$

Computing T_R

- In general, if x_1, x_2 and x_3 are collinear,
  - then: $T_r(\mathbf{x}_1 \leftrightarrow \mathbf{x}_3) = T_r(\mathbf{x}_1 \leftrightarrow \mathbf{x}_2)\, T_r(\mathbf{x}_2 \leftrightarrow \mathbf{x}_3)$

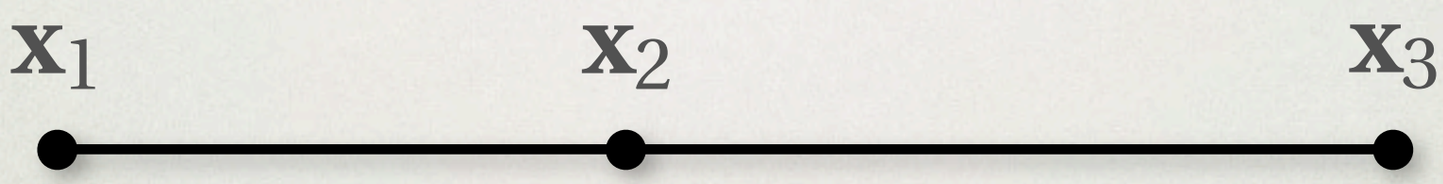

Computing T_R

- In general, if x_1, x_2 and x_3 are collinear,
  - then: $T_r(\mathbf{x}_1 \leftrightarrow \mathbf{x}_3) = T_r(\mathbf{x}_1 \leftrightarrow \mathbf{x}_2)\, T_r(\mathbf{x}_2 \leftrightarrow \mathbf{x}_3)$

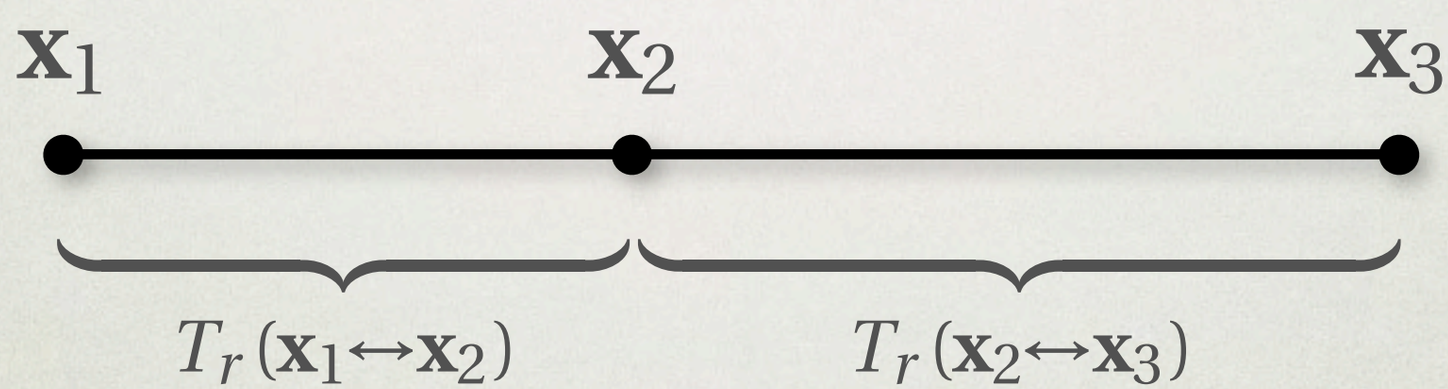

Computing T_R

- In general, if x_1, x_2 and x_3 are collinear,
  - then: $T_r(\mathbf{x}_1 \leftrightarrow \mathbf{x}_3) = T_r(\mathbf{x}_1 \leftrightarrow \mathbf{x}_2)\, T_r(\mathbf{x}_2 \leftrightarrow \mathbf{x}_3)$

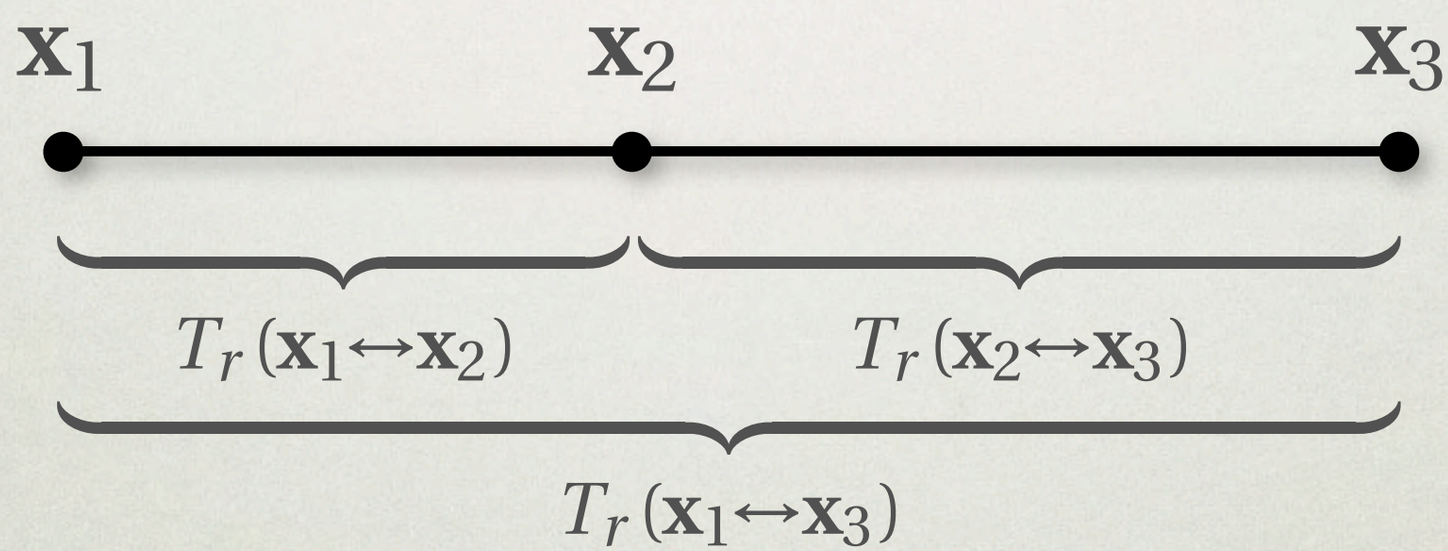

Ray Marching

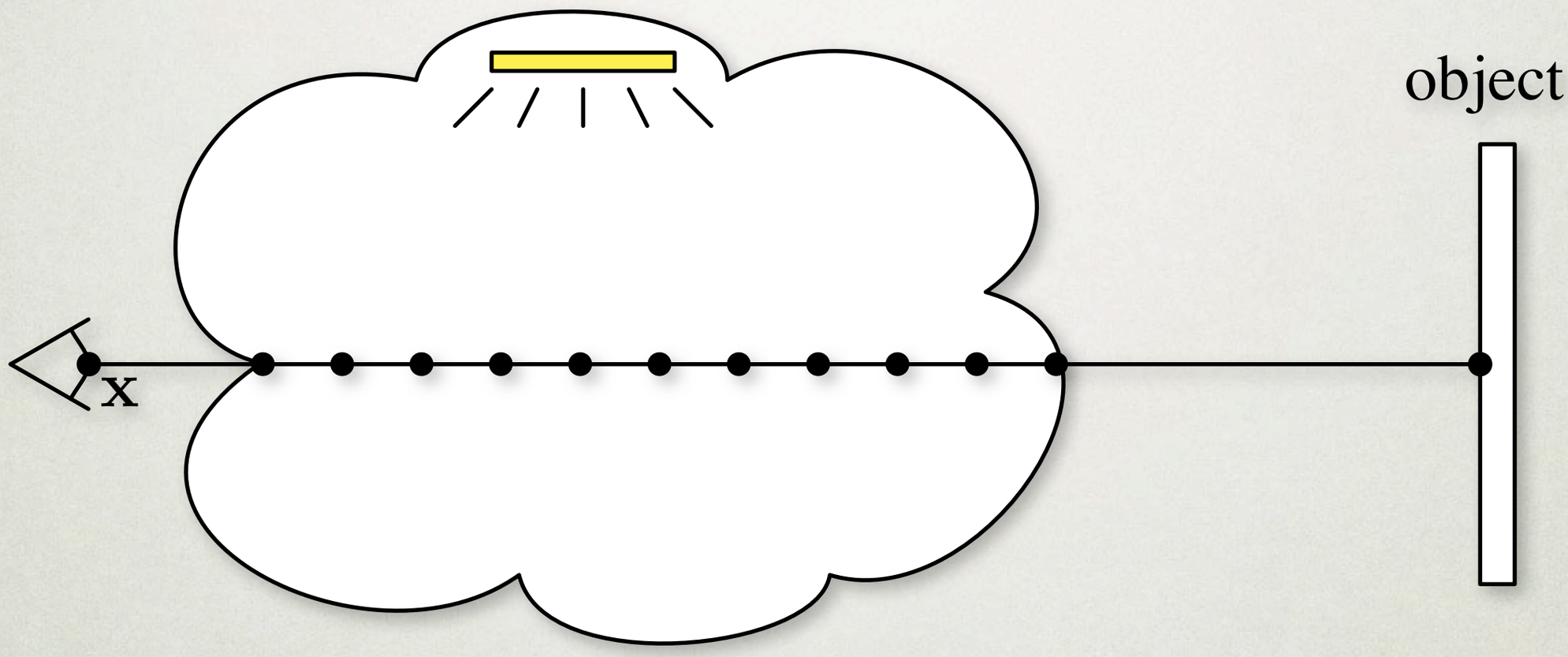

$$L(\mathbf{x}, \vec{\omega}) \approx \sum_{t=0}^{S-1} T_r(\mathbf{x} \leftrightarrow \mathbf{x}_t)\sigma_s(\mathbf{x}_t)L_i(\mathbf{x}_t, \vec{\omega})\Delta_t + T_r(\mathbf{x} \leftrightarrow \mathbf{x}_s)L(\mathbf{x}_s, \vec{\omega})$$

- compute T_r incrementally

Ray Marching

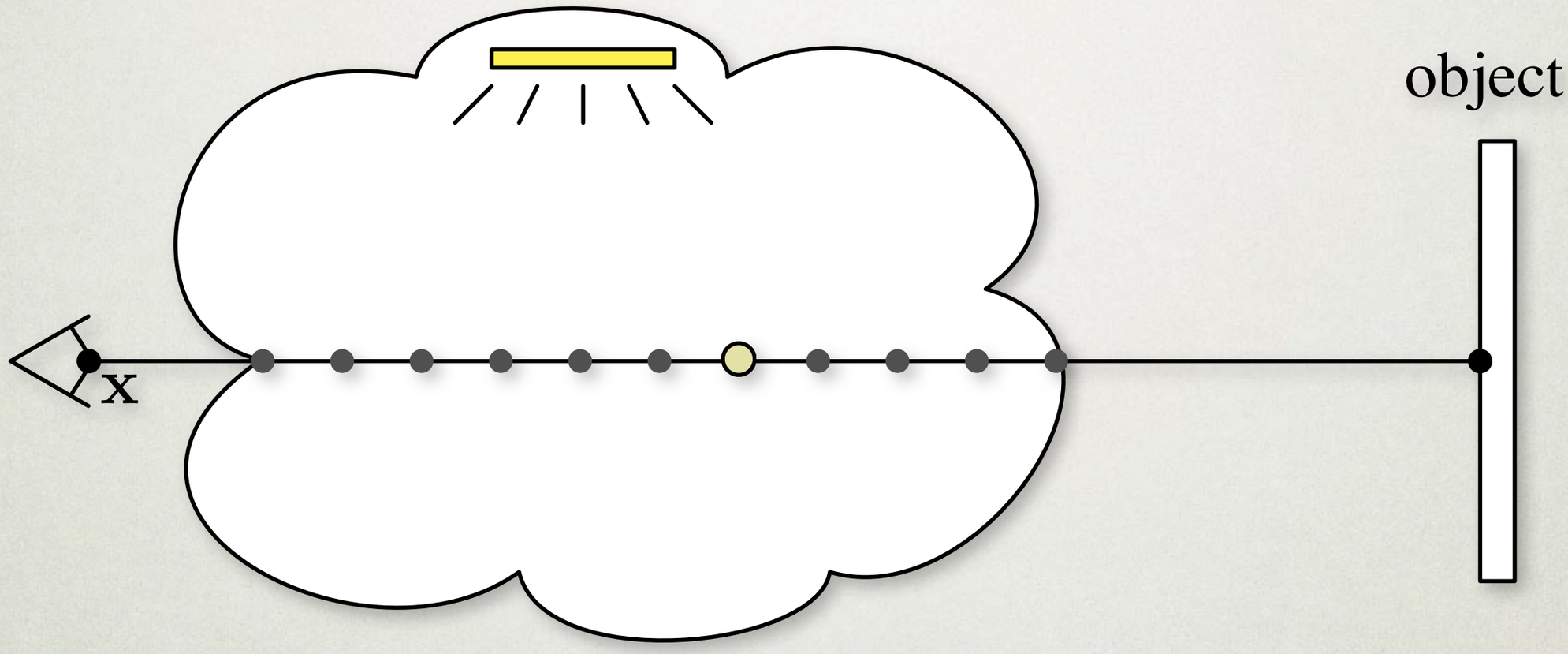

$$L(\mathbf{x}, \vec{\omega}) \approx \sum_{t=0}^{S-1} T_r(\mathbf{x} \leftrightarrow \mathbf{x}_t)\sigma_s(\mathbf{x}_t)\boxed{L_i(\mathbf{x}_t, \vec{\omega})}\Delta_t + T_r(\mathbf{x} \leftrightarrow \mathbf{x}_s)L(\mathbf{x}_s, \vec{\omega})$$

Ray Marching

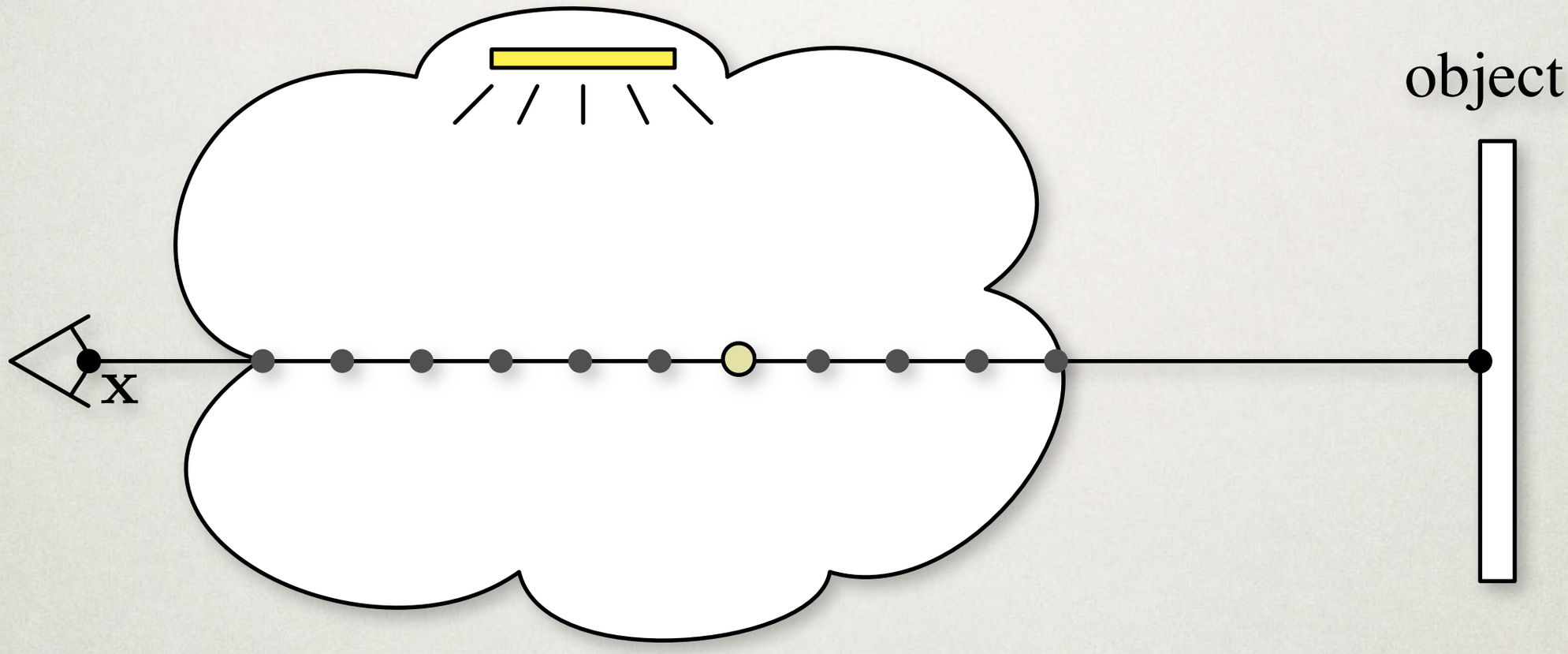

$$L(\mathbf{x}, \vec{\omega}) \approx \sum_{t=0}^{S-1} T_r(\mathbf{x} \leftrightarrow \mathbf{x}_t)\sigma_s(\mathbf{x}_t)\boxed{L_i(\mathbf{x}_t, \vec{\omega})}\Delta_t + T_r(\mathbf{x} \leftrightarrow \mathbf{x}_s)L(\mathbf{x}_s, \vec{\omega})$$

$$L_i(\mathbf{x}_t, \vec{\omega}) = \int_{\Omega_{4\pi}} p(\mathbf{x}_t, \vec{\omega}_t, \vec{\omega})L(\mathbf{x}_t, \vec{\omega}_t)\ d\omega_t$$

Ray Marching (Single Scattering)

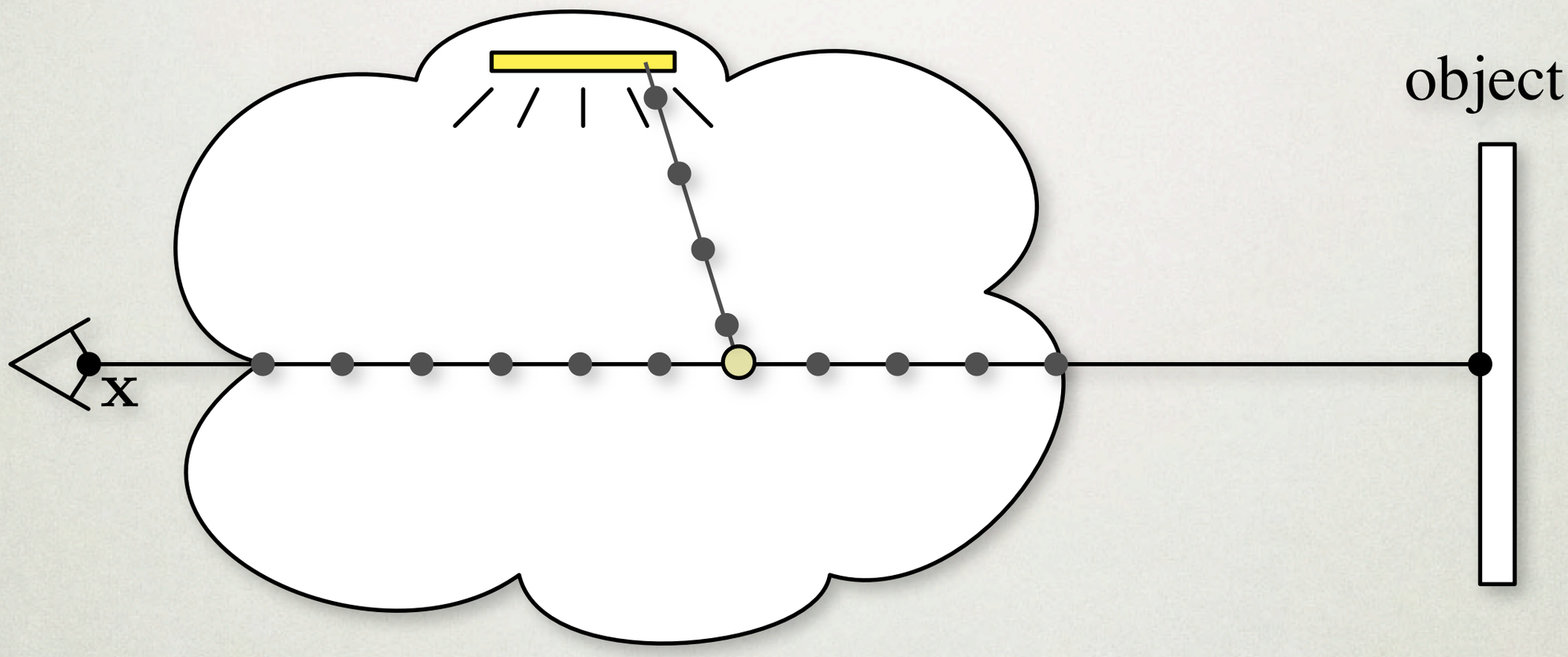

$$L(\mathbf{x},\vec{\omega}) \approx \sum_{t=0}^{S-1} T_r(\mathbf{x}\leftrightarrow\mathbf{x}_t)\sigma_s(\mathbf{x}_t)\boxed{L_i(\mathbf{x}_t,\vec{\omega})}\Delta_t + T_r(\mathbf{x}\leftrightarrow\mathbf{x}_s)L(\mathbf{x}_s,\vec{\omega})$$

- assume only single scattering (direct lighting)

Ray Marching (Single Scattering)

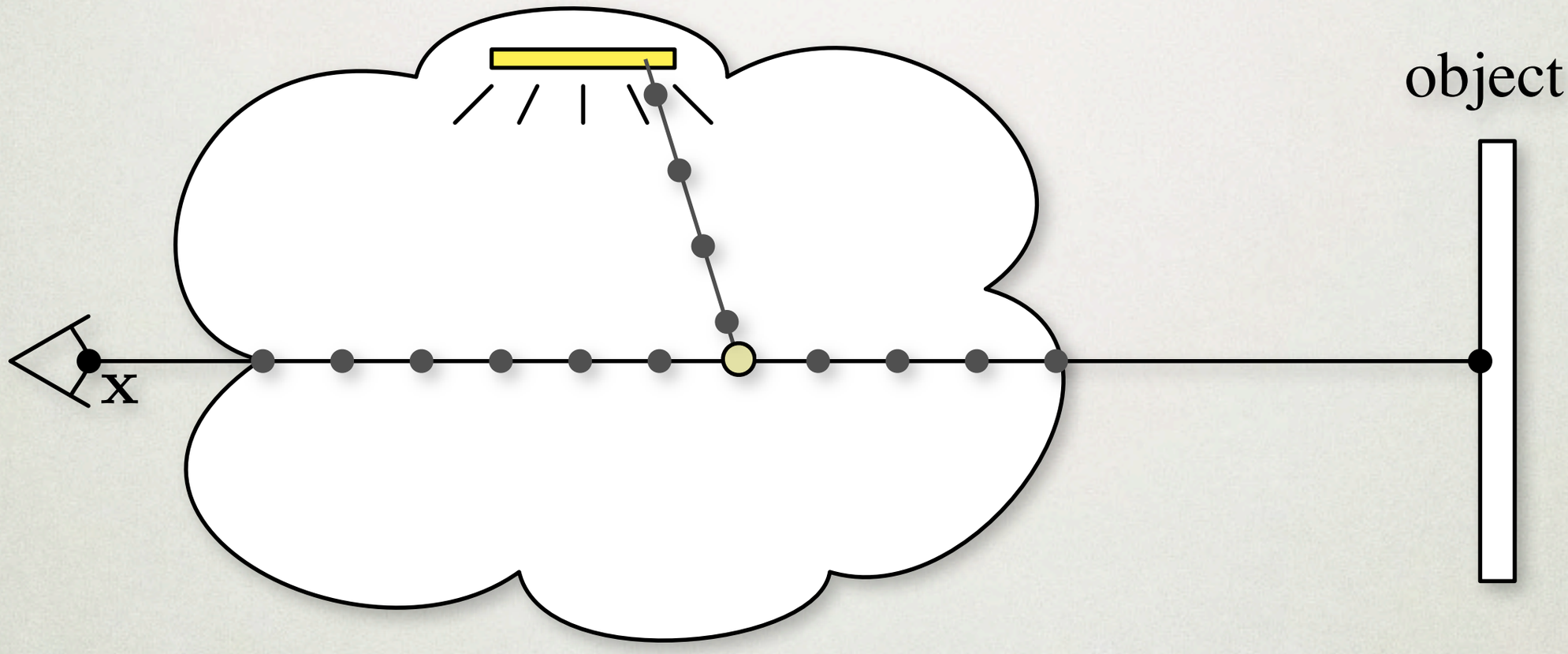

$$L(\mathbf{x},\vec{\omega}) \approx \sum_{t=0}^{S-1} T_r(\mathbf{x}\leftrightarrow\mathbf{x}_t)\sigma_s(\mathbf{x}_t)\boxed{L_i(\mathbf{x}_t,\vec{\omega})}\Delta_t + T_r(\mathbf{x}\leftrightarrow\mathbf{x}_s)L(\mathbf{x}_s,\vec{\omega})$$

- assume only single scattering (direct lighting)
- trace shadow ray for volumetric shadows

Ray Marching (Multiple Scattering)

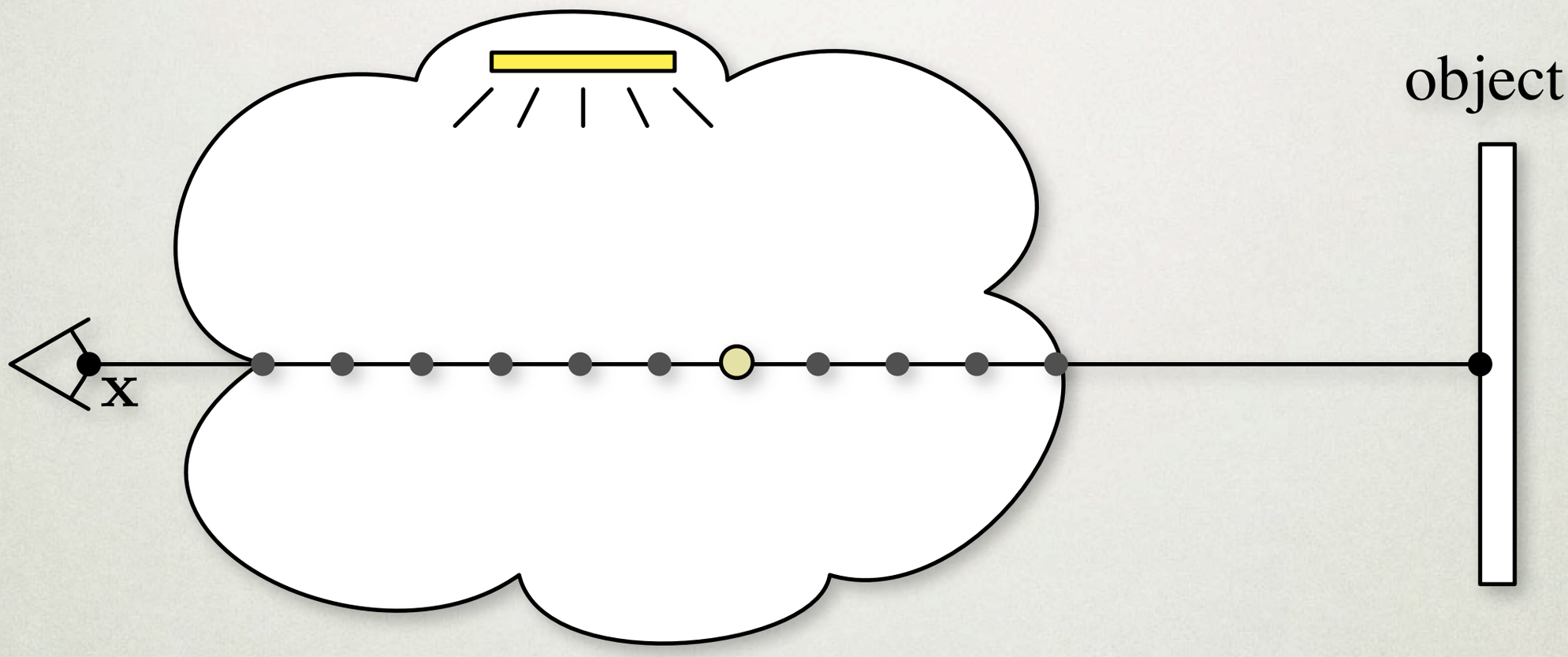

$$L(\mathbf{x},\vec{\omega}) \approx \sum_{t=0}^{S-1} T_r(\mathbf{x}\leftrightarrow\mathbf{x}_t)\sigma_s(\mathbf{x}_t)\boxed{L_i(\mathbf{x}_t,\vec{\omega})}\Delta_t + T_r(\mathbf{x}\leftrightarrow\mathbf{x}_s)L(\mathbf{x}_s,\vec{\omega})$$

- recursive ray marching
- exponential growth! expensive!

Ray Marching (Multiple Scattering)

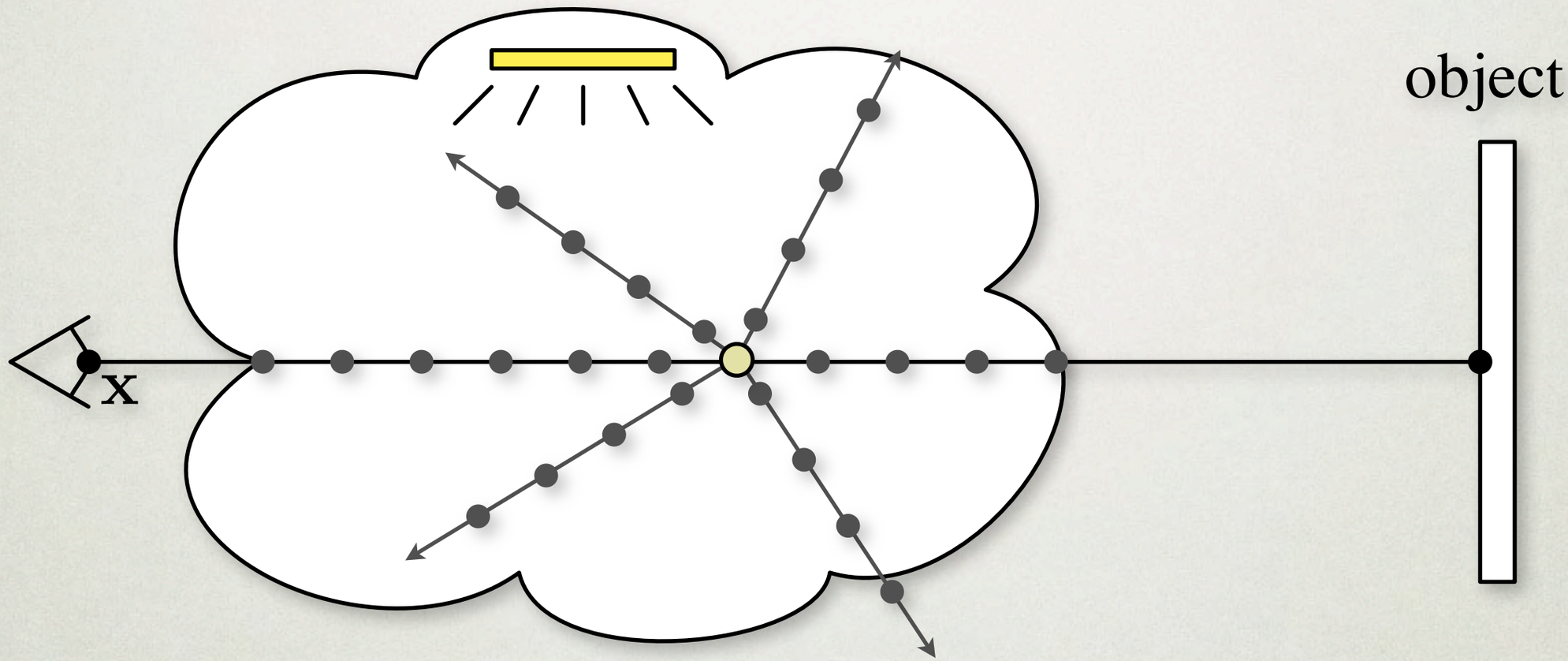

$$L(\mathbf{x},\vec{\omega}) \approx \sum_{t=0}^{S-1} T_r(\mathbf{x}\leftrightarrow\mathbf{x}_t)\sigma_s(\mathbf{x}_t)\boxed{L_i(\mathbf{x}_t,\vec{\omega})}\Delta_t + T_r(\mathbf{x}\leftrightarrow\mathbf{x}_s)L(\mathbf{x}_s,\vec{\omega})$$

- recursive ray marching
- exponential growth! expensive!

Ray Marching (Multiple Scattering)

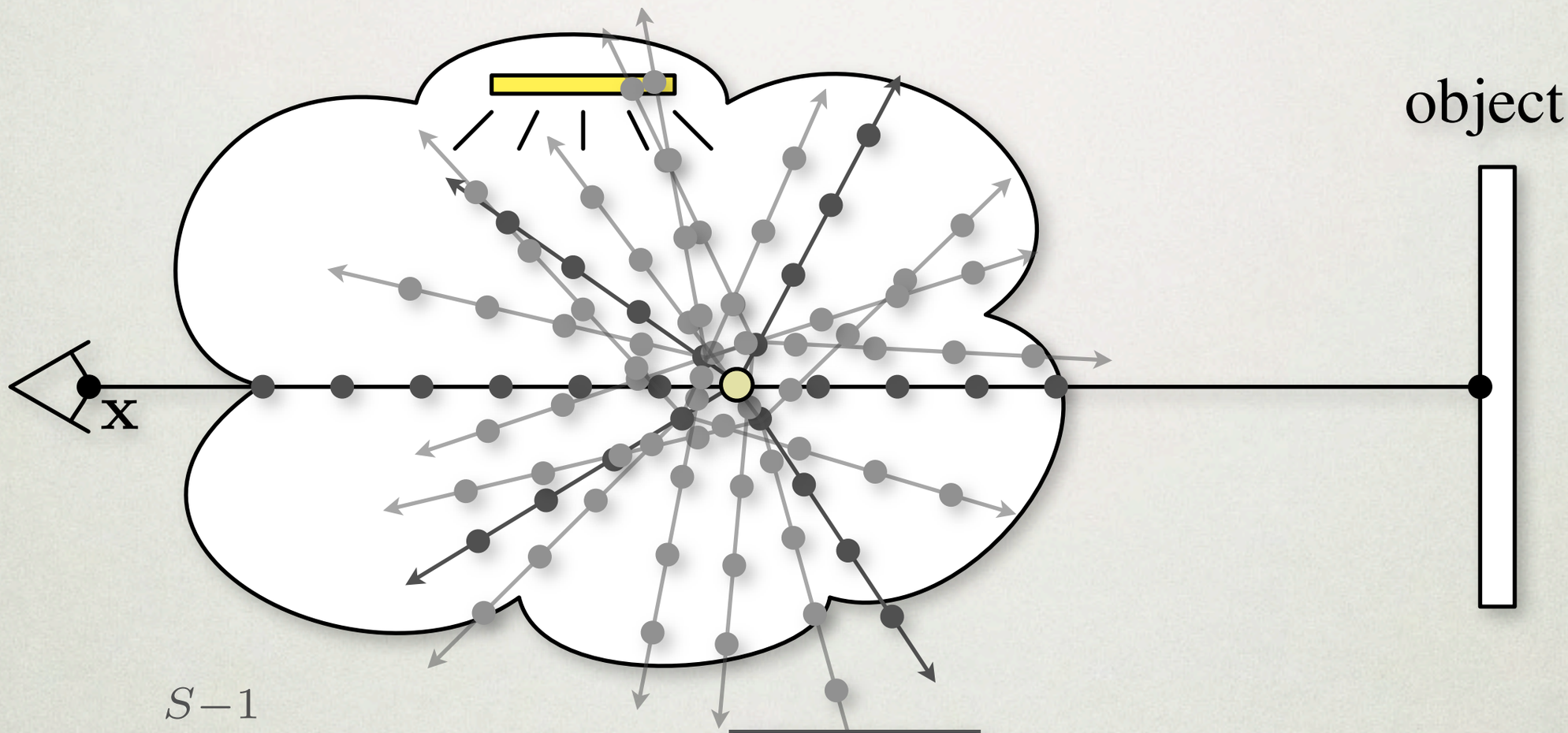

$$L(\mathbf{x},\vec{\omega}) \approx \sum_{t=0}^{S-1} T_r(\mathbf{x}\leftrightarrow\mathbf{x}_t)\sigma_s(\mathbf{x}_t)\boxed{L_i(\mathbf{x}_t,\vec{\omega})}\Delta_t + T_r(\mathbf{x}\leftrightarrow\mathbf{x}_s)L(\mathbf{x}_s,\vec{\omega})$$

- recursive ray marching
- exponential growth! expensive!

Ray Marching (Multiple Scattering)

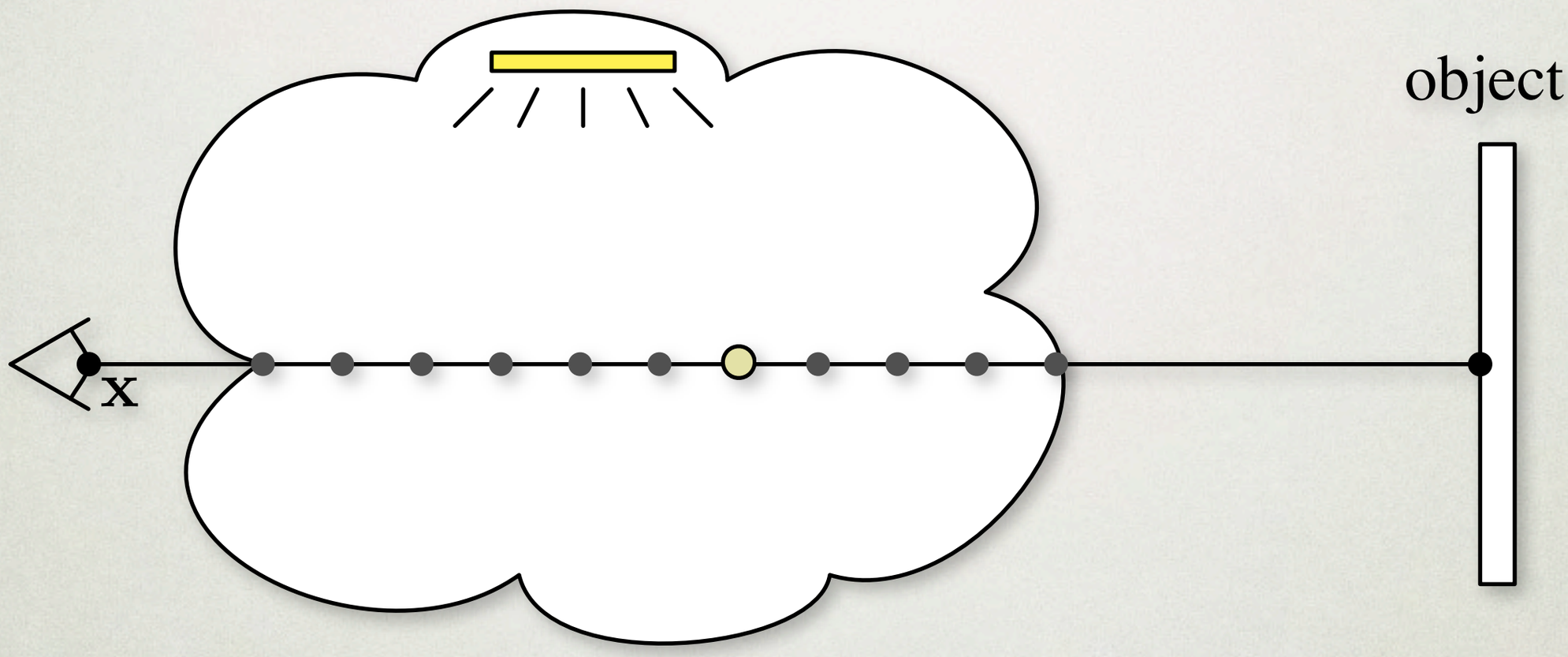

$$L(\mathbf{x},\vec{\omega}) \approx \sum_{t=0}^{S-1} T_r(\mathbf{x}\leftrightarrow\mathbf{x}_t)\sigma_s(\mathbf{x}_t)\boxed{L_i(\mathbf{x}_t,\vec{\omega})}\Delta_t + T_r(\mathbf{x}\leftrightarrow\mathbf{x}_s)L(\mathbf{x}_s,\vec{\omega})$$

- random walk sampling (path tracing)
- linear growth, but still expensive.

Ray Marching (Multiple Scattering)

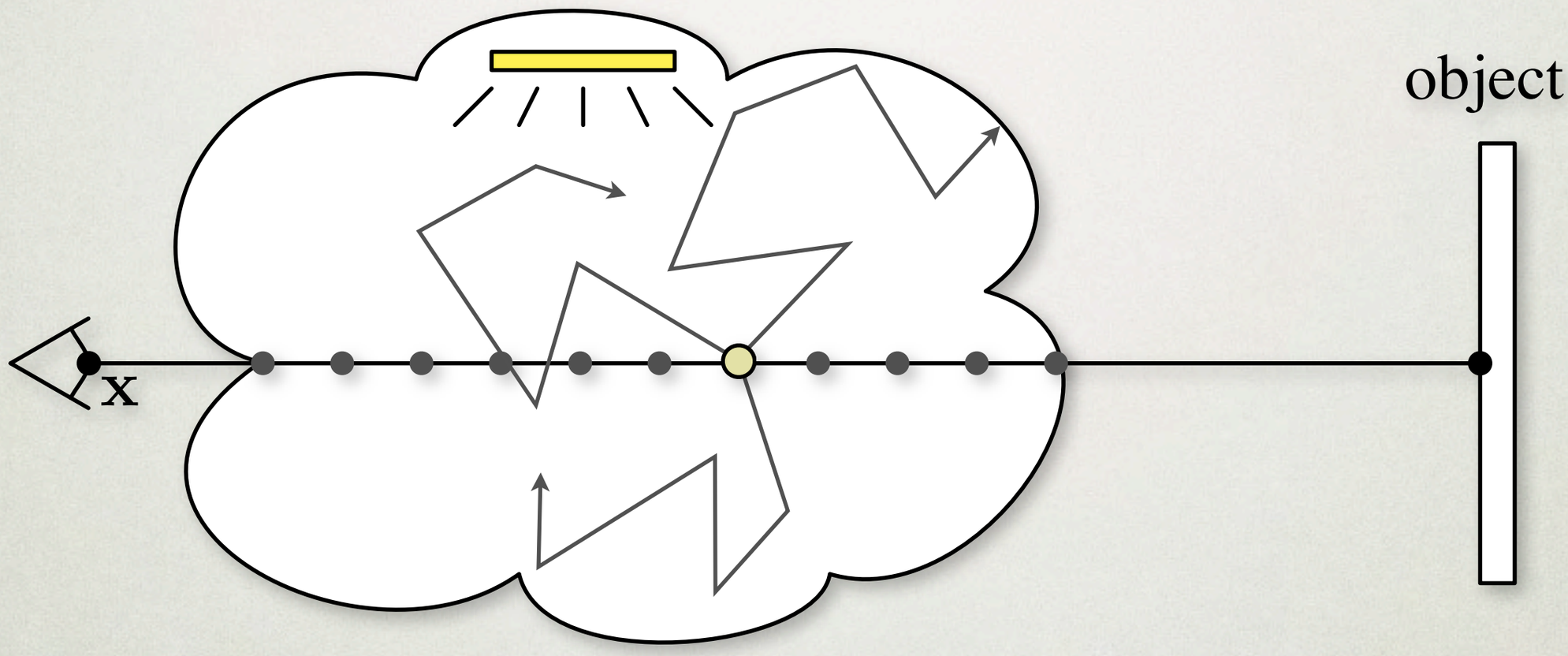

$$L(\mathbf{x},\vec{\omega}) \approx \sum_{t=0}^{S-1} T_r(\mathbf{x}\leftrightarrow\mathbf{x}_t)\sigma_s(\mathbf{x}_t)\boxed{L_i(\mathbf{x}_t,\vec{\omega})}\Delta_t + T_r(\mathbf{x}\leftrightarrow\mathbf{x}_s)L(\mathbf{x}_s,\vec{\omega})$$

- random walk sampling (path tracing)
- linear growth, but still expensive.

Ray Marching (Multiple Scattering)

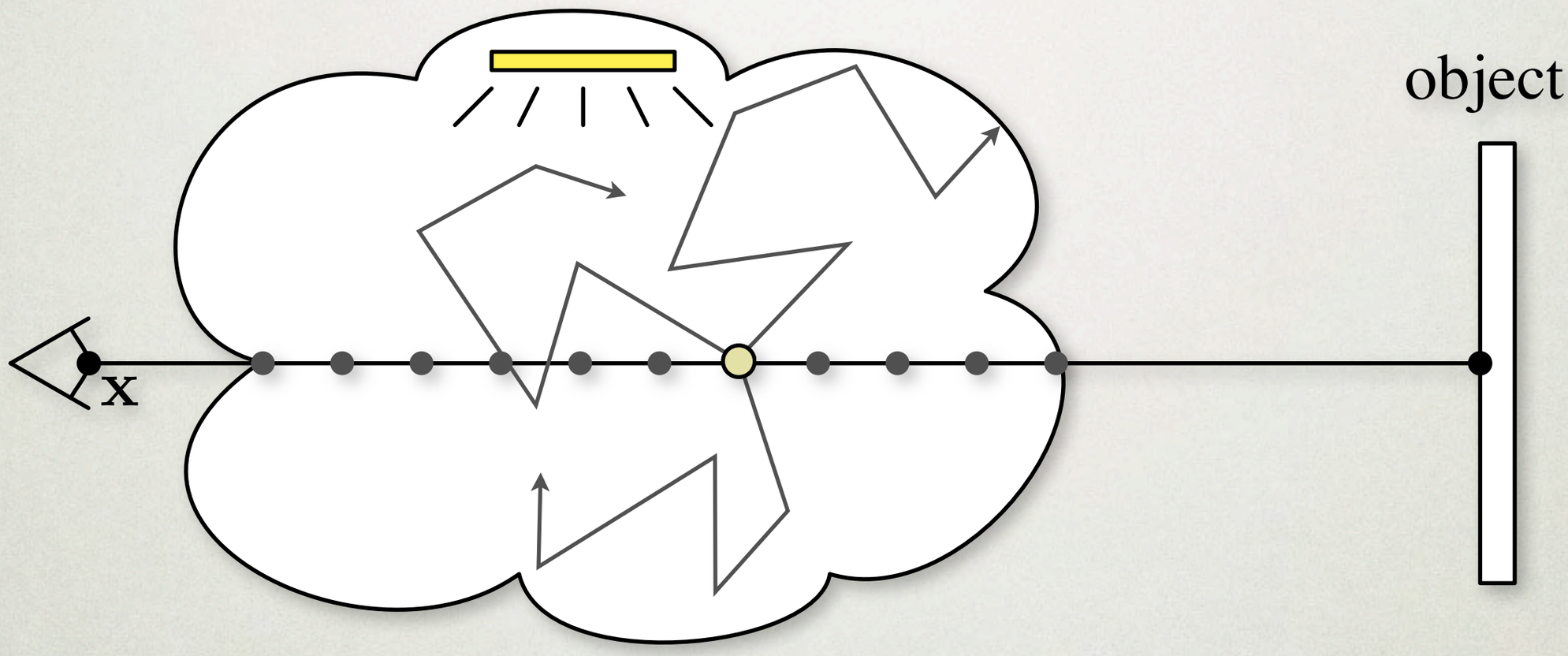

$$L(\mathbf{x},\vec{\omega}) \approx \sum_{t=0}^{S-1} T_r(\mathbf{x}\leftrightarrow\mathbf{x}_t)\sigma_s(\mathbf{x}_t)\boxed{L_i(\mathbf{x}_t,\vec{\omega})}\Delta_t + T_r(\mathbf{x}\leftrightarrow\mathbf{x}_s)L(\mathbf{x}_s,\vec{\omega})$$

- random walk sampling (path tracing)
- linear growth, but still expensive.

So Far

- Single scattering relatively in-expensive
- Multiple scattering **very** expensive

Volumetric Photon Tracing

Two-pass algorithm:

1) Photon tracing
   - Simulate the scattering of photons
2) Rendering
   - Reuse the photons to estimate multiple scattering
     - VPL methods or density estimation

Volumetric Photon Tracing

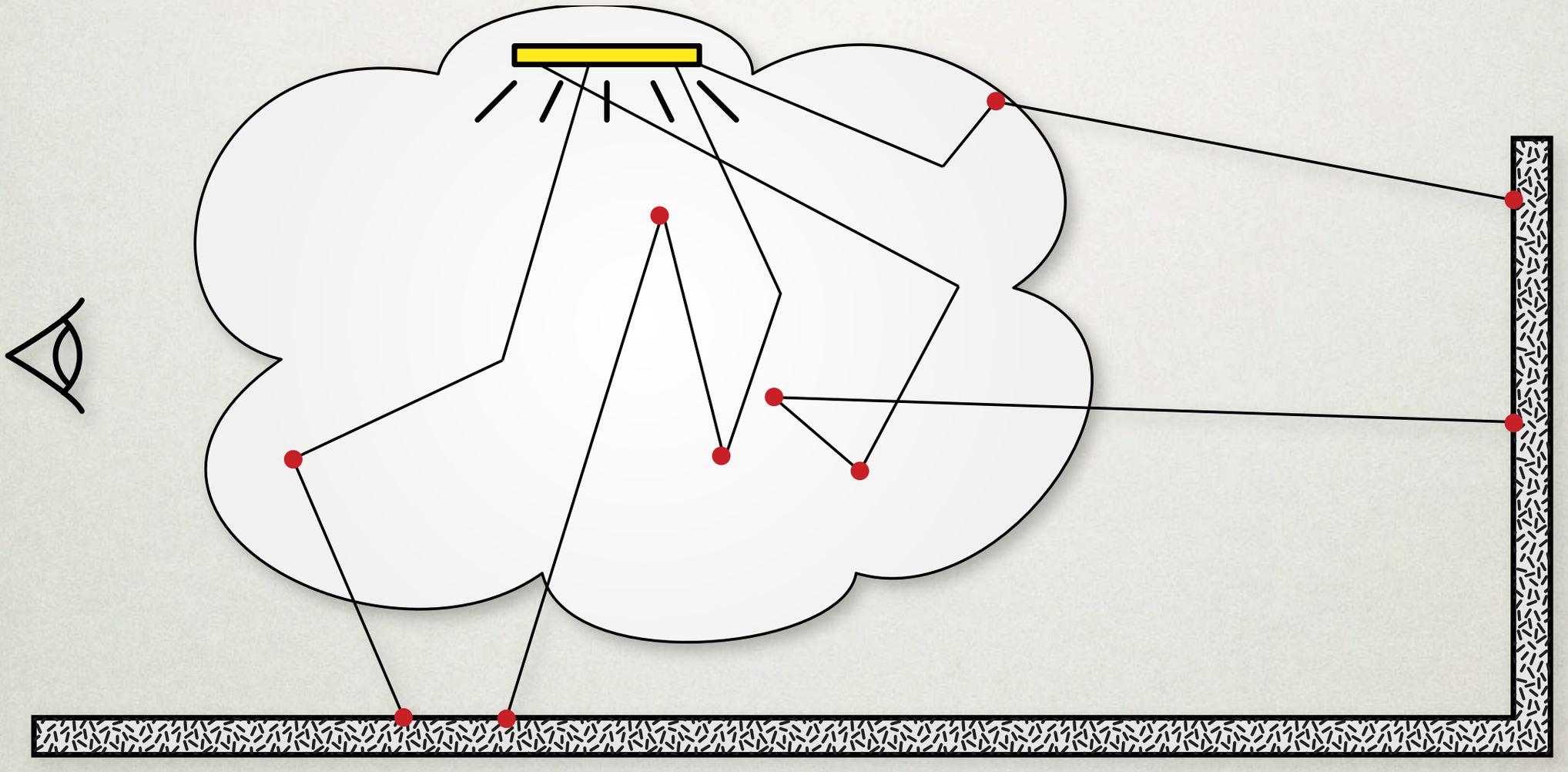

Volume Photon Map

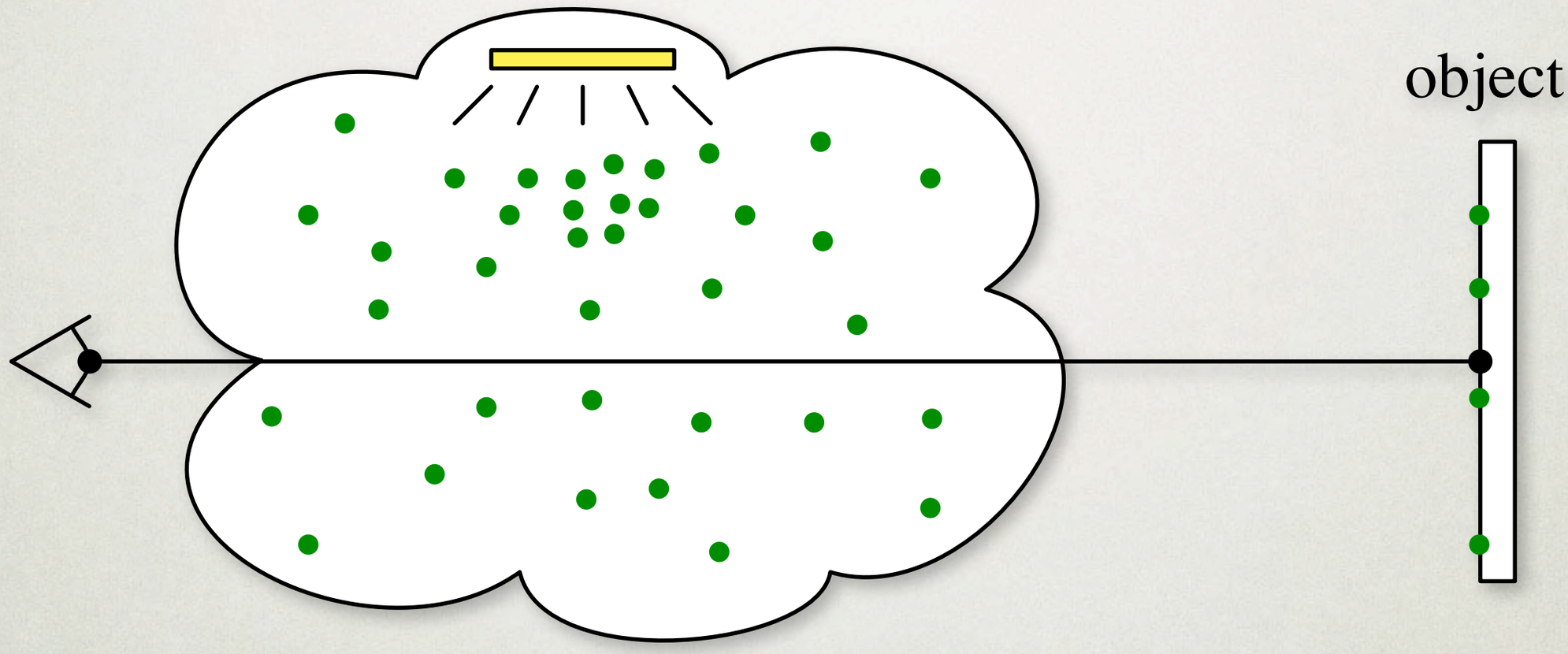

$$L(\mathbf{x}, \vec{\omega}) = \int_0^s T_r(\mathbf{x} \leftrightarrow \mathbf{x}_t)\sigma_s(\mathbf{x}_t)L_i(\mathbf{x}_t, \vec{\omega})\ dt + T_r(\mathbf{x} \leftrightarrow \mathbf{x}_s)L(\mathbf{x}_s, \vec{\omega})$$

VPL (Virtual Point Light) Methods

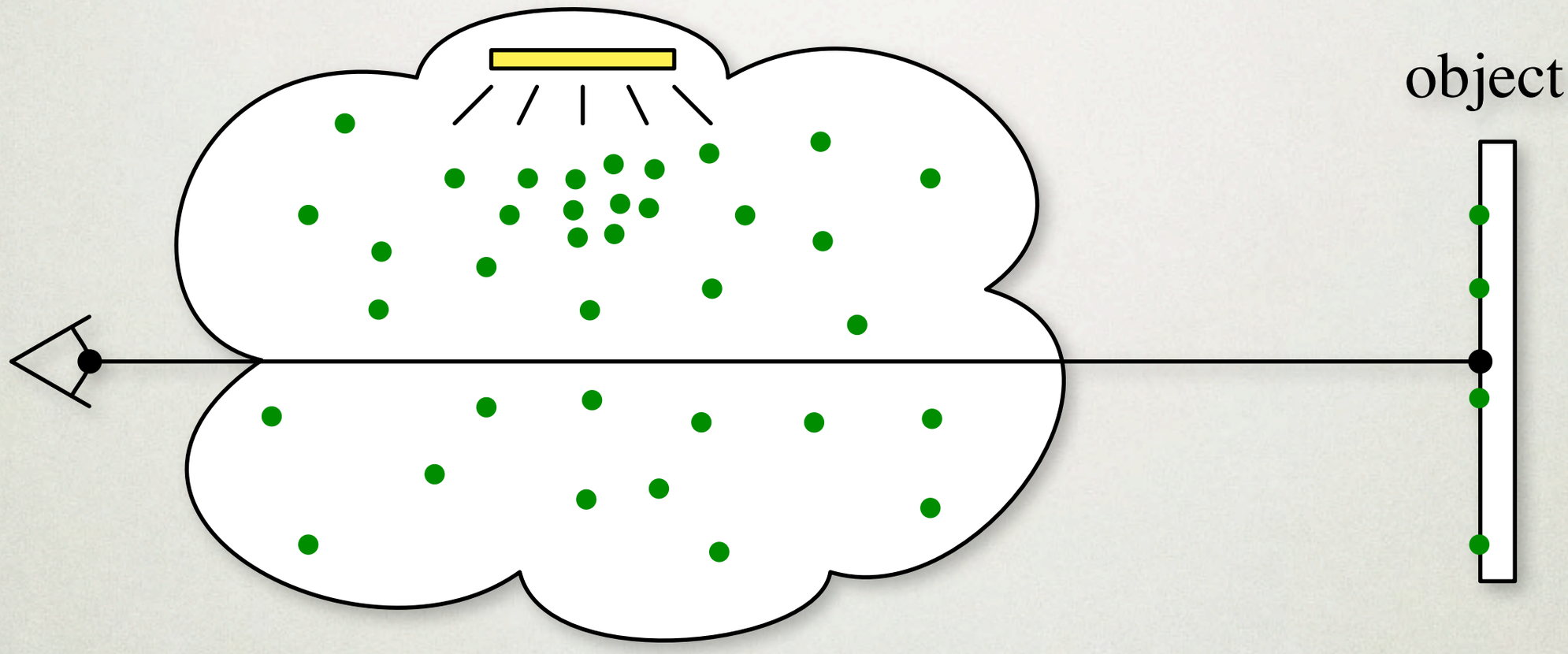

1. Treat each photon as a “virtual point light”

VPL Methods (Instant Radiosity)

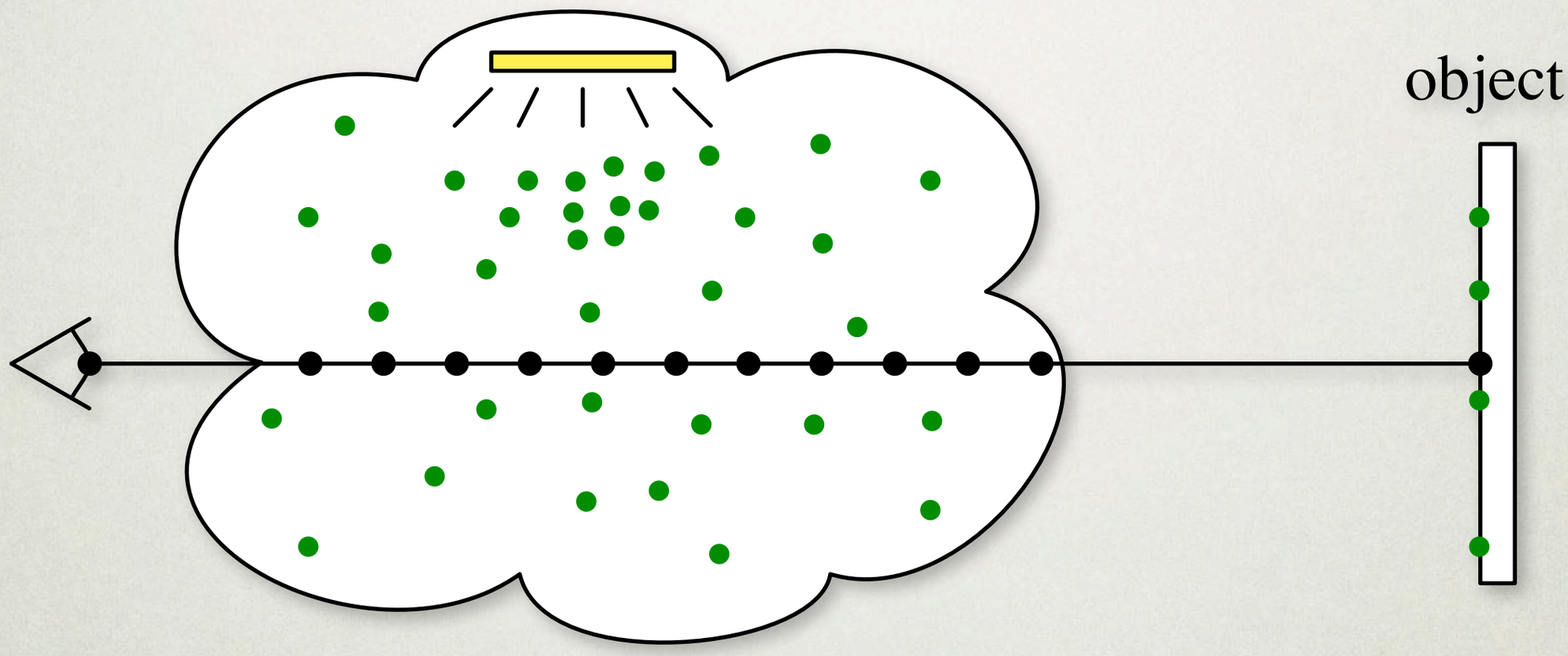

1. Treat each photon as a “virtual point light”
2. Perform ray marching
   - At each step: shoot shadow rays to VPLs

VPL Methods (Instant Radiosity)

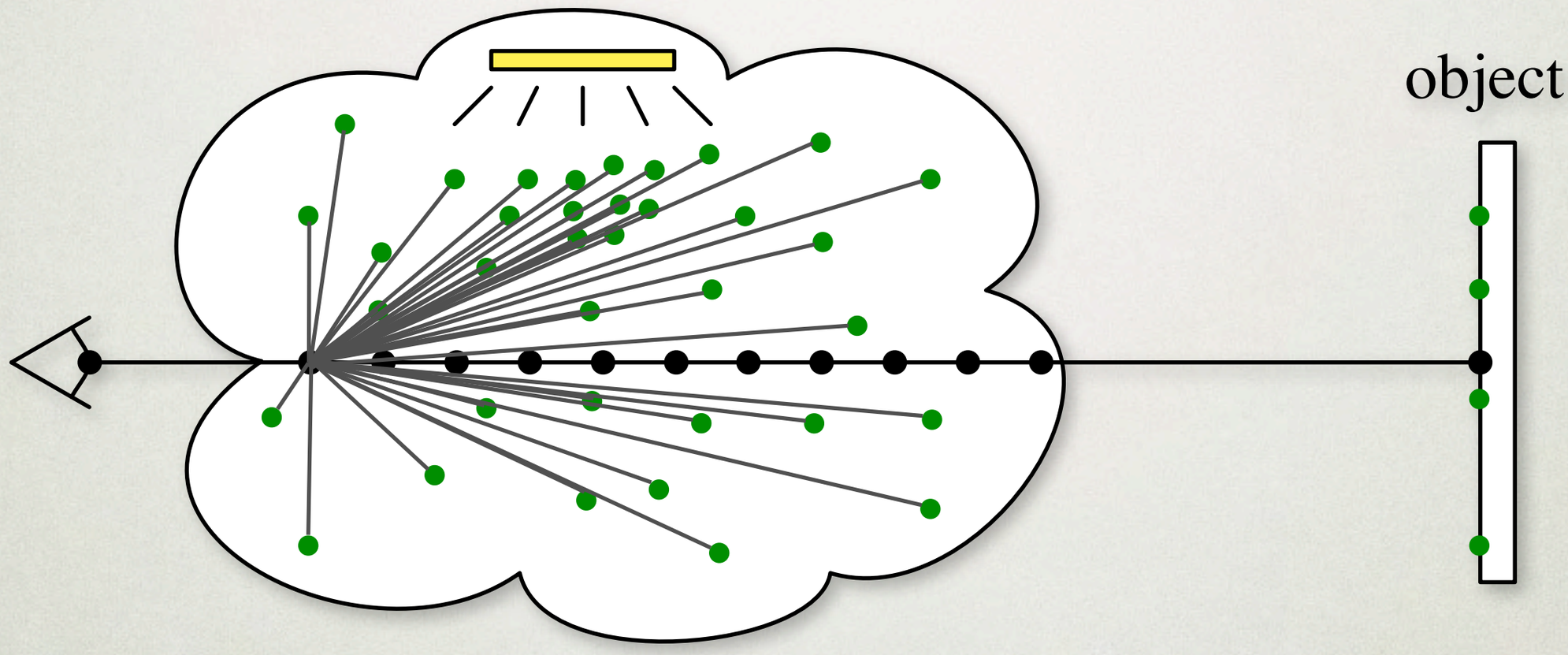

1. Treat each photon as a “virtual point light”
2. Perform ray marching
   - At each step: shoot shadow rays to VPLs

VPL Methods (Instant Radiosity)

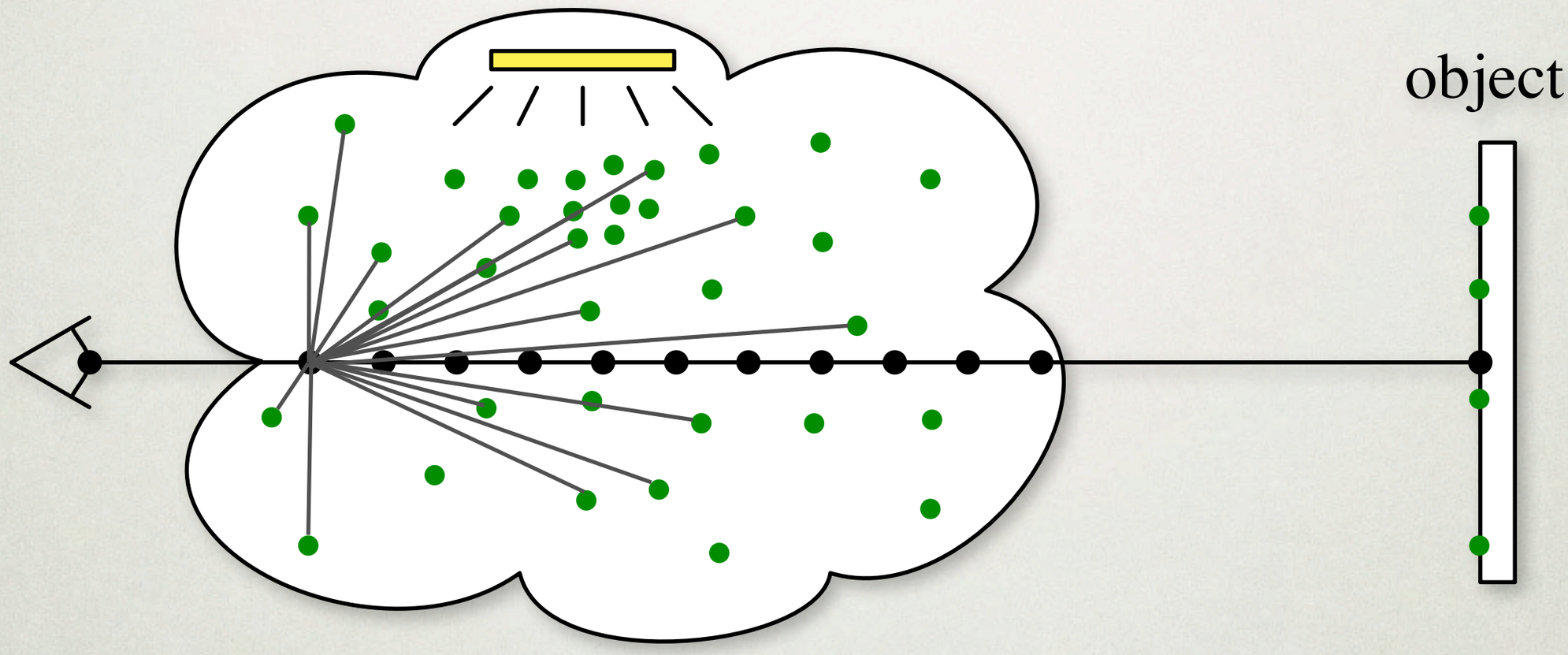

1. Treat each photon as a "virtual point light"
2. Perform ray marching
   - At each step: choose a **subset** of VPLs (faster performance, introduces noise)

VPL Methods (Lightcuts)

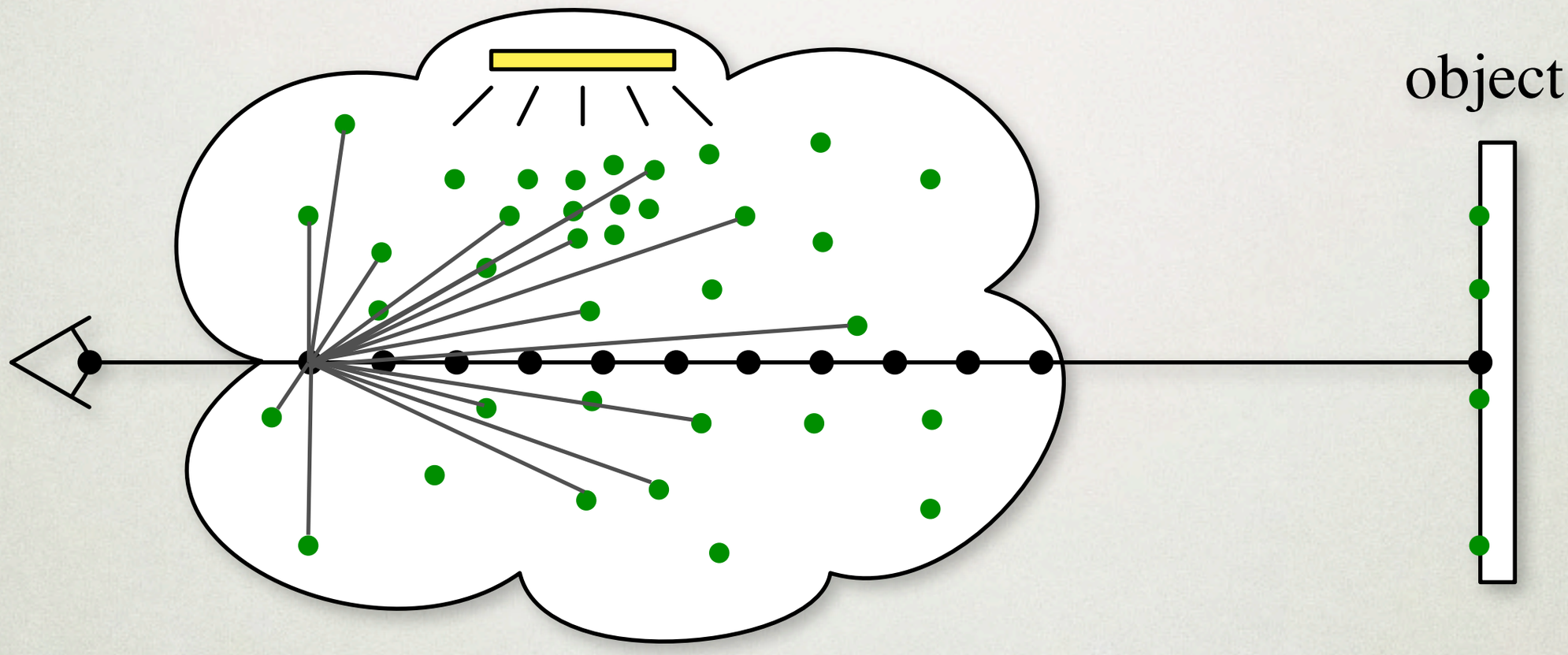

1. Create VPL **hierarchy**
2. Perform ray marching
   - At each step: choose **hierarchical subset** (faster performance, tries to limit noise)

Caustics

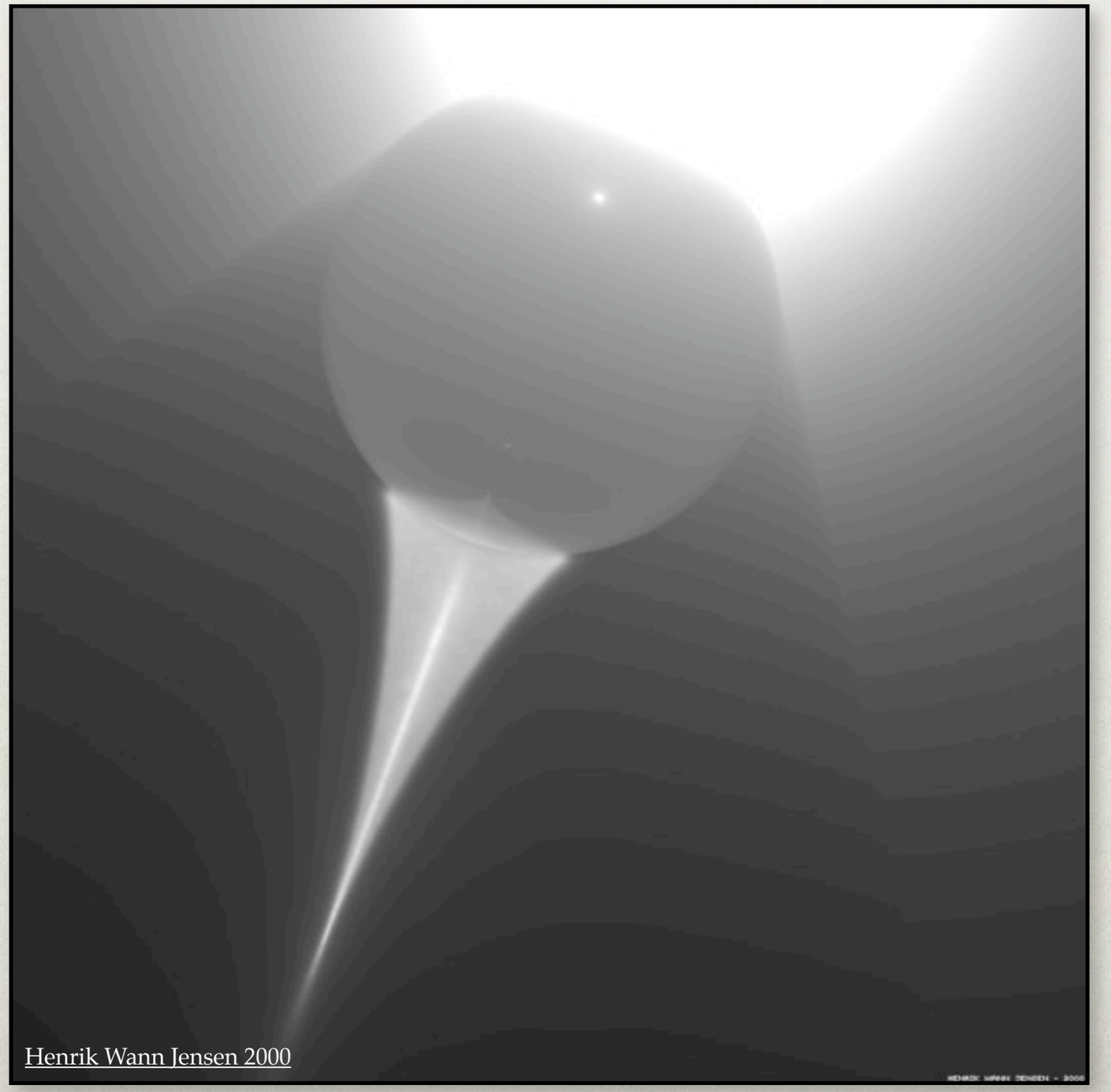

Volumetric Photon Mapping

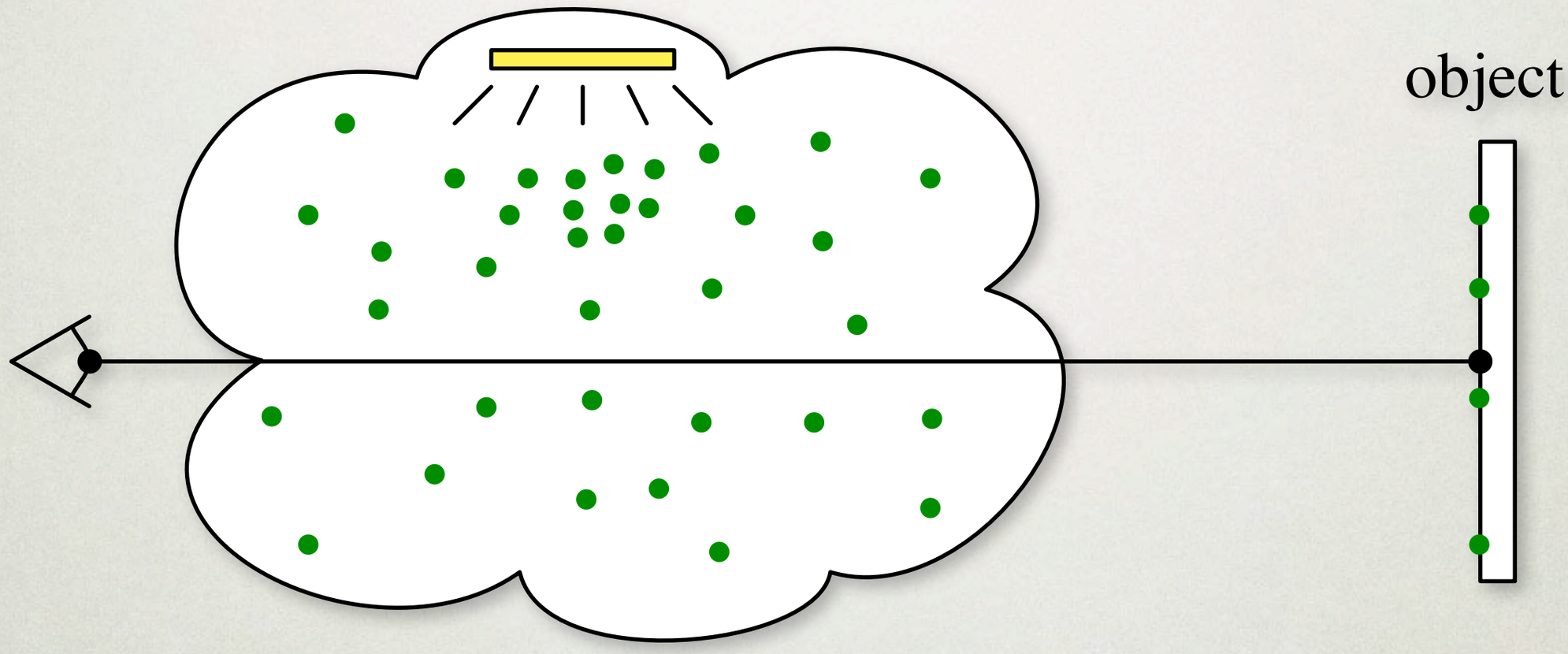

$$L(\mathbf{x}, \vec{\omega}) = \int_0^s T_r(\mathbf{x} \leftrightarrow \mathbf{x}_t)\sigma_s(\mathbf{x}_t)L_i(\mathbf{x}_t, \vec{\omega})\ dt + T_r(\mathbf{x} \leftrightarrow \mathbf{x}_s)L(\mathbf{x}_s, \vec{\omega})$$

Volumetric Photon Mapping

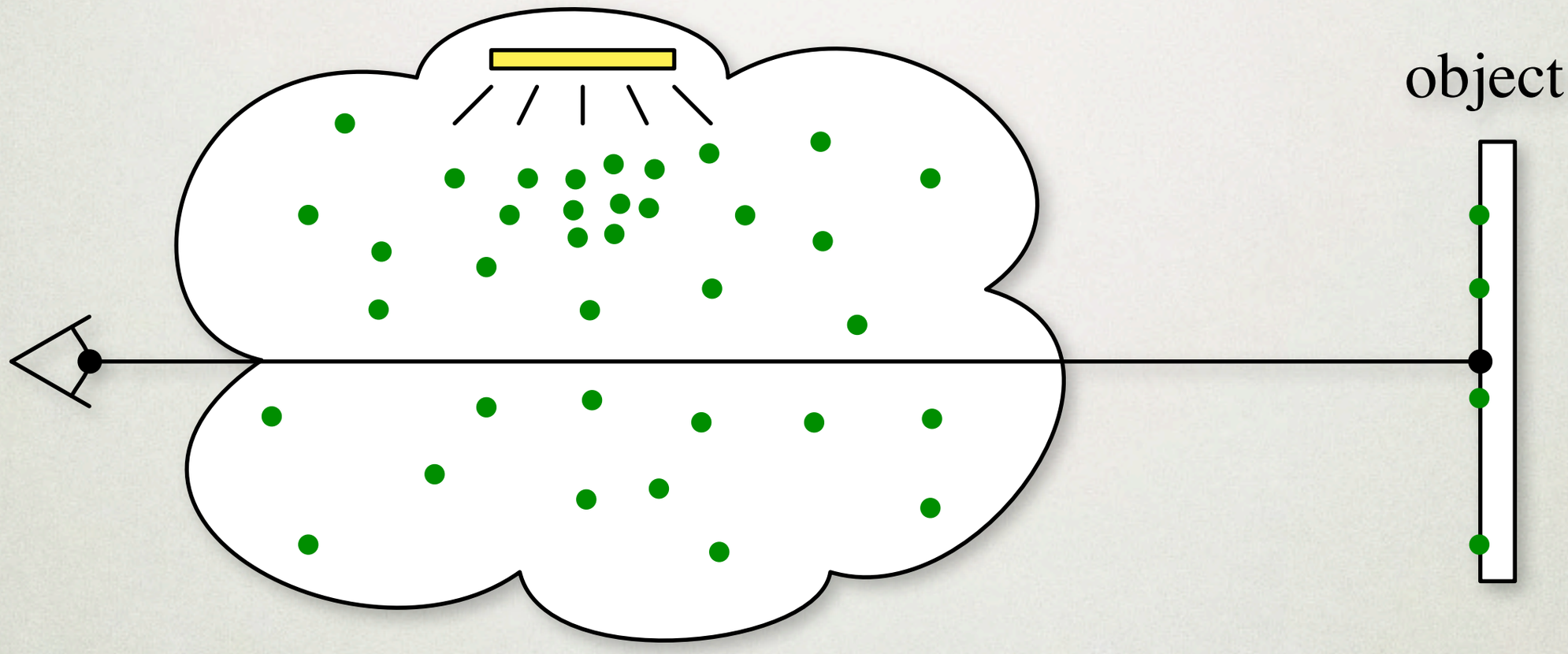

$$L(\mathbf{x}, \vec{\omega}) = \int_0^s T_r(\mathbf{x} \leftrightarrow \mathbf{x}_t)\sigma_s(\mathbf{x}_t)L_i(\mathbf{x}_t, \vec{\omega})\ dt + T_r(\mathbf{x} \leftrightarrow \mathbf{x}_s)L(\mathbf{x}_s, \vec{\omega})$$

Two approaches: traditional & beam estimation

Traditional Photon Mapping (Ray Marching)

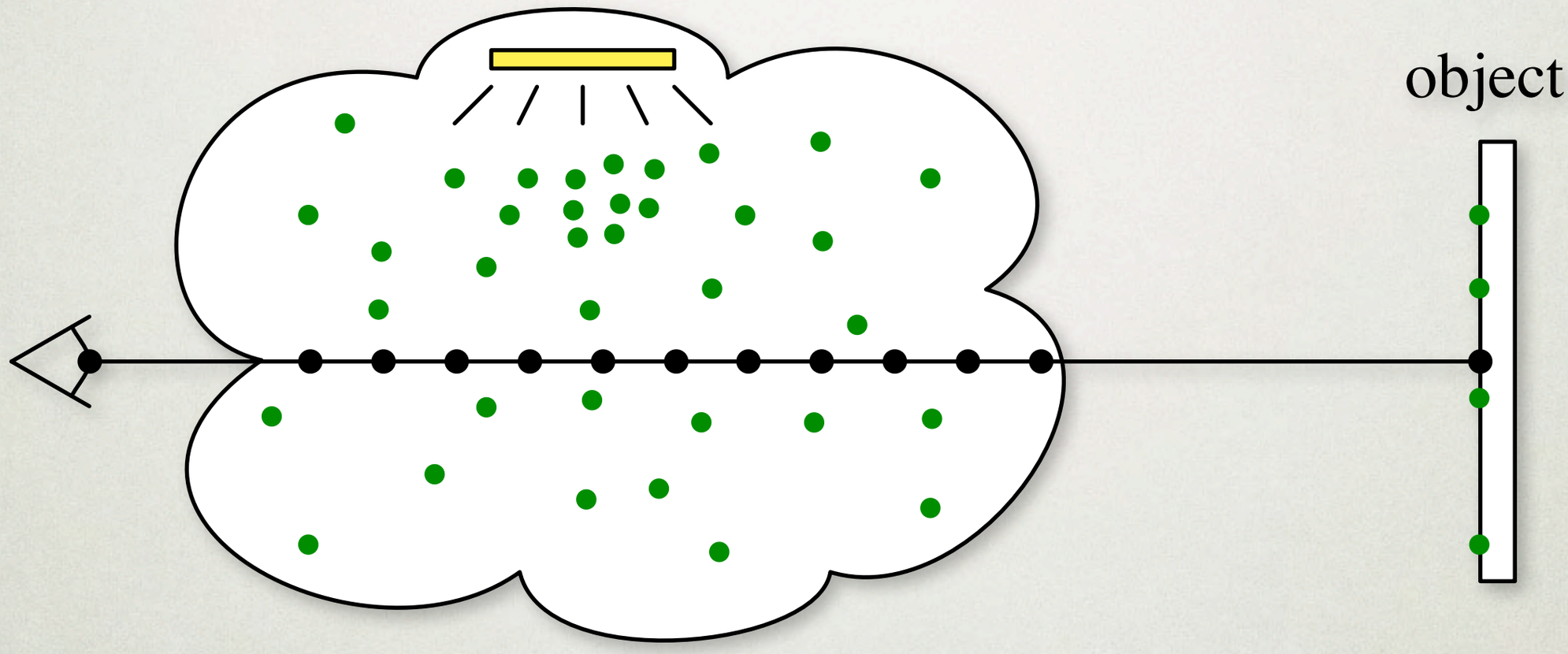

$$L(\mathbf{x}, \vec{\omega}) \approx \sum_{t=0}^{S-1} T_r(\mathbf{x} \leftrightarrow \mathbf{x}_t)\sigma_s(\mathbf{x}_t)L_i(\mathbf{x}_t, \vec{\omega})\Delta_t + T_r(\mathbf{x} \leftrightarrow \mathbf{x}_s)L(\mathbf{x}_s, \vec{\omega})$$

Traditional Photon Mapping (Ray Marching)

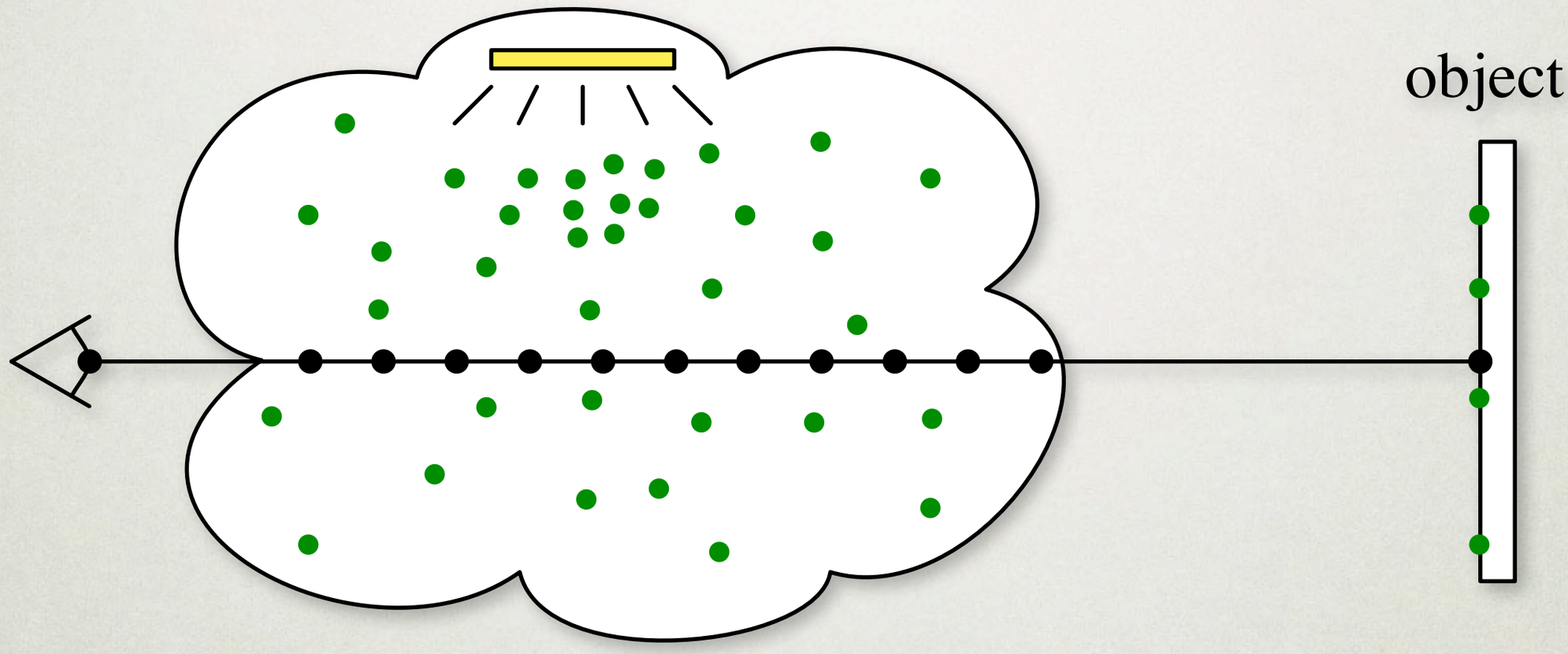

$$L(\mathbf{x},\vec{\omega}) \approx \sum_{t=0}^{S-1} T_r(\mathbf{x}\leftrightarrow\mathbf{x}_t)\sigma_s(\mathbf{x}_t)\boxed{L_i(\mathbf{x}_t,\vec{\omega})}\Delta_t + T_r(\mathbf{x}\leftrightarrow\mathbf{x}_s)L(\mathbf{x}_s,\vec{\omega})$$

Traditional Photon Mapping (Multiple Scattering)

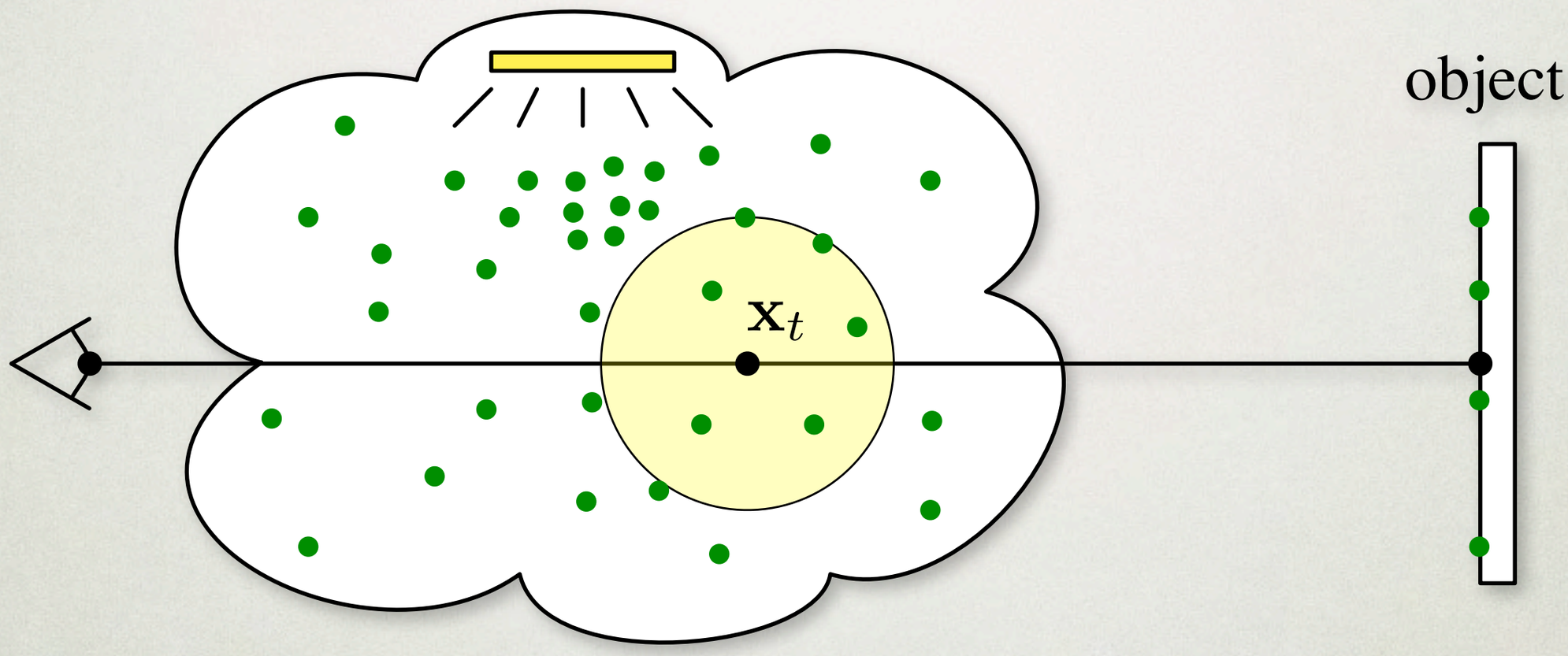

$$L(\mathbf{x},\vec{\omega}) \approx \sum_{t=0}^{S-1} T_r(\mathbf{x}\leftrightarrow\mathbf{x}_t)\sigma_s(\mathbf{x}_t)\boxed{L_i(\mathbf{x}_t,\vec{\omega})}\Delta_t + T_r(\mathbf{x}\leftrightarrow\mathbf{x}_s)L(\mathbf{x}_s,\vec{\omega})$$

$L_i(\mathbf{x}_t,\vec{\omega})$ photon map for multiple scattering

Volumetric Radiance Estimate

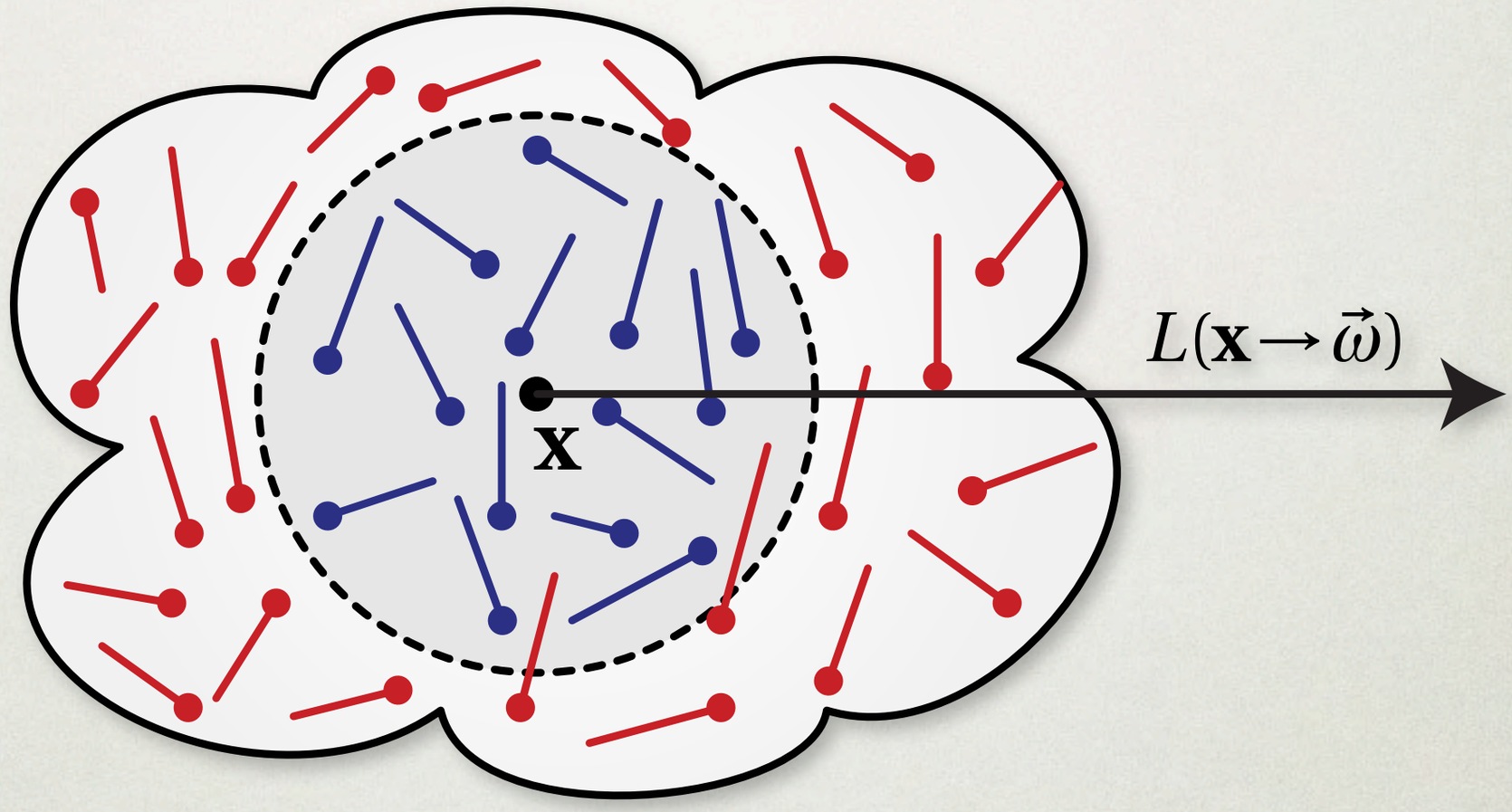

$$L_i(\mathbf{x} \rightarrow \vec{\omega}) \approx \sum_{p=1}^{k} p(\mathbf{x}, \vec{\omega}_p, \vec{\omega}) \frac{\Phi_p(\mathbf{x}, \vec{\omega}_p)}{\mathcal{V}(\mathbf{x})}$$

Volumetric Radiance Estimate

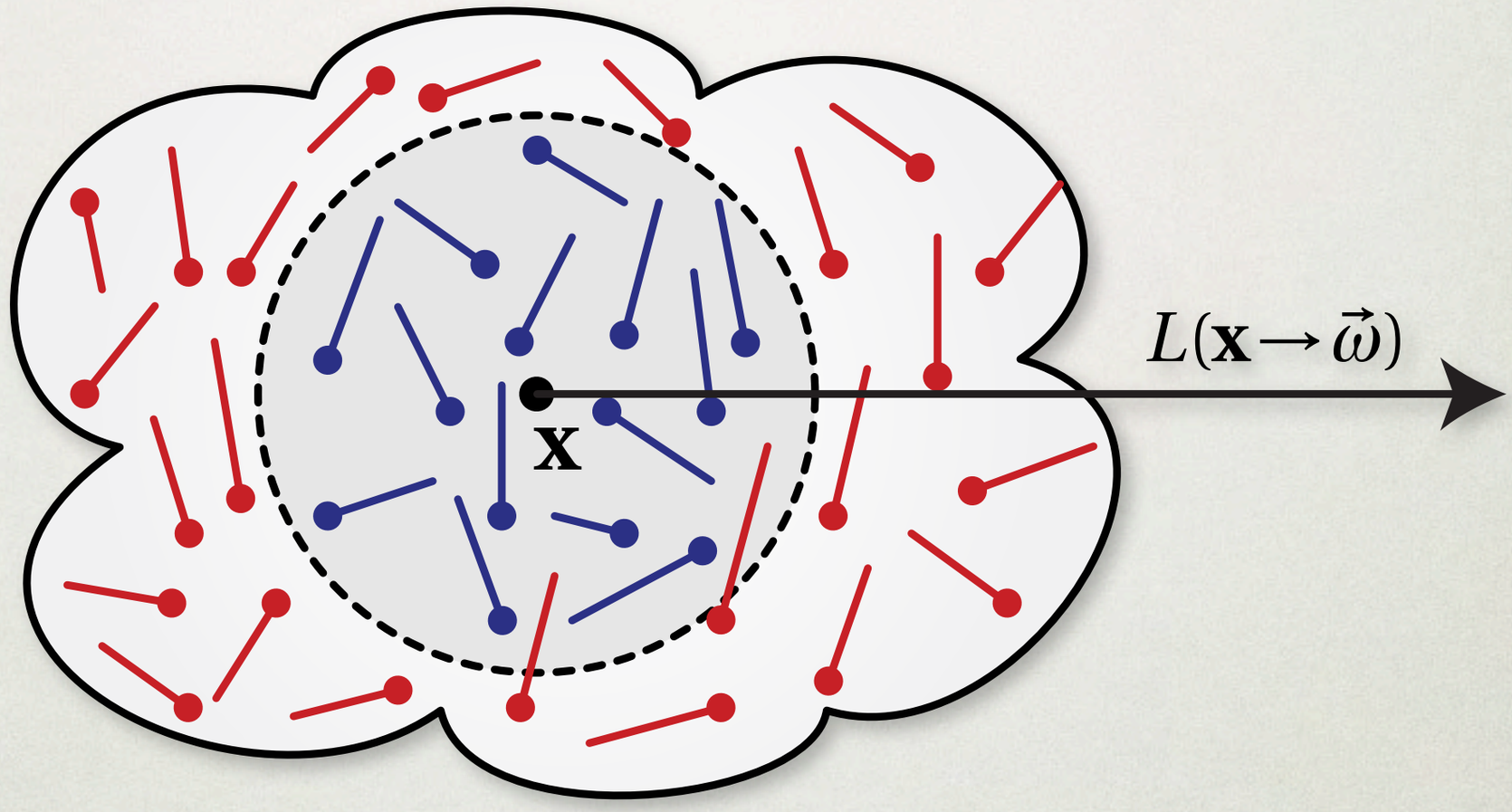

$$L_i(\mathbf{x} \rightarrow \vec{\omega}) \approx \sum_{p=1}^{k} p(\mathbf{x}, \vec{\omega}_p, \vec{\omega}) \frac{\Phi_p(\mathbf{x}, \vec{\omega}_p)}{\frac{4}{3}\pi r(\mathbf{x})^3}$$

A Volume Caustic

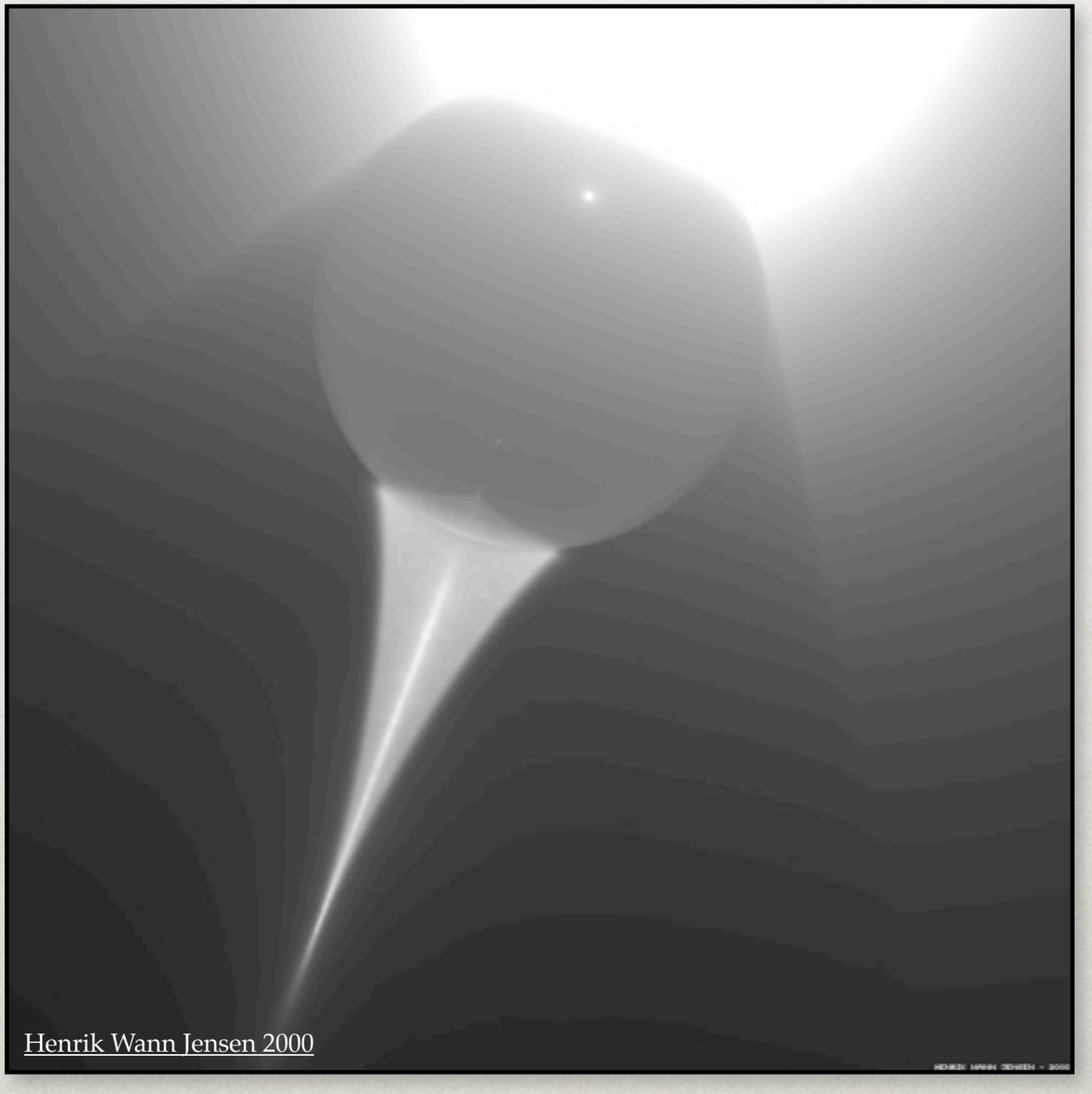

500,000 photons. 1 minute

Rising Smoke

Smoke flowing past a sphere

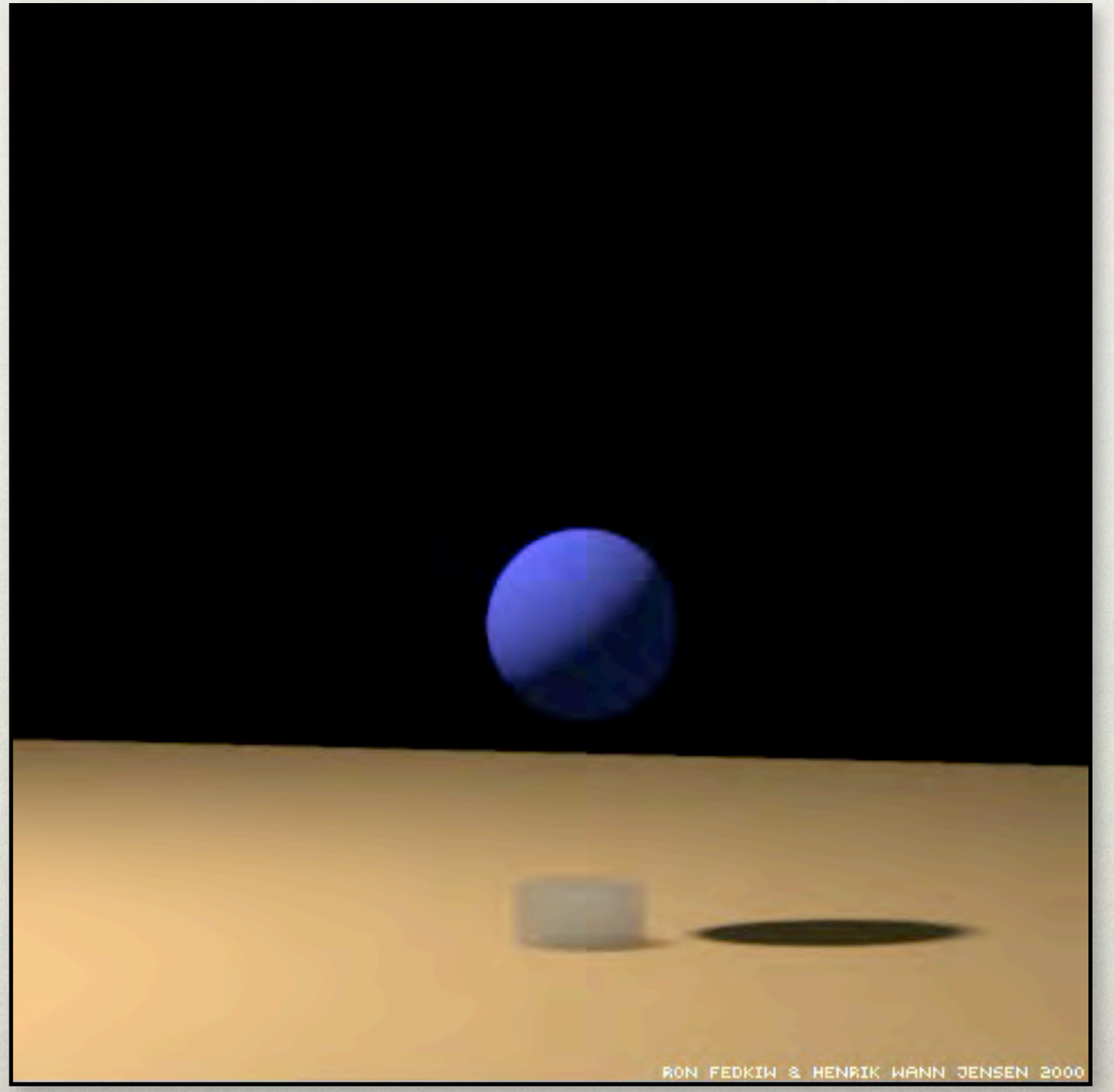

Volumetric Photon Mapping

Conventional Radiance Estimate

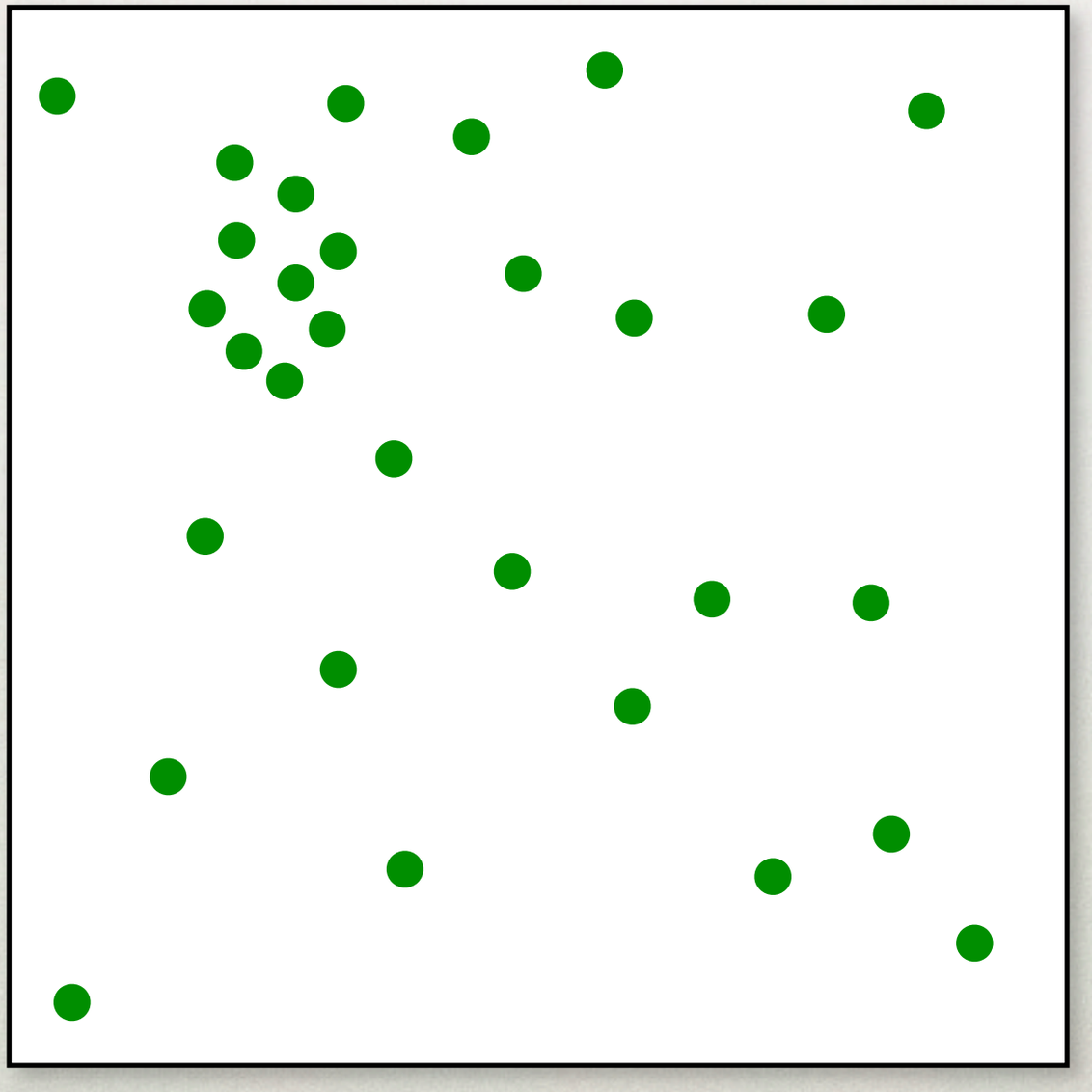

Volumetric Photon Mapping

Conventional Radiance Estimate

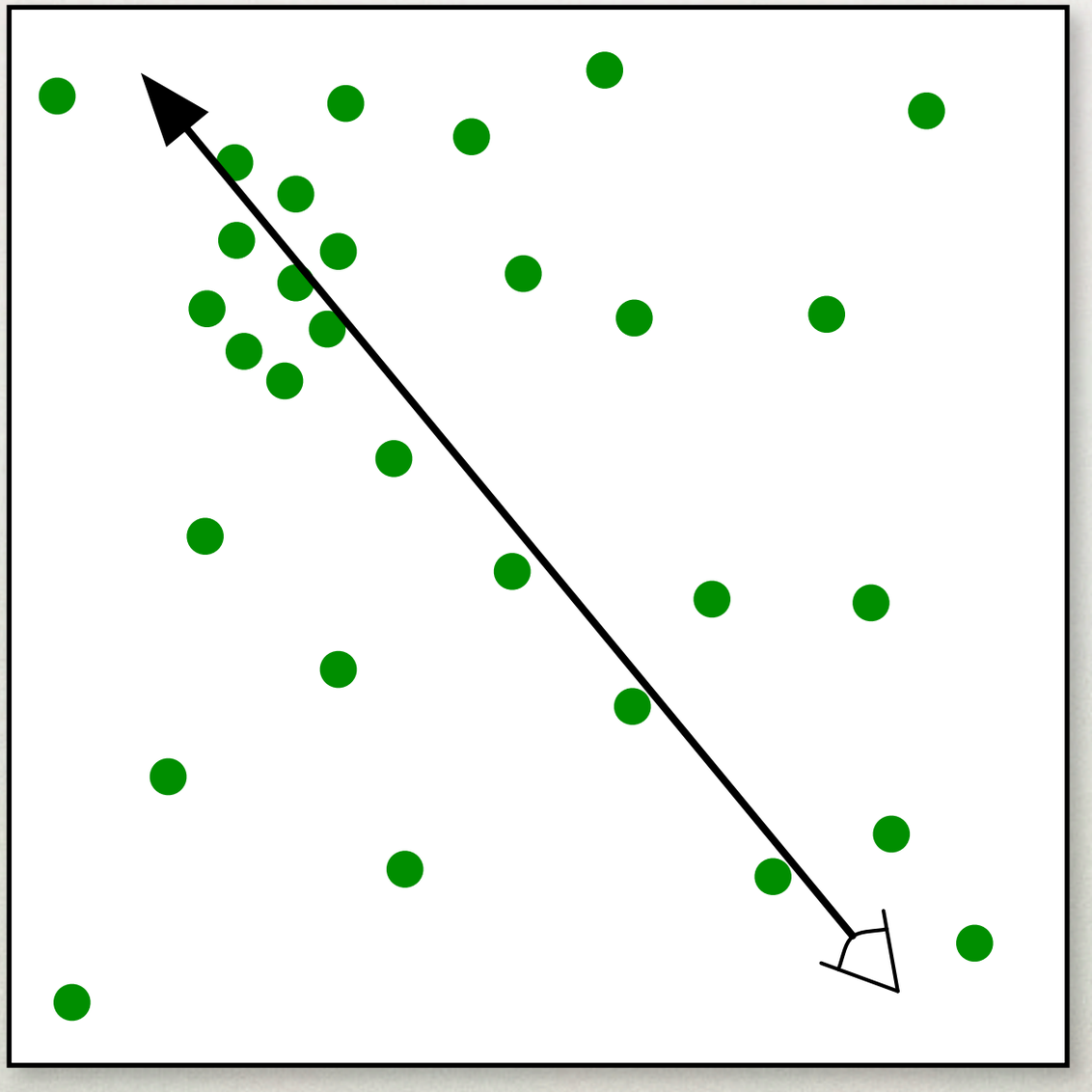

Volumetric Photon Mapping

Conventional Radiance Estimate

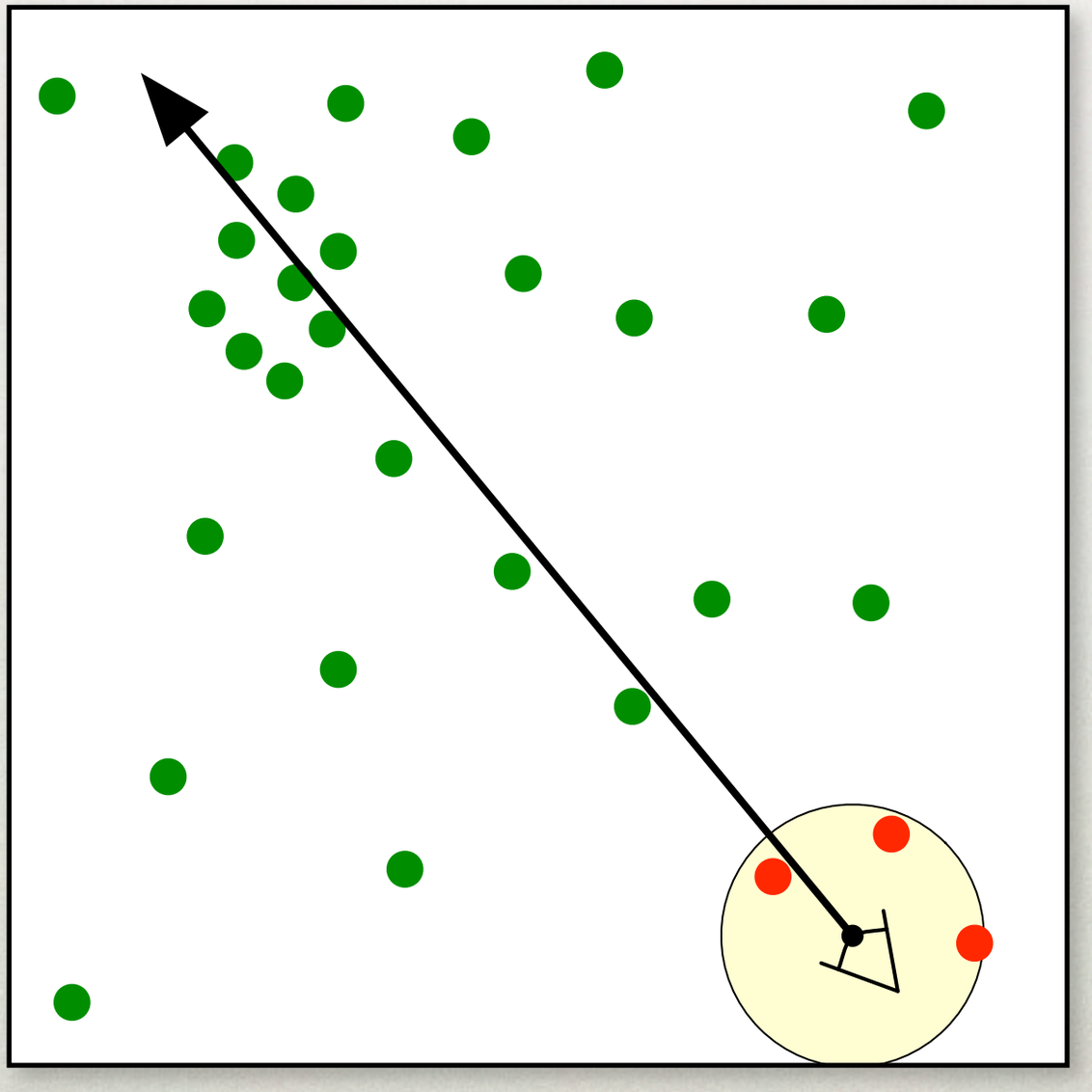

Volumetric Photon Mapping

Conventional Radiance Estimate

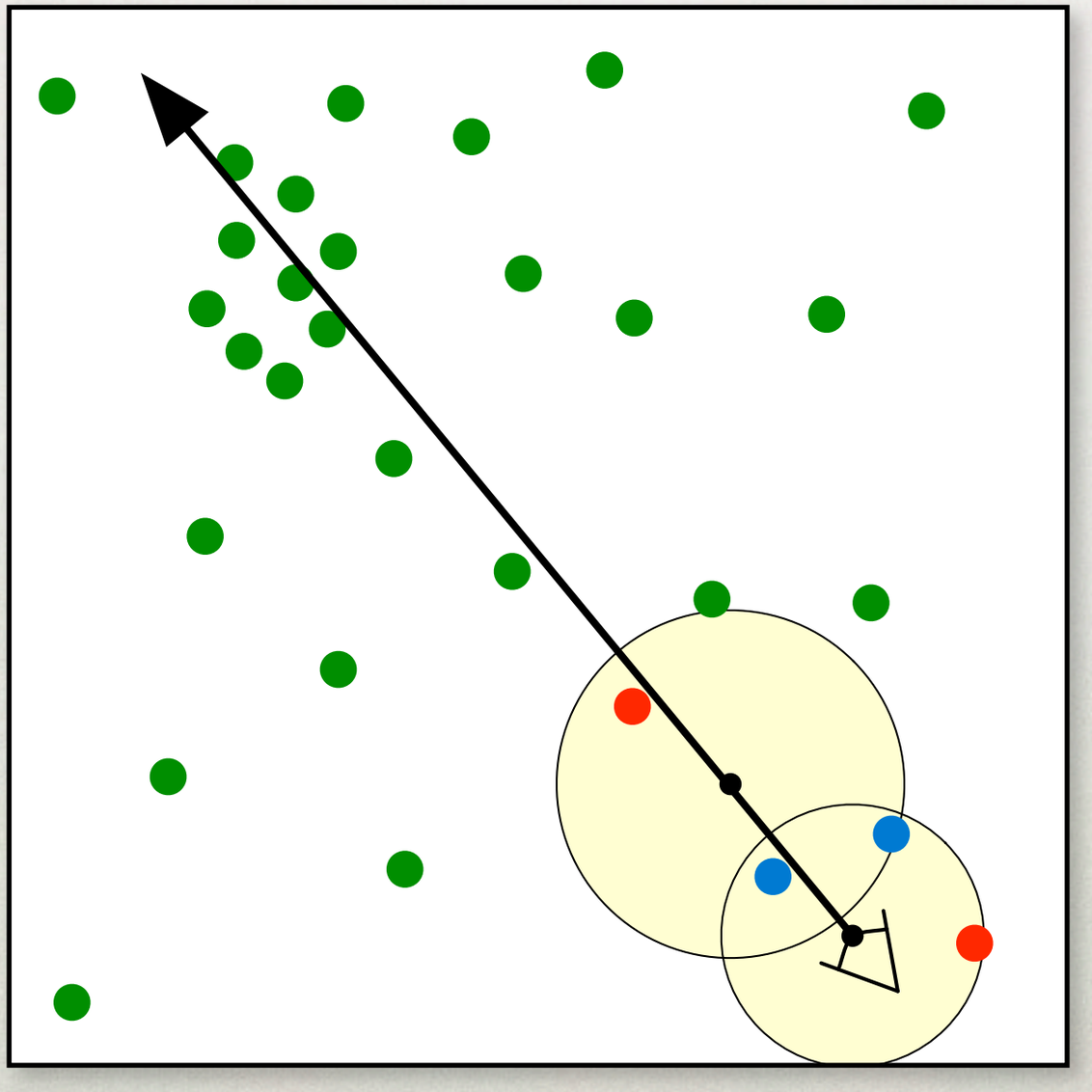

Volumetric Photon Mapping

Conventional Radiance Estimate

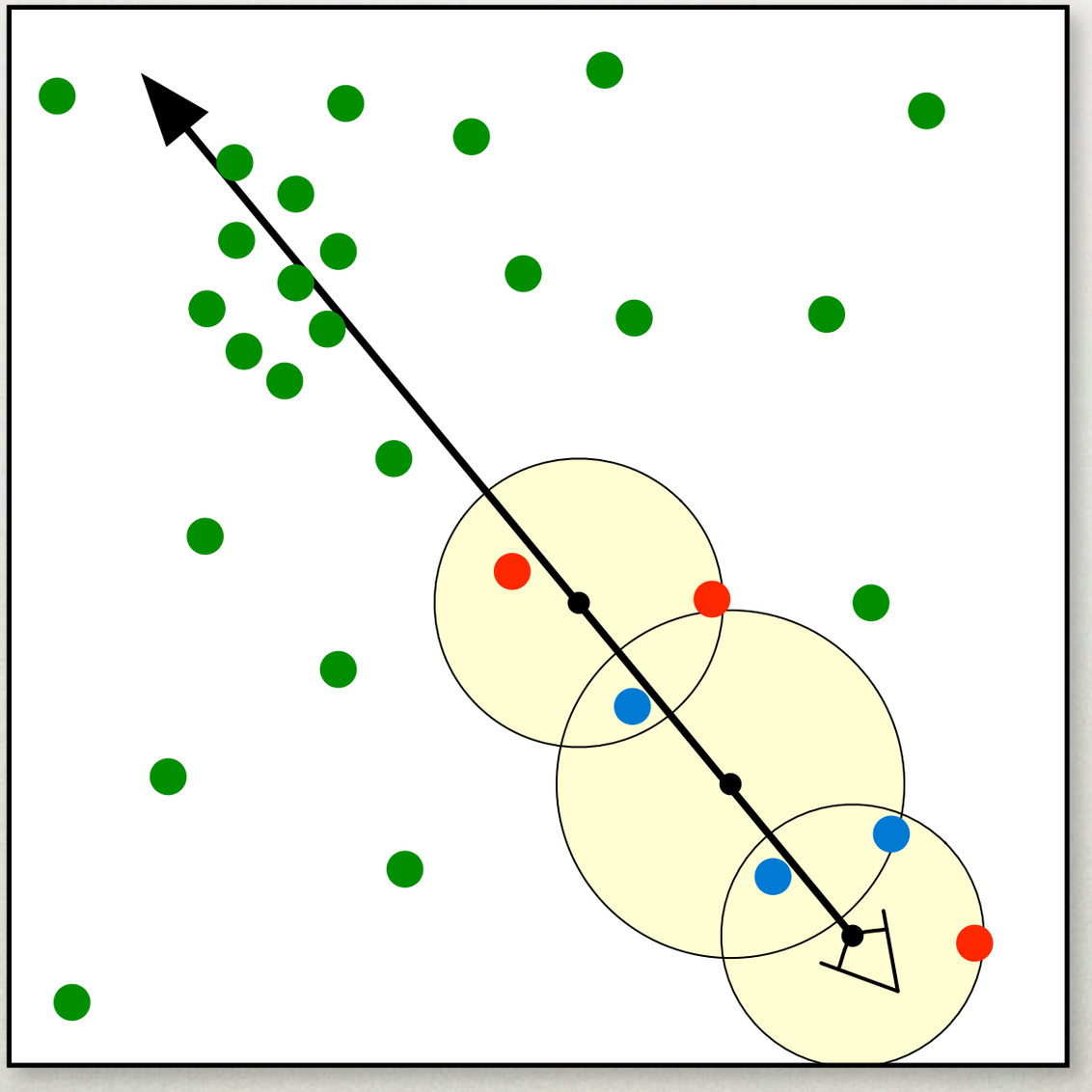

Volumetric Photon Mapping

Conventional Radiance Estimate

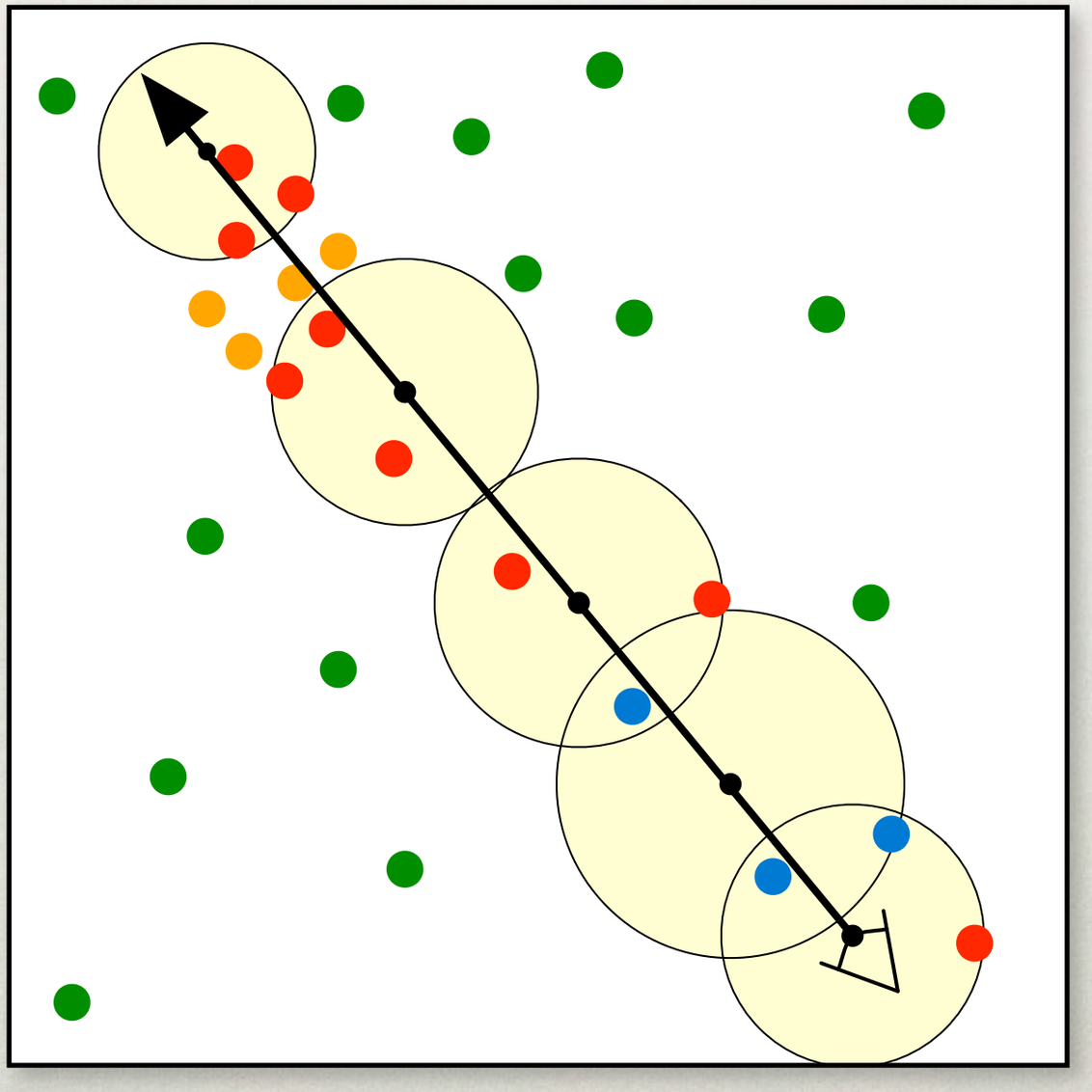

Drawbacks

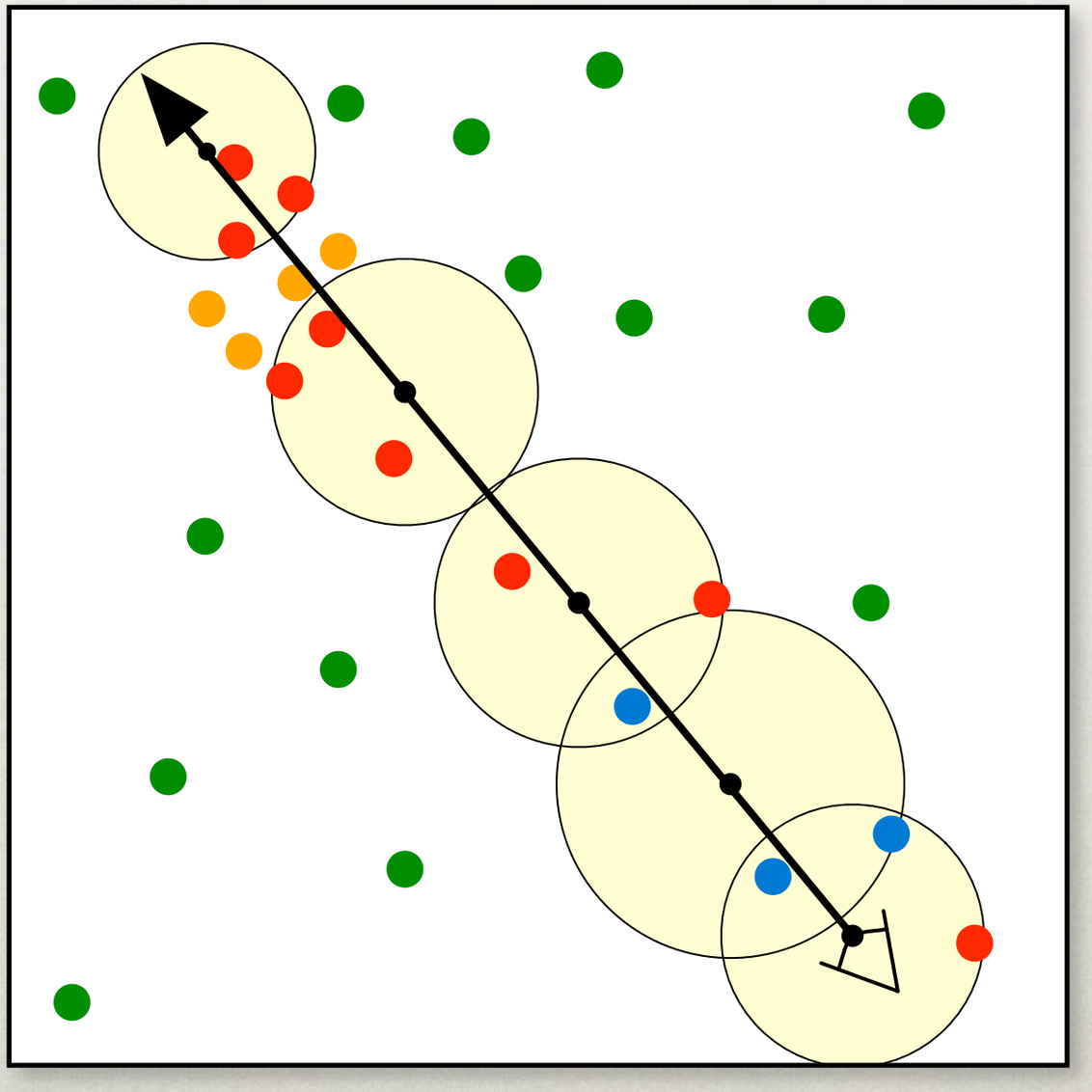

Drawbacks

- Radiance estimation is expensive
  - Requires range search in photon map
  - Performed numerous times per ray

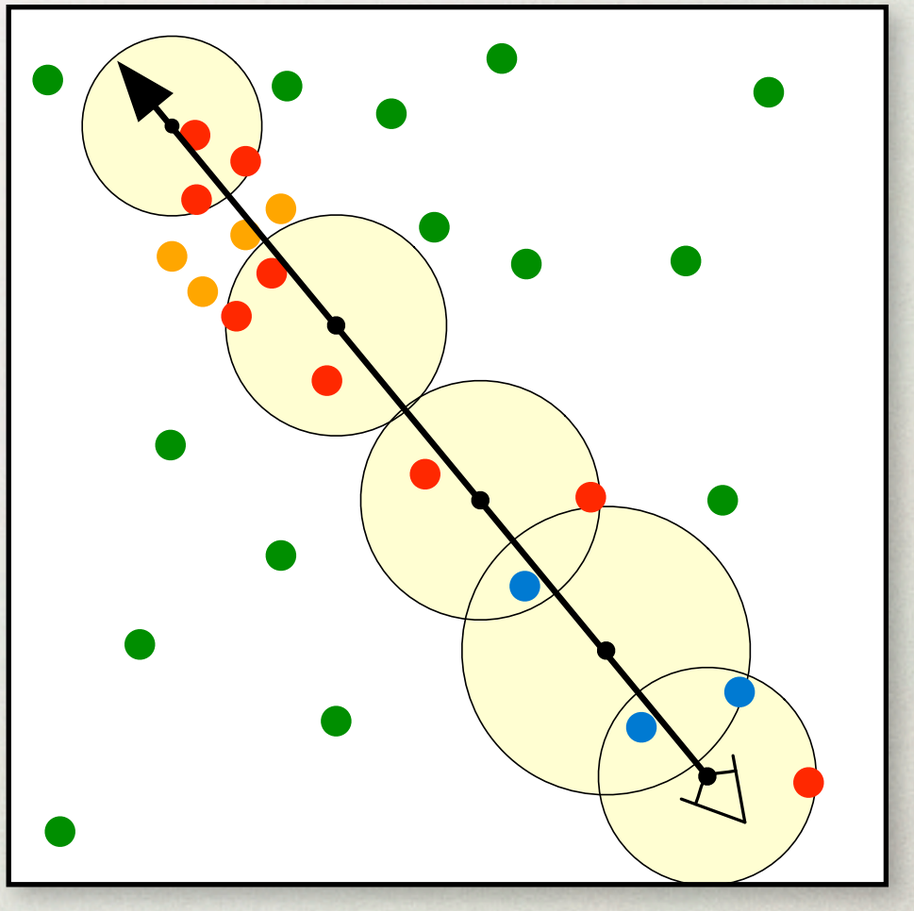

Drawbacks

Large Step-size

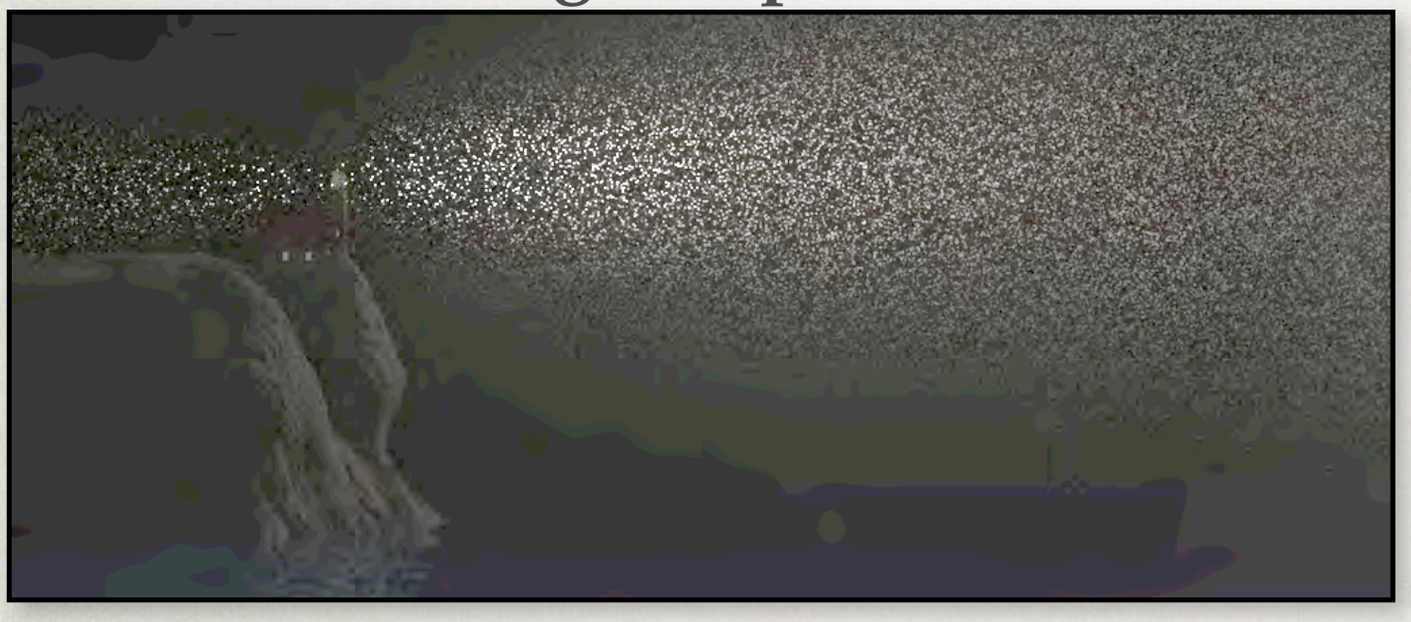

Drawbacks

Large Step-size

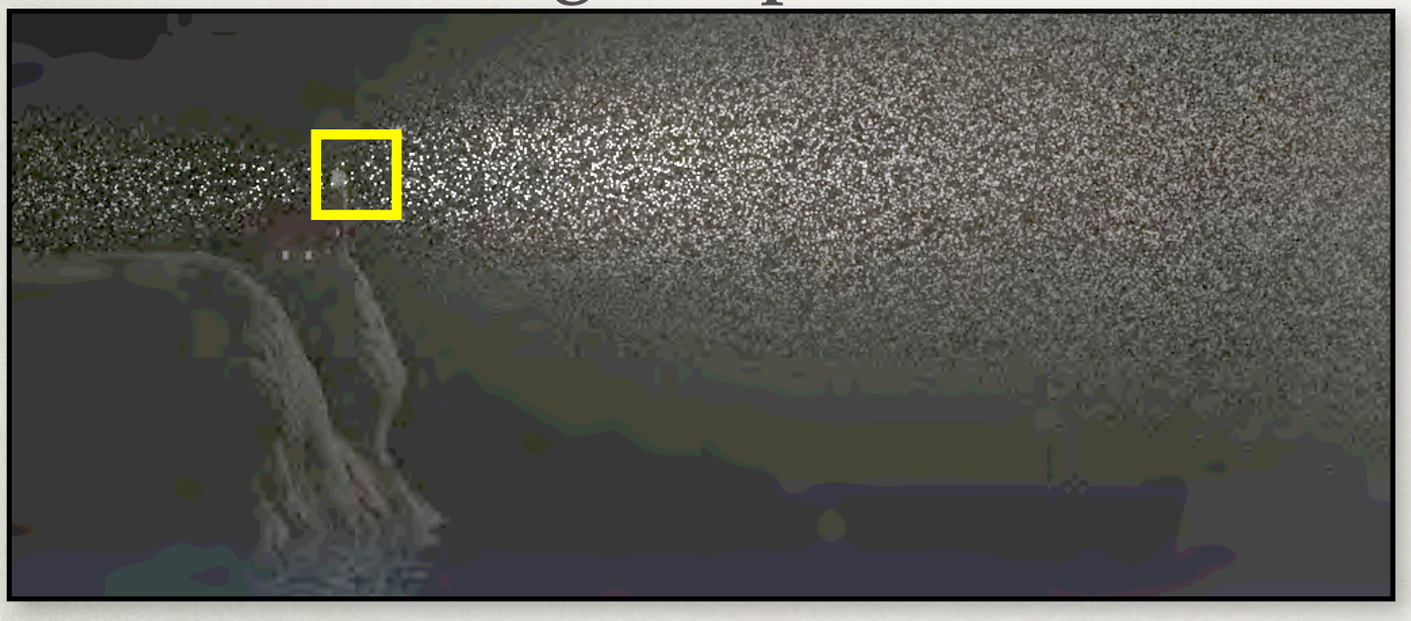

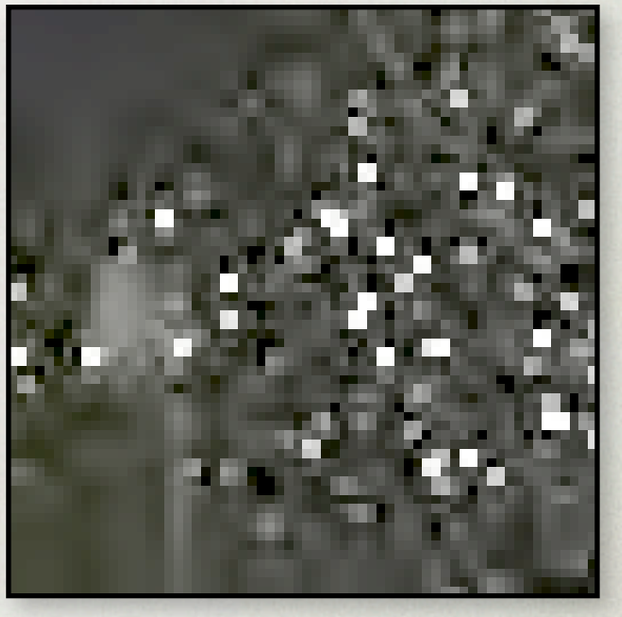

Drawbacks

Large Step-size

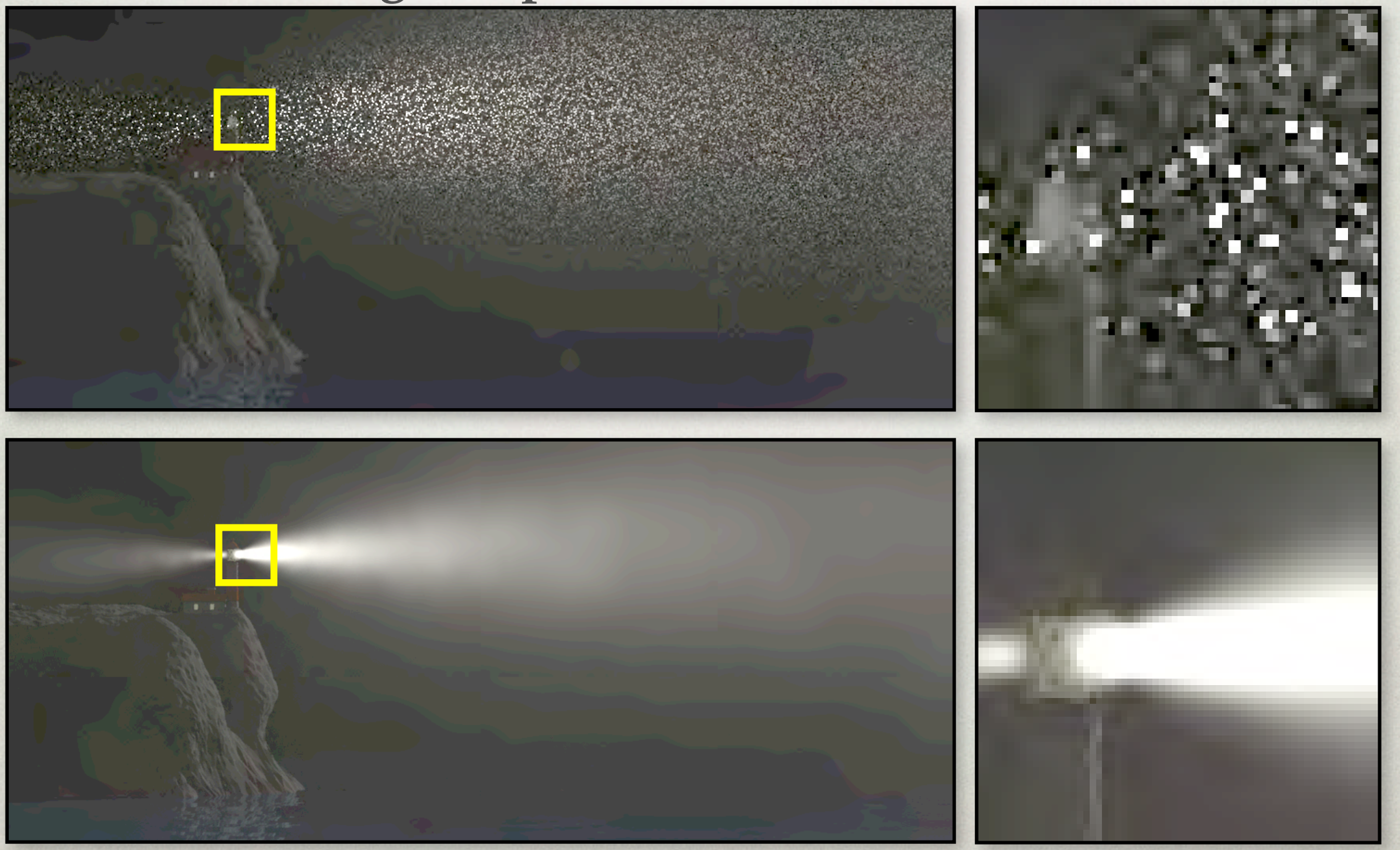

Very Small Step-size

Volumetric Photon Mapping

Conventional Radiance Estimate

$$L(\mathbf{x}, \vec{\omega}) \approx T_r(\mathbf{x} \leftrightarrow \mathbf{x}_s) L(\mathbf{x}_s, \vec{\omega}) + \left(\sum_{t=0}^{S-1} T_r(\mathbf{x} \leftrightarrow \mathbf{x}_t) \sigma_s(\mathbf{x}_t) L_i(\mathbf{x}_t, \vec{\omega}) \Delta_t \right)$$

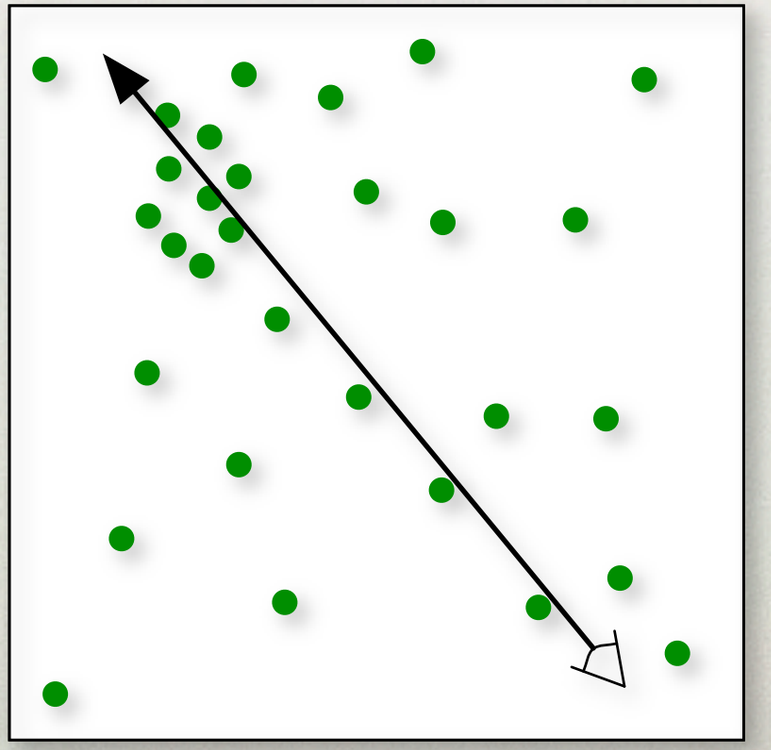

Volumetric Photon Mapping

Conventional Radiance Estimate

$$L(\mathbf{x},\vec{\omega}) \approx T_r(\mathbf{x}\leftrightarrow\mathbf{x}_s)L(\mathbf{x}_s,\vec{\omega}) + \left(\sum_{t=0}^{S-1} T_r(\mathbf{x}\leftrightarrow\mathbf{x}_t)\sigma_s(\mathbf{x}_t)\boxed{L_i(\mathbf{x}_t,\vec{\omega})}\Delta_t\right)$$

$$\boxed{L_i(\mathbf{x}_t,\vec{\omega})} \approx \sum_{p=1}^{n} \frac{p(\mathbf{x}_t,\vec{\omega},\vec{\omega}_p)\Delta\Phi_p}{\frac{4}{3}\pi r^3}$$

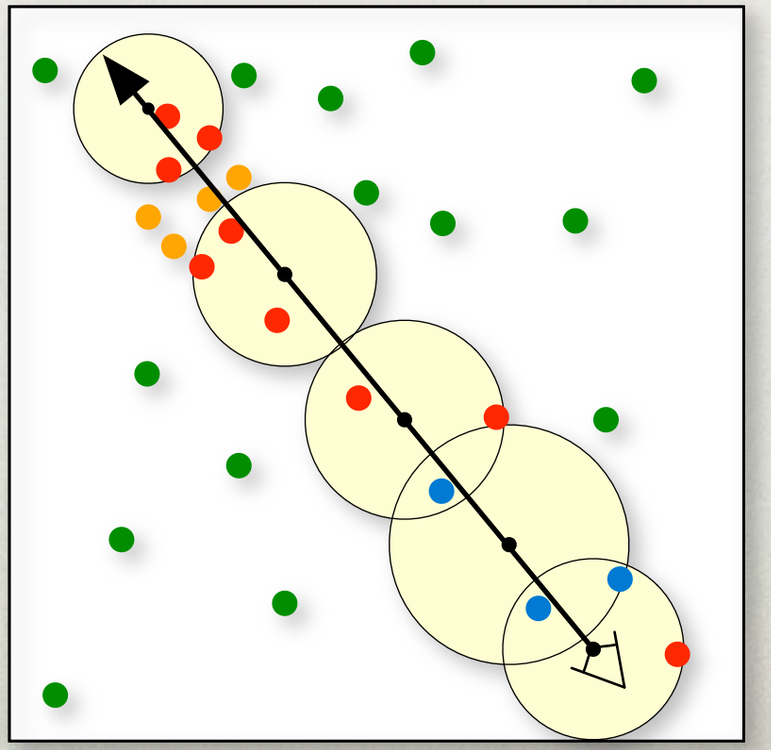

Volumetric Photon Mapping

Conventional Radiance Estimate

$$L(\mathbf{x},\vec{\omega}) \approx T_r(\mathbf{x}\leftrightarrow\mathbf{x}_s)L(\mathbf{x}_s,\vec{\omega}) + \left(\sum_{t=0}^{s-1} T_r(\mathbf{x}\leftrightarrow\mathbf{x}_t)\sigma_s(\mathbf{x}_t)L_i(\mathbf{x}_t,\vec{\omega})\Delta_t\right)$$

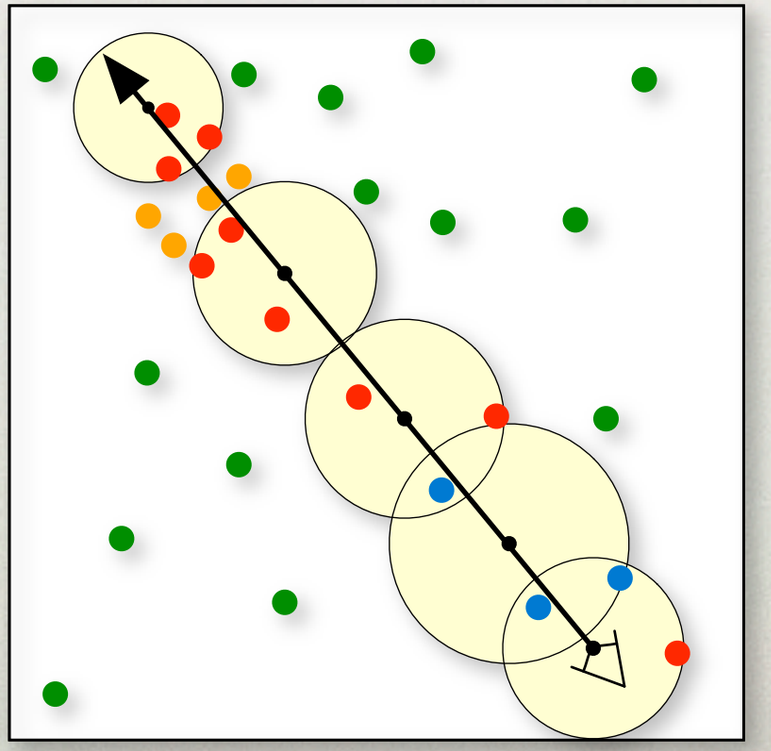

Volumetric Photon Mapping

Beam Radiance Estimate

$$L(\mathbf{x}, \vec{\omega}) \approx T_r(\mathbf{x} \leftrightarrow \mathbf{x}_s) L(\mathbf{x}_s, \vec{\omega}) + L_b(\mathbf{x}, \vec{\omega})$$

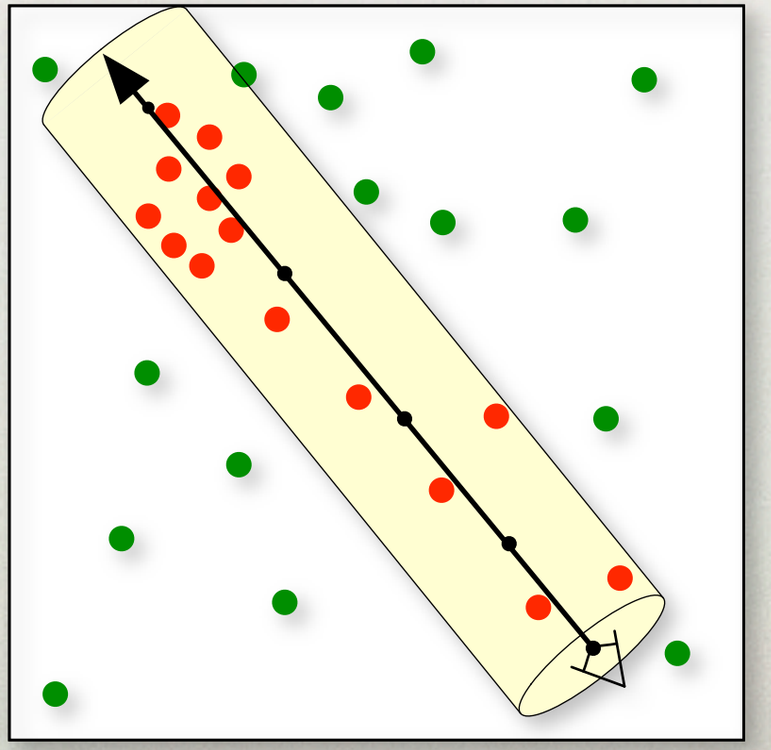

Volumetric Photon Mapping

Beam Radiance Estimate

$$L(\mathbf{x}, \vec{\omega}) \approx T_r(\mathbf{x} \leftrightarrow \mathbf{x}_s) L(\mathbf{x}_s, \vec{\omega}) + L_b(\mathbf{x}, \vec{\omega})$$

$$L_b(\mathbf{x}, \vec{\omega}) = \frac{1}{N} \sum_{i=1}^{N} K_i T_r(\mathbf{x} \leftrightarrow \mathbf{x}_i) \sigma_s(\mathbf{x}_i) p(\mathbf{x}_i, \vec{\omega}, \vec{\omega}_i) \alpha_i$$

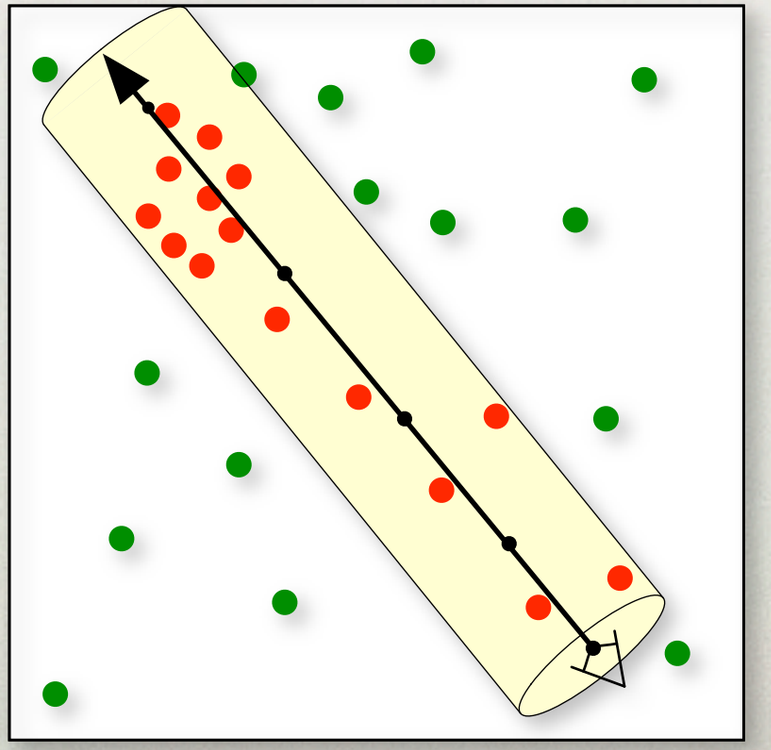

Adaptive Radius Comparison

Beam Estimate

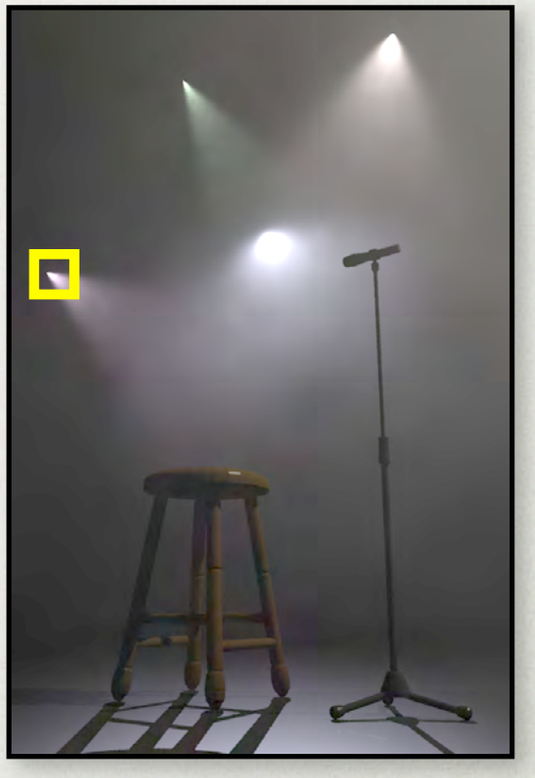

(6:22)

Adaptive Radius Comparison

Conv. Estimate Beam Estimate

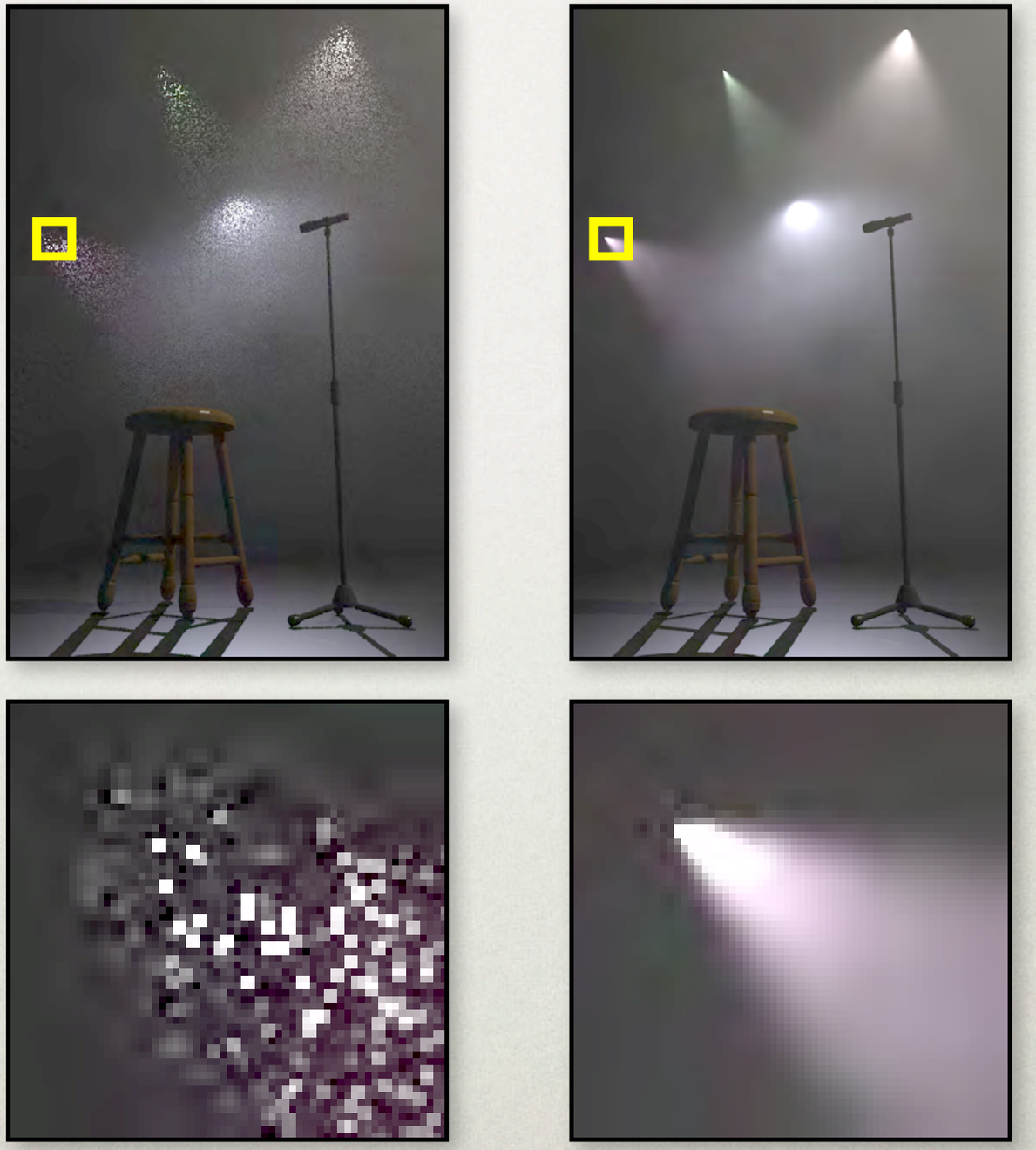

(6:38) (6:22)

Adaptive Radius Comparison

Conv. Estimate | Conv. Estimate | Beam Estimate

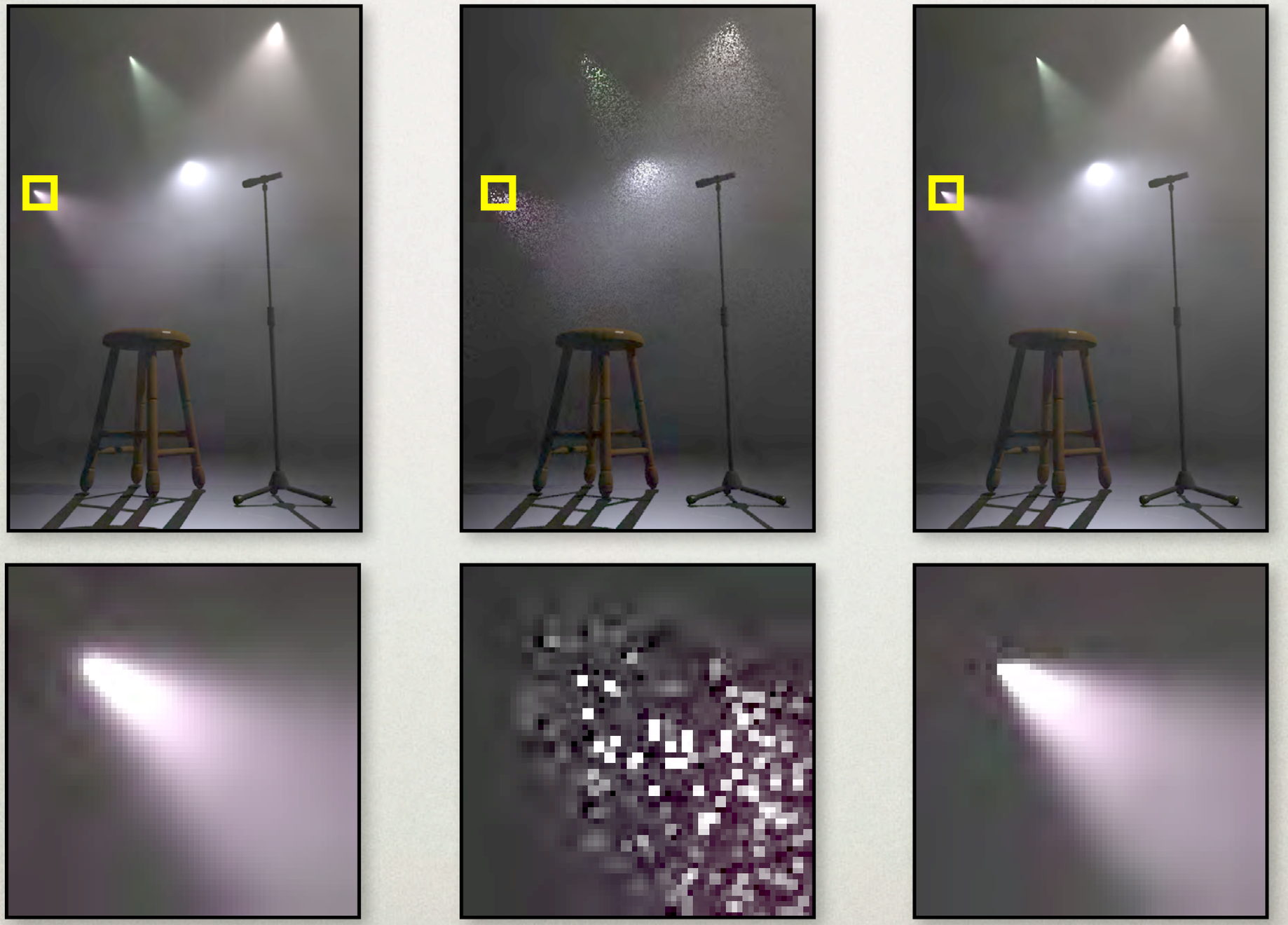

(∞) | (6:38) | (6:22)

Smoky Cornell Box

Conv. Estimate

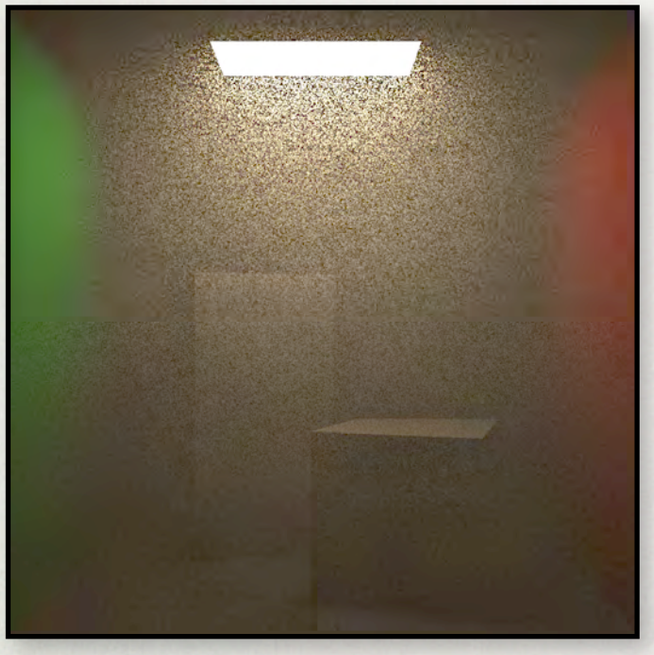

Beam Estimate

Smoky Cornell Box

Conv. Estimate

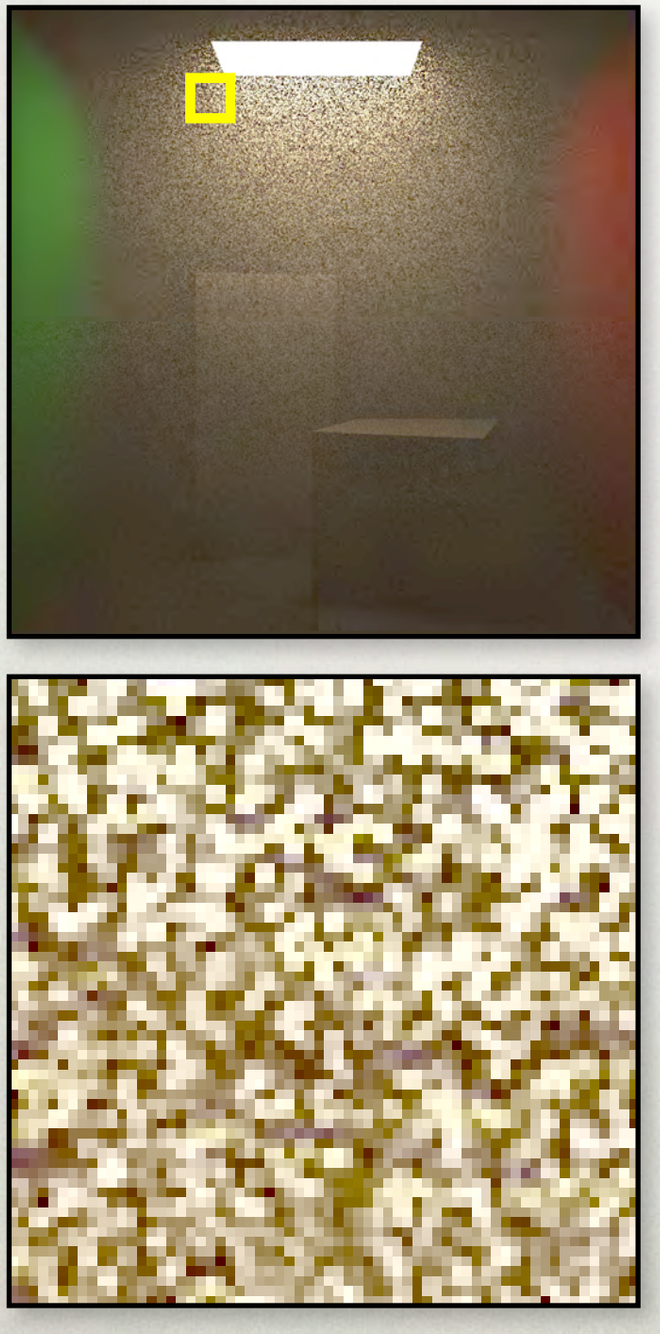

(4:03)

Beam Estimate

(3:35)

Lighthouse

Beam Estimate

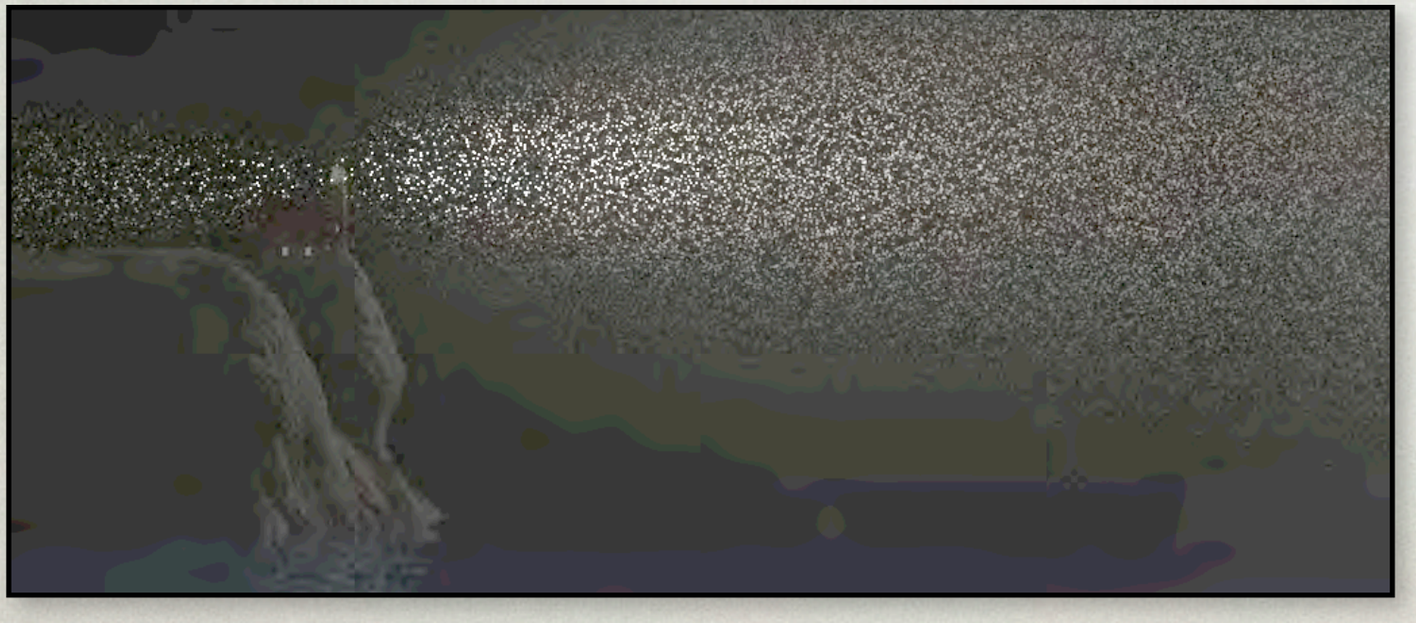

Conventional Estimate

Lighthouse

Beam Estimate (1:05)

Conventional Estimate (1:12)

Cars on Foggy Street

Beam Estimate

Conventional Estimate

Cars on Foggy Street

Beam Estimate (1:53)

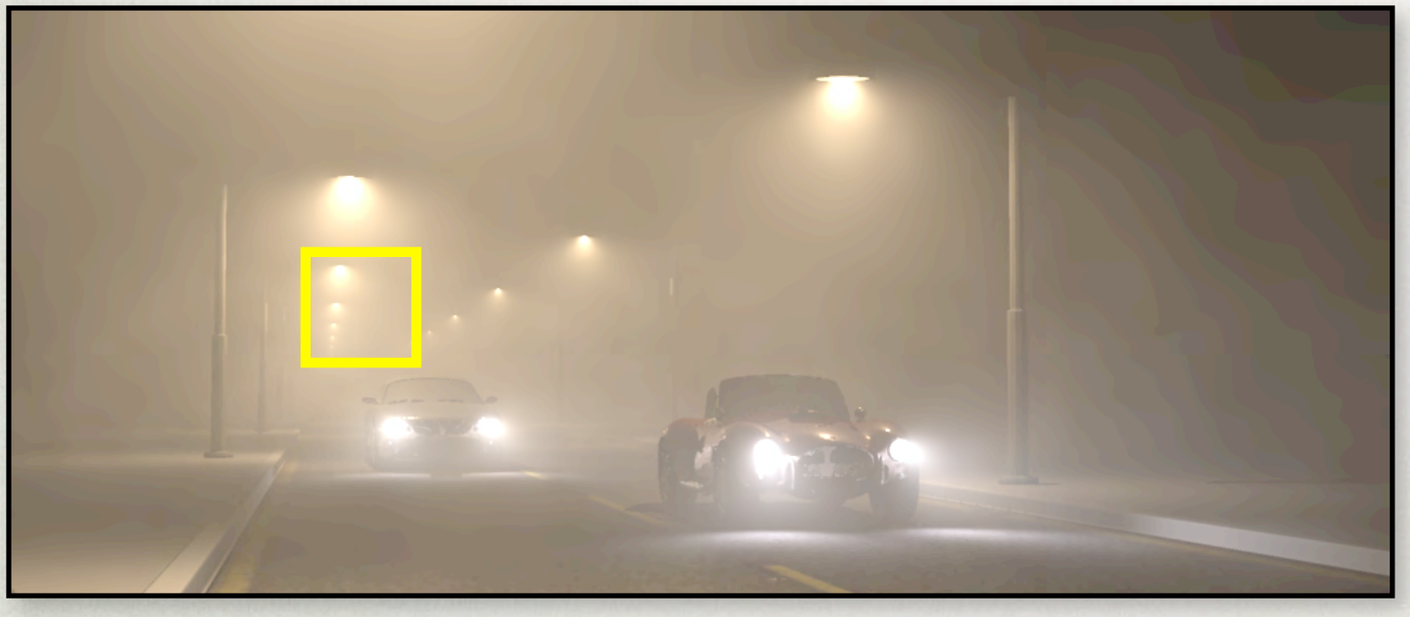

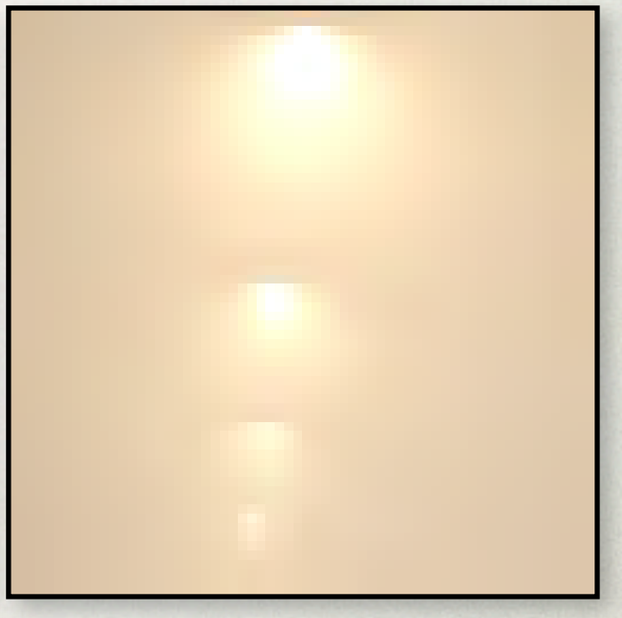

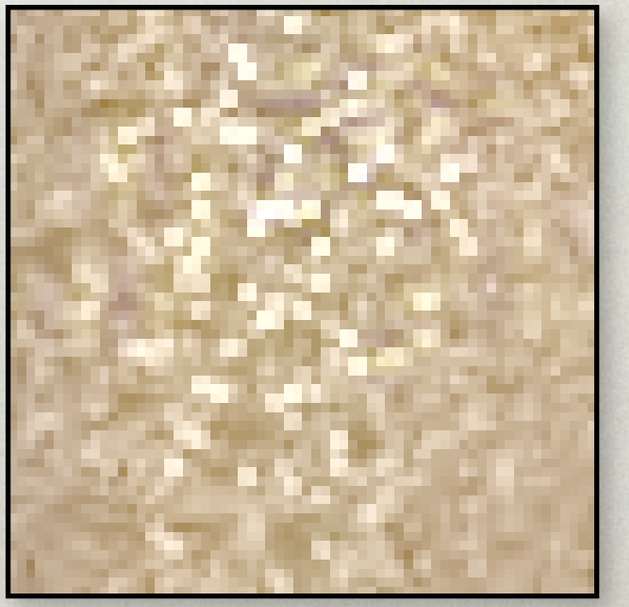

Conventional Estimate (2:02)

For More Information

Physically Based Rendering.
Matt Pharr and Greg Humphreys

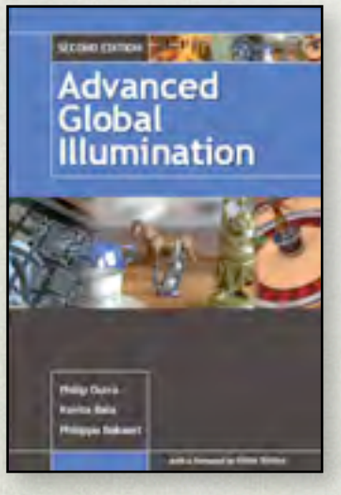

Advanced Global Illumination.
Philip Dutre, Kavita Bala, and Philippe Bekaert

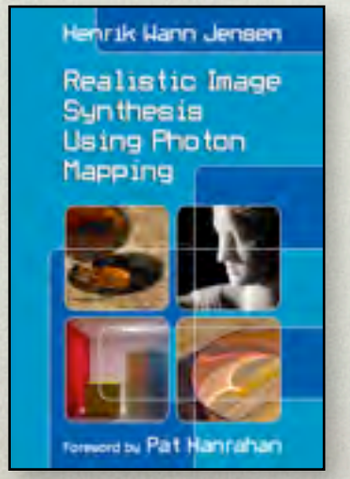

Realistic Image Synthesis Using Photon Mapping.
Henrik Wann Jensen

Questions?

Inelastic Scattering

Diego Gutiérrez

Scattering

Scattering

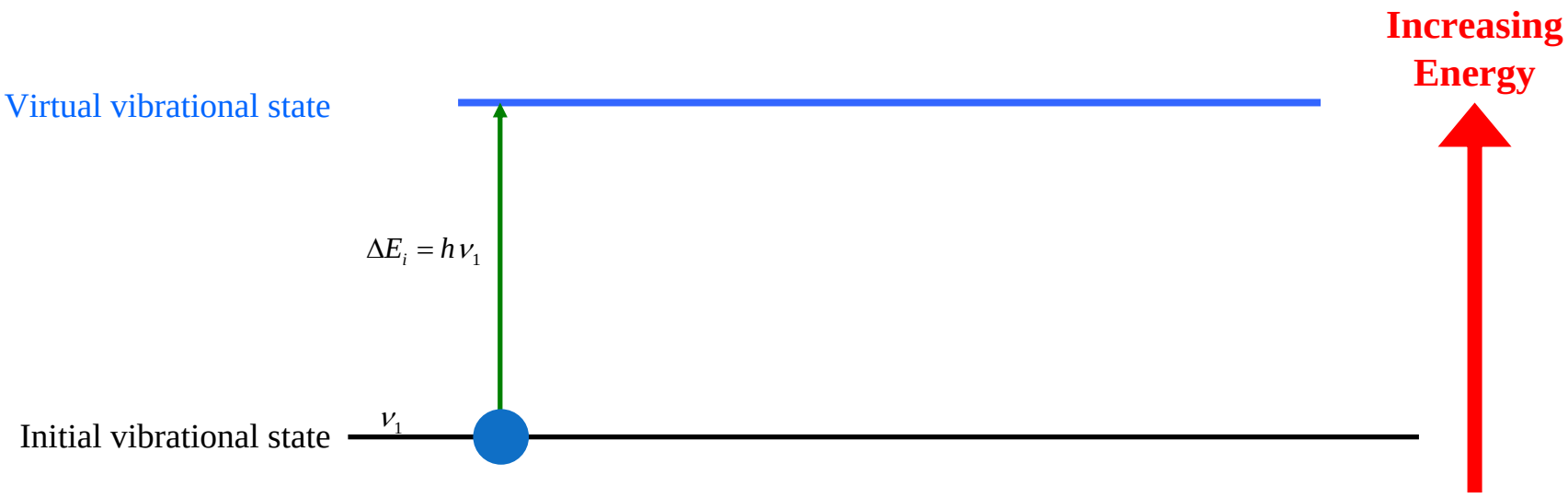

Atom, molecule, ion….

Scattering

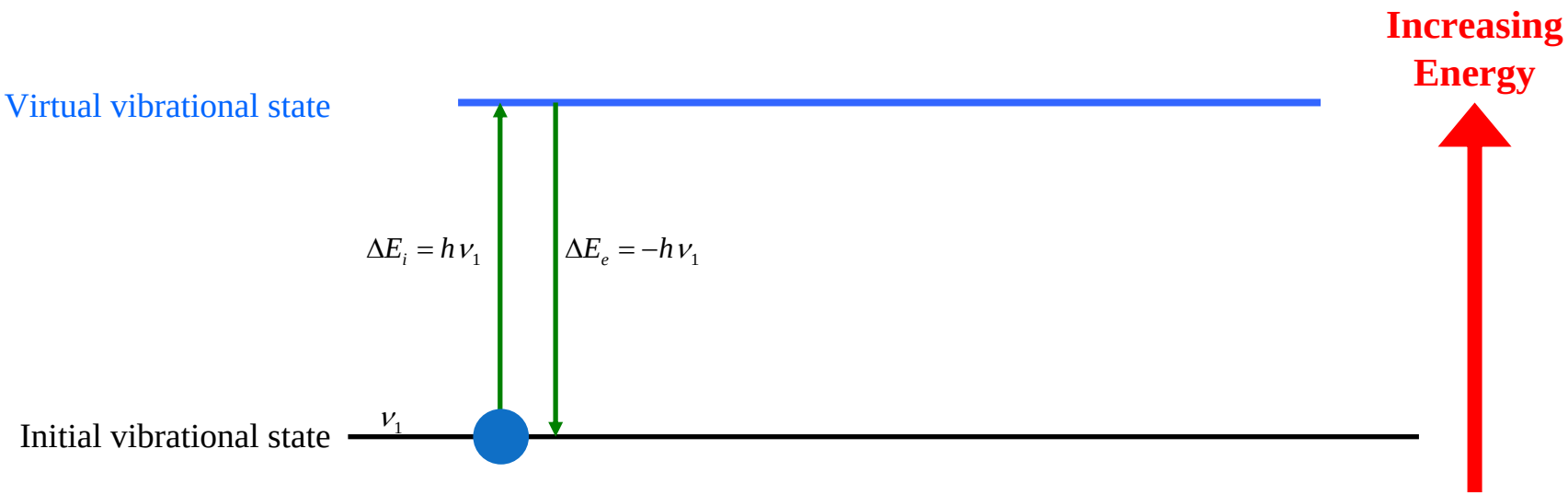
Increasing Energy
Virtual vibrational state
$\Delta E_i = h\nu_1$
$\Delta E_e = -h\nu_1$
ν_1
Initial vibrational state

Scattering

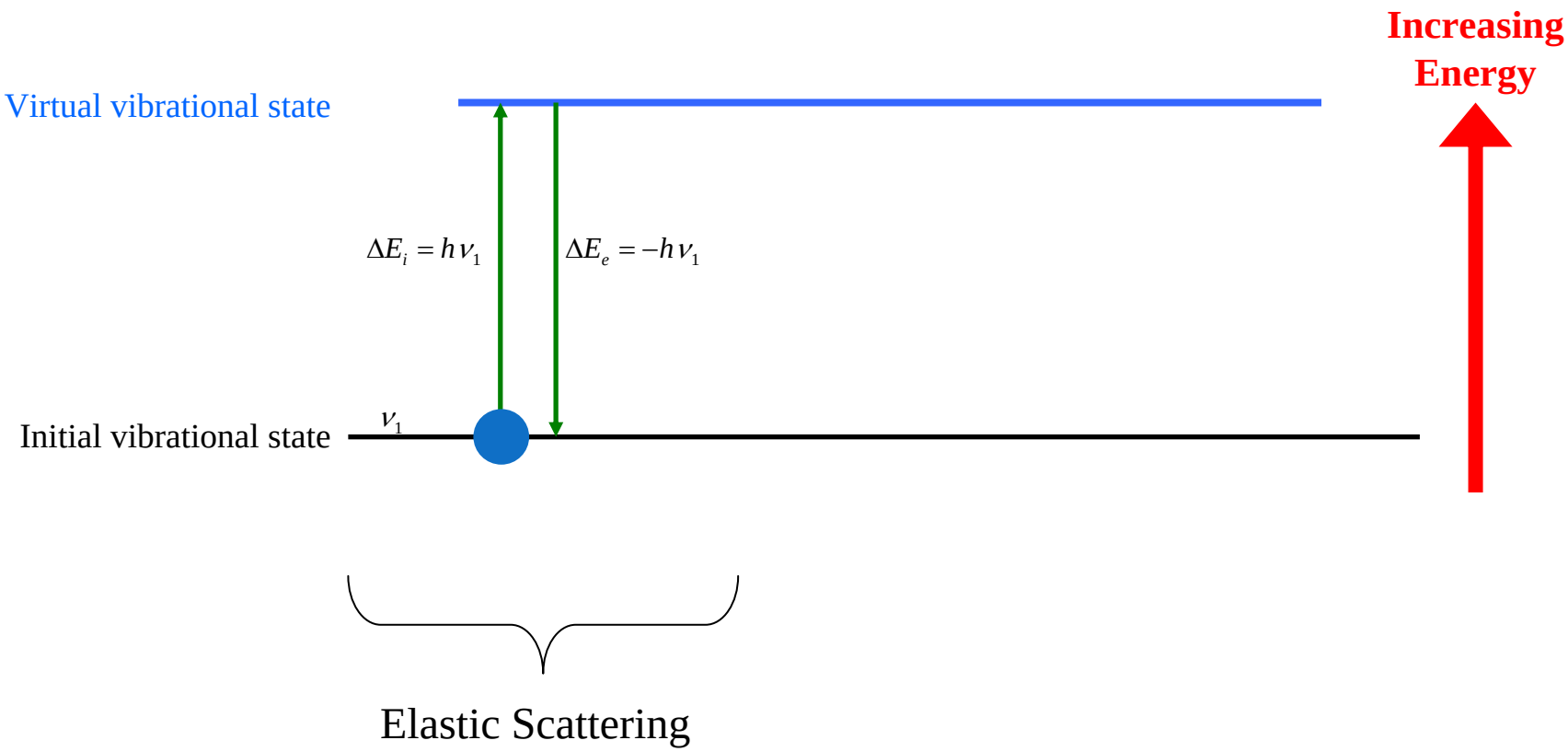
Increasing Energy
Virtual vibrational state
$\Delta E_i = h\nu_1$
$\Delta E_e = -h\nu_1$
ν_1
Initial vibrational state
Elastic Scattering

Scattering

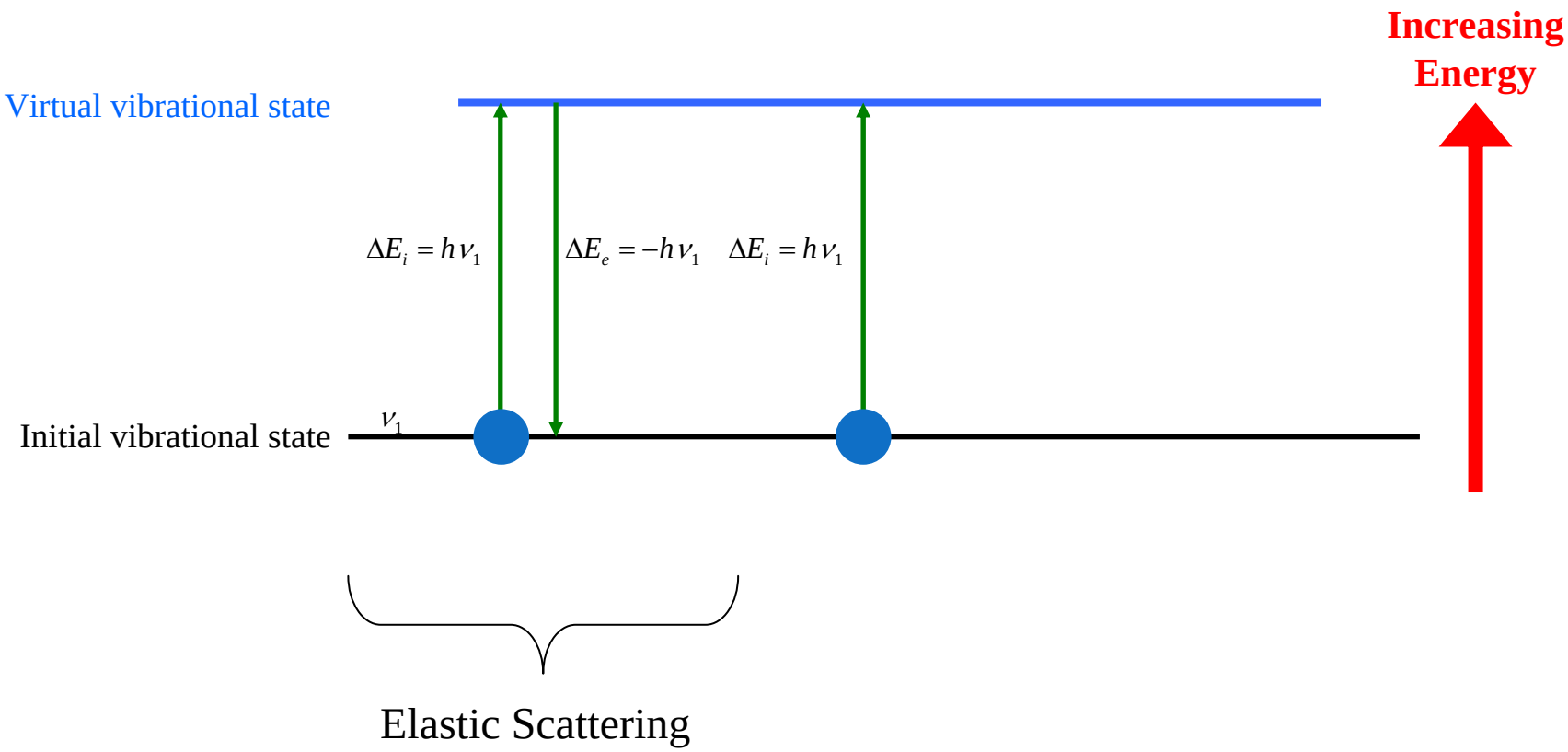
Increasing Energy
Virtual vibrational state
$\Delta E_i = h\nu_1$
$\Delta E_e = -h\nu_1$
$\Delta E_i = h\nu_1$
Initial vibrational state
ν_1
Elastic Scattering

Scattering

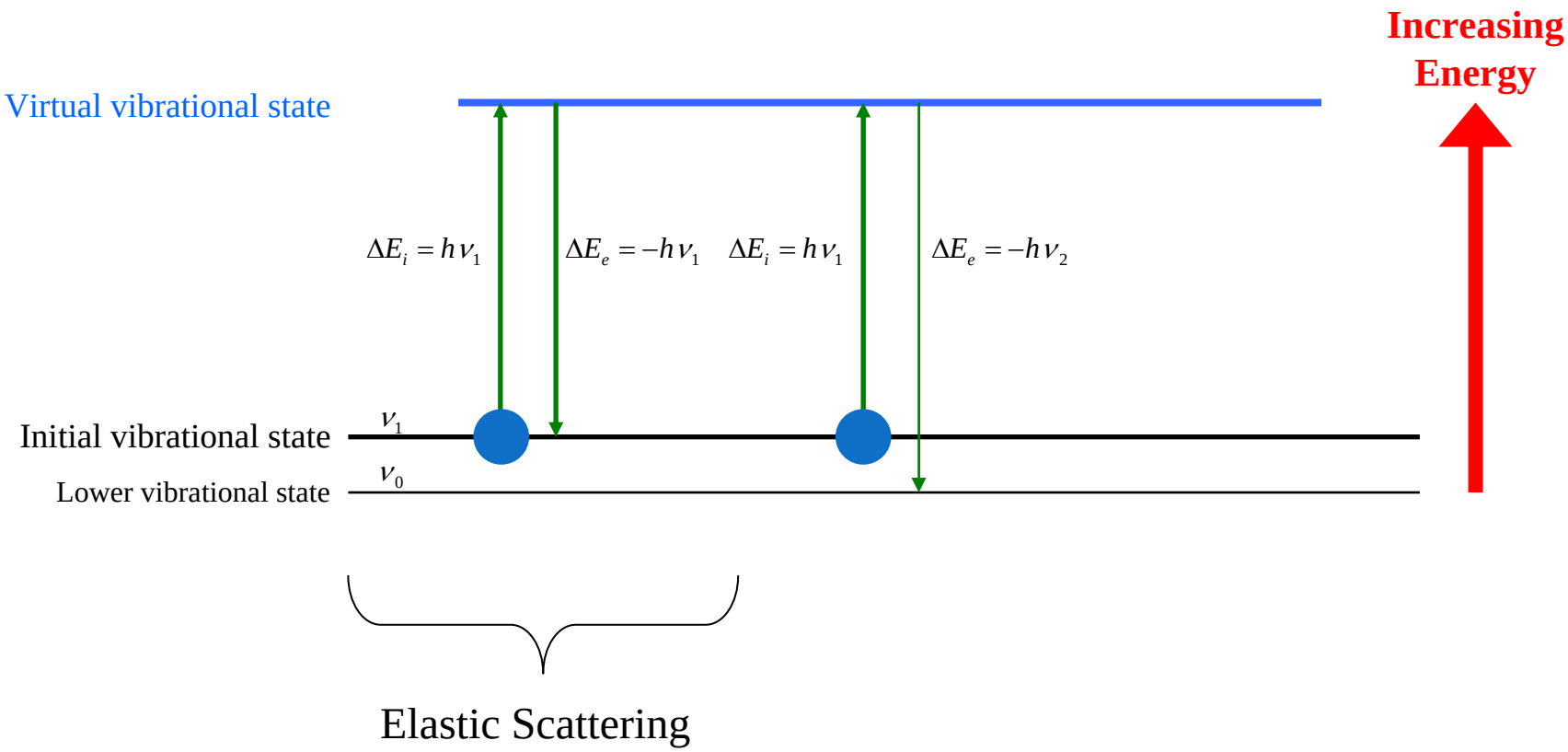
Increasing Energy
Virtual vibrational state
$\Delta E_i = h\nu_1$
$\Delta E_e = -h\nu_1$
$\Delta E_i = h\nu_1$
$\Delta E_e = -h\nu_2$
Initial vibrational state
ν_1
ν_0
Lower vibrational state
Elastic Scattering

Scattering

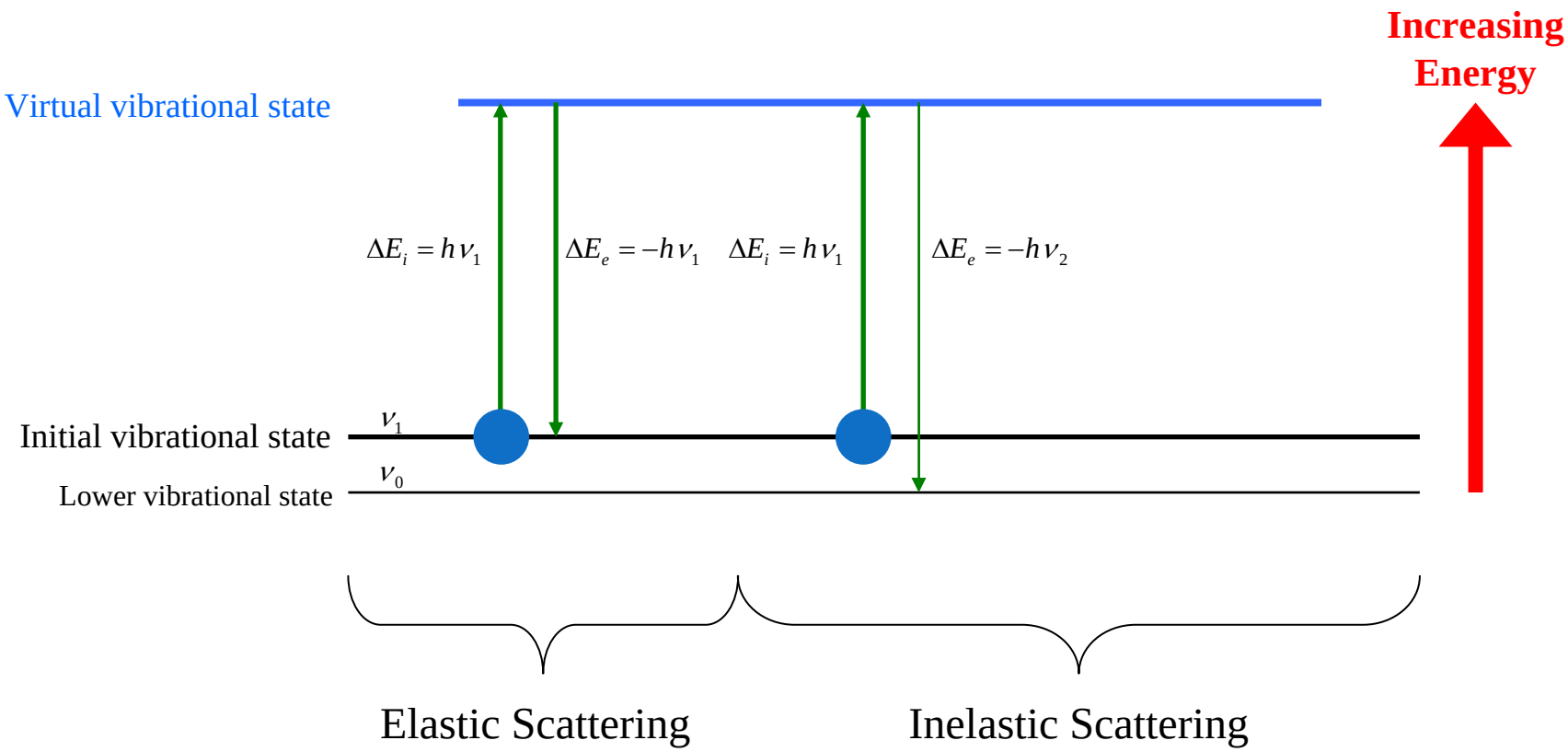
Increasing Energy
Virtual vibrational state
$\Delta E_i = h\nu_1$
$\Delta E_e = -h\nu_1$
$\Delta E_i = h\nu_1$
$\Delta E_e = -h\nu_2$
Initial vibrational state
ν_1
ν_0
Lower vibrational state
Elastic Scattering
Inelastic Scattering

Scattering

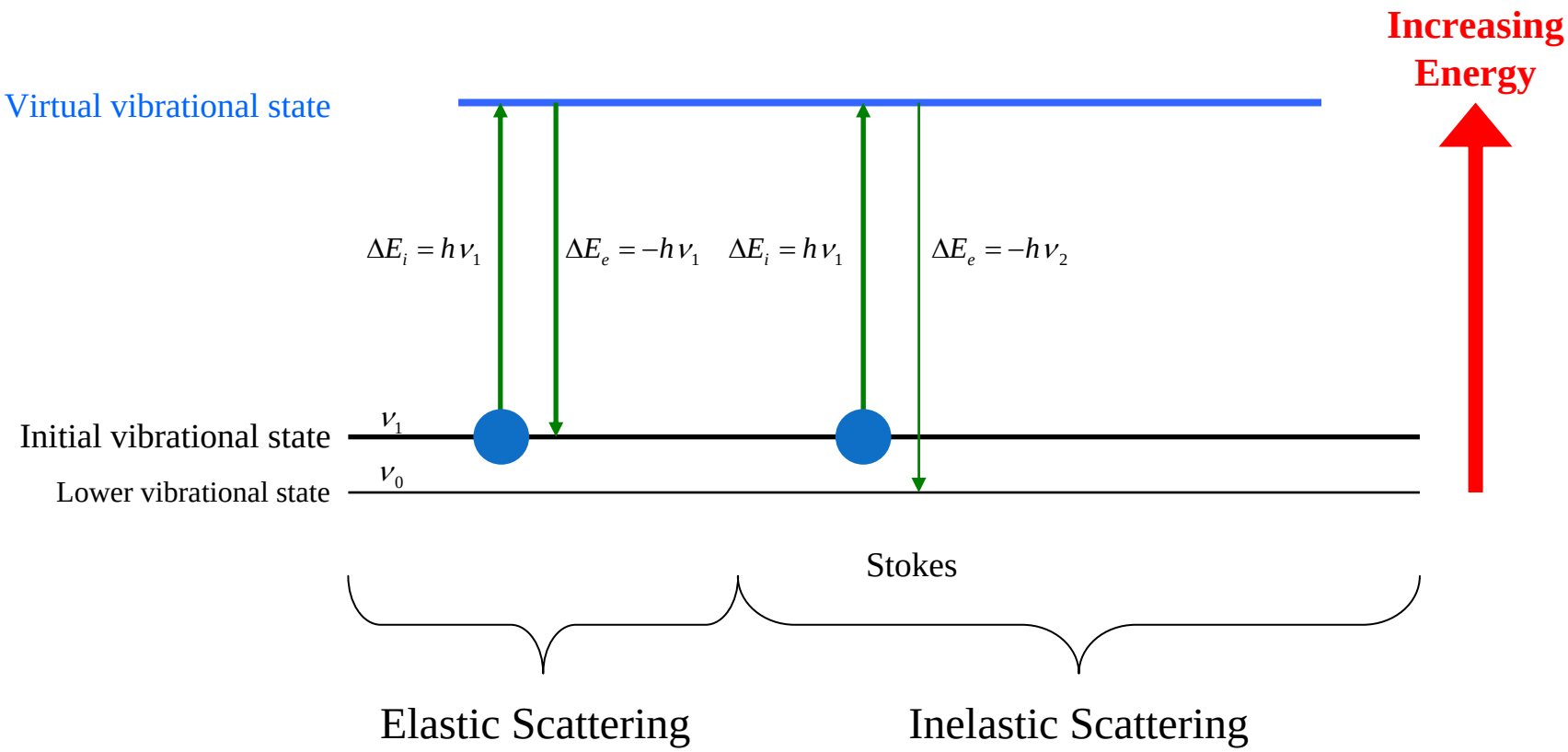
Increasing Energy
Virtual vibrational state
$\Delta E_i = h\nu_1$
$\Delta E_e = -h\nu_1$
$\Delta E_i = h\nu_1$
$\Delta E_e = -h\nu_2$
Initial vibrational state
ν_1
ν_0
Lower vibrational state
Stokes
Elastic Scattering
Inelastic Scattering

Scattering

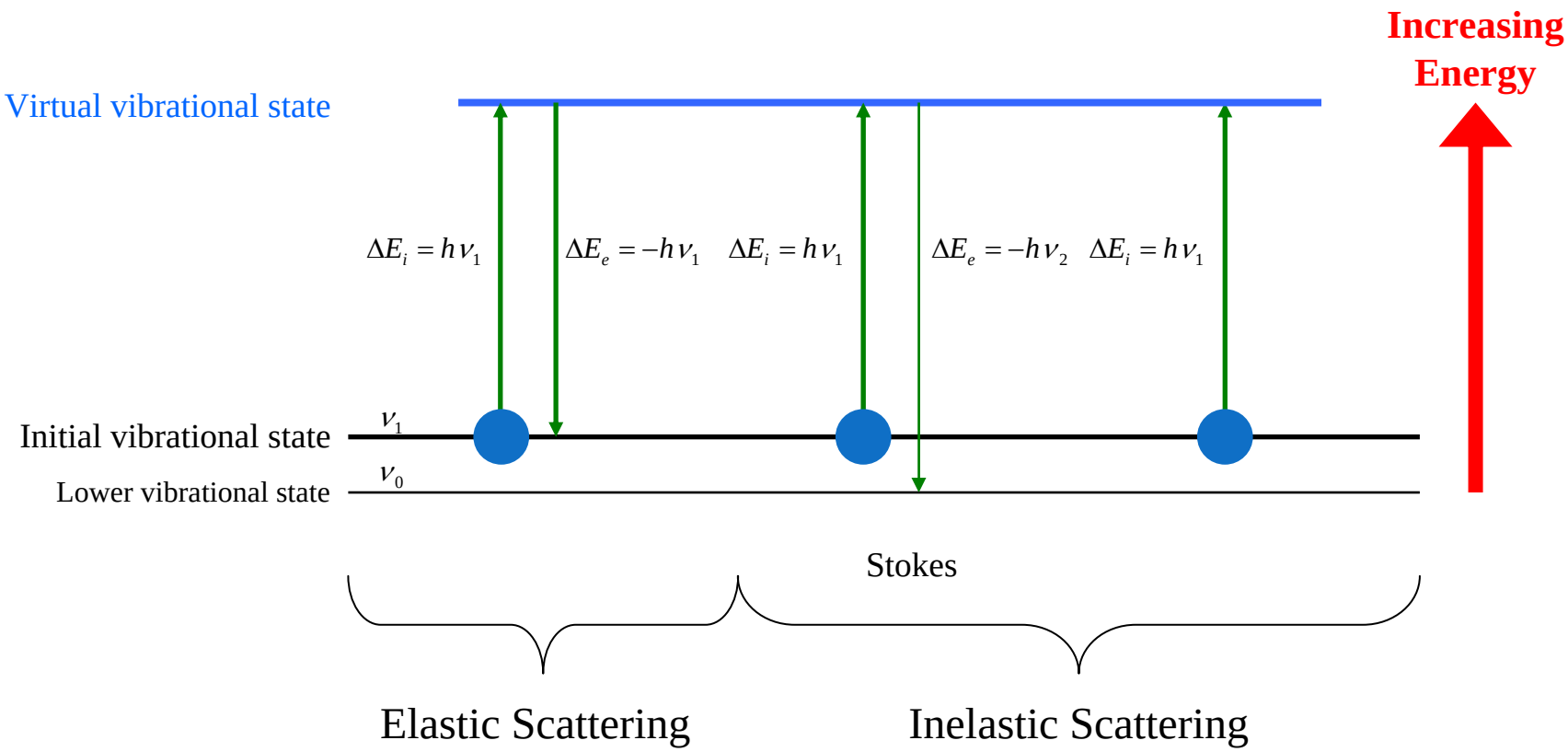
Increasing Energy
Virtual vibrational state
$\Delta E_i = h\nu_1$
$\Delta E_e = -h\nu_1$
$\Delta E_i = h\nu_1$
$\Delta E_e = -h\nu_2$
$\Delta E_i = h\nu_1$
Initial vibrational state
ν_1
ν_0
Lower vibrational state
Stokes
Elastic Scattering
Inelastic Scattering

Scattering

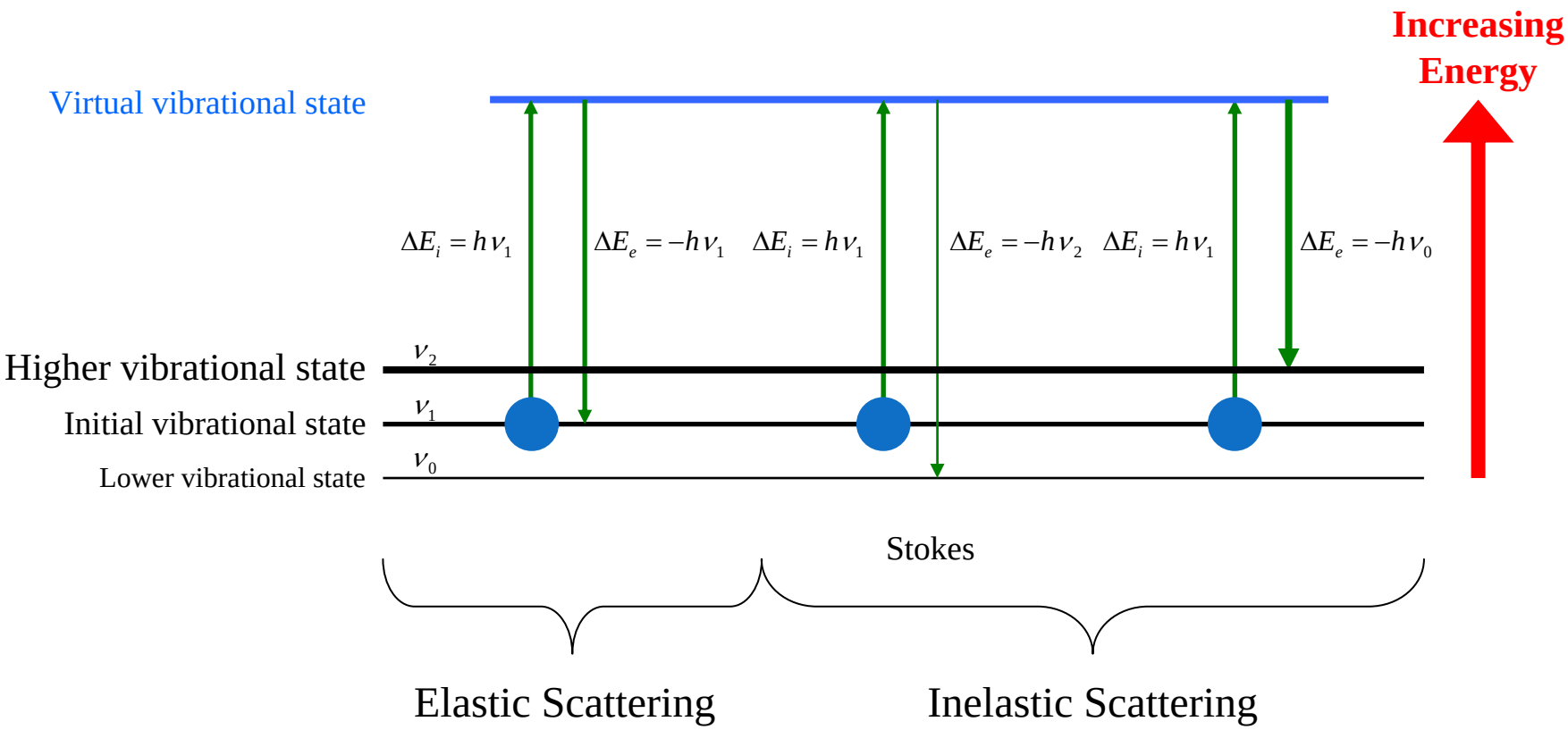
Increasing Energy
Virtual vibrational state
$\Delta E_i = h\nu_1$
$\Delta E_e = -h\nu_1$
$\Delta E_i = h\nu_1$
$\Delta E_e = -h\nu_2$
$\Delta E_i = h\nu_1$
$\Delta E_e = -h\nu_0$
Higher vibrational state
ν_2
Initial vibrational state
ν_1
Lower vibrational state
ν_0
Stokes
Elastic Scattering
Inelastic Scattering

Scattering

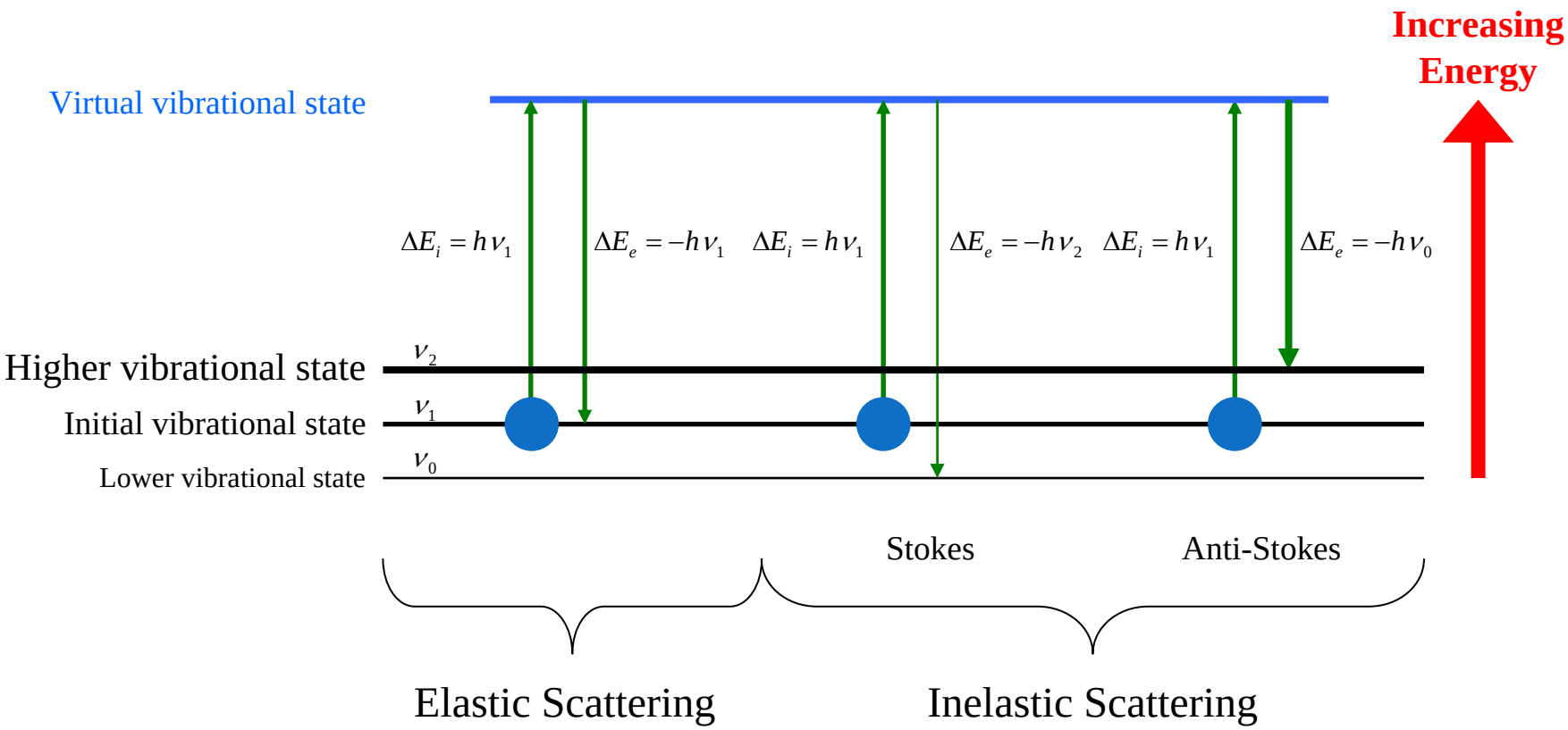
Increasing Energy
Virtual vibrational state
$\Delta E_i = h\nu_1$
$\Delta E_e = -h\nu_1$
$\Delta E_i = h\nu_1$
$\Delta E_e = -h\nu_2$
$\Delta E_i = h\nu_1$
$\Delta E_e = -h\nu_0$
Higher vibrational state
ν_2
Initial vibrational state
ν_1
Lower vibrational state
ν_0
Stokes
Anti-Stokes
Elastic Scattering
Inelastic Scattering

Scatter

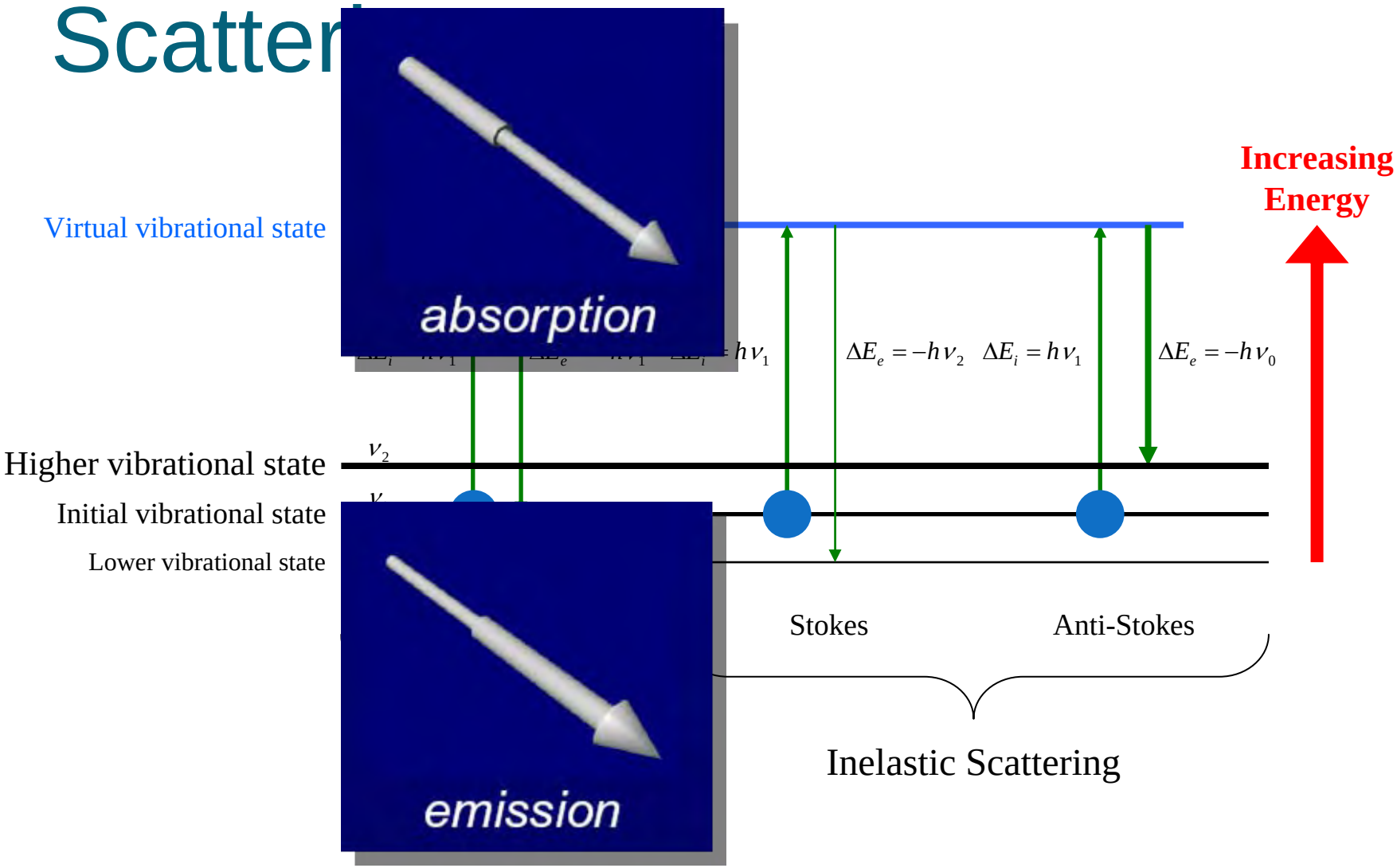
Virtual vibrational state
absorption
Increasing Energy
$\Delta E_e = -h\nu_2$
$\Delta E_i = h\nu_1$
$\Delta E_e = -h\nu_0$
Higher vibrational state
ν_2
Initial vibrational state
Lower vibrational state
Stokes
Anti-Stokes
Inelastic Scattering
emission

Inelastic scattering

It can cause very prominent effects, but has traditionally been neglected:

- It can be faked (actually, just like everything else)
- Real-world data is not easy to obtain
- It requires a spectral renderer

430nm

480nm

530nm

580nm

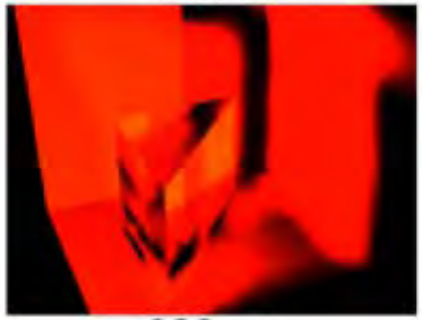

630nm

680nm

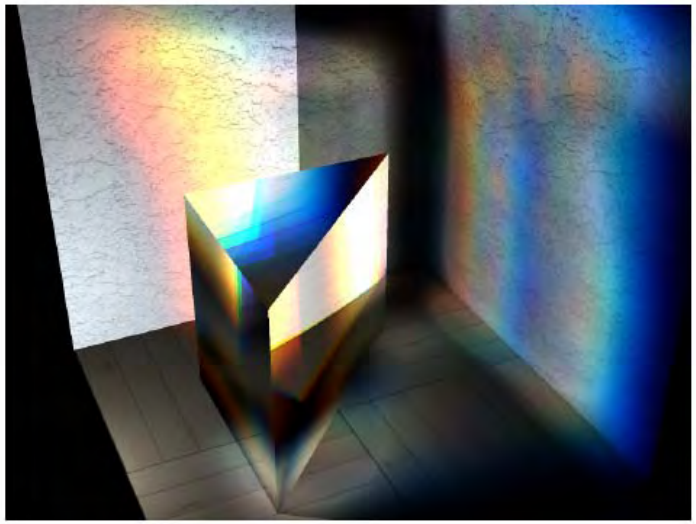

[Glassner 94]

$$\frac{\partial L(\lambda, w)}{\partial x} = \underbrace{\sigma_a(\lambda)\, L_e(\lambda, w)}_{\text{Emission}} - \underbrace{\sigma_t(\lambda)\, L(\lambda, w)}_{\text{Extinction}}$$

$$\underbrace{+\,\sigma_s(\lambda) \int_{\Omega} p(\lambda, w, w')\, L(\lambda, w')\, dw'}_{\text{Elastic Scattering}}$$

[Glassner 94]

$$\frac{\partial L(\lambda, w)}{\partial x} = \underbrace{\sigma_a(\lambda)\, L_e(\lambda, w)}_{\text{Emission}} \underbrace{- \sigma_t(\lambda)\, L(\lambda, w)}_{\text{Extinction}}$$

$$\underbrace{+ \sigma_s(\lambda) \int_{\Omega} p(\lambda, w, w')\, L(\lambda, w')\, dw'}_{\text{Elastic Scattering}}$$

$$\underbrace{+ \int_{\Omega} \int_{W} \left\{ \sigma_s(\lambda', \lambda)\, p(\lambda', \lambda, w, w')\; L(\lambda', w') \right\} d\lambda'\, dw'}_{\text{Inelastic Scattering}}$$

Full Radiative Transfer Equation

Inelastic phase function

Wavelength redistribution function

$$+\int_{\Omega}\int_{W}\left\{\sigma_s(\lambda',\lambda)\,p(\lambda',\lambda,w,w')\;L(\lambda',w')\right\}d\lambda'\,dw'$$

$$\sigma_a(\lambda')\,f(\lambda',\lambda)$$

Inelastic Scattering

[Glassner 94]

- First application of inelastic scattering to CG
  - Fluorescence (modified version of *rayshade*)

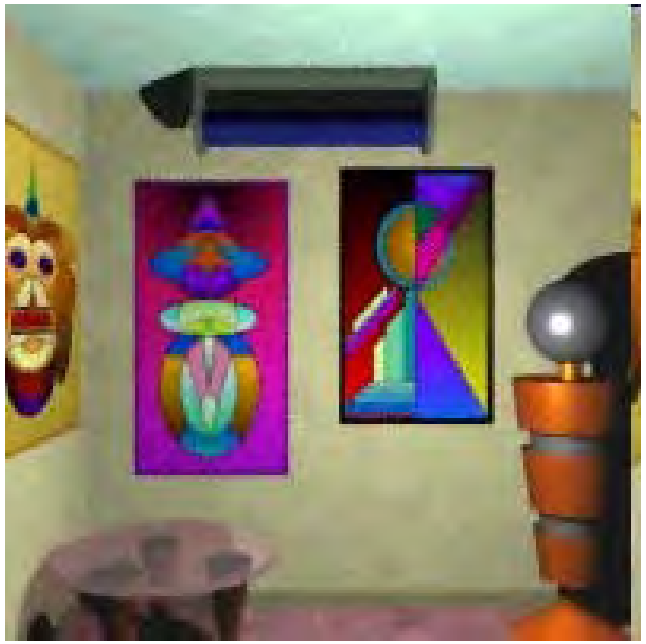

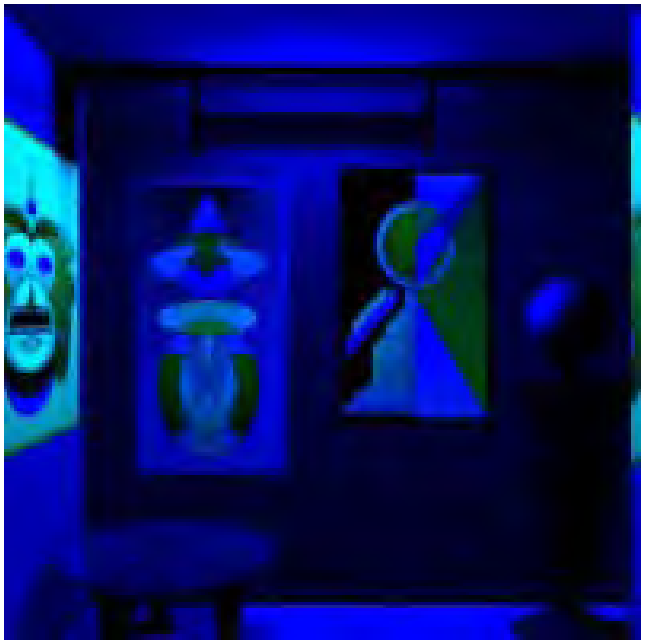

[Glassner 94]

- First application of inelastic scattering to CG
  - Phosphorescence

- Re-formulation of the rendering equation in the presence of these phenomena

[Glassner 94][Wilkie et al. 01]

- Re-radiation matrix

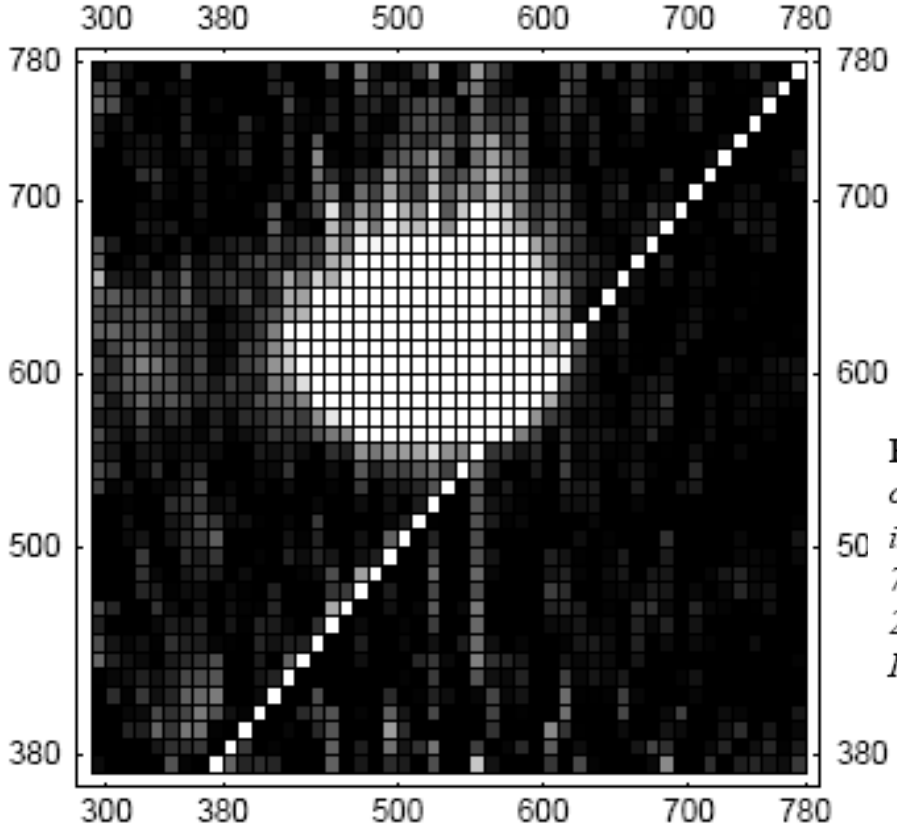

Figure 8: *Bispectral reflectivity measurements of pink fluorescent 3M Post-It® notes. The re–radiation matrix is shown for excitation wavelengths between 300nm and 780nm, and emission wavelengths from 380nm to 780nm, as 2D density plot and 3D graph. Data courtesy of Labsphere Inc.*

[Devlin et al. 02]

Scattering

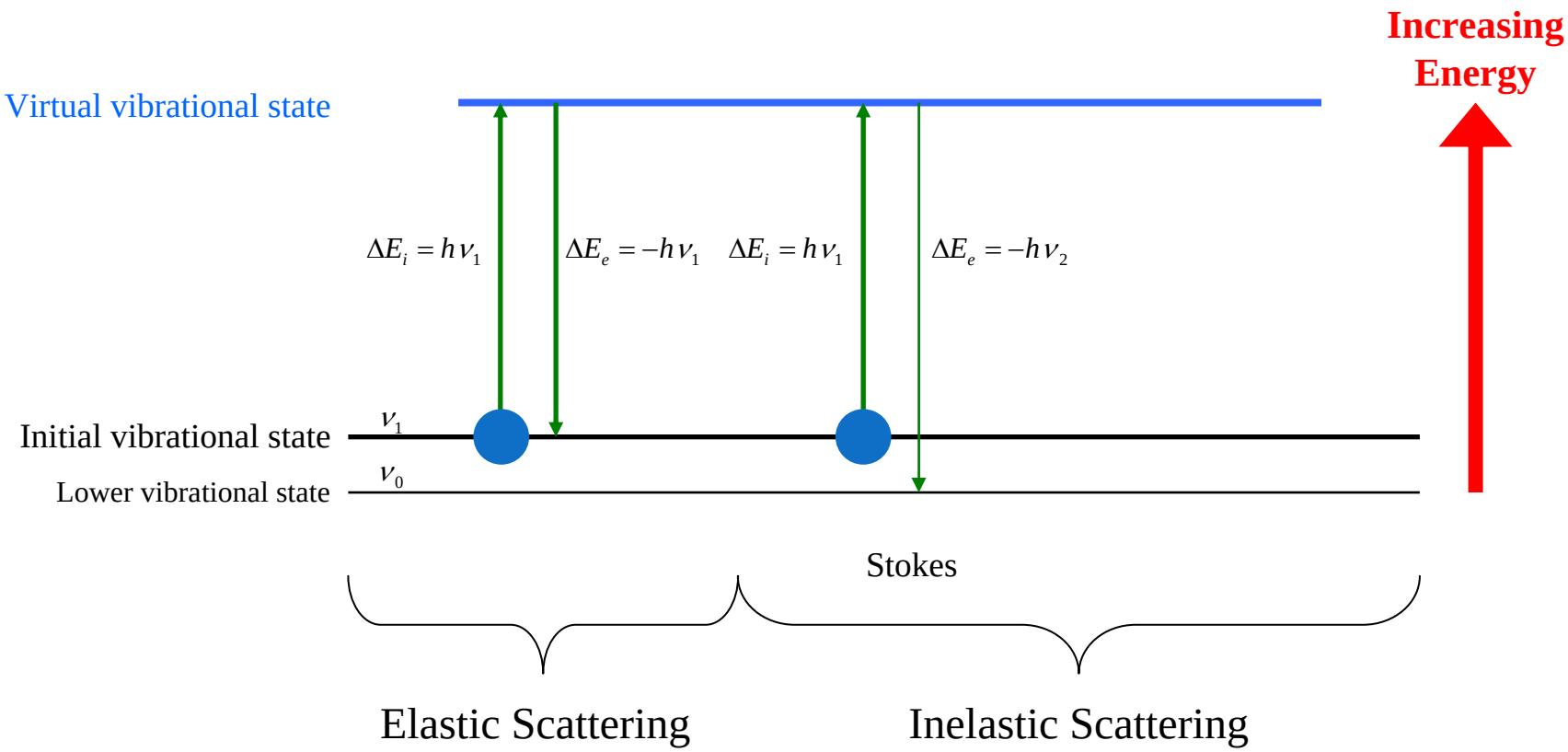
Increasing Energy
Virtual vibrational state
$\Delta E_i = h\nu_1$
$\Delta E_e = -h\nu_1$
$\Delta E_i = h\nu_1$
$\Delta E_e = -h\nu_2$
Initial vibrational state
ν_1
ν_0
Lower vibrational state
Stokes
Elastic Scattering
Inelastic Scattering

[Glassner 94][Wilkie et al. 01]

- Re-radiation matrix

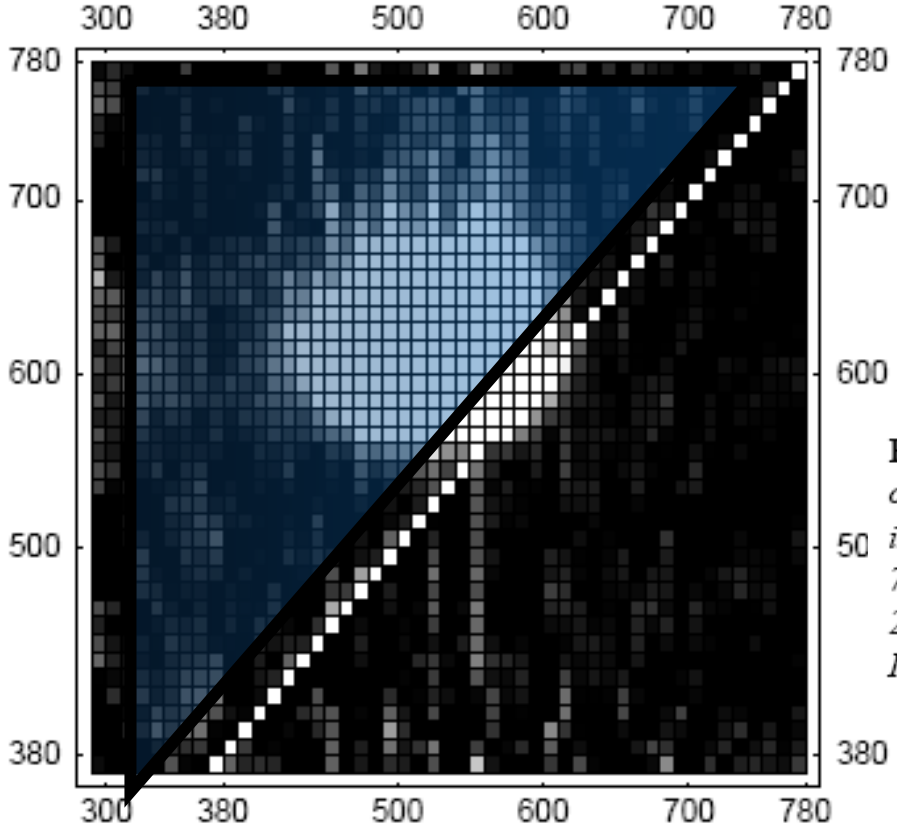

Figure 8: *Bispectral reflectivity measurements of pink fluorescent 3M Post-It® notes. The re–radiation matrix is shown for excitation wavelengths between 300nm and 780nm, and emission wavelengths from 380nm to 780nm, as 2D density plot and 3D graph. Data courtesy of Labsphere Inc.*

[Devlin et al. 02]

[Wilkie et al. 01]

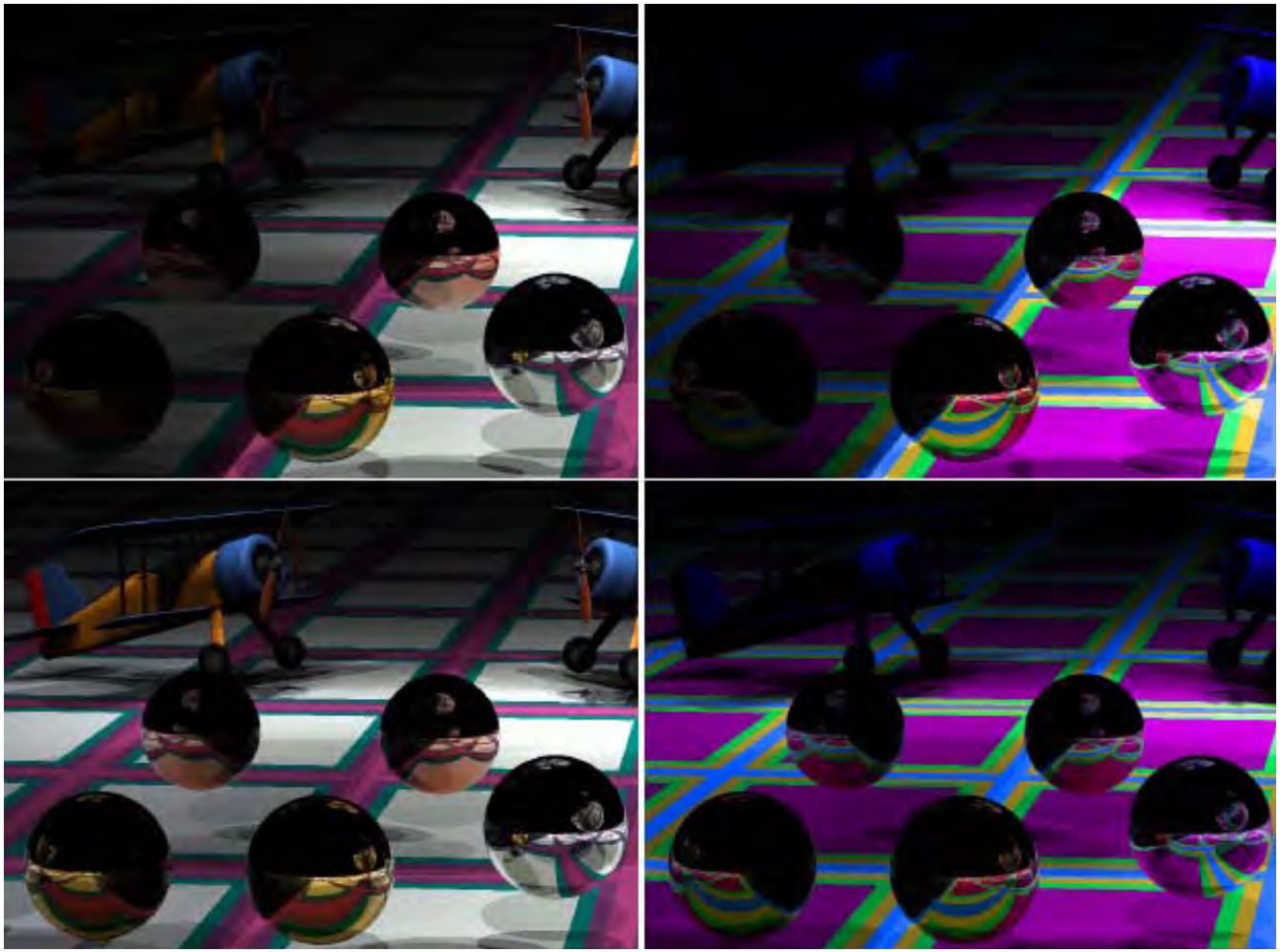

[Wilkie et al. 06]

- Previous works dealt with color computations
- Analyze the reflection behaviour of fluorescent surfaces: energy shift is highly dependant on exitant angle
- Provide an analytical BRDF model for fluorescent surfaces based on a layered microfacet approach

[Wilkie et al. 06]

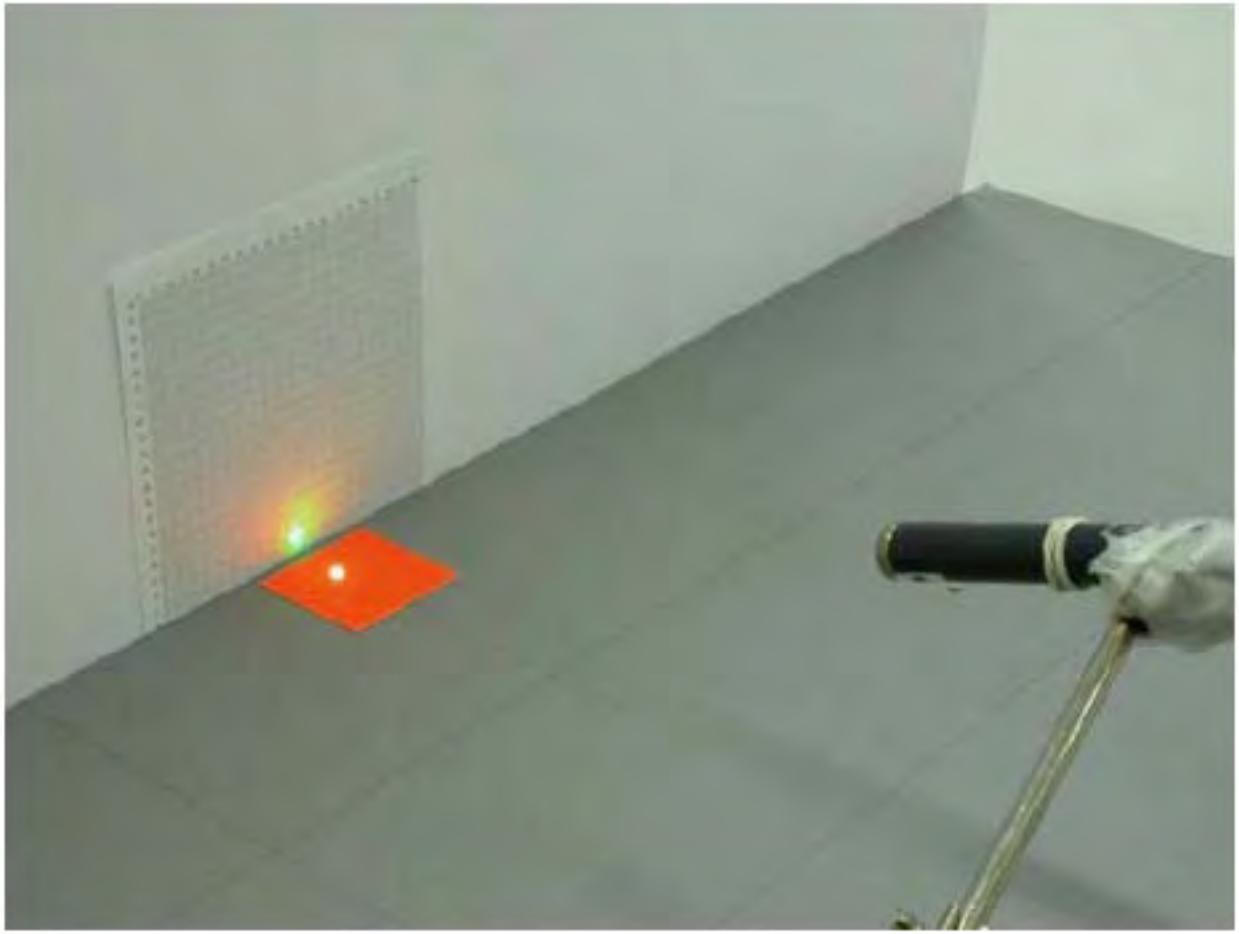

[Wilkie et al. 06]

- Diffuse orange card hit by green laser
  - Left: plain
  - Right: fluorescent (day-glo)

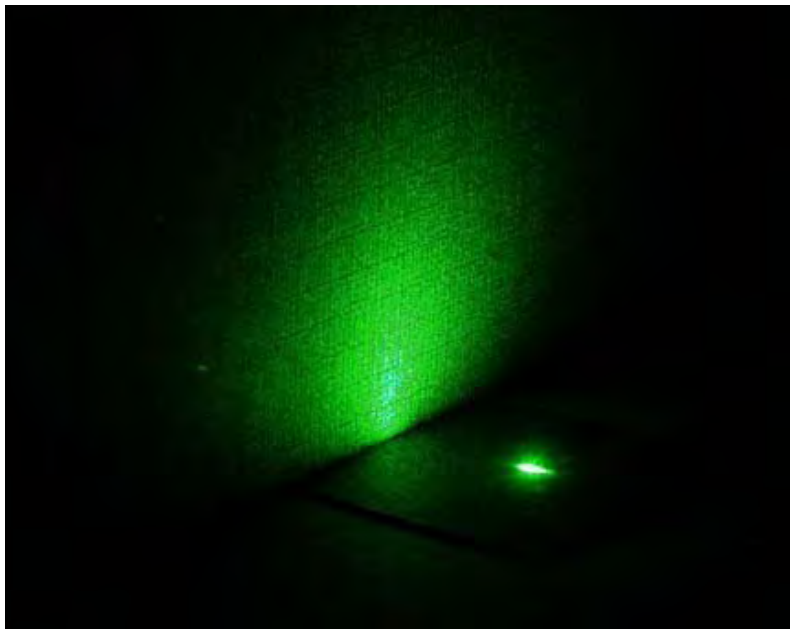

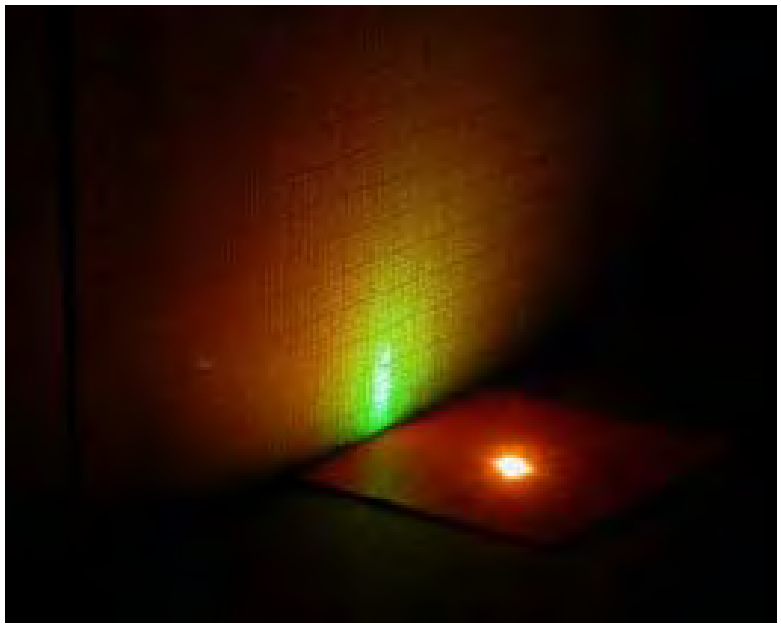

- From almost specular to fully fluorescent

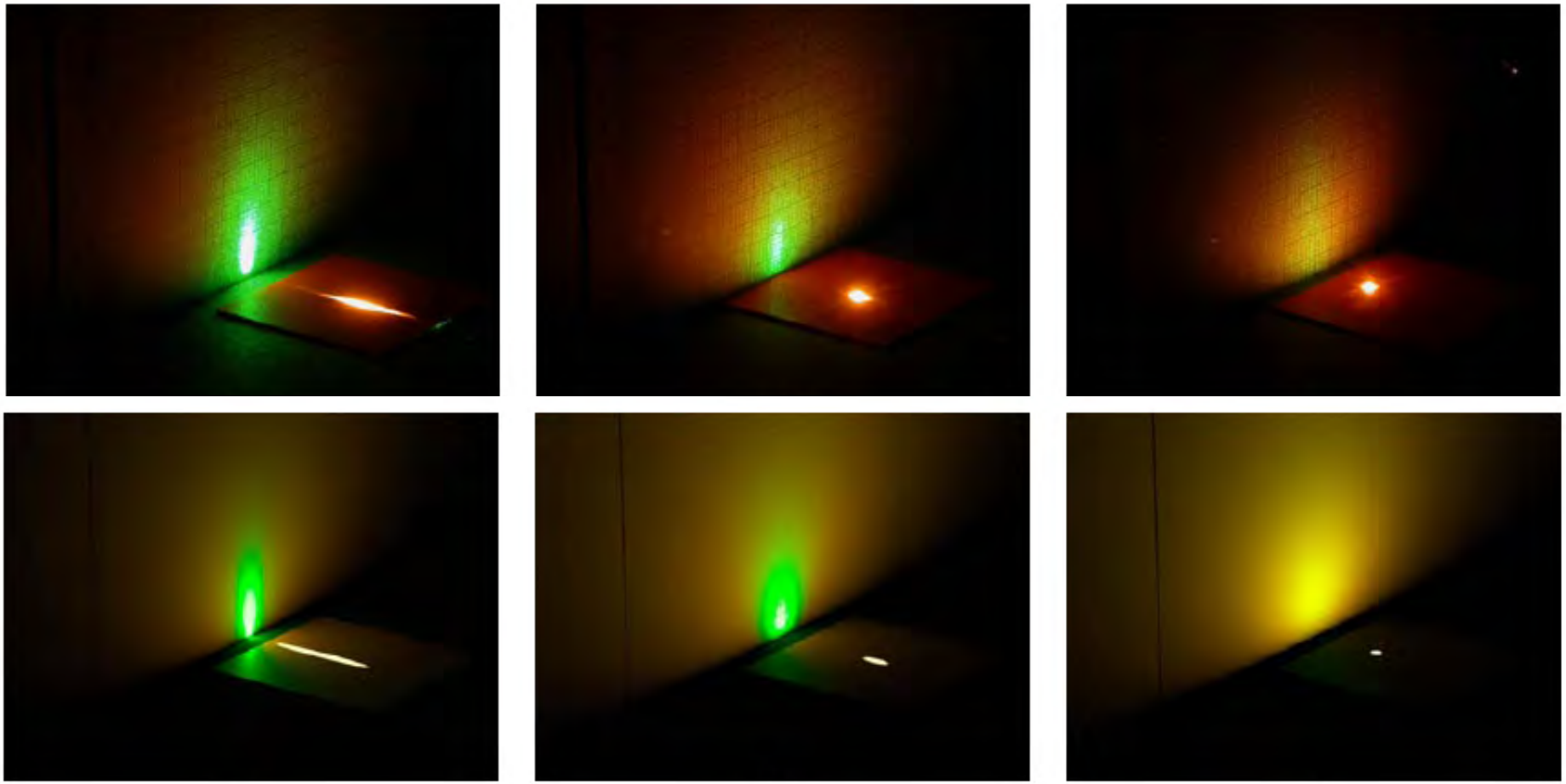

- Re-radiation matrices not enough

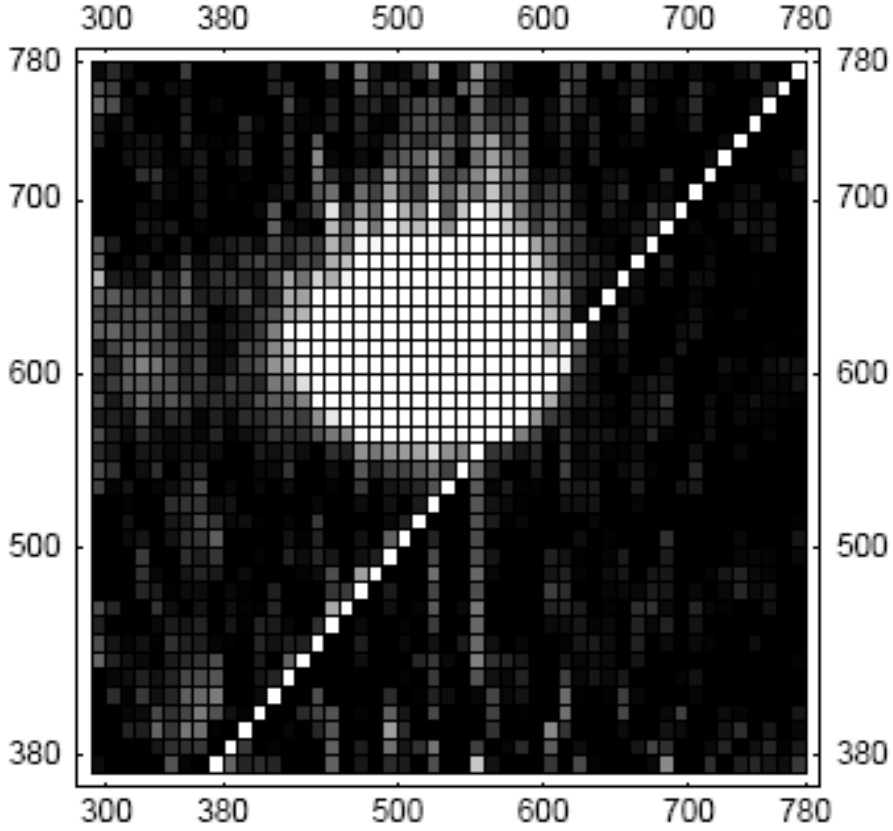

[Wilkie et al. 06]

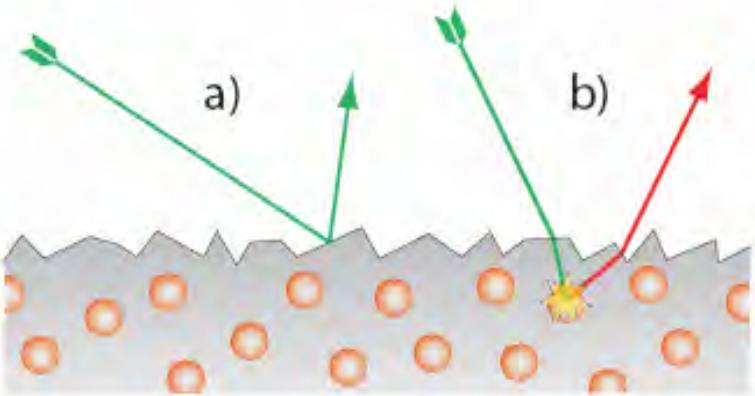

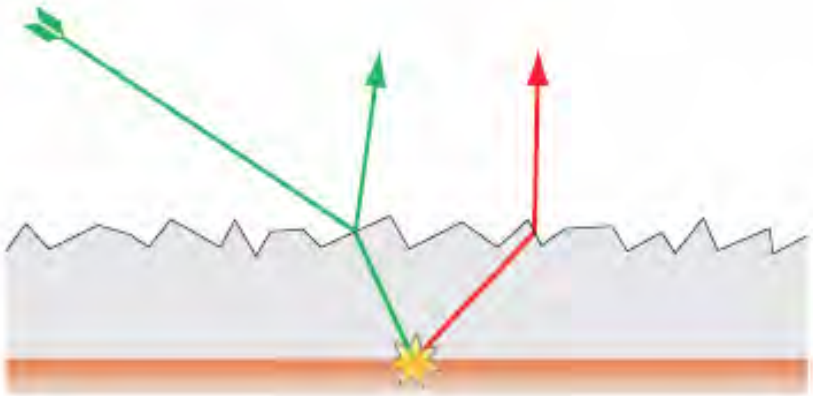

- BRDF made up of:
  - Non-fluorescent semigloss specular component
  - Fluorescent diffuse component
  - No SSS

[Wilkie et al. 06]


1/8/04
500
1995
reag alc
uinine
tener

[Cerezo and Serón 04]

- *Volume* inelastic scattering
- Rendering system based on the discrete ordinates method
- Generalizes [Languénou et al. 95] to inelastic events. Energy is transmitted from voxel to voxel in a cascading scheme
  - Limited to pure chlorophyl
  - Requires voxelization (simple scenes)

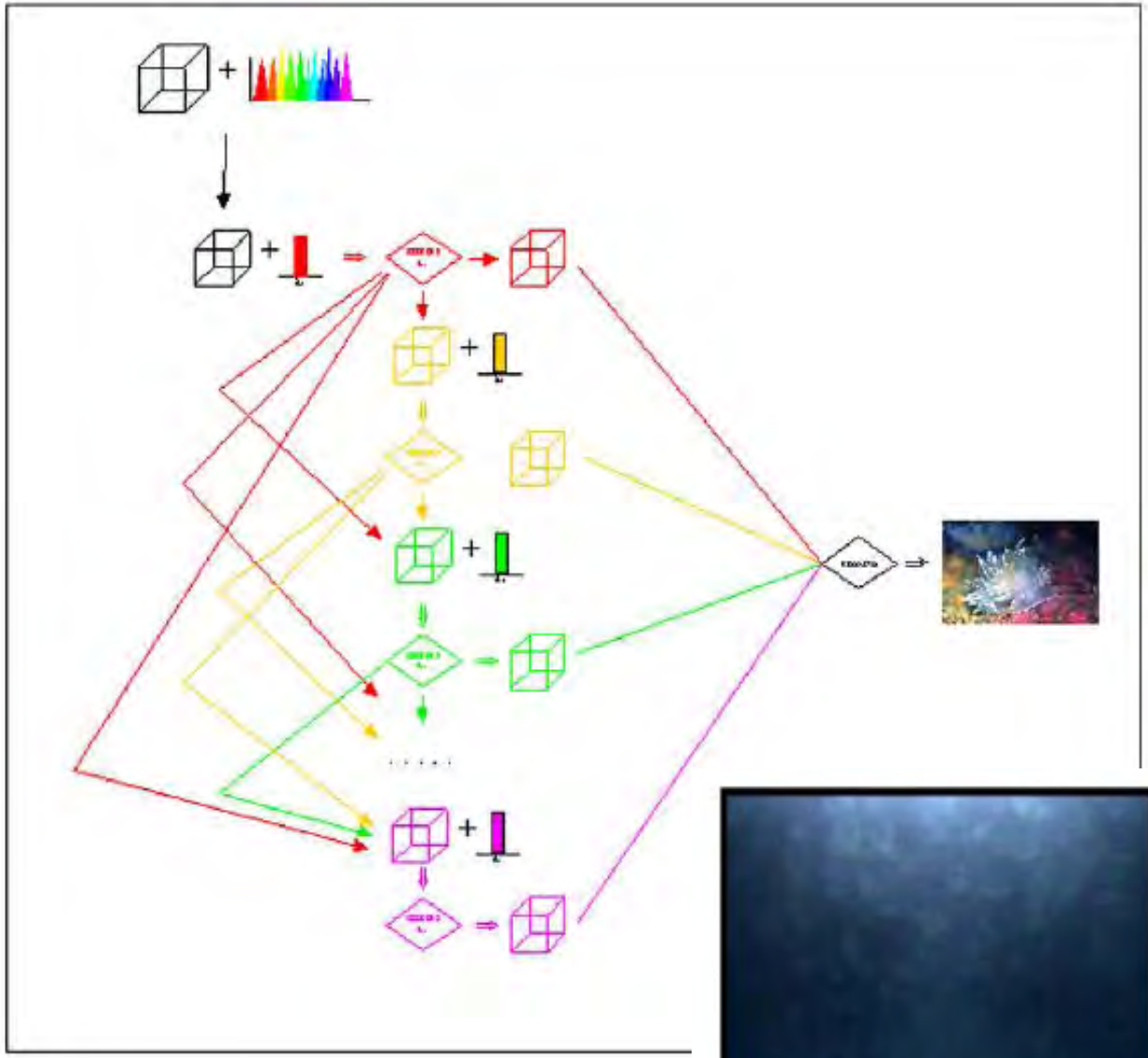

The figure from the paper (shown here) should actually show the opposite cascading scheme

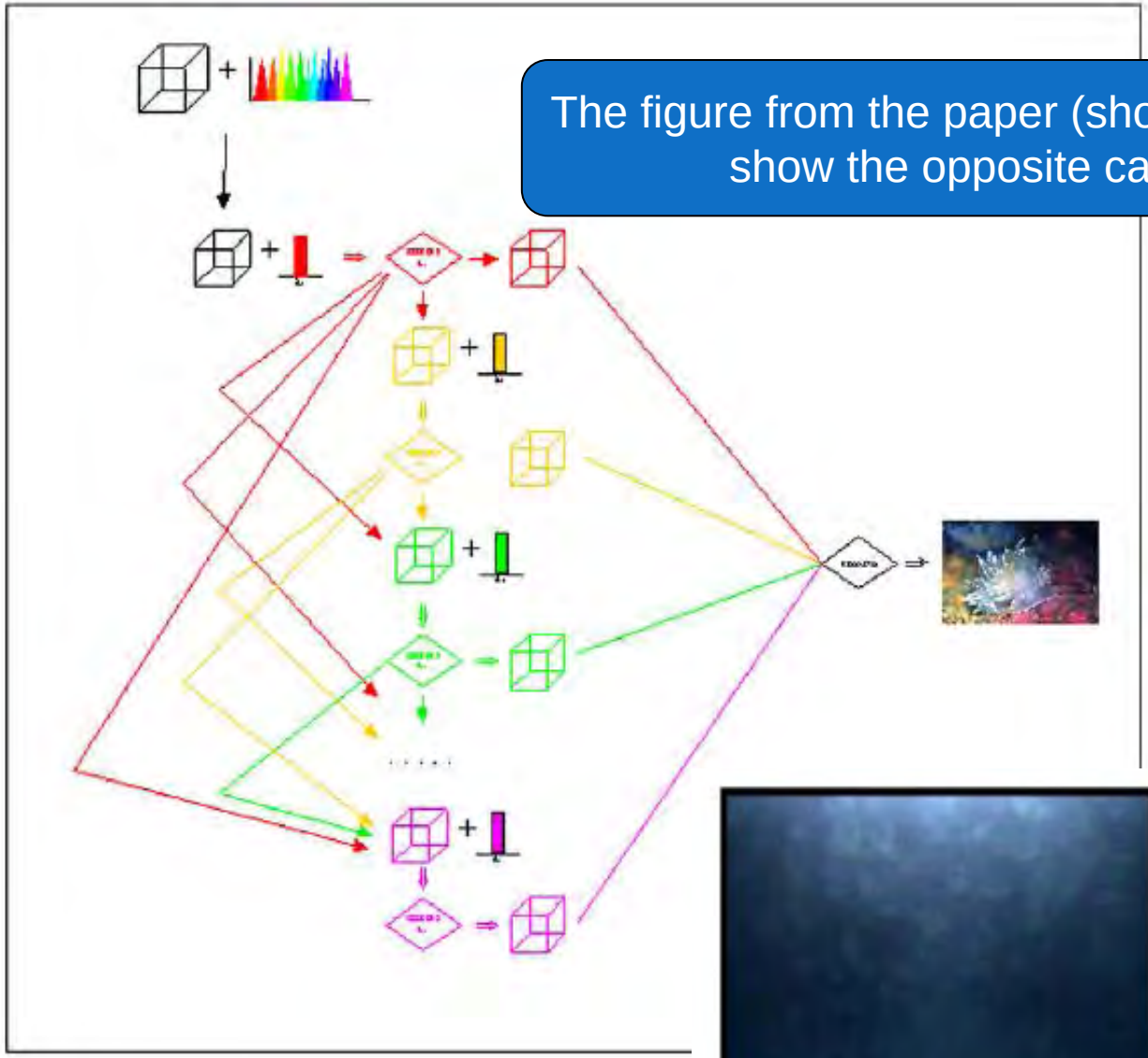

[Gutiérrez et al. 05]

- Generalized volume inelastic scattering: photon mapping extension
  - No need to voxelize
  - Not limited to chlorophyl: Stokes behavior

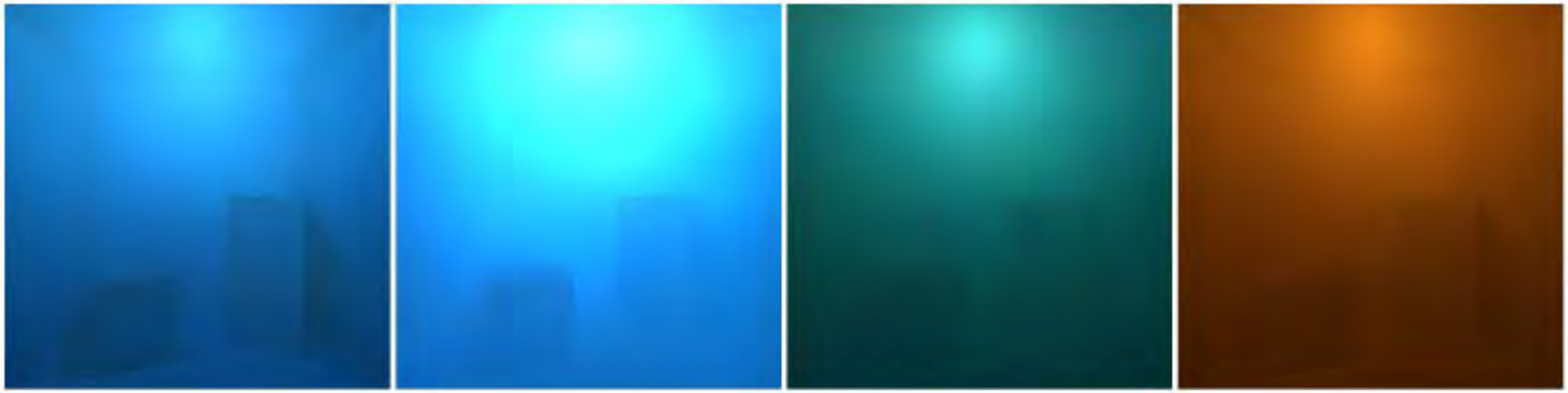

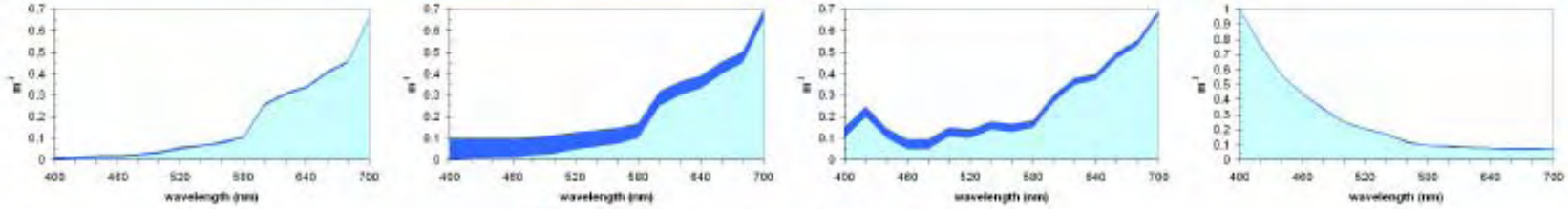

Absorption coef. Extinction coef.

[Gutiérrez et al. 08]

- Extension to the previous PM extension
  - *Full* volumetric inelastic scattering (Stokes, anti-Stokes)

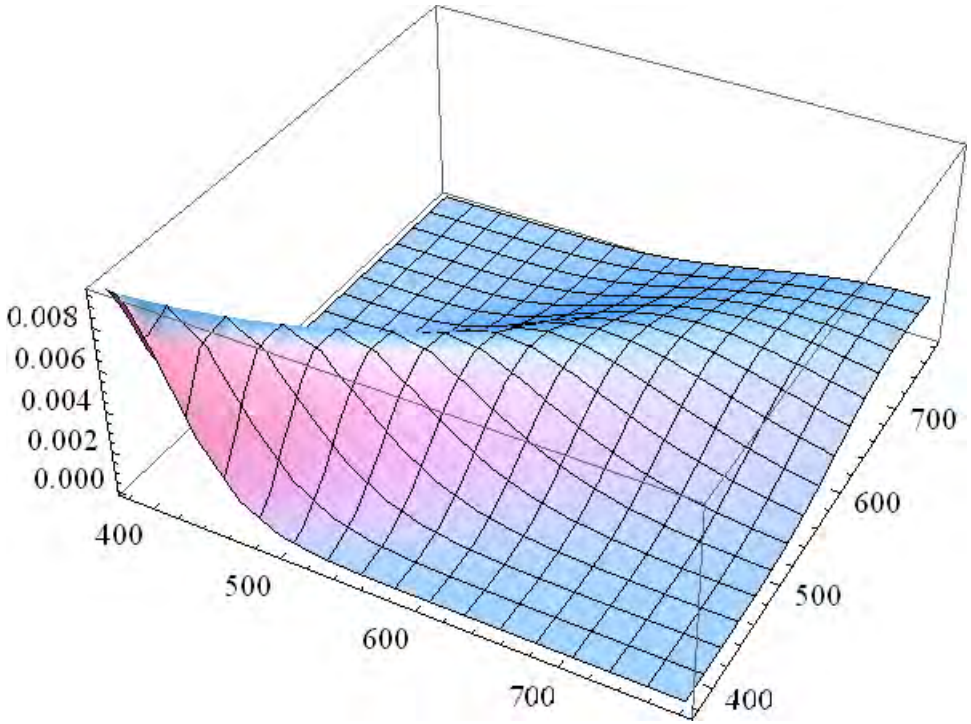

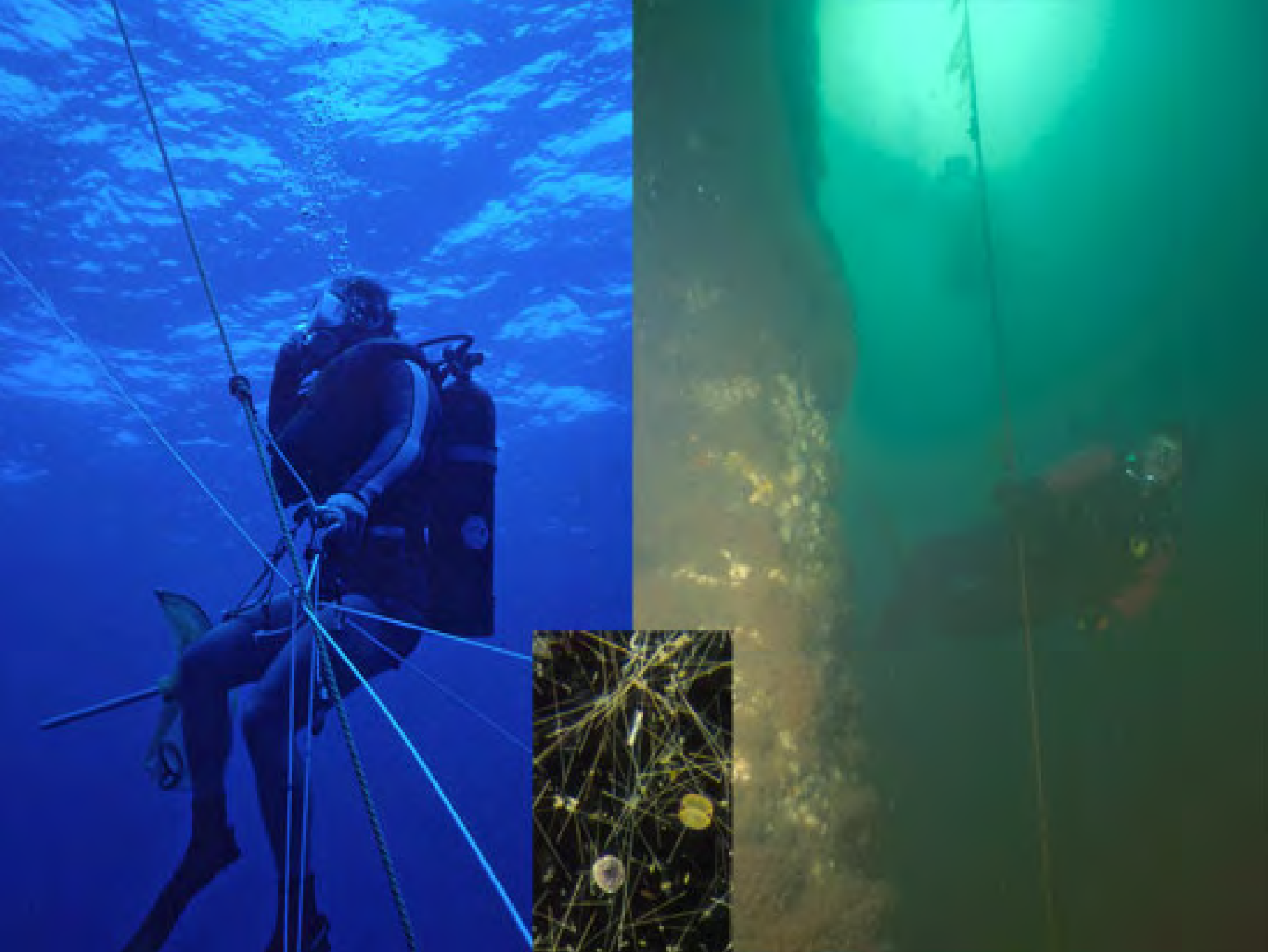

- Constituents = f(Parameters of the model)

$$\alpha_d(\lambda) = \alpha_d(\lambda_0)\, e^{-S_d(\lambda-\lambda_0)}$$

$$\alpha_p(\lambda) = C\,\alpha_p^*(\lambda)$$

λ	$[nm]$	380	440	500	550	610	670	720	780
α_w	$[cm^{-1}]$	0.00022	0.000145	0.000257	0.000638	0.00289	0.0043	0.01169	0.0236
α_p^*	$[m^2 \cdot mg^{-1}]$	0.025	0.035	0.02	0.01	0.007	0.015	0.001	0.0001

$$\alpha_y(\lambda) = \alpha_y(\lambda_0)\, e^{-S_y(\lambda-\lambda_0)}$$

$$\sigma_w(\lambda) = 16.06\,\beta_w(\lambda_0, 90^\circ)\left(\frac{\lambda_0}{\lambda}\right)^{4.32}$$

	λ	$[nm]$	380	440	500	550	610	670	720	780
detritus	σ_{dt}	$[m^{-1}]$	0.045	0.0375	0.0325	0.03	0.0285	0.0275	0.027	0.027
minerals	σ_m	$[m^{-1}]$	0.0675	0.0525	0.05	0.045	0.04	0.036	0.034	0.032
total	σ_d	$[m^{-1}]$	0.1125	0.09	0.0825	0.075	0.0685	0.0635	0.061	0.059

$$\sigma_p(\lambda) = \left(\frac{550}{\lambda}\right) 0.30\,C^{0.62}$$

$$p_w(\theta) = 0.06225\left(1 + 0.835\cos^2\theta\right)$$

$$p_d(\theta, \zeta, g_f, g_b) = \zeta\, p_{HG}(\theta, g_f) + (1-\zeta)\, p_{HG}(\theta, g_b)$$

$$p_{HG}(\theta, g) = \frac{1-g^2}{(1+g^2-2g\cos\theta)^{3/2}} \qquad p_p = 1/\pi$$

$$f_w(\lambda', \lambda) = \frac{10^7}{\lambda'^2}\,\frac{\sum_{j=1}^{4} A_i \frac{1}{\Delta\tilde{\nu}_i} \exp\left\{-\frac{\left[10^7\left(\frac{1}{\lambda'}-\frac{1}{\lambda}\right)-\tilde{\nu}_i\right]^2}{\Delta\tilde{\nu}_i^{\,2}}\right\}}{\sqrt{\frac{\pi}{4\ln 2}}\sum_{j=1}^{4} A_j}$$

$$f_y(\lambda', \lambda) = A_0(\lambda')\exp\left\{-\left(\frac{\frac{1}{\lambda}-\frac{A_1}{\lambda'}-B_1}{0.6\left(\frac{A_2}{\lambda'}+B_2\right)}\right)^2\right\}\frac{\lambda'}{\lambda}$$

$$f_p(\lambda', \lambda) = \eta_p(\lambda', \lambda)\frac{\lambda'}{\lambda} \equiv \Gamma_p\, g_p(\lambda')\, h_p(\lambda)\,\frac{\lambda'}{\lambda}$$

$$h_p(\lambda) = \frac{1}{\sqrt{2\pi}\,\lambda_\sigma}\exp\left\{-\frac{(\lambda-\lambda_0)^2}{2(\lambda_\sigma)^2}\right\}$$

$$g_p(\lambda') \equiv \begin{cases} 1 & \text{if } 370 \le \lambda' \le 690 \text{ nm} \\ 0 & \text{otherwise} \end{cases}$$

Fluorescence → isotropic phase function

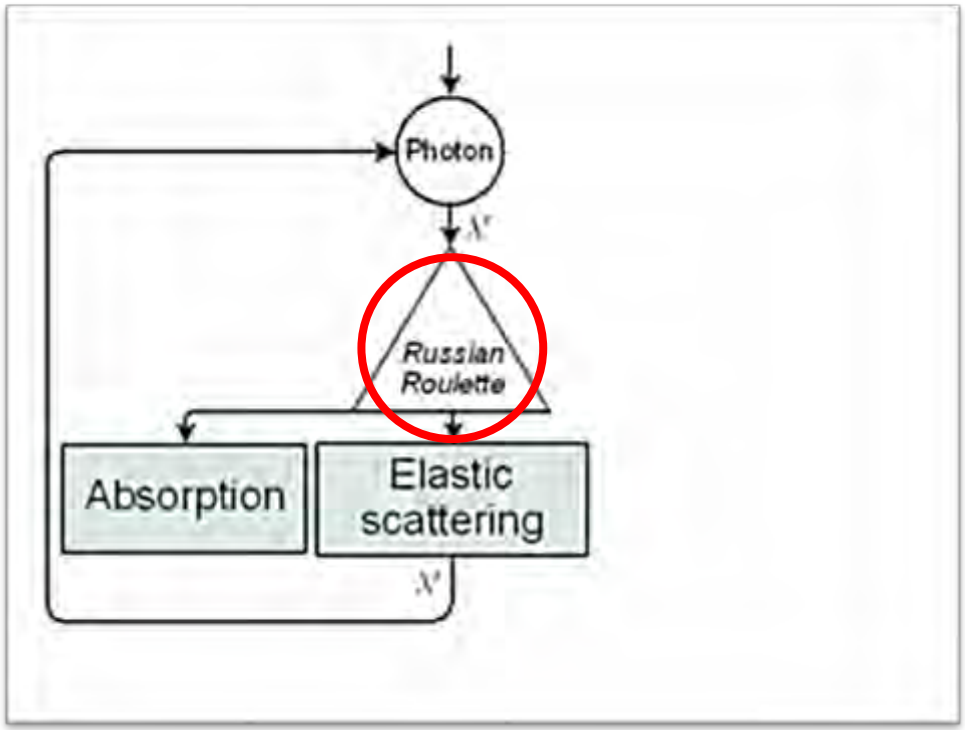

Photon tracing

Ray marching

Radiance estimate

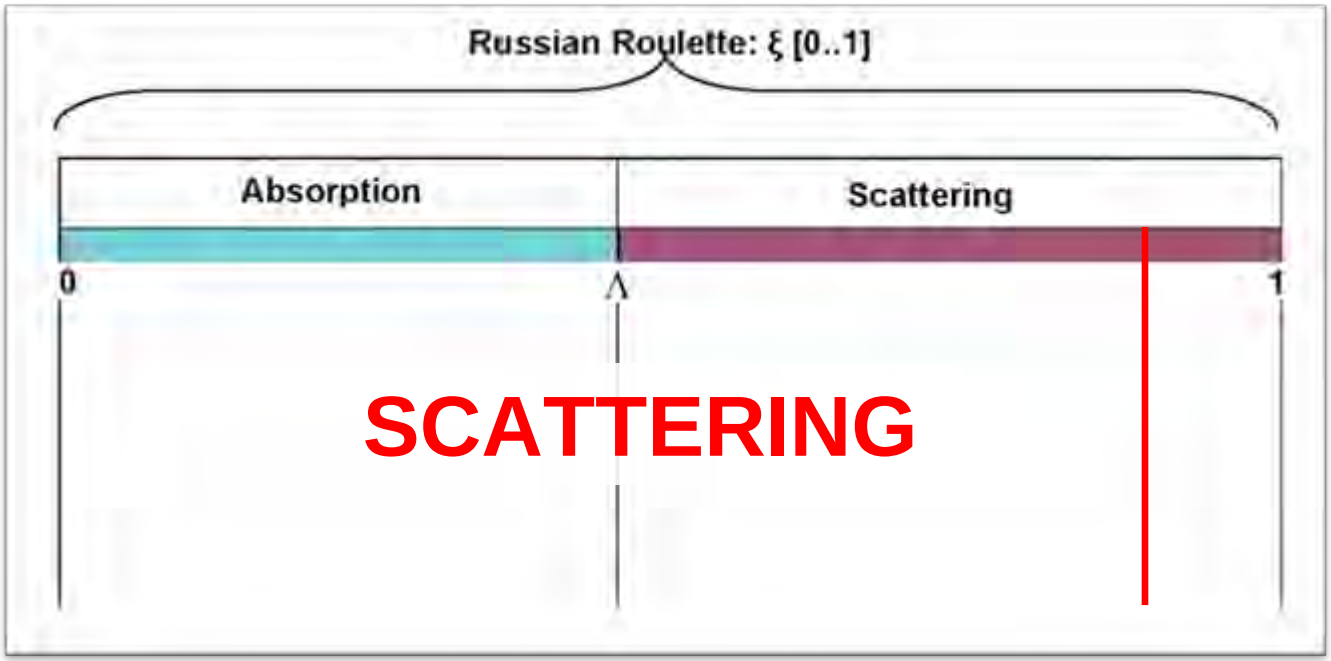

Photon tracing

Ray marching

Radiance estimate

Absorption

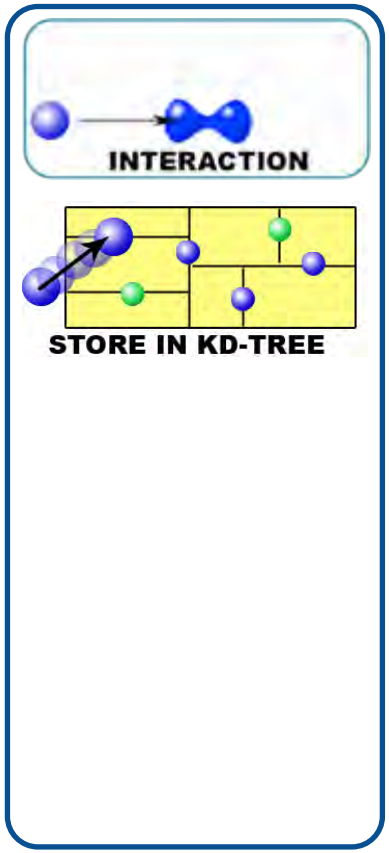

Elastic scattering

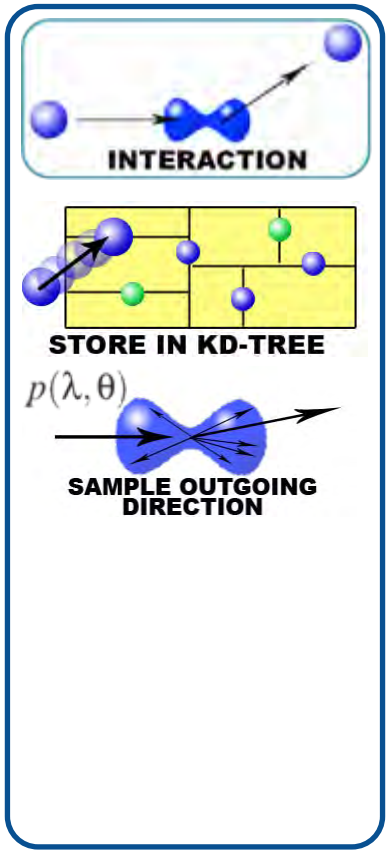

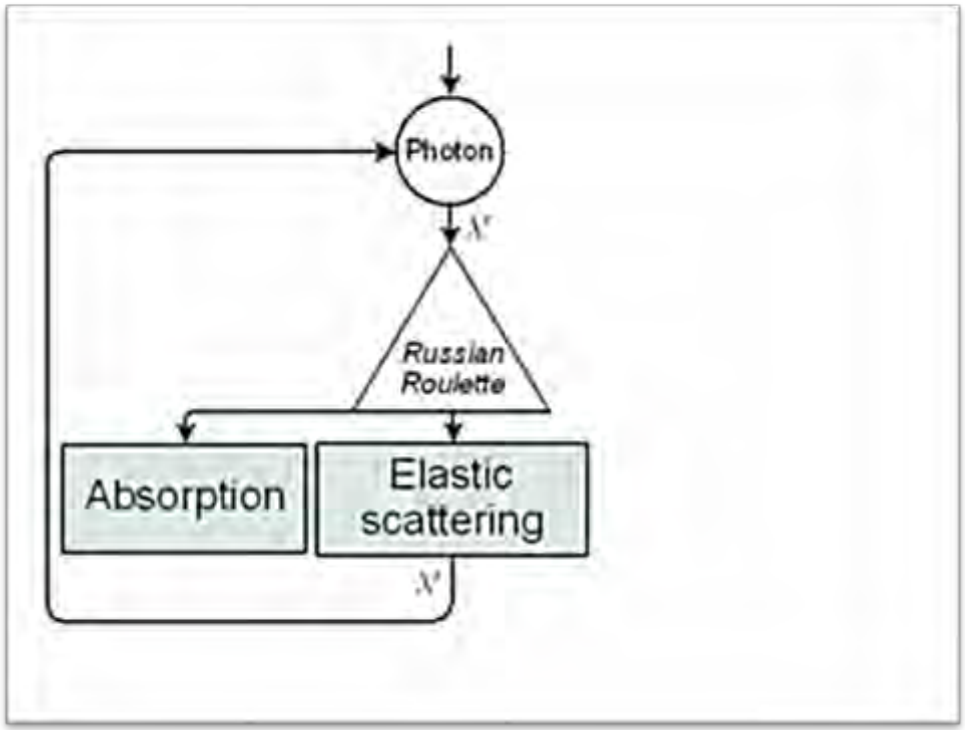

Photon tracing

Ray marching

Radiance estimate

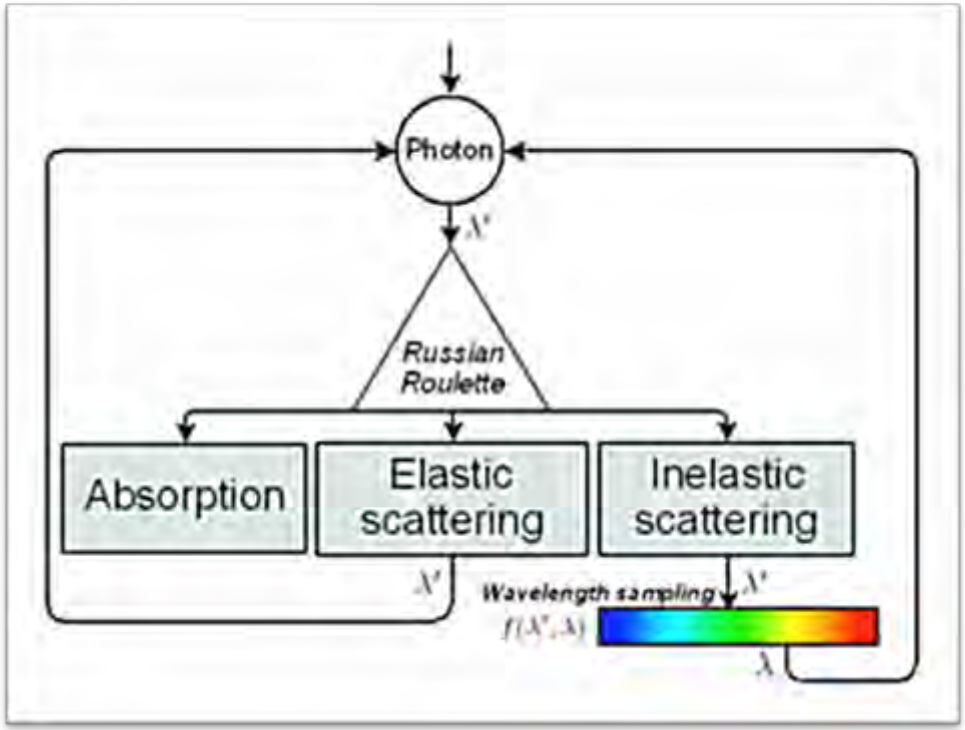

Photon tracing

Ray marching

Radiance estimate

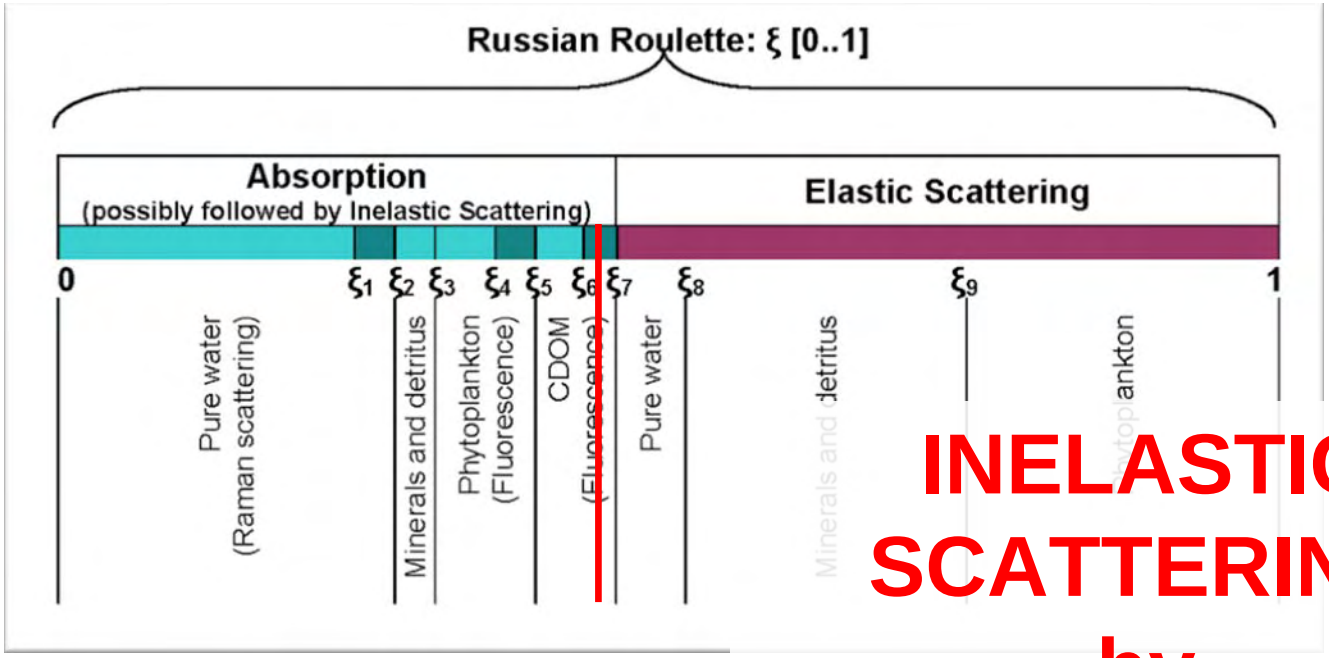

Photon tracing

Ray marching

Radiance estimate

INELASTIC SCATTERING by YELLOW MATTER

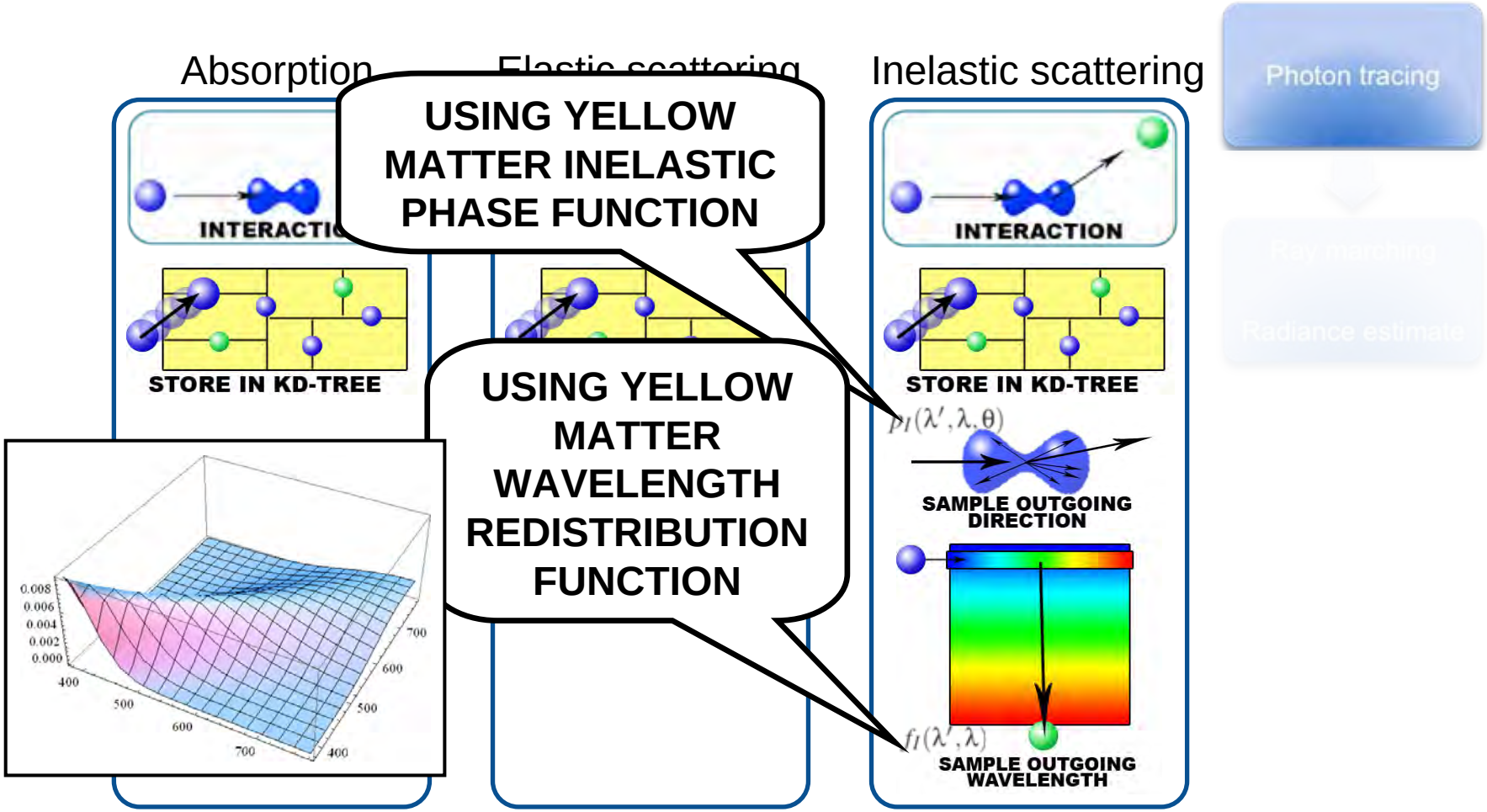
Absorption
Elastic scattering
Inelastic scattering
Photon tracing
Ray marching
Radiance estimate
INTERACTION
STORE IN KD-TREE
INTERACTION
STORE IN KD-TREE
$p_I(\lambda', \lambda, \theta)$
SAMPLE OUTGOING DIRECTION
$f_I(\lambda', \lambda)$
SAMPLE OUTGOING WAVELENGTH
USING YELLOW MATTER INELASTIC PHASE FUNCTION
USING YELLOW MATTER WAVELENGTH REDISTRIBUTION FUNCTION
0.008
0.006
0.004
0.002
0.000
400
500
600
700
400
500
600
700

- Radiance estimate
  - Single scattering

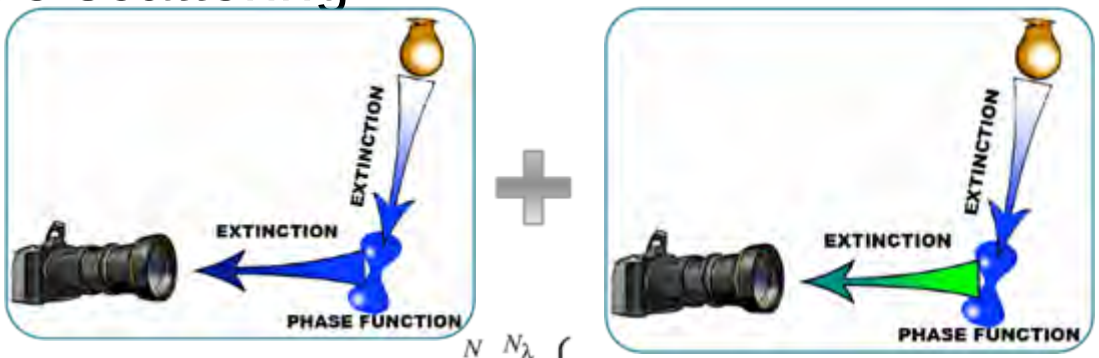

$$\sum_{l=1}^{N}\sum_{i=1}^{N_\lambda}\left\{L_l\left(\lambda_i',\vec{w}_l\right)p_I\left(\lambda_i',\lambda,\vec{w}_l,\vec{w}_o\right)\alpha_I\left(\lambda_i'\right)f_I\left(\lambda_i',\lambda\right)\Delta x\right\}$$

  - Multiple scattering

$$\sum_{k=1}^{n}\left\{p_I\left(\lambda_k',\lambda,\vec{w}_k,\vec{w}_o\right)f_I\left(\lambda_k',\lambda\right)\frac{\Delta\Phi_k}{\frac{4}{3}\pi r^2}\right\}$$

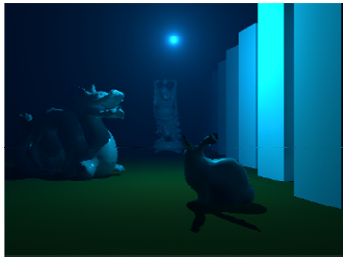

(a) $C = 0, \alpha_d = 0, \alpha_y = 0$

(b) $C = 0.01, \alpha_d = 0, \alpha_y = 0$

(c) $C = 0.1, \alpha_d = 0, \alpha_y = 0$

(d) $C = 1, \alpha_d = 0, \alpha_y = 0$

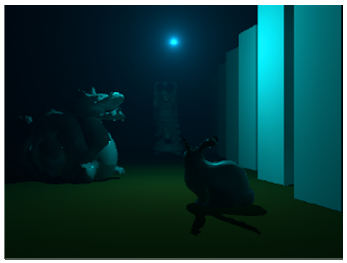

(e) $C = 0, \alpha_d = 0.1, \alpha_y = 0$

(f) $C = 0.01, \alpha_d = 0.1, \alpha_y = 0$

(g) $C = 0.1, \alpha_d = 0.1, \alpha_y = 0$

(h) $C = 1, \alpha_d = 0.1, \alpha_y = 0$

(i) $C = 0, \alpha_d = 0, \alpha_y = 0.1$

(j) $C = 0.01, \alpha_d = 0, \alpha_y = 0.1$

(k) $C = 0.1, \alpha_d = 0, \alpha_y = 0.1$

(l) $C = 1, \alpha_d = 0, \alpha_y = 0.1$

- The effect of inelastic scattering

Without inelastic scattering

With inelastic scattering

[Hullin et al. 08]

- Fluorescent immersion range scanning

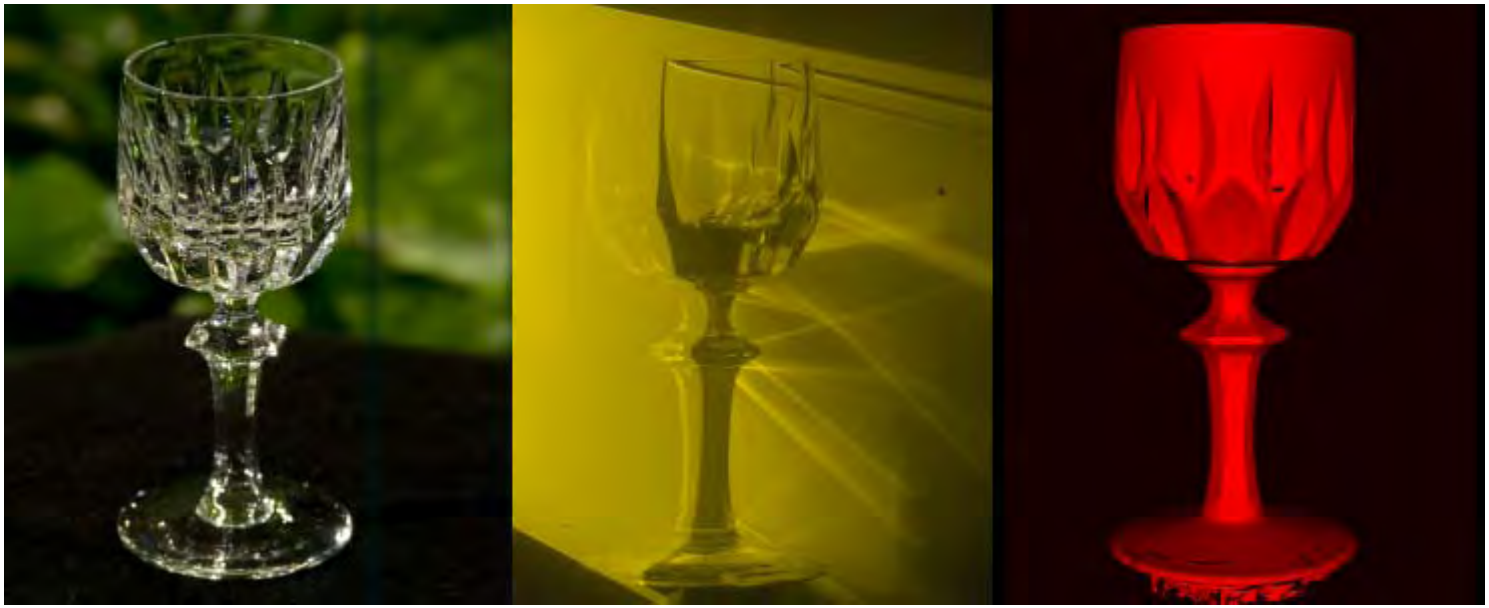

Acquisition of Optically Complex Objects and Phenomena
Tuesday, 4 August, 08:30 – 10:15
http://www.mpi-inf.mpg.de/resources/FIRS/

[Hullin et al. 08]

- Fluorescent immersion range scanning

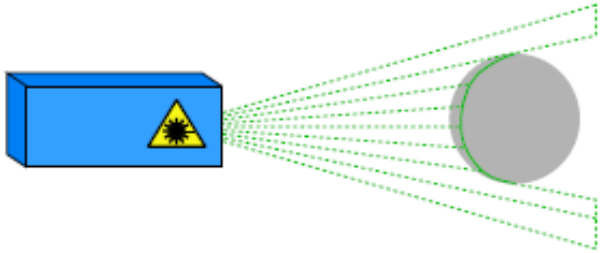

(a)

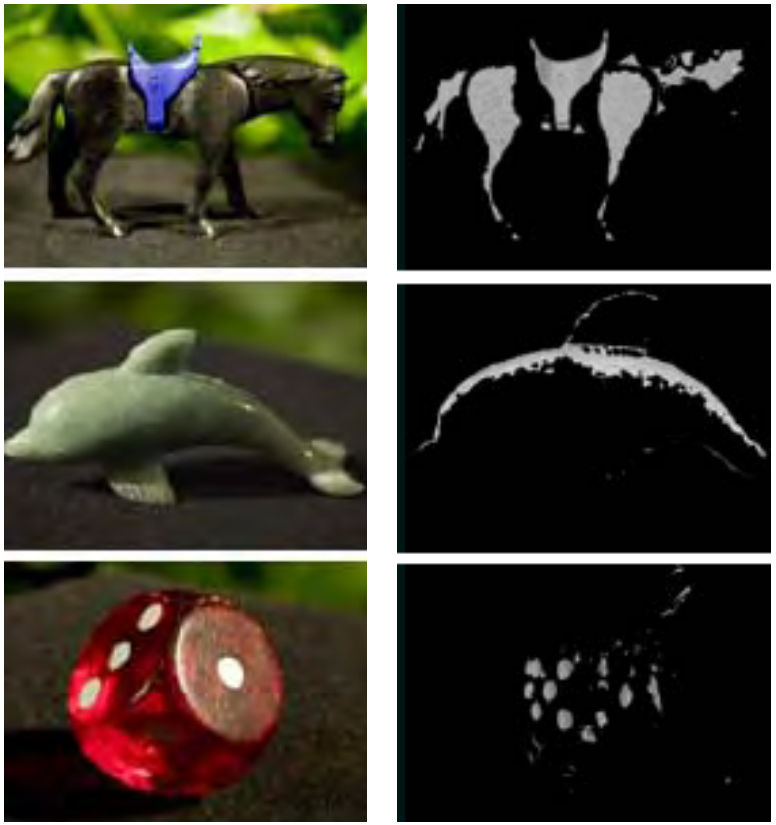

[Hullin et al. 08]

- Fluorescent immersion range scanning

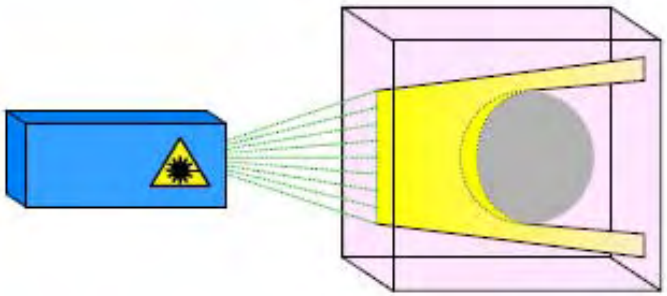

(b)

[Hullin et al. 08]

- 1. Get rid of multiple scattering

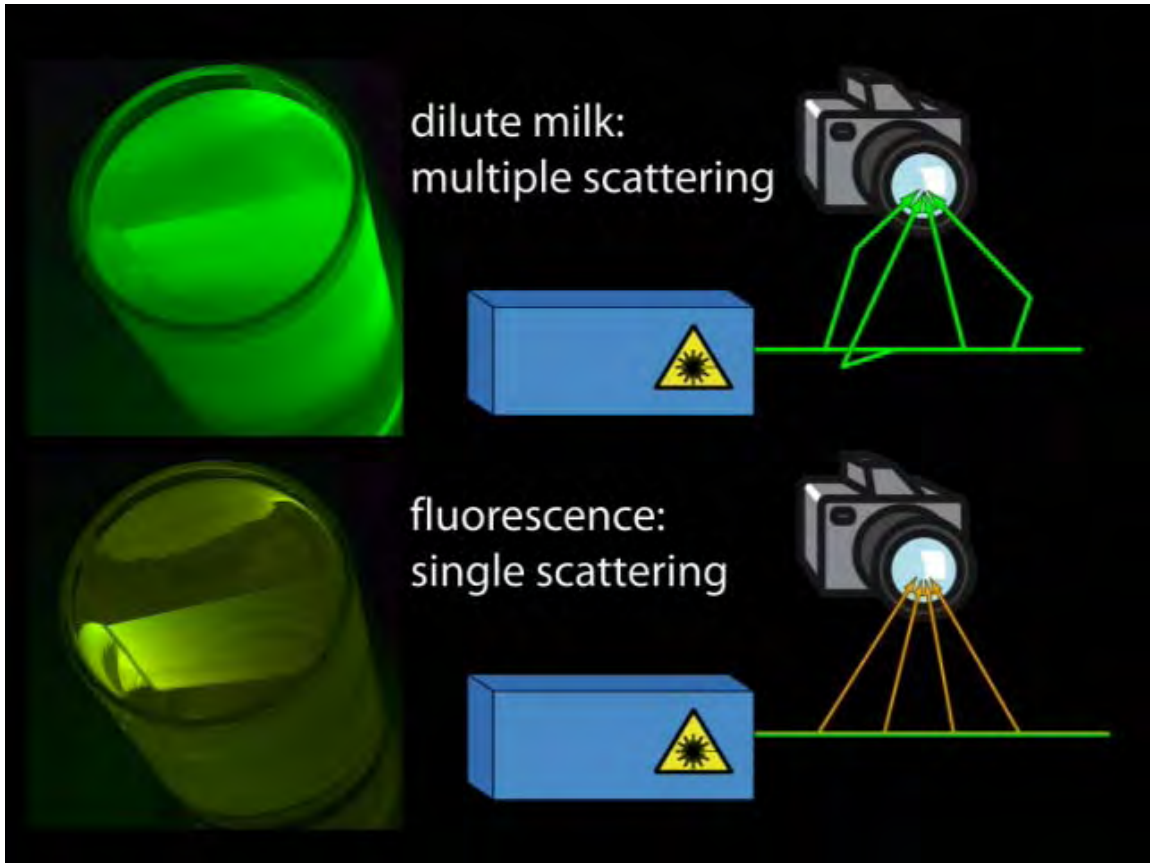

[Hullin et al. 08]

- 1. Get rid of multiple scattering
  - Structured Light in Scattering Media [Narasimhan et al. 2005]: finding a suitable concentration of milk seems almost impossible
  - Fluorescent dye avoids the problem

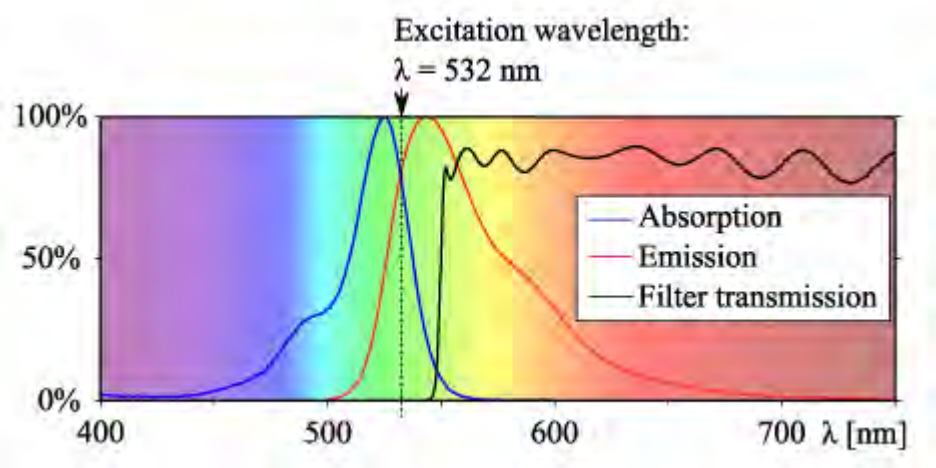

[Hullin et al. 08]

http://www.mpi-inf.mpg.de/~hullin/projects/FIRS/virtuallab.html

- Milk: murky
- Fluorescent dye: almost no multiple scattering

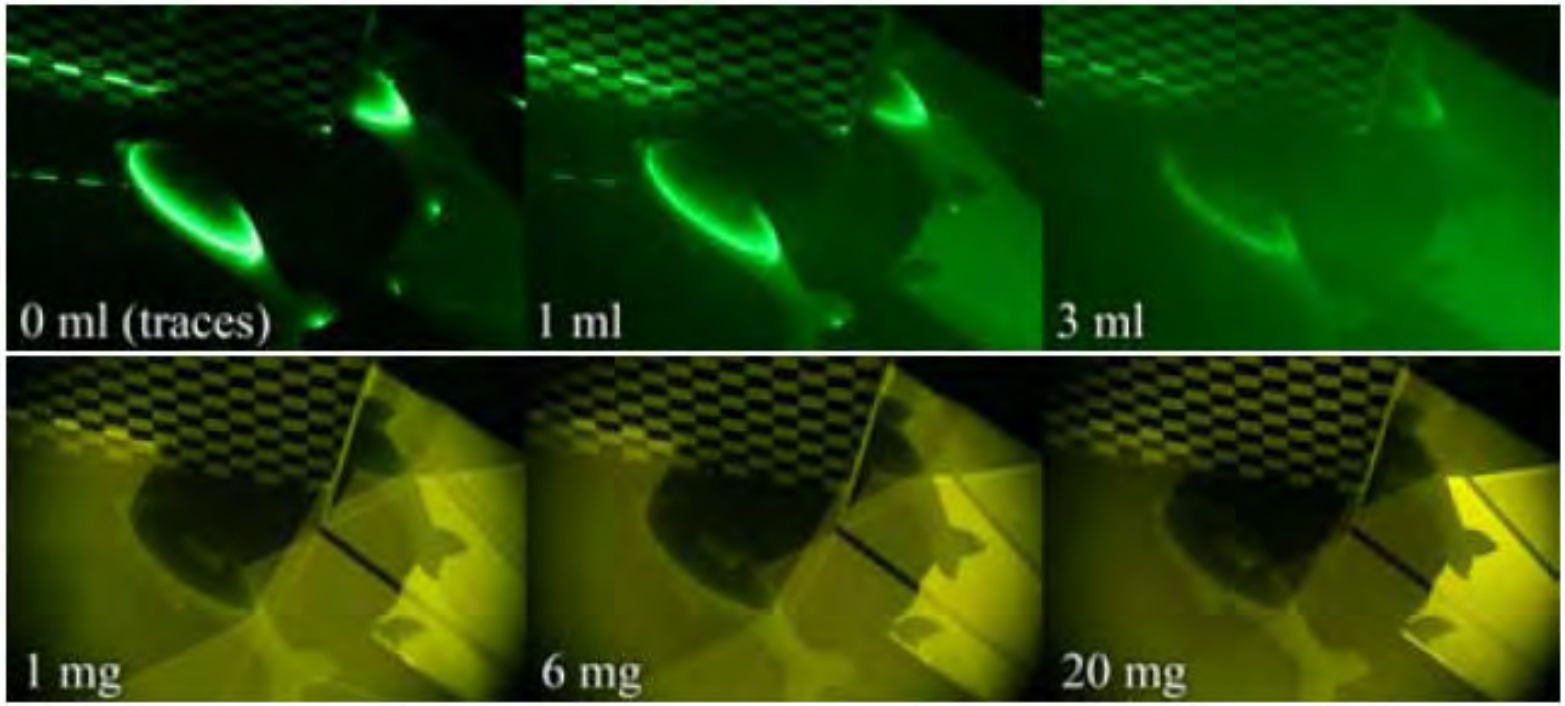

[Hullin et al. 08]

- 2. Filter out unwanted rays

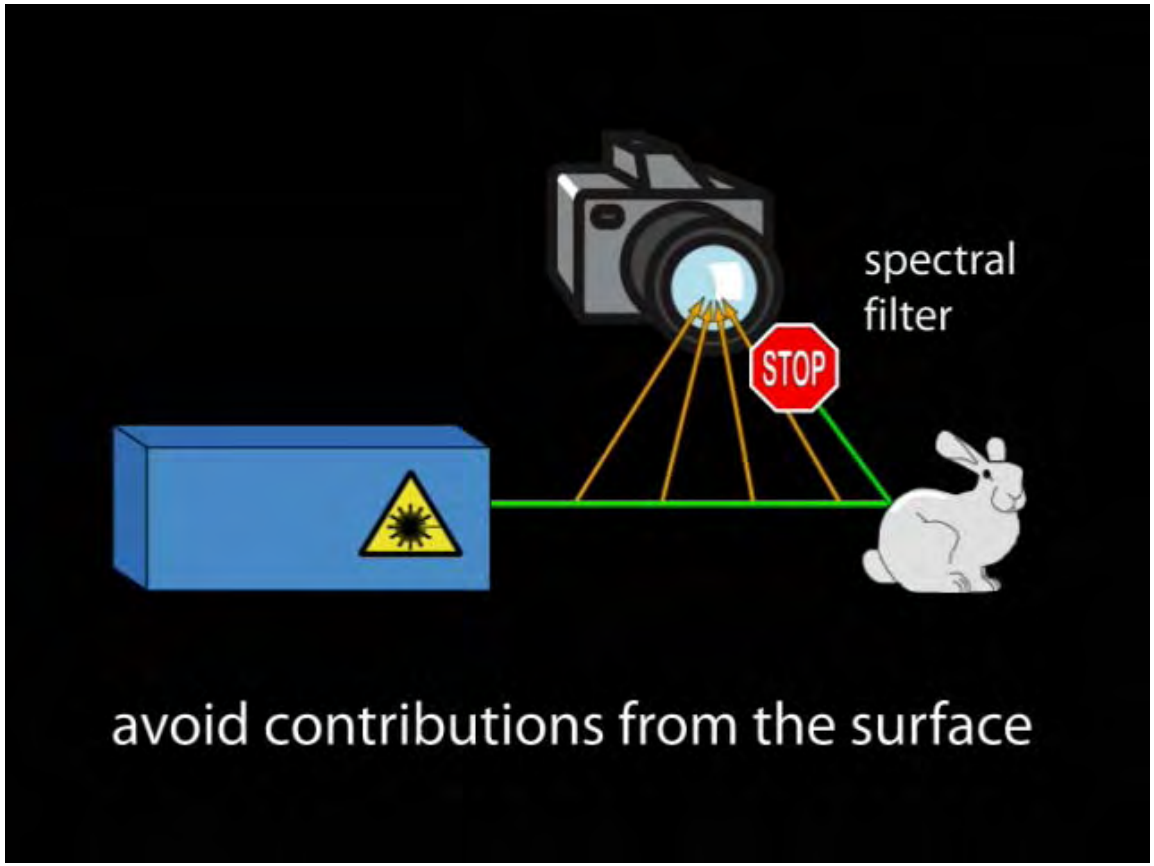

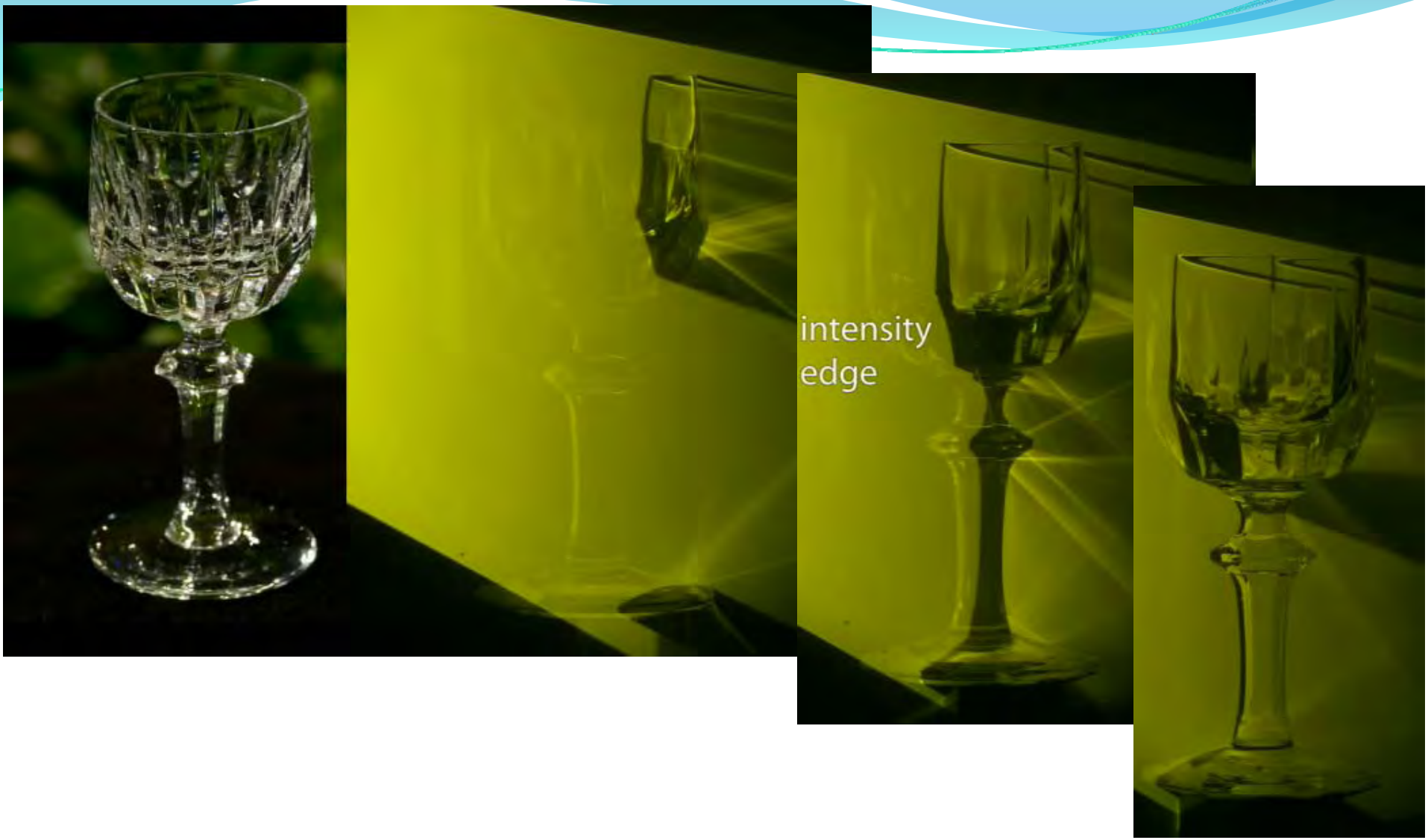
intensity
edge

[Hullin et al. 08]

- Fluorescent immersion range scanning

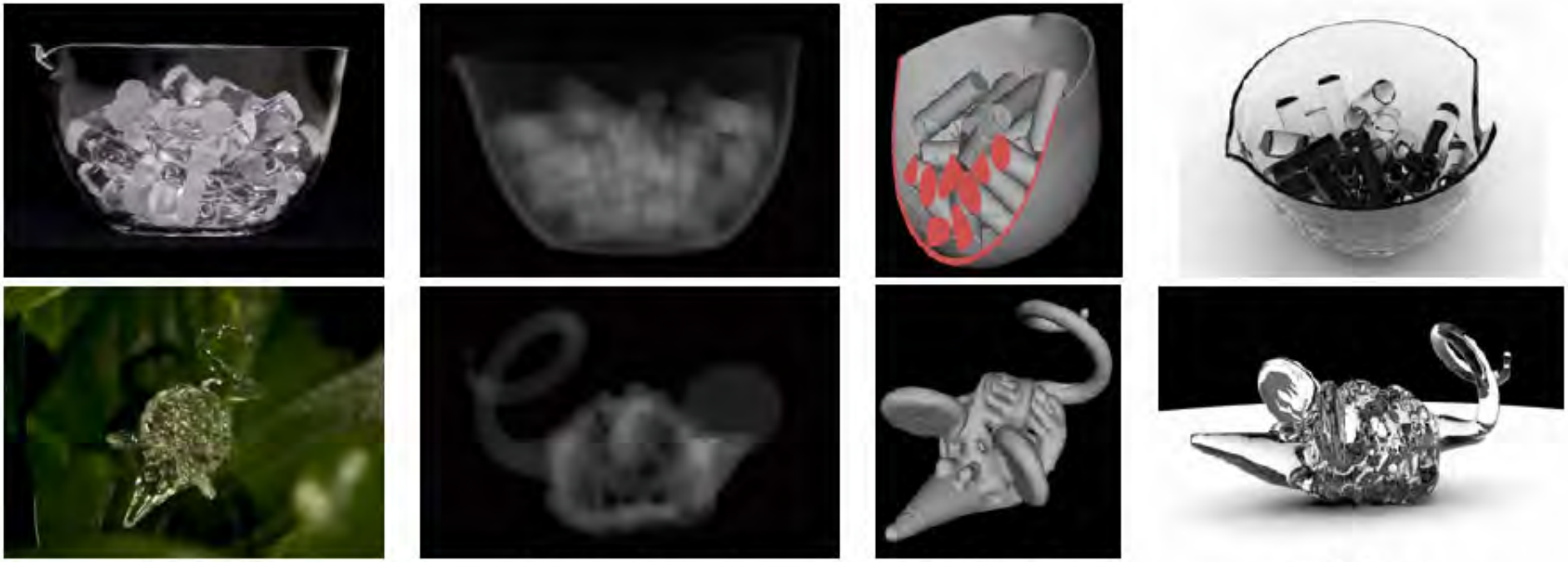

photograph of real object (a) | X-ray rendering of recovered volume (b) | Marching Cubes output mesh (c) | rendering in virtual environment (d)

To summarize

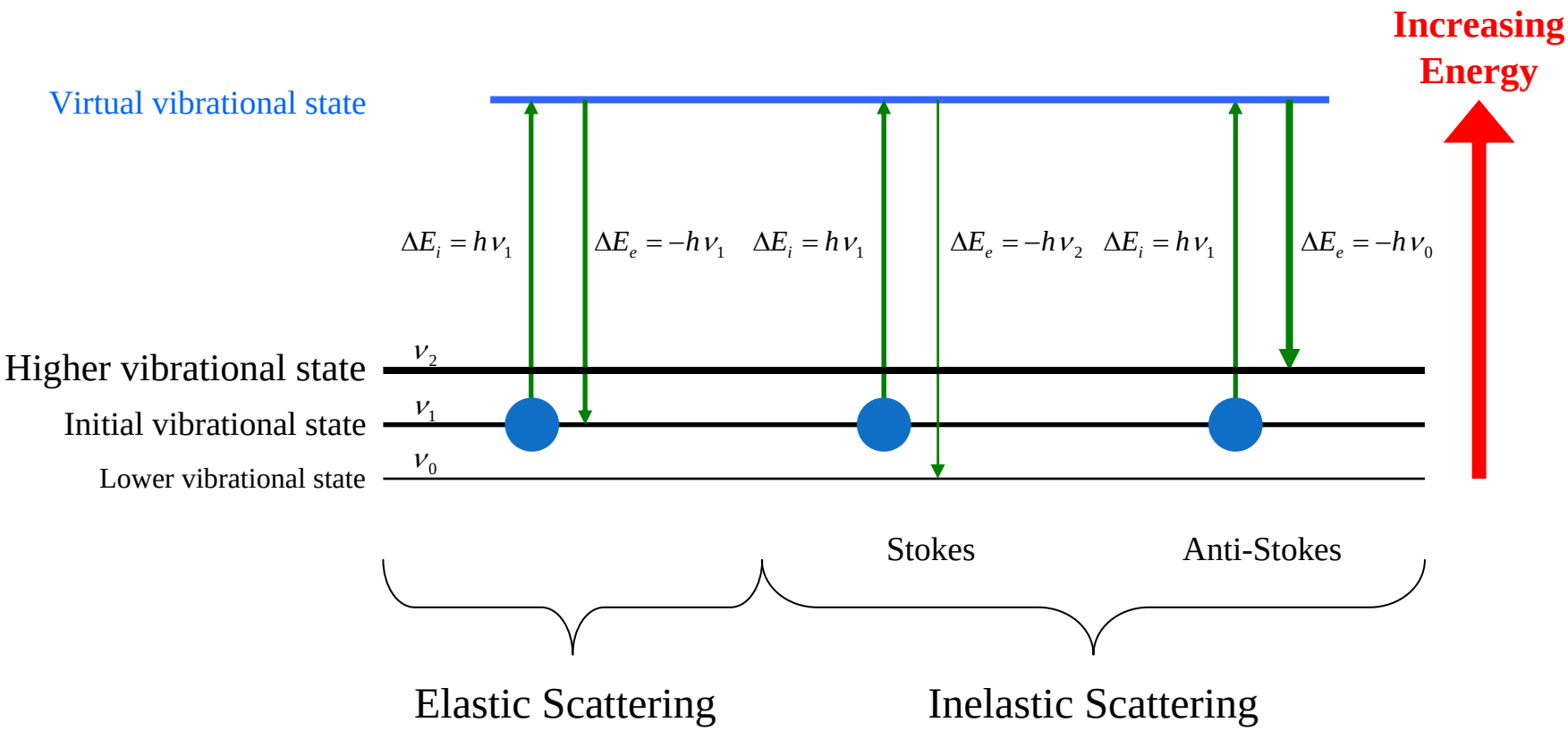

To summarize

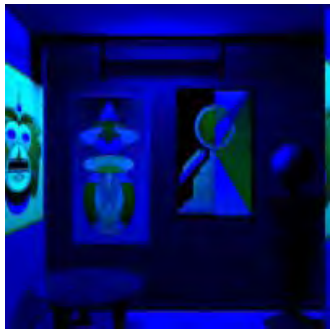

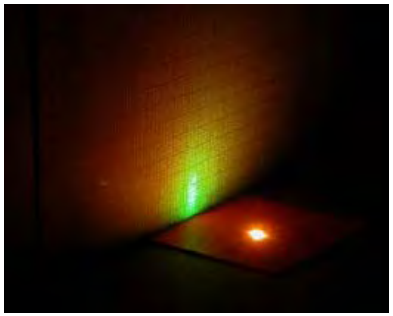

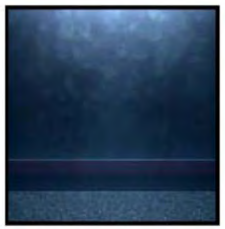

(a) $C = 0, \alpha_d = 0, \alpha_y = 0$ (b) $C = 0.01, \alpha_d = 0, \alpha_y = 0$ (c) $C = 0.1, \alpha_d = 0, \alpha_y = 0$ (d) $C = 1, \alpha_d = 0, \alpha_y = 0$

(e) $C = 0, \alpha_d = 0.1, \alpha_y = 0$ (f) $C = 0.01, \alpha_d = 0.1, \alpha_y = 0$ (g) $C = 0.1, \alpha_d = 0.1, \alpha_y = 0$ (h) $C = 1, \alpha_d = 0.1, \alpha_y = 0$

(i) $C = 0, \alpha_d = 0, \alpha_y = 0.1$ (j) $C = 0.01, \alpha_d = 0, \alpha_y = 0.1$ (k) $C = 0.1, \alpha_d = 0, \alpha_y = 0.1$ (l) $C = 1, \alpha_d = 0, \alpha_y = 0.1$

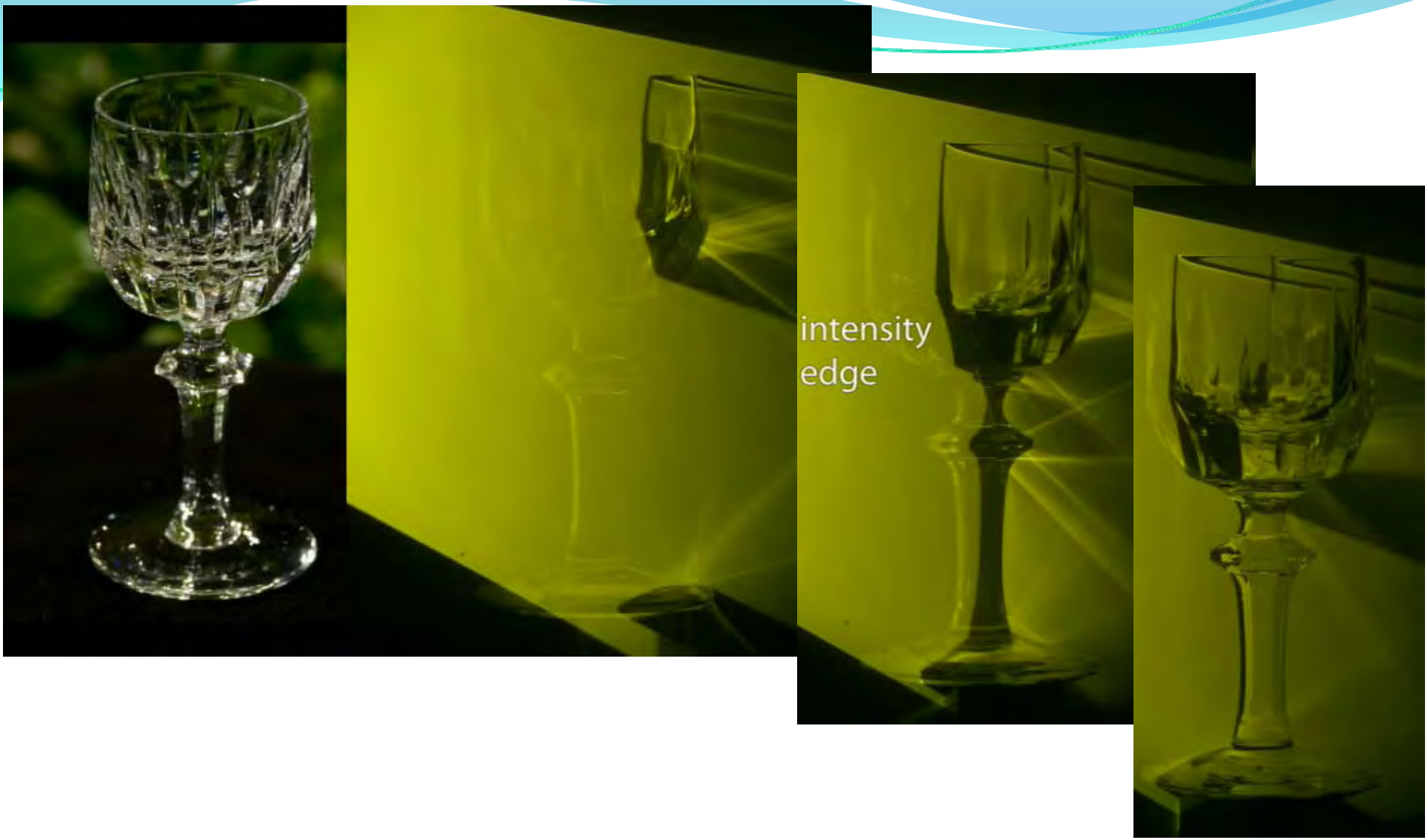
intensity
edge

Thanks for your attention!

Acquiring Scattering Properties of Participating Media by Dilution

Srinivasa Narasimhan, Craig Donner, Ravi Ramamoorthi
Mohit Gupta, Henrik Wann Jensen, Shree Nayar

Carnegie Mellon University
UC San Diego
Columbia University

SIGGRAPH 2006

Sponsors: NSF, ONR, Sloan

Scattering in Participating Media

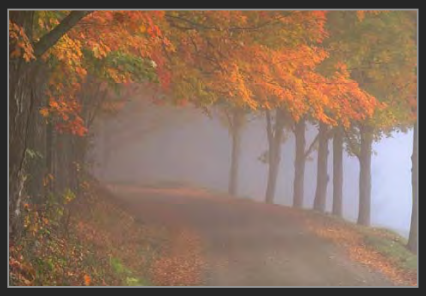


Accurate Rendering of Media Critical for Realism

Significant Progress in Volumetric Rendering

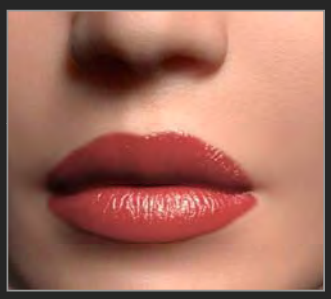

[Jensen et al, 01]

[Donner, 03]

[Jensen, 02]

[Fedkiw et al, 01]

Accuracy Limited by the Input Medium Parameters

Measuring Surface Reflectance [’95 - ’06]

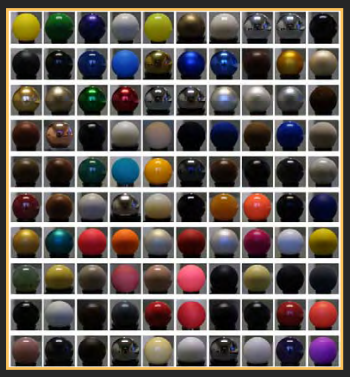

BRDF [Matusik et al, 03]

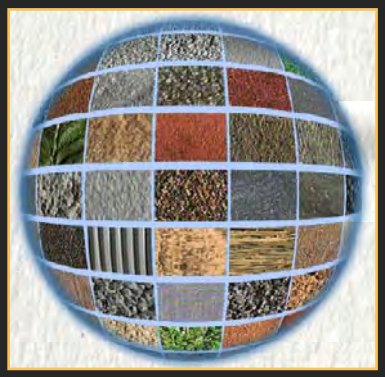

BTF [Dana et al, 97]

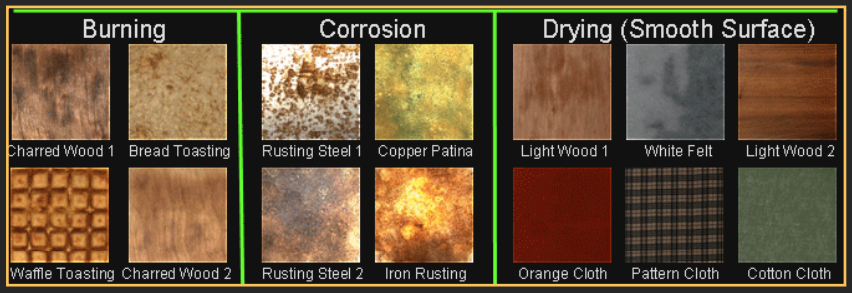

Time varying BTF [Gu et al, 06]

Measurement Work in Graphics

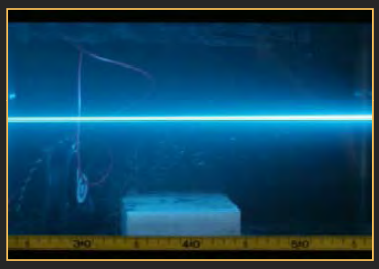

Attenuation of Laser Beams [Hawkins et al, 05]

No Scattering

Directional Scattering using a Mirror [Hawkins et al, 05]

No Attenuation

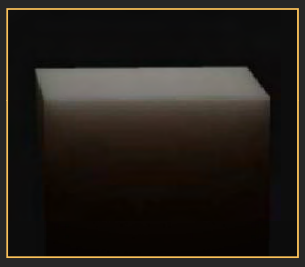

Diffusion-based BSSRDF Measurement [Jensen et al, 01; Joshi et al, 05]

High Scattering

Measurement Work in Graphics

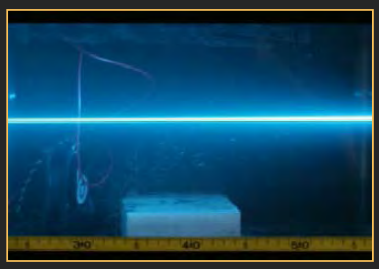

Attenuation of Laser Beams [Hawkins et al, 05]

No Scattering

Directional Scattering using a Mirror [Hawkins et al, 05]

No Attenuation

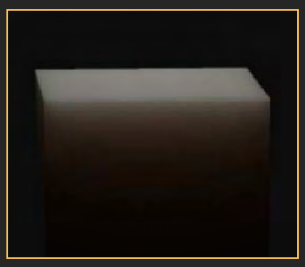

Diffusion-based BSSRDF Measurement [Jensen et al, 01; Joshi et al, 05]

High Scattering

One Simple Setup
Robust Parameter Estimation from a Photograph
Cover Entire Parameter Space

Our Measurement Setup

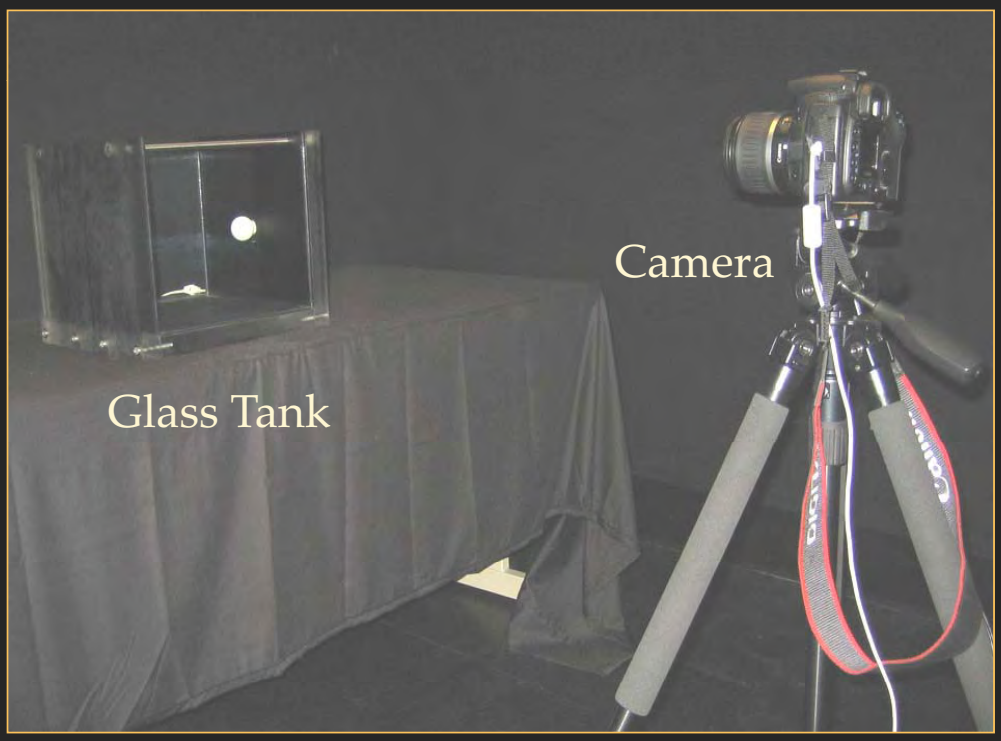

Our Measurement Setup

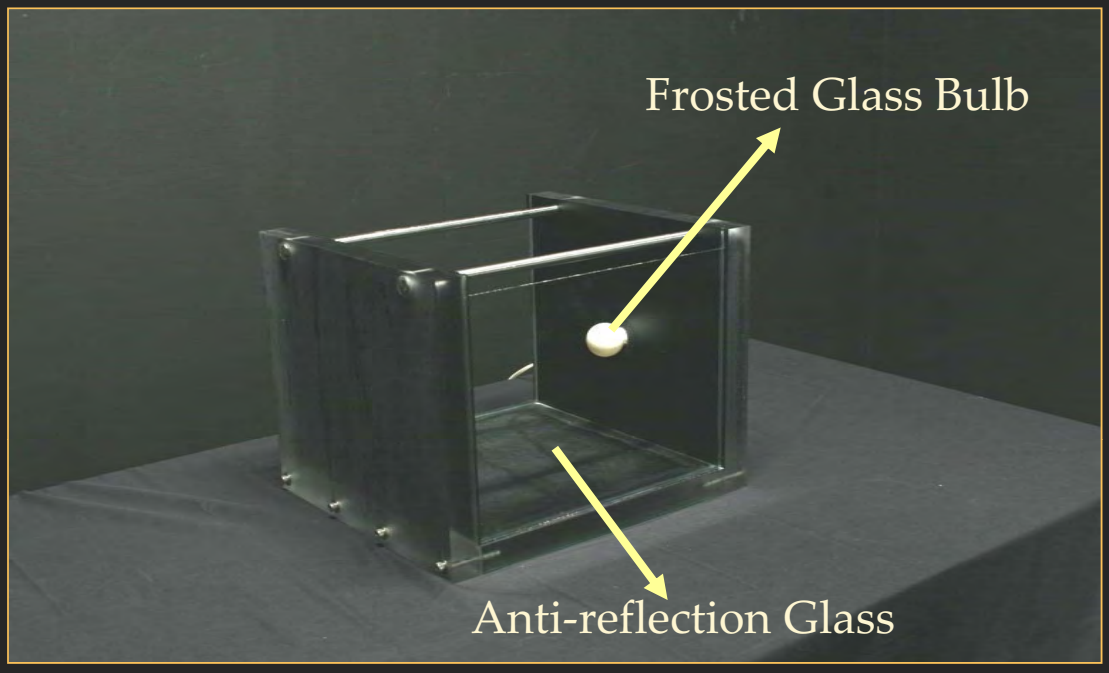

Dimensions of Tank: 25cm x 30 cm x 30 cm

Problem: Multiple Scattering

- Causes significant Blurring of Incident Light
- Inverse Estimation is Ill-conditioned and Not Unique

[Ishimaru 75,97; McCormick et al., 79-83]

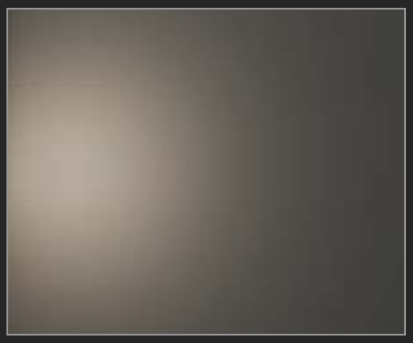

Photo of Milk in Setup

Problem: Multiple Scattering

- Causes significant Blurring of Incident Light
- Inverse Estimation is Ill-conditioned and Not Unique

[Ishimaru 75,97; McCormick et al., 79-83]

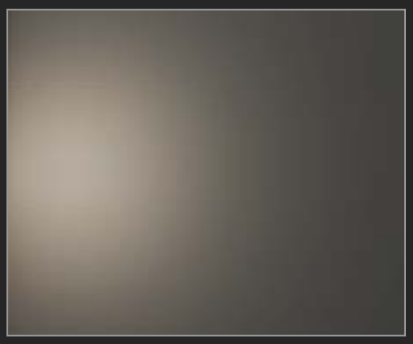

Photo of Milk in Setup

- Key Idea: Avoid Multiple Scattering

At "low" concentrations:

- Single Scattering dominant
- Multiple Scattering negligible

[Ishimaru 97; Narasimhan et al 99-03]

Increasing Milk Concentrations

So…dilute media “sufficiently” with water to simplify light transport.

Single Scattering Ray Geometry

Physical Apparatus

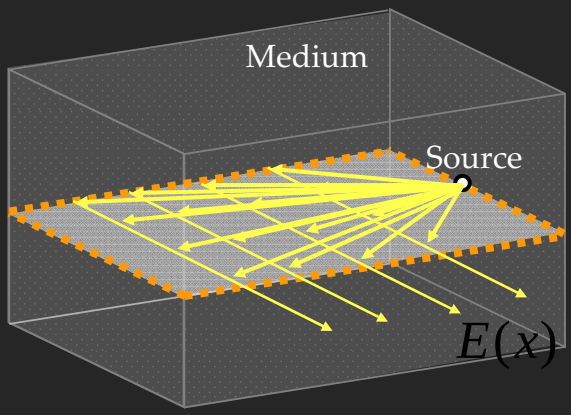

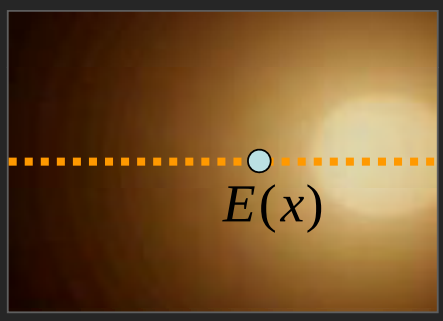

Captured Ortho-Photo

- Range of Scattering Angles: [0 deg, 175 deg]
- Range of Path-lengths: [125 mm, 610mm]
- All Path-length and Angle Combinations

Single Scattering Model and Estimation

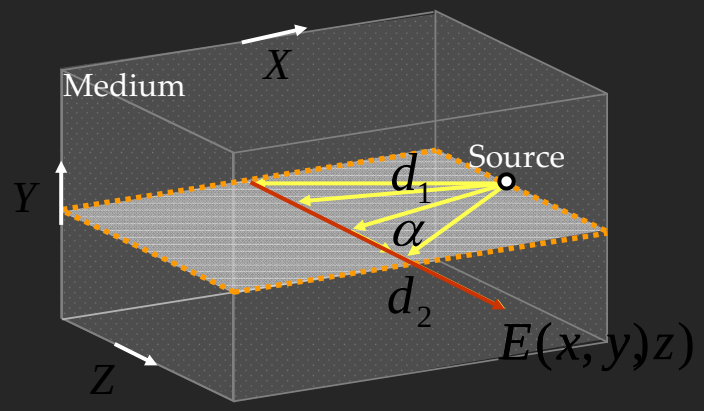

- Image Formation Model:

Scattering Coefficient — Phase function — Extinction Coefficient

$$E(x,y,z) = \int \frac{I_0}{d_1^2} \exp(-\sigma d_1) \bullet \beta\, P(\alpha, g) \bullet \exp(-\sigma d_2)\, dz$$

Single Scattering Model and Estimation

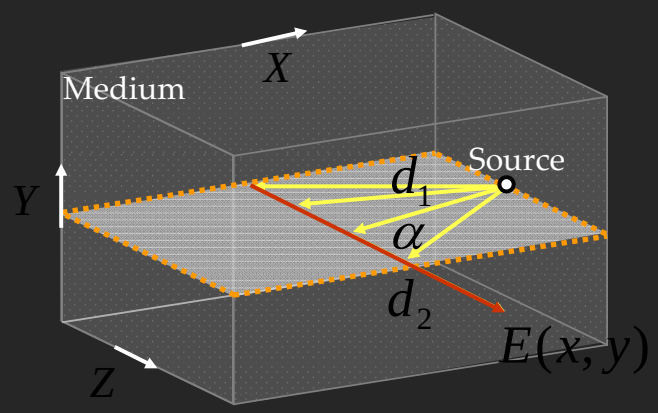

- Image Formation Model:

Scattering Coefficient — Phase function — Extinction Coefficient

$$E(x,y) = \int \frac{I_0}{d_1^2} \exp(-\sigma d_1) \bullet \beta\, P(\alpha, g) \bullet \exp(-\sigma d_2)\, dz$$

- Parameter Estimation: Nelder-Meade Search in Matlab

$$\arg\min_{\sigma,\beta,g} \| E^{\text{measured}}(x,y) - E^{\text{model}}(x,y) \|$$

Single Scattering Model and Estimation

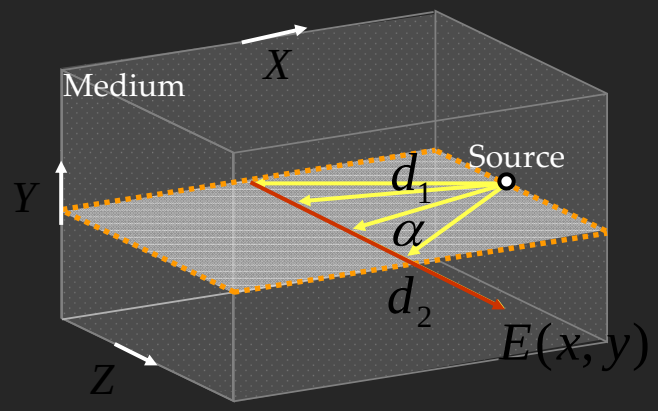

- Image Formation Model:

Scattering Coefficient — Phase function — Extinction Coefficient

$$E(x,y) = \int \frac{I_0}{d_1^2} \exp(-\sigma d_1) \bullet \beta\, P(\alpha, g) \bullet \exp(-\sigma d_2)\, dz$$

- Parameter Estimation: Nelder-Meade Search in Matlab

$$\arg\min_{\sigma,\beta,g} \| E^{\text{measured}}(x,y) - E^{\text{model}}(x,y) \|$$

Unique and Robust!

How Much to Dilute?

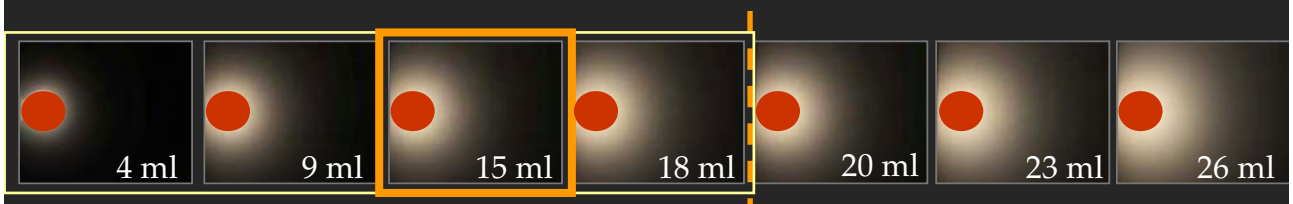

Increasing Milk Concentration

Single Scattering

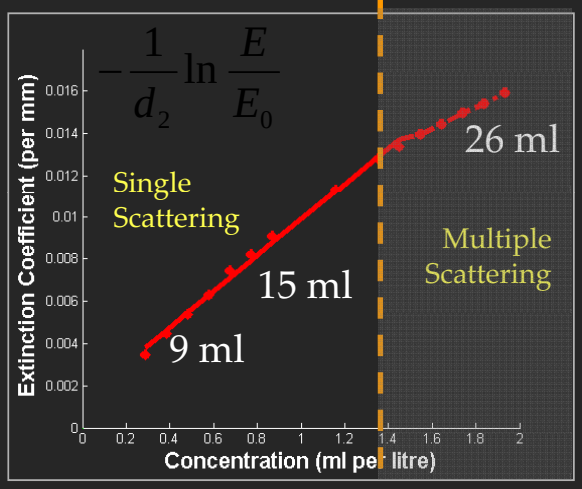

Multiple Scattering

Database of 40 Common Materials

- Alcoholic Beverages – 3 wines, 3 beers…
- Coffees – black, with cream, cappuccino,…
- Milks – chocolate, whole, 2% fat, vitamin A & D,…
- Juices – grape, apple, cranberry,…
- Soft-drinks – coke, pepsi, lemonade…
- Cleaning supplies – detergents, shampoos,…
- Powders and Crystals – sugar, salt, tang,…
- Pacific Ocean Water – bay, different depths,…

Sample Photographs: Highly Scattering Media

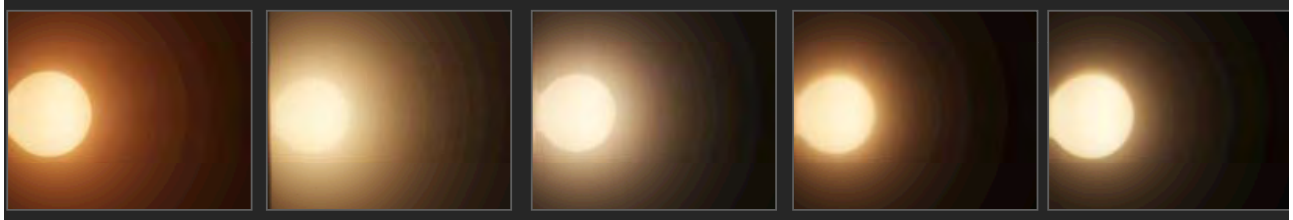

Pink Lemonade Powder | Regular Chocolate Milk | Low Fat Choc Milk | Ruby Grapefruit Juice | Salt Powder

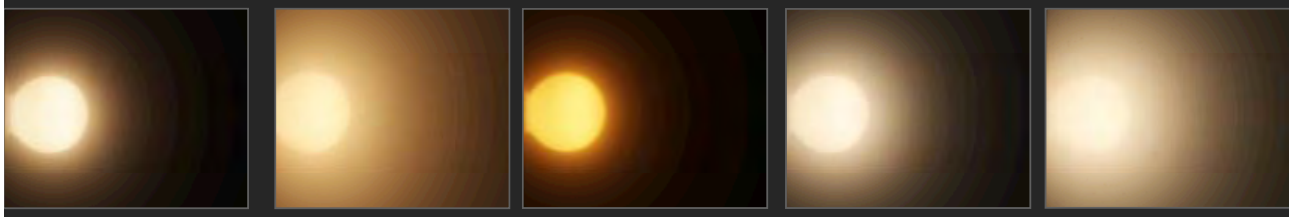

Espresso Coffee | Cappuccino Powder | Orange Powder | Low Fat Milk | Regular Milk

Sample Photographs: Highly Absorbing Media

Merlot Wine | Coke | Grape Juice | Yuengling Beer | Pacific Ocean Water

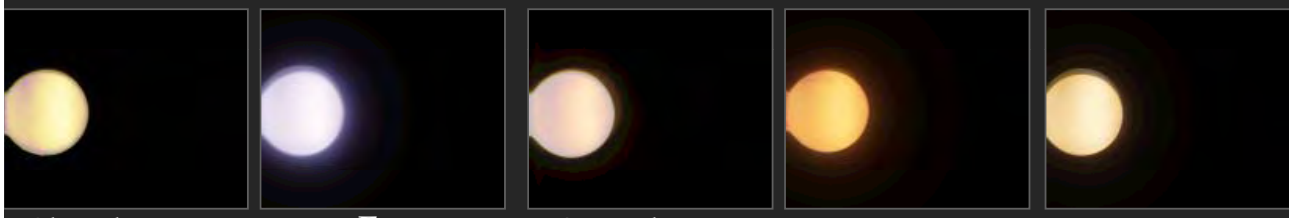

Chardonnay Wine | Era Detergent | Strawberry Shampoo | Lemon Tea Powder | Brown Sugar

Sample Parameters: Highly Scattering Media

Medium	Volume		Extinction Coefficient (σ) (x 10^{-2} mm^{-1})	Scattering Coefficient (β) (x 10^{-2} mm^{-1})	Average Cosine (g)
Low-Fat Milk	16 ml	R	0.9126	0.9124	0.932
		G	1.0748	1.0744	0.902
		B	1.2500	1.2492	0.859
Regular Milk	15 ml	R	1.1874	1.1873	0.750
		G	1.3296	1.3293	0.714
		B	1.4602	1.4589	0.681
Regular Chocolate Milk	16 ml	R	0.7359	0.7352	0.862
		G	0.9172	0.9142	0.838
		B	1.0688	1.0588	0.806

Sample Parameters: Highly Absorbing Media

Medium	Volume		Extinction Coefficient (σ) (x 10^{-2} mm^{-1})	Scattering Coefficient (β) (x 10^{-2} mm^{-1})	Average Cosine (g)
Yuengling Beer	2900 ml	R	0.1535	0.0495	0.969
		G	0.3322	0.0521	0.969
		B	0.7452	0.0597	0.975
Merlot Wine	1500 ml	R	0.7639	0.0053	0.974
		G	1.6429	0.0000	-
		B	1.9196	0.0000	-
Era Detergent	2300 ml	R	0.7987	0.0553	0.949
		G	0.5746	0.0586	0.950
		B	0.2849	0.0906	0.971


Merlot Wine
Coke
Era Detergent
Orange Powder
Pink Lemonade Powder
Strawberry Shampoo
Ruby Grape Fruit Juice
Chardonnay
Coors Light
Ocean Water
Sprite
Regular Choc Milk
Regular Milk
Low Fat Choc Milk
Low Fat Milk
Absorption Coefficient
Scattering Coefficient

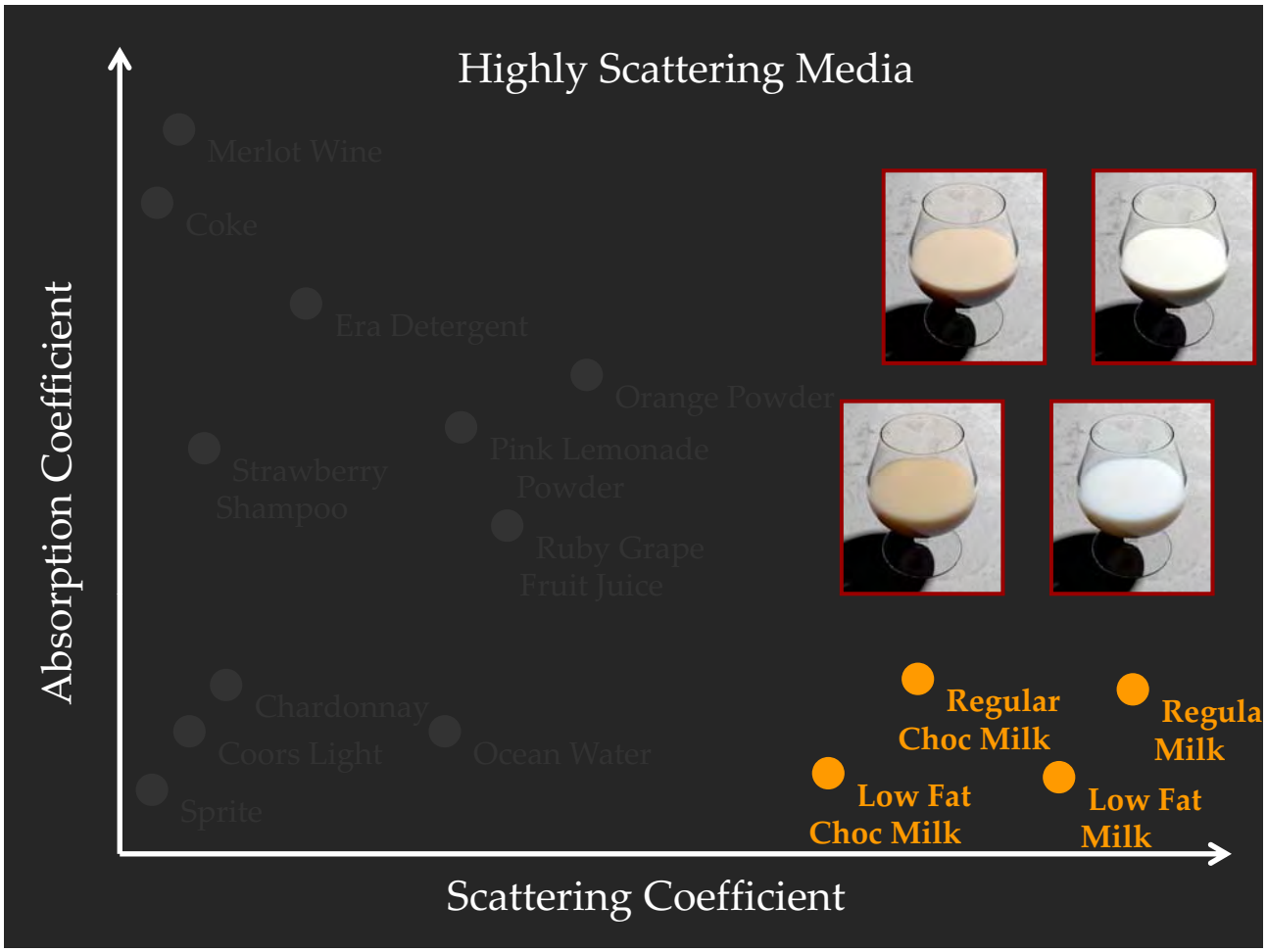
Highly Scattering Media
Merlot Wine
Coke
Era Detergent
Orange Powder
Pink Lemonade Powder
Strawberry Shampoo
Ruby Grape Fruit Juice
Chardonnay
Coors Light
Ocean Water
Sprite
Regular Choc Milk
Regular Milk
Low Fat Choc Milk
Low Fat Milk
Absorption Coefficient
Scattering Coefficient

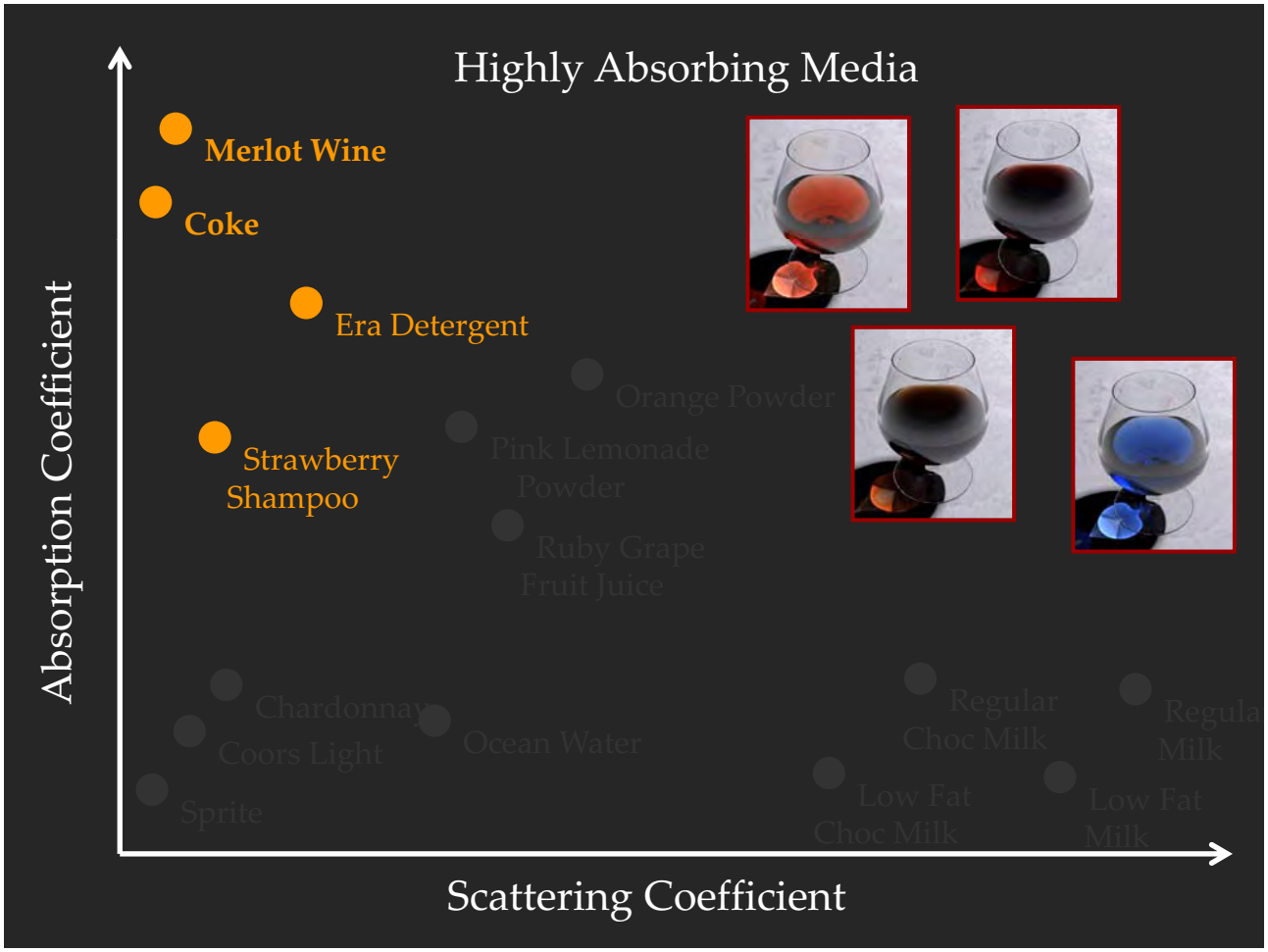
Highly Absorbing Media
Merlot Wine
Coke
Era Detergent
Strawberry Shampoo
Orange Powder
Pink Lemonade Powder
Ruby Grape Fruit Juice
Chardonnay
Coors Light
Ocean Water
Sprite
Regular Choc Milk
Low Fat Choc Milk
Low Fat Milk
Absorption Coefficient
Scattering Coefficient

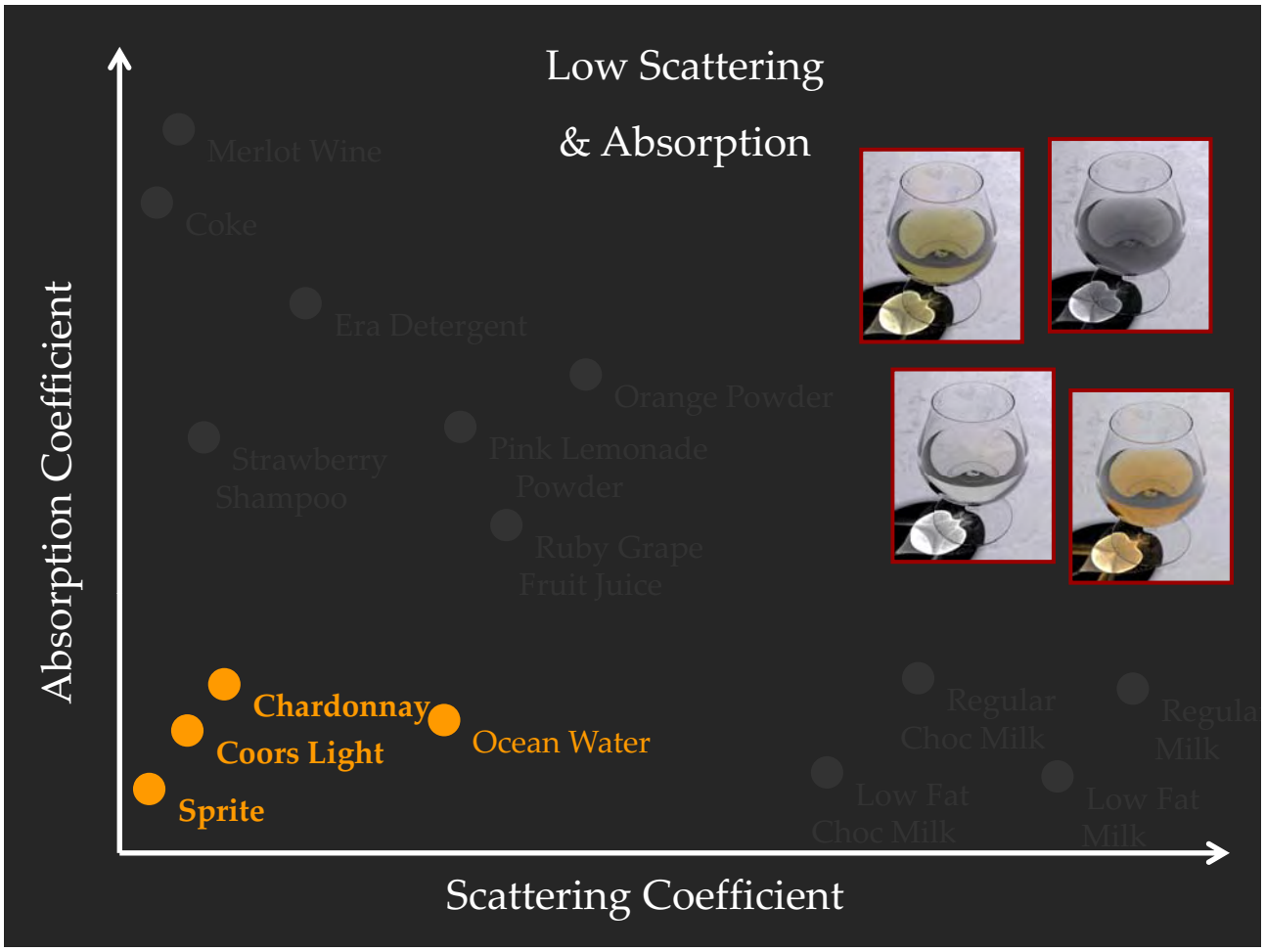
Low Scattering
& Absorption
Merlot Wine
Coke
Era Detergent
Orange Powder
Strawberry Shampoo
Pink Lemonade Powder
Ruby Grape Fruit Juice
Chardonnay
Coors Light
Ocean Water
Sprite
Regular Choc Milk
Low Fat Choc Milk
Low Fat Milk
Absorption Coefficient
Scattering Coefficient

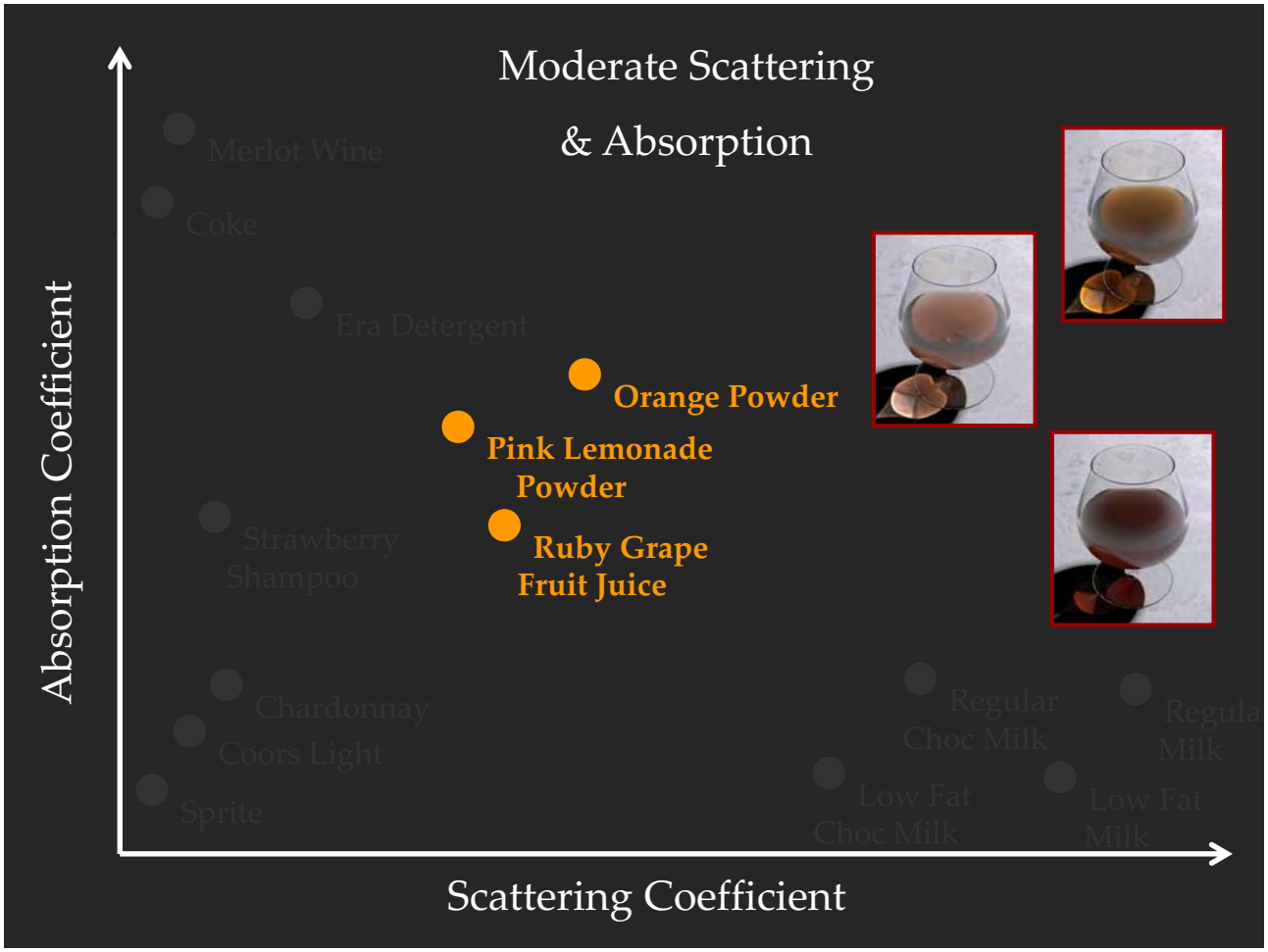

Material Name	Volume	Extinction Coefficient (σ) ($\times 10^{-2}$ mm^{-1})			Scattering Coefficient (β) ($\times 10^{-2}$ mm^{-1})			Average Cosine (g)			% RMS Error
		R	G	B	R	G	B	R	G	B	
Milk (lowfat)	16ml	0.9126	1.0748	1.2500	0.9124	1.0744	1.2492	0.932	0.902	0.859	0.95
Milk (reduced)	18ml	1.0750	1.2213	1.3941	1.0748	1.2209	1.3931	0.819	0.797	0.746	1.27
Milk (regular)	15ml	1.1874	1.3296	1.4602	1.1873	1.3293	1.4589	0.750	0.714	0.681	1.56
Coffee (espresso)	8ml	0.4376	0.5115	0.6048	0.2707	0.2828	0.2970	0.907	0.896	0.880	1.90
Coffee (mint mocha)	6ml	0.1900	0.2600	0.3500	0.0916	0.1081	0.1460	0.910	0.907	0.914	2.00
Soy Milk (lowfat)	16ml	0.1419	0.1625	0.2740	0.1418	0.1620	0.2715	0.850	0.853	0.842	1.75
Soymilk (regular)	12ml	0.2434	0.2719	0.4597	0.2433	0.2714	0.4563	0.873	0.858	0.832	1.68
Chocolate Milk (lowfat)	10ml	0.4282	0.5014	0.5791	0.4277	0.4998	0.5723	0.934	0.927	0.916	1.04
Chocolate Milk (regular)	16ml	0.7359	0.9172	1.0688	0.7352	0.9142	1.0588	0.862	0.838	0.806	2.19
Soda (coke)	1600ml	0.7143	1.1688	1.7169	0.0177	0.0208	0.0000	0.965	0.972	–	4.86
Soda (pepsi)	1600ml	0.6433	0.9990	1.4420	0.0058	0.0141	0.0000	0.926	0.979	–	2.92
Soda (sprite)	15000ml	0.1299	0.1283	0.1395	0.0069	0.0089	0.0089	0.943	0.953	0.952	3.22
Sports Gatorade	1500ml	0.4009	0.4185	0.4324	0.2392	0.2927	0.3745	0.933	0.933	0.935	3.42
Wine (chardonnay)	3300ml	0.1577	0.1748	0.3512	0.0030	0.0047	0.0069	0.914	0.958	0.975	5.10
Wine (white zinfandel)	3300ml	0.1763	0.2370	0.2913	0.0031	0.0048	0.0066	0.919	0.943	0.972	5.49
Wine (merlot)	1500ml	0.7639	1.6429	1.9196	0.0053	0.0000	0.0000	0.974	–	–	4.56
Beer (budweiser)	2900ml	0.1486	0.3210	0.7360	0.0037	0.0069	0.0074	0.917	0.956	0.982	5.61
Beer (coorslight)	1000ml	0.0295	0.0663	0.1521	0.0027	0.0055	0.0000	0.918	0.966	–	4.89
Beer (yuengling)	2900ml	0.1535	0.3322	0.7452	0.0495	0.0521	0.0597	0.969	0.969	0.975	4.48
Detergent (Clorox)	1200ml	0.1600	0.2500	0.3300	0.1425	0.1723	0.1928	0.912	0.905	0.892	1.99
Detergent (Era)	2300ml	0.7987	0.5746	0.2849	0.0553	0.0586	0.0906	0.949	0.950	0.971	4.17
Apple Juice	1800ml	0.1215	0.2101	0.4407	0.0201	0.0243	0.0323	0.947	0.949	0.945	4.92
Cranberry Juice	1500ml	0.2700	0.6300	0.8300	0.0128	0.0155	0.0196	0.947	0.951	0.974	4.60
Grape Juice	1200ml	0.5500	1.2500	1.5300	0.0072	0.0000	0.0000	0.961	–	–	5.19
Ruby Grapefruit Juice	240ml	0.2513	0.3517	0.4305	0.1617	0.1606	0.1669	0.929	0.929	0.931	2.68
White Grapefruit Juice	160ml	0.3609	0.3800	0.5632	0.3513	0.3669	0.5237	0.548	0.545	0.565	2.84
Shampoo (balancing)	300ml	0.0288	0.0710	0.0952	0.0104	0.0114	0.0147	0.910	0.905	0.920	4.86
Shampoo (strawberry)	300ml	0.0217	0.0788	0.1022	0.0028	0.0032	0.0033	0.927	0.935	0.994	2.47
Head & Shoulders	240ml	0.3674	0.4527	0.5211	0.2791	0.2890	0.3086	0.911	0.896	0.884	1.91
Lemon Tea Powder	5tsp	0.3400	0.5800	0.8800	0.0798	0.0898	0.1073	0.946	0.946	0.949	2.83
Orange Powder	4tbsp	0.3377	0.5573	1.0122	0.1928	0.2132	0.2259	0.919	0.918	0.922	2.25
Pink Lemonade Powder	5tbsp	0.2400	0.3700	0.4500	0.1235	0.1334	0.1305	0.902	0.902	0.904	1.02
Cappuccino Powder	0.25tsp	0.2574	0.3536	0.4840	0.0654	0.0882	0.1568	0.849	0.843	0.926	0.67
Salt Powder	1.75cup	0.7600	0.8685	0.9363	0.2485	0.2822	0.3216	0.802	0.793	0.821	1.34
Sugar Powder	5cup	0.0795	0.1759	0.2780	0.0145	0.0162	0.0202	0.921	0.919	0.931	1.80
Suisse Mocha Powder	0.5tsp	0.5098	0.6476	0.7944	0.3223	0.3583	0.4148	0.907	0.894	0.888	1.33
Mission Bay Surface Water (1-2 hours)		3.3623	3.2929	3.2193	0.2415	0.2762	0.3256	0.842	0.865	0.912	2.48
Pacific Ocean Surface Water (1 hour)		3.3645	3.3158	3.2428	0.1800	0.1834	0.2281	0.902	0.825	0.914	2.57
Mission Bay 10ft deep Water (30 min)		3.4063	3.3410	3.2810	0.0990	0.1274	0.1875	0.726	0.820	0.921	5.10
Mission Bay 10ft deep Water (8 hours)		3.3997	3.3457	3.2928	0.1018	0.1033	0.1611	0.929	0.910	0.945	5.13

Experimental Validation: Fits to Measurements

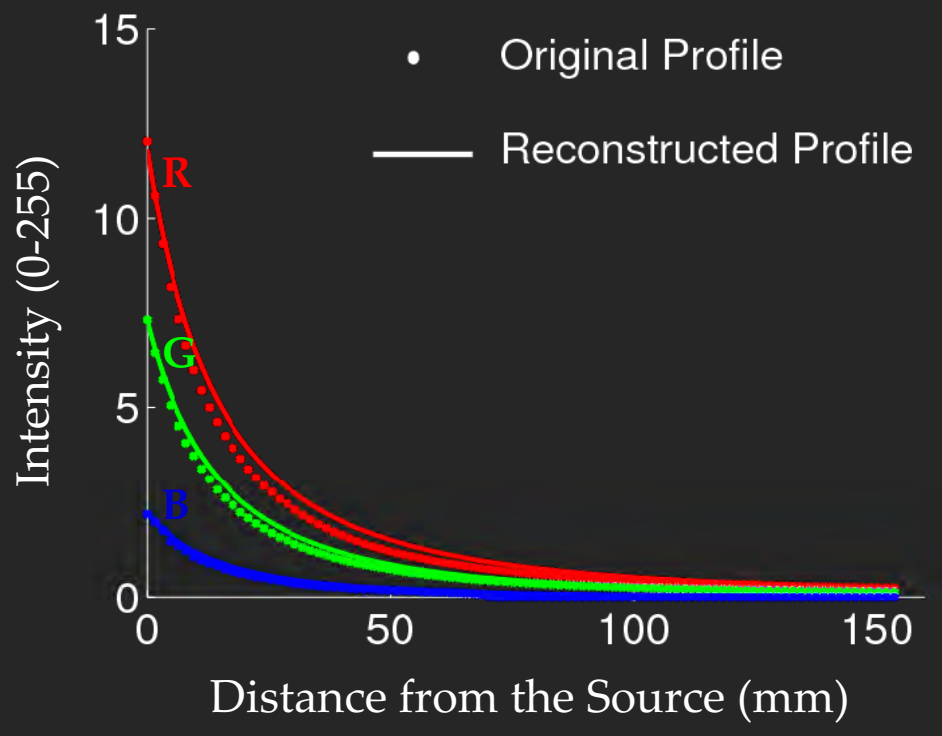

Orange Powder

Sample Fits: Highly Absorbing Media

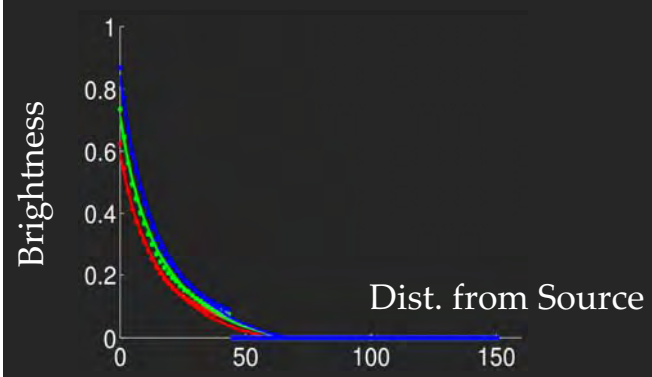

Era Detergent

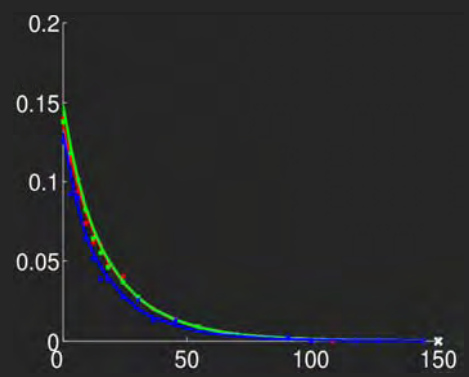

Pacific Ocean Surface Water

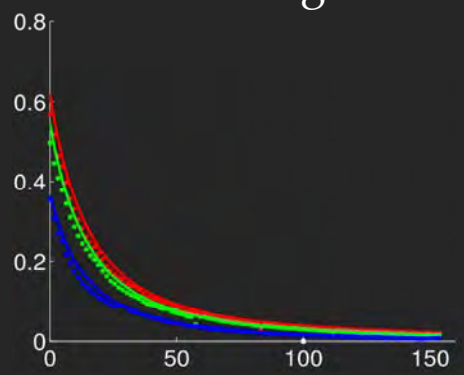

Yuengling Beer

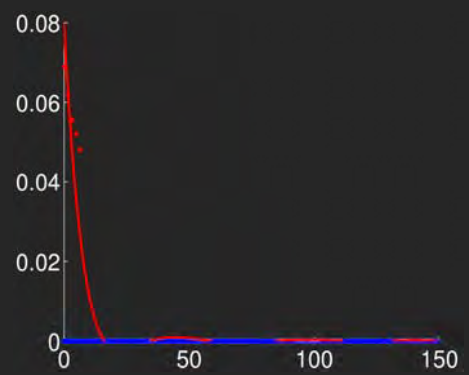

Merlot Wine

Sample Fits: Highly Scattering Media

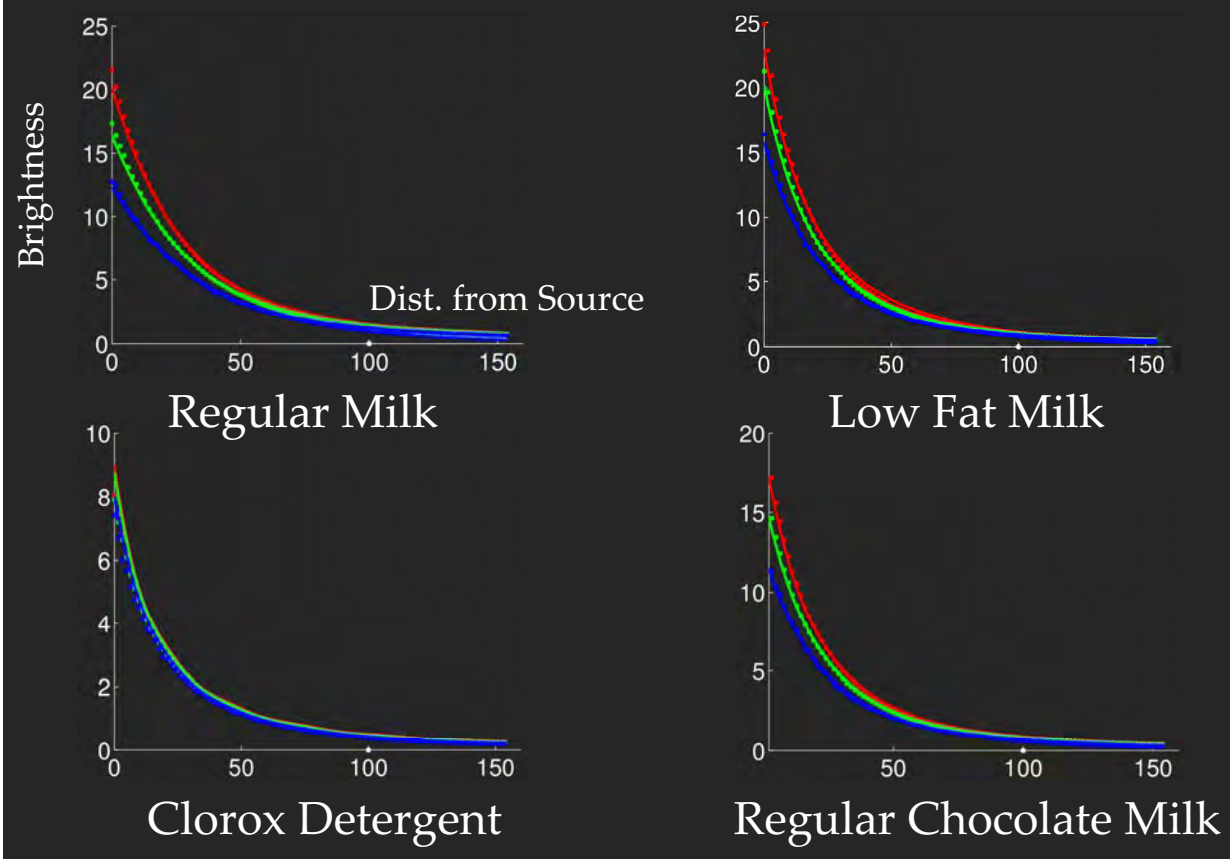

Renderings with the "Kitchen" Environment Map

[Debevec et al]

Merlot Wine

Chardonnay Wine

Yuengling Beer

Coca-Cola

Yuengling Beer

Milk

Renderings with a Single Directional Light Source

Yuengling Beer

Coca-cola

Chardonnay Wine

Orange Powder

Strawberry Shampoo

Era Detergent

Blending Parameters

75% Espresso

+

25% Milk

=

Light Coffee

Blending Parameters

+

=

50% Wine 50% Milk ?

Transitions between Media

Wine → Water → Milk → Espresso

Concentrations at which Parameters Measured

Real Concentrations

Summary

Simple Apparatus

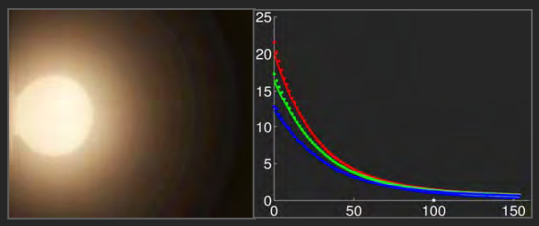

Robust Parameter Estimation

Render Any Concentration

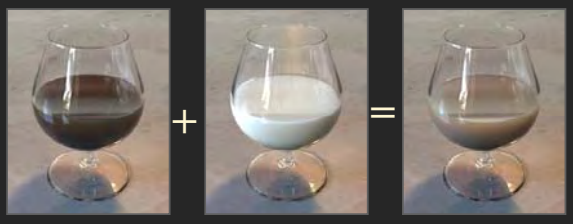

Mixing Media

http://graphics.cs.cmu.edu

Rendering Scattering Materials

Simulating the Appearance of Natural Materials

Henrik Wann Jensen

Computer Science and Engineering

University of California, San Diego

The Natural World

Mist

A Sunset

The Green Flash

A Halo

Human Skin

Simulating Natural Materials

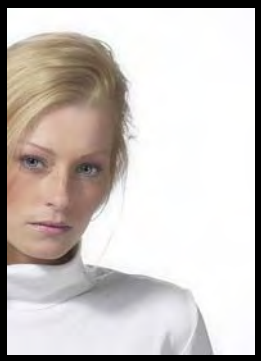

Simulating the appearance of scattering media and materials

Appearance Modeling

Film

Computer Games

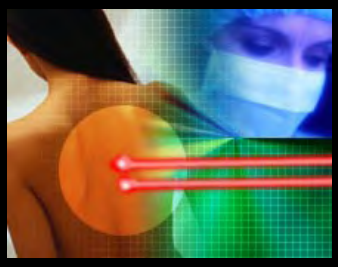

Medicin

Radiative Transport

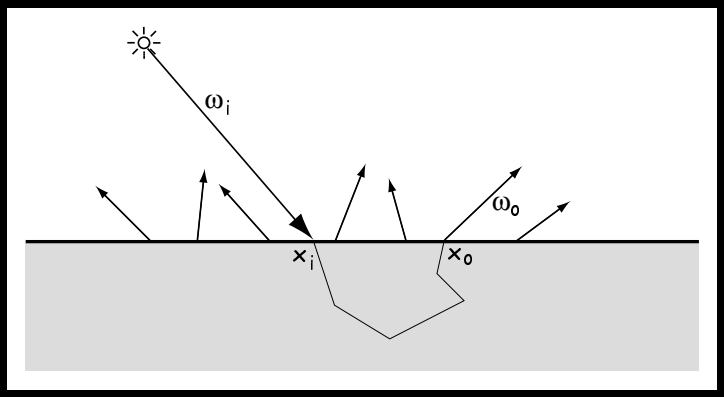

$$
\begin{aligned}
(\vec{\omega}\cdot\nabla)L(x,\vec{\omega}) \;=\; & -\sigma_t L(x,\vec{\omega}) + \\
& \sigma_s \int_{4\pi} p(\vec{\omega},\vec{\omega}')L(x,\vec{\omega}')d\vec{\omega}' + \\
& s(x,\vec{\omega})
\end{aligned}
$$

Marble Bust

Monte Carlo photon tracing, rendering time = days

Photon Mapping

[Jensen and Christensen, SIGGRAPH 1998]

Wet Materials

[Jensen, Legakis, and Dorsey -- EGWR 1999]

Rising Smoke Simulation

[Fedkiw, Stam, and Jensen -- SIGGRAPH 2001]

Campfire Simulation

[Nguyen, Fedkiw, and Jensen -- SIGGRAPH 2002]

BRDF

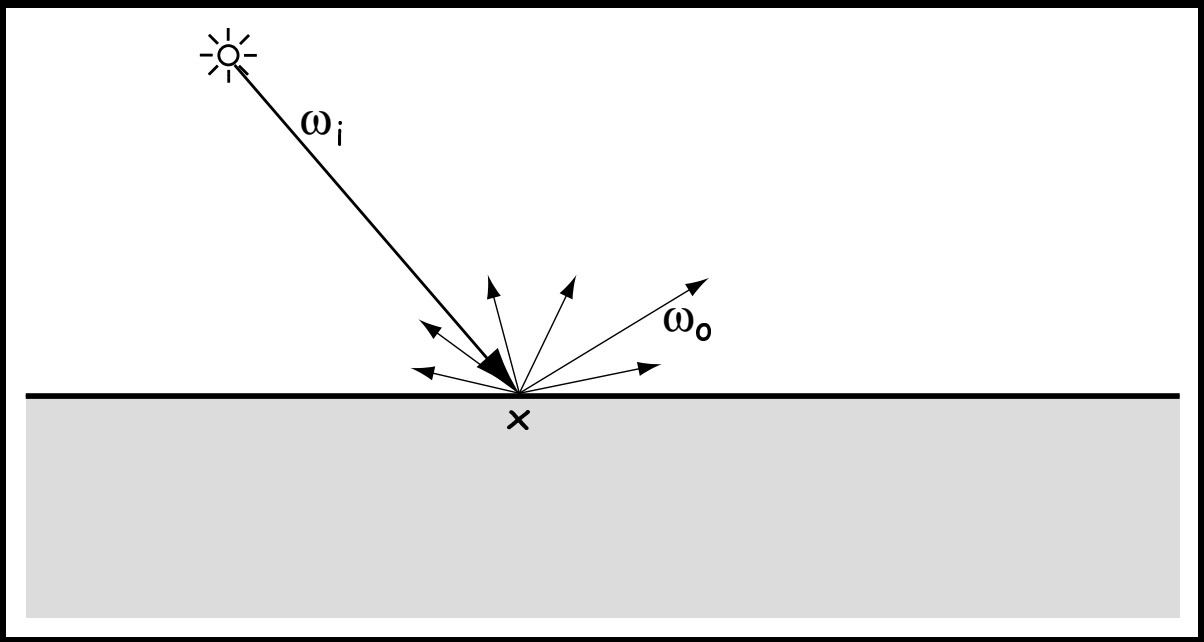

BRDF: $f_r(x, \vec{\omega}_i, \vec{\omega}_o) = \frac{dL(x,\vec{\omega}_i)}{dE(x,\vec{\omega}_o)}$

Marble Bust (BRDF)

BSSRDF

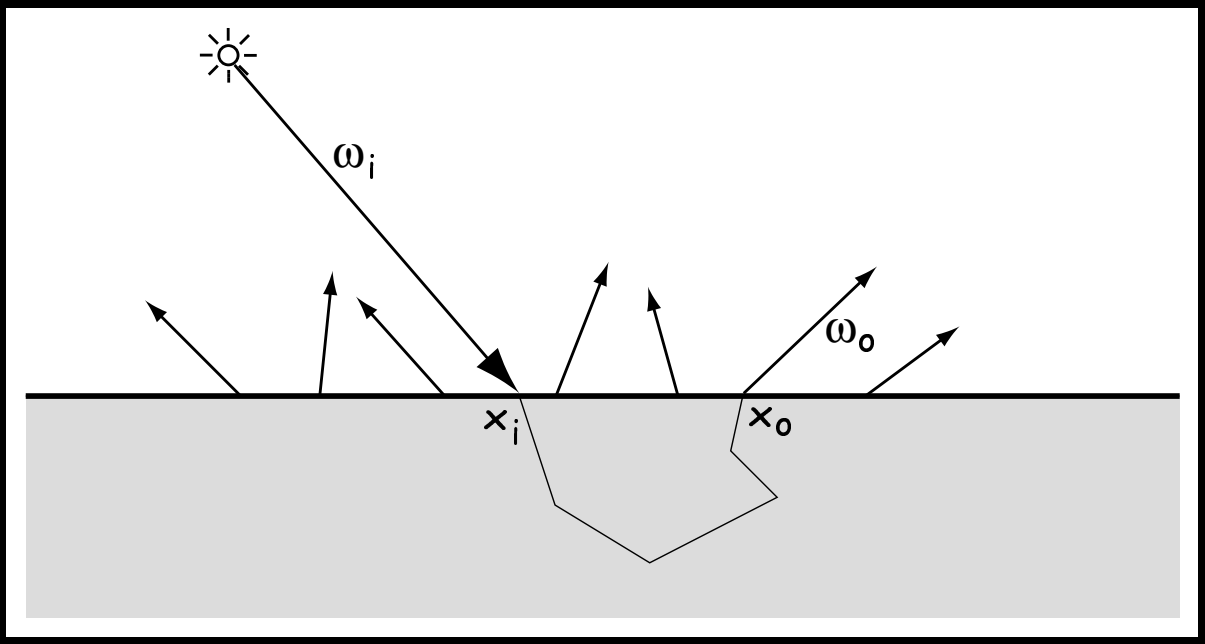

BSSRDF: $S(x_i, \vec{\omega}_i, x_o, \vec{\omega}_o) = \frac{dL(x_o, \vec{\omega}_o)}{d\Phi(x_i, \vec{\omega}_i)}$

Radiative Transport

$$
\begin{aligned}
(\vec{\omega} \cdot \nabla) L(x, \vec{\omega}) \;=\; & -\sigma_t L(x, \vec{\omega}) + \\
& \sigma_s \int_{4\pi} p(\vec{\omega}, \vec{\omega}') L(x, \vec{\omega}') d\vec{\omega}' + \\
& s(x, \vec{\omega})
\end{aligned}
$$

- Costly for highly scattering materials
- Highly scattering materials are common

Human Skin

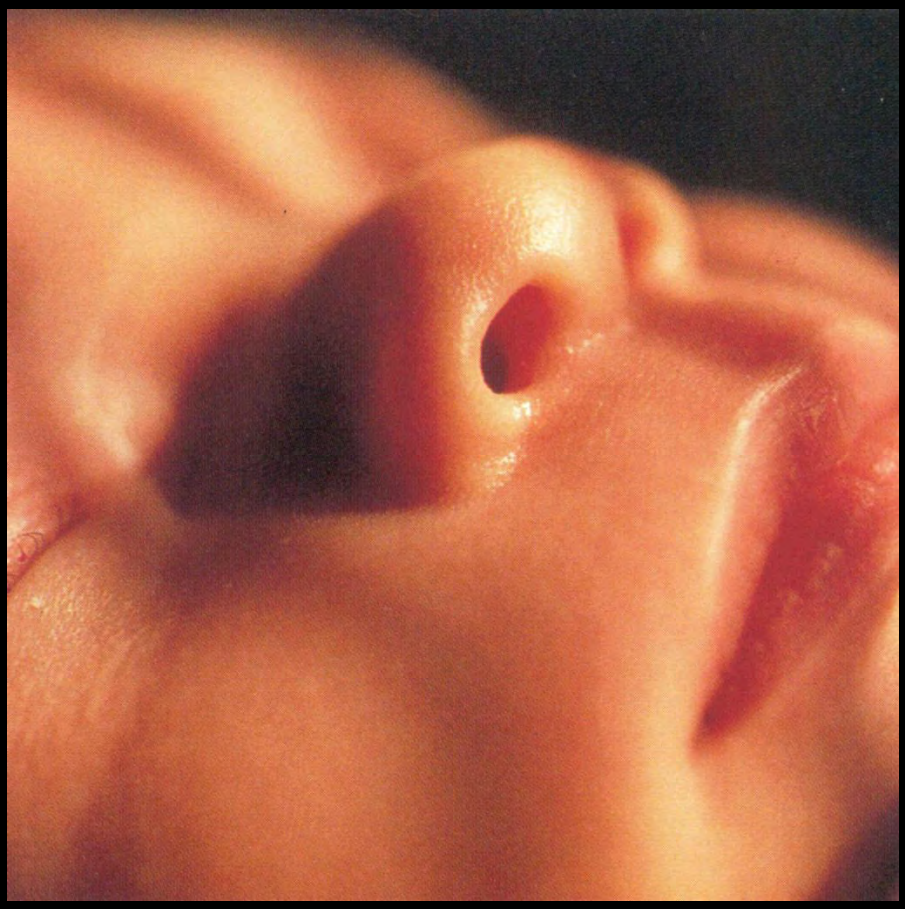

The Diffusion Approximation

$$L(x,\vec{\omega}) = L_u(x,\vec{\omega}) + L_d(x,\vec{\omega})$$

$$L_d(x,\vec{\omega}) \approx F_t(x) + \frac{3}{4}\pi\vec{E}(x)\cdot\vec{\omega}$$

The diffusion equation

$$\frac{1}{3\sigma_t'}\nabla^2 F_t(x) = \sigma_a F_t(x) - S_0(x) + \frac{1}{\sigma_t'}\nabla\cdot\vec{S}_1(x)$$

The BSSRDF Model

Multiple scattering:

$$dM_o(x_o) = d\Phi_i(x_i)\frac{\alpha'}{4\pi}\left\{C_1\frac{e^{-\sigma_{tr}d_r}}{d_r^2} + C_2\frac{e^{-\sigma_{tr}d_v}}{d_v^2}\right\}$$

where

$$C_1 = z_r\left(\sigma_{tr} + \frac{1}{d_r}\right) \quad \text{and} \quad C_2 = z_v\left(\sigma_{tr} + \frac{1}{d_v}\right)$$

Single scattering:

$$L_o^{(1)}(x_o,\vec{\omega}_o) = \sigma_s(x_o)\int_{2\pi} F\,p(\vec{\omega}_i'\cdot\vec{\omega}_o')\int_0^\infty e^{-\sigma_{tc}s}L_i(x_i,\vec{\omega}_i)\,ds\,d\vec{\omega}_i$$

$$= \int_A\int_\Omega S^{(1)}(x_i,\vec{\omega}_i;x_o,\vec{\omega}_o)\,L_i(x_i,\vec{\omega}_i)\,(\vec{n}\cdot\vec{\omega}_i)\,d\vec{\omega}_i dA(x_i)$$

[Jensen, Marschner, Levoy, and Hanrahan - SIGGRAPH 2001]

The BSSRDF Model

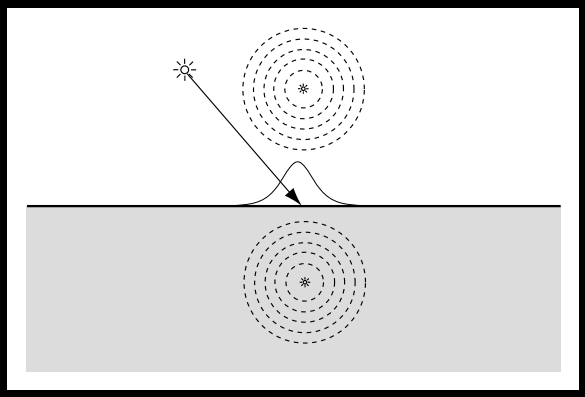

Multiple Scattering

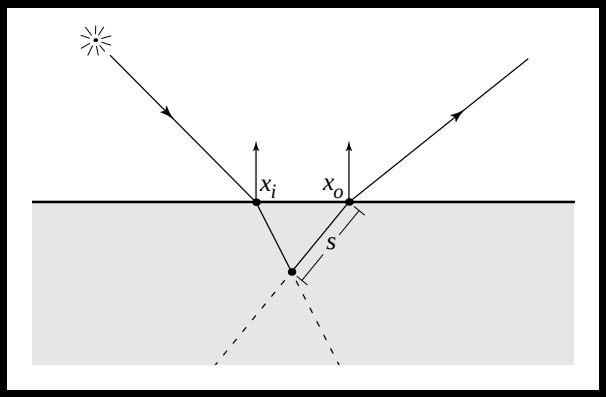

Single Scattering

Marble Bust (BSSRDF)

Marble: MCRT versus BSSRDF

MCRT

BSSRDF

Marble: BRDF versus BSSRDF

BRDF

BSSRDF

A Face (BSSRDF Model)

Modeled by Steven Stahlberg

A Face (BRDF Approximation)

Modeled by Steven Stahlberg

Virtual Skin

[Swerdlow, National Geographic 2002]

Shrek

[Jensen and Buhler, SIGGRAPH 2002]

Structure of Skin

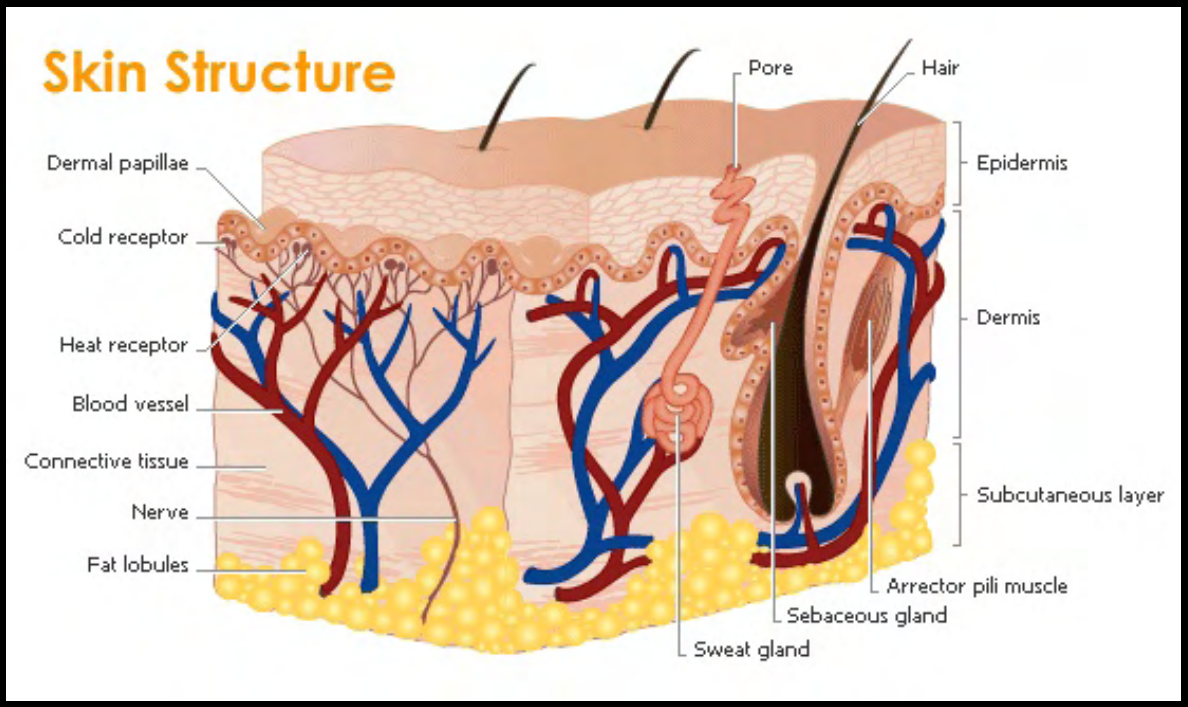

Scattering in a Layer

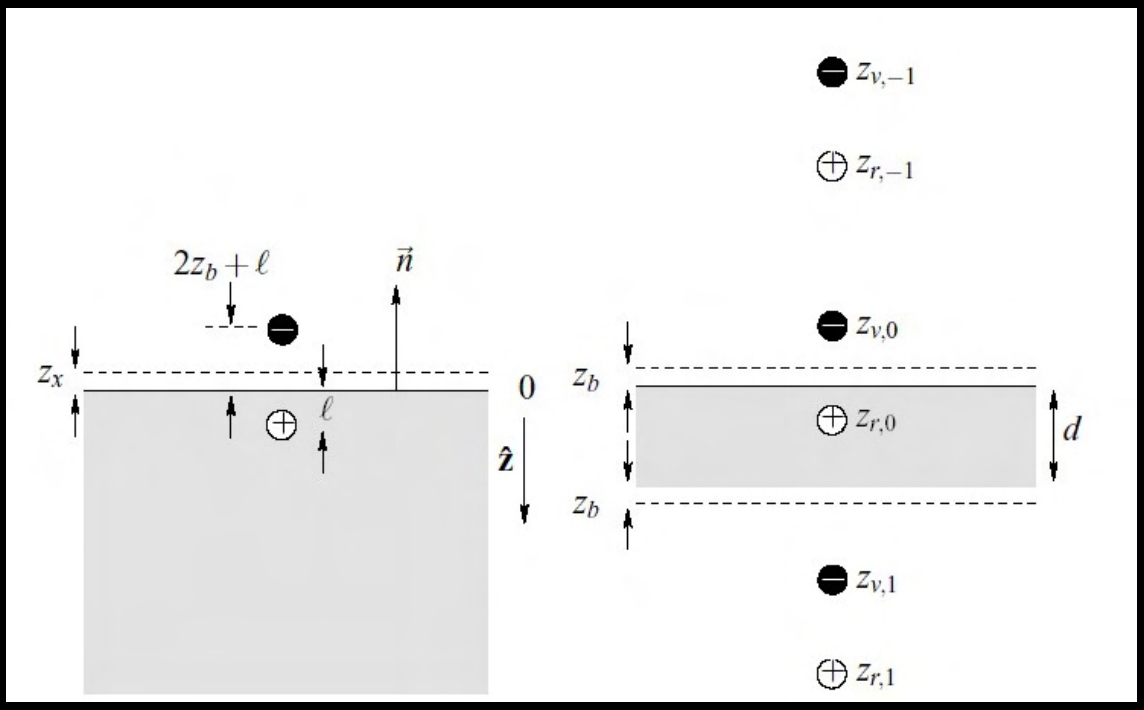

Multipole Diffusion

$$R(r) = \sum_{i=-n}^{n} \frac{\alpha' z_{r,i}(1+\sigma_{tr} d_{r,i}) e^{-\sigma_{tr} d_{r,i}}}{4\pi d_{r,i}^3} - \frac{\alpha' z_{v,i}(1+\sigma_{tr} d_{v,i}) e^{-\sigma_{tr} d_{v,i}}}{4\pi d_{v,i}^3}$$

$$T(r) = \sum_{i=-n}^{n} \frac{\alpha'(d - z_{r,i})(1+\sigma_{tr} d_{r,i}) e^{-\sigma_{tr} d_{r,i}}}{4\pi d_{r,i}^3} - \frac{\alpha'(d - z_{v,i})(1+\sigma_{tr} d_{v,i}) e^{-\sigma_{tr} d_{v,i}}}{4\pi d_{v,i}^3}$$

[Donner and Jensen, SIGGRAPH 2005]

Scattering in Two Layers

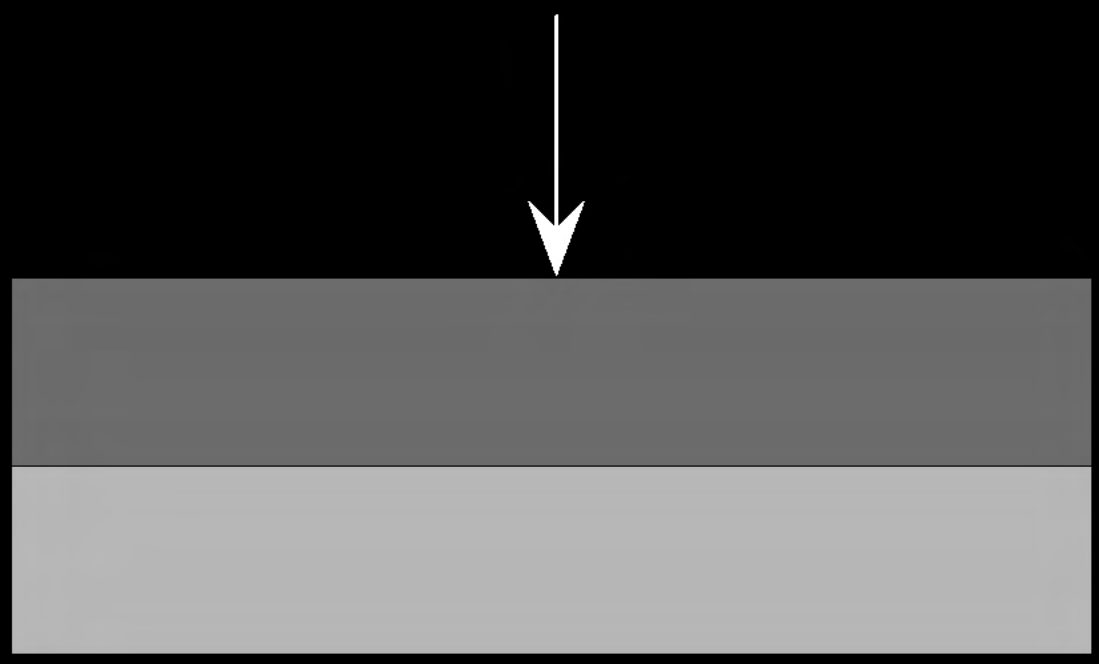

Scattering in Two Layers

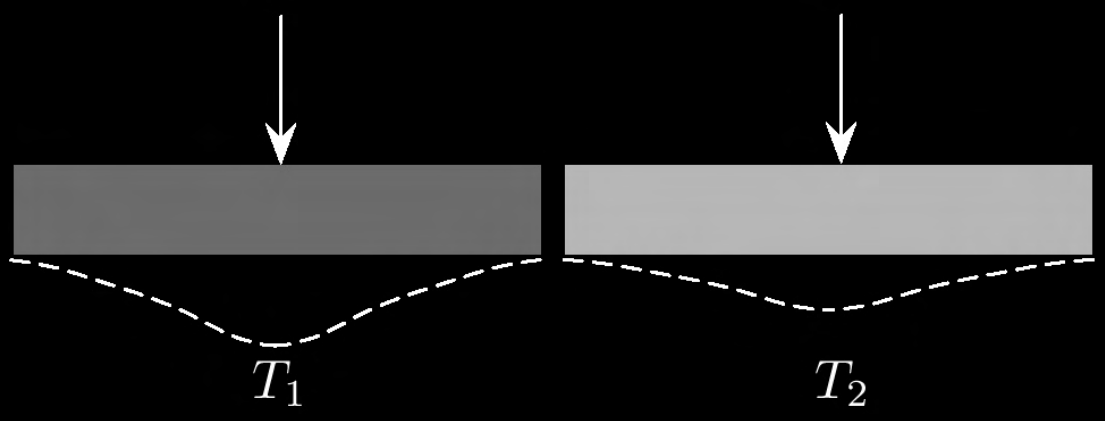

Scattering in Two Layers

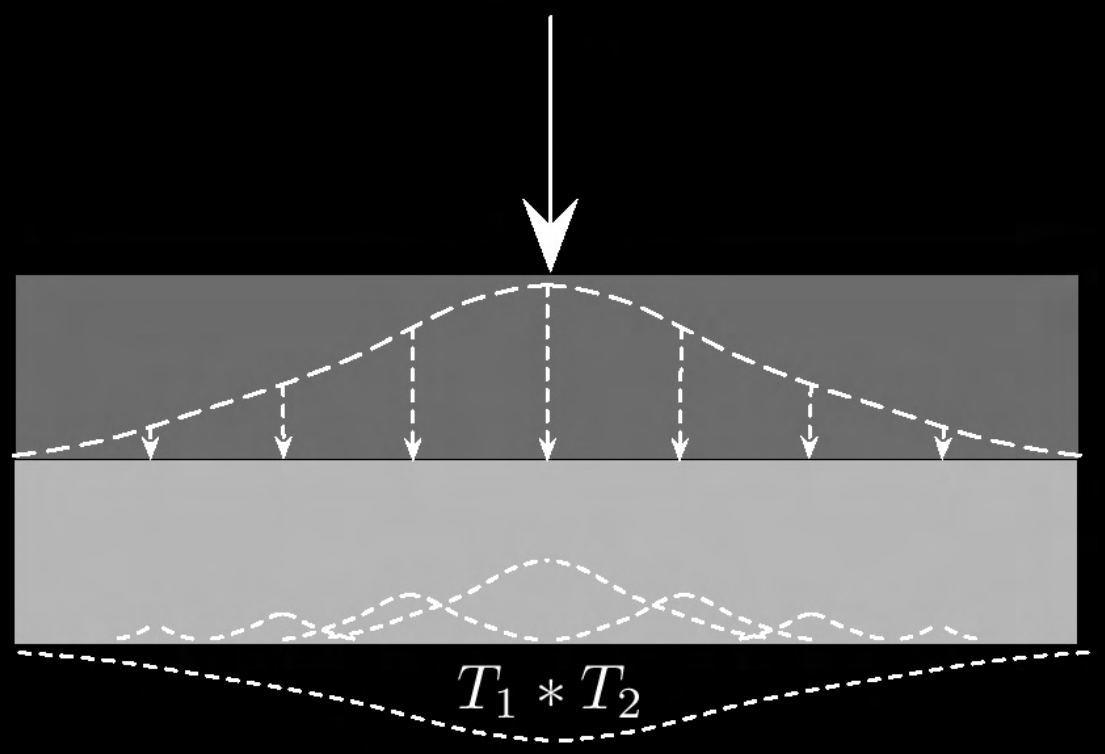

Interlayer Scattering

$$
\begin{aligned}
T_{12} &= T_1 * T_2 + T_1 * R_2 * R_1 * T + 2 + \\
&\quad T_1 * R_2 * R_1 * R_2 * R_1 * T_2 + \ldots
\end{aligned}
$$

$$
\begin{aligned}
\mathcal{T}_{12} &= \mathcal{T}_1\mathcal{T}_2 + \mathcal{T}_1\mathcal{R}_2\mathcal{R}_1\mathcal{T}_2 + \mathcal{T}_1\mathcal{R}_2\mathcal{R}_1\mathcal{R}_2\mathcal{R}_1\mathcal{T}_2 + \ldots \\
&= \frac{\mathcal{T}_1\mathcal{T}_2}{1 - \mathcal{R}_2\mathcal{R}_1}
\end{aligned}
$$

Multilayer Diffusion Model

$$
R(r) = \sum_{i=-n}^{n} \frac{\alpha' z_{r,i}(1+\sigma_{tr} d_{r,i}) e^{-\sigma_{tr} d_{r,i}}}{4\pi d_{r,i}^3} - \frac{\alpha' z_{v,i}(1+\sigma_{tr} d_{v,i}) e^{-\sigma_{tr} d_{v,i}}}{4\pi d_{v,i}^3}
$$

$$
\begin{aligned}
T(r) &= \sum_{i=-n}^{n} \frac{\alpha'(d - z_{r,i})(1+\sigma_{tr} d_{r,i}) e^{-\sigma_{tr} d_{r,i}}}{4\pi d_{r,i}^3} - \\
&\quad \frac{\alpha'(d - z_{v,i})(1+\sigma_{tr} d_{v,i}) e^{-\sigma_{tr} d_{v,i}}}{4\pi d_{v,i}^3}
\end{aligned}
$$

$$
\begin{aligned}
\mathcal{T}_{12} &= \mathcal{T}_1\mathcal{T}_2 + \mathcal{T}_1\mathcal{R}_2\mathcal{R}_1\mathcal{T}_2 + \mathcal{T}_1\mathcal{R}_2\mathcal{R}_1\mathcal{R}_2\mathcal{R}_1\mathcal{T}_2 + \ldots \\
&= \frac{\mathcal{T}_1\mathcal{T}_2}{1 - \mathcal{R}_2\mathcal{R}_1}
\end{aligned}
$$

[Donner and Jensen, JOSA 2006]

A 3 Layer Skin Model

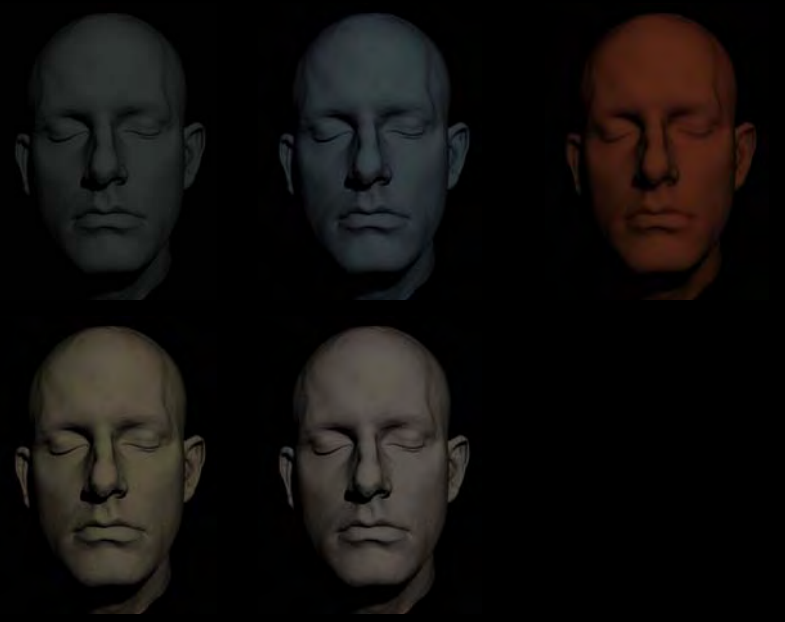

Epidermis Dermis Bloody Dermis

[Skin parameters from Tuchin 2000, 3D Model XYZRGB]

Face (3 Layer Skin Model)

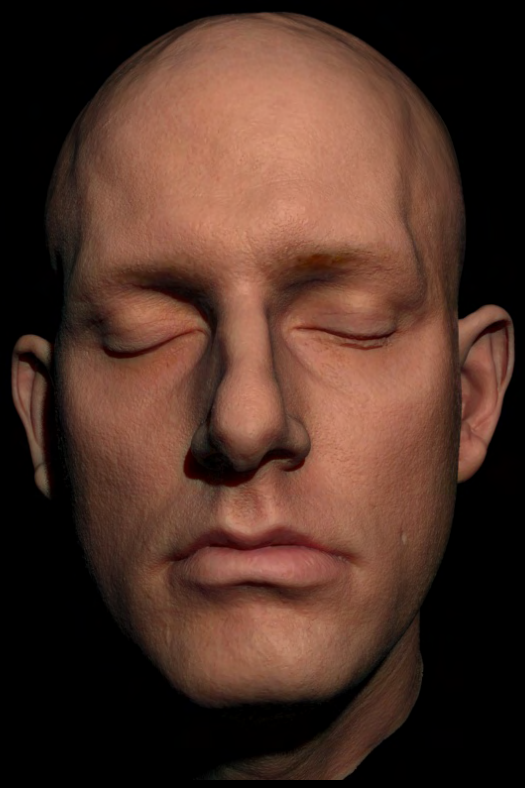

Face (3 Layer Skin Model)

Face (Single Layer Model)

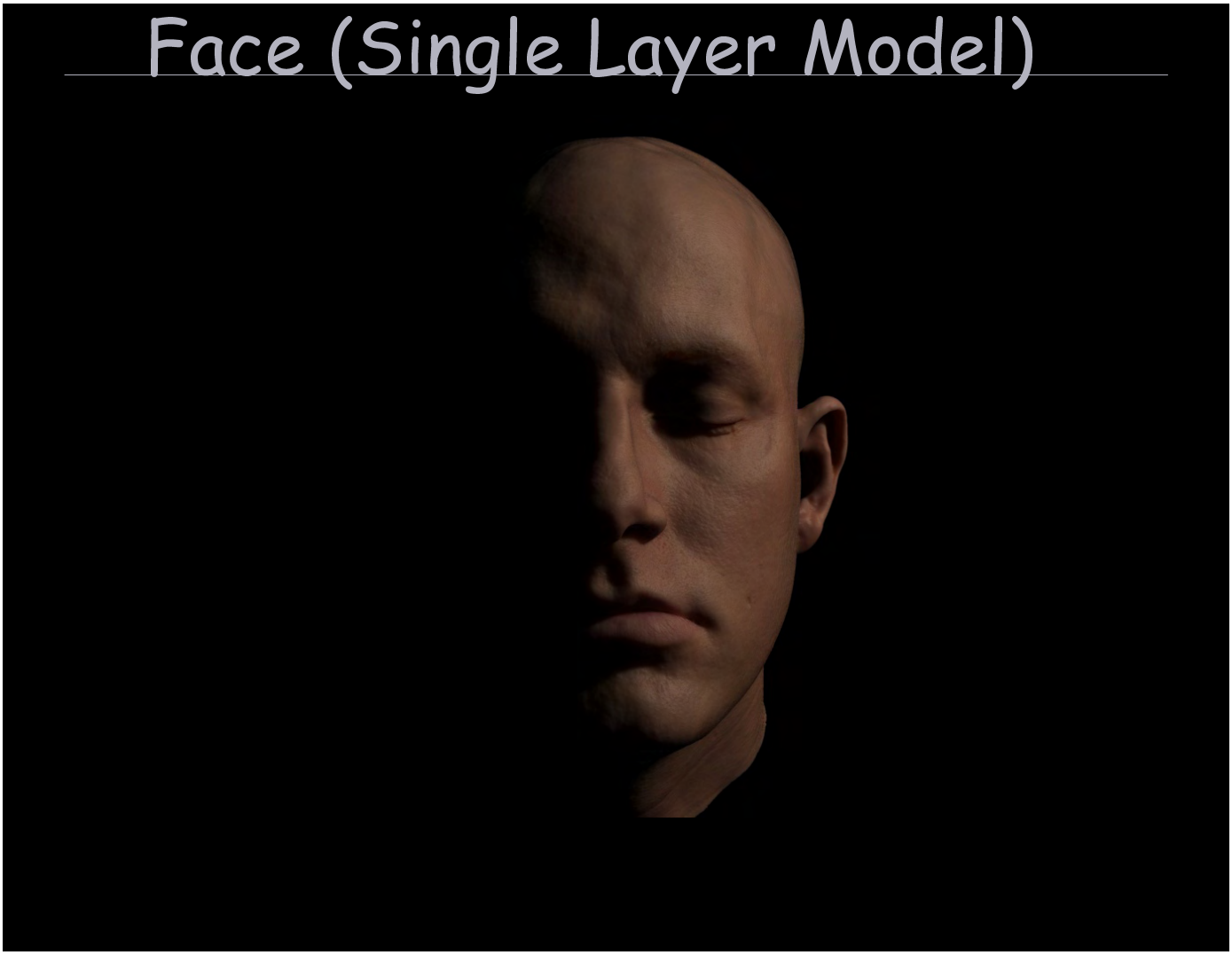

Spectral BSSRDF for Human Skin

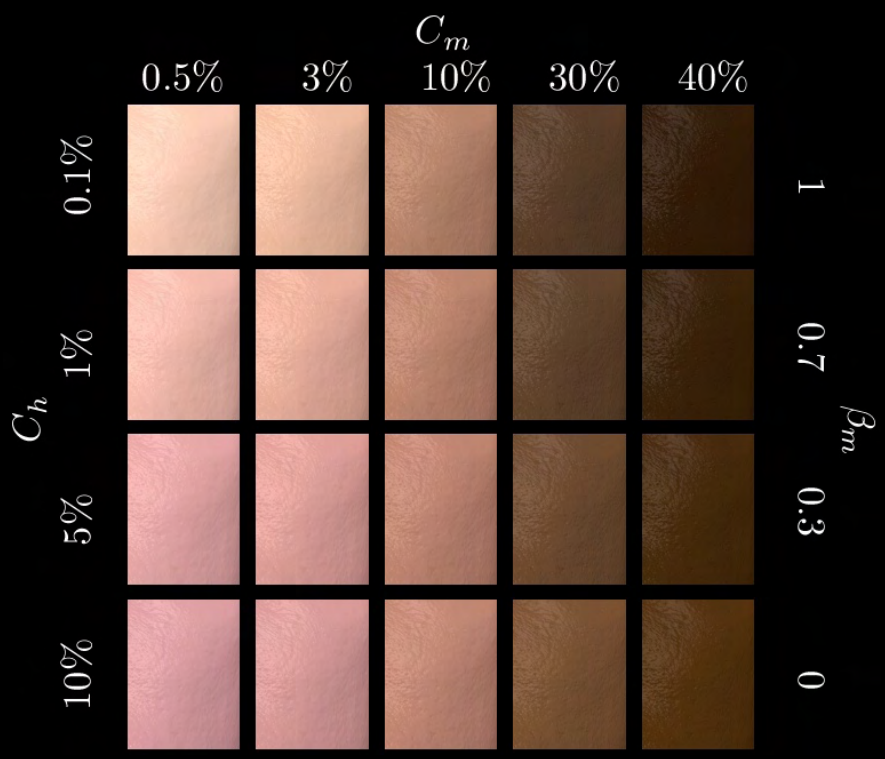

[Donner and Jensen, EGSR 2006]

Spectral BSSRDF for Human Skin

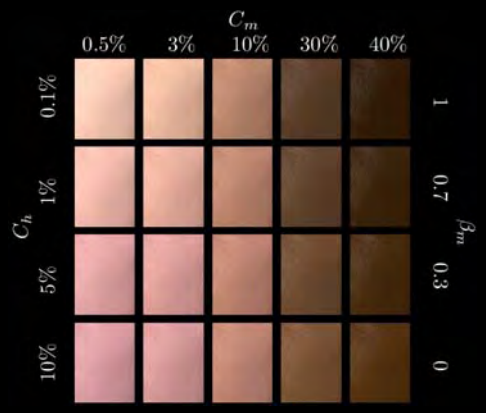

- Few parameters
- Subsurface scattering
- Surface reflections
- Surface texture

A Two-Layer Skin Model

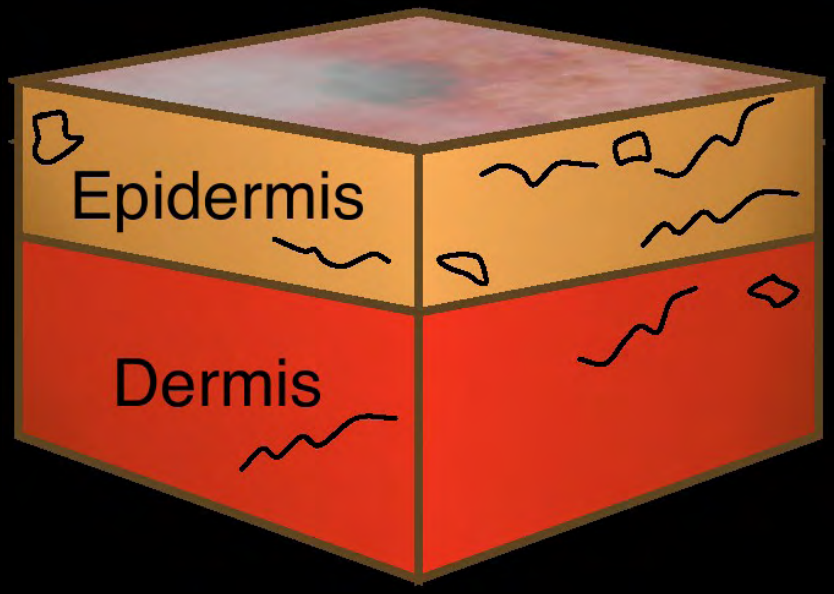

A Two-Layer Skin Model

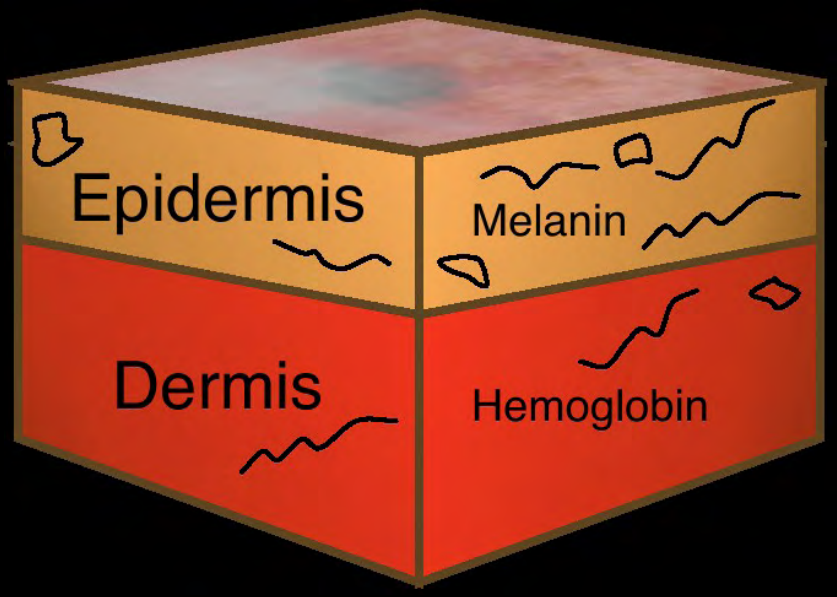

Chromophore Spectra

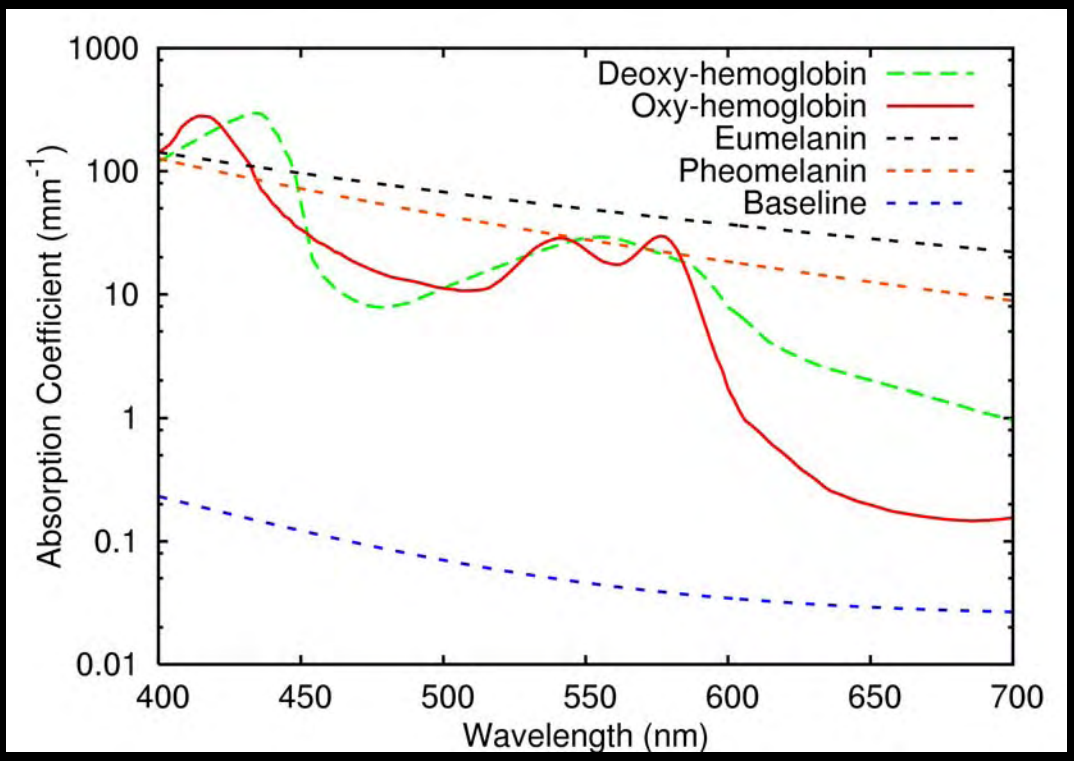

Layer Absorption

Epidermis absorption:

$$\sigma_a^{epi}(\lambda) = C_m(\beta_m \sigma_a^{em}(\lambda) + (1-\beta_m)\sigma_a^{pm}(\lambda)) + (1-C_m)\sigma_a^{baseline}$$

Melanin type $\beta_m \in [0,1]$ and concentration $C_m \in [0,1]$

Dermis absorption:

$$\sigma_a^{derm}(\lambda) = C_h(\gamma \sigma_a^{oxy}(\lambda) + (1-\gamma)\sigma_a^{deoxy}(\lambda)) + (1-C_h)\sigma_a^{baseline}$$

Hemoglobin oxygenation $\gamma = 0.7$ and concentration $C_h \in [0,1]$

Layer Scattering

Epidemis scattering:

$$\sigma_s^{epi}(\lambda) = 14.74 \cdot \lambda^{-0.22} + 2.2 \cdot 10^{11} \cdot \lambda^{-4}$$

Dermis scattering:

$$\sigma_s^{derm}(\lambda) = 29.48 \cdot \lambda^{-0.22} + 4.4 \cdot 10^{11} \cdot \lambda^{-4}$$

Surface Scattering

- Torrance-Sparrow BRDF

$$f_{r,TS} = \rho_s \frac{F(x, \vec{\omega}_o, \vec{\omega}_i) \cdot D(x, \vec{\omega}_o, \vec{\omega}_i, \sigma) \cdot G(x, \vec{\omega}_o, \vec{\omega}_i)}{4(\vec{\omega}_i \cdot \vec{n})(\vec{\omega}_o \cdot \vec{n})}$$

$$\sigma \approx 0.3$$

Oiliness: ρ_s

Total surface reflectance: ρ_{dr}

$$\rho_{dr}(x, \vec{\omega}_i) = \int_{2\pi} f_{r,TS}(r, \vec{\omega}_o, \vec{\omega}_i)(\vec{\omega}_i \cdot \vec{n}) d\vec{\omega}_o$$

Modulate BSSRDF by $(1 - \rho_{dr})$

Melanin Concentration

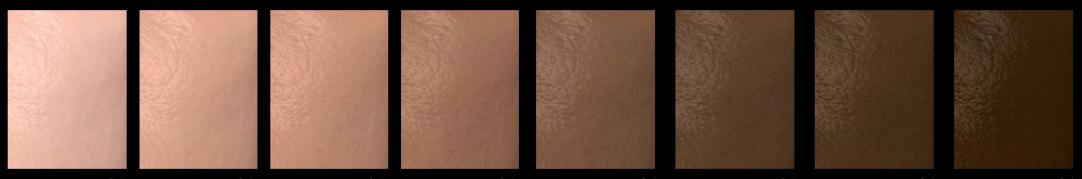

$C_m = 0.1\%$ $C_m = 1\%$ $C_m = 2\%$ $C_m = 5\%$ $C_m = 10\%$ $C_m = 20\%$ $C_m = 30\%$ $C_m = 50\%$

Melanin type $\beta_m = 0.7$, hemoglobin concentration $C_h = 0.5\%$

Melanin Type

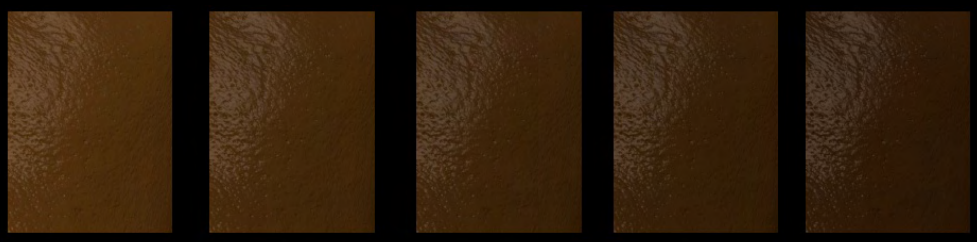

$\beta_m = 0$ $\beta_m = 0.25$ $\beta_m = 0.5$ $\beta_m = 0.7$ $\beta_m = 1$

Melanin concentration $C_m = 50\%$, hemoglobin concentration $C_h = 1\%$

Hemoglobin Concentration

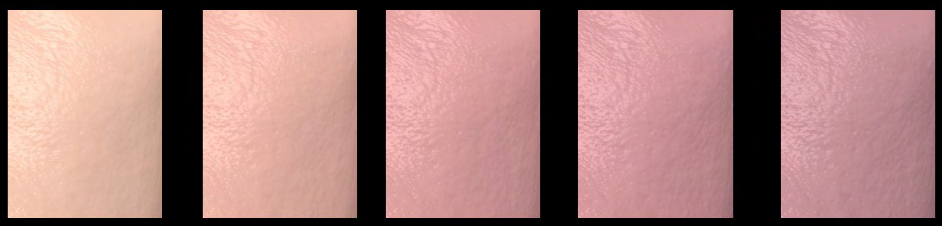

$C_h = 0.1\%$ $C_h = 1\%$ $C_h = 5\%$ $C_h = 10\%$ $C_h = 20\%$

Melanin concentration $C_m = 1\%$ and type $\beta_m = 0.5$

Skin Oiliness

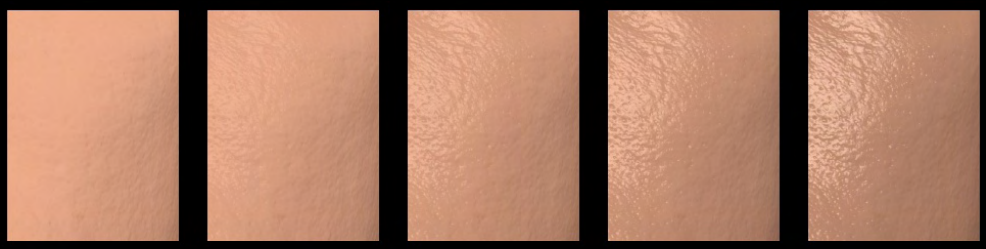

$\rho_s = 0$ $\rho_s = 0.25$ $\rho_s = 0.5$ $\rho_s = 0.75$ $\rho_s = 1$

Skin Matrix

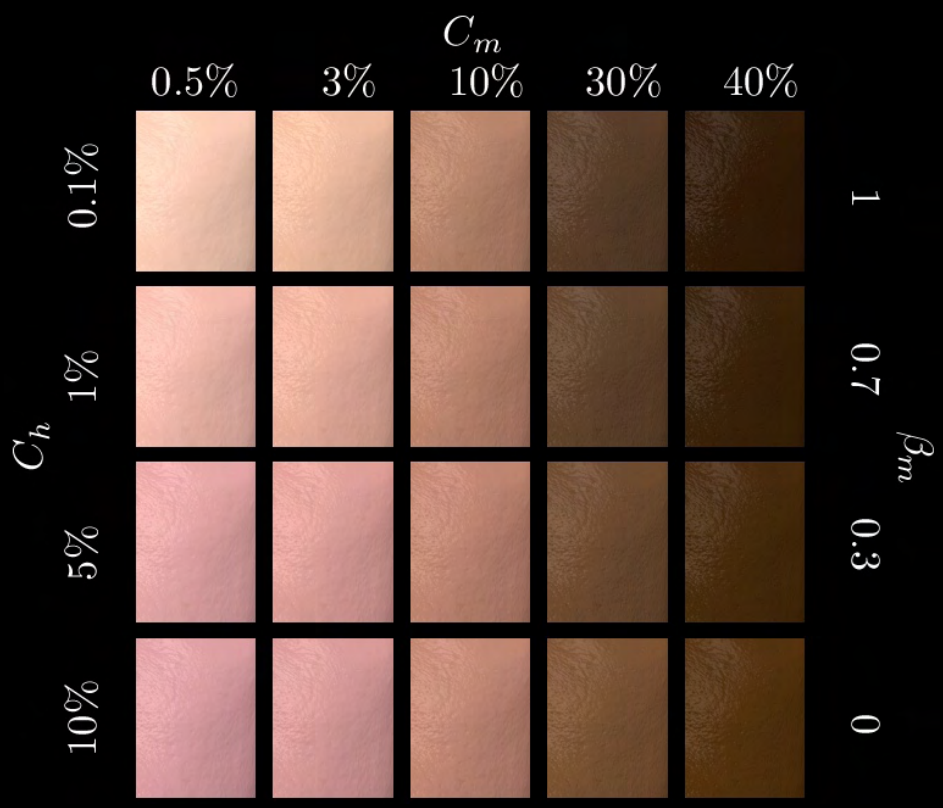

Skin Types

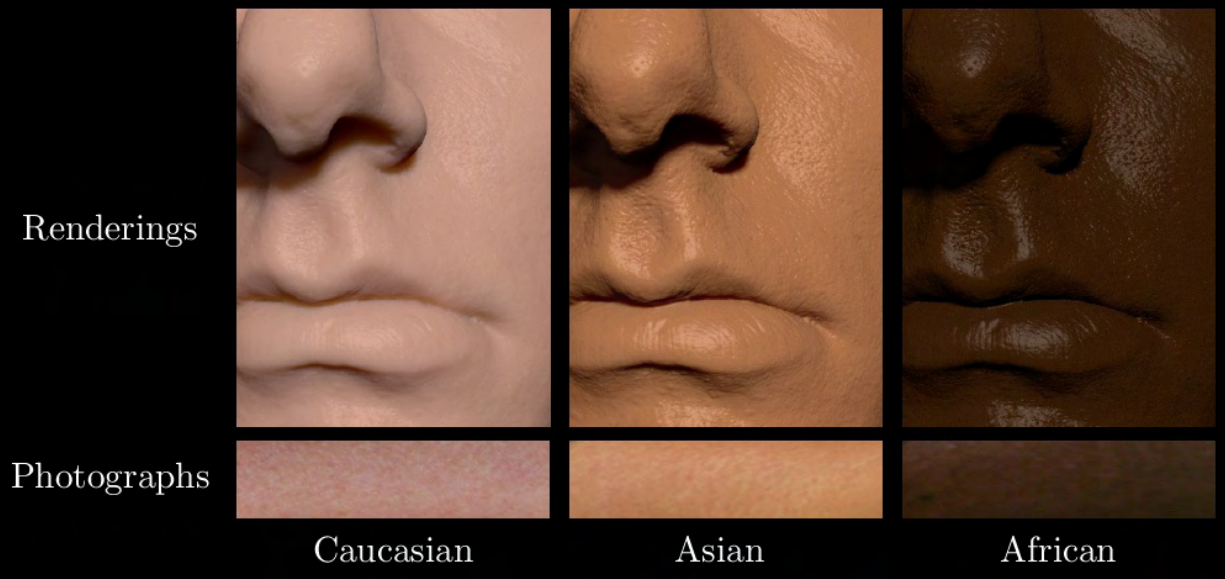

Skin Texture

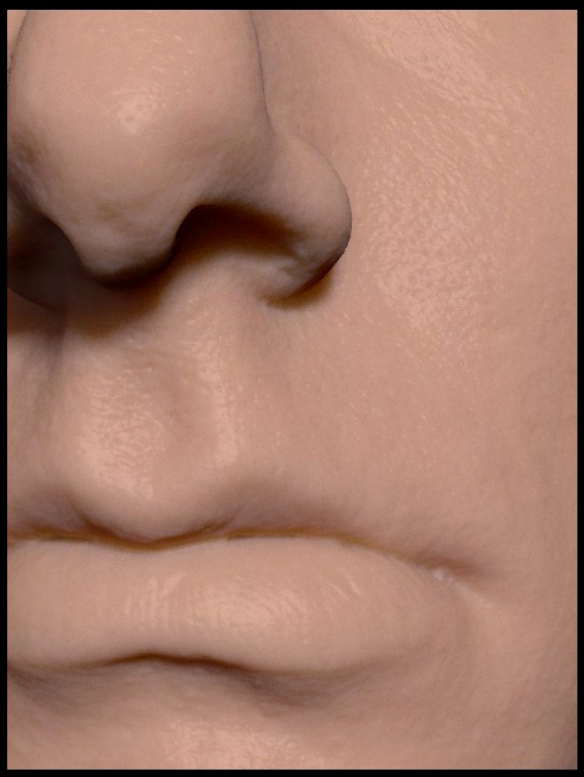

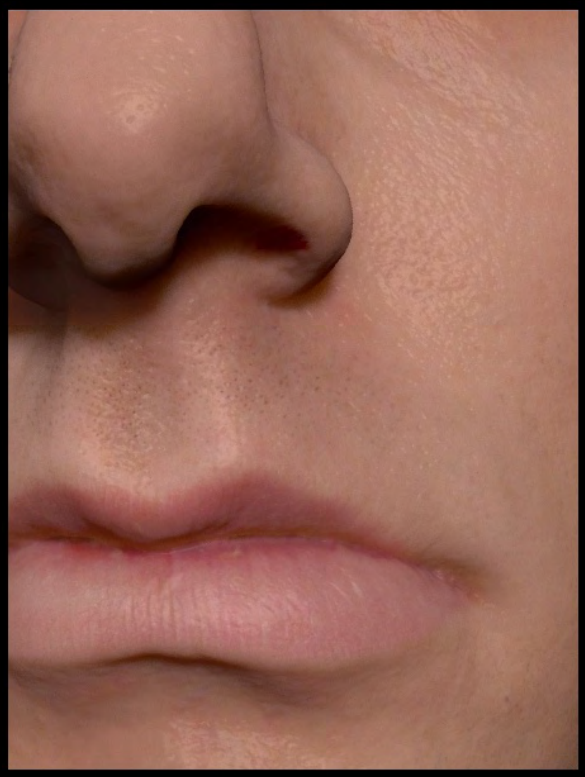

Modulate BSSRDF using albedo map normalized by the skin reflectance

Skin Pale

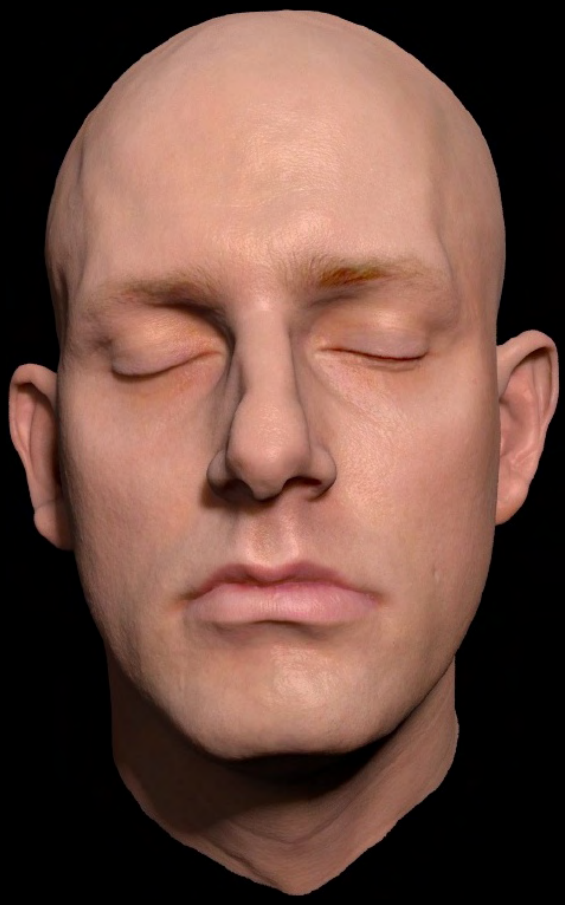

Skin Tan

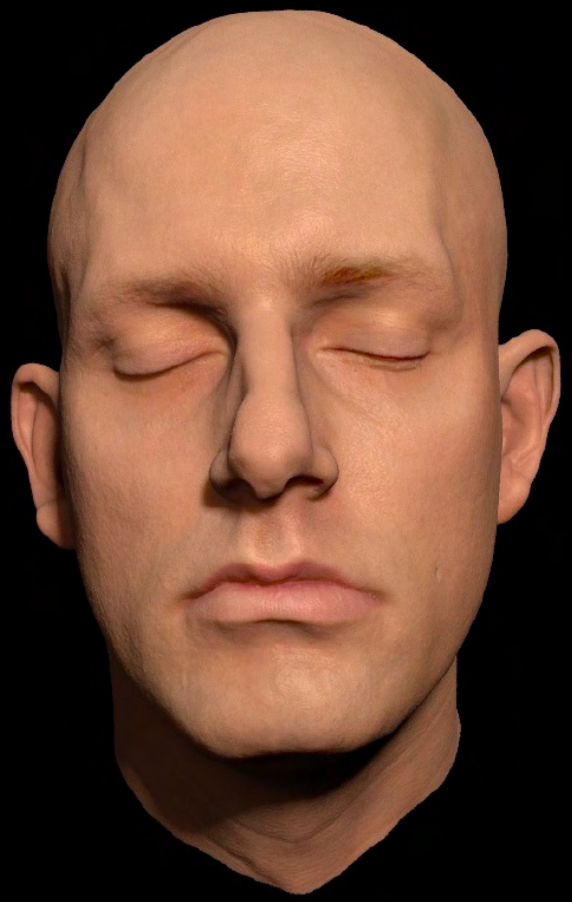

Skin Ear Closeup

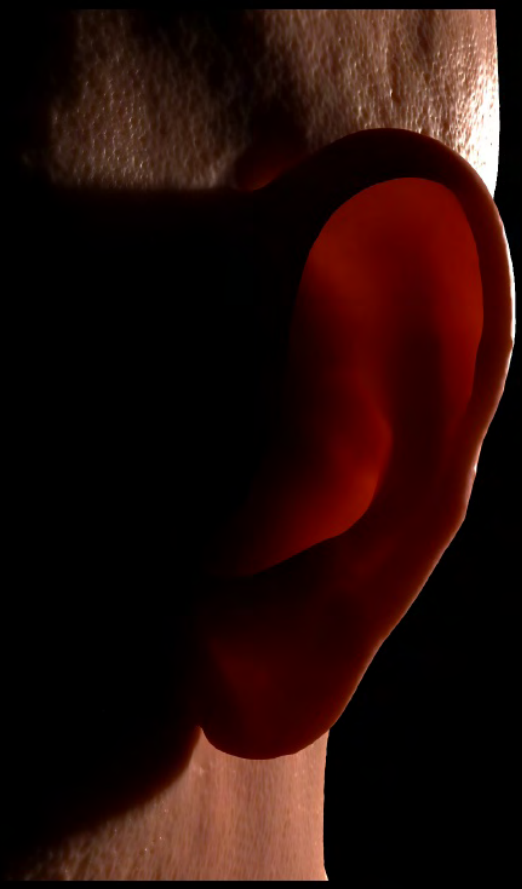

Skin Normal Lighting

Reflectance Prediction

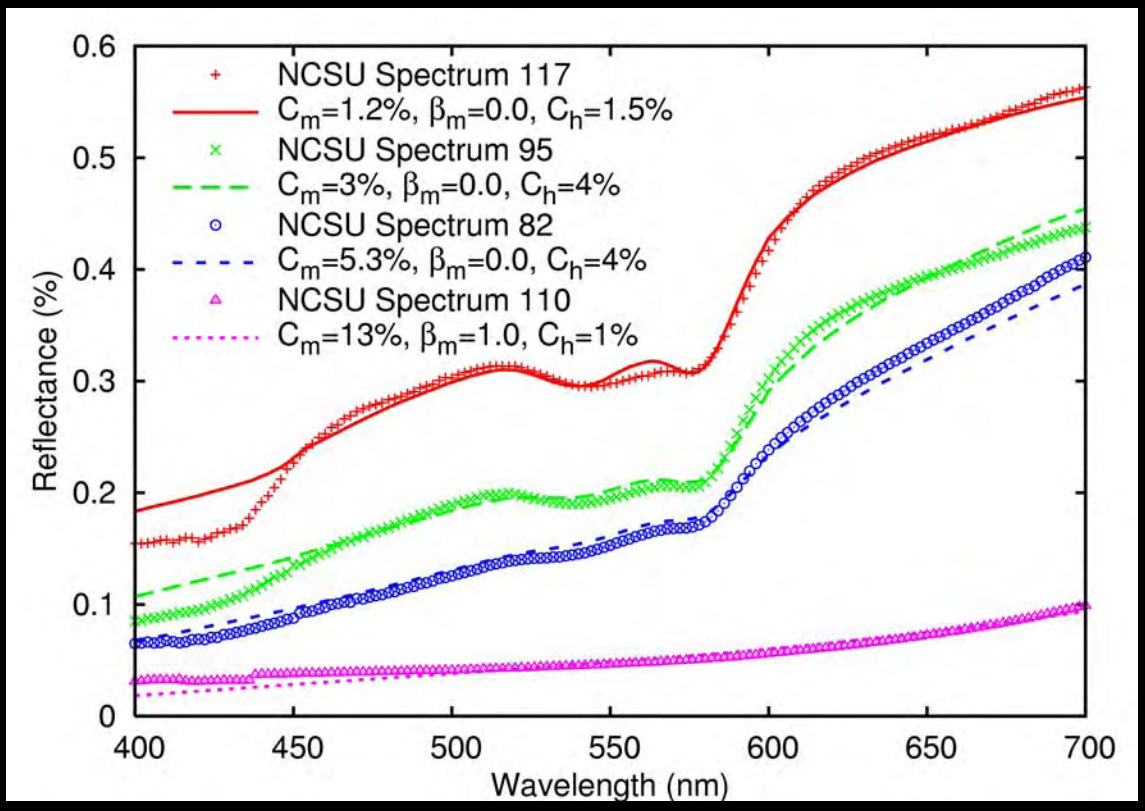

Acquiring Scattering Properties

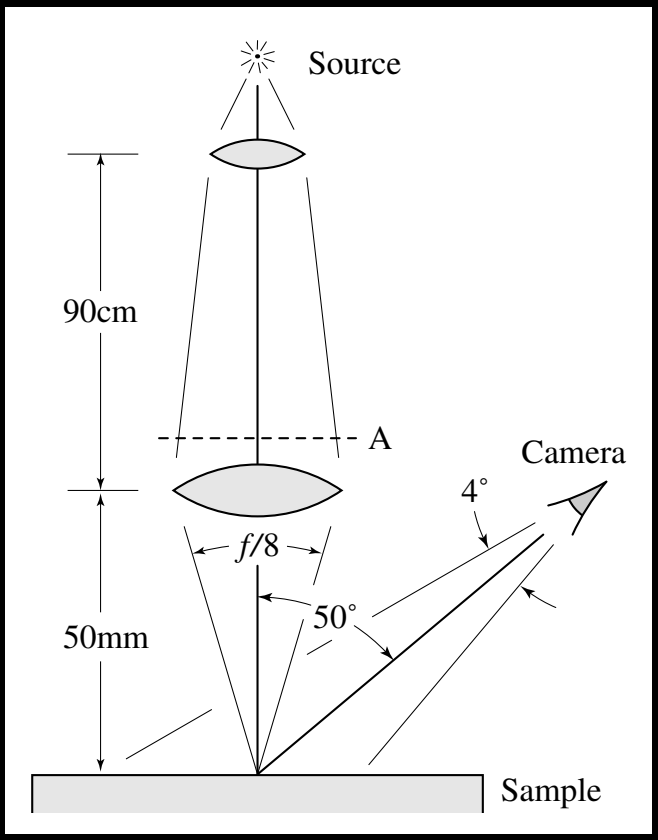

A High-Dynamic Range Image

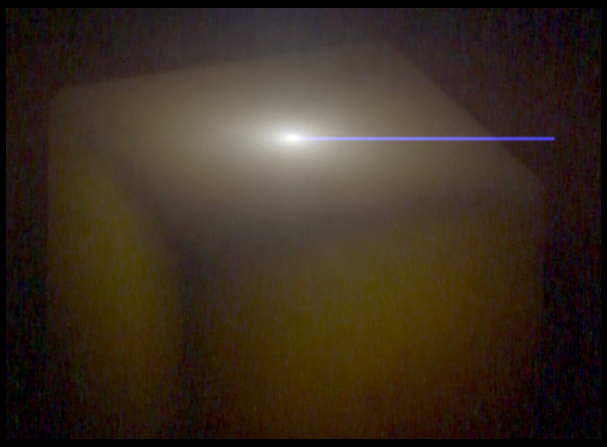

Monte Carlo Verification

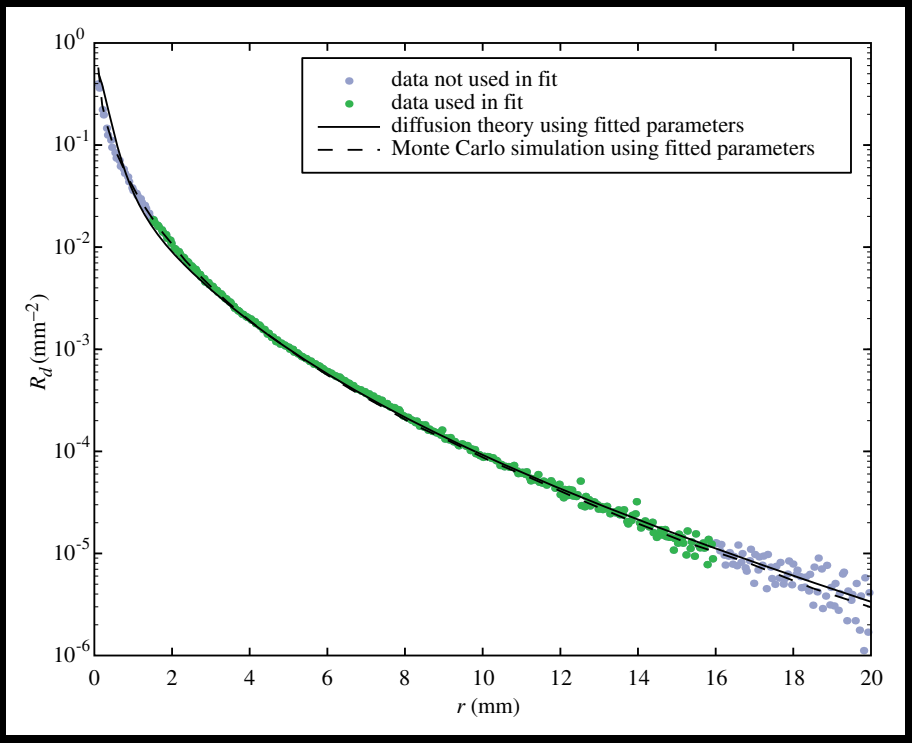

Measured Materials

Material	σ_s' [mm^{-1}]			σ_a [mm^{-1}]		
	R	G	B	R	G	B
Apple	2.29	2.39	1.97	0.0030	0.0034	0.046
Chicken1	0.15	0.21	0.38	0.015	0.077	0.19
Chicken2	0.19	0.25	0.32	0.018	0.088	0.20
Cream	7.38	5.47	3.15	0.0002	0.0028	0.0163
Ketchup	0.18	0.07	0.03	0.061	0.97	1.45
Marble	2.19	2.62	3.00	0.0021	0.0041	0.0071
Potato	0.68	0.70	0.55	0.0024	0.0090	0.12
Skimmilk	0.70	1.22	1.90	0.0014	0.0025	0.0142
Skin1	0.74	0.88	1.01	0.032	0.17	0.48
Skin2	1.09	1.59	1.79	0.013	0.070	0.145
Spectralon	11.6	20.4	14.9	0.00	0.00	0.00
Wholemilk	2.55	3.21	3.77	0.0011	0.0024	0.014

Measuring Scattering Anisotropy

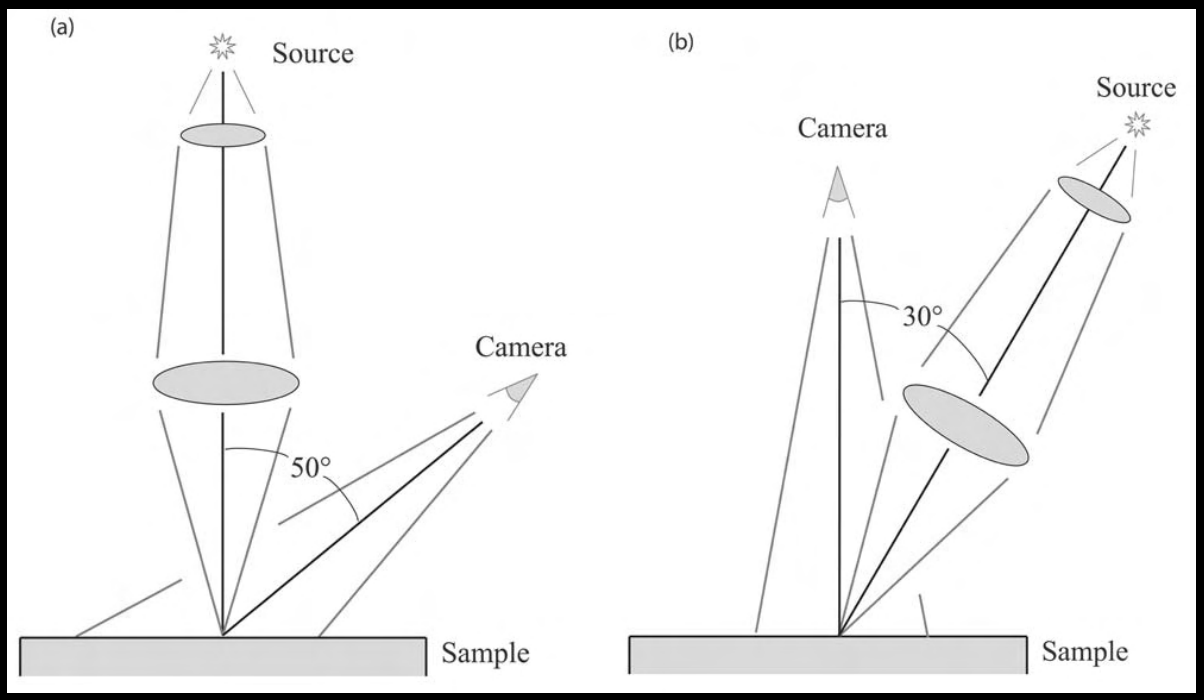

[Joshi, Donner, and Jensen - Optics Letters 2006]

Measuring Scattering Anisotropy

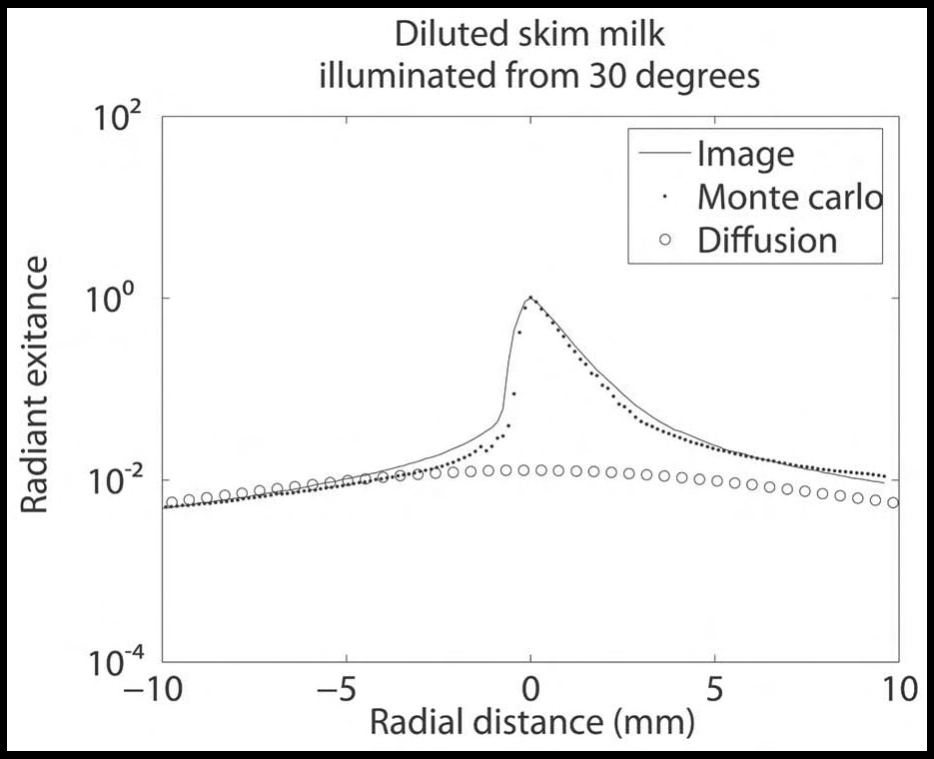

Measurement via Dilution

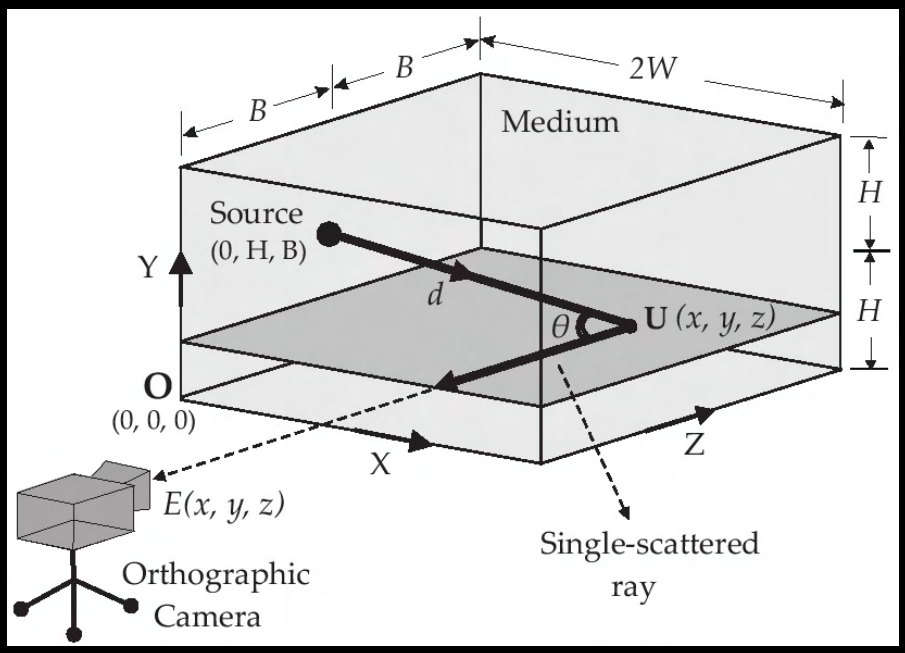

[Narasimhan, Gupta, Donner, Ramamoorthi, Nayar, and Jensen - SIGGRAPH 2006]

Measurement via Dilution

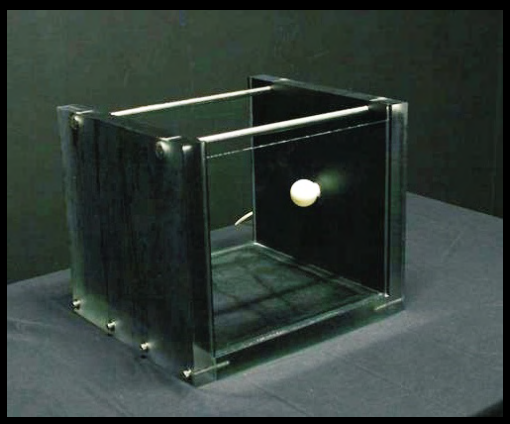

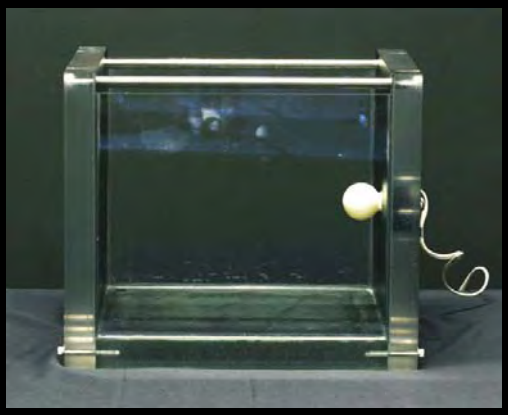

Measurement via Dilution

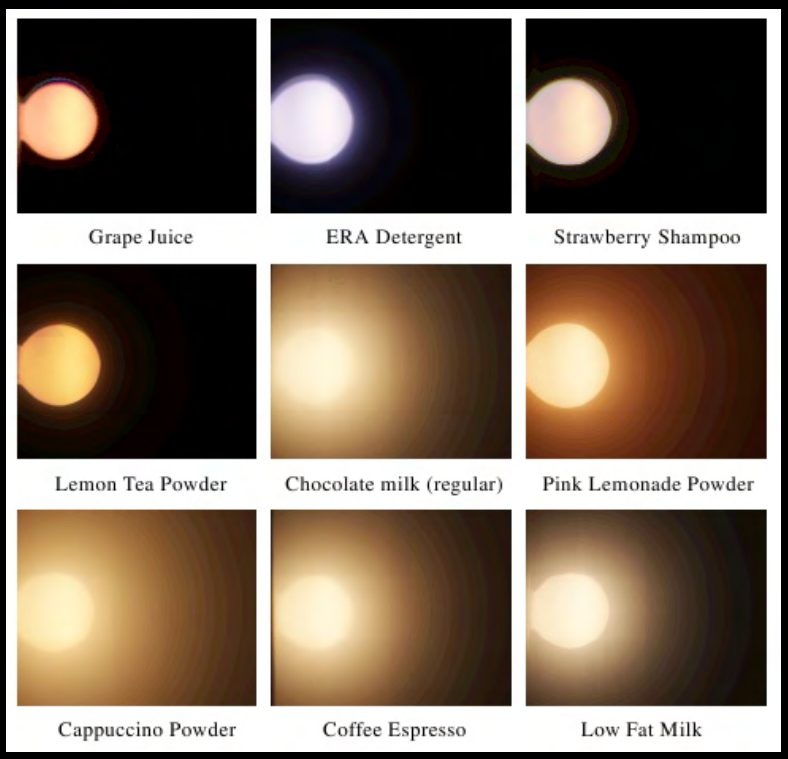

Measurement via Dilution

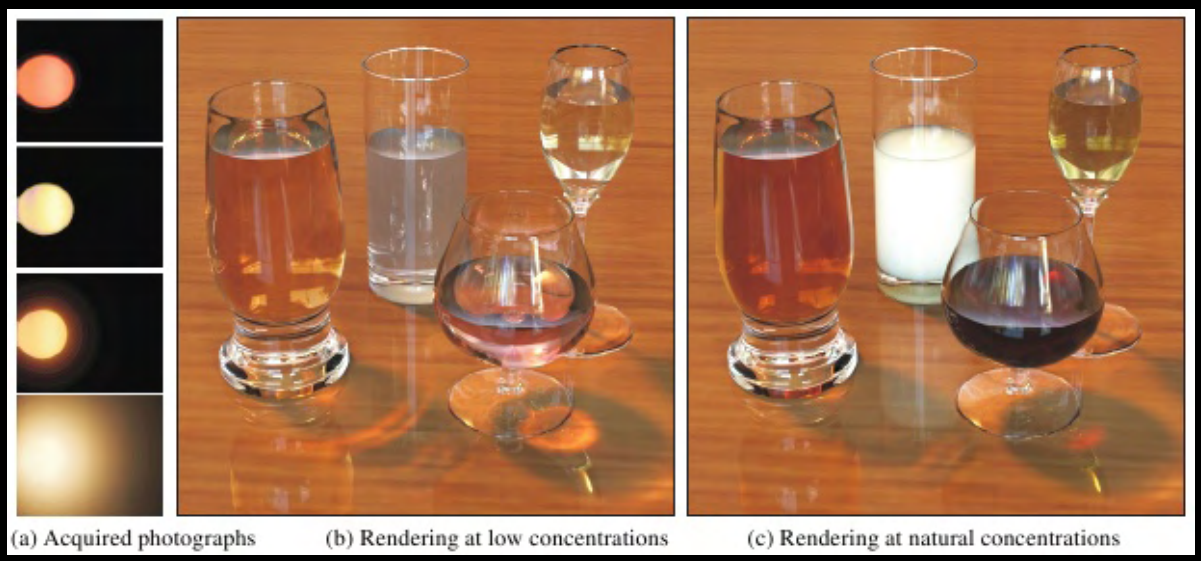

(a) Acquired photographs (b) Rendering at low concentrations (c) Rendering at natural concentrations

Skin Acquisition

[Weirich et al., SIGGRAPH 2006]

Translucency Acquisition

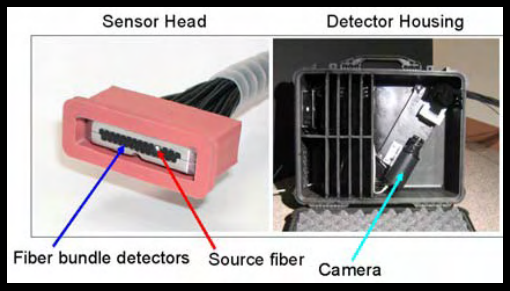

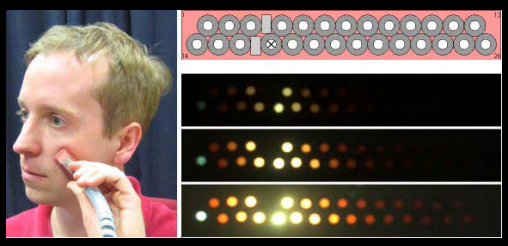

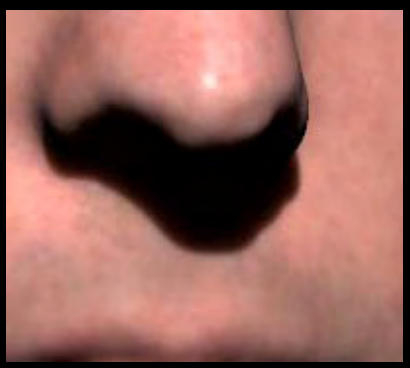

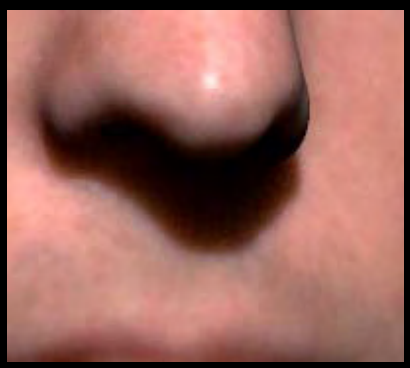

Skin Rendering

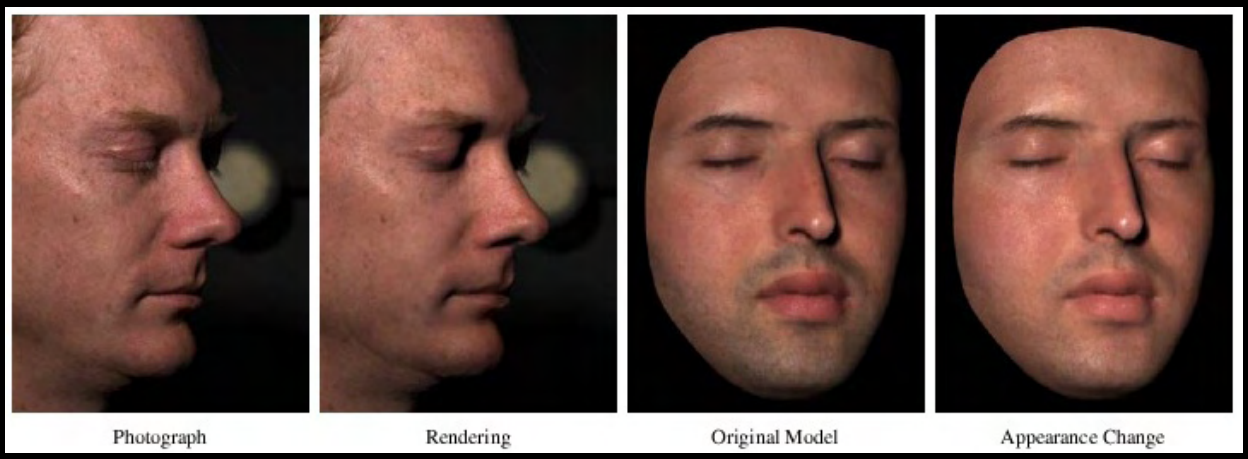

Hair Measurements

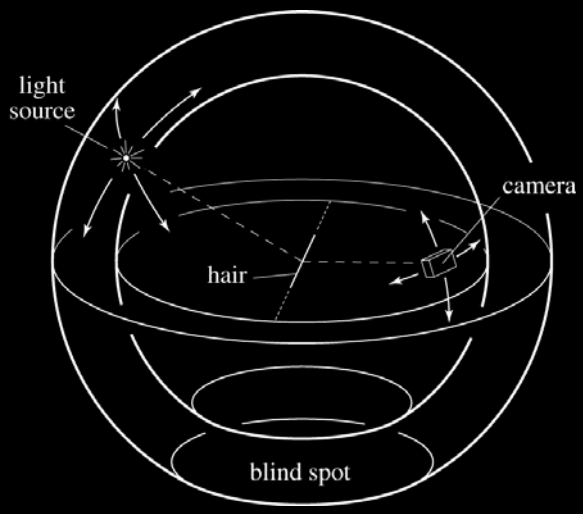

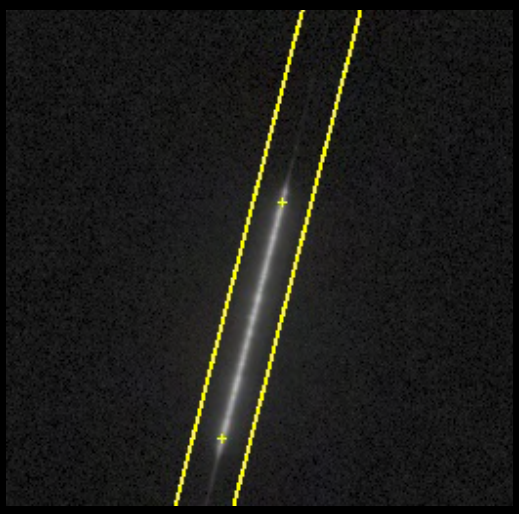

Black Hair

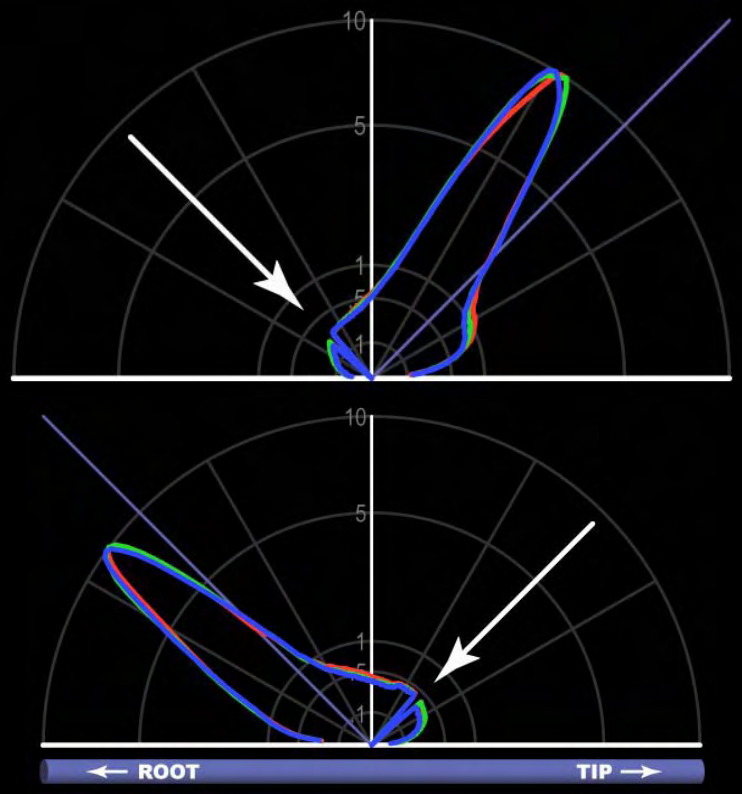

Blond Hair

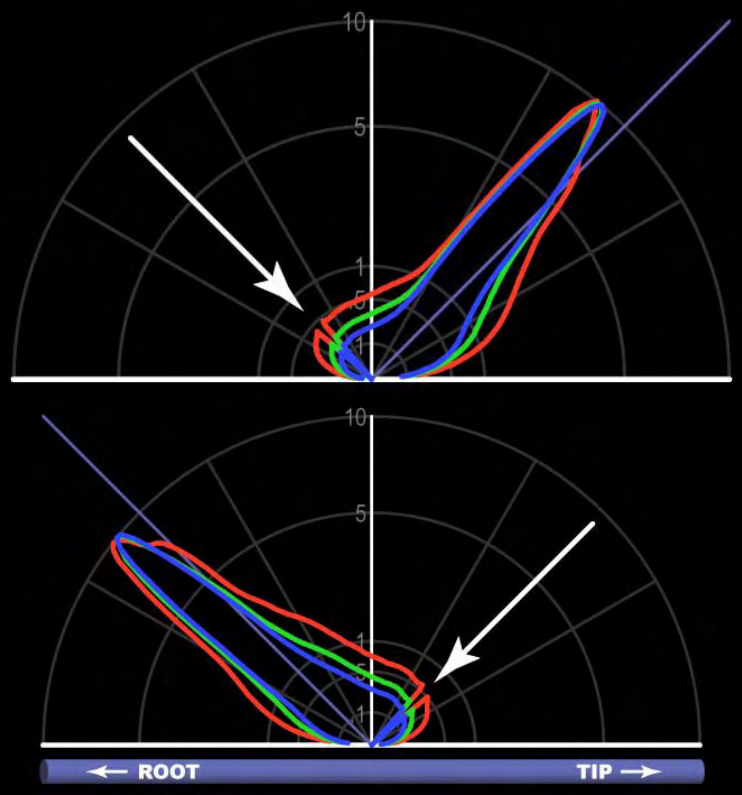

Synthetic Hair

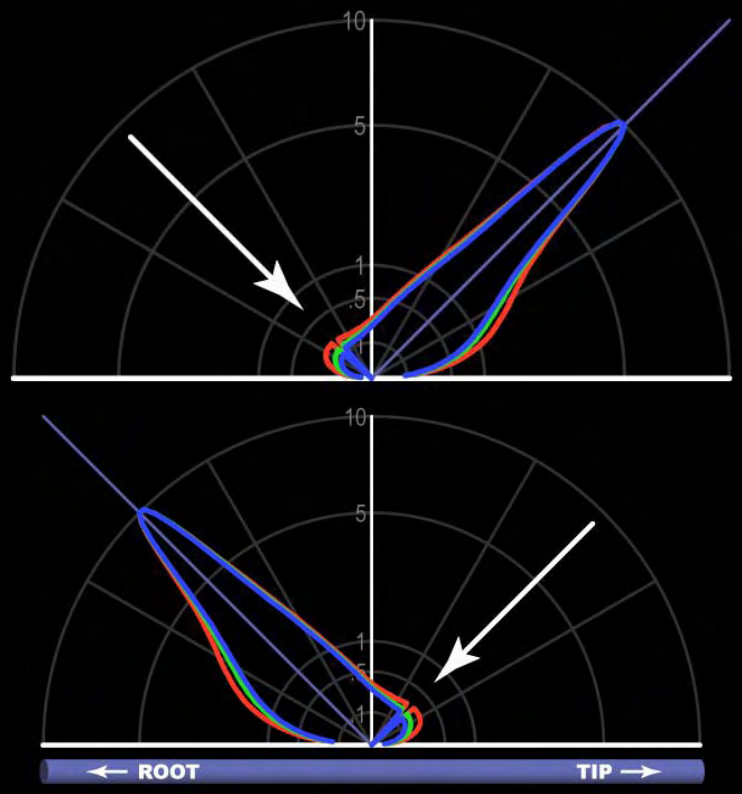

Tilted Cuticle Scales

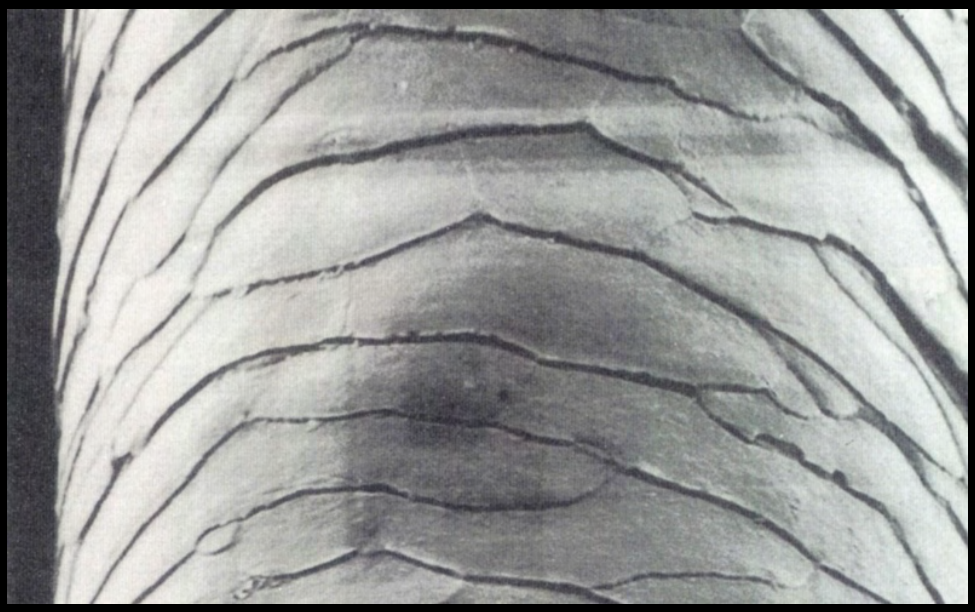

Hair Model

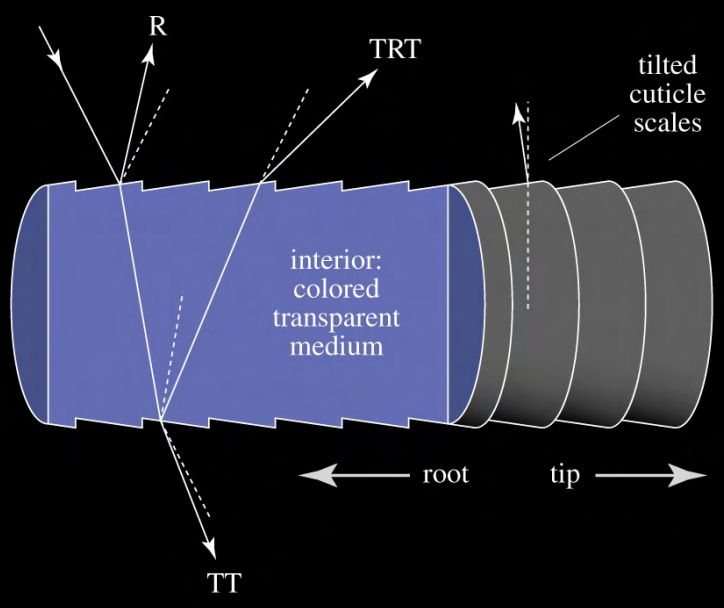

Real Hair

Real Black Hair

Real Brown Hair

The Final Measurement

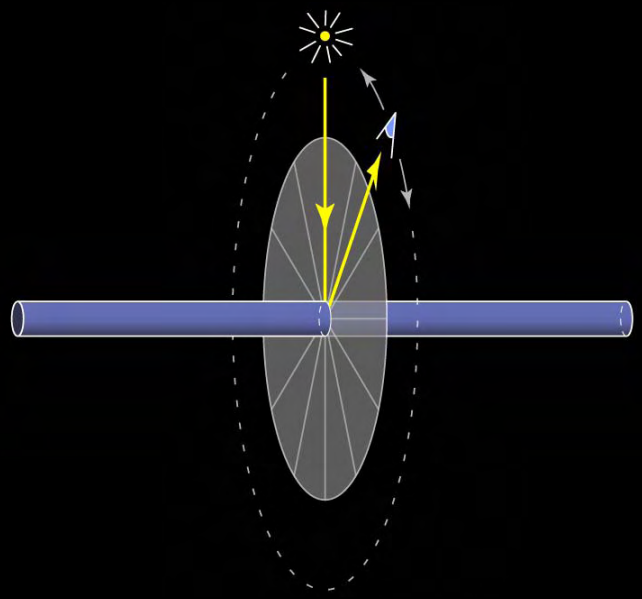

Caustics

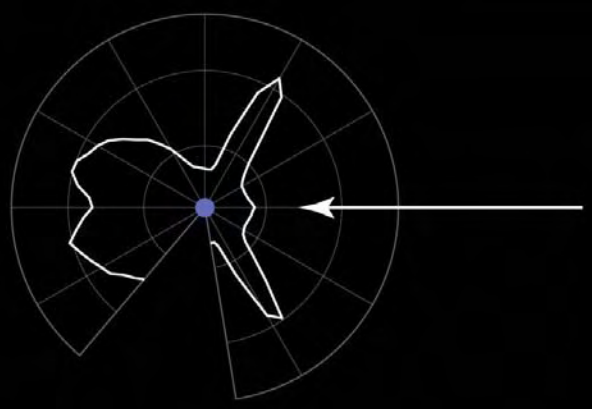

Hair Glints

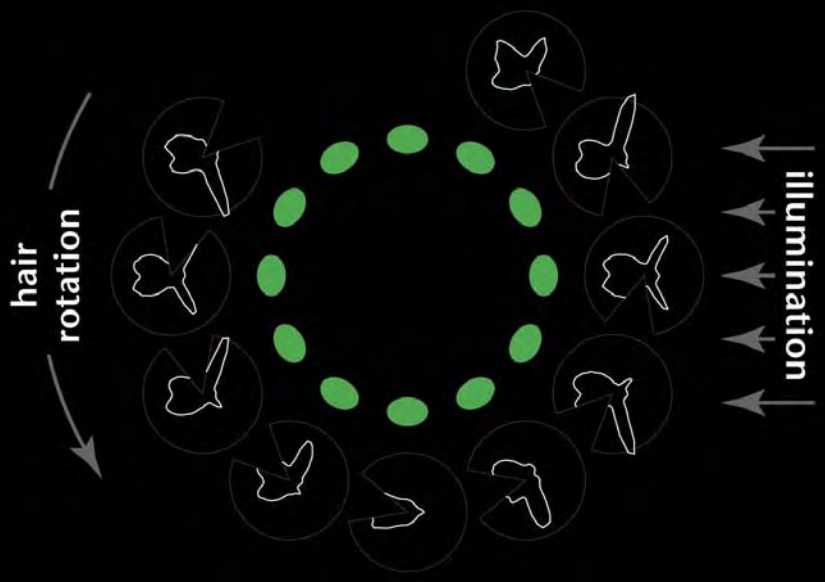

Hair Scattering

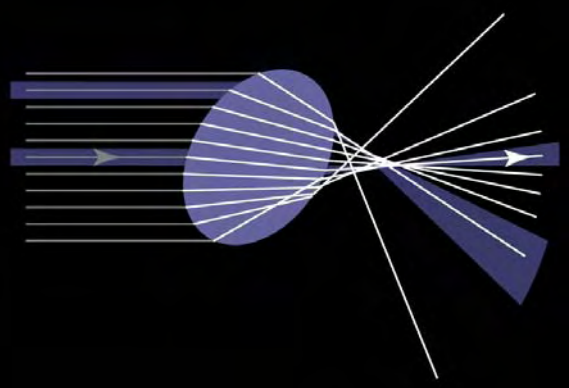

Hair Model

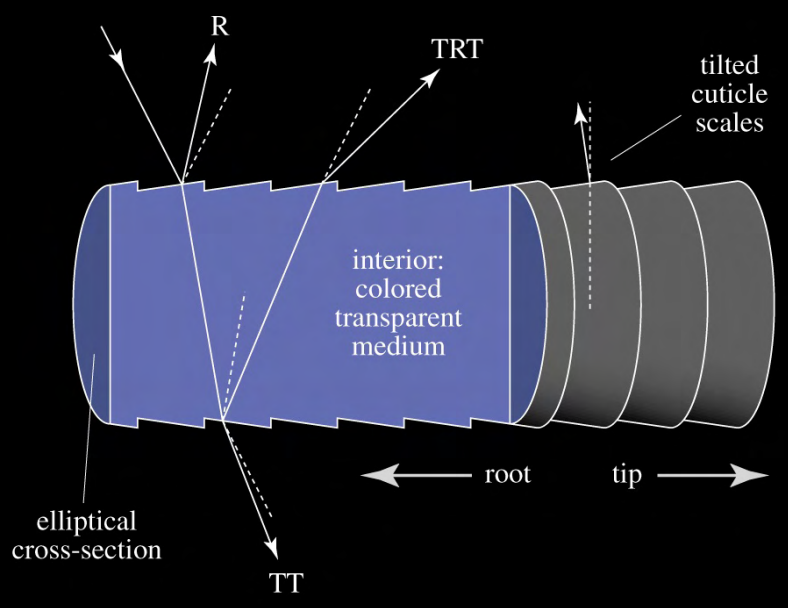

Real Hair

Photograph

Gray 1997

Photograph

Gray 1997

Photograph vs. Kajiya-Kay

Photograph

Kajiya-Kay

Photograph vs. New Model

Photograph

New Model

Components of the New Model

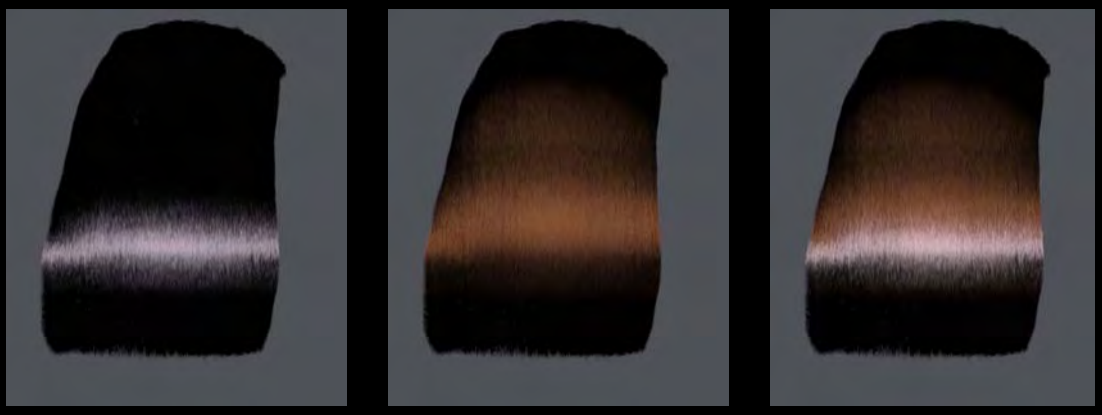

Components of the New Model

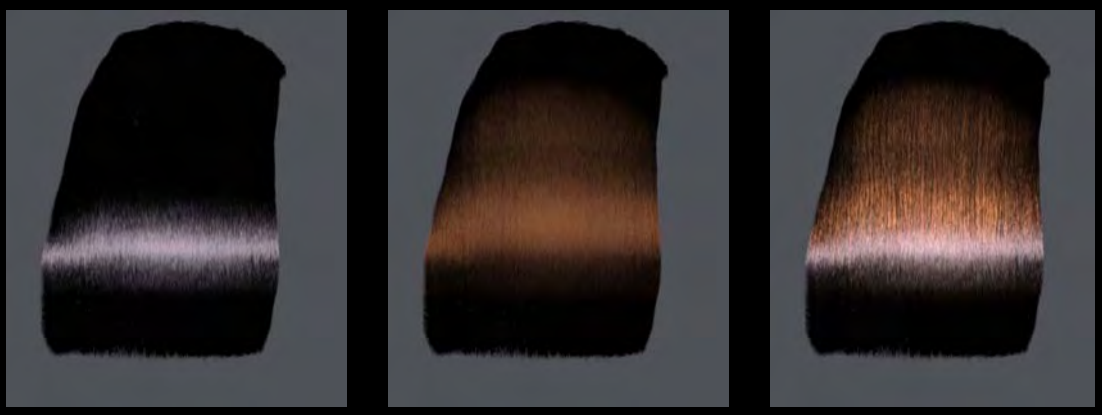

Glints

Different Lighting Directions

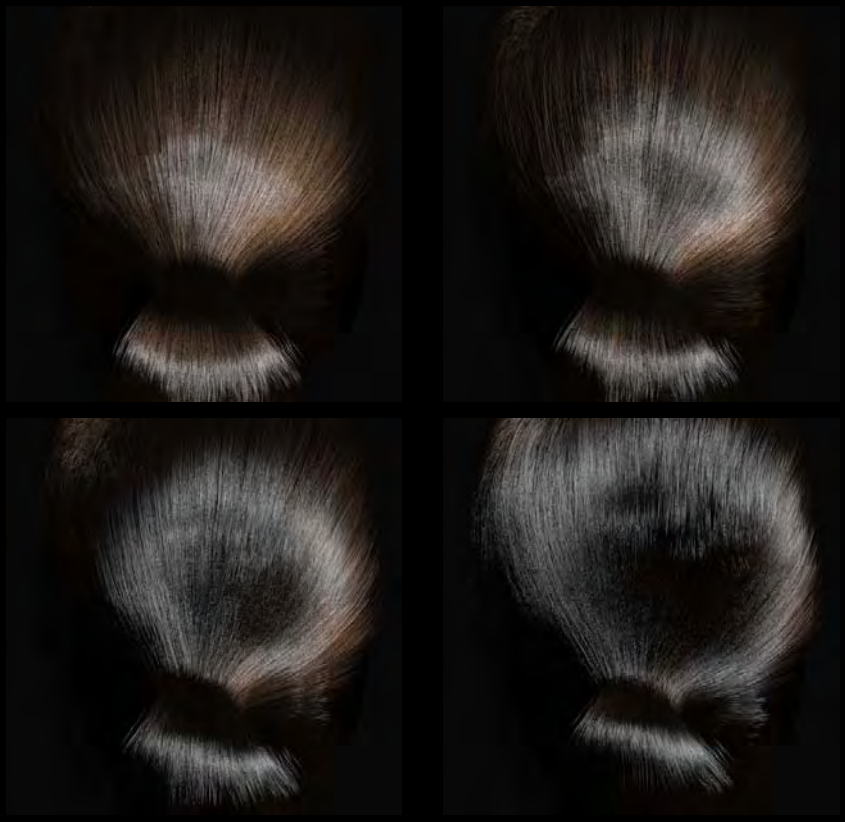

Lorenz-Mie Theory

$$S_1(\theta) = \sum_{n=1}^{\infty} \frac{2n+1}{n(n+1)} (a_n \pi_n(\cos\theta) + b_n \tau_n(cos\theta)) \ ,$$

$$S_2(\theta) = \sum_{n=1}^{\infty} \frac{2n+1}{n(n+1)} (b_n \pi_n(\cos\theta) + a_n \tau_n(cos\theta)) \ .$$

[Revall, Christensen, and Jensen - SIGGRAPH 2007]

Milk Components

Computed scattering properties of milk components

Milk

Milk with varying fat concentration

Ice Dragons

Pure

Compacted

White

Green Icebergs

10 am

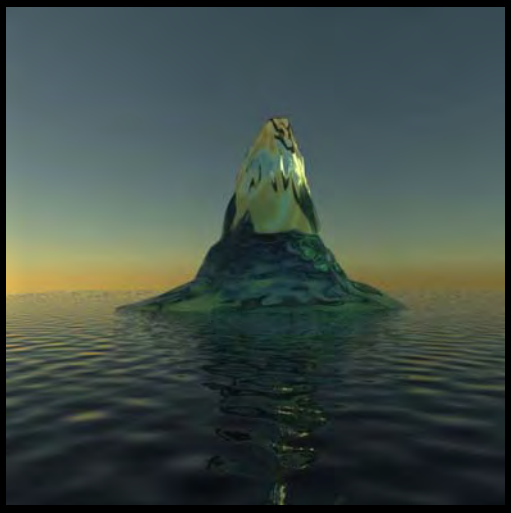

7 pm

Ocean Water

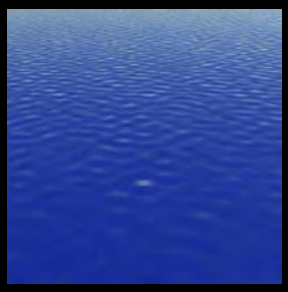

Atlantic

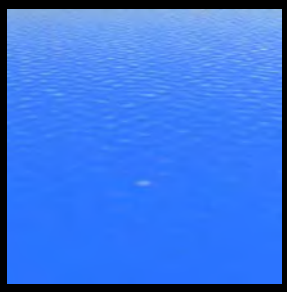

Mediterranean

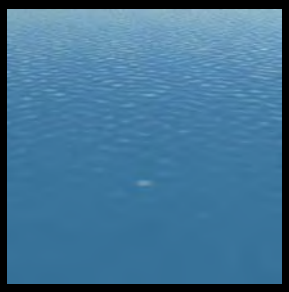

Baltic

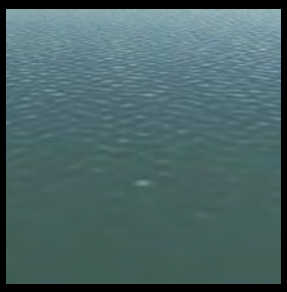

North Sea

What's Next?

Acquiring Scattering Properties of Participating Media by Dilution

Srinivasa G. Narasimhan[1], Mohit Gupta[1], Craig Donner[2], Ravi Ramamoorthi[3], Shree K. Nayar[3], Henrik Wann Jensen[2]

[1]Carnegie Mellon University* [2]University of California, San Diego [3]Columbia University

(a) Acquired photographs (b) Rendering at low concentrations (c) Rendering at natural concentrations

Figure 1: *(a) Photographs of our simple setup consisting of a glass tank and a bulb, filled with diluted participating media (from top, MERLOT, CHARDONNAY, YUENGLING beer and milk). The colors of the bulb and the glow around it illustrate the scattering and absorption properties in these media. At low concentrations, single scattering of light is dominant while multiple scattering of light is negligible. From a single HDR photograph, we robustly estimate all the scattering properties of the medium. Once these properties are estimated, a standard volumetric Monte Carlo technique can be used to create renderings at any concentration and with multiple scattering, as shown in (b) and (c). While the colors are only slightly visible in the diluted setting in (b), notice the bright colors of the liquids - deep red and golden-yellow wines, soft white milk, and orange-red beer - in their natural concentrations. Notice, also the differences in the caustics and the strong interreflections of milk onto other liquids.*

Abstract

The visual world around us displays a rich set of volumetric effects due to participating media. The appearance of these media is governed by several physical properties such as particle densities, shapes and sizes, which must be input (directly or indirectly) to a rendering algorithm to generate realistic images. While there has been significant progress in developing rendering techniques (for instance, volumetric Monte Carlo methods and analytic approximations), there are very few methods that measure or estimate these properties for media that are of relevance to computer graphics. In this paper, we present a simple device and technique for robustly estimating the properties of a broad class of participating media that can be either (a) diluted in water such as juices, beverages, paints and cleaning supplies, or (b) dissolved in water such as powders and sugar/salt crystals, or (c) suspended in water such as impurities. The key idea is to dilute the concentrations of the media so that single scattering effects dominate and multiple scattering becomes negligible, leading to a simple and robust estimation algorithm. Furthermore, unlike previous approaches that require complicated or separate measurement setups for different types or properties of media, our method and setup can be used to measure media with a complete range of absorption and scattering properties from a single HDR photograph. Once the parameters of the diluted medium are estimated, a volumetric Monte Carlo technique may be used to create renderings of any medium concentration and with multiple scattering. We have measured the scattering parameters of forty commonly found materials, that can be immediately used by the computer graphics community. We can also create realistic images of combinations or mixtures of the original measured materials, thus giving the user a wide flexibility in making realistic images of participating media.

*e-mail:srinivas@cs.cmu.edu

1 Introduction

Very often in our daily lives, we see participating media such as fluids (juices, beverages, milks) and underwater impurities (natural ocean, river and lake waters). The propagation of light through these media results in a broad range of effects, including softer appearance of milk, coloring of wines and juices, the transformation of appearances when liquids are mixed (coffee with milk, and cocktails), the brilliant caustics from glasses containing these liquids, and low visibility in underwater situations. These effects inherently depend on several physical properties of the media such as

scattering nature, sizes, shapes, and densities of particles [Hulst 1957; Chandrasekhar 1960]. Rendering these effects accurately is critical to achieving photo-realism in computer graphics.

In the past few years, there has been a considerable effort towards developing efficient and accurate rendering algorithms for participating media, based on Monte Carlo simulation and analytic approximations. All these algorithms and models contain parameters (scattering coefficient, absorption coefficient, phase function) that directly or indirectly represent the physical properties of the medium. In order to faithfully render the effects of any participating medium, the right parameters must be input. Given the progress in developing rendering algorithms, the quality of images is now often limited by the quality of these input parameters. Since there has so far been relatively little work in measuring or estimating scattering properties of media relevant to computer graphics, the parameters are currently often set in an ad-hoc manner.

This situation is similar in some ways to that of standard surface rendering. In that case, global illumination algorithms have progressed to the point of creating almost photo-realistic images, leaving the realism limited by the quality of the reflectance models, and leading to much recent effort on measuring BRDFs. [Marschner 1998; Dana et al. 1997; Matusik et al. 2003]. However, existing methods for directly measuring physical properties for media usually require very expensive equipment, such as the particle sizing apparatus used in colloidal chemistry [Finsy and Joosten 1991; Jaeger et al. 1991], resulting in little usable data for graphics.

Earlier efforts to estimate scattering properties from images of media have often yielded ill-conditioned and non-unique results, because of the difficulties of solving the inverse light transport problem. The reasoning for the ill-conditioning of the inverse problem is mainly due to multiple scattering, which blurs the incident light field and results in significant loss of information [McCormick 1981; McCormick 1985; Antyufeev 2000]. This is analogous to the ill-conditioning of BRDF estimation under complex illumination [Ramamoorthi and Hanrahan 2001]. In this paper, we take a completely different approach. The key idea is to estimate properties of media by acquiring the data in a state where multiple scattering effects are negligible. Instead, the data is acquired when single scattering (which does not degrade the incident light significantly) is the dominant effect. This is achieved by diluting the material to low concentrations.

We present a simple and inexpensive experimental setup, along with a robust and accurate technique for measuring the scattering properties of a broad class of participating media that can be either (a) diluted in water such as juices, beverages, paints and cleaning supplies, or (b) suspended in natural waters such as impurities and organisms, or even (c) dissolved in water such as powders and sugar or salt crystals. These media collectively have a wide range of scattering and absorption properties. We first derive a simple image formation model for single scattering of light in our setup. Through extensive simulations of both our model and ground truth (with multiple scattering), we then determine the space of concentrations and scattering properties of media for which single scattering is dominant. Within this regime of valid concentrations, we conduct simulations to demonstrate that our estimation technique uniquely solves the inverse single scattering light transport problem. Finally, we present a simple experimental procedure to determine the best concentration (dilution) for any material despite no prior knowledge of its scattering properties.

We have used our approach to create a dataset of scattering parameters for **forty commonly found materials**, which can be directly used for computer graphics rendering. Once the scattering parameters have been estimated, they can be used to render realistic images of arbitrary concentrations of the material with multiple scattering, using a standard physically based volumetric rendering algorithm. Figure 1 shows two renderings of a scene with four liquids in their natural high density states and their diluted states. The scattering parameters of each material were computed using a single HDR photograph of our setup. Notice the bright saturated colors obtained despite the murky appearance of the diluted states. We can also create realistic images of mixtures of the original measured materials, thus giving the user a wide flexibility in creating realistic images of participating media.

Medium Property	Notation
Concentration or Volume Fraction	C
Scattering Coefficient (mm^{-1})	β
Absorption Coefficient (mm^{-1})	κ
Extinction Coefficient (mm^{-1})	$\sigma = \beta + \kappa$
Single Scattering Albedo	$\omega = \beta / \sigma$
Scattering Angle	θ
Henyey-Greenstein (H-G) Parameter	g
H-G Phase Function	$P(g,\theta) = \frac{1}{4\pi} \frac{1-g^2}{(1+g^2-2g\cos\theta)^{3/2}}$

Figure 2: *The different scattering properties of a participating medium and their notations used in this paper. Light transport equations are usually written in terms of three parameters σ, β and g. We estimate these parameters for participating media based on single scattering.*

2 Related Work

Figure 2 shows the most common properties of participating media including the scattering and absorption coefficients, and the phase function (angular scattering distribution represented by the Henyey-Greenstein (H-G) model [Henyey and Greenstein 1941]). The scattering and absorption coefficients are proportional to the concentration or volume fraction of the particulate medium. We will briefly review some of the representative works on the direct measurement and indirect estimation of these parameters.

Estimation based on analytic approximations to light transport. Surprisingly, little work has been done in computer graphics on the measurement of scattering properties of media. A recent work is that of [Jensen et al. 2001], on the diffusion model for subsurface scattering. They present a measurement of a number of translucent materials. However, the diffusion approximation assumes multiple scattering for optically dense media, so that only a limited amount of information on the scattering parameters can be estimated. For instance, this approximation is independent of the phase function of the medium, and therefore this important property cannot be estimated. Furthermore, the diffusion is a poor approximation when scattering is comparable to absorption [Prahl 1988]. The analytic multiple scattering model presented in [Narasimhan and Nayar 2003] has also been used to estimate properties of only purely scattering media (visibility and type of weather such as fog and mist). Our focus is somewhat different in considering fluids like juices or beverages, instead of subsurface scattering in translucent solids like marble and skin, or weather conditions such as fog. Nevertheless, our approach is valid for media with the entire range of absorbing and scattering properties, significantly extending the class of measurable media for graphics.

Most recently, Hawkins et. al., [2005] measure the extinction coefficient of optically thin smoke from the exponential attenuation of a laser beam in a tank. They also use a separate mirror setup to directly measure the phase function (see below). In contrast, our setup uses divergent beams from a simple bulb to include more light in the volume (than a single laser beam) for robust measurements, and requires only a single photograph to measure all scattering properties shown in Figure 2.

Numerical solution to inverse light transport: In cases where there are no analytic solutions to light transport, several works have taken a numerical approach to estimate scattering properties [McCormick 1996; Antyufeev 2000]. However, it is widely

known, that inverse problems in radiative transfer that take into account multiple scattering are ill-conditioned and require regularizing assumptions to obtain reliable estimates. See the reports and critiques by McCormick et al [1981; 1985]. Furthermore, the computational complexity of such inverse estimation techniques make it hard for measuring large sets of media for computer graphics or vision applications. Our focus here is on estimating scattering properties of media that can be measured in a state where multiple scattering is negligible.

The observation that single scattering is dominant for optically thin media has been made by [Hawkins et al. 2005; Sun et al. 2005]. We exploit this observation and apply the single scattering model for the first time to a large class of materials which exhibit significant multiple scattering in their natural states of existence. We also determine the exact range of optical thicknesses for which single scattering is dominant for media with arbitrary scattering properties, and propose an experimental procedure to ensure the dominance of single scattering in real data.

Goniophotometry is often used to directly measure the phase function. Here, several detectors measure radiance in different directions after being scattered by a very small volume of the medium. [Fuchs and Jaffe 2002] use thin laser light sheet microscopy for detecting and localizing microorganisms in ocean waters. [Boss and Pegau 2001; Oishi 1990] investigate the relationship of light scattering at a single angle and the extinction coefficient using specialized receivers and transmitters. However, all these techniques assume that there is no attenuation of light through the sample and require expensive devices with precise alignment of detectors and transmitters. In contrast, our setup is extremely simple (consisting of a glass tank and an off the shelf bulb), and our technique robustly estimates all properties from only a single photograph, thus making it inexpensive and easy to measure a large number of participating media.

3 Single Scattering in Dilute Media

Our approach is to measure media in a state where single scattering is dominant and multiple scattering is negligible. This is achieved by diluting the otherwise optically thick media, such as fluids, in water. The process of dilution does not usually corrupt the inherent scattering properties of media[1] since the scattering and absorption of pure water itself is negligible for very small distances (less than 50 cm) [Sullivan 1963]. We begin by presenting our acquisition setup and an image formation model for single scattered light transport within the measurement volume. We will then present extensive simulations of this model and compare with traditional Monte-Carlo approaches that include multiple scattering, to derive a valid space of scattering parameters over which single scattering is dominant. Based on this simulation, we design a simple experimental procedure to choose the best concentration for any particular medium. Later, we will describe our algorithm to estimate the scattering parameters using our image formation model.

3.1 Acquisition Setup

The measurement apparatus, shown in Figure 3, consists of a $25 \times 30 \times 30\,\text{cm}^3$ tank that is filled with the diluted scattering medium. The depth of the tank is large enough to ensure the scattering angles are adequately covered (0 to 175 degrees). The volume of the tank is designed to be large enough to dilute concentrated media such as milk. Two sides of the tank are constructed using anti-reflection glass and the other sides using diffuse black coated acrylic. A small frosted (diffuse) glass bulb fixed to a side

[1] When crystals are dissolved in water, they may exhibit different scattering properties due to ionization.

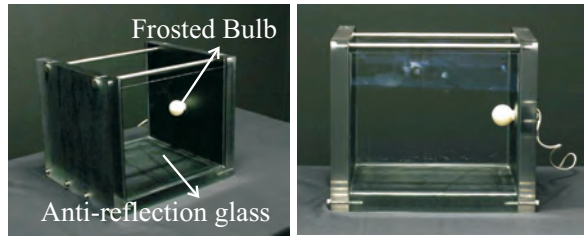

Figure 3: *Two views of the apparatus used to measure scattering properties of water-soluble media. A glass tank with rectangular cross-section is fitted with a small light bulb. The glass is anti-reflection coated. Different volumes of participating media are diluted with water in the tank, to simulate different concentrations. A camera views the front face of the tank at normal incidence to avoid refractions at the medium-glass-air boundaries.*

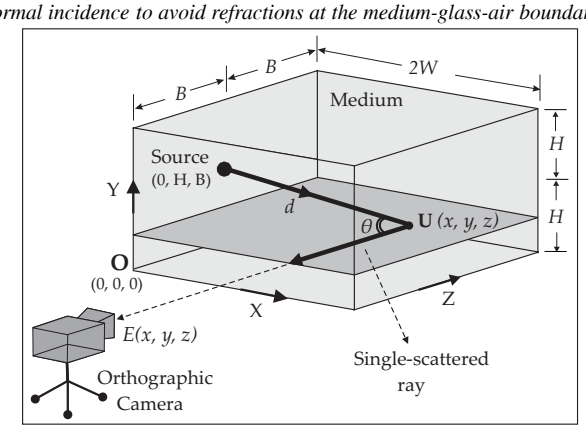

Figure 4: *A volume filled with a homogeneous participating medium and illuminated by an isotropic point light source. A camera views the front face of the volume at normal incidence. The path of one single-scattered ray as it travels from the source to the camera is shown. This ray is first attenuated in intensity over a distance d, is then scattered at an angle $\pi - \theta$, and finally, is attenuated again over a distance z, before reaching the camera. The irradiances due to all the rays that scatter into a viewing direction must be integrated to obtain the final camera irradiance.*

of the tank illuminates the medium. A Canon EOS-20D 12-bit 3504x2336 pixel digital camera with a zoom lens is placed five meters away from the tank and observes a face of the tank at normal incidence. The field of view occupied by the tank in the image is three degrees and is therefore approximately orthographic. Orthographic projection avoids the need for modeling refractions of light rays at the medium-glass-air interfaces. In all our experiments, about 25 different exposures (1/500s to 10s) were used to acquire HDR images.

3.2 Image Formation Model

Although the basic principles of single scattering are well known, the exact nature of the image formation model depends on the geometry of the volume and the locations of the source and the camera. Figure 4 illustrates the illumination and measurement geometry based on our acquisition setup. For simplicity, we will assume that the medium is illuminated by an isotropic point light source (later we extend the analysis to area sources) of intensity I_0 that is located at the coordinates $(0, B, H)$.

Consider the path of one single-scattered light ray (thick ray in Figure 4) in the medium as it travels from the source to the camera. This ray is first exponentially attenuated in intensity for a distance d. At location $\mathbf{U}\ (x, y, z)$, depending on the phase function P, a fraction of the light intensity is scattered at an angle $\pi - \theta$. Finally, the ray is attenuated again for a distance z, before it reaches the camera. Mathematically, the irradiance at the camera produced by

this ray is written as [Sun et al. 2005],

$$E(x,y,z) = \frac{I_0}{d^2} \,.\, e^{-\sigma d} \,.\, \beta P(g,\pi-\theta) \,.\, e^{-\sigma z}.$$
$$d = \sqrt{x^2+(y-H)^2+(z-B)^2} \;,\; \cos\theta = (z-B)/d \quad (1)$$

Here, $P(g,\pi-\theta)$ is the Henyey-Greenstein (H-G) phase function, and β and σ are the scattering and extinction coefficients (Figure 2). Then, the total irradiance E at pixel (x,y) in the camera is obtained by integrating intensities due to all rays that are scattered at various angles along the pixel's line of sight (Z-direction),

$$E(x,y) = \int_0^{2B} E(x,y,z)\,dz$$
$$= \beta \int_0^{2B} \frac{I_0\, e^{-\sigma(z+\sqrt{x^2+(y-H)^2+(z-B)^2})}}{x^2+(y-H)^2+(z-B)^2}\, P(g,\pi-\theta)\,dz. \quad (2)$$

The above equation relates the camera irradiances as a function of the three medium parameters, σ, β and g. Although obtaining an analytic (closed-form) solution to the above integral is hard [Sun et al. 2005], it is straightforward to evaluate it numerically.

3.3 Space of valid medium parameters

Different materials have their own natural densities and scattering properties, which are all unknown before experimentation. So, how do we know if single scattering is dominant at a particular concentration for a given material? Note that the scattering β, absorption κ and extinction σ, coefficients are proportional to the concentration (fraction of volume diluted in water) of the medium. Thus, we performed exhaustive simulations to derive the complete space of parameters for which the above image formation model is accurate[2]. For ground truth, we simulated the irradiances obtained using multiple scattering for the same set of parameter values, using a standard volumetric Monte Carlo technique. Figure 5 shows a plot of the differences between energies captured by the single scattering and multiple scattering simulations for a set of parameter values. From the RMS errors in the plot, we can define the upper bounds on the parameters κ and $\sigma = \beta + \kappa$ as those for which the energy differences between our model and the ground truth are less than five percent. For example, the valid domain where single scattering is dominant, is approximately $\sigma < 0.04$ for $\kappa < 0.004$.

3.4 How to choose the best concentration?

Based on the simulations, we present an experimental method to determine the best concentration for our measurements. Figure 6 shows images acquired of different concentrations of milk and MERLOT. Which among these images should we use to measure the scattering properties? Several heuristics may be used to decide on a particular concentration. For instance, the extent of blurring of the light source provides us a good clue to determine whether multiple scattering is significant (rightmost image in Figure 6). A better heuristic is to compute an approximation to the extinction coefficient σ from the attenuated brightness of the light source. Under single scattering, the radiance in the direction of the source (distance d) can be approximated using exponential attenuation as:

$$E(0) \approx \left(\frac{I_0}{d^2}\right) e^{-\hat{\sigma} d}, \quad (3)$$

[2]This extends the simulations in [Sun et al. 2005], where a small part of the possible parameter space (pure isotropic scattering) was considered.

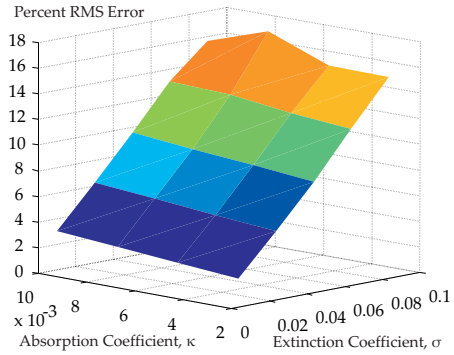

Figure 5: *Plot showing the differences between irradiances obtained by simulating single scattering and multiple scattering (ground truth) models, for a large space of parameter values σ and $\kappa = \sigma - \beta$. An upper bound on the differences of, say, 5%, can be used to define the range of parameters for which single scattering is a valid approximation. From the plot, the valid range is approximately $\sigma < 0.04$ for $\kappa < 0.004$.*

where $\hat{\sigma}$ is an estimate of the extinction coefficient σ. In the absence of multiple scattering, this estimate is closer to the true value of σ (and varies linearly with concentration), whereas, in the presence of multiple scattering, this estimate is called *diffuse or reduced attenuation coefficient* [Ishimaru 1978] and is usually much lesser than σ. Thus, we can determine whether the concentration can be used for measurement by observing the plot (Figure 7 of $\hat{\sigma}$ versus the volume fraction of the medium diluted with water). Figure 7 shows that after a certain amount of milk is added to water, the $\hat{\sigma}$ no longer remains linear with concentration (dashed line), and must not be used for measurements. For a purely absorbing liquid like wine (MERLOT), the plot is completely linear and any image that has the best signal-to-noise ratio may be used. Similarly, the plot shows that coke scatters, albeit weakly, and ESPRESSO coffee scatters light strongly. We use this simple procedure to try several concentrations and observe where the linearity in the plot fails to determine the best concentration. As a further test, we check if the estimated parameters from this concentration lie within the valid space of parameters simulated above.

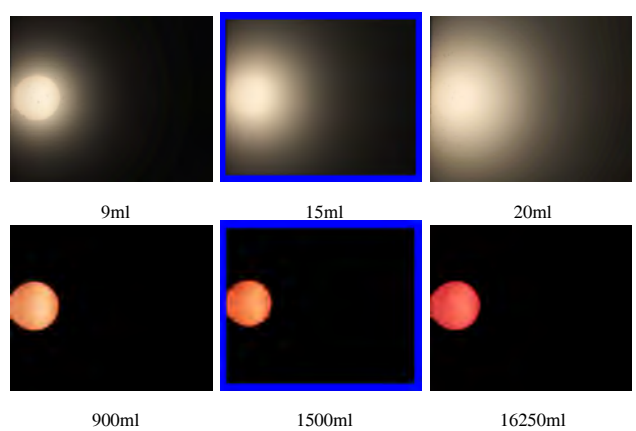

Figure 6: *Images illustrating different degrees of scattering and absorption. [Top row] Images of milk at various concentrations. Since milk is a highly scattering liquid, we observe an increase in blurring with increasing concentration. [Bottom Row] Images of red wine at various concentrations. Red wine is a highly absorbing liquid, showing only a saturation of the bulb color with increasing concentration, and no blurring. The highlighted images are chosen for estimating the parameters.*

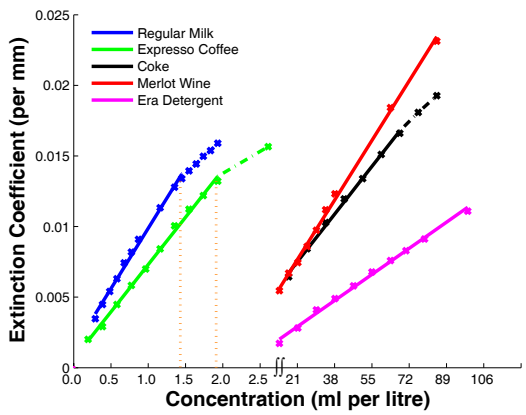

Figure 7: *Plot of extinction coefficient estimate $\hat{\sigma}$ as a function of the volume of the media diluted in water in the measurement apparatus. The plots are linear when multiple scattering is negligible and single scattering is dominant. As the concentrations of media (and hence multiple scattering) increase, the estimated $\hat{\sigma}$ is less than the true extinction coefficient σ. For a highly scattering medium such as milk, the linearity fails at very low concentrations, while for an absorbing medium such as MERLOT, the linearity is always preserved.*

4 Estimating Medium Properties based on Single Scattering

In this section, we present a non-linear minimization algorithm to estimate the properties of the medium (σ, β and g), from the measured image irradiances $E(x,y)$ (see Equation (2)). We then demonstrate the accuracy of the algorithm through extensive simulations.

4.1 Formulating the Error Function

The error at each pixel is written as the difference between the measured irradiance $E(x,y)$ and the irradiance predicted by the model in equation 2,

$$\mathscr{F}(x,y) = E(x,y) - RHS(x,y)\,. \tag{4}$$

Here $RHS(x,y)$ is the numerically evaluated right hand side integral in the model of equation 2. Then, the parameters σ, β and g can be estimated by computing the global minimum of the sum of squares of the errors of all the pixels, as,

$$\min_{\beta,\sigma,g} \sum_y \sum_x \mathscr{F}^2(x,y)\,. \tag{5}$$

The above function essentially requires a 3-parameter search. However, note that the parameter β is a global scale factor. Thus, we can eliminate β by defining a normalized error function as,

$$\mathscr{F}_{norm}(x,y) = \frac{E(x,y)}{\max\limits_{x,y} E(x,y)} - \frac{RHS(x,y)}{\max\limits_{x,y} RHS(x,y)}\,. \tag{6}$$

Now, instead of requiring a 3-parameter search, the above problem can be reduced to a 2-parameter search that minimizes the normalized objective function to estimate σ and g:

$$\min_{\sigma,g} \sum_y \sum_x \mathscr{F}^2{}_{norm}(x,y)\,. \tag{7}$$

Then, the scale factor β can be recovered using the original function $\mathscr{F}$. To compute the global minimum, we use Nelder-Meade search implemented by the Matlab^{TM} function "fminsearch".

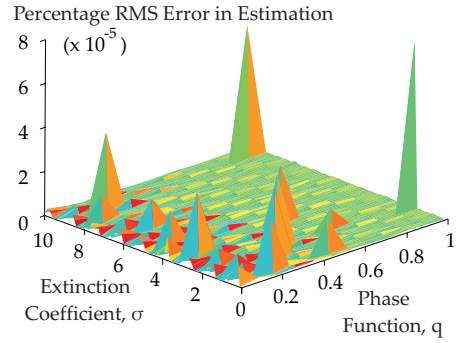

Figure 8: *Plot showing the errors in reconstruction of the single scattering parameters σ and $q = |g|$, where $-1 < g < 1$, compared to ground truth values. The low errors indicate the accuracy of our estimation technique. The maximum of the errors for positive or negative g is shown.*

4.2 Estimation Accuracy using Simulations

Fortunately, since the space of the possible parameters is small (see Section 3.3), exhaustive simulation of the above algorithm is possible. We only show the correctness of the estimated parameters σ and g, using Equation (7). The estimation of the scale factor β then follows trivially. Gaussian noise of unit standard deviation was added in all our simulations. The non-linear search was initialized randomly for both the parameters σ and g. The plot in Figure 8 shows the error in the estimated parameters as compared to ground truth values. In all the cases, the estimation errors were less than 0.0001%, and the number of iterations required for convergence was less than 100. Since the numerical evaluation of the integral is very fast, the time for convergence is usually of the order of a few minutes. This demonstrates that the inverse estimation is fast and results in unique and correct parameters.

4.3 Implementation Issues

We present two issues that need careful implementation for our algorithm to be successful on real images.

Calibrating the area source: Our method does not rely on isotropic point sources but requires only a calibrated divergent source to take advantage of the different phase angles measured in the same view and hence, any off-the-shelf bulb suffices. For our real setup, we have implemented a spherical diffuse area source. To compute the irradiance at any point P within the tank, we sample (using roughly 10x10 samples) the hemisphere of the bulb that is visible to that point P. The non-uniform directional intensities and intensity fall-off were calibrated carefully by using a light meter at discrete 3D locations within the tank. The camera also measures a pure water image (without any scattering or absorption) to give the image irradiance of each source element (sample). This irradiance along with the fall-off value and the pixel solid angle is used to determine the intensity without scattering.

Instabilities in the H-G phase function for highly absorbing media: The H-G phase function was designed for scattering media and is not defined for purely absorbing media. However, for highly absorbing media, the scattering coefficient β is very low and the average cosine $g \approx 1$ since rays only pass straight through, much like highly forward scattering media. Even though this was not a problem in simulations, the instability for $g > 0.95$ can be high in real experiments. For this special case, we simply use a truncated legendre polynomial expansion of the H-G phase function as $P(g,\theta) = \sum_i (2i+1)\, g^i\, L_i(\theta)$, and truncate to less than 100 terms. As an undesirable byproduct the fits may show some "ringing" at the tail of the phase function. However, this truncated function still fits higher brightness well and thus does not affect appearance strongly. Despite this instability, the H-G phase function is flexible enough to model the scattering behavior of all our materials.

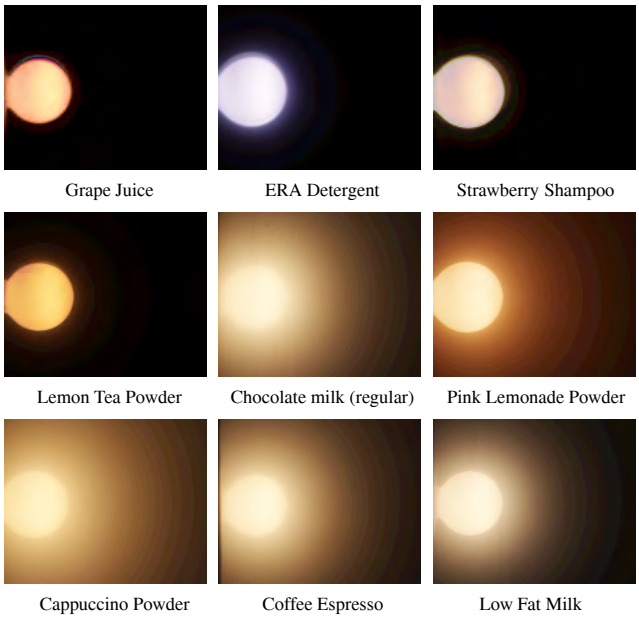

Figure 9: *Captured photographs of a variety of water-soluble media illustrating different degrees of scattering and absorption. For highly scattering media such as milk, chocolate milk and espresso, we observe a significant blur around the bulb. For highly absorbing media such as grape juice, there is very little scattering. All the images have wide dynamic range of intensities and hence, we have tone-mapped them for illustration.* **Please see supplementary material for more images.**

5 Actual Measurements and Validation

Using our approach, we have measured the scattering properties of a broad class of **forty** commonly found participating media that can be either (a) diluted in water such as juices (for example, apple, strawberry, orange), beverages (for example, coffee, soft drinks, milks, wines, beers), cleaning supplies (detergents), or (b) suspended in natural waters such as impurities and organisms, or even (c) dissolved in water such as powders and sugar, salt crystals. In addition to liquids available at the usual supermarkets, we have also collected four samples from different locations and depths in the Pacific ocean. We then present detailed validation by showing that our parameters extrapolate correctly to higher concentrations as well, where multiple scattering is prominent.

A subset of nine photographs of the diluted set of liquids contained in the glass tank is shown in Figure 9, similar to the four in Figure 1. Together, these include representative types of media such as highly scattering, highly absorbing and moderate levels of absorption and scattering. The images show a high dynamic range of brightness and are enhanced to show the scattering effects. The set of scattering parameters for all the media is shown in Table 1. The extinction (σ) and scattering (β) coefficients are given for each of the three color channels, red, green and blue. The phase function parameter g is also shown for the three color channels. Note that all the extinction and scattering coefficients are less than 0.04 in accordance with our simulations in Section 3.3. Also, as expected, in all cases, the scattering coefficient does not increase with wavelength.

5.1 Fits to Measured Brightness Profiles

We demonstrate the accuracy of our technique by reconstructing the photographs using the estimated parameters. Although we considered the brightness at all pixels in the captured photographs, for illustration purposes we show only the profile of intensity values in the direction that is radially outward from the source. Figure 10

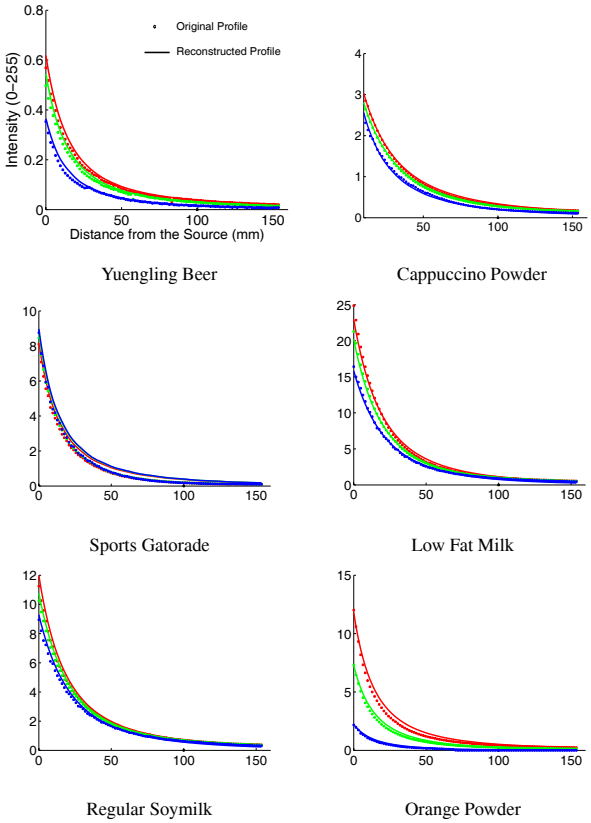

Figure 10: *Fits obtained using the estimated parameters as compared against the corresponding measured brightness profiles in the captured photographs. The brightness profile is measured radially outward from the source in the image. The red, green and blue plots correspond to the three color channels of the camera. The match between the estimated and measured data demonstrates the accuracy of the estimation technique. The fits for six (out of 40) representative materials with varying degrees of absorption and scattering are shown.* **Please see the supplementary material for more plots.**

shows the good fits obtained using the estimated parameters compared against the measured profiles for a subset of six materials of varying degrees of scattering and absorption properties (please review supplementary document for plots of other materials). When there is no scattering (pure absorption), fitting a scattering model can induce some "ringing" effect in the dark tail end of the profile. We can detect this special case and use the attenuation model to compute the absorption coefficient ($\kappa = \sigma$).

5.2 Extrapolation to higher concentrations

The extinction and scattering coefficients are proportional to the concentration of the medium. Thus, if β_1 and σ_1 are estimated at concentration c_1, then the coefficients β_2 and σ_2 at another concentration c_2 can be extrapolated using:

$$\beta_2 = \beta_1 \left(\frac{c_2}{c_1}\right) \ , \ \sigma_2 = \sigma_1 \left(\frac{c_2}{c_1}\right) . \tag{8}$$

Note, however, that g is independent of the medium concentration. While we estimate the parameters from lower concentrations, it is important to ensure that the parameters can be scaled to any concentration (where multiple scattering cannot be ignored) to produce accurate scattering effects. We show an example validation using fits obtained in comparison to the measured brightness profiles of chocolate milk at various concentrations. Figure 11 shows the fits

Material Name	Volume	Extinction Coefficient (σ) ($\times 10^{-2}$ mm^{-1})			Scattering Coefficient (β) ($\times 10^{-2}$ mm^{-1})			Average Cosine (g)			% RMS Error
		R	G	B	R	G	B	R	G	B	
Milk (lowfat)	16ml	0.9126	1.0748	1.2500	0.9124	1.0744	1.2492	0.932	0.902	0.859	0.95
Milk (reduced)	18ml	1.0750	1.2213	1.3941	1.0748	1.2209	1.3931	0.819	0.797	0.746	1.27
Milk (regular)	15ml	1.1874	1.3296	1.4602	1.1873	1.3293	1.4589	0.750	0.714	0.681	1.56
Coffee (espresso)	8ml	0.4376	0.5115	0.6048	0.2707	0.2828	0.2970	0.907	0.896	0.880	1.90
Coffee (mint mocha)	6ml	0.1900	0.2600	0.3500	0.0916	0.1081	0.1460	0.910	0.907	0.914	2.00
Soy Milk (lowfat)	16ml	0.1419	0.1625	0.2740	0.1418	0.1620	0.2715	0.850	0.853	0.842	1.75
Soymilk (regular)	12ml	0.2434	0.2719	0.4597	0.2433	0.2714	0.4563	0.873	0.858	0.832	1.68
Chocolate Milk (lowfat)	10ml	0.4282	0.5014	0.5791	0.4277	0.4998	0.5723	0.934	0.927	0.916	1.04
Chocolate Milk (regular)	16ml	0.7359	0.9172	1.0688	0.7352	0.9142	1.0588	0.862	0.838	0.806	2.19
Soda (coke)	1600ml	0.7143	1.1688	1.7169	0.0177	0.0208	0.0000	0.965	0.972	–	4.86
Soda (pepsi)	1600ml	0.6433	0.9990	1.4420	0.0058	0.0141	0.0000	0.926	0.979	–	2.92
Soda (sprite)	15000ml	0.1299	0.1283	0.1395	0.0069	0.0089	0.0089	0.943	0.953	0.952	3.22
Sports Gatorade	1500ml	0.4009	0.4185	0.4324	0.2392	0.2927	0.3745	0.933	0.933	0.935	3.42
Wine (chardonnay)	3300ml	0.1577	0.1748	0.3512	0.0030	0.0047	0.0069	0.914	0.958	0.975	5.10
Wine (white zinfandel)	3300ml	0.1763	0.2370	0.2913	0.0031	0.0048	0.0066	0.919	0.943	0.972	5.49
Wine (merlot)	1500ml	0.7639	1.6429	1.9196	0.0053	0.0000	0.0000	0.974	–	–	4.56
Beer (budweiser)	2900ml	0.1486	0.3210	0.7360	0.0037	0.0069	0.0074	0.917	0.956	0.982	5.61
Beer (coorslight)	1000ml	0.0295	0.0663	0.1521	0.0027	0.0055	0.0000	0.918	0.966	–	4.89
Beer (yuengling)	2900ml	0.1535	0.3322	0.7452	0.0495	0.0521	0.0597	0.969	0.969	0.975	4.48
Detergent (Clorox)	1200ml	0.1600	0.2500	0.3300	0.1425	0.1723	0.1928	0.912	0.905	0.892	1.99
Detergent (Era)	2300ml	0.7987	0.5746	0.2849	0.0553	0.0586	0.0906	0.949	0.950	0.971	4.17
Apple Juice	1800ml	0.1215	0.2101	0.4407	0.0201	0.0243	0.0323	0.947	0.949	0.945	4.92
Cranberry Juice	1500ml	0.2700	0.6300	0.8300	0.0128	0.0155	0.0196	0.947	0.951	0.974	4.60
Grape Juice	1200ml	0.5500	1.2500	1.5300	0.0072	0.0000	0.0000	0.961	–	–	5.19
Ruby Grapefruit Juice	240ml	0.2513	0.3517	0.4305	0.1617	0.1606	0.1669	0.929	0.929	0.931	2.68
White Grapefruit Juice	160ml	0.3609	0.3800	0.5632	0.3513	0.3669	0.5237	0.548	0.545	0.565	2.84
Shampoo (balancing)	300ml	0.0288	0.0710	0.0952	0.0104	0.0114	0.0147	0.910	0.905	0.920	4.86
Shampoo (strawberry)	300ml	0.0217	0.0788	0.1022	0.0028	0.0032	0.0033	0.927	0.935	0.994	2.47
Head & Shoulders	240ml	0.3674	0.4527	0.5211	0.2791	0.2890	0.3086	0.911	0.896	0.884	1.91
Lemon Tea Powder	5tsp	0.3400	0.5800	0.8800	0.0798	0.0898	0.1073	0.946	0.946	0.949	2.83
Orange Powder	4tbsp	0.3377	0.5573	1.0122	0.1928	0.2132	0.2259	0.919	0.918	0.922	2.25
Pink Lemonade Powder	5tbsp	0.2400	0.3700	0.4500	0.1235	0.1334	0.1305	0.902	0.902	0.904	1.02
Cappuccino Powder	0.25tsp	0.2574	0.3536	0.4840	0.0654	0.0882	0.1568	0.849	0.843	0.926	0.67
Salt Powder	1.75cup	0.7600	0.8685	0.9363	0.2485	0.2822	0.3216	0.802	0.793	0.821	1.34
Sugar Powder	5cup	0.0795	0.1759	0.2780	0.0145	0.0162	0.0202	0.921	0.919	0.931	1.80
Suisse Mocha Powder	0.5tsp	0.5098	0.6476	0.7944	0.3223	0.3583	0.4148	0.907	0.894	0.888	1.33
Mission Bay Surface Water (1-2 hours)		3.3623	3.2929	3.2193	0.2415	0.2762	0.3256	0.842	0.865	0.912	2.48
Pacific Ocean Surface Water (1 hour)		3.3645	3.3158	3.2428	0.1800	0.1834	0.2281	0.902	0.825	0.914	2.57
Mission Bay 10ft deep Water (30 min)		3.4063	3.3410	3.2810	0.0990	0.1274	0.1875	0.726	0.820	0.921	5.10
Mission Bay 10ft deep Water (8 hours)		3.3997	3.3457	3.2928	0.1018	0.1033	0.1611	0.929	0.910	0.945	5.13

Table 1: Scattering properties for 40 different water-soluble materials estimated using our technique. The second column lists the volumes V of the materials dissolved in $23-V$ litres of water to achieve the desired levels of dilution where single scattering is dominant. These parameters can be proportionately scaled to any other volume V_n, using a scale factor of V_n/V. The percentage RMS errors (obtained over all pixels) quantify the accuracy of fits achieved with the estimated parameters to the measured intensity profiles. Errors for all the highly scattering media are less than 3%. For low-scattering materials, the total intensity of profiles is relatively low, thus making the estimation more sensitive to noise. Even for such low-scattering media, the errors are less than $5-6\%$. The last four rows are the parameters for various ocean water samples at their original concentrations. The **time elapsed** between the collection of samples and the image acquisition is listed in the parentheses. Since the suspended particles in ocean water settle down with time, we observe a small decrease in scattering coefficients in the sample for which 8 hours had been elapsed as compared to the one which was imaged just 30 minutes after collection. Note that all the extinction and scattering coefficients are less than 0.04 in accordance with our simulations in Section 3.3. As expected, the scattering coefficients do not decrease with wavelength. The scattering albedos (ratio of scattering coefficients to the extinction coefficients) is much higher for the scattering media (milk, coffee, orange powder) as compared to the absorbing ones (coke, wine). For materials that have $\beta = 0$, the phase function parameter g is undefined. As seen from the values of g which are closer to 1, several media are predominantly forward scattering. The parameters for the milks match those in [Jensen et al. 2001] up to a scale factor (due to the different fat contents in the milks used), providing further support for our estimation.

in this validation experiment. First, we estimate the parameters from the photograph of only 8ml of chocolate milk diluted in water, where single scattering is dominant. In (a), we show the fit obtained compared against the measured intensity profile. However, for higher concentrations of 50ml, 100ml and 150ml, multiple scattering cannot be ignored. For these cases, we scaled the coefficients (σ and β) by factors of $\{50/8, 100/8, 150/8\}$ (see Equation 8) and use them in a standard volumetric Monte Carlo renderer that includes multiple scattering. The plots in (b) - (d) demonstrate the strong fits obtained. This demonstrates that our parameters are robust enough to be extrapolated to higher concentrations. In fact, we will show renderings of most of the liquids at their natural concentrations (Section 6) despite measuring the parameters at significantly dilute states.

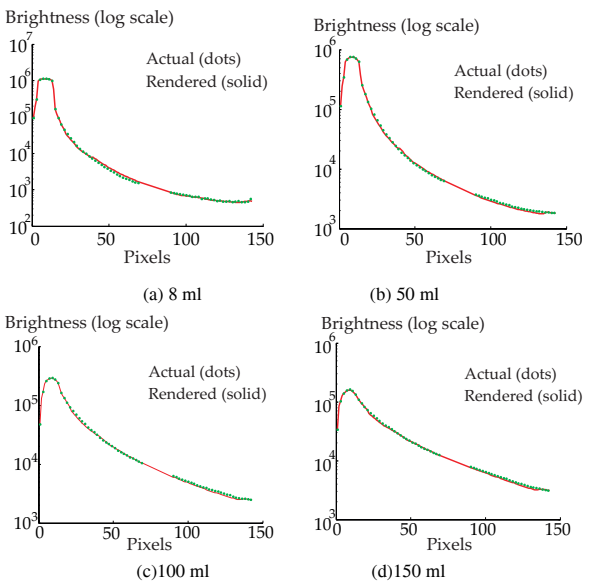

Figure 11: *Extrapolation of parameters to higher concentrations with multiple scattering. (a) 8 ml of chocolate milk is diluted in water and the parameters are estimated using the measured brightness profile. (b) - (d) The parameters estimated in (a) are scaled to higher concentrations (50ml, 100ml and 150ml) where multiple scattering cannot be ignored. Plots show a good fit between the brightness profile obtained by extrapolating our estimated parameters with a Monte Carlo renderer, and the ground truth measurements. The fits are shown in logarithmic scale.*

Figure 12: *Rendered scenes of liquids in a cognac glass under complex lighting. The KITCHEN environment map [Debevec 1998] was used for the lighting. The natural colors, shading and caustics indicate the high accuracy of our parameters.*

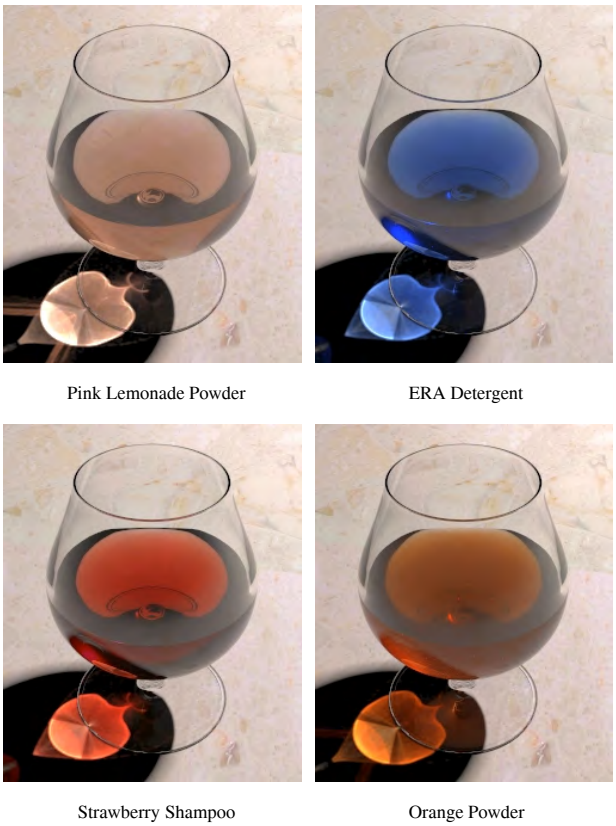

Figure 13: *Rendered scenes of liquids and powders in a cognac glass illuminated with a single directional white light source. The bright caustics show the colors transmitted through the media.*

6 Example Volumetric Renderings

The scattering properties estimated in this work can be input to any volumetric rendering algorithm to create visual effects of participating media. Here, we chose brute-force volumetric Monte-Carlo path tracing since it can be used to render arbitrary materials[3]. We use photon mapping for rendering caustics. For display purposes, we have applied a tone-mapping operator [Ward-Larson et al. 1997] to the renderings. Indices of refraction (IOR) of these media are also important for rendering. In initial experiments, we found the IOR to be between 1.33 (water) and 1.42 (milk) and varying linearly with concentrations, by using location of total internal reflection from the top of the water surface in the tank. In current renderings, we have simply used an IOR proportionate to the medium concentrations between 1.33 and 1.42, since this does not alter the visual appearance of the liquid drastically. We wish to perform thorough experiments in the future.

Figure 12 shows a mosaic of images of liquids rendered in their natural concentrations, partially filled in a cognac glass and illuminated by the "Kitchen Environment Map" [Debevec 1998]. These include two different types of wine (deep red MERLOT and golden-yellow CHARDONNAY), dark brown coffee ESPRESSO, and the golden-orange YUENGLING beer. Notice the color differences between MERLOT (no scattering) and ESPRESSO (moderate scattering) even though both of them are dark liquids. Observe that while beer and CHARDONNAY are very clear liquids, coffee is noticeably more opaque. Similarly, Figure 13 shows a mosaic of predominantly bright colored liquids such as the deep

[3]Under-sampling of path-traces can cause speckle noise seen in the renderings, and is not an artifact of our estimation.

Figure 14: *Effect of changing concentrations of a highly absorbing (MERLOT) and a highly scattering (milk) liquid. In the case of wine, notice that while the color gradually becomes deep red, the liquid remains clear, due to the lack of scattering. In the case of milk, however, we see a quick transition from a murky appearance to a soft white appearance, due to the high scattering albedo of milk.*

blue ERA detergent, the reddish strawberry shampoo, and powders dissolved in water such as the "pinkish" strawberry lemonade and orange powders. These images are illuminated only by a strong directional source to illustrate the bright caustics whose colorings are primarily due to absorption. We also present different types of novel visual effects obtained by changing or blending the parameters of different media to create realistic images of dilutions and mixtures of the original measured materials.

Effect of changing concentrations: Figure 14 illustrates the effects of changing concentrations of media in water. The top row shows a transition from pure water to MERLOT, obtained by scaling parameters of wine as in Equation 8. Notice the changes in caustics and the gradual deepening of the red color of the liquid. Note that as the transition occurs, the liquid remains clear even though the color changes; this is due to the pure absorbing nature of wine, as depicted by our parameters. The bottom row shows the effect of changing milk concentration in water. Since milk is a highly scattering medium, as expected, the appearance quickly changes from murky whitish water to soft and thick white milk. This is because the scattering albedo β/σ is high and the phase function parameter g is such that a significant amount of light diffuses into different directions.

Blending parameters for mixtures of media: For example, what are the properties of a mixture of ESPRESSO and milk, or otherwise known as *light coffee*? Consider a medium containing a mixture of two types of media, A and B. The properties of the individual media are denoted with the subscripts A and B. The scattering coefficient of the mixture is obtained by a weighted average,

$$\beta_{mix} = \frac{V_A\beta_A + V_B\beta_B}{V_A + V_B}\,. \tag{9}$$

The absorption and extinction coefficients are similarly defined. Unlike above where we just changed the scattering and absorption coefficients, here a new phase function parameter must be defined for the mixture as the weighted average [Key 2005],

$$g_{mix} = \frac{g_A\beta_A + g_B\beta_B}{\beta_{mix}}\,. \tag{10}$$

These equations can be used to render mixtures of participating media or morph from one medium into another. Figure 15 shows mixing of different proportions of milk and wine. The second example shows a more common mixing of milk and coffee. Such mixing between materials, for the first time, gives a user the flexibility to create novel renderings of participating media.

7 Conclusion

Rendering the rich visual effects of participating media, like fluids or underwater impurities, requires precise measurements of their scattering properties. In this paper, we have developed a simple device and method for accurately estimating the scattering properties of a variety of media that can be diluted in water. Our approach only requires a single high dynamic range photograph. By diluting the medium, we work in the single scattering regime, where the inverse light transport problem is well conditioned—however, we can later render at arbitrary concentrations and even mix materials. We have presented a database of scattering parameters for 40 commonly found materials. This database is the first of its kind, and enables computer graphics practitioners to accurately render a wide variety of participating media, rather than having to set parameters in an ad-hoc fashion. In the future, we would like to improve this work by investigating different phase functions and measuring indices of refraction more accurately.

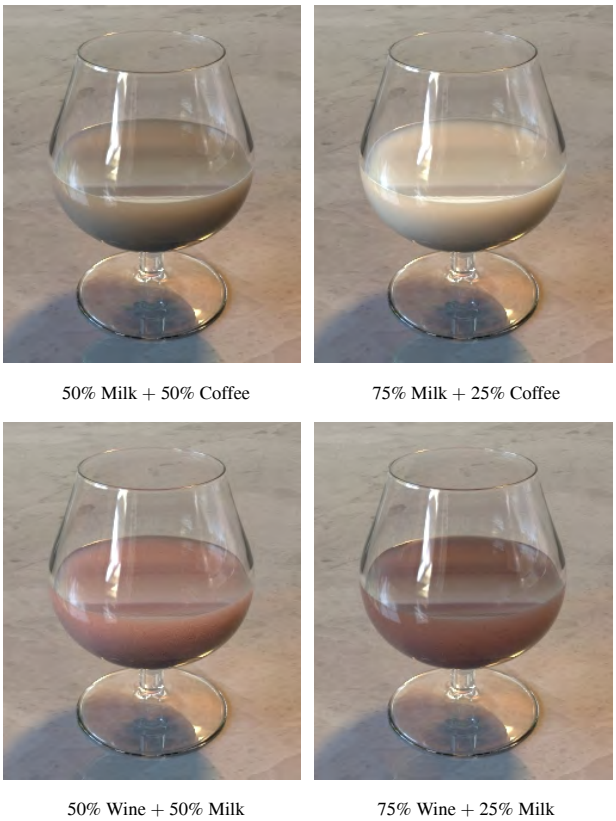

Figure 15: *Mixing two liquids - milk and coffee (top) and milk and wine (bottom), in different proportions. The wine-milk combination produces a soft pink appearance while the ESPRESSO-milk combination produces soft but brown appearance. (Minor noise due to Monte-Carlo under-sampling.)*

Acknowledgements: This work was supported by NSF Grants 0541307, 0305322, 0446916 and 0305399, and an ONR grant N00014-05-1-0188. Ramamoorthi, Jensen and Donner were supported also by Sloan Fellowships. The authors thank Terrence Boult for ocean water samples, Chao-Kuo Lin for help with experiments, and Simon Premoze for early discussions.

References

ANTYUFEEV, S. 2000. *Monte Carlo Method for Solving Inverse Problems of Radiative Transfer*. Inverse and Ill-Posed Problems Series, VSP Publishers.

BOSS, E., AND PEGAU, W. S. 2001. Relationship of light scattering at an angle in the backward direction to the backscattering coefficient. *Applied Optics 40 (30)*, 5503–5507.

CHANDRASEKHAR, S. 1960. *Radiative Transfer*. Oxford University Press.

DANA, K., NAYAR, S., VAN GINNEKEN, B., AND KOENDERINK, J. 1997. Reflectance and texture of real-world surfaces. In *Proc CVPR*, 151–157.

DEBEVEC, P. 1998. Rendering synthetic objects into real scenes: Bridging traditional and image-based graphics with global illumination and high dynamic range photography. *Proc. SIGGRAPH 98*, 189–198.

FINSY, E. G., AND JOOSTEN, J. 1991. Maximum entropy inversion of static light scattering data for the particle size distribution by number and volume. In *Advances in measurements and control of colloidal processes. Butterworth-Heineman, Ch. 30*.

FUCHS, E., AND JAFFE, J. S. 2002. Thin laser light sheet microscope for microbial oceanography. *OPTICS EXPRESS 10 (2)*, 145–154.

HAWKINS, T., EINARSSON, P., AND DEBEVEC, P. 2005. Acquisition of time-varying participating media. *ACM Trans. on Graphics (SIGGRAPH) 24*, 3, 812–815.

HENYEY, L., AND GREENSTEIN, J. 1941. Diffuse radiation in the galaxy. vol. 93, 70–83.

HULST, V. D. 1957. *Light Scattering by small Particles*. John Wiley and Sons.

ISHIMARU, A. 1978. *Wave Propagation and Scattering in Random Media. Volume 1: Single Scattering and Transport Theory*. Academic Press.

JAEGER, D., DEMEYERE, H., FINSY, R., SNEYERS, R., VANDERDEELEN, J., VAN-DER-MEEREN, P., AND VAN-LAETHEM, M. 1991. Particle sizing by photon correlation spectroscopy. part i: Monodisperse latices: influence of scattering angle and concentration of dispersed material. In *Part. Syst. Charact. 8, 179*.

JENSEN, H., MARSCHNER, S., LEVOY, M., AND HANRAHAN, P. 2001. A practical model for subsurface light transport. In *Proc. SIGGRAPH 01*, 511–518.

KEY, J. R. 2005. Streamer: User's guide. *Tech Report, NOAA/NESDIS, Madison, Wisconsin*.

MARSCHNER, S. 1998. Inverse rendering for computer graphics. *PhD Thesis, Cornell University*.

MATUSIK, W., PFISTER, H., BRAND, M., AND MCMILLAN, L. 2003. A data-driven reflectance model. *ACM Trans. on Graphics (SIGGRAPH) 22*, 3, 759–769.

MCCORMICK, N. J. 1981. A critique of inverse solutions to slab geometry transport problems. *Prog. Nucl. Energy 8*.

MCCORMICK, N. J. 1985. Sensitivity of multiple-scattering inverse transport methods to measurement errors. *JOSA A 2*.

MCCORMICK, N. J. 1996. Analytical transport theory applications in optical oceanography. *Annals of Nuclear Energy 23*, 381–395.

NARASIMHAN, S. G., AND NAYAR, S. K. 2003. Shedding light on the weather. In *CVPR 03*, 665–672.

OISHI, T. 1990. Significant relationship between the backward scattering coefficient of sea water and the scatterance at 120 degrees. *Applied Optics 29 (31)*, 4658–4665.

PRAHL, S. A. 1988. Light transport in tissue. *PhD Thesis, University of Texas at Austin*.

RAMAMOORTHI, R., AND HANRAHAN, P. 2001. A signal processing framework for inverse rendering. *Proc. SIGGRAPH 01*, 117–128.

SULLIVAN, S. A. 1963. Experimental study of the absorption in distilled water, artificial sea water, and heavy water in the visible region of the spectrum. *JOSA 53*.

SUN, B., RAMAMOORTHI, R., NARASIMHAN, S. G., AND NAYAR, S. K. 2005. A practical analytic single scattering model for real time rendering. *ACM Trans. on Graphics (SIGGRAPH) 24*, 3, 1040–1049.

WARD-LARSON, RUSHMEIER, H., AND PIATKO. 1997. A visibility matching tone reproduction operator for high dynamic range scenes. *IEEE Trans. on Visualization and Computer Graphics 3*, 4, 291–306.

Eurographics Symposium on Rendering (2005)
Kavita Bala, Philip Dutré (Editors)

Non-Linear Volume Photon Mapping

Diego Gutierrez†, Adolfo Munoz, Oscar Anson and Francisco J. Seron

GIGA, Universidad de Zaragoza, Spain

Abstract

This paper describes a novel extension of the photon mapping algorithm, capable of handling both volume multiple inelastic scattering and curved light paths simultaneously. The extension is based on the Full Radiative Transfer Equation (FRTE) and Fermat's law, and yields physically accurate, high-dynamic data than can be used for image generation or for other simulation purposes, such as driving simulators, underwater vision or lighting studies in architecture. Photons are traced into the participating medium with a varying index of refraction, and their curved trajectories followed (curved paths are the cause of certain atmospheric effects such as mirages or rippling desert images). Every time a photon is absorbed, a Russian roulette algorithm based on the quantum efficiency of the medium determines whether the inelastic scattering event takes place (causing volume fluorescence). The simulation of both underwater and atmospheric effects is shown, providing a global illumination solution without the restrictions of previous approaches.

Categories and Subject Descriptors (according to ACM CCS): I.3.7 [Computer Graphics]: Three-Dimensional Graphics and Realism

1. Introduction

Simulation of nature has always been one of the loftiest goals of computer graphics, providing a rich range of visual phenomena. Most of the times, the effect to be reproduced can be faked using a top-down approach, where the final desired result guides the implementation. This usually turns out relatively fast, ad-hoc methods that yield more than acceptable results. However, a physically correct simulation is necessary in certain fields where accuracy is a must. Underwater vision, driving simulators, the military, architectural lighting design etc. are fields where it is not enough to render an image which resembles reality. Predictive algorithms must be developed instead, where the image is the final visualization of the physically correct data generated. A bottom-up approach is then necessary: first, the basic laws of physics that govern the phenomenon need to be described and fed to the rendering system; the phenomenon itself will just be the logical, inevitable output. This approach sacrifices rendering speed in exchange for reliable, physically accurate numerical data that can be used for purposes beyond image generation.

Two of the greatest sources of visually appealing phenomena in nature are participating media and a varying index of refraction. Participating media are the cause of such well-known effects such as fog, clouds or blurry underwater vision, whereas a varying index of refraction yields mirages, rippling images, twinkling stars or some spectacular sunsets. Sources of inelastic scattering in ocean waters can greatly affect visibility and alter its color, whereas distortions caused by temperature differences can further alter the perception of things in such environment. Simulating underwater rescue missions, laying submarine data cables or even the correct interpretation of ancient World Heritage sites can benefit from an accurate description of light that includes an ampler range of phenomena.

We present in this paper a physically-based spectral simulation of light, solving the Full Radiative Transfer Equation (FRTE) and applying Fermat's law, which includes multiple inelastic scattering as well as an accurate description of the non-linear paths followed by the light rays in media with a varying index of refraction. It is based on an extension of the volume photon map algorithm presented by Wann Jensen and Christensen [JC98]. The main contributions are a full global illumination solution which supports non-linear light

† e-mail: diegog@unizar.es

paths and is free of the restrictions of previous works, and the physically-correct simulation of volume fluorescence in participating media, caused by inelastic scattering, including efficient computation of caustics. Atmospheric effects and underwater imagery are simulated as case studies to demonstrate the algorithm. To our knowledge, there is no previous research in computer graphics literature that models together physically-based inelastic scattering in participating, inhomogeneous media where the index of refraction varies continuously. Related previous works therefore span two different categories: inelastic scattering in participating media and non-linear light propagation.

Rendering participating media is not a new field in computer graphics, and an exhaustive review can be found in [PPS97]. There are two types of scattering events in a participating medium: *elastic* scattering, where no transfer of energy occurs between wavelengths, and *inelastic* scattering, where such energy transfers do occur, from shorter to longer wavelengths. Spectral global illumination algorithms that handle participating media only take into account elastic scattering, with the strategy consisting on decoupling the solutions for each sampled wavelength, then adding them to obtain the final image. No interaction between wavelengths is computed. To the authors' knowledge, the only previous work that simulates volume inelastic scattering in participating media is owed to Cerezo and Seron [CS03], using a discrete ordinate method. Unfortunately their method requires both rectangular meshing of the geometry, as well as an angular and spatial discretization which imposes high memory requirements, thus limiting the complexity of the scenes that can be reproduced (the problem is aggravated when simulating highly anisotropic scattering). They also cannot provide a full solution, failing to render caustics. Surface inelastic scattering works include [Gla95b] or [WTP01], but their methods are not extensible to participating media.

With respect to non-linear ray tracing, the first method to deal with non-straight light paths is owed to Berger et al. [BTL90], refracting the ray according to Snell's law in each of a series of flat homogeneous layers, thus achieving a piece-wise linear approximation of a curved path. This was challenged by Musgrave [Mus90], who develops a purely reflective model where rays follow a parabolic path, following the Kuhlar/Fabri physical model [FFLV82]. A more general approach to non-linear ray tracing is proposed by Gröller [Grö95], although the work does not study the influence of the index of refraction in the curvature of the rays, visualizing mathematical and physical systems instead. In the paper by Stam and Languenou [SL96], the authors use geometrical optics to describe how light bends if the index of refraction of the medium varies continuously. They nevertheless fail to provide a physically-based analytical expression for the index of refraction as a function of temperature and wavelength, and solve the equations only for two specific cases, thus losing generality. Seron et al. [SGGC05] implement a method of curved ray tracing capable of simulating the inferior mirage and some sunset effects, although they do not attempt to calculate any lighting, deforming pre-lit textures instead. In [HW01] gravitational light bending is visualized according to the theory of general relativity, whereas other relativity- and physics-related papers include the bending caused by neutron stars or black holes [Nem93], so they cannot (nor pretend to) simulate the phenomena described in this paper. Yngve et al. [YOH00] describe a simple method to simulate the bending of light by interpolating a density field, but they need to exaggerate the variation of the index of refraction tenfold for the effect to be visible.

The paper is organized as follows: section 2 provides the physically-based background, with an overview of inelastic scattering, the FRTE and the Fermat's law. In section 3 we describe our extension of the volume photon map algorithm to include inelastic scattering and curved light paths, with sections 4 and 5 providing case studies of underwater imagery and atmospheric effects respectively. The discussion of the results and some additional images are presented in section 6, to finish the paper in section 7 with the conclusions and future work.

2. Physically-based Framework

We now present the physical framework of our work, by first introducing what inelastic scattering is, then deriving the FRTE that needs to be solved to account for it. In order to be able to compute non-linear light paths, we will use Fermat's law to obtain the correct trajectories.

2.1. Inelastic scattering

Inelastic scattering implies an energy transfer from wavelength λ' to λ, with $\lambda' < \lambda$ within the visible spectrum, and gives rise to fluorescence and phosphorescence phenomena. Fluorescence occurs when a molecule absorbs a photon of wavelength λ' (called excitation wavelength), and re-emits it at a longer wavelength λ according to a *fluorescence efficiency function* $P_f(\lambda)$. The time lapse between the two events is 10^{-11} to 10^{-8} seconds, so for computer graphics it can be taken as an instantaneous process. For pure substances, re-emission is isotropic and the wavelength of the re-emitted photons is independent of the different excitation wavelengths, although the intensity of the re-emission does depend on them. Phosphorescence is a similar process, governed by the *phosphorescence efficiency function*, with the main difference being that the re-emitted energy declines with time according to a function $d(t)$.

2.2. Full Radiative Transfer Equation

Usually, participating media algorithms solve the integro-differential Radiative Transfer Equation (RTE), which takes into account emission, absorption and elastic scattering, but

does not yield a solution for inelastic scattering events. Following the notation in [JC98], and reformulating to include wavelength dependencies, the RTE can be written as:

$$\frac{\partial L_\lambda(x,\overrightarrow{w})}{\partial x} = \alpha_\lambda(x)L_{e,\lambda}(x,\overrightarrow{w}) + \sigma_\lambda(x)L_{i,\lambda}(x,\overrightarrow{w}) - \alpha_\lambda(x)L_\lambda(x,\overrightarrow{w}) - \sigma_\lambda(x)L_\lambda(x,\overrightarrow{w}) \quad (1)$$

where $\frac{\partial L(x,\overrightarrow{w})}{\partial_x}$ represents the variation of radiance L at a point x in the direction $\overrightarrow{w}$, α and σ are the absorption and scattering coefficients, L_e is the emitted radiance and L_i is the in-scattered radiance. Defining the extinction coefficient as $\kappa_\lambda(x) = \alpha_\lambda(x) + \sigma_\lambda(x)$ and integrating $L_{i,\lambda}$ over the sphere Ω we get:

$$\frac{\partial L_\lambda(x,\overrightarrow{w})}{\partial x} = \alpha_\lambda(x)L_{e,\lambda}(x,\overrightarrow{w}) + \sigma_\lambda(x)\int_\Omega p_\lambda(x,\overrightarrow{w}',\overrightarrow{w})L_\lambda(x,\overrightarrow{w}')d\overrightarrow{w}' - \kappa_\lambda(x)L_\lambda(x,\overrightarrow{w}) \quad (2)$$

which is the integro-differential, wavelength-dependent RTE governing the transport of light in participating media, with $p_\lambda(x,\overrightarrow{w}',\overrightarrow{w})$ being the phase function that defines the re-emission direction. However, this equation does not account for energy transfers between wavelengths, the phenomenon known as inelastic scattering. To be able to compute these inelastic scattering events, we need to develop the RTE equation further, by adding a term that accounts for such energy transfers. This term can be expressed as a double integral over the domains of the solid angle and wavelength:

$$\int_\Omega \int_\lambda \alpha_{\lambda_i}(x) f(x,\lambda_i \to \lambda) L_{\lambda_i}(x,\overrightarrow{w}') \frac{p_\lambda(x,\overrightarrow{w}'_i,w)}{4\pi} d\overrightarrow{w}_i d\lambda_i \quad (3)$$

where α_{λ_i} is the absorption coefficient for wavelength λ_i (remember there is no inelastic scattering without previous absorption), $f(x,\lambda_i \to \lambda)$ is the function that governs the efficiency of the energy transfer between wavelengths, defined as the probability of a photon of λ_i being re-emitted at λ. For fluorescence and phosphorescence, this phase function is isotropic [Mob94]. Adding this term to the RTE (equation 2) we obtain the FRTE:

$$\frac{\partial L_\lambda(x,\overrightarrow{w})}{\partial x} = \alpha_\lambda(x)L_{e,\lambda}(x,\overrightarrow{w}) + \sigma_\lambda(x)\int_\Omega p_\lambda(x,\overrightarrow{w}',\overrightarrow{w})L_\lambda(x,\overrightarrow{w}')d\overrightarrow{w}' - \kappa_\lambda(x)L_\lambda(x,\overrightarrow{w}) + \int_\Omega \int_\lambda \alpha_{\lambda_i}(x) f(x,\lambda_i \to \lambda) L_{\lambda_i}(x,\overrightarrow{w}') \frac{p_\lambda(x,\overrightarrow{w}'_i,w)}{4\pi} d\overrightarrow{w}_i d\lambda_i \quad (4)$$

which is the equation that must be solved to take into account multiple inelastic scattering in participating media, thus being able to render volume fluorescence effects.

2.3. Varying index of refraction in inhomogeneous media

A varying index of refraction n_λ defines an inhomogeneous medium where light travels in curved paths. These curved paths result in a distorted image, with the mirages being probably the best known manifestation of the effect. To be able to simulate this type of inhomogeneous medium, we therefore need to obtain the curved trajectory of light as it traverses it. The direction $\overrightarrow{w}$ in equation 4 therefore needs to be recomputed at each differential step, accounting for the changes in n_λ. We obtain this corrected direction at each step by solving Fermat's law, which defines how light traverses one given medium.

The following derivation of Fermat's law uses the work of Gutierrez et al. [GSMA04] and is not meant to be exhaustive. As stated in [Gla95a], *a ray of light, when travelling from one point to another, follows a path that corresponds to a stationary value of the optical path length* (OPL). The OPL is defined as the index of refraction times the travelled path (or the distance the light would have travelled in a vacuum during the flight time through the material), and in its differential form it can be formulated as $d(OPL) = ndl$, where l is the path travelled by the light ray. The equation shows how light gets bent towards the areas with a greater index of refraction, as Snell's law also predicts for the boundary of two homogeneous media. A stationary value corresponds to a maximum or a minimum in the function, thus the derivative equals zero. We can therefore write:

$$\delta(OPL) = \delta\int_A^B ndl = \int_A^B \delta ndl + \int_A^B n\delta(dl) = \int_A^B \frac{\delta n}{\delta x_i}\delta x_i dl + \int_A^B n\delta(dl) = 0 \quad (5)$$

where x_i are the vector components of l. Considering dx_i as variables and taking increments we get $\delta(dl) = \frac{dx_i}{dl}\delta(dx_i)$. Since light trajectories start and end at the stationary points A and B, we get $\delta x_i(A) = 0$ and $\delta x_i(B) = 0$. Equation 5 then results:

$$\delta L = \int_A^B \left[\frac{\partial n}{\partial x_i} - \frac{d}{dl}\left(n\frac{dx_i}{dl}\right)\right]\delta x_i dl = 0 \quad (6)$$

Since this equation must hold for any value of δx_i, the integrand must equal zero, so we finally come up with the equation that must be solved to obtain the path followed by light while traversing any medium, as a function of the index of refraction at each point:

$$\frac{d}{dl}\left(n\frac{d\overrightarrow{r}}{dl}\right) - \nabla n = 0 \Leftrightarrow \frac{d}{dl}\left(n\frac{dx_j}{dl}\right) - \frac{\partial n}{\partial x_j} = 0\,(j = 1,2,3) \quad (7)$$

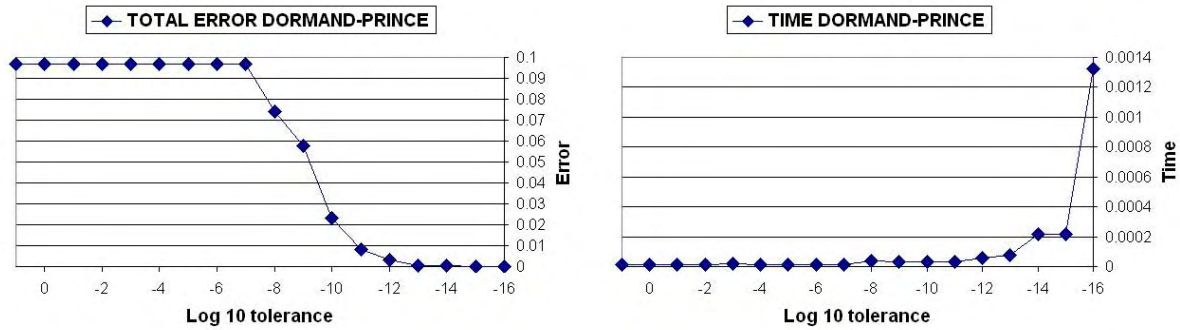

Figure 1: *Error and rendering time (secs.) as functions of the error tolerance in the Dormand-Prince RK5(4)7M method for a test scene.*

where $\vec{r} = x_j$ are the coordinates (x, y, z) of each point. This equation cannot be solved analytically, and thus we must apply a numerical method. We now need to rewrite equation 7 in order to solve it in a more efficient way than the Euler method presented in [GSMA04]:

$$\frac{d^2 x_j}{dl^2} = \frac{1}{n}\left(\frac{\partial n}{\partial x_j} - \frac{dn}{dl}\frac{dx_j}{dl}\right) \tag{8}$$

Doing the change of variable $y_j = \frac{dx_j}{dl}$ we obtain:

$$y_j' = \frac{1}{n}\left(\frac{\partial n}{\partial x_j} - \frac{dn}{dl} y_j\right) \tag{9}$$

where $\frac{dn}{dl} = \frac{dn}{dx_j}\frac{dx_j}{dl}$. The change of variable can also be written as:

$$x_j' = y_j \tag{10}$$

Equations 9 and 10 define a system where x_j represents the position and y_j the velocity at a given point in the trajectory, which can be written in matrix form as:

$$\begin{pmatrix} x_j \\ y_j \end{pmatrix}' = \begin{pmatrix} y_j \\ \frac{1}{n}\left(\frac{\partial n}{\partial x_j} - \frac{dn}{dl} y_j\right) \end{pmatrix} \tag{11}$$

This equation 11 has the form $Y' = f(l, Y)$, which defines an Initial Value Problem with $Y(0) = \alpha$. We solve this problem by applying the embedded Runge-Kutta method RK5(4)7M from the Dormand-Prince family. A detailed description of the method and the error tolerance can be found in [DP80].

We have tested the implementation in a simple scene where the index of refraction varies according to the equation $n = 1 + ky$, with y representing height, and k varying from -0.1 to 0.1. This distribution of n can be solved analytically, so we can measure the numerical error against the exact solution. Figure 1 shows the error of the Dormand-Prince RK5(4)7M method as the tolerance is reduced, along with the time it takes to reach the solution. As it can be seen, error tolerances in the range of 10^{-8} to 10^{-12} yield good results without much of a time penalty. Error tolerances beyond 10^{-14} start increasing rendering times considerably.

3. Extension of the Volume Photon Mapping Algorithm

Ray tracing techniques involve shooting rays into the scene from the camera and following them to detect hits with the geometry, then shooting shadow rays to the lights to find out direct illumination. With curved light paths this turns out to be highly impractical, though, since finding the ray with the physically-correct curvature which goes from the intersection point to the light is computationally very expensive (or the solution might not even exist). Groeller [Grö95] proposes three solutions: considering shadow rays to follow straight paths, retrieving all lighting information straight from the textures, and finally voxelizing the space and prestoring the approximated incident directions of light sources for each voxel, by launching rays from the light sources into the scene prior to the render pass. The first two are clearly not physically-based, while the third only approximates the solution with a preprocessing step.

In order to obtain a physically-based solution for multiple inelastic scattering in inhomogeneous media with a varying index of refraction n, we have extended the volume photon mapping algorithm [JC98] to account both for volume fluorescence and the distortions caused by the changing n.

For inelastic scattering, we need to model the possibility of an absorbed photon being re-emitted at a different wavelength. Equation 4 includes a term $f(x, \lambda_i \rightarrow \lambda)$ known as *wavelength redistribution function*, which represents the ef-

ficiency of the energy transfer between wavelengths. It is defined as the quotient between the energy of the emitted wavelength and the energy of the absorbed excitation wavelength, per wavelength unit. Reformulating in terms of photons instead of energy we have the *spectral quantum efficiency function* $\eta(x, \lambda_i \rightarrow \lambda)$, defined as the number of photons emitted at λ per wavelength unit, divided by the number of absorbed photons at λ_i. Both functions are dimensional (nm^{-1}), and are related as follows:

$$f(x, \lambda_i \rightarrow \lambda) = \eta(x, \lambda_i \rightarrow \lambda)\frac{\lambda_i}{\lambda} \tag{12}$$

A related dimensionless function that describes inelastic scattering is the *quantum efficiency* Γ, defined as the total number of photons emitted at all wavelengths divided by the number of photons absorbed at excitation wavelength λ_i. It is related to the spectral quantum efficiency function by the equation:

$$\Gamma(\lambda_i) = \int_{\lambda} \eta(x, \lambda_i \rightarrow \lambda) d\lambda \tag{13}$$

Our extension to the volume photon mapping algorithm includes a) solving Fermat's law to obtain the curved trajectory of each photon if the index of refraction varies (and also for the eye rays shot during the radiance estimate phase), thus being able to overcome the shadow ray problem presented above and to obtain a full solution including effects such as color bleeding and caustics; and b) the inclusion of the quantum efficiency Γ to govern the probability of an inelastic scattering event. As shown in figure 2, once the albedo-based Russian roulette determines that a certain photon has been absorbed by the medium, a second Russian roulette based on the quantum efficiency determines whether an inelastic scattering event takes place, and therefore the photon has to be re-emitted at a different wavelength. This is done by generating a random number $\xi_{in}[0,1]$ so that:

$$\xi_{in}[0,1] \rightarrow \begin{cases} \xi_{in} \leq \Gamma & \text{Photon is re-emitted} \\ \xi_{in} > \Gamma & \text{Photon remains absorbed} \end{cases} \tag{14}$$

If re-emitted, the new wavelength must be obtained, for which we must sample the spectral quantum efficiency function $\eta(x, \lambda_i \rightarrow \lambda)$ for the excitation wavelength λ_i. This can be simply done by rejection sampling the function, but to increase efficiency we perform importance sampling using the inverse of its cumulative distribution function (cdf). A random number $\psi[0,1]$ therefore yields the new wavelength for the re-emitted photon. Steeper areas of the cdf increase the probability of a photon being re-emitted at the corresponding wavelengths.

Figure 2 shows the basic scheme of the algorithm. The sequence of events in the original volume photon mapping by [JC98] is represented inside the grey area.

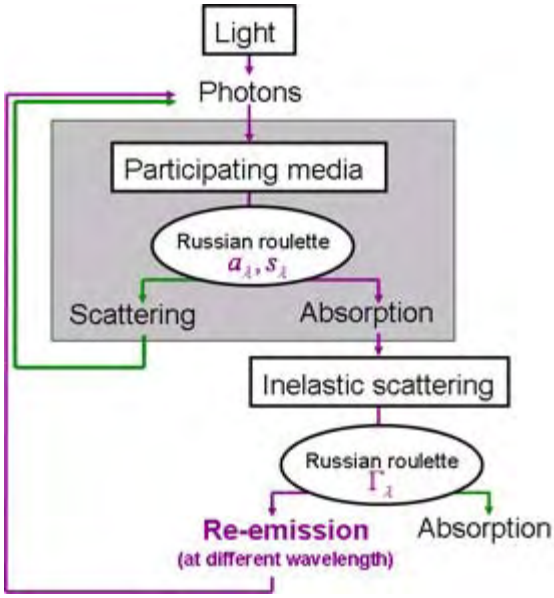

Figure 2: *Our extended volume photon mapping algorithm.*

4. Case Study: Underwater Imagery

We chose deep ocean waters as our first case study, given its rich range of elastic and inelastic scattering phenomena and the fact that it is a medium well studied by oceanographers. Pure seawater absorbs most wavelengths except for blue: the absorption coefficient peaks at 760 nanometers, and reaches a minimum at 430 nm. The phase function p is modelled as the phase function in pure sea water plus the phase function of the scattering by suspended particles, as proposed in [Mob94] ($p = p_w + p_p$). For pure water we use a phase function similar to Rayleigh's:

$$p_w(\theta) = 0.06225(1 + 0.835cos^2\theta) \tag{15}$$

while the scattering caused by particles is modelled using a Henyey-Greenstein phase function with $g = 0.924$:

$$p_p(\theta, g) = \frac{1 - g^2}{(1 + g^2 - 2gcos\theta)^{3/2}} \tag{16}$$

It is very common in ocean waters to see a color shift ranging from greenish to very bright green, or even yellowish. These hue shifts are due to the variation in the concentration and type of the suspended microorganisms, mainly phytoplankton, which presents a maximum absorption at 350 nm. rapidly decreasing to almost zero beyond 500 nm. The

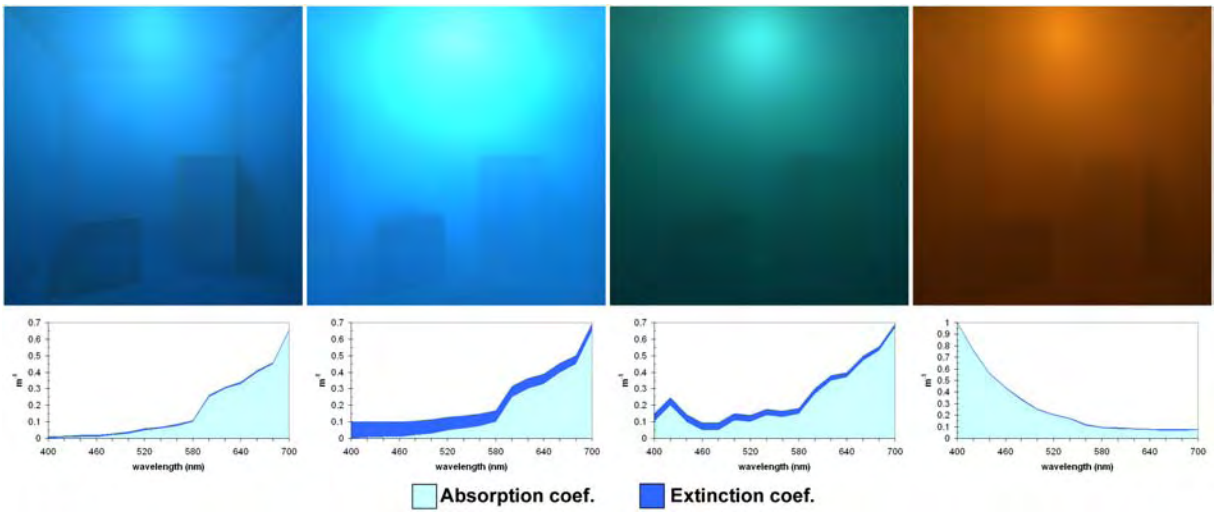

Figure 3: *Fluorescent ocean water in Cornell rooms. (a), (b) and (c) show varying concentrations of chlorophyll* ($0.05mg/m^3$, $0.1mg/m^3$ *and* $5mg/m^3$ *respectively). (d) High concentration of yellow matter* ($5mg/m^3$).

most important element in the phytoplankton is chlorophyll, which presents spectral absorption peaks in the blue and red ends of the spectrum and is the most important source of volume fluorescence in the waters. For chlorophyll, $\Gamma^c(\lambda_i)$ is wavelength-independent, with values ranging from 0.01 to 0.1 (we use the superscript c for chlorophyll). As with most inelastic scattering event, the re-emission phase function is isotropic.

Another important source of fluorescence is the Color Dissolved Organic Matter (CDOM), also called yellow matter, present in shallow ocean waters and harbors. $\Gamma^y(\lambda_i)$ is also wavelength-independent, with values between 0.005 and 0.025, and re-emission is also isotropic [Haw92].

All the images in the paper have been rendered on a Beowulf system composed of six nodes, each one being a Pentium 4 @ 2.8 GHz. with 1 Gb. of RAM. Figure 3 shows different colorations of ocean water, according to varying chlorophyll and yellow matter concentrations which trigger inelastic scattering events with different probabilities. The images were rendered with 250,000 photons stored in the volume photon map and 200 photons used for the radiance estimate. This high numbers are needed to obtain accurate results, since we use the volume photon map to compute both direct and indirect illumination. Direct illumination in participating media with a varying index of refraction cannot be efficiently computed using ray tracing techniques, as explained at the beginning of section 3. The spectrum was sampled at nine intervals. Below each picture, the resulting absorption and extinction curves (functions of the different concentrations of chlorophyll in the modelled waters) are shown for each case. Image (a) shows little fluorescence (low chlorophyll concentration of $0.05mg/m^3$), and the waters are relatively clear. When chlorophyll concentration increases, fluorescence events become more prominent and the image first gets a milky aspect (b), losing visibility and reaching a characteristic green hue when chlorophyll reaches $5mg/m^3$. Image (d) shows fluorescence owed to yellow matter. The absorption function in this case has been modelled after [Mob94]: $a_y(\lambda) = a_y(440)^{-0.014(\lambda-440)}$ where $a_y(440)$ is the empirical absorption at 440 nm. Rendering times for the images were six minutes.

5. Case Study: Atmospheric Phenomena

The images in this section illustrate some of the most relevant effects in nature owed to curved light paths. To achieve physically correct results we have modelled the Earth as a sphere with a radius of 6371 units (one unit equals one kilometer); the atmosphere is another concentric sphere with a thickness of 40 kilometers. Taking the 1976 *USA Standard Atmosphere* (USA76) [USG76], we first obtain a standard temperature and pressure profile of the whole 40 kilometers, with temperature decreasing at an approximate rate of 0.6°C per 100 meters. In order to curve light correctly according to Fermat's law, we need to obtain the wavelength-dependent index of refraction as a function of both the temperature and pressure given by the USA76. To do so, we follow the method described in [GSMA04], by first obtaining density as a function of temperature $T(h)$ and pressure $P(h)$ using the Perfect Gas law $\rho(h) = \frac{P(h)M}{RT(h)}$, where M and R are constants of values $28.93 \cdot 10^{-3}\, kg/mol$ and $8.3145\, J/mol \cdot K$ respectively. The Gladstone-Dale law [GD58] relates $n(\lambda, h)$ as a function of both $\rho(h)$ and $n(\lambda)$, given by the expression:

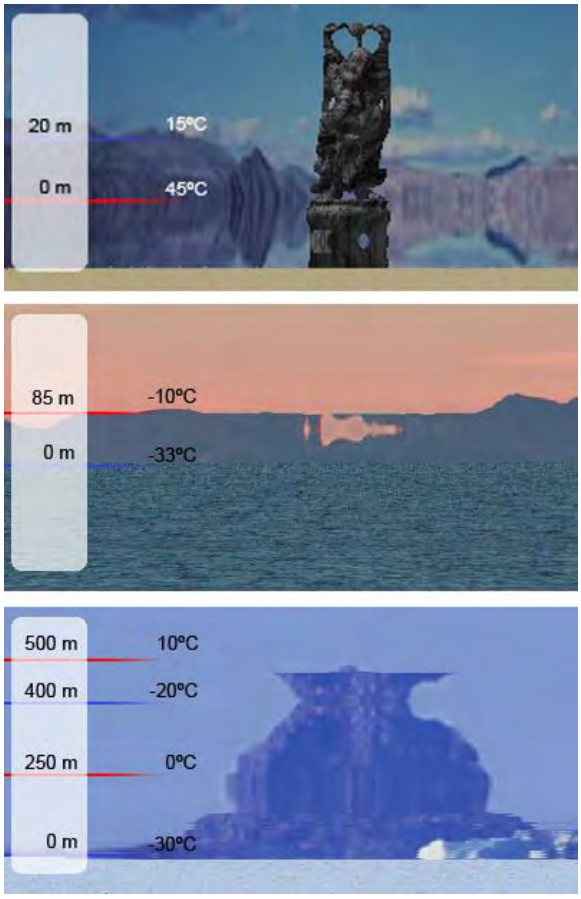

Figure 4: *Simulation of several atmospheric phenomena. Top: inferior mirage. Middle: superior mirage. Bottom: Fata Morgana.*

$$n(h,\lambda) = \rho(h) \cdot (n(\lambda) - 1) + 1 \tag{17}$$

The only missing function is now $n(\lambda)$, which we obtain from Cauchy's analytical formula [BW02]:

$$n(\lambda) = a \cdot \left(1 + \frac{b}{\lambda^2}\right) + 1 \tag{18}$$

where a and b depend on the medium considered (for air, their values are $a = 29.79 \cdot 10^{-5}$ and $b = 5.67 \cdot 10^{-5}$). Sellmeier [BW02] provides a slightly more elaborated formula, but we have chosen Cauchy's for efficiency reasons.

Combining equations 17 and 18 we finally obtain our profile for $n(\lambda, h)$, which we can alter at will to obtain the desired effects. To interpolate the complete, altered profiles for the whole 40 km. we use Fermi's distribution, as proposed in [VDWGL00].

The camera in the scenes is placed far from the mirages at a specific height for each effect to be seen (they can only appear if the observer's line of vision forms an angle less than one degree with the horizon). The error tolerance in the Dormand-Prince RK5(4)7M method has been set to 10^{-9}, and the spectrum has been sampled in three wavelengths. Figure 4 (top) shows our simulation of an inferior mirage, which occurs when the ground is very hot and heats up the air layers right above it, thus creating a steep temperature gradient (30°C in 20 meters). As a consequence, light rays get bent upwards, and an inverted image of the Happy Buddha and the background appears on the ground. The camera is placed 10 meters above the ground. The image took 14 minutes to render.

Inversion layers are caused by an increase of air temperature with height, reversing the standard behavior where temperature decreases as a function of height. This happens most commonly above cold sea waters, and the light rays get bent downward, giving rise to the superior mirage. Figure 4 (middle) shows our simulation, modelling an inversion layer with a temperature gradient of 23°C. The apparent hole in the mountains is actually formed by the superior inverted image of the real mountains. The camera is placed also 10 meters above the ground, and the image took four minutes and 32 seconds to render. The great decrease in rendering time compared to the inferior mirage is owed to the simpler geometry of the scene, since the far away mountains are textured low-resolution objects.

Maybe less known than the two previous examples, the Fata Morgana occurs as a concatenation of both superior and inferior mirages, and is a much rarer phenomenon. Figure 4 (bottom) shows our simulation with two inversion layers with steep temperature gradients. There is an inferior mirage image across the middle of the mountain plus a superior mirage with the inverted image on top. The shape of the mountain gets greatly distorted; the Fata Morgana has historically tricked arctic expeditions, making them believe they were seeing huge mountains that were just a complicated pattern of upright and inverted images of the real, much lower hill (*Fata Morgana* is in fact the name of a fairly enchantress skilled in the art of changing shape, which she learnt from Merlin the Magician). The camera is placed at 300 meters (for the Fata to be visible it needs to be between the inversion layers), and the rendering time was five minutes.

6. Discussion

The method described has been implemented in Lucifer, our in-house global illumination renderer. It can handle multiple inelastic scattering in inhomogeneous participating media with a varying index of refraction, thus rendering effects such as mirages or fluorescence in ocean waters with full lighting computation. It deals well with strong anisotropy in the phase functions and the effects of backscattering, since no discretizations of the scene must be performed,

and thus the shortcoming of the only previous work on volume fluorescence [CS03] is overcome. It also supports real light sources, with photometric data input specified in the standard CIBSE TM14 format [CIB88]. This is a must for predictive rendering and for generating physically accurate data. The real light sources are sampled so that photons are emitted proportionally to the distribution of the light, given by its photometry.

Spectral images are calculated in high dynamic range, in order to obtain accurate data from the simulations. For tone reproduction purposes we map luminances to the display based on the work by Ward et al. [LRP97] and Pattanaik et al. [PTYG00]. To increase realism during the visualization of the images, an additional operator has been added which simulates the effects of chromatic adaptation in the human eye. This operator is specially important in the realistic depiction of underwater imagery, where the cones in the human eye might undergo a loss of spectral sensitivity after having been exposed to the same wavelength for a long period of time (underwater imagery being usually blue or green mostly). The complete description of such operator can be found in [GSMA04].

As stated in the introduction, the algorithm implemented is general and physically-based. This allows us to use the radiometric and photometric data obtained from the simulations for any purpose other than rendering, such as professional architectural lighting or accurate simulations of deep underwater vision, given the exact description of the luminaire to be used and the water conditions. This accuracy obviously increases rendering times compared to faked, ad-hoc solutions. To improve efficiency, we impose an early light path termination and an adaptive integration step while solving Fermat's law. Choosing the Dormand-Prince RK5(4)7M numerical method over the more standard Euler method has produced speedups of up to 106.4. We have also used a parallel implementation on a six-PC Beowulf system of our non-linear photon mapping algorithm, achieving additional speedups between 4.2 and 4.8.

The non-linear photon mapping implementation allows us to extend several sunset effects similar to the ones simulated in [GSMA04], by including a thin layer of fog between the observer and the sun. The solar disk gets distorted into different shapes, while light is scattered through the layer of fog, thus achieving a "winter sunset" look (figure 5, left and middle). Figure 5 right shows volume caustics generated by a crystal sphere in a fluorescent medium.

Figure 6 shows several renders obtained with Lucifer. All of them are lit by a Philips SW-type© luminaire, specified according to the CIBSE TM14 format. The only light source is immersed in the medium, so no caustics from the interaction of sunlight with the surface appear. The medium modelled does not emit light, although adding that to the model is straightforward and would allow us to simulate effects such as bioluminiscence in the water. Fluorescence

Figure 5: *Sunset effects through a layer of fog. Left: flattened sun. Middle: split sun. Right: Volume caustics in a fluorescent medium.*

owed to inelastic scattering is computed according to the varying concentrations of chlorophyll in each image (between 0.01 and $0.1 mg/m^3$). The volume photon map in all the images contains 500.000 photons, and the radiance estimate used 250. Again, these high numbers are needed since we compute direct lighting with the photon map. The top two images represent a sunken boat along a Happy Buddha in clear, shallow waters (left) or deep underwater with a chlorophyll concentration of $0.05 mg/m^3$(right). For the bottom-left image, we have added a volume temperature field that simulates a heat source outside the image as explained in [SGGC05], deriving the index of refraction using the formula $n = 1 + \frac{T_o}{T}(n_o - 1)$ as proposed by Stam and Languenou [SL96]. The distortions caused by the varying index of refraction are visible, similar to the characteristic rippling in a real desert scene. The bottom-middle image uses a smoke-like medium, modelled as a 3D turbulence function, whereas the last to the right shows the effects of a highly anisotropic medium. The images are 400 pixels wide and took between 30 and 40 minutes to render, without any penalty imposed by the anisotropy in the last image.

7. Conclusion and Future Work

We proposed a novel extension of the widely used photon mapping technique, which accounts for multiple inelastic scattering and can provide a full global illumination solution in inhomogeneous media with a varying index of refraction, where light paths are bent. No pre-lit textures are needed in this case, since both direct and indirect lighting is calculated from the photon map. The method is physically-based and yields accurate high-dynamic results that can either be output as an image to a display device (via tone mapping), or used in other fields as raw data. Inelastic scattering is calculated during the photon tracing stage, so the extra cost required is just a second Russian roulette per absorption. The accompanying video shows the feasibility of the approach for animations.

Practically all inelastic scattering effects in the visible range of the spectrum mean a transfer of energy from shorter to longer wavelengths. Nevertheless, the algorithm presented in this work can handle rarer inelastic scattering events where energy gets transferred from longer to shorter wave-

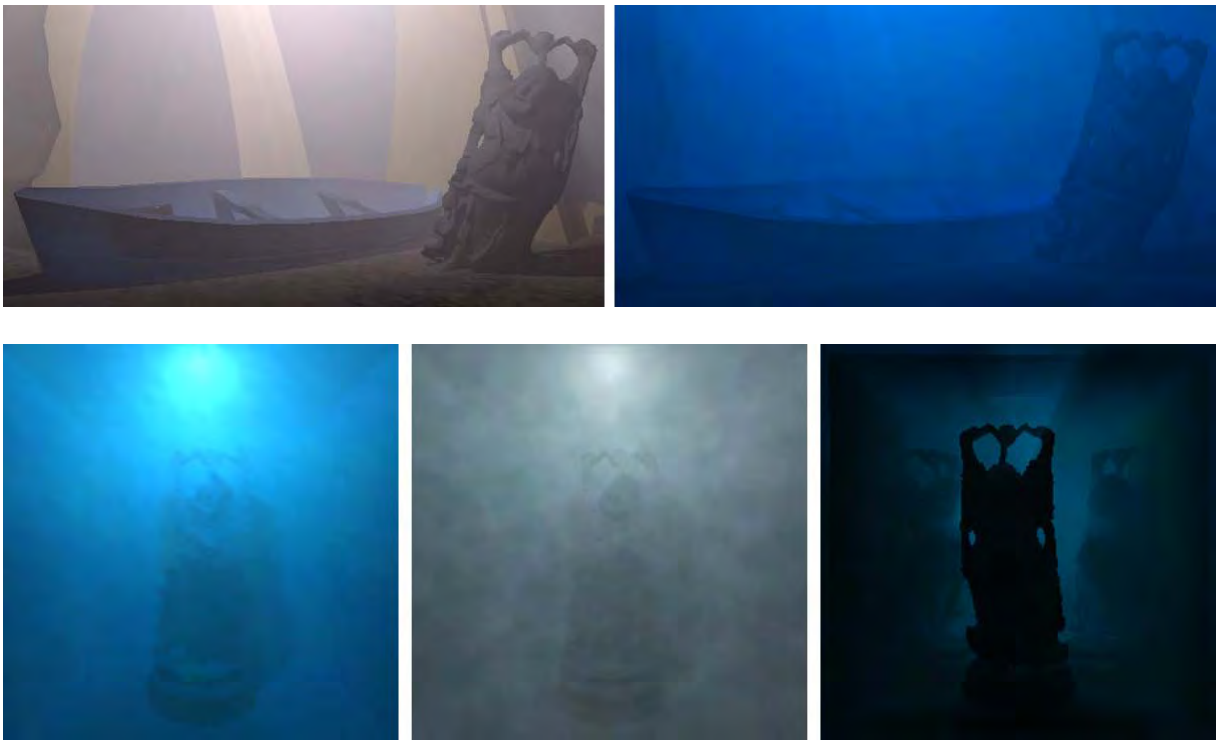

Figure 6: *Different images with inelastic scattering in participating media. Top left: very low chlorophyll concentration. Top right: higher concentration yields more inelastic scattering events. Bottom left: distortions caused by a 3D temperature field. Bottom middle: 3D turbulence field simulating smoke. Bottom right: highly anisotropic medium.*

lengths (such as a fraction of the Raman scattering that occurs naturally in several solids, liquids and gases [Mob94]), since it does not follow a cascade, one-way scheme from the blue end to the red end of the spectrum. The application of these type of inelastic scattering to computer graphics is probably just marginal, but the data generated can be very useful to physicists or oceanographers. Adding phosphorescence effects could make use of the work by Cammarano and Wann Jensen [CJ02], although a more straightforward approach would be to use the decay function $d(t)$ in each frame. Any number of light sources can be used in the scene, even with different photometric descriptions.

The bottleneck of the algorithm is solving the paths for each photon and eye-ray using Fermat's law. Although the use of a Dormand-Prince method has drastically reduced rendering times by two orders of magnitude, additional work needs to be done to achieve near real-time frame rates. Importance maps could be used for this purpose, although two other promising fields of research lay ahead: the first one is the implementation of the algorithm on GPUs, as proposed by Purcell et al. [PDC*03]. The second would try to take advantage of temporal coherence of light distribution, as presented by Myszkowski et al. [MTAS01].

8. Acknowledgements

This research was partly done under the sponsorship of the Spanish Ministry of Education and Research through the project TIN2004-07672-C03-03. The authors would also like to thank Eduardo Jiménez for his initial contribution to this work.

References

[BTL90] BERGER M., TROUT T., LEVIT N.: Ray tracing mirages. *IEEE Computer Graphics and Applications 10*, 3 (May 1990), 36–41.

[BW02] BORN M., WOLF E.: *Principles of Optics: Electromagnetic Theory of Propagation, Interference and Diffraction of Light*. Cambridge University Press, 2002.

[CIB88] CIBSE: *Standard File Format for Transfer of Luminaire Photometric Data*. The Chartered Institution of Building Services Engineers, 1988.

[CJ02] CAMMARANO M., JENSEN H. W.: Time dependent photon mapping. In *Proceedings of the 13th Eurographics workshop on Rendering* (2002), Eurographics Association, pp. 135–144.

[CS03] CEREZO E., SERON F.: Inelastic scattering in participating media. application to the ocean. In *Proceedings of the Annual Conference of the European Association for Computer Graphics, Eurographics 2003* (2003), pp. CD–ROM.

[DP80] DORMAND J., PRINCE P.: A family of embeded runge-kutta formulae. *Journal of Computational and Applied Mathematics 6(1)* (1980), 19–26.

[FFLV82] FABRI E., FIORZO G., LAZZERI F., VIOLINO P.: Mirage in the laboratory. *Am. J. Physics 50(6)* (1982), 517–521.

[GD58] GLADSTONE J. H., DALE J.: On the influence of temperature on the refraction of light. *Phil. Trans. 148* (1858), 887.

[Gla95a] GLASSNER A.: *Principles of Digital Image Synthesis*. Morgan Kaufmann, San Francisco, California, 1995.

[Gla95b] GLASSNER A. S.: A model for fluorescence and phosphorescence. In *Photorealistic Rendering Techniques* (1995), Sakas P. S. G., Müller S., (Eds.), Eurographics, Springer-Verlag Berlin Heidelberg New York, pp. 60–70.

[Grö95] GRÖLLER E.: Nonlinear ray tracing: visualizing strange worlds. *The Visual Computer 11*, 5 (1995), 263–276.

[GSMA04] GUTIERREZ D., SERON F., MUNOZ A., ANSON O.: Chasing the green flash: a global illumination solution for inhomogeneous media. In *Spring Conference on Computer Graphics* (2004), (in cooperation with ACM SIGGRAPH A. P., Eurographics), (Eds.), pp. 95–103.

[Haw92] HAWES S.: *Quantum Fluorescence Efficiencies of Marine Fulvic and Humid Acids*. PhD thesis, Dept. of Marince Science, Univ. of South Florida, 1992.

[HW01] HANSON A. J., WEISKOPF D.: Visualizing relativity. siggraph 2001 course 15, 2001.

[JC98] JENSEN H. W., CHRISTENSEN P. H.: Efficient simulation of light transport in scenes with participating media using photon maps. In *SIGGRAPH 98 Conference Proceedings* (jul 1998), Cohen M., (Ed.), Annual Conference Series, ACM SIGGRAPH, Addison Wesley, pp. 311–320. ISBN 0-89791-999-8.

[LRP97] LARSON G. W., RUSHMEIER H., PIATKO C.: A visibility matching tone reproduction operator for high dynamic range scenes. *IEEE Transactions on Visualization and Computer Graphics 3*, 4 (Oct. 1997), 291–306.

[Mob94] MOBLEY C.: *Light and Water. Radiative Transfer in Natural Waters*. Academic Press, Inc., 1994.

[MTAS01] MYSZKOWKSI K., TAWARA T., AKAMINE A., SEIDEL H. P.: Perception-guided global illumination solution for animation. In *Computer Graphics Proceedings, Annual Conference Series, 2001 (ACM SIGGRAPH 2001 Proceedings)* (Aug. 2001), pp. 221–230.

[Mus90] MUSGRAVE F. K.: A note on ray tracing mirages. *IEEE Computer Graphics and Applications 10*, 6 (Nov. 1990), 10–12.

[Nem93] NEMIROFF R. J.: Visual distortions near a neutron star and black hole. *American Journal of Physics 61(7)* (1993), 619–632.

[PDC*03] PURCELL T. J., DONNER C., CAMMARANO M., JENSEN J., HANRAHAN P.: Photon mapping on programmable graphics hardware. In *SIGGRAPH/Eurographics Workshop on Graphics Hardware* (2003), Eurographics Association, pp. 041–050.

[PPS97] PEREZ F., PUEYO X., SILLION F.: Global illumination techniques for the simulation of participating media. In *Proc. of the Eigth Eurographics Workshop on Rendering* (1997), pp. 16–18.

[PTYG00] PATTANAIK S., TUMBLIN J. E., YEE H., GREENBERG. D. P.: Time-dependent visual adaptation for realistic image display. In *SIGGRAPH 2000, Computer Graphics Proceedings* (2000), Akeley K., (Ed.), Annual Conference Series, ACM Press / ACM SIGGRAPH / Addison Wesley Longman, pp. 47–54.

[SGGC05] SERON F., GUTIERREZ D., GUTIERREZ G., CEREZO E.: Implementation of a method of curved ray tracing for inhomogeneous atmospheres. *Computers and Graphics 29(1)* (2005).

[SL96] STAM J., LANGUÉNOU E.: Ray tracing in non-constant media. In *Eurographics Rendering Workshop 1996* (New York City, NY, June 1996), Pueyo X., Schröder P., (Eds.), Eurographics, Springer Wien, pp. 225–234. ISBN 3-211-82883-4.

[USG76] USGPC: *U.S. Standard Atmosphere*. United State Government Printing Office, Washington, D.C., 1976.

[VDWGL00] VAN DER WERF S., GUNTHER G., LEHN W.: Novaya zemlya effects and sunsets. *Applied Optics 42*, 3 (2000).

[WTP01] WILKIE A., TOBLER R., PURGATHOFER W.: Combined rendering of polarization and fluorescence effects. In *Rendering Techniques '01 (Proc. Eurographics Workshop on Rendering 2001)* (2001), Gortler S.J. M. K. e., (Ed.), Eurographics, Springer-Verlag, pp. 197–204.

[YOH00] YNGVE G. D., O'BRIEN J. F., HODGINS H.: Animating explosions. In *Proceedings of the Computer Graphics Conference 2000 (SIGGRAPH-00)* (New York, July 23–28 2000), Hoffmeyer S., (Ed.), ACMPress, pp. 29–36.

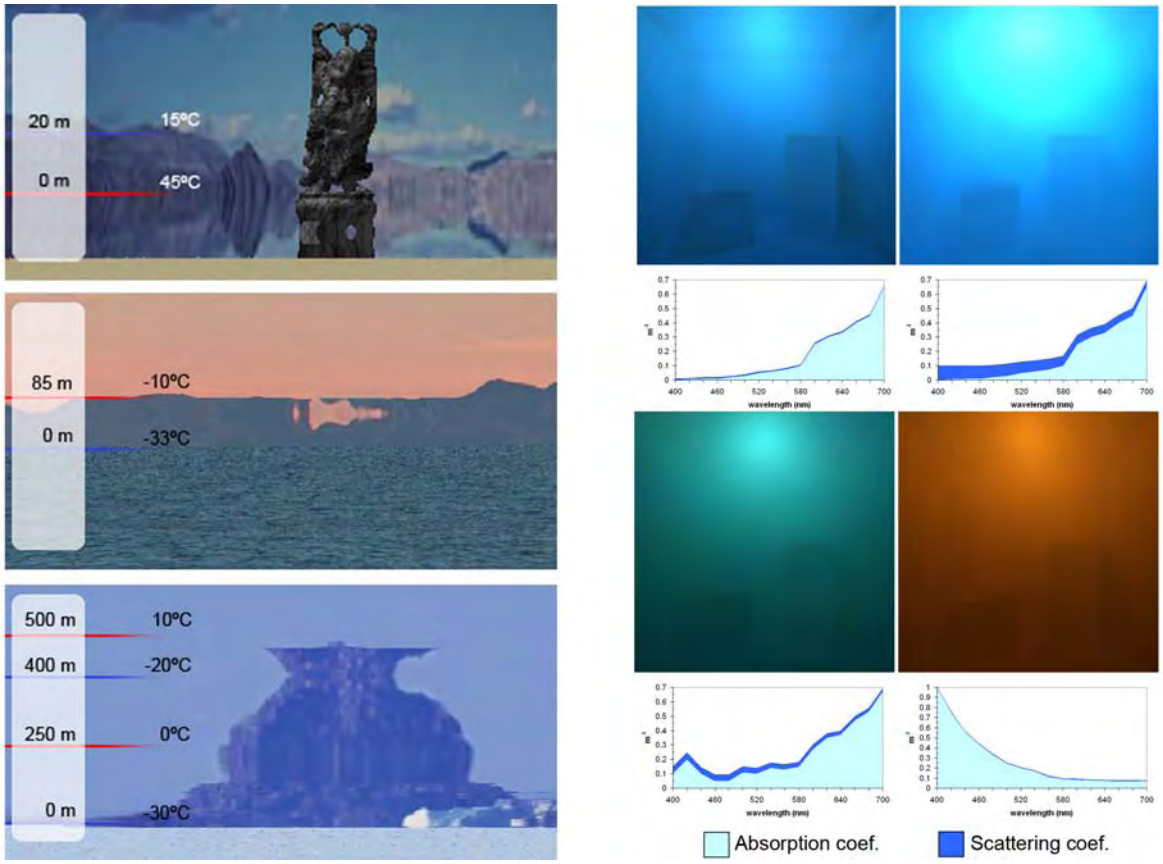

EUROGRAPHICS 2008 / G. Drettakis and R. Scopigno
(Guest Editors)

Volume 27 (2008), Number 2

Visualizing Underwater Ocean Optics

Diego Gutierrez, Francisco J. Seron, Adolfo Munoz and Oscar Anson

University of Zaragoza, Spain

Abstract

Simulating the in-water ocean light field is a daunting task. Ocean waters are one of the richest participating media, where light interacts not only with water molecules, but with suspended particles and organic matter as well. The concentration of each constituent greatly affects these interactions, resulting in very different hues. Inelastic scattering events such as fluorescence or Raman scattering imply energy transfers that are usually neglected in the simulations. Our contributions in this paper are a bio-optical model of ocean waters suitable for computer graphics simulations, along with an improved method to obtain an accurate solution of the in-water light field based on radiative transfer theory. The method provides a link between the inherent optical properties *that define the medium and its* apparent optical properties*, which describe how it looks. The bio-optical model of the ocean uses published data from oceanography studies. For inelastic scattering we compute all frequency changes at higher and lower energy values, based on the spectral quantum efficiency function of the medium. The results shown prove the usability of the system as a predictive rendering algorithm. Areas of application for this research span from underwater imagery to remote sensing; the resolution method is general enough to be usable in any type of participating medium simulation.*

Categories and Subject Descriptors (according to ACM CCS): I.3.7 [Computer Graphics]: Three-Dimensional Graphics and Realism

1. Introduction

Ocean water is arguably the richest participating medium in terms of optical thickness and the number and type of interactions that occur in it. This paper deals with the physically-based rendering of underwater scenes by simulating the in-water light field, based on a compact bio-optical model that takes into account the *dissolved* and *particulate* matter, optically influential constituents of the water. To ensure accuracy, we use published data obtained from a wide range of literature in the field of oceanography. Our model is not restricted to just the visible spectrum and can be adapted to any type of known ocean water in particular, or to any kind of participating medium in general.

Scattering in water is caused by interactions of light at molecular level and with particles [Mob94]. It can be classified in two broad categories: *elastic* or *inelastic* scattering, depending on whether the scattered photon maintains or changes its energy in the process. The inelastic scattering events can be further subclassified according to the nature of the energy transfer: *Stokes* scattering, when a molecule of the medium absorbs the photon and re-emits it with a lower energy, and *anti-Stokes* scattering, when the re-emitted photon has a higher energy. Both cases are covered by our model. The process implies an energy transfer from wavelength λ' to λ, with λ' being the excitation wavelength and λ the re-emitted wavelength. The former case implies a shift towards longer wavelengths, whereas in the latter the scattered photon has a shorter wavelength. Major forms of elastic events in water include Einstein-Smoluchowski scattering (see Section 3.2), whereas for inelastic events, *Raman* scattering and *fluorescence* are the two most prominent (see Section 3.3).

The presence and concentrations of the constituents in the water determine its optical properties. These optical properties are divided in two classes: *inherent* and *apparent*. The *inherent optical properties* (IOP) only depend on the constituents of the water, whereas the *apparent optical properties* (AOP) are not properties of the aquatic medium itself, although they do depend on its characteristics. Typical IOP are the absorption coefficient, the scattering coefficient or the scattering phase function. Some of the AOP include irradiance reflectance, attenuation coefficients or the average cosines [Pre76]. To obtain the in-water light field,

we rely on the physically based theory of *radiative transfer* [Cha60], which relates the IOP and AOP. More precisely, the link is provided through the Radiative Transfer Equation (RTE) [SCP94], which takes into account emission, absorption and elastic scattering. Unfortunately this equation can not account for the phenomenon known as *inelastic scattering* described previously, which is of significant importance in ocean waters. We consequently expand the RTE by adding an extra term, thus obtaining the Full Radiative Transfer Equation (FRTE) [Gla95] and solving it by using an extended version of the method presented by Gutierrez et al. [GMAS05]:

$$\begin{aligned}\frac{\partial L(\lambda,\vec{\omega}_o)}{\partial x} &= \alpha(\lambda)\,L_e(\lambda,\vec{\omega}_o) - \kappa(\lambda)\,L(\lambda,\vec{\omega}_o)\\ &\quad + \sigma(\lambda)\int_{\Omega} p(\lambda,\vec{\omega}_i,\vec{\omega}_o)\,L(\lambda,\vec{\omega}_i)\,d\vec{\omega}_i\\ &+ \int_{\Omega}\int_{W}\left\{\sigma(\lambda',\lambda)\,p(\lambda',\lambda,\vec{\omega}_i,\vec{\omega}_o)\,L(\lambda',\vec{\omega}_i)\right\}d\lambda'\,d\vec{\omega}_i \qquad (1)\end{aligned}$$

where L is the radiance and $\vec{\omega}_i$ and $\vec{\omega}_o$ are, respectively, the incoming and outgoing directions of that radiance. α, σ and κ are the absorption, scattering and extinction coefficients respectively. We assume $L_e(\lambda,\vec{\omega}_o)$ to be zero, thus making the medium non-emissive. Note that the last term models the inelastic scattering events and is expressed as a double integral over the domains of the solid angle Ω and wavelength W. Here $p(\lambda',\lambda,\vec{\omega}_i,\vec{\omega}_o)$ is the phase function for inelastic events and $\sigma(\lambda',\lambda)$ is the inelastic scattering function for the energy exchange between λ' and λ. For simplicity, when considering elastic interactions ($\lambda = \lambda'$) parameters λ,λ' are simplified to a single parameter λ. For processes such as fluorescence, where the photons are inelastic scattered to longer wavelengths, the function $\sigma(\lambda',\lambda)$ is usually expressed as:

$$\sigma(\lambda',\lambda) = \alpha(\lambda')\,f(\lambda',\lambda) \qquad (2)$$

where $\alpha(\lambda')$ is the inelastic absorption coefficient and $f(\lambda',\lambda)$ is the *wavelength redistribution function*, which governs the efficiency of the energy transfer between wavelengths. It is defined as the probability of a photon of λ' that inelastically scatters being re-emitted at λ. Therefore, (2) expresses the inelastic scattering as a percentage of the inelastic absorption coefficient. Section 3.3 gives more details on how to model this redistribution function $f(\lambda',\lambda)$.

Our research on water simulation encompasses the fields of both computer graphics and oceanography, and it is free from the restrictions of previous works. The main contributions of this paper are:

- A compact, parameterized bio-optical model of ocean waters which can be used in computer graphics applications.
- A resolution method based on the theory of radiative transfer, which solves the FRTE by handling *all* kinds of inelastic scattering events and modeling both absorption and elastic scattering accurately. This method is based on photon mapping [Jen01].
- A link between the IOP of water and the resulting light field, which in turn defines its AOP, based on radiative transfer theory.

The remainder of this paper is organized as follows: Section 2 presents previous work on the simulation of light transport in water bodies. In Section 3 a comprehensive bio-optical model is developed, whilst section 4 presents our simulation method. The paper ends with the results and conclusions.

2. Related work

The simulation of light transport in participating media usually either relies on Monte-Carlo techniques for ray tracing (Rushmeier and Torrance [RT87]; Nakamae et al. [NKON90]; Tadamura and Nakamae [TN95]) or attempts to solve the RTE, such as the method proposed by Kaneda et al. [KYNN91]. Nishita et al. [NSTN93] display water from outer space modifying this method, but both works only take into account single scattering. In the work of Premoze and Ashikhmin [PA01], no radiance due to scattering is calculated at all, using empirical equations based on experimental data instead. Mobley [Mob94] developed a method to solve the RTE analytically, but it cannot be extended to take into account inelastic scattering. Recently, the Lorenz-Mie theory has been generalized and applied to rendering natural waters by Frisvad, Christensen and Jensen [FCJ07], also neglecting the effects of inelastic scattering. Cerezo and Seron [CS04] also develop a bio-optical model. Whilst the goal of their work is closely related to ours, we overcome here significant shortcomings:

- They use a discrete ordinate method, which requires an angular and spatial discretization of the volume to be rendered. This imposes high memory requirements which seriously limit the complexity of the scenes that can be reproduced.
- In their work, inelastic scattering simulations are limited to fixed re-emissions in the 680 *nm*. wavelength..
- They cannot provide a full solution to the light transport problem.

Gutierrez et al. [GMAS05] present a method that deals with participating media in which the index of refraction is not homogeneous, while also taking into account the simulation of some inelastic scattering events. They apply their method to the simulation of underwater imagery using a simplified, four-parameter model of ocean waters. In this regard, our paper offers improvement in the following ways:

- Our bio-optical model of ocean waters is more complete, thus making the simulations more accurate.
- They also fail to develop a complete description for the complex inelastic scattering events that occur underwater, and the method is limited to re-emissions at lower energy levels and at fixed wavelengths. In this paper *all* inelastic scattering events can be modeled, including *Anti Stokes* scattering events like *Raman scattering* (see Section 3.3).

- We additionally offer simulations using real data from different seas as a means of visual validation.

3. The Bio-Optical Model

The various constituents of ocean water have a great influence in its optical properties. In order to solve the forward problem in ocean optics, the IOP have to be modeled and used in the FRTE. The values of these IOP can be obtained as the sum of the contributions of pure water and the dissolved particles and particulate matter present in the water, as proposed in [Mob94]. Optically pure water is devoid of any dissolved or suspended matter, and thus there is no scattering or absorption owed to particles or organic material [Mor74]. For *saline* pure water the salt concentration (35 to 39 parts per thousand) does influence the scattering and absorption functions. In particular it absorbs most wavelengths except for blue, with the absorption coefficient peaking at 760 *nm*, and reaching a minimum at 430 *nm*.

We develop our bio-optical model from three main IOP, with others like the extinction coefficient or the albedo derived from those three. These IOP are the absorption coefficient (3), the scattering coefficient (4) and the phase function (5), which for the elastic case can be written as (see Table 4 for a more detailed description of the functions used, including both the elastic and inelastic cases):

$$\alpha(\lambda) = \alpha_w(\lambda) + \sum_i \alpha_i(\lambda) \tag{3}$$

$$\sigma(\lambda) = \sigma_w(\lambda) + \sum_i \sigma_i(\lambda) \tag{4}$$

$$p(\lambda,\theta) = \frac{\sigma_w(\lambda)}{\sigma(\lambda)} p_w(\lambda,\theta) + \sum_i \frac{\sigma_i(\lambda)}{\sigma(\lambda)} p_i(\lambda,\theta) \tag{5}$$

where θ is the angle between the incoming $\vec{\omega}_i$ and outgoing $\vec{\omega}_o$ directions, the subscript w stands for the contribution of the pure water (fresh or salty) and the subscript i stands for the constituents in the water body such as biological particles or dissolved substances. We include three types of such constituents in our model, namely CDOM (Colored Dissolved Organic Matter, also know as yellow matter, present mainly in shallow ocean waters and harbors), phytoplankton (microscopic plants rich in chlorophyll) and minerals and organic detritus. The rest of this section will characterize the three main IOP (with elastic and inelastic scattering treated separately) for pure water and the three constituents. The next section will show how radiative transfer theory is applied to simulate the light field (which define the AOP) and render the final images.

3.1. Modeling Absorption

For the spectral absorption function of pure water $\alpha_w(\lambda)$ we rely on the work of Smith and Baker [SB81], whose tabulated values are well known in oceanography studies (shown in Table 1). Following further studies by Pope and Fry [PF97], we use those values as an upper bound, to account for the fact that the true absorption can be, in fact, lower. The function shows that absorption is more prominent both in the UV and red ends of the spectrum. [PF97] also shows that absorption by salt in oceanic water is negligible. Based on the data by Bricaud, Morel and Prieur [BMP81], we model absorption by CDOM by fitting an exponential curve of the form:

$$\alpha_y(\lambda) = \alpha_y(\lambda_0)\, e^{-S_y(\lambda-\lambda_0)} \tag{6}$$

where the subscript y denotes the constituent CDOM. λ_0 is a reference wavelength, often chosen to be 440 *nm* for yellow matter, and S_y is the slope of the semilogarithmic absorption curve [Kir94]. S_y is usually taken to be constant, with a value of 0.014 nm^{-1}, but has been found to vary both geographically and temporally, and is also dependent on the wavelength range over which it is calculated [BMP81]. The values of absorption $\alpha_y(\lambda_0)$ at reference wavelengths also vary in a range between 0.01 m^{-1} to 20 m^{-1}, as a function of turbidity [Kir94].

Phytoplankton absorbs a great amount of visible light, due to its chlorophyll pigment. The absorption function for chlorophyll peaks strongly at 430 *nm* and 670 *nm*, being very weak in the mid range of the visible spectrum (thus the more phytoplankton the greener the hue of the water). The concentration of the chlorophyll in the water usually ranges from 0.01 mg/m^3 for open waters to 100 mg/m^3. The spectral absorption coefficient of the phytoplankton is usually expressed as a function of this concentration C as:

$$\alpha_p(\lambda) = C\,\alpha_p^*(\lambda) \tag{7}$$

where C can be defined as the concentration of the main pigment chlorophyll-a (Chl_a) or as the sum of the concentrations of Chl_a and its degradation products, the pheopigments. α_p^* is the *specific spectral absorption coefficient* (the absorption per unit of concentration) for a particular species of phytoplankton, given in m^2/mg. Typical values for specific absorptions of different species of phytoplankton can be found in the work of Sathyendranath, Lazzara and Prieur [SLP87] (see Table 1). A rough correspondence between chlorophyll concentrations and several oceanic water types is given by Morel [Mor88]. The absorption owed to organic detritus and minerals can be approximated by an exponential function, according to Roesler, Perry and Carder [RPC89]:

$$\alpha_d(\lambda) = \alpha_d(\lambda_0)\, e^{-S_d(\lambda-\lambda_0)} \tag{8}$$

Here the reference wavelength 400 *nm* is selected for λ_0 and typical values for the exponent coefficient S_d will be in the range between 0.006 nm^{-1} to 0.014 nm^{-1}, although 0.011 nm^{-1} is the most common value [RPC89]. Further studies confirm that the absorption spectra of minerals and detritus is well described by an exponential function with an average slope S_d of 0.0123 nm^{-1}, with slightly lower values than predicted at wavelengths below 440 *nm* [BSF*03].

Table 1: *Absorption coefficient for a clear water body α_w (after Smith and Baker [SB81]) and specific absorption coefficient for phytoplankton α_p^* (after Sathyendranath, Lazzara and Prieur [SLP87]).*

λ	$[nm]$	380	440	500	550	610	670	720	780
α_w	$[cm^{-1}]$	0.00022	0.000145	0.000257	0.000638	0.00289	0.0043	0.01169	0.0236
α_p^*	$[m^2 \cdot mg^{-1}]$	0.025	0.035	0.02	0.01	0.007	0.015	0.001	0.0001

3.2. Modeling Elastic Scattering

For the pure water term we use the volume scattering function defined by the Einstein-Smoluchowski theory [Maz02], which models scattering at molecular level as small-scale fluctuations. Whilst usually Rayleigh's scattering is used instead, Einstein-Smoluchowski provides more accurate results, is well defined and imposes no overheads in the simulations. Its scattering coefficient and phase function are given by:

$$\sigma_w(\lambda) = 16.06\,\beta_w(\lambda_0, 90^\circ)\left(\frac{\lambda_0}{\lambda}\right)^{4.32} \tag{9}$$

$$p_w(\theta) = 0.06225\left(1 + 0.835\cos^2\theta\right) \tag{10}$$

Typical values for $\beta_w(\lambda_0, 90^\circ)$ for both fresh and saline pure water are given in [Mor74]. These values range from $14.1 \cdot 10^{-4}\ m^{-1}$ to $134.5 \cdot 10^{-4}\ m^{-1}$. All the scattering produced by CDOM has inelastic nature and thus will be described in next section.

Gordon and Morel [GM83] found that phytoplankton, even in small concentrations, also contribute to the total elastic scattering in the water. Its contribution is given by:

$$\sigma_p(\lambda) = \left(\frac{550}{\lambda}\right) 0.30\,C^{0.62} \tag{11}$$

where the constant 0.30 is selected to fit the data collected from many types of waters. The actual upper bound for this constant has a value of 0.45 [GM83]. The phase function due to phytoplankton is given by an isotropic function ($p_p = 1/\pi$).

The elastic scattering caused by organic detritus and minerals can be modeled based on Mie theory [GSO03]. The Henyey-Greenstein phase function models forward scattering fairly well but fails to reproduce backscattering with the same precision. We found that we can achieve a better fit by using a Two-Terms Henyey-Greenstein phase function (TTHG) [HG41]:

$$p_d(\theta, \zeta, g_f, g_b) = \zeta\, p_{HG}(\theta, g_f) + (1-\zeta)\, p_{HG}(\theta, g_b) \tag{12}$$

where ζ is a weighting function between zero and one. This common way of utilizing this combination defines a forward scattering lobe (first term), plus a backscattering lobe (second term), with $g_f \in [0..1]$ and $g_b \in [-1..0]$. p_{HG} represents a simple Henyey-Greenstein phase function (HG):

$$p_{HG}(\theta, g) = \frac{1-g^2}{(1+g^2-2g\cos\theta)^{3/2}} \tag{13}$$

The TTHG function not only models backscattering more precisely, but it can describe more complex particle scattering models, improving the fit at large and small angles as well. The shape of each of the two HG functions can be approximated by an ellipsoid, avoiding the relatively expensive exponent in its evaluation. The observation was first introduced by Schlick [BLSS93]. Due to the great variety of particulate matter, the scattering coefficient σ_d can adopt a wide range of values. Table 2 shows typical values of this function (data after Stramski et al. [SBM01]).

3.3. Modeling Inelastic Scattering

For inelastic scattering, we need to model the possibility of an absorbed photon being re-emitted at a different wavelength. (2) includes a term $f(\lambda', \lambda)$ known as *wavelength redistribution function*, which represents the efficiency of the energy transfer between wavelengths. It is defined as the quotient between the energy of the emitted wavelength and the energy of the absorbed excitation wavelength, per wavelength unit. Reformulating in terms of photons instead of energy we have the *spectral quantum efficiency function* $\eta(\lambda', \lambda)$, defined as the ratio between the number of photons emitted at λ per wavelength unit, and the number of absorbed photons at λ'. Both functions are dimensional (nm^{-1}), and are related as follows:

$$f(\lambda', \lambda) = \eta(\lambda', \lambda)\,\frac{\lambda'}{\lambda} \tag{14}$$

The wavelength redistribution function f, and therefore its associated spectral quantum efficiency function η, can be seen as a re-radiation matrix. A related dimensionless function that describes inelastic scattering is the *quantum yield* $\Gamma(\lambda')$, defined as the total number of photons emitted at all wavelengths divided by the number of photons absorbed at excitation wavelength λ'. It is related to the spectral quantum efficiency function by:

$$\Gamma(\lambda') = \int_W \eta(\lambda', \lambda)\, d\lambda \tag{15}$$

The three functions $\Gamma(\lambda')$, $f(\lambda', \lambda)$ and $\eta(\lambda', \lambda)$, depend on both the medium and the type of inelastic event. The two inelastic events with more influence in the in-water light field are fluorescence and Raman scattering. Phytoplankton and CDOM are important fluorescence sources, whilst Raman scattering is produced by pure water; minerals and detritus, on the other hand, do not produce any inelastic event.

Table 2: *Scattering coefficient for detritus σ_{dt} and minerals σ_m (After Stramski et al. [SBM01]).*

	λ	$[nm]$	380	440	500	550	610	670	720	780
detritus	σ_{dt}	$[m^{-1}]$	0.045	0.0375	0.0325	0.03	0.0285	0.0275	0.027	0.027
minerals	σ_m	$[m^{-1}]$	0.0675	0.0525	0.05	0.045	0.04	0.036	0.034	0.032
total	σ_d	$[m^{-1}]$	0.1125	0.09	0.0825	0.075	0.0685	0.0635	0.061	0.059

3.3.1. Fluorescence

Fluorescence occurs when a molecule absorbs a photon of wavelength λ', and re-emits it at a longer wavelength λ according to the *fluorescence efficiency function* $\eta_F(\lambda',\lambda)$. For the two main sources of fluorescence (phytoplankton and CDOM), re-emission follows an isotropic phase function. For phytoplankton, the wavelength of the re-emitted photons is independent of the excitation wavelength, although the intensity does show wavelength dependency [Mob94].

It is very common in ocean waters to see a color shift ranging from greenish to very bright green, or even yellowish. These hue shifts are mainly due to the variation in the concentration and type of the suspended microorganisms, specially phytoplankton and its related chlorophyll concentration, which presents an absorption function peaking at 350 *nm* and rapidly decaying to almost zero beyond 500 *nm*. Only wavelengths between 370 and 690 *nm* can trigger fluorescence due to phytoplankton. This can be modeled as a dimensionless function $g_p(\lambda')$ so that:

$$g_p(\lambda') \equiv \begin{cases} 1 & \text{if } 370 \leq \lambda' \leq 690 \text{ nm} \\ 0 & \text{otherwise} \end{cases} \tag{16}$$

The wavelength-independent quantum yield for phytoplankton $\Gamma_p(\lambda')$ ranges from 0.01 to 0.1. Using (14) and (16), the relationship between the wavelength redistribution function $f_p(\lambda',\lambda)$ and the spectral quantum efficiency function $\eta_p(\lambda',\lambda)$ is:

$$f_p(\lambda',\lambda) = \eta_p(\lambda',\lambda)\frac{\lambda'}{\lambda} \equiv \Gamma_p\, g_p(\lambda')\, h_p(\lambda)\, \frac{\lambda'}{\lambda} \tag{17}$$

where $h_p(\lambda)$ is the *fluorescence emission function* per unit wavelength, and can be approximated by a gaussian [Mob94]:

$$h_p(\lambda) = \frac{1}{\sqrt{2\pi}\lambda_\sigma} \exp\left\{-\frac{(\lambda-\lambda_0)^2}{2(\lambda_\sigma)^2}\right\} \tag{18}$$

$\lambda_0 = 685\,nm$ is the wavelength of maximum emission and $\lambda_\sigma = 10.6\,nm$ represents the standard deviation. Using (7) and (17) we can now compute the inelastic scattering coefficient owed to phytoplankton $\sigma_p(\lambda',\lambda)$ following (2).

The other important source of fluorescence in water is CDOM. For relatively high concentrations of CDOM, its quantum yield $\Gamma_y(\lambda')$ varies between 0.005 and 0.025. Following the work of Hawes [Haw92] we use the following formula to describe its spectral fluorescence quantum efficiency function:

Table 3: *Water constituents and interactions*

Constituent	Absorption	Elastic Scat.	Inelastic Scat.
Pure water (w)	Yes	Yes	Raman Scattering
Minerals, detritus (d)	Yes	Yes	No
Phytoplankton (p)	Yes	Yes	Fluorescence
CDOM (y)	Yes	No	Fluorescence

$$f_y(\lambda',\lambda) = A_0(\lambda')\exp\left\{-\left(\frac{\frac{1}{\lambda}-\frac{A_1}{\lambda'}-B_1}{0.6\left(\frac{A_2}{\lambda'}+B_2\right)}\right)^2\right\}\frac{\lambda'}{\lambda} \tag{19}$$

where A_0, A_1, A_2, B_1 and B_2 are empirical parameters whose values depend on the specific composition of the CDOM and can be found in [Mob94] (see Table 5). A_1 and A_2 are dimensionless, whereas the rest are given in nm^{-1}. Like fluorescence due to phytoplankton, we can use (6) and (19) to compute the inelastic scattering coefficient $\sigma_y(\lambda',\lambda)$ following (2).

Our model can be easily extended to account for phosphorescence phenomena, which are intrinsically similar to fluorescence and are governed by the *phosphorescence efficiency function*. The only difference is that the re-emitted energy declines with time according to a function $d(t)$.

3.3.2. Raman scattering

Raman scattering influences the in-water light field, specially at great depths where sun irradiance becomes zero and only Raman radiance remains. It occurs when vibration and rotation in water molecules exchange energy with incoming photons, re-emitting them with approximately the same wavelength, but allowing for small shifts towards longer or shorter wavelengths. It can also be considered a spontaneous process. To isolate Raman inelastic events from fluorescence and other scattering events, it is usually studied in pure water, filtered several times, so that the second term in (4) becomes zero.

The Raman wavelength redistribution function $f_w(\lambda',\lambda)$ is usually described in terms of a sum of four Gaussian functions [Mob94]:

$$f_w(\lambda',\lambda) = \frac{10^7}{\lambda'^2}\frac{\sum_{j=1}^{4} A_i \frac{1}{\Delta\tilde{\nu}_i}\exp\left\{-\frac{\left[10^7\left(\frac{1}{\lambda'}-\frac{1}{\lambda}\right)-\tilde{\nu}_i\right]^2}{\Delta\tilde{\nu}_i{}^2}\right\}}{\sqrt{\frac{\pi}{4\ln 2}}\sum_{j=1}^{4} A_j} \tag{20}$$

where $\tilde{\nu}$ is the wavenumber ($\tilde{\nu} = 10^7/\lambda$) given in cm^{-1}. Typical parameter values A_i, $\tilde{\nu}_i$ and $\Delta\tilde{\nu}_i$ for the Raman redistribution function are given by Walrafen [Wal69] and are

shown in Table 5. The inelastic scattering coefficient can now be obtained using α_w and f_w in (2).

4. The simulation method

Having so far developed our bio-optical model, we can now formalize it into a set of parameters and equations to fully simulate the in-water light field. To summarize, the four constituents of the model and their interactions with light are given in Table 3. Table 4 shows how the main functions that define the model are derived from IOP and related functions at constituent level.

Table 4: *The main functions of the model*

Equations	
$\alpha(\lambda)$	$= \alpha_d(\lambda)+\alpha_p(\lambda)+\alpha_w(\lambda)+\alpha_y(\lambda)$
$\sigma(\lambda)$	$= \sigma_w(\lambda)+\sigma_d(\lambda)+\sigma_p(\lambda)$
$p(\lambda,\theta)$	$= \frac{\sigma_w(\lambda)p_w(\lambda,\theta)+\sigma_d(\lambda)p_d(\lambda,\theta)+\sigma_p(\lambda)p_p(\lambda,\theta)}{\sigma(\lambda)}$
$\kappa(\lambda)$	$= \alpha(\lambda)+\sigma(\lambda)$
$\alpha_I(\lambda')$	$= \alpha_p(\lambda')+\alpha_w(\lambda')+\alpha_y(\lambda')$
$p_I(\lambda',\lambda,\theta)$	$= \frac{\alpha_p(\lambda')p_p(\lambda',\lambda,\theta)+\alpha_w(\lambda')p_w(\lambda',\lambda,\theta)+\alpha_y(\lambda')p_y(\lambda',\lambda,\theta)}{\alpha_I(\lambda')}$
$f_I(\lambda',\lambda)$	$= \frac{\alpha_p(\lambda')f_p(\lambda',\lambda)+\alpha_w(\lambda')f_w(\lambda',\lambda)+\alpha_y(\lambda')f_y(\lambda',\lambda)}{\alpha_I(\lambda')}$

Table 5: *Parameters of the model*

Parameter	Equations	Simulated values	Units
C	(7) (11)	$[0..1.0]$	$\frac{mg}{m^3}$
$\alpha_d(400)$	(8)	$[0..0.1]$	m^{-1}
$\alpha_y(440)$	(6)	$[0..0.1]$	m^{-1}
S_y	(6)	0.014	nm^{-1}
S_d	(8)	0.011	nm^{-1}
A_0	(19)	$\frac{150}{700}$	nm^{-1}
A_1	(19)	4	-
A_2	(19)	4	-
B_0	(19)	$\frac{1}{450\cdot 10^{-7}}$	nm^{-1}
B_1	(19)	$\frac{1}{650\cdot 10^{-7}}$	nm^{-1}
Γ_p	(17)	0.1	-
Γ_y	(19)	0.025	-
A_i, $i = 1..4$	(20)	$0.41, 0.39, 0.10, 0.10$	-
$\widetilde{\nu}_i$, $i = 1..4$	(20)	$3250, 3425, 3530, 3625$	-
$\Delta\widetilde{\nu}_i$, $i = 1..4$	(20)	$210, 175, 140, 140$	-

The model allows for easy adjusting of its parameters to simulate different types of water and thus obtain different in-water light fields. As well as minerals and detritus, other particulate components of water can be added from oceanographic studies (although minerals and detritus have the greatest influence in the final appearance of water). Mie theory can again be used to model the scattering by these new particles, and the phase function can be approximated by using a Two Terms Henyey-Greenstein phase function (12). An overview of the most significant parameters of the model, the equations in which they can be found and the corresponding values used for the simulations in this paper can be found in Table 5. Note that for simplicity we have not included the values that are already specified throughout the text during the explanation of the bio-optical model (more specifically, those included in tables 1 and 2). The first three correspond to the parameters analyzed in Figure 2.

Once we have formalized the model into a set of equations, we rely on radiative transfer theory to obtain a solution for the in-water light field. We solve the Full Radiative Transfer Equation (1) by extending the traditional photon mapping algorithm [Jen01] by taking into account all ten different events specified in Table 3, while allowing for both Stokes or anti-Stokes inelastic scattering. This enhancement is done in both stages: photon tracing and radiance estimation.

During the photon tracing stage in the original photon mapping method [Jen01], a Russian roulette algorithm is triggered at each interaction with the medium, deciding whether the photon is scattered or absorbed. In [GMAS05] the authors add a second Russian roulette which separates absorption from inelastic scattering; in the latter case, a new photon is generated at a different wavelength, but the algorithm considers just a single type of inelastic event with Stokes behavior. No anti-Stokes events are simulated. In contrast, our method uses just a single Russian roulette to choose between ten different kinds of interactions (including three types of inelastic events where the photons may gain or lose energy), and can be easily extended to handle an arbitrary number of different interactions. Finally, we improve the radiance estimation stage over previous methods by adding a term to take into account the contributions from the inelastic scattering events. The next subsections present the algorithm in more detail.

4.1. Stage 1: Photon tracing

We shoot photons from the light sources and let them interact with the geometry and the medium according to its optical distance, which is a function of the extinction coefficient (as in the original photon mapping method). We statistically decide at each interaction which type of event occurs (refer to Table 3) with just a single Russian roulette. At the interactions, photons are stored in a kd-tree as in traditional photon mapping.

The wavelength spectrum is box sampled into N_λ samples, so absorption ($\alpha(\lambda)$) and scattering coefficients ($\sigma(\lambda)$) are implemented as N_λ-dimensional arrays while wavelength redistribution functions ($f(\lambda',\lambda)$) are implemented as $N_\lambda \times N_\lambda$ square matrices. Each of the photons carries information about a portion of flux ($\Delta\Phi$) at a certain sampled wavelength (λ'). Importance sampling is used for computing the optical distance, so $\Delta\Phi$ does not change along the photon tracing stage, while λ' changes for inelastic scattering events.

In order to apply the Russian roulette algorithm, we will define an albedo $\Lambda_j(\lambda)$ for each interaction j as follows:

- If interaction j represents an elastic scattering event, then $\Lambda_j(\lambda) = \frac{\sigma_j(\lambda)}{\kappa(\lambda)}$
- If j represents an absorption interaction that does not

show inelastic scattering (detritus and minerals, basically), then $\Lambda_j(\lambda) = \frac{\alpha_j(\lambda)}{\kappa(\lambda)}$

- For each absorption interaction that could generate inelastic scattering (pure water, phytoplankton and CDOM) we define its *inelastic probability* (χ_j), the probability that an absorption event generates an inelastic scattering event:

$$\chi_j(\lambda') = \int_{\lambda_a}^{\lambda_b} f_I(\lambda',\lambda)d\lambda \approx \sum_{i=1}^{N_\lambda} f_I(\lambda',\lambda_i) \qquad (21)$$

where λ_a and λ_b are the lower and upper limits of the simulated wavelengths, and $i \in [1..N_\lambda]$ refer to samples in wavelength domain:

  - If interaction j represents the effective inelastic scattering event within the absorption interaction: $\Lambda_j(\lambda) = \frac{\alpha_j(\lambda)}{\kappa(\lambda)}\chi_j(\lambda)$
  - If interaction j represents the pure absorption event (no inelastic scattering happening at all): $\Lambda_j(\lambda) = \frac{\alpha_j(\lambda)}{\kappa(\lambda)}(1-\chi_j(\lambda))$

Thus, at each interaction a random number ξ between 0 and 1 is generated resulting in (between parenthesis, example values of Λ_j at $\lambda = 500nm$ that determine the size of the corresponding interval are included):

- $\xi\varepsilon[0,\xi_1) \rightarrow$ absorption by pure water ($2.51 \cdot 10^{-1}$).
- $\xi\varepsilon[\xi_1,\xi_2) \rightarrow$ Raman scattering, inelastic scattering by pure water ($1.21 \cdot 10^{-9}$).
- $\xi\varepsilon[\xi_2,\xi_3) \rightarrow$ absorption by minerals and detritus ($7.12 \cdot 10^{-2}$).
- $\xi\varepsilon[\xi_3,\xi_4) \rightarrow$ absorption by phytoplankton ($4.90 \cdot 10^{-3}$).
- $\xi\varepsilon[\xi_4,\xi_5) \rightarrow$ inelastic scattering by phytoplankton ($2.18 \cdot 10^{-3}$).
- $\xi\varepsilon[\xi_5,\xi_6) \rightarrow$ absorption by CDOM ($7.83 \cdot 10^{-2}$).
- $\xi\varepsilon[\xi_6,\xi_7) \rightarrow$ inelastic scattering by CDOM ($1.21 \cdot 10^{-2}$).
- $\xi\varepsilon[\xi_7,\xi_8) \rightarrow$ elastic scattering by pure water ($7.44 \cdot 10^{-3}$)
- $\xi\varepsilon[\xi_8,\xi_9) \rightarrow$ elastic scattering by minerals and detritus ($2.94 \cdot 10^{-1}$).
- $\xi\varepsilon[\xi_9,1] \rightarrow$ elastic scattering by phytoplankton ($2.79 \cdot 10^{-1}$).

where $\xi_i(\lambda)$ is given by $\xi_i(\lambda) = \sum_{j=1}^{i}\Lambda_j(\lambda)$

To compute the new re-emitted wavelength after a inelastic scattering event i, the normalized wavelength redistribution function $\frac{f_i(\lambda',\lambda)}{\chi_i(\lambda')}$ is treated as a probability distribution function (PDF) given the excitation wavelength λ'. To sample it efficiently we first build its normalized cumulative distribution function (CDF) and then inverse importance sample this CDF. Greater values of the PDF for a given wavelength will translate to steeper areas of the CDF, thus increasing the probability of a re-emission at such wavelength. Note that the definition of $f_i(\lambda',\lambda)$ is not limited to the visible spectrum, which might result in re-emissions happening at wavelengths beyond the visible spectrum. However, as $\chi_i(\lambda')$ is limited to the simulated (visible) spectrum, only inelastic interactions within this spectrum are considered. It could happen that a photon inelastically scattered at such wavelengths suffers a second inelastic scattering event that brings it back to the visible light range. Given the low probability of this chain of events and our computer graphics approach, we assume that a photon beyond the visible spectrum is definitely absorbed. Figure 1 shows a global overview of the algorithm during the photon tracing stage.

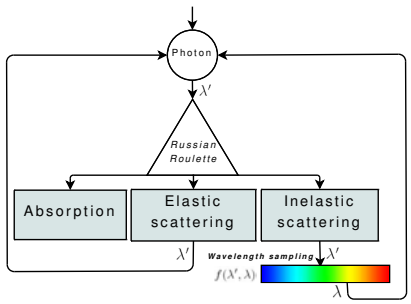

Figure 1: *Photon tracing algorithm. Inelastic scattering events generate a photon with a different associated wavelength according to the wavelength redistribution function.*

4.2. Stage 2: radiance estimate

To estimate radiance we adopt a tradeoff between speed and memory requirements similar to the proposed by Jensen and Christensen [JC98]: we only store photons in the photon map if they have been reflected or transmitted from surfaces, or if they have already been scattered at least once. Thus, we can compute single scattering more efficiently by ray marching through the medium and sampling the light sources by casting shadow rays. Taking into account the wavelength redistribution function for inelastic scattering, a new addend will be added at each step of the ray marching process:

$$\sum_{l=1}^{N}\sum_{i=1}^{N_\lambda}\left\{L_l\left(\lambda_i',\vec{w}_l\right)p_I\left(\lambda_i',\lambda,\vec{w}_l,\vec{w}_o\right)\alpha_I\left(\lambda_i'\right)f_I\left(\lambda_i',\lambda\right)\Delta x\right\} \qquad (22)$$

where $i \in [1..N_\lambda]$ and $l \in [1..N]$ refer to samples in the wavelength and light source domain respectively, $\vec{w}_l$ is the direction to the light with an incoming radiance L_l and Δx represent the ray marching steps.

Multiple scattering will be computed from the photon map, finding in the kd-tree the n photons which are closest to the estimation point by using the typical nearest neighbours algorithm. To account for multiple *inelastic* scattering we modify the radiance estimate expression of [JC98] by including a new term:

$$\sum_{k=1}^{n}\left\{p_I\left(\lambda_k',\lambda,\vec{w}_k,\vec{w}_o\right)f_I\left(\lambda_k',\lambda\right)\frac{\Delta\Phi_k}{\frac{4}{3}\pi r^2}\right\} \qquad (23)$$

where r is the radius of the sphere that contains the n closest photons, and k represents each of the stored photons.

5. Results

We have used the values from Table 5 for our simulations. In the images produced we only vary the chlorophyll concentration C, minerals and detritus turbidity $\alpha_d(400)$ and

(a) $C = 0, \alpha_d = 0, \alpha_y = 0$ (b) $C = 0.01, \alpha_d = 0, \alpha_y = 0$ (c) $C = 0.1, \alpha_d = 0, \alpha_y = 0$ (d) $C = 1, \alpha_d = 0, \alpha_y = 0$

(e) $C = 0, \alpha_d = 0.1, \alpha_y = 0$ (f) $C = 0.01, \alpha_d = 0.1, \alpha_y = 0$ (g) $C = 0.1, \alpha_d = 0.1, \alpha_y = 0$ (h) $C = 1, \alpha_d = 0.1, \alpha_y = 0$

(i) $C = 0, \alpha_d = 0, \alpha_y = 0.1$ (j) $C = 0.01, \alpha_d = 0, \alpha_y = 0.1$ (k) $C = 0.1, \alpha_d = 0, \alpha_y = 0.1$ (l) $C = 1, \alpha_d = 0, \alpha_y = 0.1$

Figure 2: *Resulting pictures varying the chlorophyll concentration C, the minerals and detritus turbidity α_d at 400nm and the CDOM turbidity α_y at 440nm.*

CDOM turbidity $\alpha_y(440)$. The choice of those three parameters to reduce the dimensionality of the model was based on their greater overall influence on the resulting light field. The photon map contains 400000 photons, with 250 used in the estimation of radiance. Ray-marching depth is set at 200 steps. Each of the images has been rendered in a Dual Xeon Pentium 4 at 2.8GHz with 2GB RAM at 512×384 resolution, casting one ray per pixel, and took approximately 20 minutes to render. This time is roughly independent of the number of parameters of the bio-optical model. In order to reduce these computation times, several optimization techniques could be adopted, like using adaptive ray-marching or radiance caching strategies [JDZJ08]. Additionally, perceptual issues could be taken into account, using just an approximate solution in areas of the image where the error is known to be perceptually negligible [SGA*07].

Energy balances show that on average almost 99% of the energy emitted by the light sources is absorbed after just a few interactions of the photons, with very incremental variation after the fourth interaction and negligible contribution after the fifth. This relatively fast convergence is due to the strong absorption in water. We have therefore limited the number of interactions per photon to five, in order to speed up the simulations. Variations of the parameters C, $\alpha_d(400)$ and $\alpha_y(440)$ yield different probabilities for absorption, elastic and inelastic scattering events, which in turn affect the in-water light field. The results can be seen in Figure 2, with each of the varying parameters influencing the final light field as follows:

- Chlorophyll concentration (C) affects mainly both elastic and inelastic scattering. The effects of inelastic scattering are mostly masked by the more predominant elastic scattering and absorption, which increases slowly. The third column in Figure 2 shows brighter images than the previous two due to in-scattering. For higher values (fourth column), out-scattering prevails and the images become darker.
- Minerals and detritus turbidity $(\alpha_d(400))$ increases absorption at lower wavelengths, thus reducing the brightness of the scene and the overall blue hue. Scattering is also increased, making the images appear murkier. Figure 2 shows variations of the minerals and detritus turbidity between the first and second rows for direct comparison.
- CDOM turbidity $(\alpha_y(440))$ slightly increases absorption (darker images) and introduces inelastic scattering (change in hue). This can be seen by comparing the first and third rows in Figure 2.

We have undergone a visual validation of our model by rendering different natural waters. Figure 3 shows the resulting underwater images for Atlantic, Mediterranean, Baltic, North Sea and shallow coastal waters rich in CDOM respectively. All the images have been simulated at the same depth

Figure 3: *Rendered images of different waters. From left to right: Atlantic, Mediterranean, Baltic, North Sea and shallow coastal waters rich in CDOM. Smaller patches below for comparison purposes by Frisvad et al. [FCJ07] (used with permission).*

and are illuminated by the same isotropic point light source. The changes in color are clearly noticeable, from a darker blue in the case of Atlantic water, to the greener hue in the image of the North Sea. The smaller patches below the first four images correspond to the simulations by Frisvad et al. [FCJ07] for the same types of water, and are shown for comparison purposes. Our simulations based on radiative transfer approximately match their simulations based on Lorenz-Mie theory. The differences are mainly owed to two factors: on the one hand, the overall darker tone in our images is due to in-water absorption, whereas [FCJ07] renders the *surface* of the water body; on the other hand, the absence of inelastic scattering effects in [FCJ07] can have a visible influence the final appearance of water, as shown in Figure 4 for the Baltic case. The properties of the water have been adjusted according to measurements found in [BSF*03] [Mob94] for our bio-optical model and [BSF*03] in the model by Frisvad et al. In both cases, it is only the changes in the constituents of the waters which yield the different colors. We have additionally performed a numerical analysis of the in-water radiance field, to quantify the influence of each constituent. The results can be seen in Figure 5.

6. Conclusion

We have presented a complete bio-optical model of ocean water based on parameterizing its intrinsic optical properties. Relying on radiative transfer theory, we obtain the resulting in-water light field by extending the rendering algorithm presented in [GMAS05]. The extension can now handle more complex interactions between light and water, including inelastic scattering with anti-Stokes behavior, where the scattered photon absorbs energy from the medium and is re-emitted at *higher* energies. We have additionally studied the influence of the parameters in the apparent optical properties of water in the scene, which are defined by the light field obtained. We have performed an energy-balance analysis, and visual validation of the method has been provided by direct comparison with images by Frisvad et al. [FCJ07], rendering different types of waters based on published constituent data.

We have included Raman scattering by pure water and fluorescence by phytoplankton and CDOM as inelastic scattering events with energy transfers. Even though their combined quantitative contribution to the overall radiance field is usually less than 2% (see Figure 5), this relatively small percentage does have a clear influence on the apparent optical properties, as Figure 4 shows. We thus argue that these events, usually overlooked in computer graphics literature, are qualitatively important for underwater imagery and should be included in a complete simulation. Other types of inelastic scattering such as *Compton*, *Bragg* or *Brillouin* could also be added, although their influence is more incremental. Other particulate elements could be easily added as well just by including their corresponding absorption and scattering coefficients in the model; however, the three constituents treated here (phytoplankton, minerals and detritus and CDOM) have the most influence in the final radiance field.

The results show how the model developed can easily be used for physically-based simulations of underwater imagery. We believe this work can be of interest not only in the computer graphics community, but in remote sense or oceanographic studies as well.

Figure 4: *The influence of inelastic scattering in the apparent optical properties of water (Baltic sea): Left, no inelastic scattering. Center, just chlorophyll inelastic scattering (as in [GMAS05]). Right, all inelastic scattering events included in the simulation.*

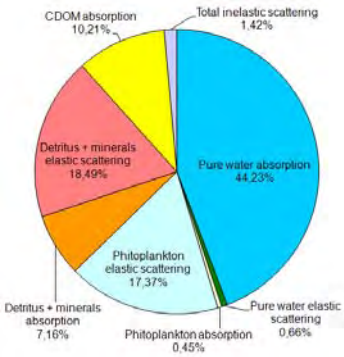

Figure 5: *Radiance distribution of the resulting in-water light field per type of event (Baltic Sea).*

Acknowledgments

We thank the anonymous reviewers for their valuable comments. This research was partly done under the sponsorship of the Spanish Ministry of Education and Research through the projects TIN2004-07672-C03-03 and TIN2007-63025.

References

[BLSS93] BLASI P., LE SAEC B., SCHLICK C.: A rendering algorithm for discrete volume density objects. *Computer Graphics Forum (Eurographics 93) 12*, 3 (1993), 201–210. 4

[BMP81] BRICAUD A., MOREL A., PRIEUR L.: Absorption by dissolved organic matter of the sea (yellow substance) in the uv and visible domains. *Limnol. Oceanogr. 26*, 1 (1981), 43–53. 3

[BSF*03] BABIN M., STRAMSKI D., FERRARI G. M., CLAUSTRE H., BRICAUD A., OBOLENSKY G., HOEPFFNER N.: Variations in the light absorption coefficients of phytoplankton, nonalgal particles, and dissolved organic matter in coastal waters around europe. *J. Geophys. Res. 108(C7)*, 3211 (2003). 3, 9

[Cha60] CHANDRASEKHAR S.: *Radiative Transfer*. Dover Publications, Inc., 1960. 2

[CS04] CEREZO E., SERON F. J.: Rendering natural waters taking fluorescence into account: Research articles. *Comput. Animat. Virtual Worlds 15*, 5 (2004), 471–484. 2

[FCJ07] FRISVAD J. R., CHRISTENSEN N. J., JENSEN H. W.: Computing the scattering properties of participating media using Lorenz-Mie theory. *ACM Trans. Graph. 26*, 3 (2007), 60. 2, 9

[Gla95] GLASSNER A. S.: *Principles of Digital Image Synthesis*. Morgan Kaufmann Publishers Inc., San Francisco, CA, USA, 1995. 2

[GM83] GORDON H. R., MOREL A.: *Remote Assessment of Ocean Color for Interpretation of Satellite Visible Imagery: A Review*, vol. 4 of *Lecture Notes on Coastal and Estuarine Studies*. Springer-Verlag, New York, 1983. 4

[GMAS05] GUTIERREZ D., MUNOZ A., ANSON O., SERÓN F. J.: Non-linear volume photon mapping. In *Proc. of the Eurographics Symposium on Rendering Techniques, Konstanz, Germany, June 29 - July 1, 2005* (2005), pp. 291–300. 2, 6, 9

[GSO03] GREEN R. E., SOSIK H. M., OLSON R. J.: Contributions of phytoplankton and other particles to inherent optical properties in new england continental shelf waters. *Limnol. Oceanogr. 48*, 6 (2003), 2377–2391. 4

[Haw92] HAWES S.: *Quantum fluorescence efficiencies of marine fulvic and humid acids*. PhD thesis, Dept. of Marince Science, Univ. of South Florida, 1992. 5

[HG41] HENYEY L., GREENSTEIN J.: Diffuse radiation in the galaxy. *Astrophysics Journal 93* (1941), 70–83. 4

[JC98] JENSEN H. W., CHRISTENSEN P. H.: Efficient simulation of light transport in scenes with participating media using photon maps. In *SIGGRAPH 98 Conference Proceedings* (jul 1998), Cohen M., (Ed.), Annual Conference Series, ACM SIGGRAPH, Addison Wesley, pp. 311–320. 7

[JDZJ08] JAROSZ W., DONNER C., ZWICKER M., JENSEN H. W.: Radiance caching for participating media. *To appear in ACM Transactions on Graphics* (2008). 8

[Jen01] JENSEN H. W.: *Realistic image synthesis using photon mapping*. A.K. Peters, Natick, Massachussets, 2001. 2, 6

[Kir94] KIRK J. T.: *Light and photosynthesis in aquatic ecosystems*. Cambridge University Press, New York, 1994. 3

[KYNN91] KANEDA K., YUAN G., NAKAMAE E., NISHITA T.: Realistic visual simulation of water surfaces taking into account radiative transfer. In *Proc. of CAD/Graphics 91* (1991), pp. 25–30. 2

[Maz02] MAZO R. M.: *Brownian Motion: Fluctuations, Dynamics and Applications*, vol. 112 of *International Series of Monographs on Physics*. Oxford University Press Inc., Great Clarendon Street, Oxford, 2002, ch. Einstein-Smoluchowski Theory, pp. 46–62. 4

[Mob94] MOBLEY C. D.: *Light and Water: Radiative Transfer in Natural Waters*. Academic Press, Inc., San Diego, 1994. 1, 2, 3, 5, 9

[Mor74] MOREL A.: *Optical Aspects of Oceanography*. Academic Press, New York, 1974. 3, 4

[Mor88] MOREL A.: Optical modeling of the upper ocean in relation to its biogenous matter content (case i waters). *Journal of Geophysical Research 93*, C9 (1988), 10749–10768. 3

[NKON90] NAKAMAE E., KANEDA K., OKAMOTO T., NISHITA T.: A lighting model aiming at drive simulators. *Computer Graphics 24*, 4 (Aug. 1990), 395–404. 2

[NSTN93] NISHITA T., SHIRAI T., TADAMURA K., NAKAMAE E.: Display of the earth taking into account atmosphere scattering. In *Computer Graphics (SIGGRAPH '93 Proceedings)* (1993), vol. 24, pp. 175–182. 2

[PA01] PREMOZE S., ASHIKHMIN M.: Rendering natural waters. *Comput. Graph. Forum 20*, 4 (2001), 189–199. 2

[PF97] POPE R. M., FRY E. S.: Absorption spectrum (380–700 nm) of pure water. ii. integrating cavity measurements. *Applied Optics 36*, 33 (1997), 8710–8723. 3

[Pre76] PREISENDORFER R. W.: *Introduction*, vol. 1 of *Hydrologic Optics*. National Technical Information Service, Springfield, IL, 1976. 1

[RPC89] ROESLER C. S., PERRY M. J., CARDER K. L.: Modeling in situ phytoplankton absorption from total absorption spectra in productive inland marine waters. *Limnol. Oceanogr. 34*, 8 (1989), 1510–1523. 3

[RT87] RUSHMEIER H. E., TORRANCE K. E.: The zonal method for calculating light intensities in the presence of a participating medium. *Computer Graphics 21*, 4 (July 1987), 293–302. 2

[SB81] SMITH R. C., BAKER K. S.: Optical properties of the clearest natural waters (200–800 nm). *Appl. Opt. 20* (1981), 177–184. 3, 4

[SBM01] STRAMSKI D., BRICAUD A., MOREL A.: Modeling the inherent optical properties of the ocean based on the detailed composition of planktonic community. *Applied Optics 40* (2001), 2929–2945. 4, 5

[SCP94] SPINRAD R. W., CARDER K. L., PERRY M. J. (Eds.): *Ocean Optics*. No. 25 in Oxford Monographs on Geology and Geophysics. Oxford University Press, 1994. 2

[SGA*07] SUNDSTEDT V., GUTIERREZ D., ANSON O., BANTERLE F., CHALMERS A.: Perceptual rendering of participating media. *ACM Transactions of Applied Perception 4*, 3 (2007). 8

[SLP87] SATHYENDRANATH S., LAZZARA L., PRIEUR L.: Variations in the spectral values of specific absorption of phytoplankton. *Limnol. Oceanogr. 32*, 2 (1987), 403–415. 3, 4

[TN95] TADAMURA K., NAKAMAE E.: *Computer Graphics: Developments in Virtual Environments*. Academic Press, 1995, ch. Modeling the colour of Water in Lightning Design, pp. 97–114. 2

[Wal69] WALRAFEN G. E.: Continuum model of water–an erroneous interpretation. *Journal of Chemical Physics 50*, 1 (January 1969), 567–569. 5

Highly Scattering Materials: Rendering and Acquisition

Craig Donner
P&G

Scattering - SIGGRAPH Asia Course
December 2009

TexasArrowheads.com


TexasArrowheads.com


TexasArrowheads.com

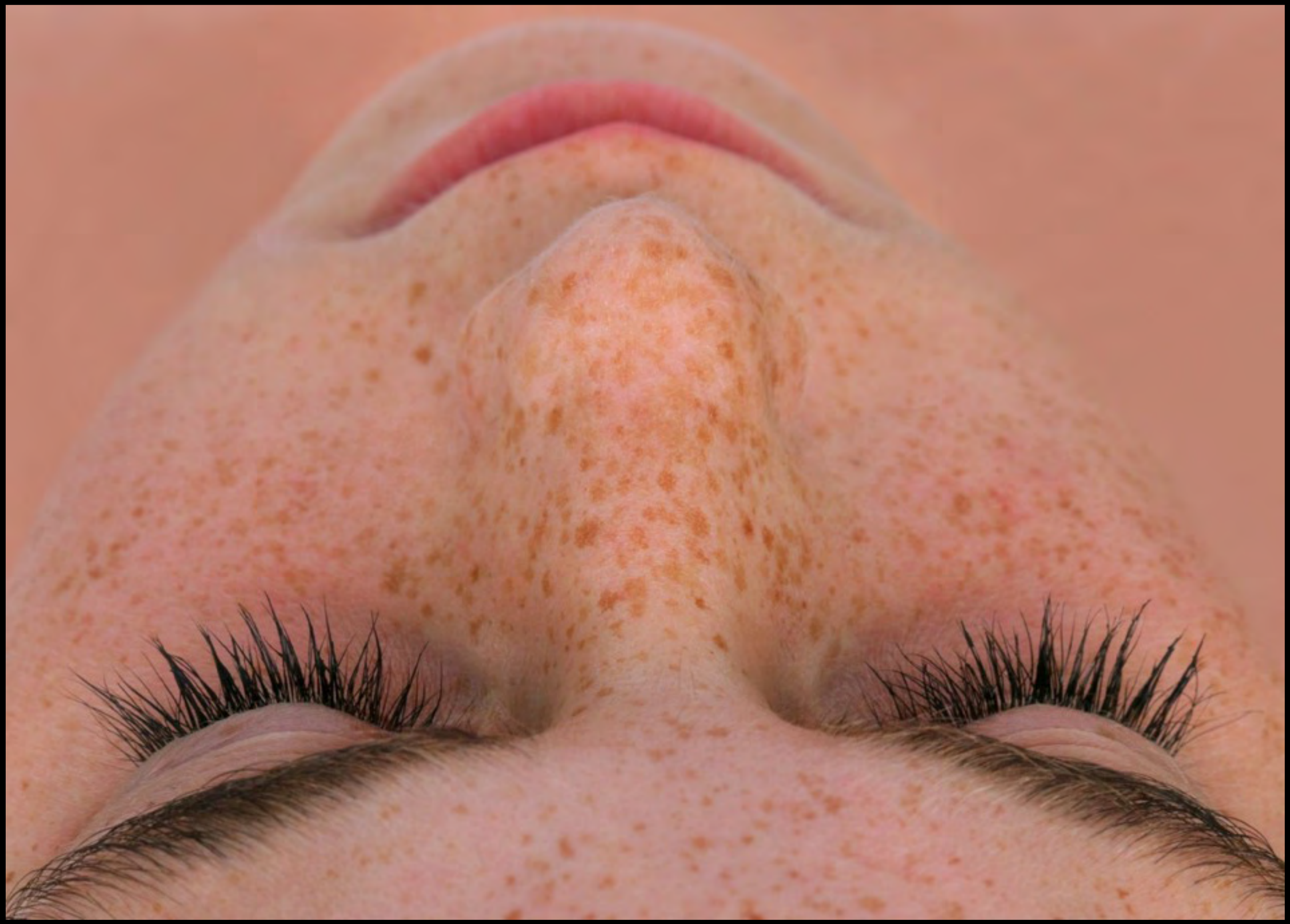

Many applications

Many applications

Many applications

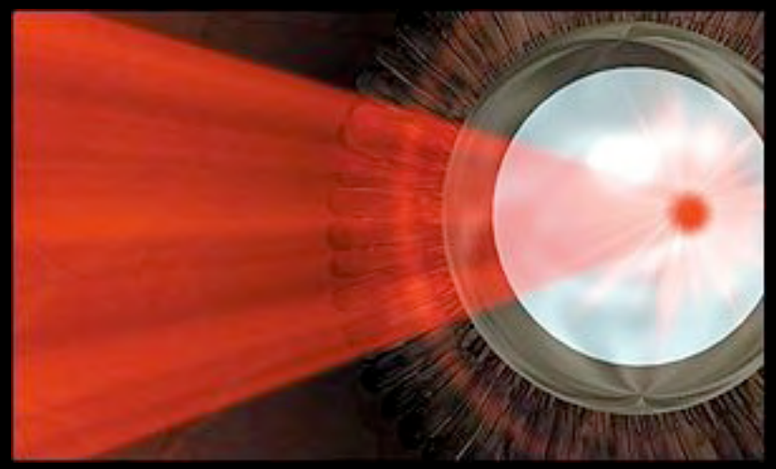

Many applications

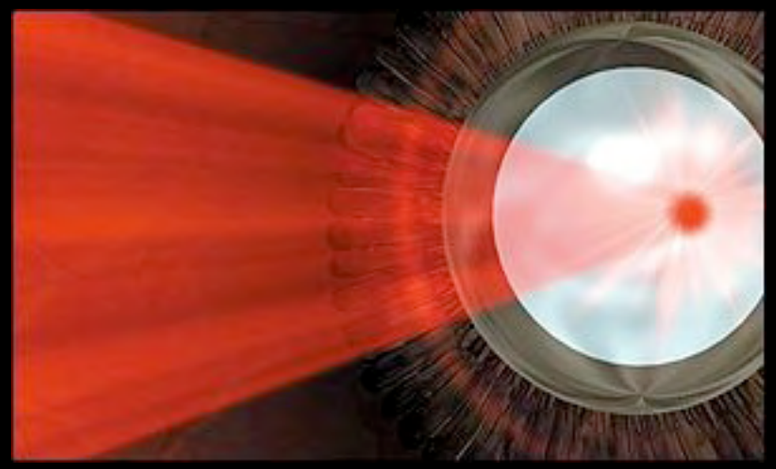

Many applications

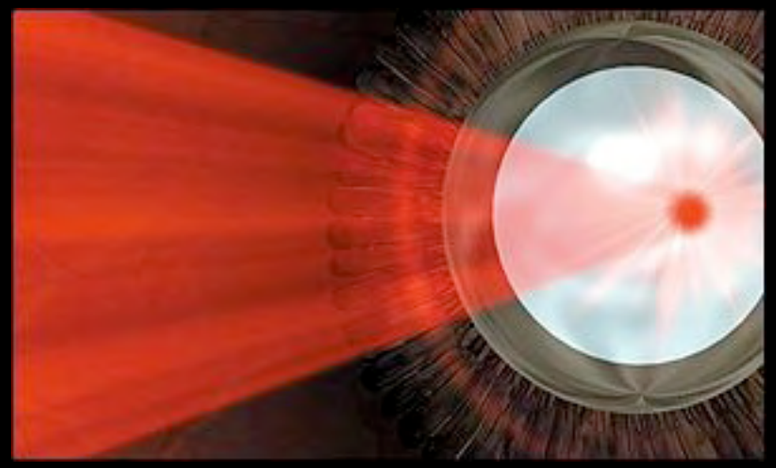

Subsurface scattering

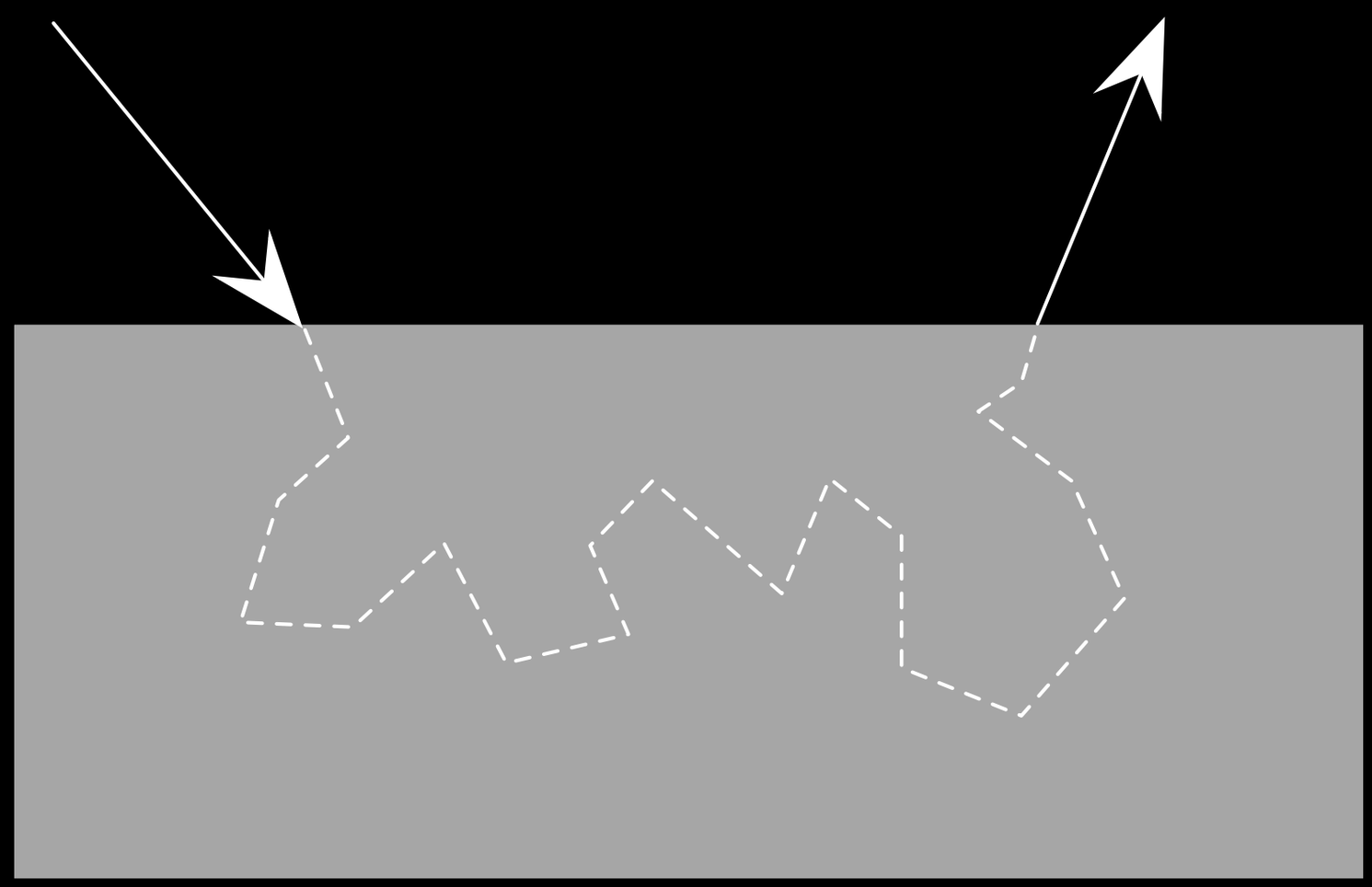

Subsurface scattering

BSSRDF

$$\frac{dL_o(x_o, \vec{\omega}_o)}{d\Phi(x_i, \vec{\omega}_i)} = S(x_i, \vec{\omega}_i; x_o, \vec{\omega}_o)$$

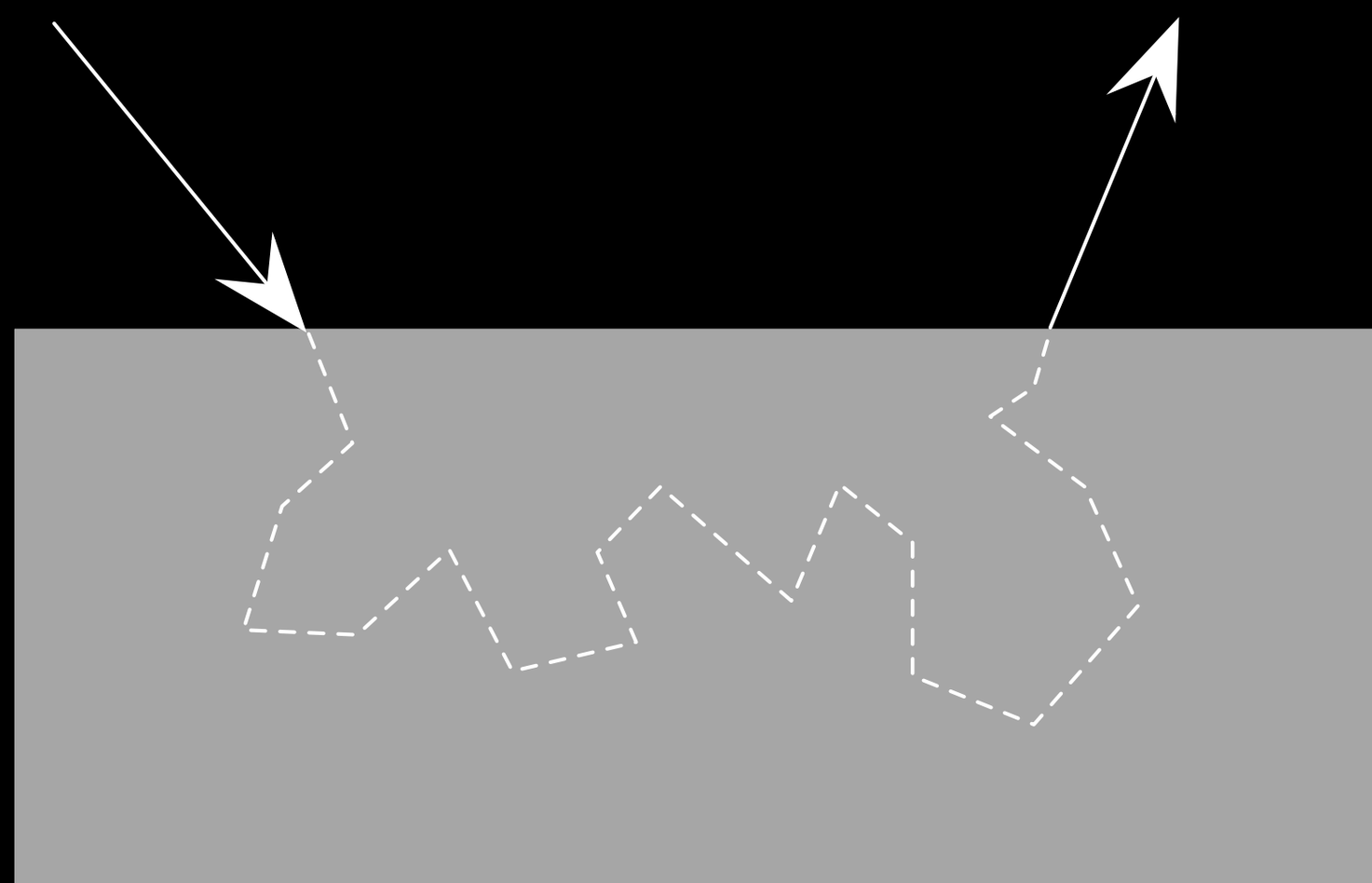

Today's menu

- Translucent materials
  - Basic acquisition
  - Thin slabs
  - Multiple layers
- Spectral BSSRDF for skin
  - Physiological properties
  - Four parameters
- Heterogeneous skin model
  - Acquisition of skin properties

Path/photon tracing

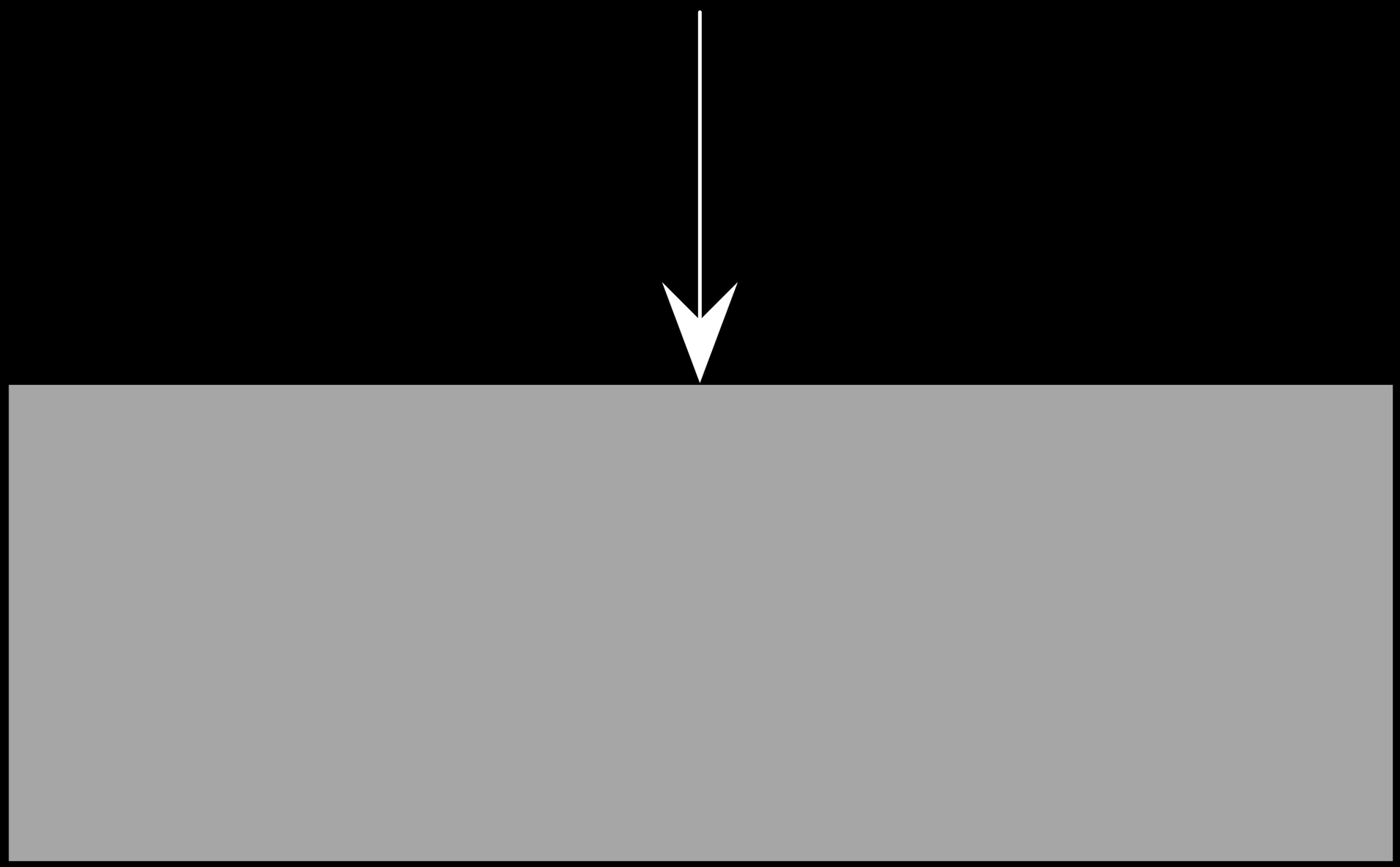

Path/photon tracing

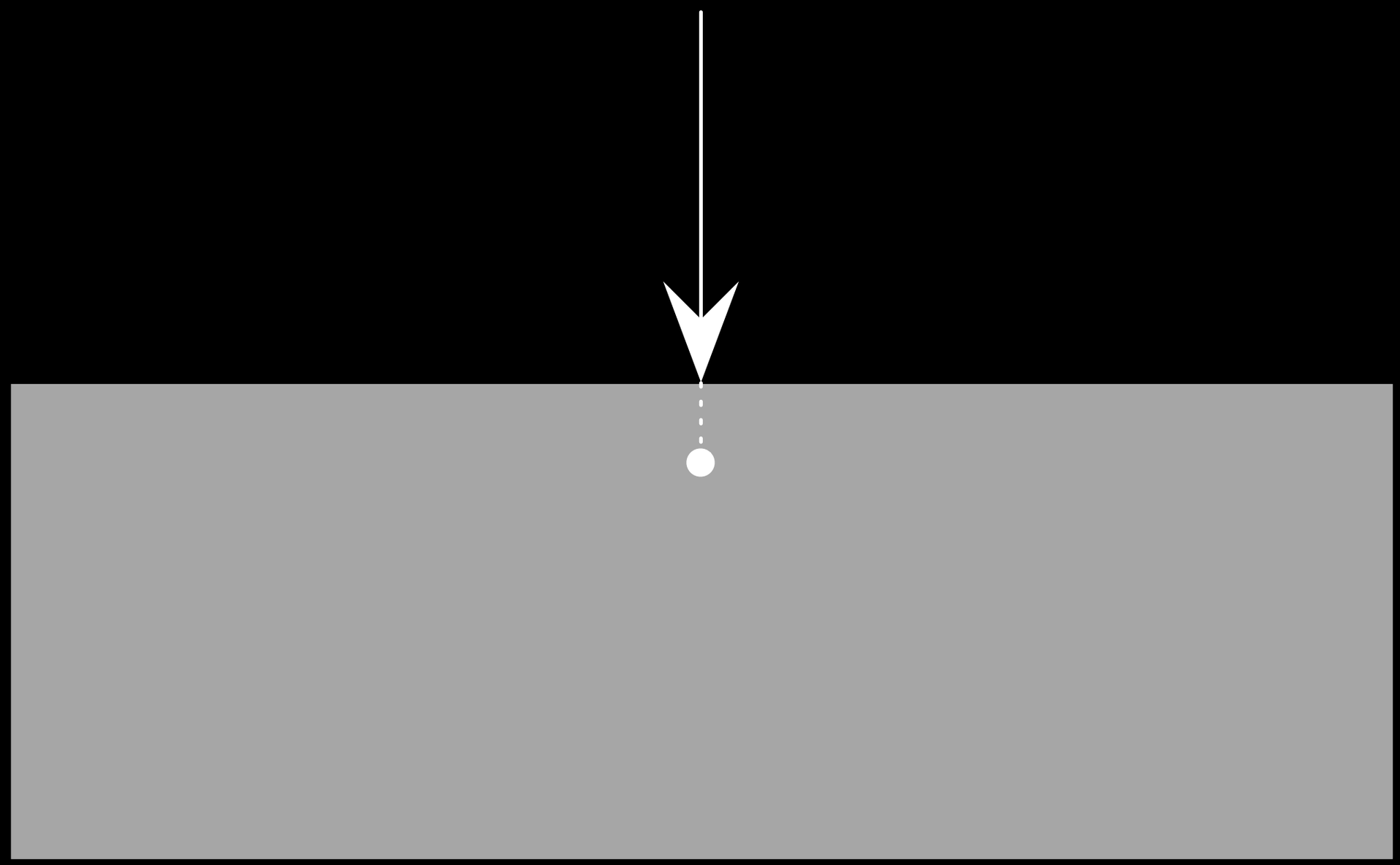

Path/photon tracing

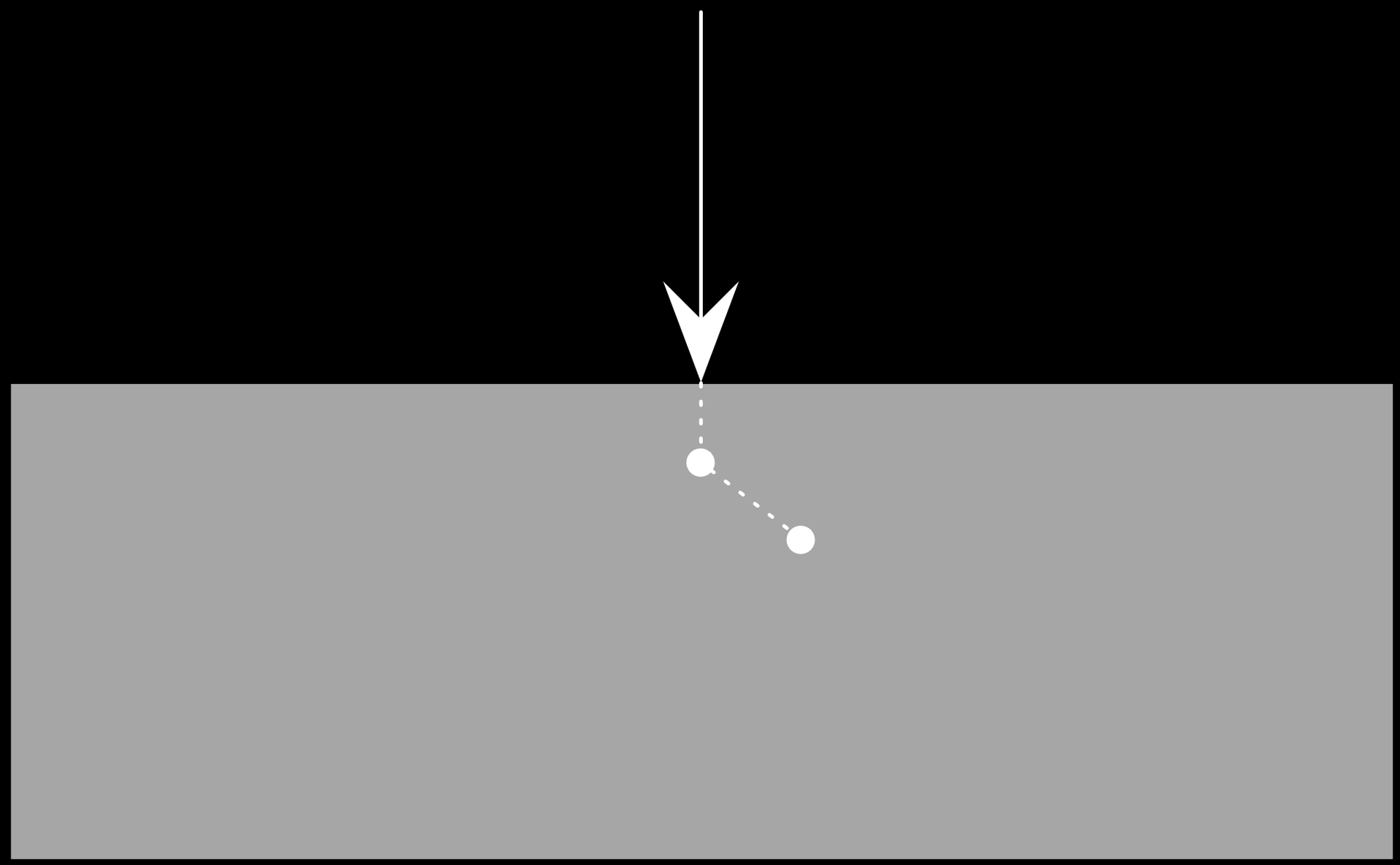

Path/photon tracing

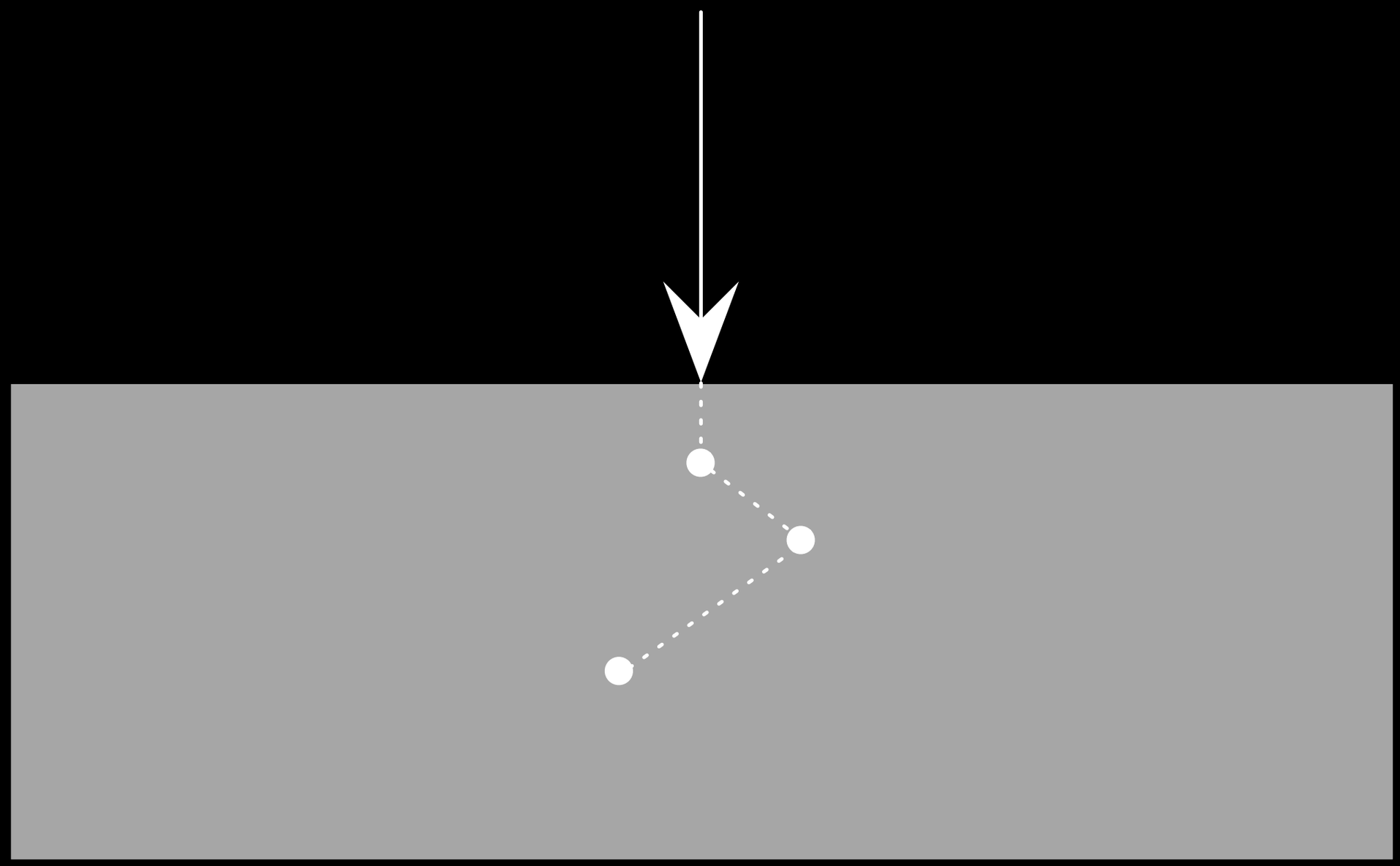

Path/photon tracing

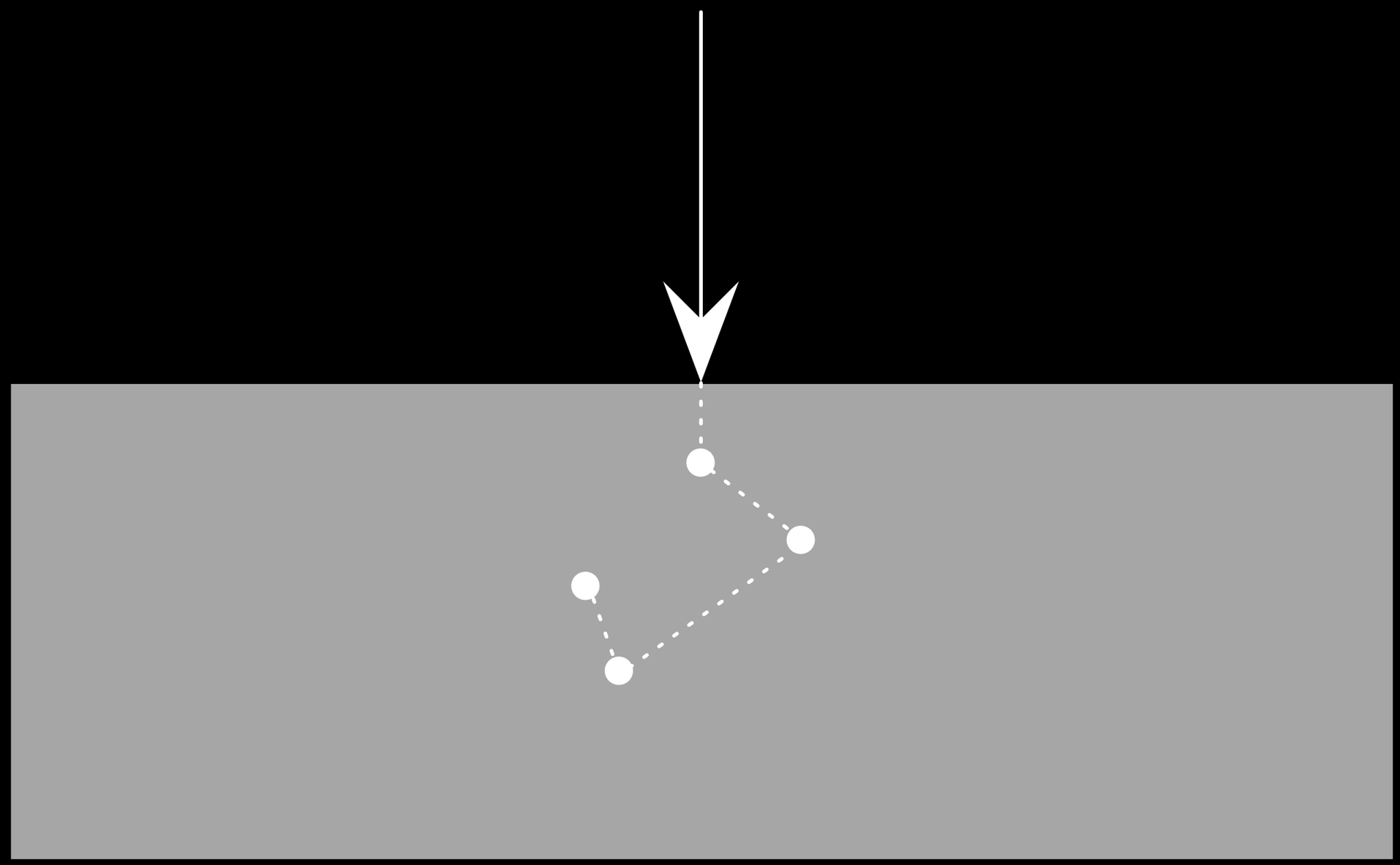

Acquisition setup

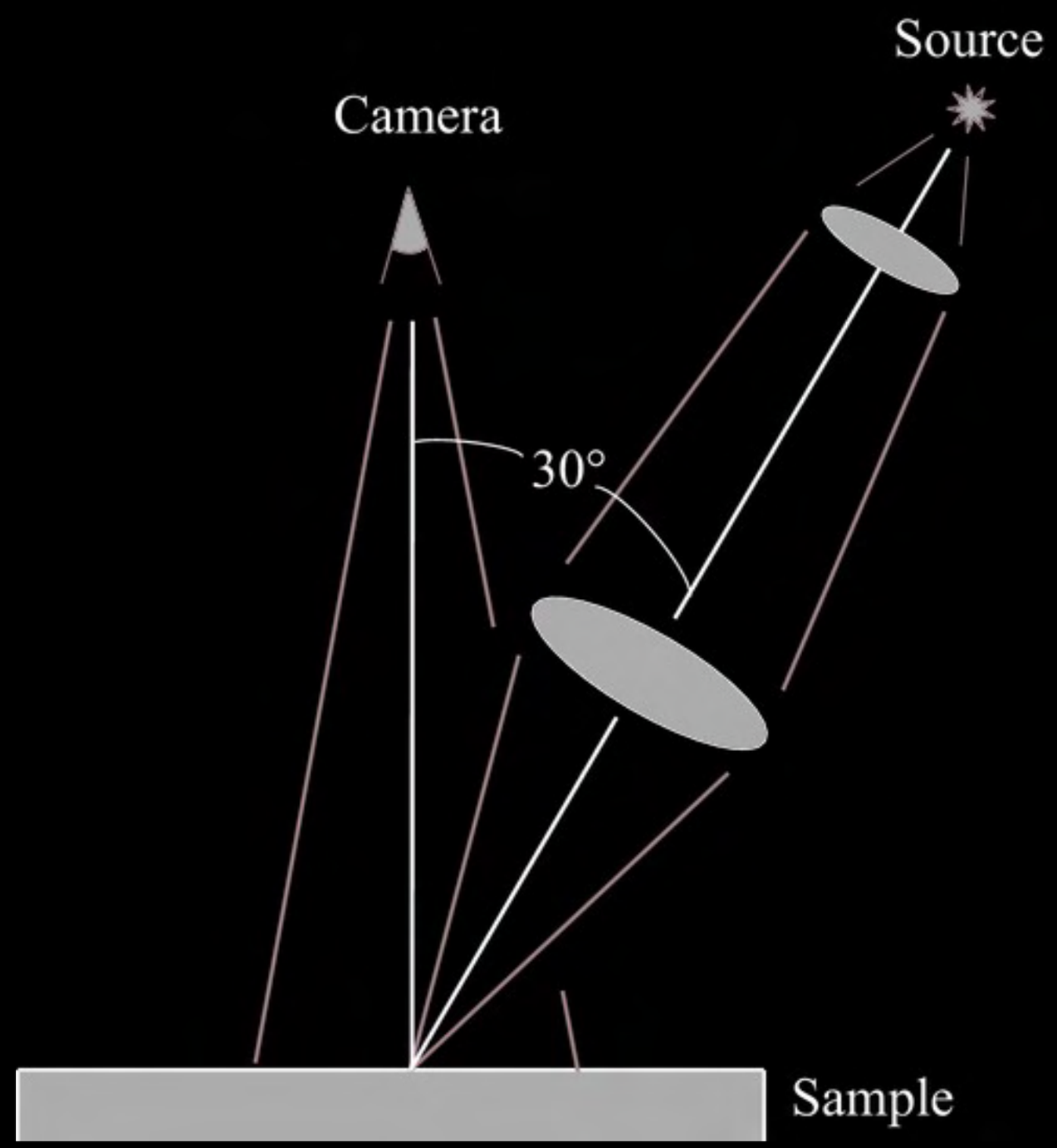

Joshi et al. 2006

Measuring asymmetry

Joshi et al. 2006

Measuring asymmetry

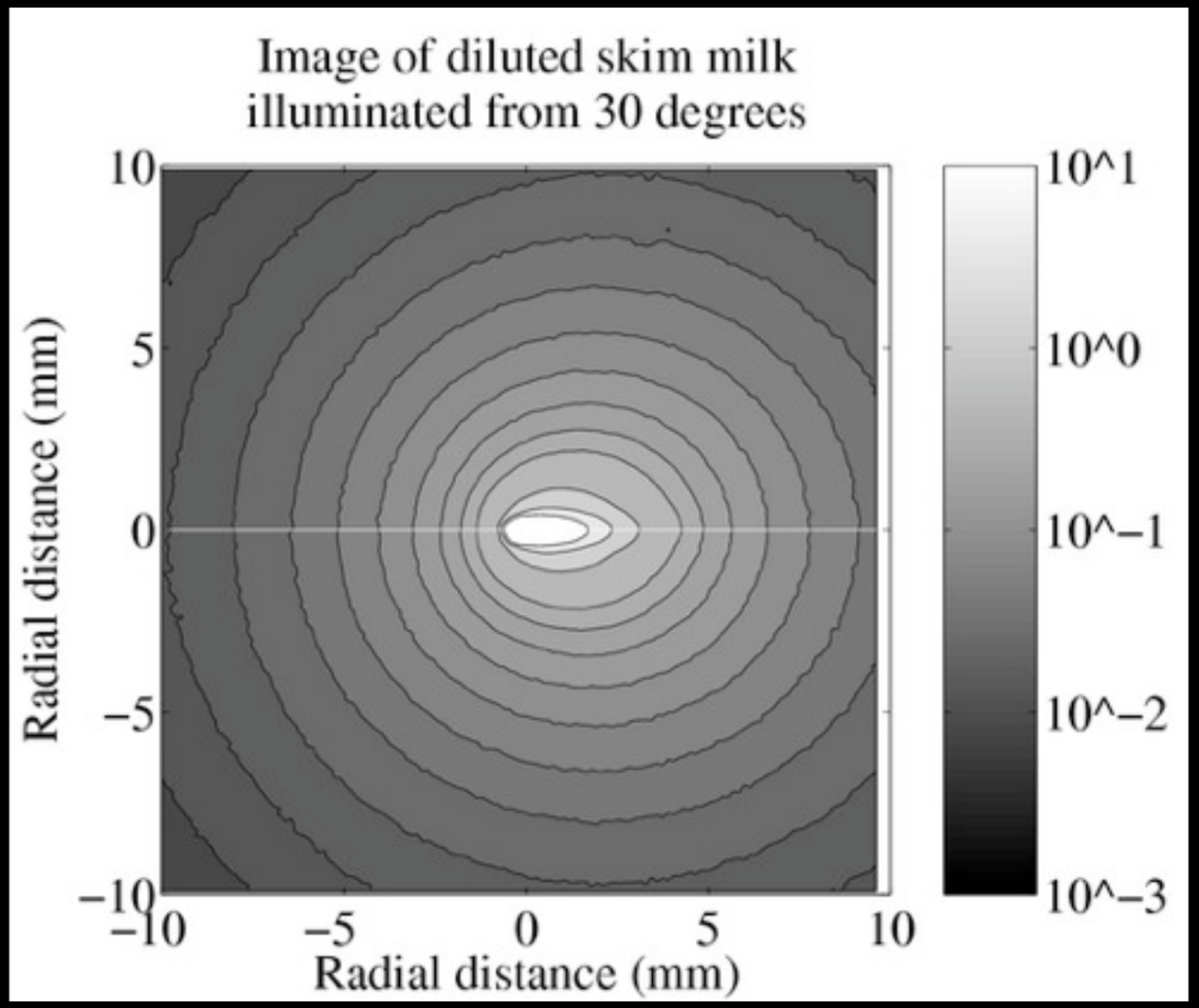

Joshi et al. 2006

Measurement and fit

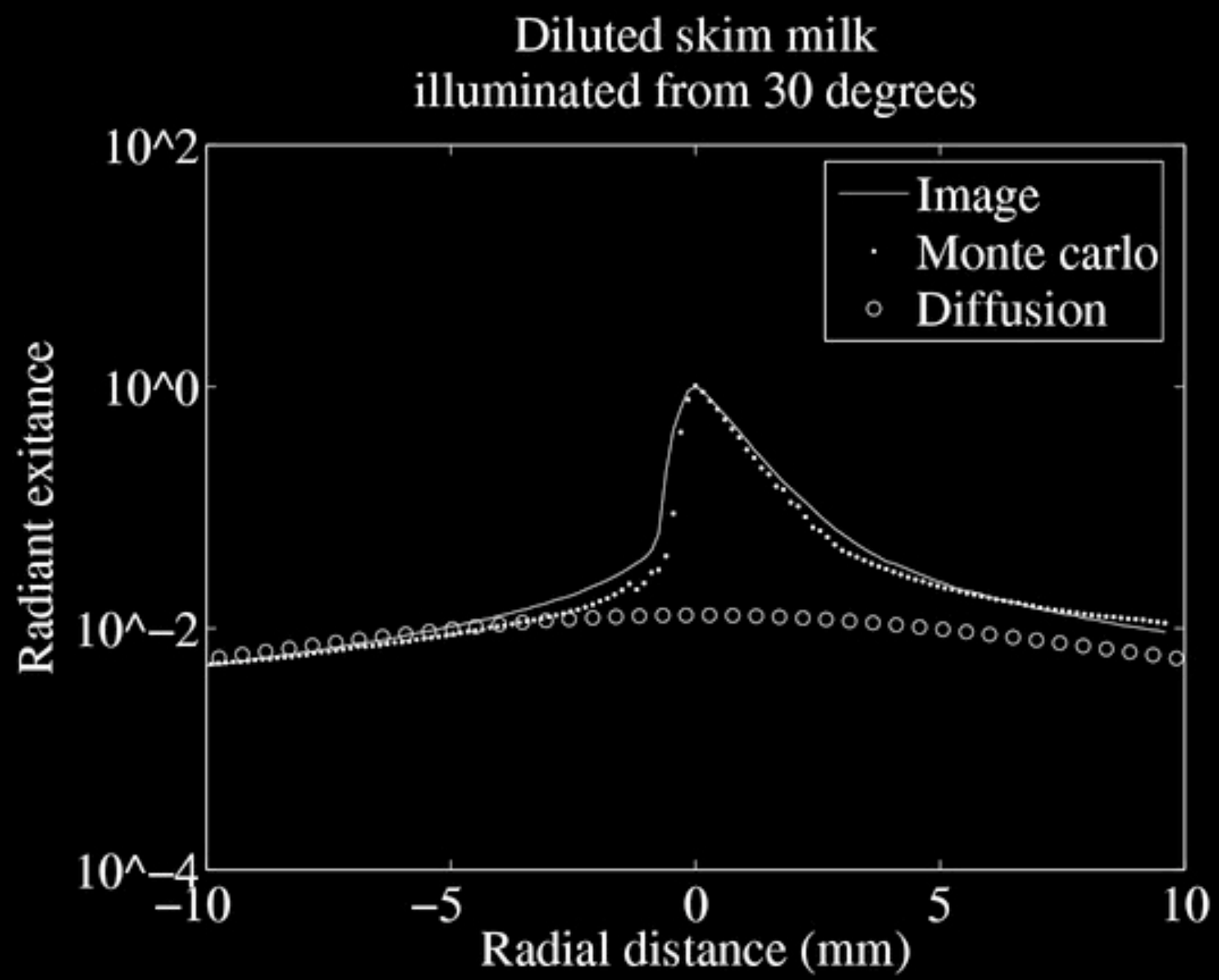

Joshi et al. 2006

Numerical methods

- Expensive
- Noisy/biased

Diffusion dipole

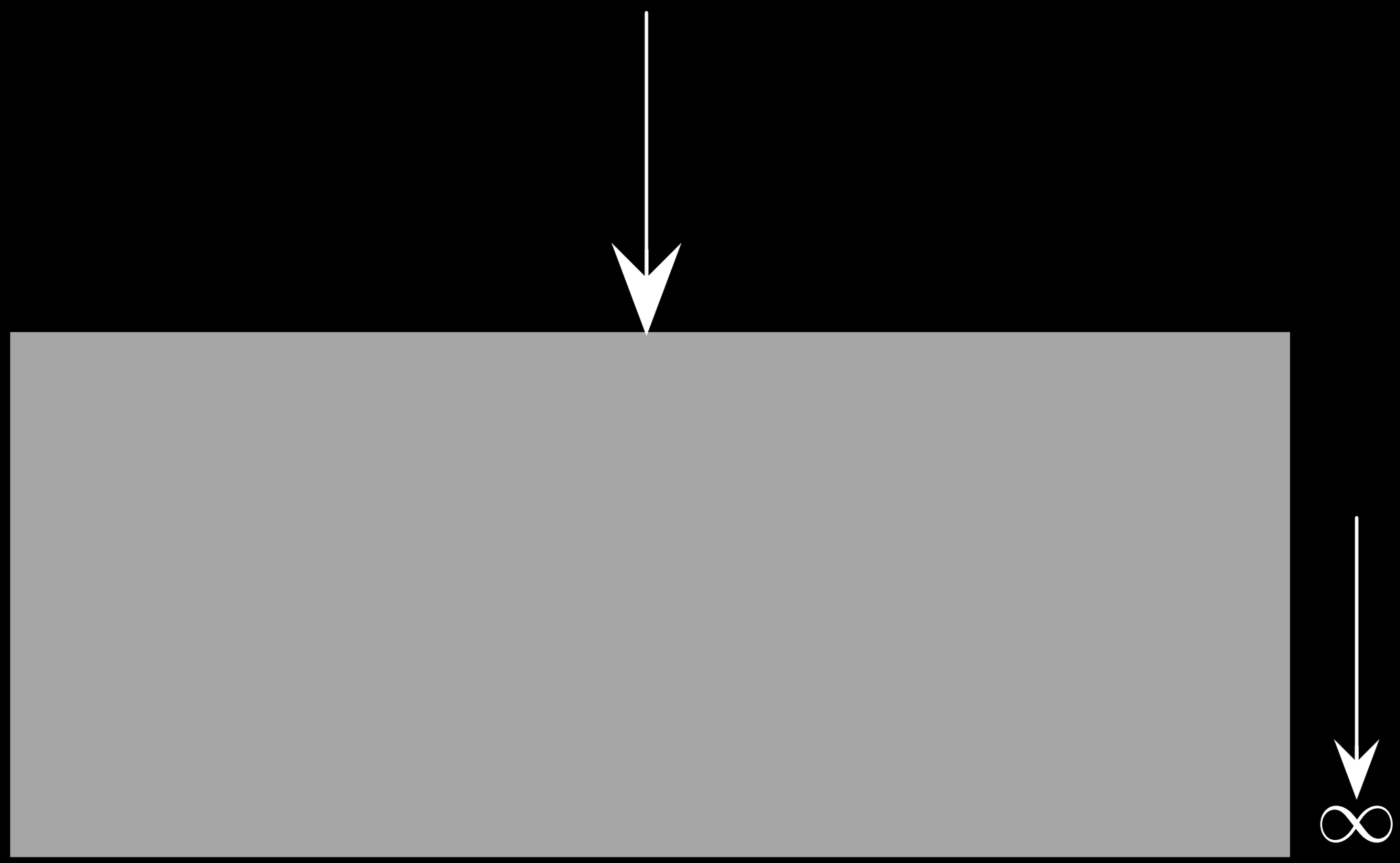

Homogeneous

Diffusion dipole

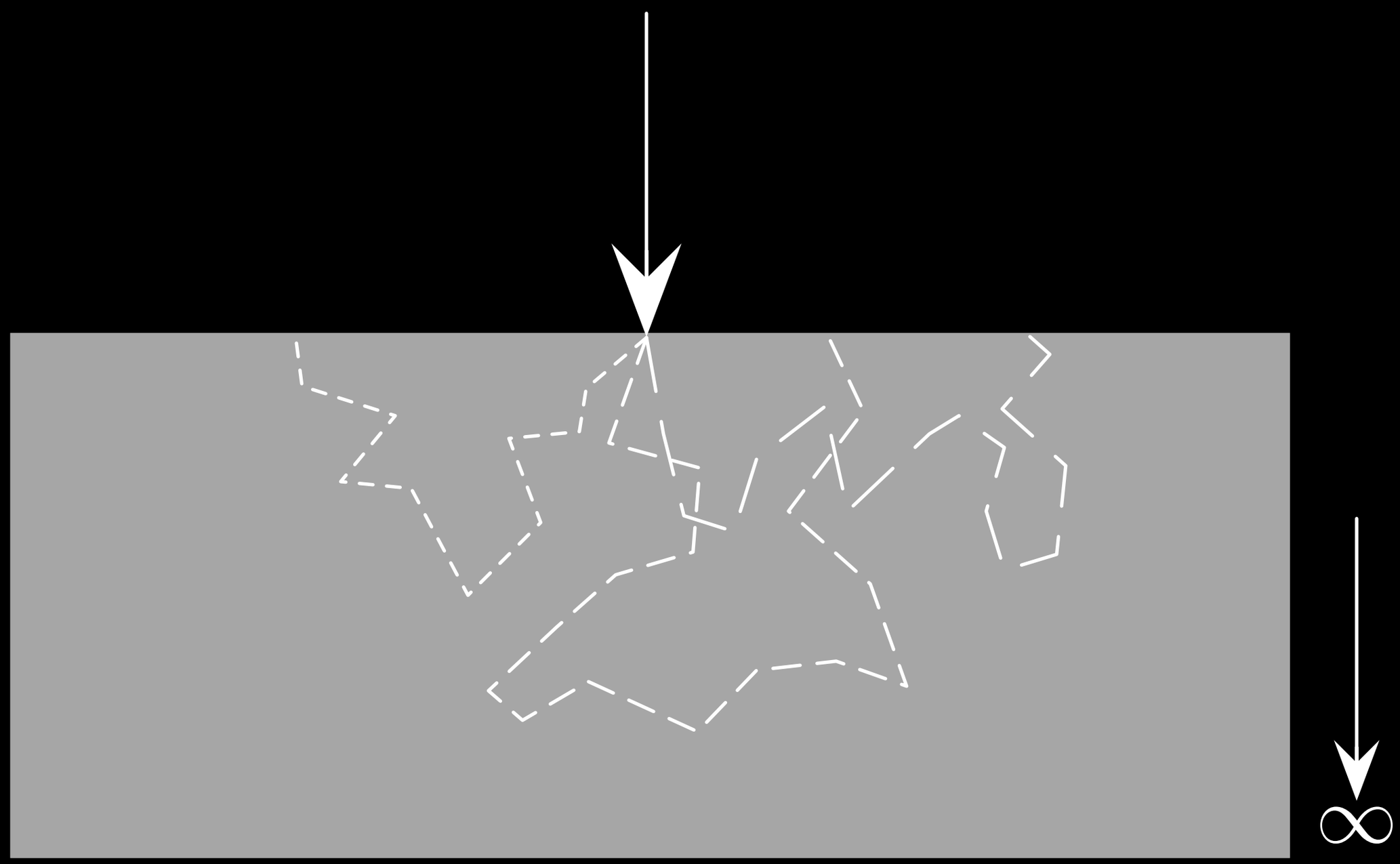

Diffusion profile

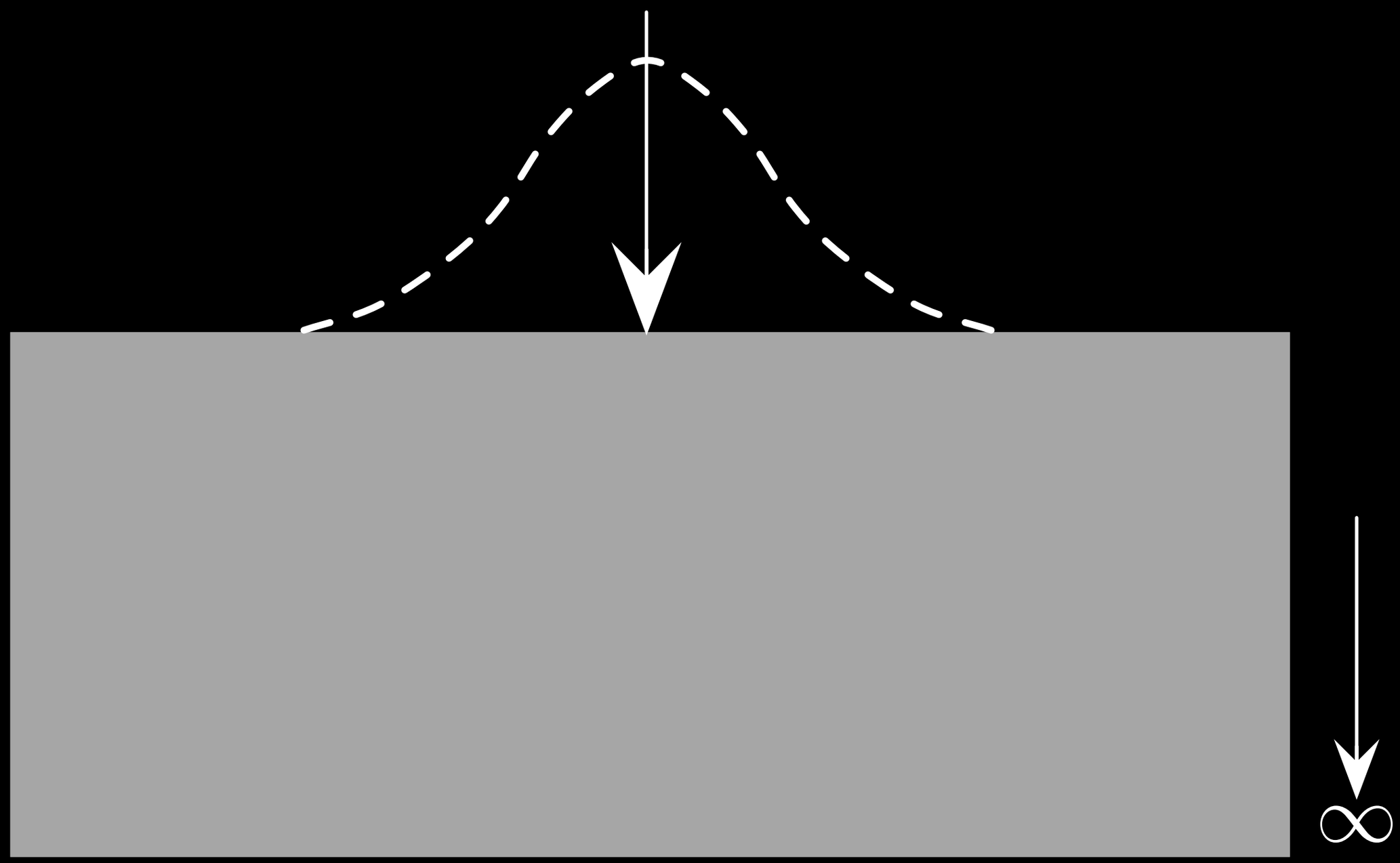

Diffusion dipole

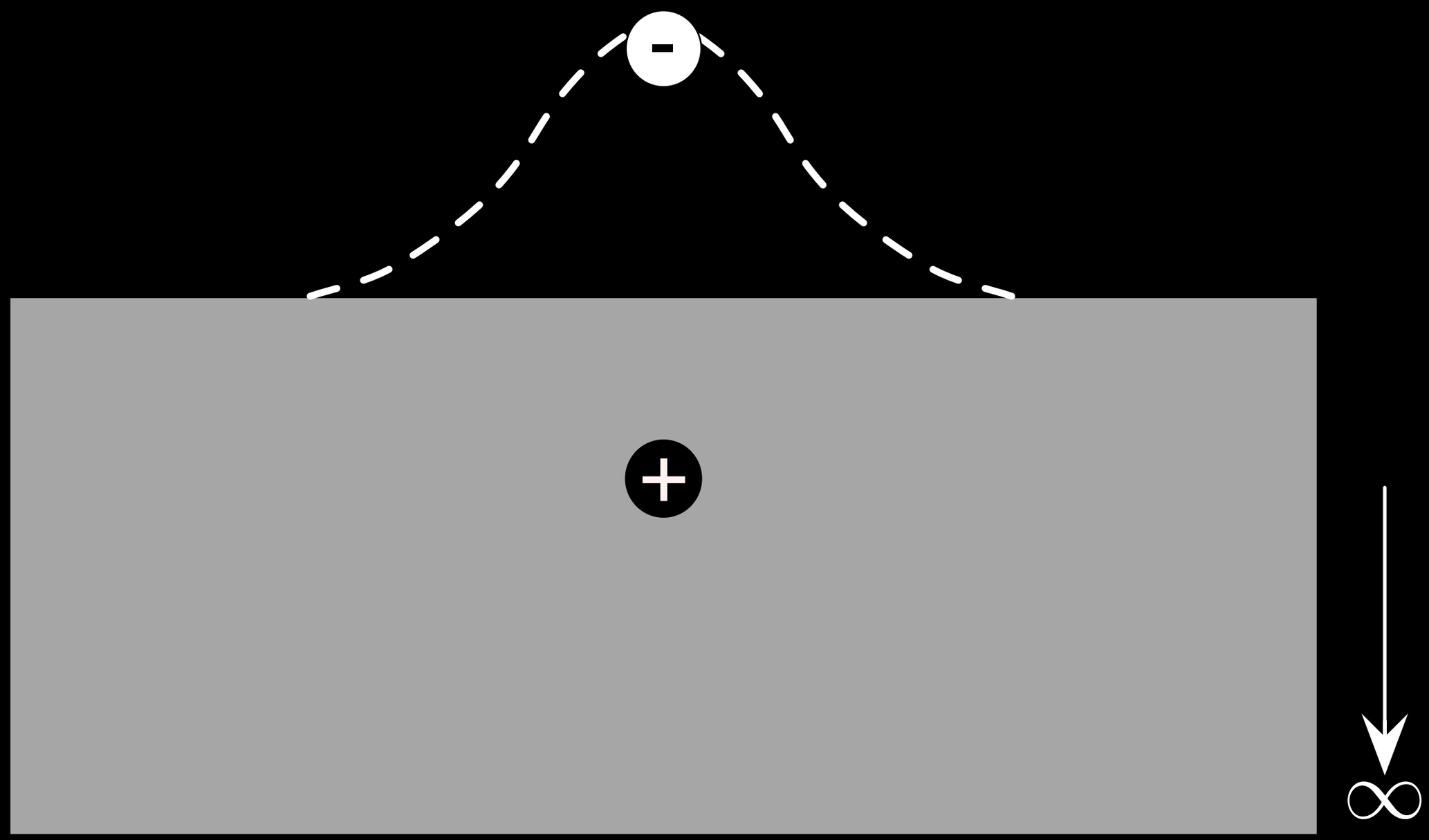

Diffusion dipole

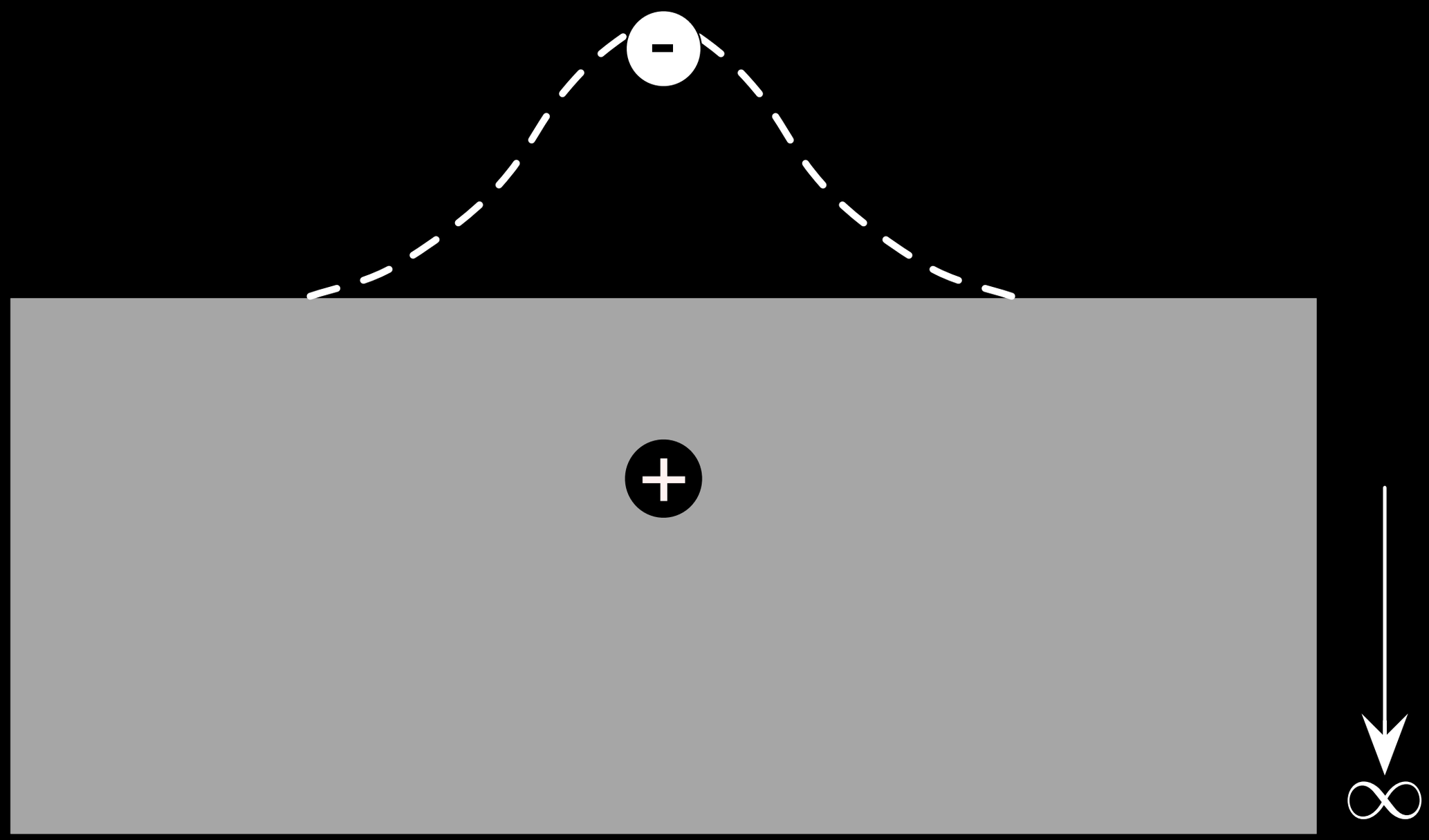

$$R(r) = \frac{\alpha' z_r (1 + \sigma_{tr} d_r) e^{-\sigma_{tr} d_r}}{4\pi d_r^3} + \frac{\alpha' z_v (1 + \sigma_{tr} d_v) e^{-\sigma_{tr} d_v}}{4\pi d_v^3}$$

Diffusion dipole

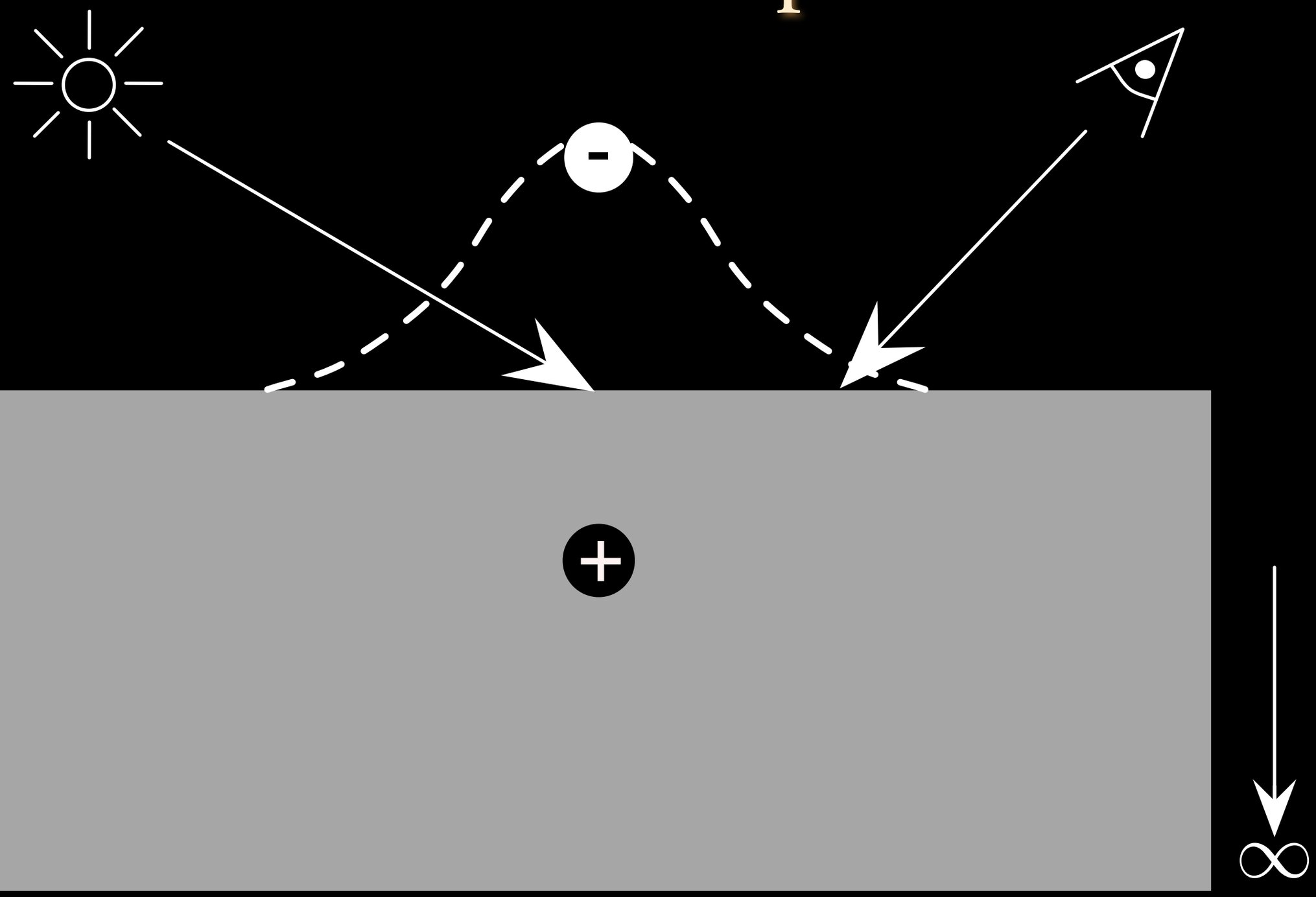

$$R(r) = \frac{\alpha' z_r (1 + \sigma_{tr} d_r) e^{-\sigma_{tr} d_r}}{4\pi d_r^3} + \frac{\alpha' z_v (1 + \sigma_{tr} d_v) e^{-\sigma_{tr} d_v}}{4\pi d_v^3}$$

Rendered images

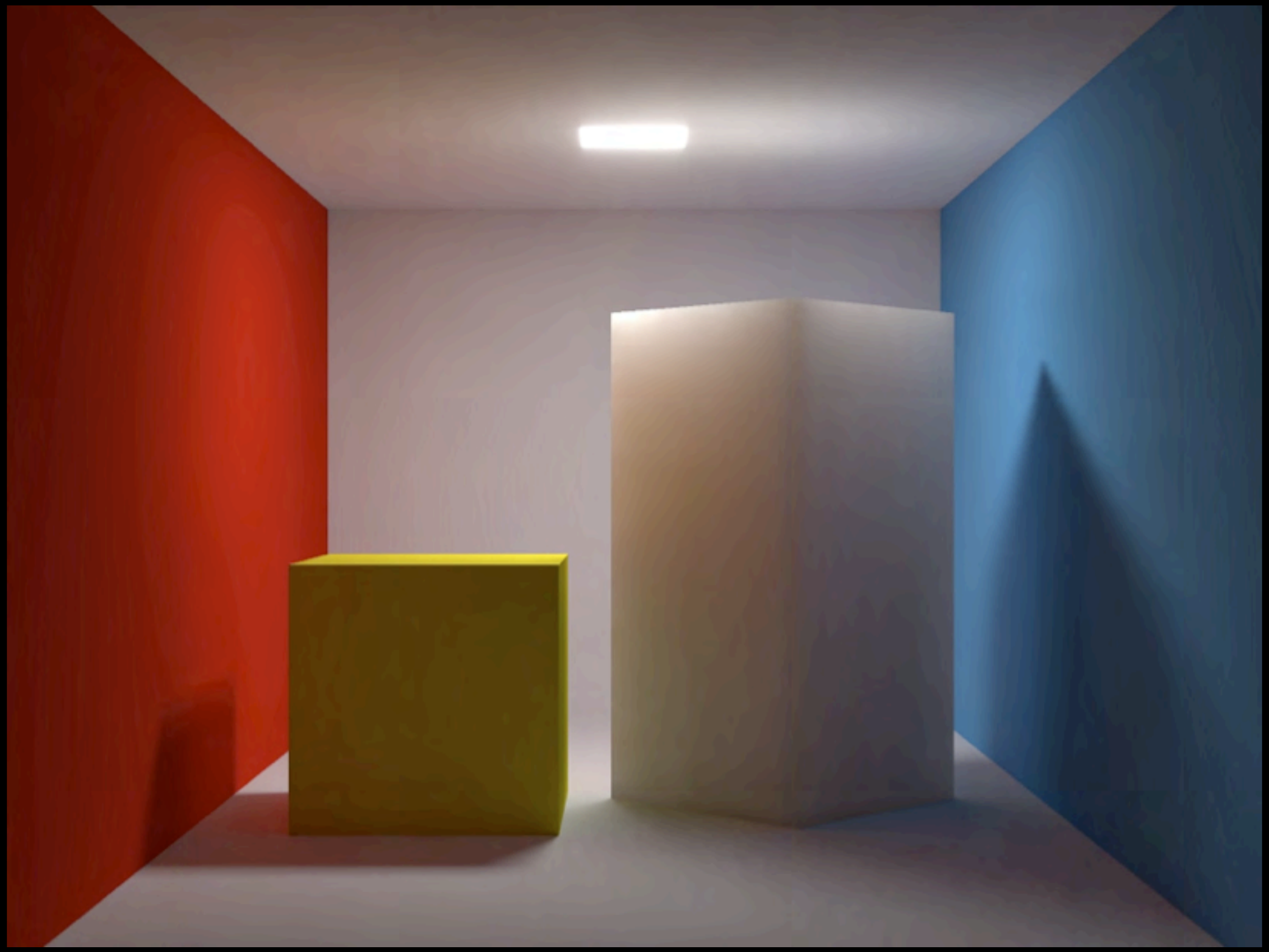

Jensen and Buhler 2002

Rendered images

Jensen et al. 2001

Rendered images

Jensen et al. 2001

Acquisition

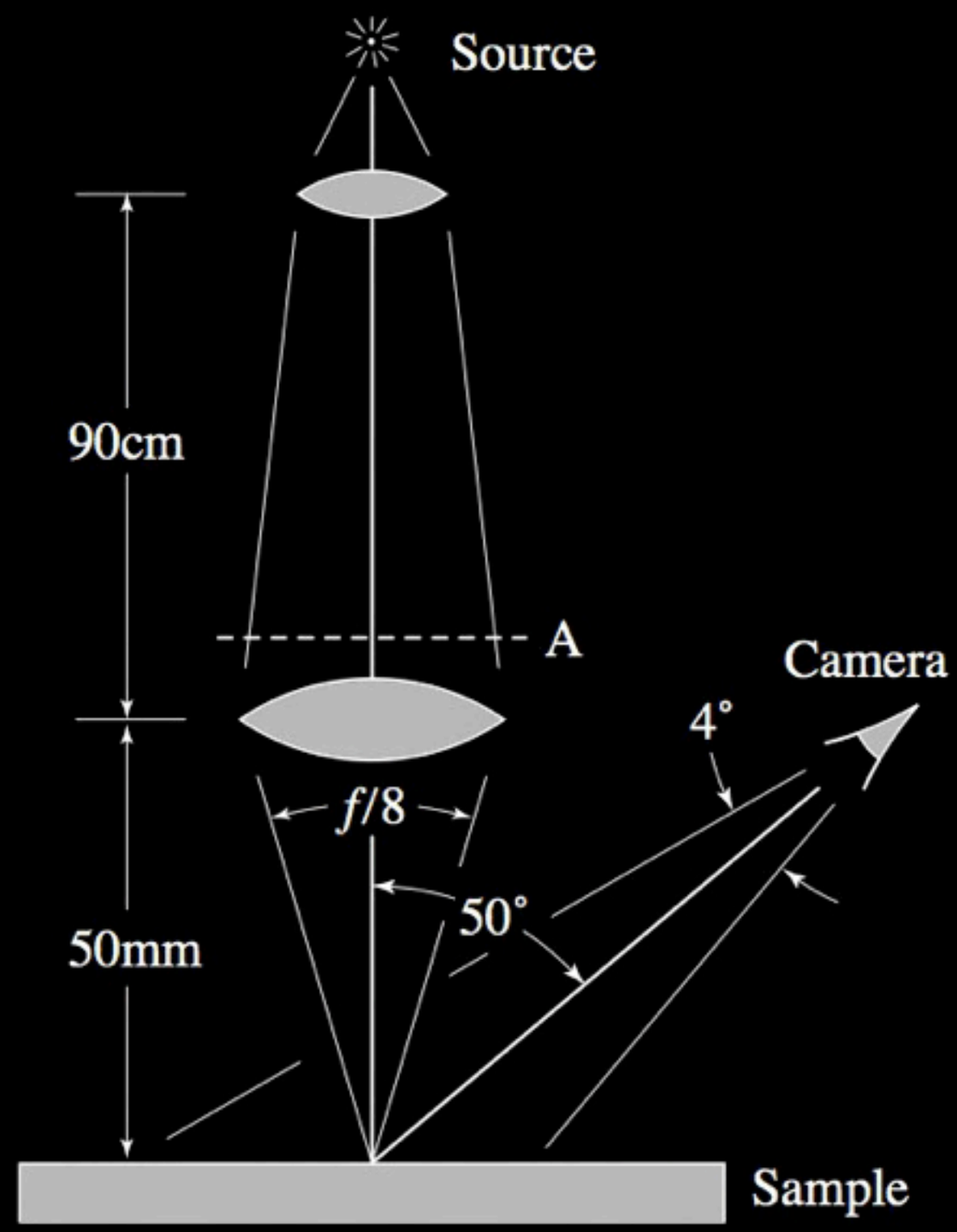

Jensen et al. 2001

High-Dynamic Range Image

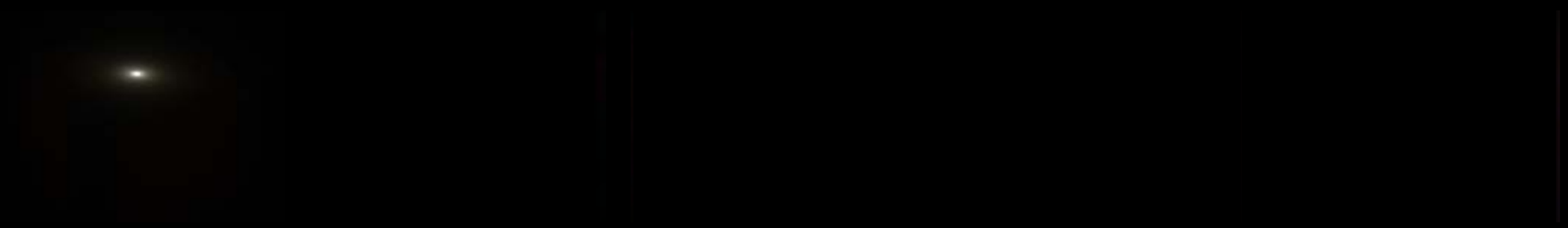

Jensen et al. 2001

High-Dynamic Range Image

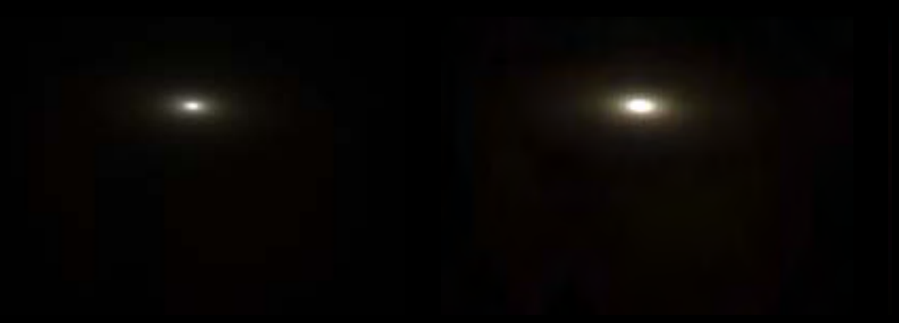

Jensen et al. 2001

High-Dynamic Range Image

Jensen et al. 2001

High-Dynamic Range Image

Jensen et al. 2001

High-Dynamic Range Image

Jensen et al. 2001

High-Dynamic Range Image

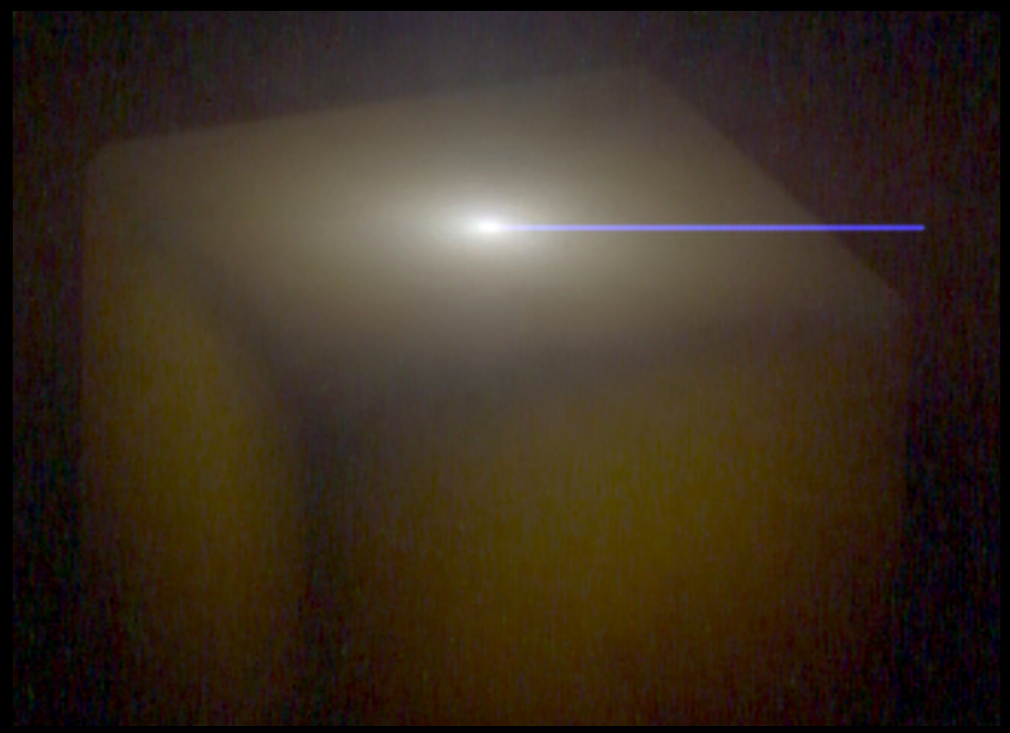

Jensen et al. 2001

Parameter Optimization

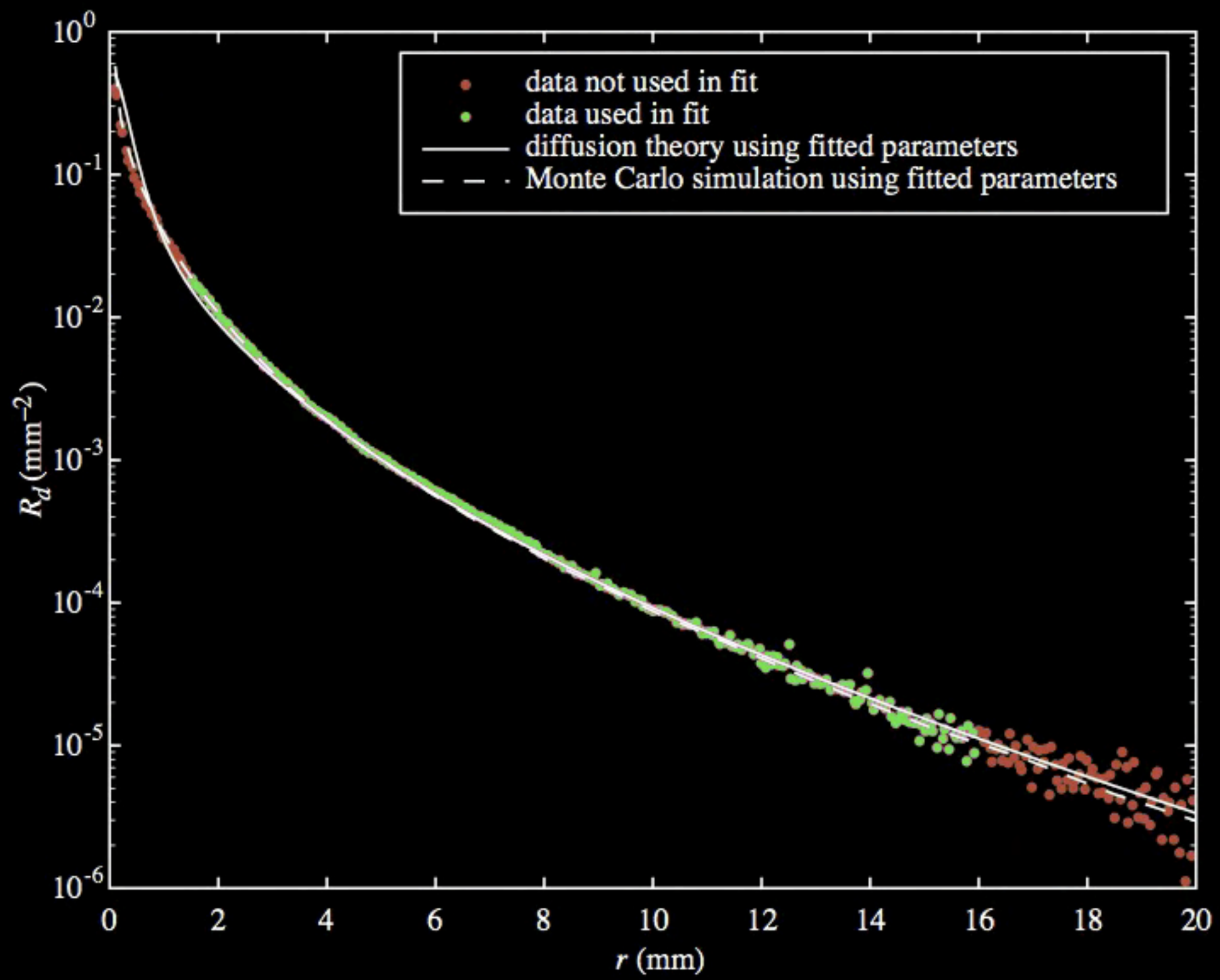

Jensen et al. 2001

Measured Materials

Material	σ_s' [mm^{-1}]			σ_a [mm^{-1}]			Diffuse Reflectance			η
	R	G	B	R	G	B	R	G	B	
Apple	2.29	2.39	1.97	0.0030	0.0034	0.046	0.85	0.84	0.53	1.3
Chicken1	0.15	0.21	0.38	0.015	0.077	0.19	0.31	0.15	0.10	1.3
Chicken2	0.19	0.25	0.32	0.018	0.088	0.20	0.32	0.16	0.10	1.3
Cream	7.38	5.47	3.15	0.0002	0.0028	0.0163	0.98	0.90	0.73	1.3
Ketchup	0.18	0.07	0.03	0.061	0.97	1.45	0.16	0.01	0.00	1.3
Marble	2.19	2.62	3.00	0.0021	0.0041	0.0071	0.83	0.79	0.75	1.5
Potato	0.68	0.70	0.55	0.0024	0.0090	0.12	0.77	0.62	0.21	1.3
Skimmilk	0.70	1.22	1.90	0.0014	0.0025	0.0142	0.81	0.81	0.69	1.3
Skin1	0.74	0.88	1.01	0.032	0.17	0.48	0.44	0.22	0.13	1.3
Skin2	1.09	1.59	1.79	0.013	0.070	0.145	0.63	0.44	0.34	1.3
Spectralon	11.6	20.4	14.9	0.00	0.00	0.00	1.00	1.00	1.00	1.3
Wholemilk	2.55	3.21	3.77	0.0011	0.0024	0.014	0.91	0.88	0.76	1.3

Jensen et al. 2001

BSSRDF gun

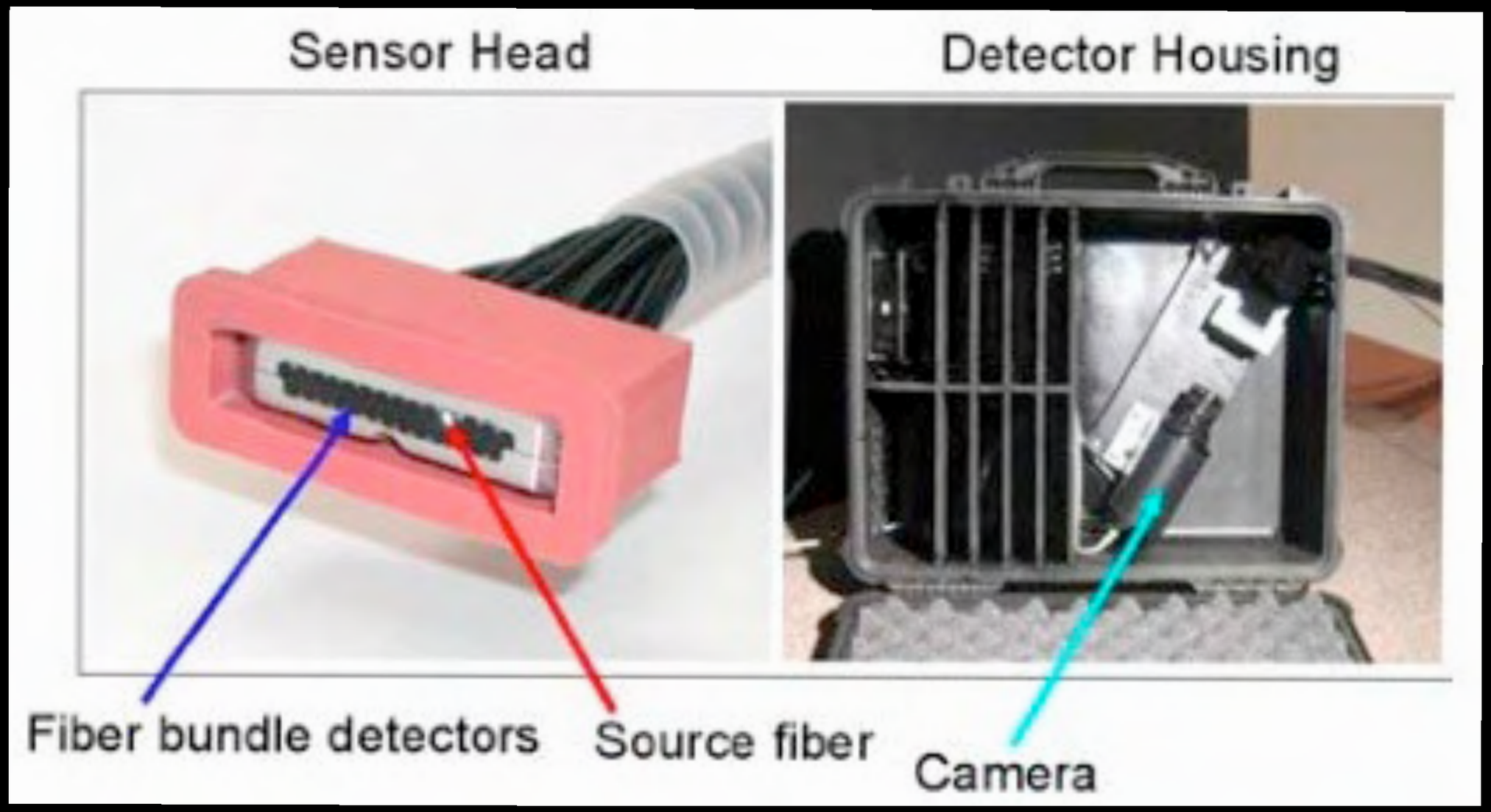

Weyrich et al. 2006

Scattering profile measurement

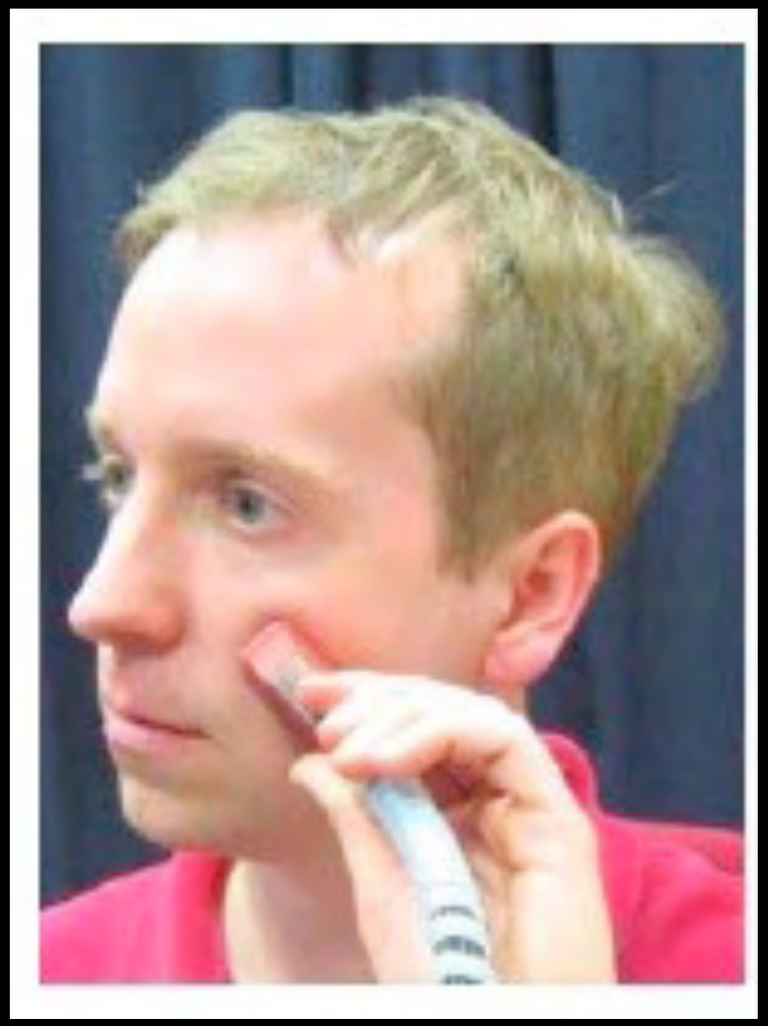

Weyrich et al. 2006

Scattering profile measurement

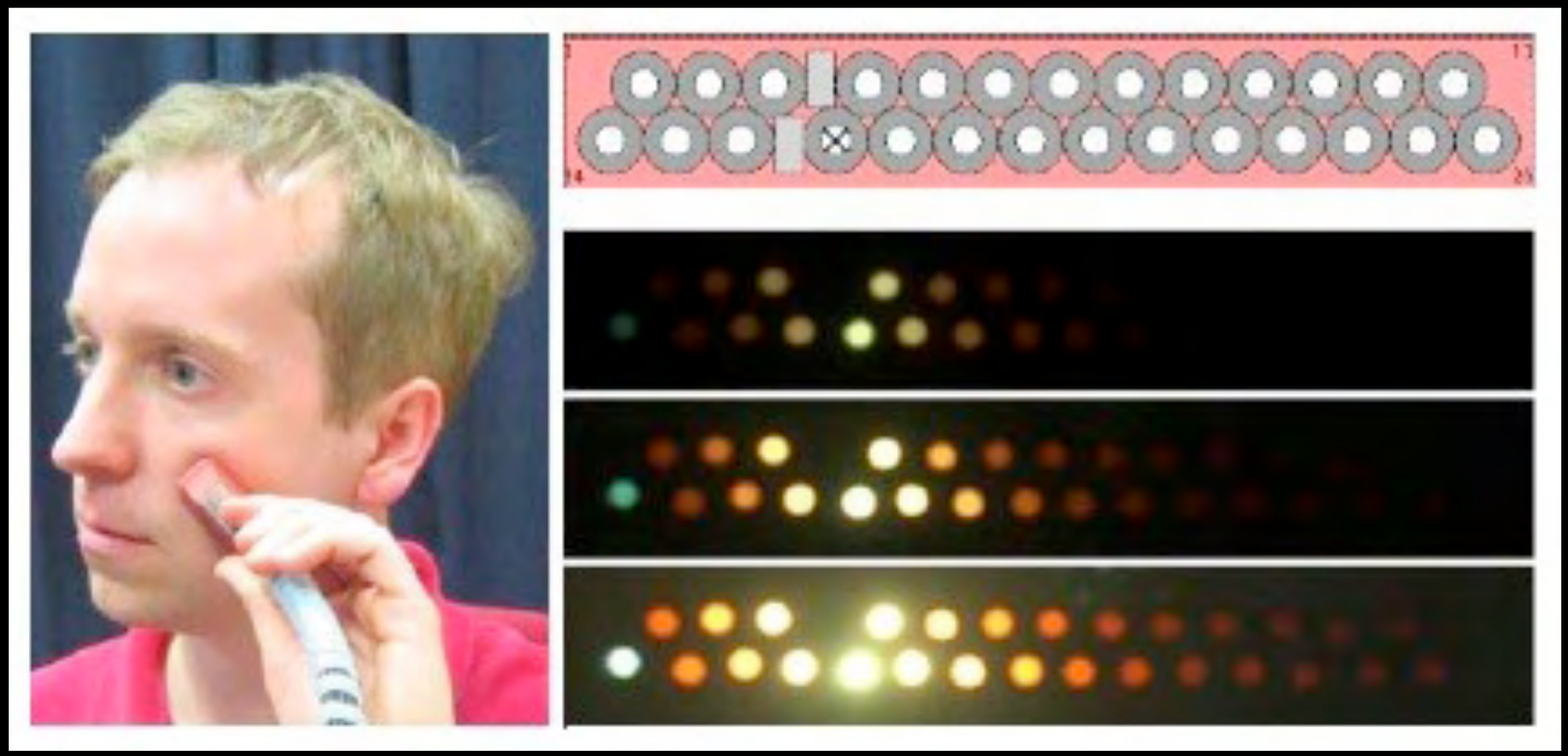

Weyrich et al. 2006

Measured profiles

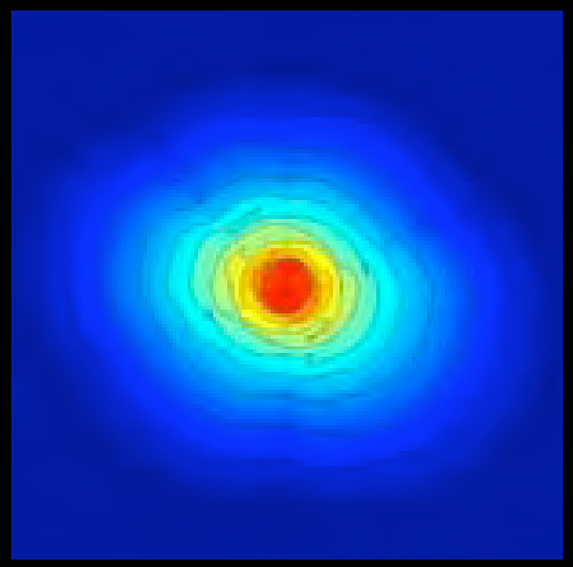

Abdomen

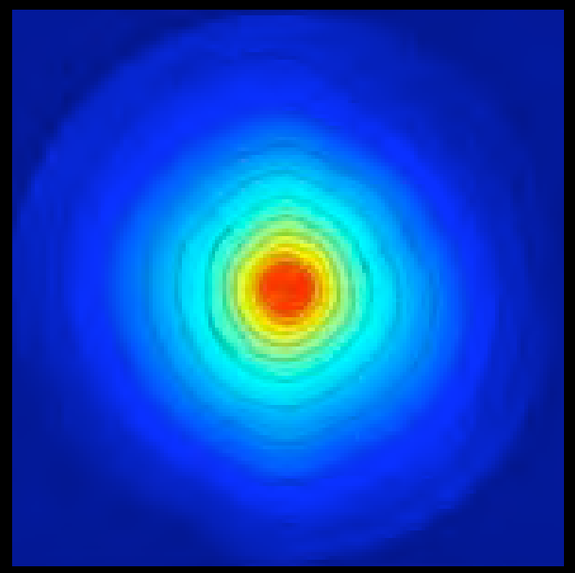

Cheek

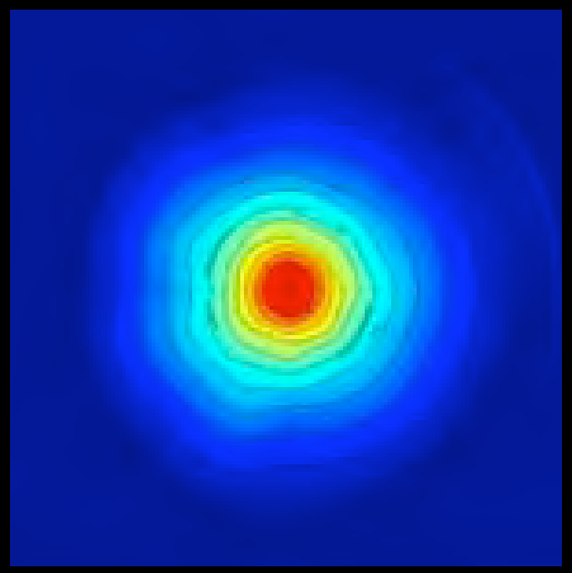

Forehead

Photo

Rendering

Weyrich et al. 2006

Thin materials

Layered materials

Diffusion dipole

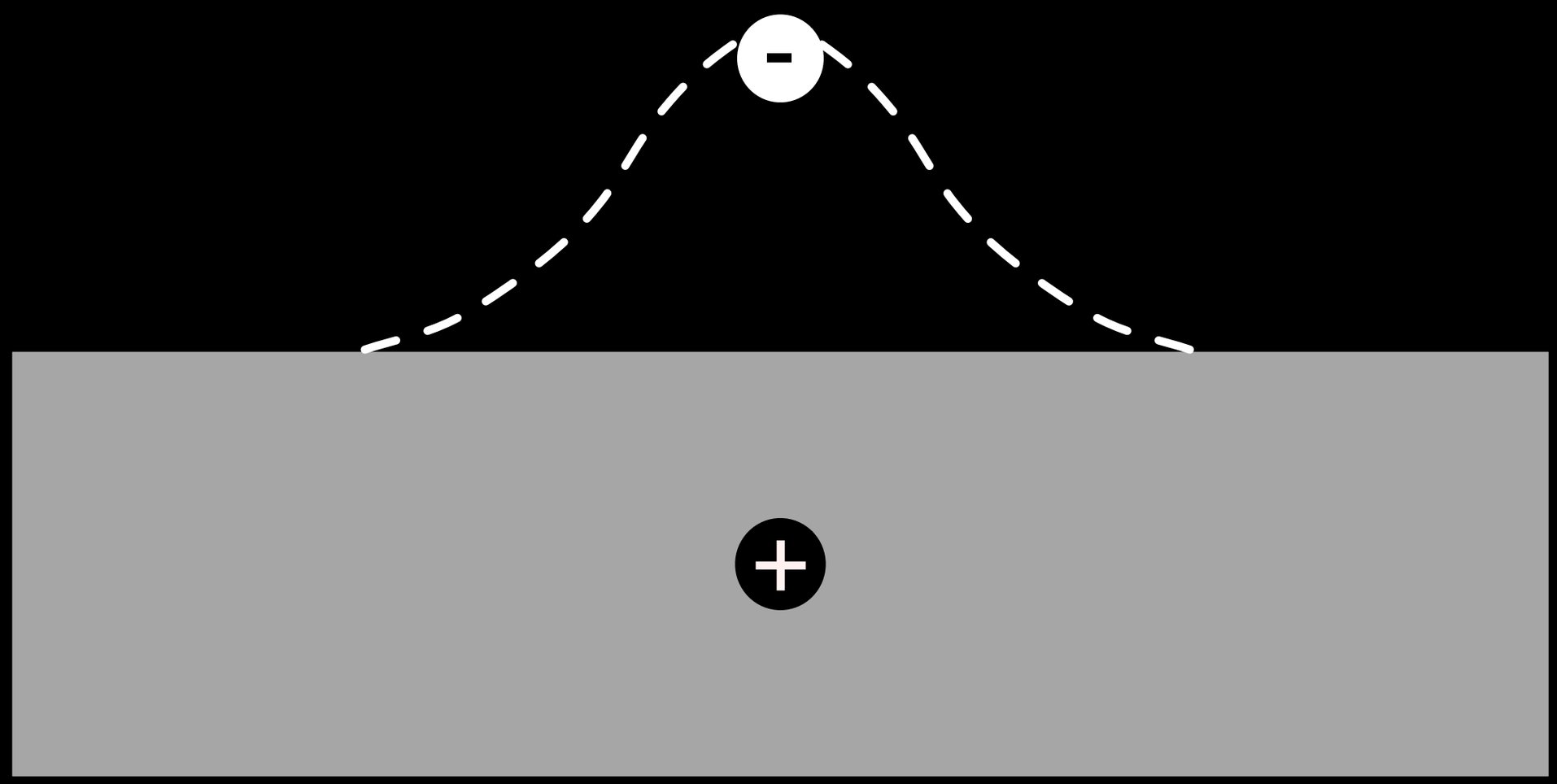

Diffusion dipole

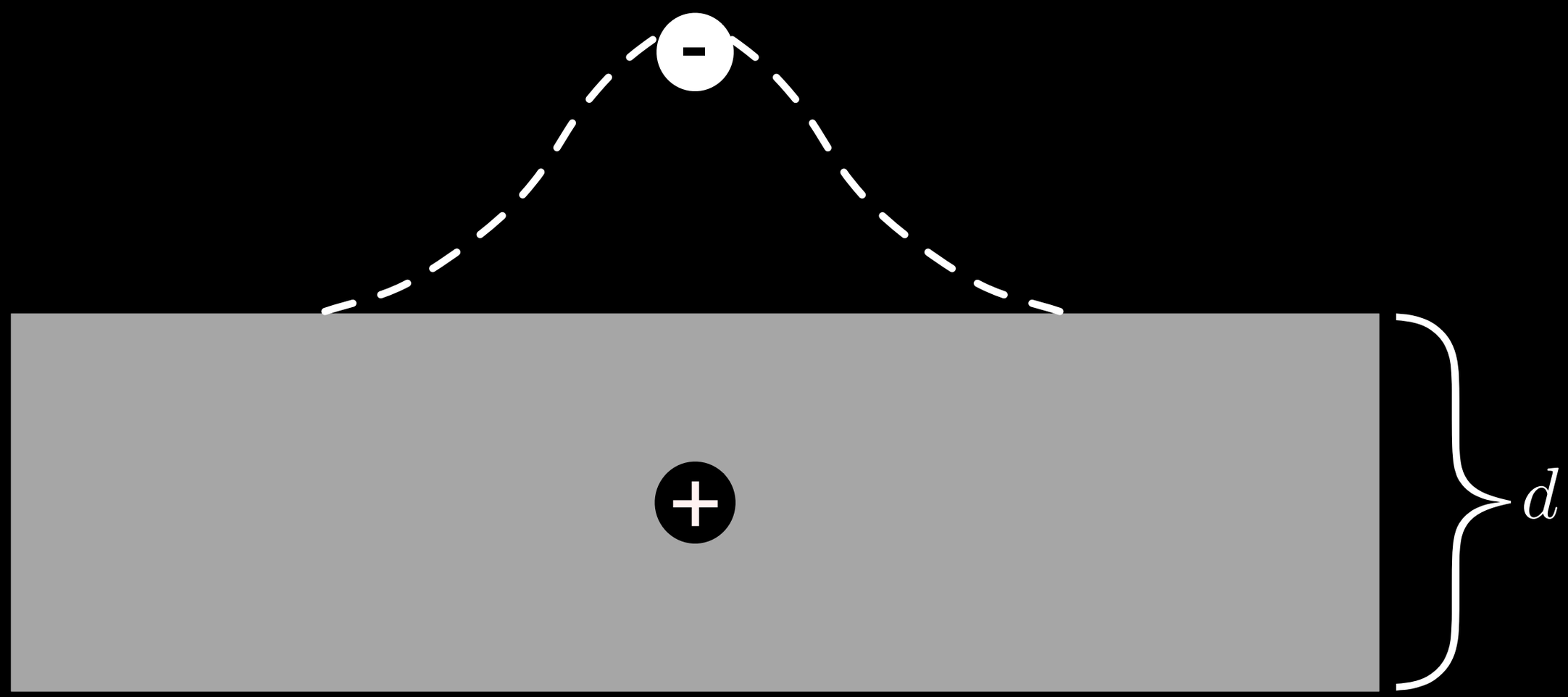

Dipole - reflectance

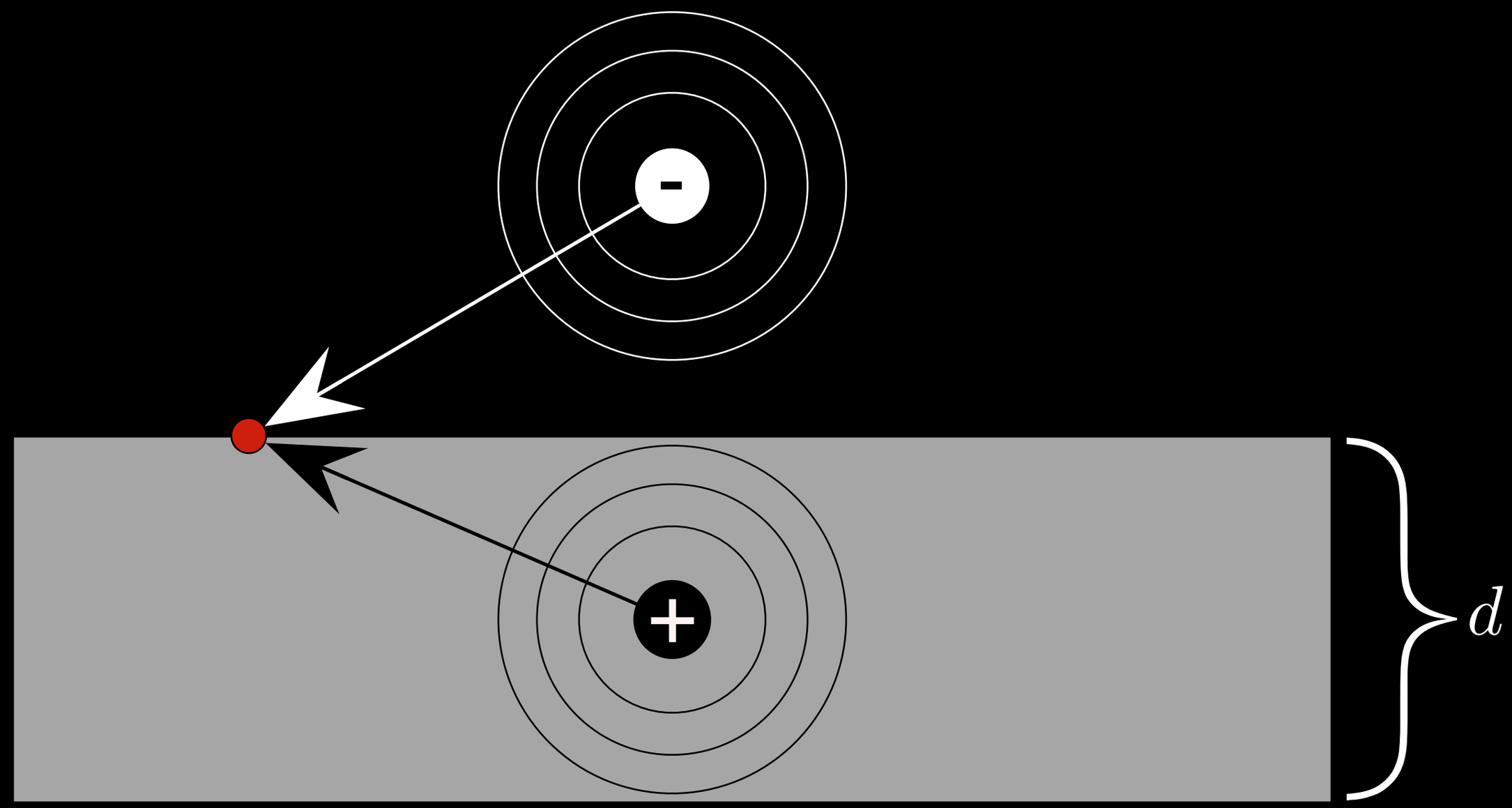

Dipole - transmittance?

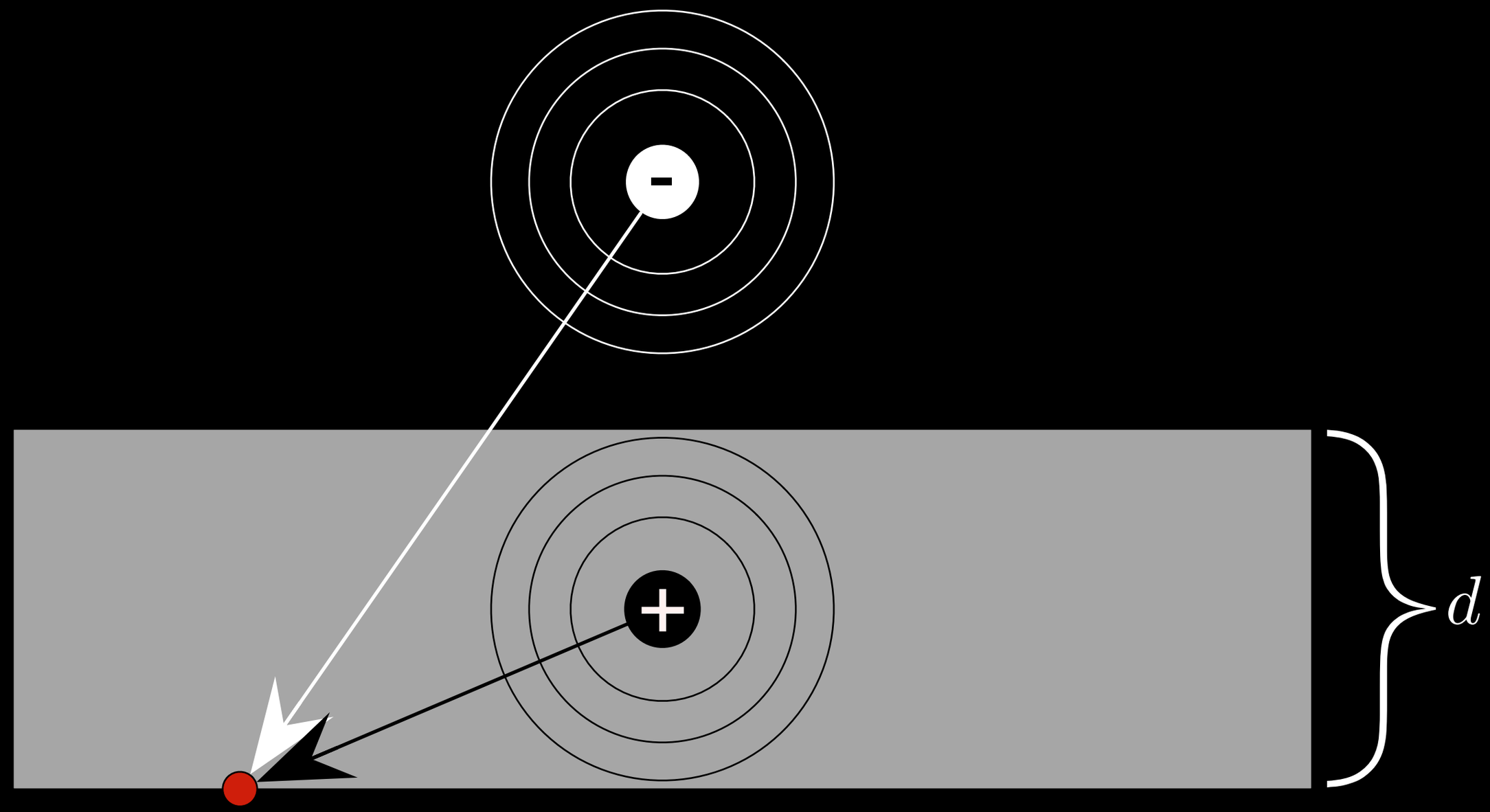

Dipole limitation

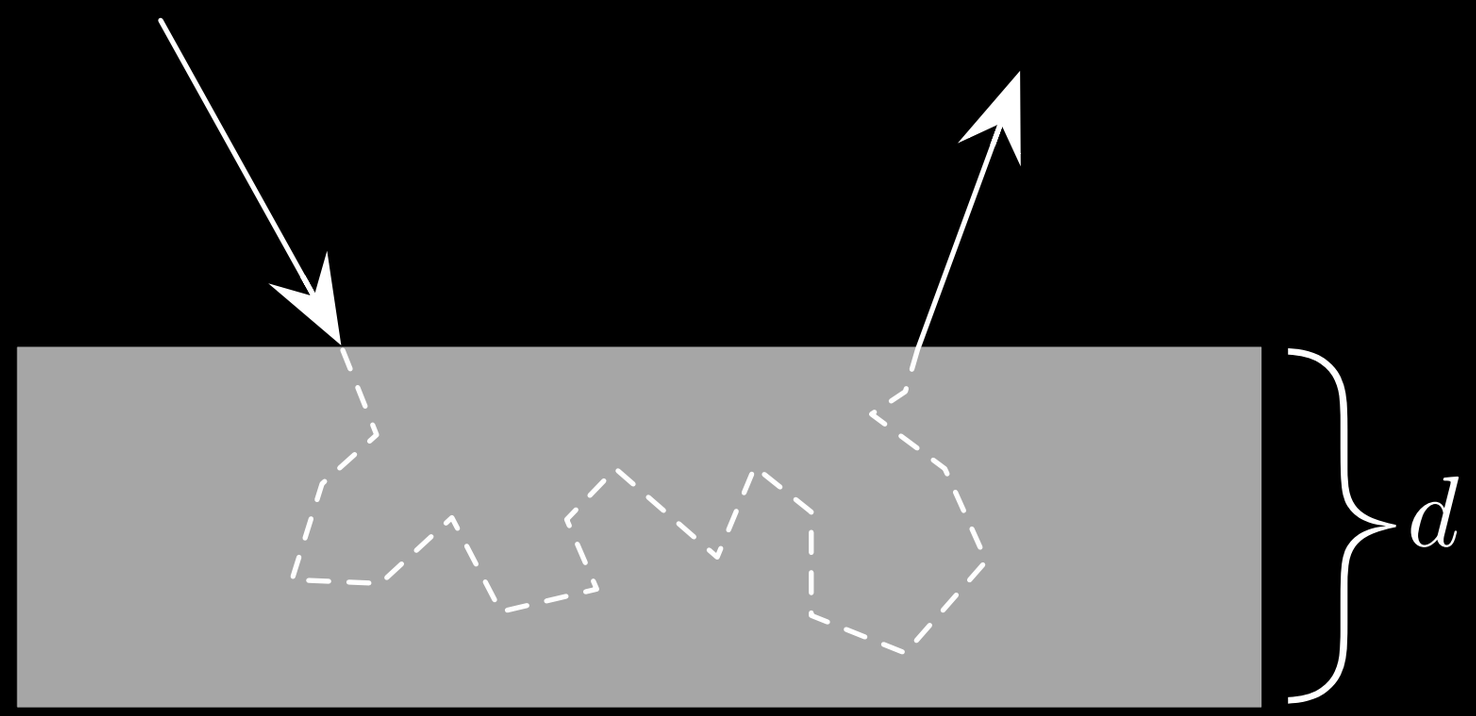

Dipole limitation

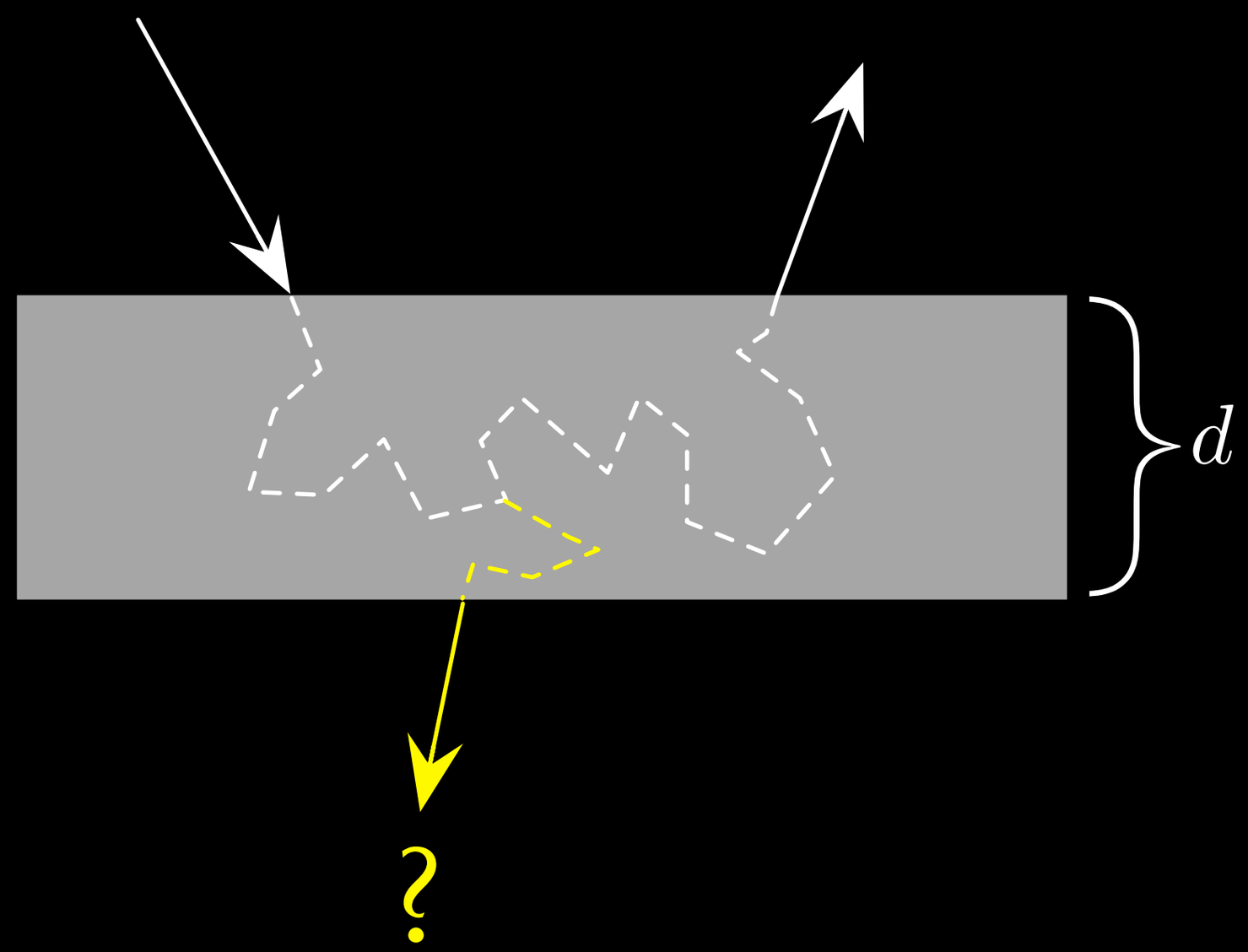

Boundary conditions

Boundary
Conditions

Boundary conditions

Boundary conditions

Boundary conditions

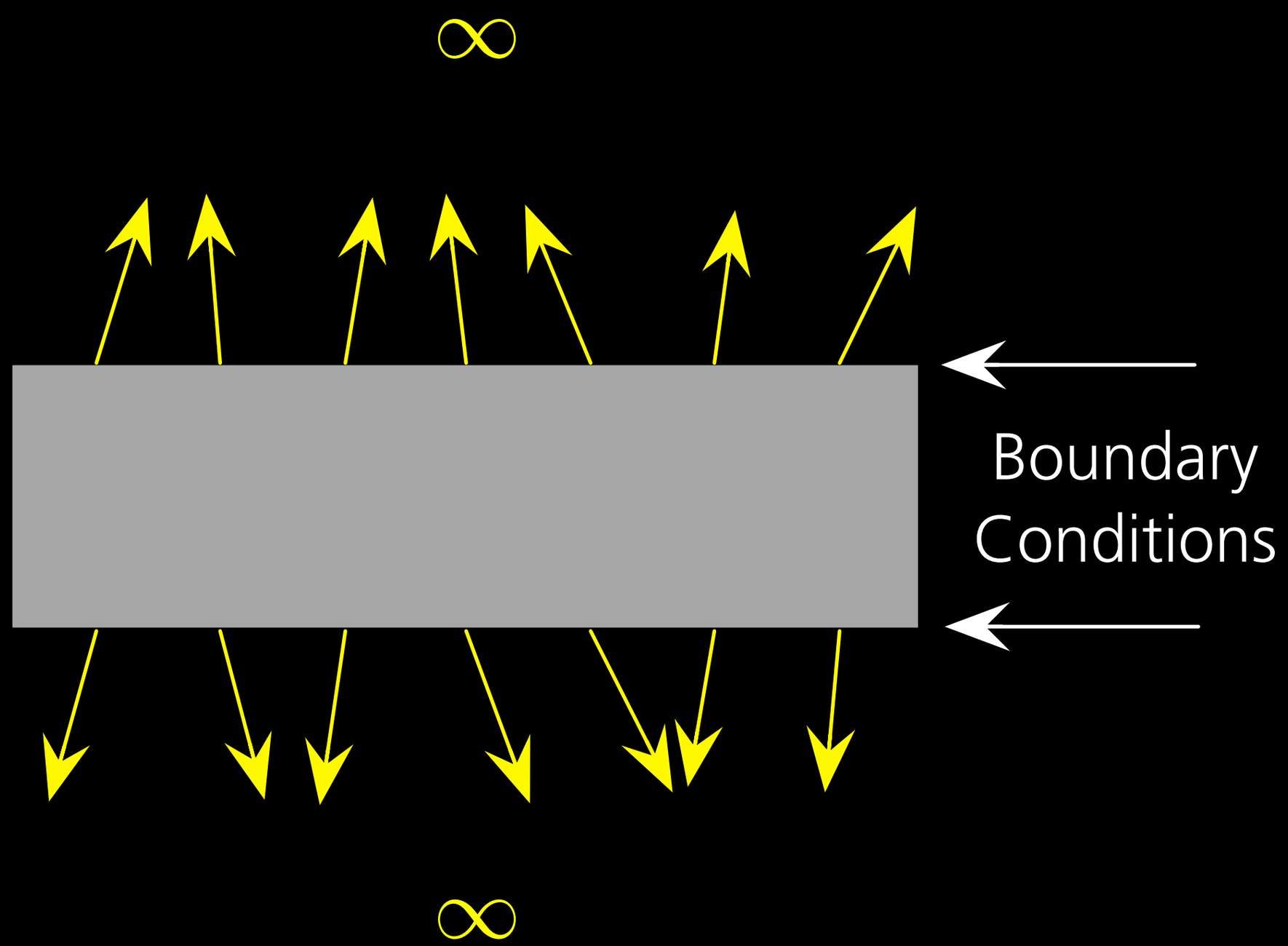

Boundary conditions

$$\int_{\Omega+} L_d(r, \vec{\omega})(-\vec{n} \cdot \vec{\omega})\, d\vec{\omega}$$

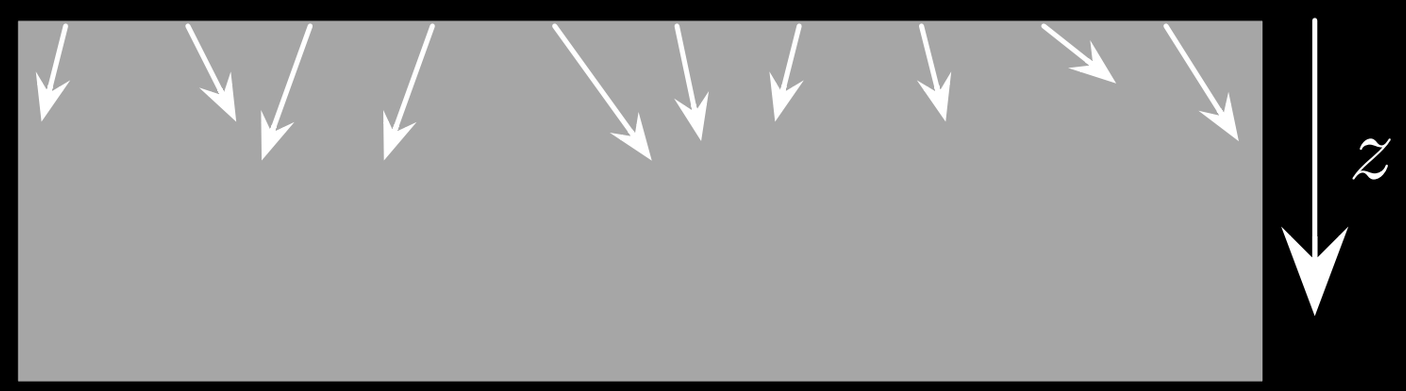

Boundary conditions

$$\int_{\Omega+} L_d(r,\vec{\omega})(-\vec{n}\cdot\vec{\omega})\ d\vec{\omega} = F_{dr}\int_{\Omega-} L_d(r,\vec{\omega})(\vec{n}\cdot\vec{\omega})\ d\vec{\omega}$$

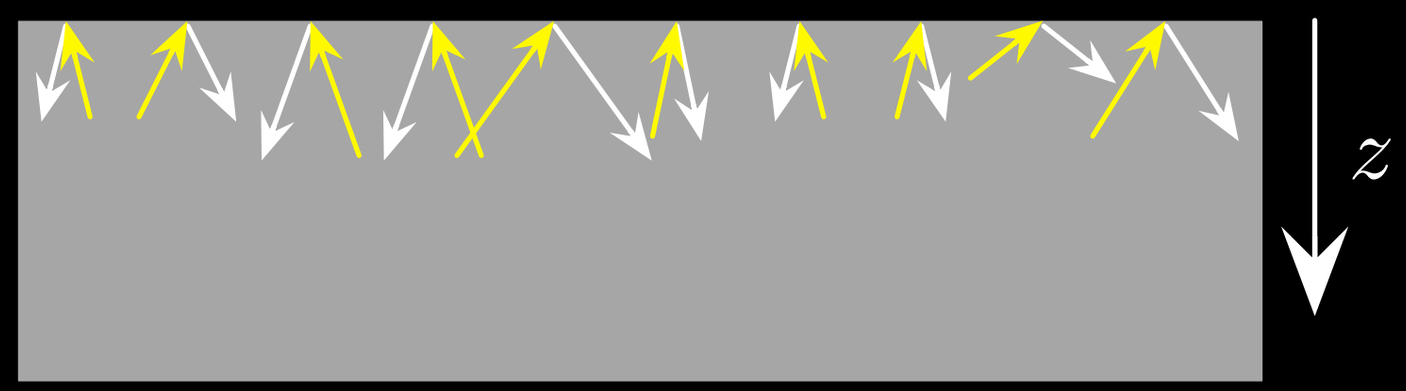

Boundary conditions

F_{dr} = Diffuse Fresnel Reflectance

$$\int_{\Omega+} L_d(r,\vec{\omega})(-\vec{n}\cdot\vec{\omega})\ d\vec{\omega} = F_{dr}\int_{\Omega-} L_d(r,\vec{\omega})(\vec{n}\cdot\vec{\omega})\ d\vec{\omega}$$

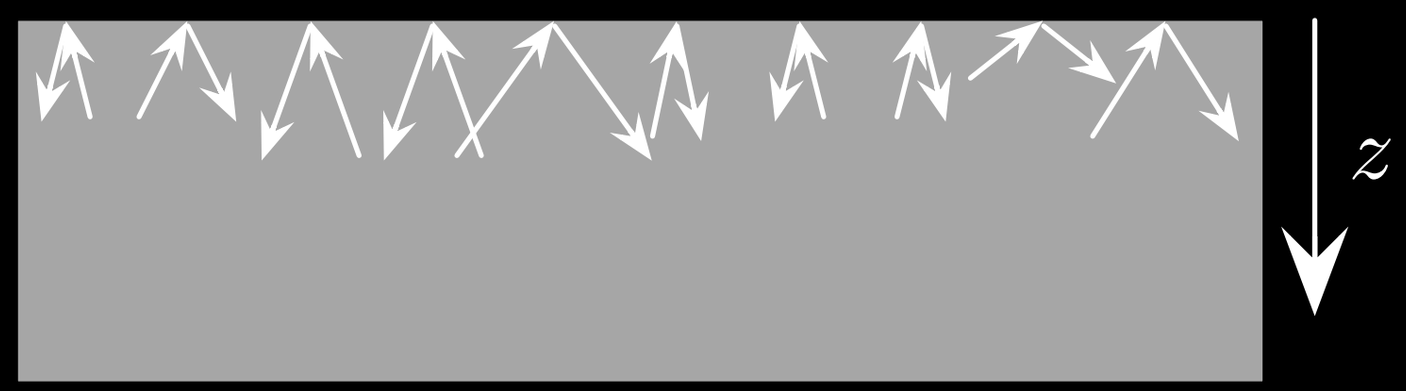

Boundary conditions

$$\int_{\Omega+} L_d(r,\vec{\omega})(-\vec{n}\cdot\vec{\omega})\ d\vec{\omega} = F_{dr}\int_{\Omega-} L_d(r,\vec{\omega})(\vec{n}\cdot\vec{\omega})\ d\vec{\omega}$$

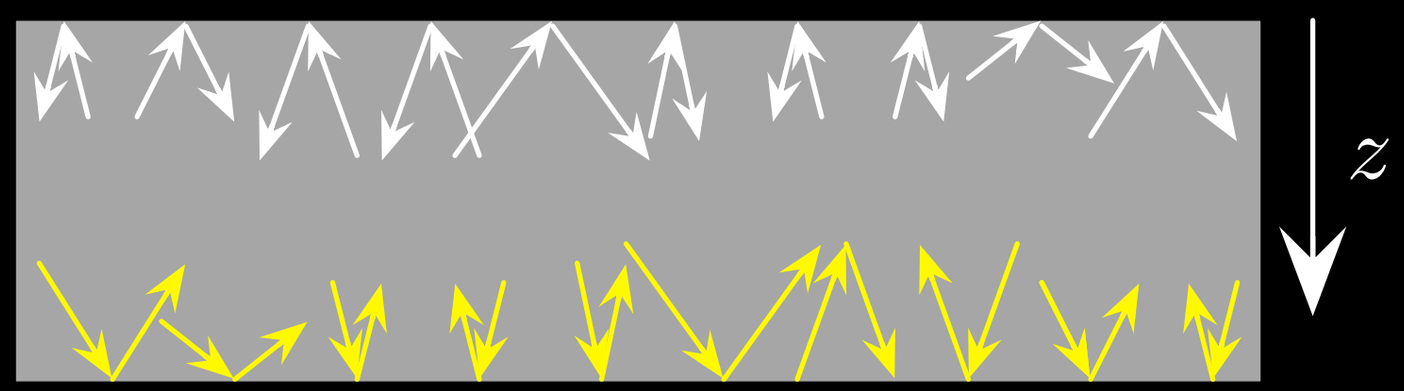

$$\int_{\Omega-} L_d(r,\vec{\omega})(\vec{n}\cdot\vec{\omega})\ d\vec{\omega} = F_{dr}\int_{\Omega+} L_d(r,\vec{\omega})(-\vec{n}\cdot\vec{\omega})\ d\vec{\omega}$$

Boundary conditions

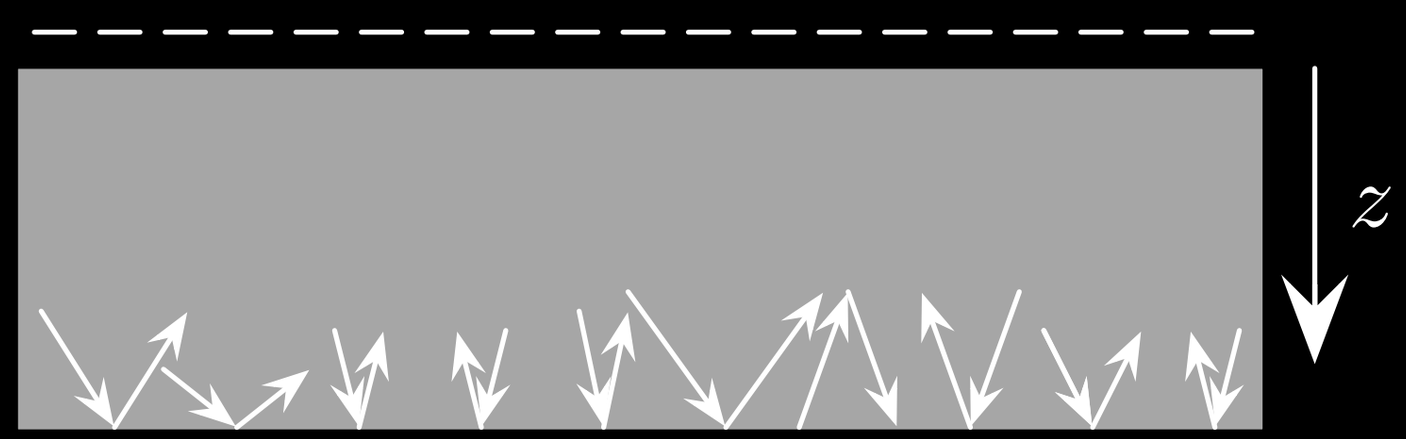

$$\int_{\Omega-} L_d(r,\vec{\omega})(\vec{n}\cdot\vec{\omega})\ d\vec{\omega} = F_{dr}\int_{\Omega+} L_d(r,\vec{\omega})(-\vec{n}\cdot\vec{\omega})\ d\vec{\omega}$$

Boundary conditions

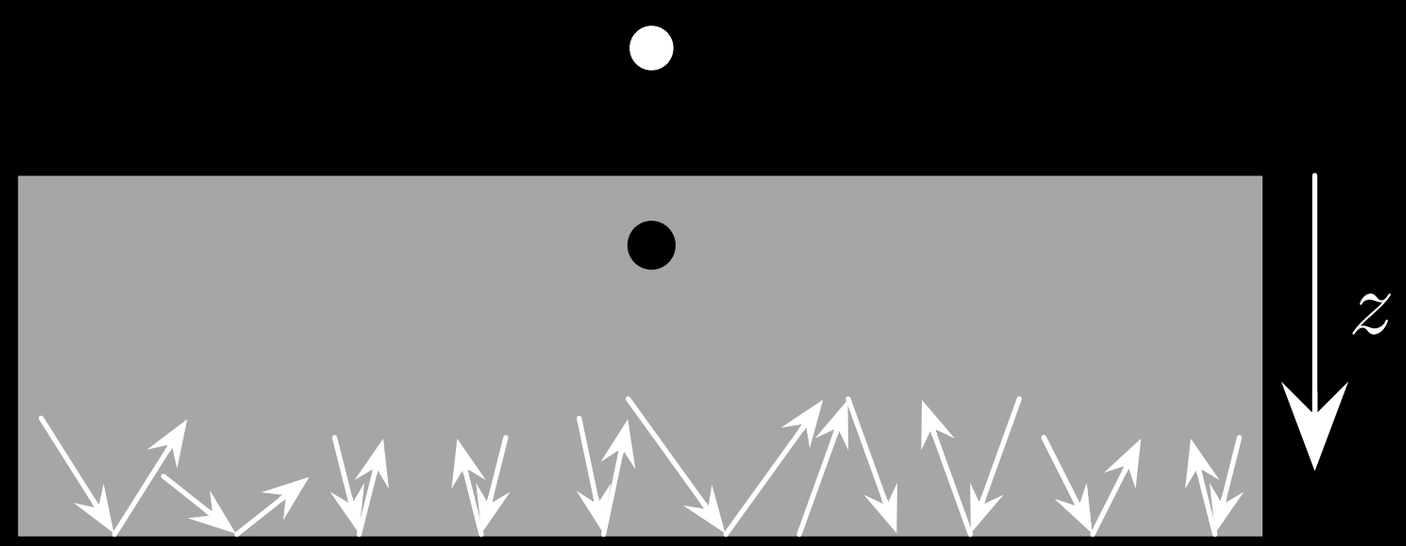

$$\int_{\Omega-} L_d(r,\vec{\omega})(\vec{n}\cdot\vec{\omega})\ d\vec{\omega} = F_{dr}\int_{\Omega+} L_d(r,\vec{\omega})(-\vec{n}\cdot\vec{\omega})\ d\vec{\omega}$$

Boundary conditions

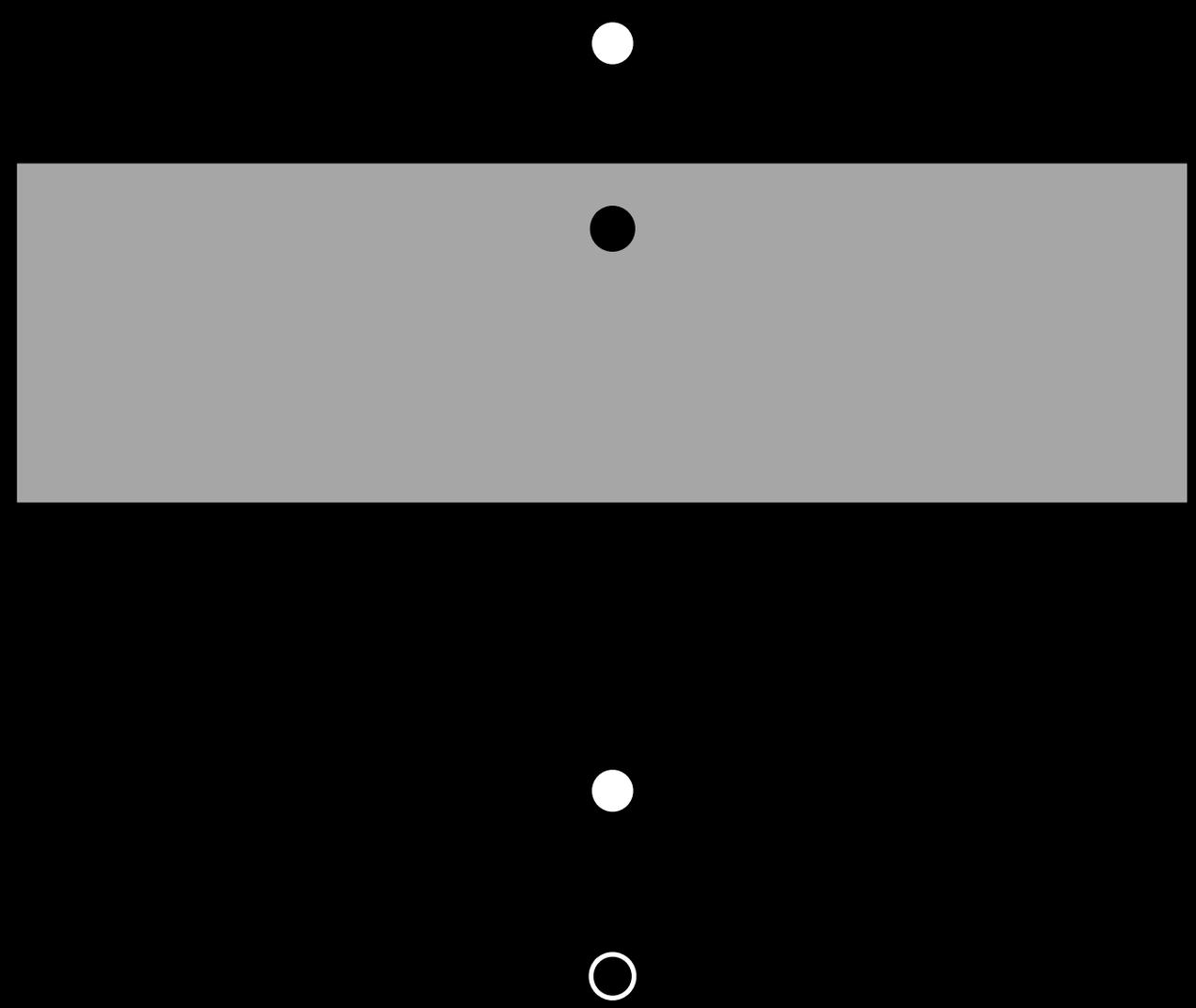

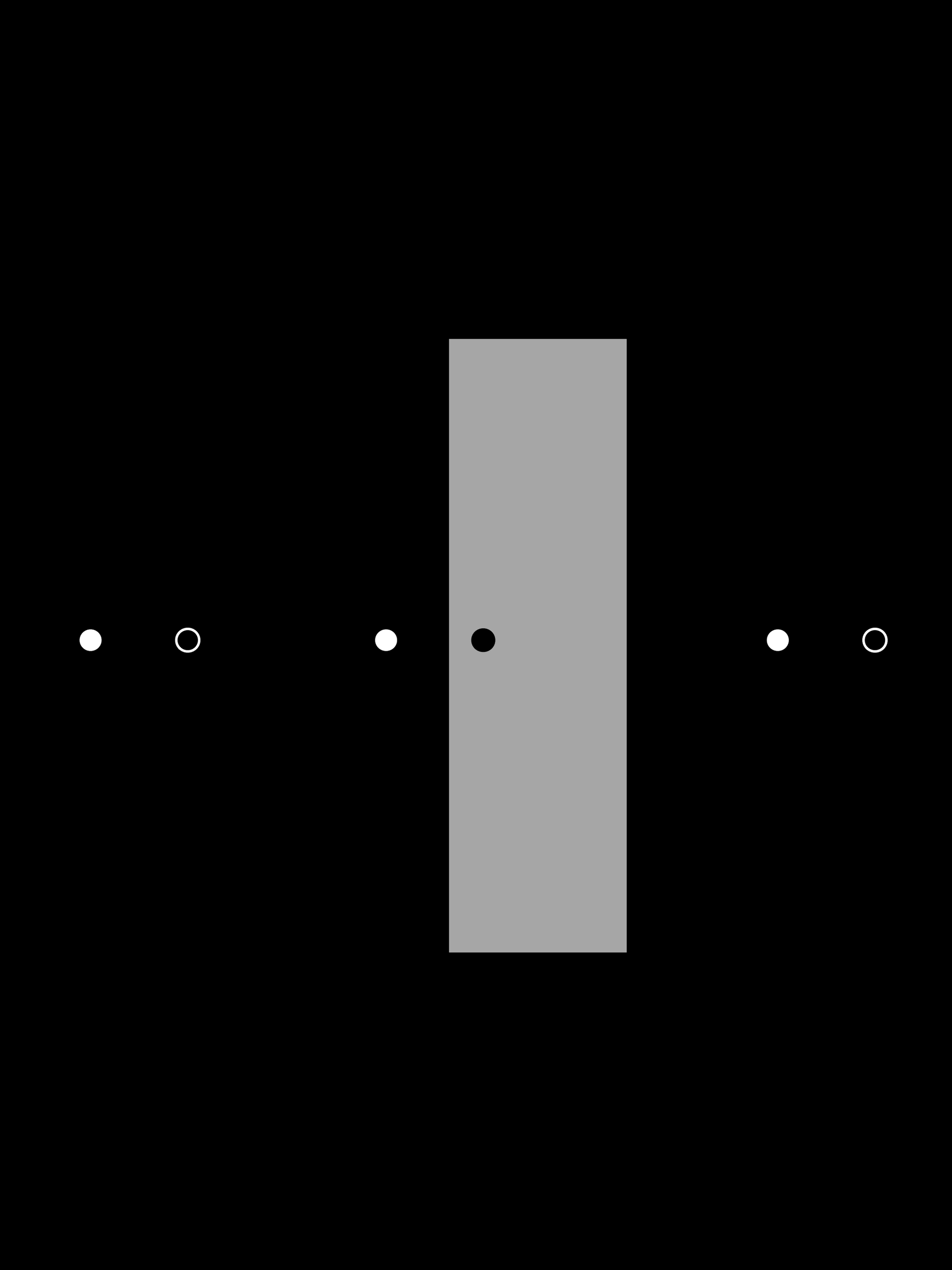

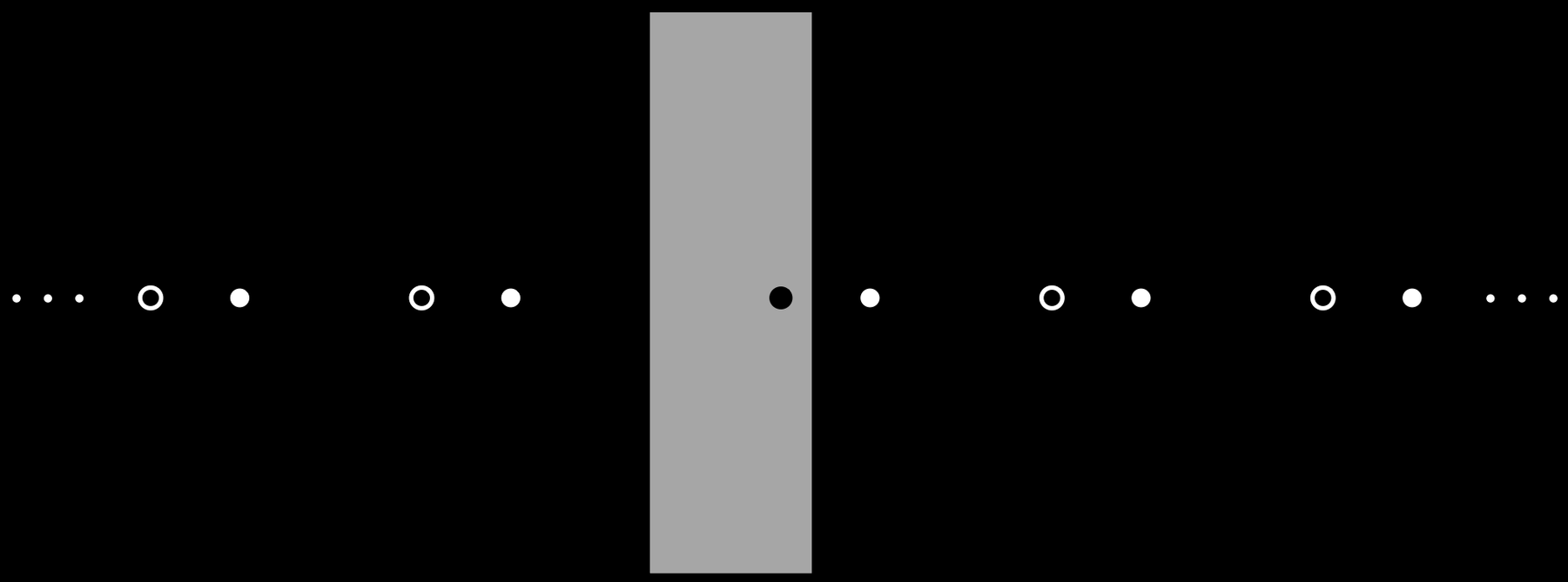

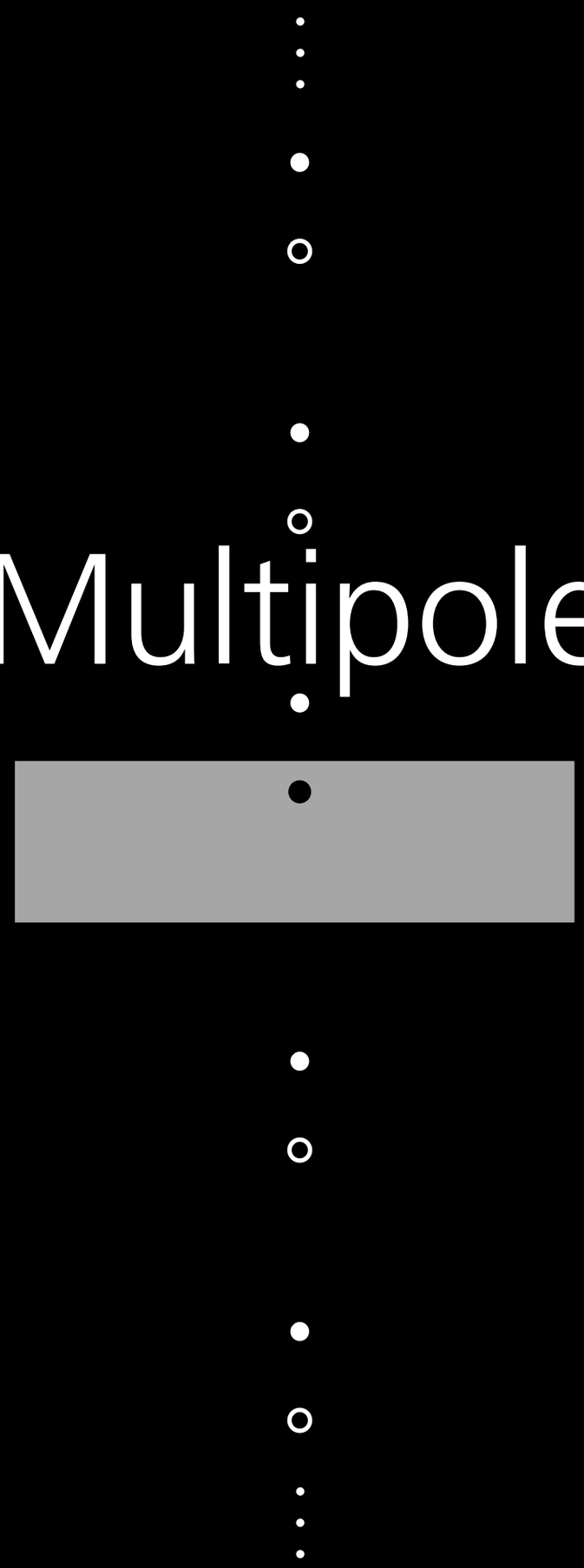

Multipole

Dipole vs Multipole

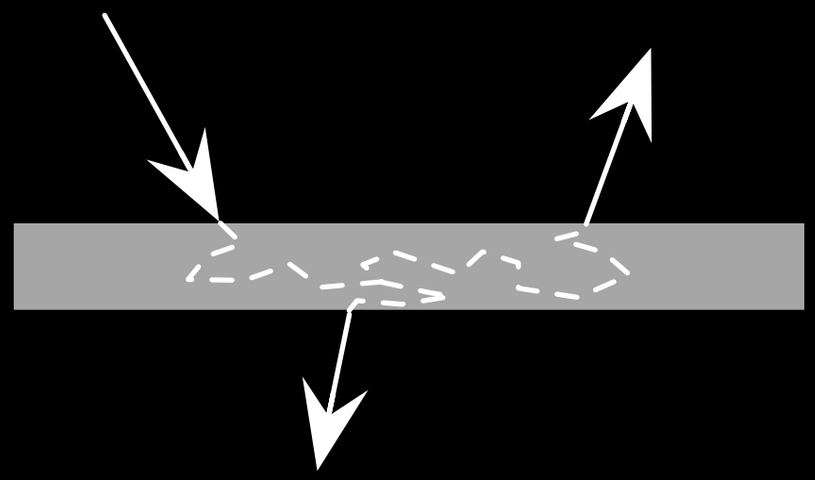

2 mean free paths

Dipole vs Multipole

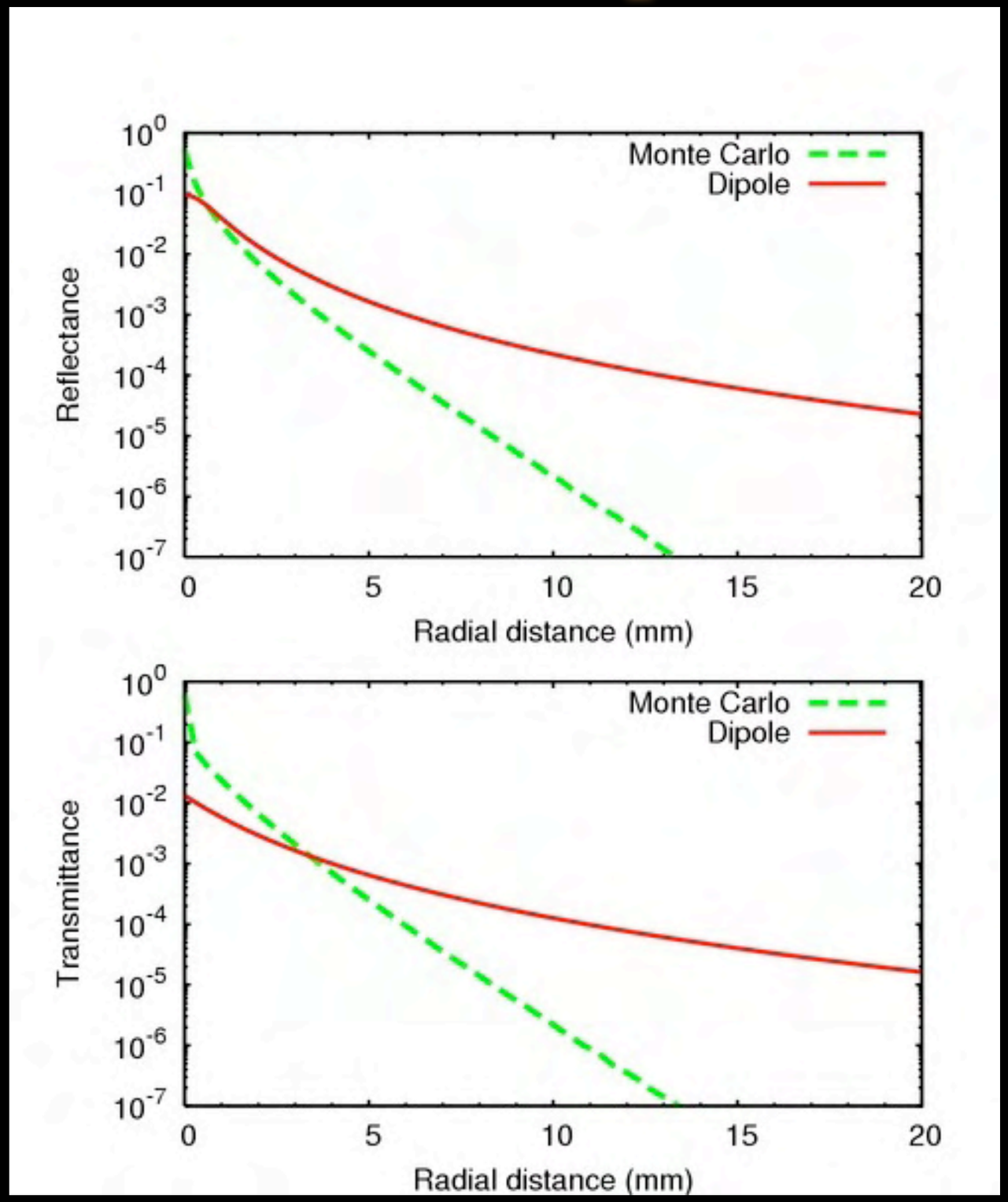

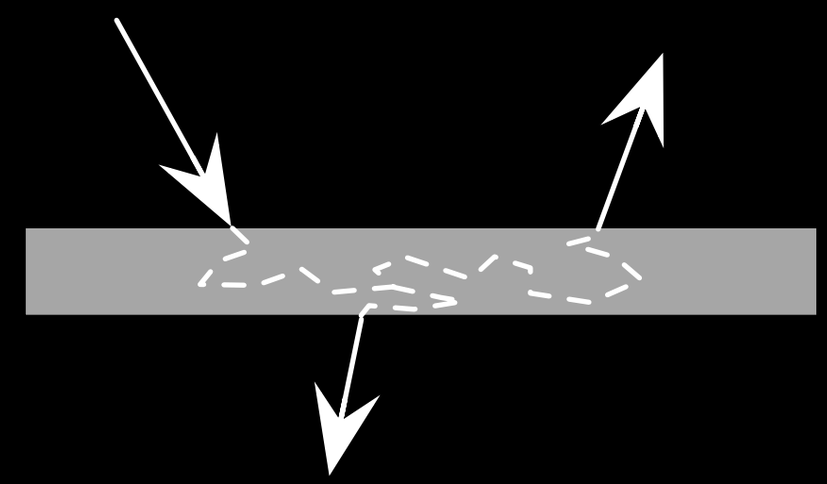

2 mean free paths

Dipole vs Multipole

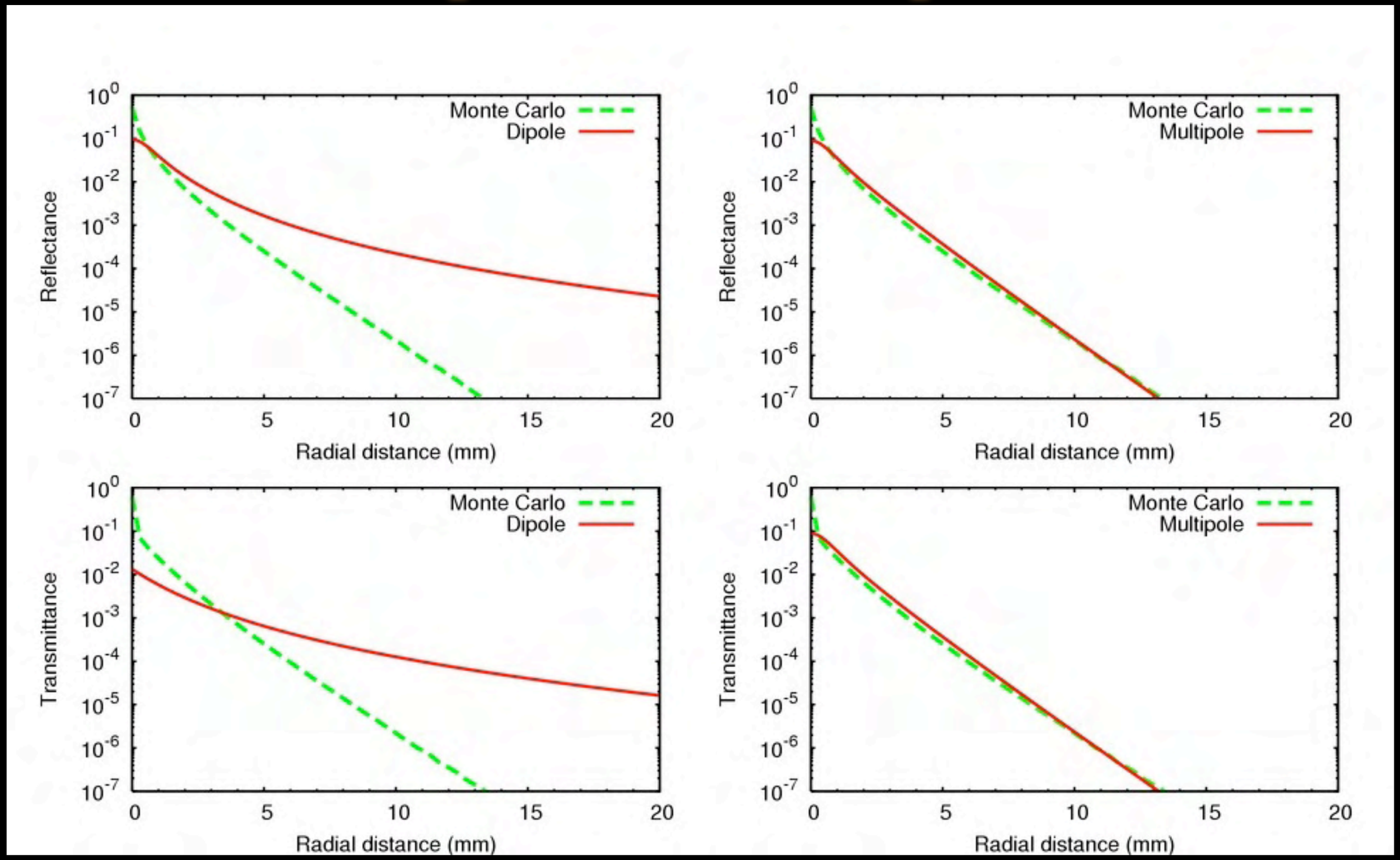

2 mean free paths

Dipole vs Multipole

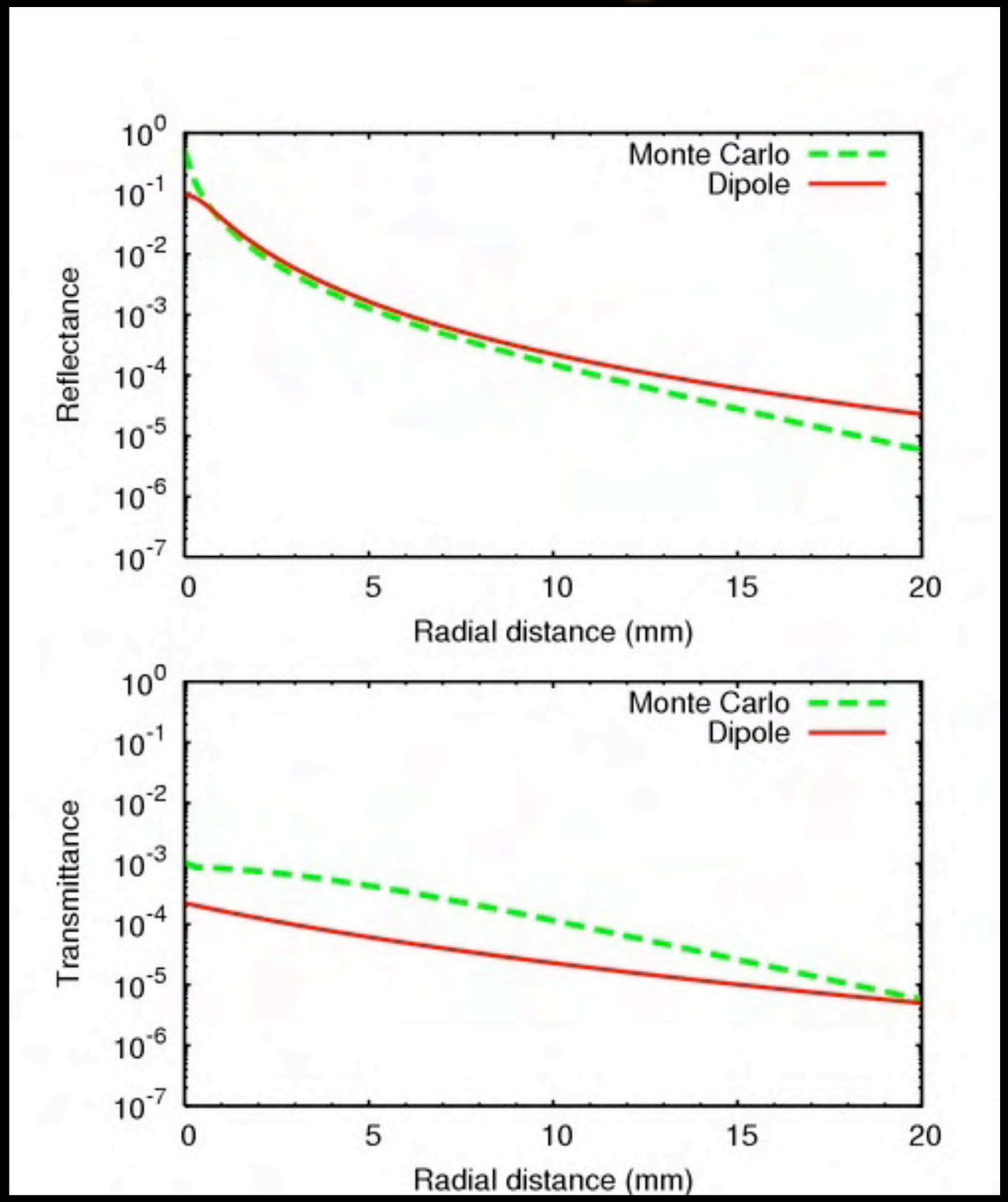

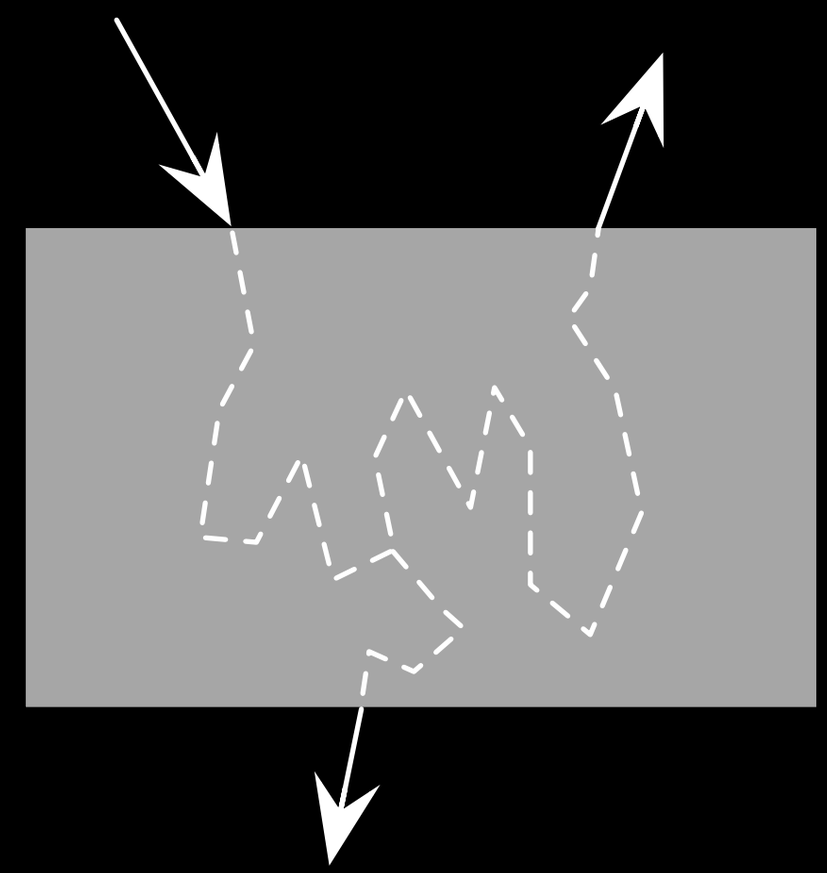

10 mean free paths

Dipole vs Multipole

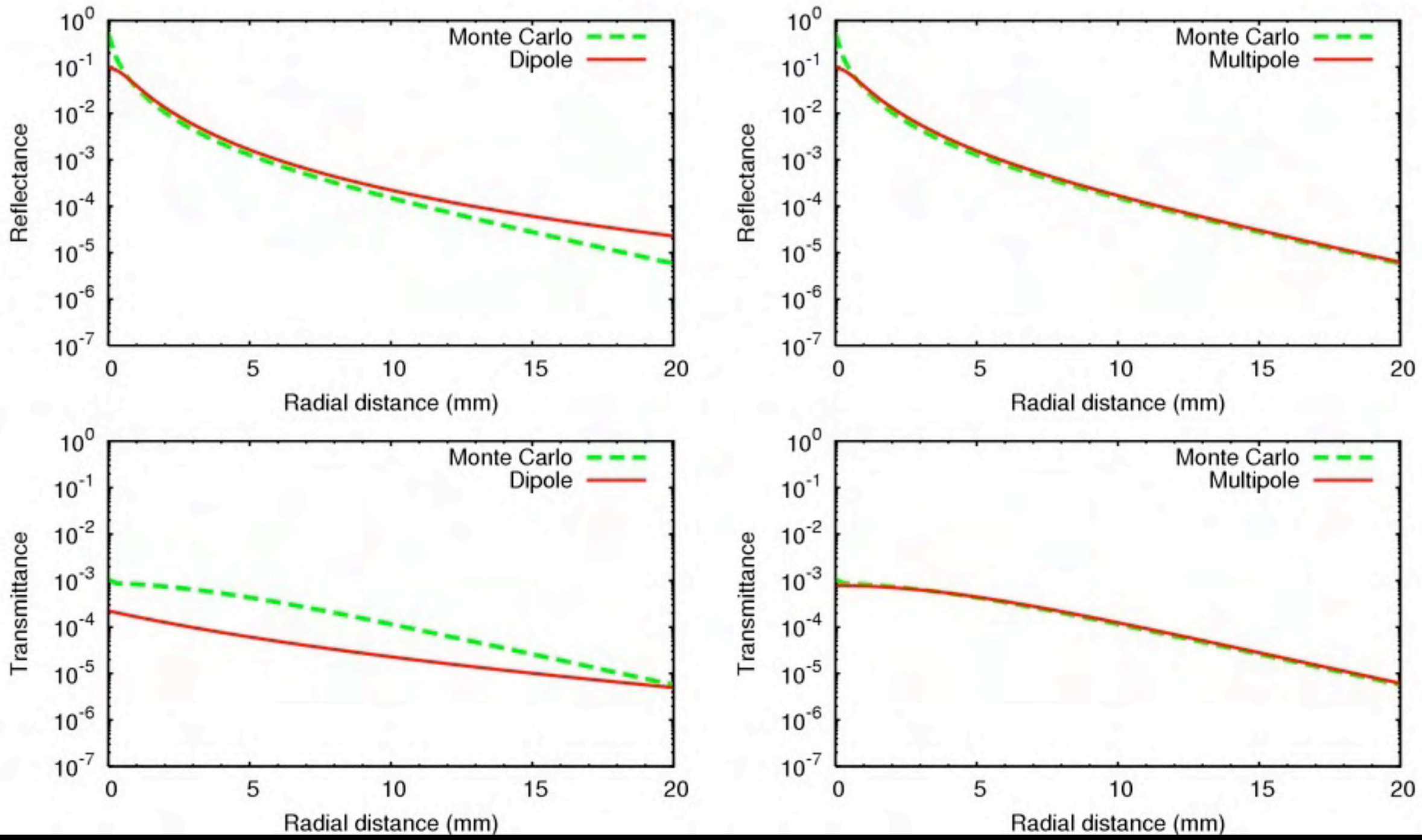

10 mean free paths

Dipole vs Multipole

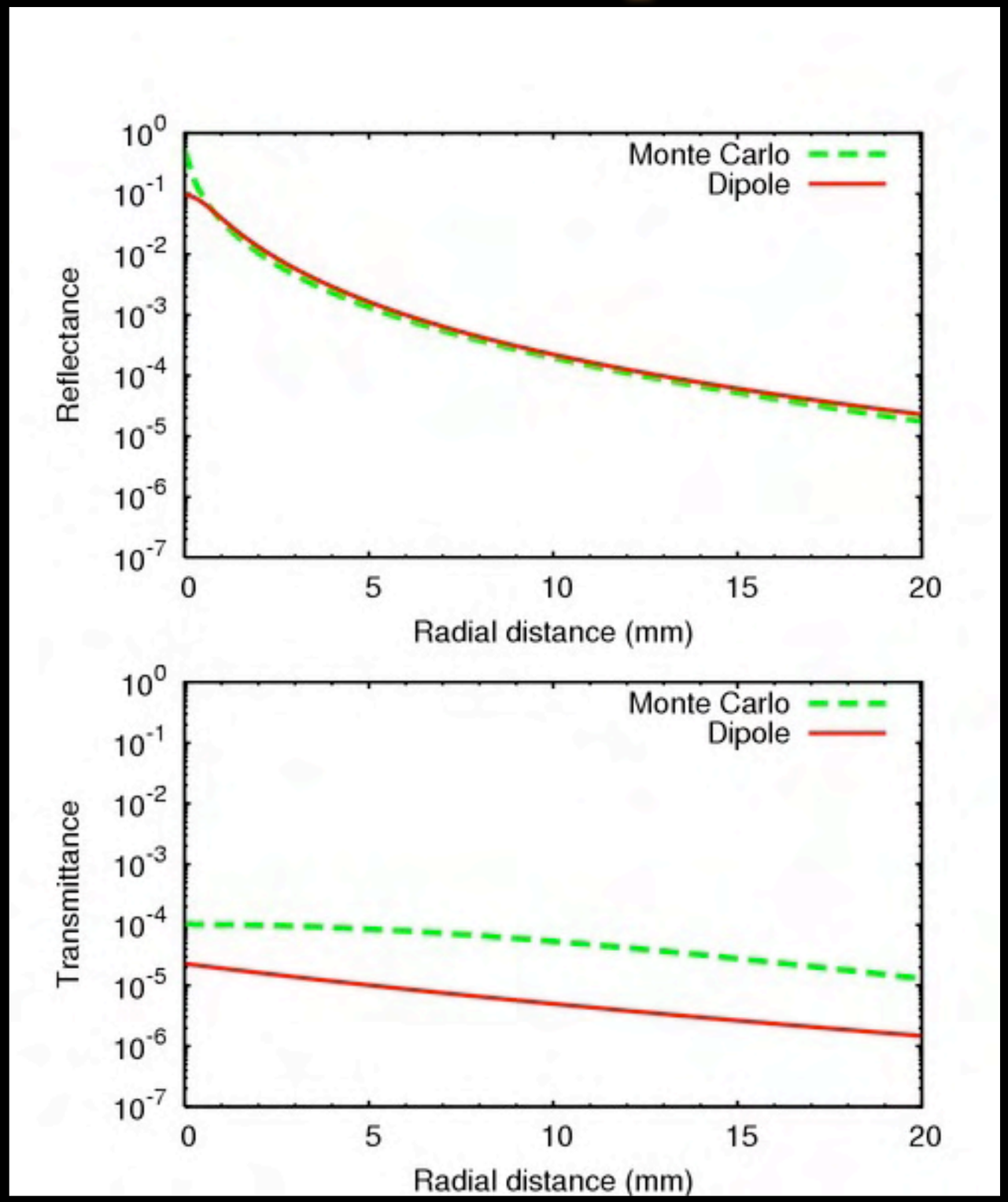

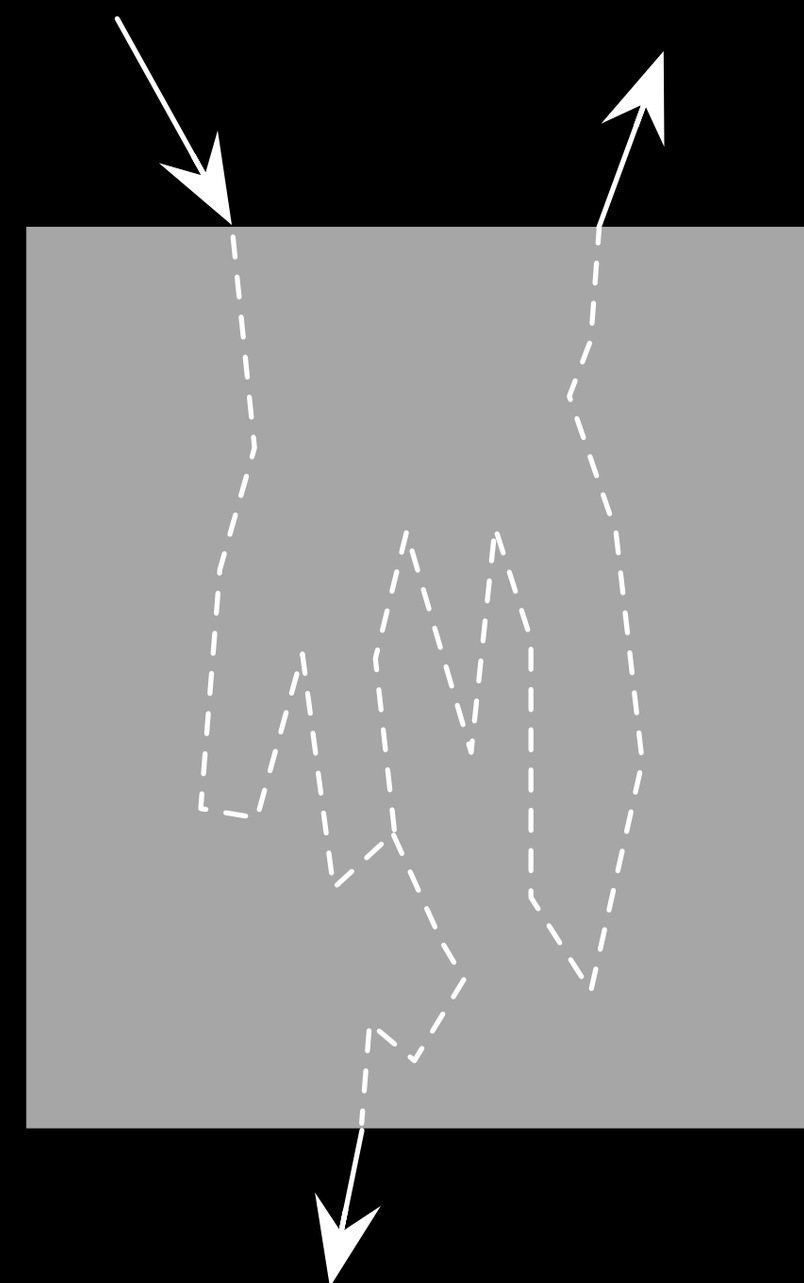

20 mean free paths

Dipole vs Multipole

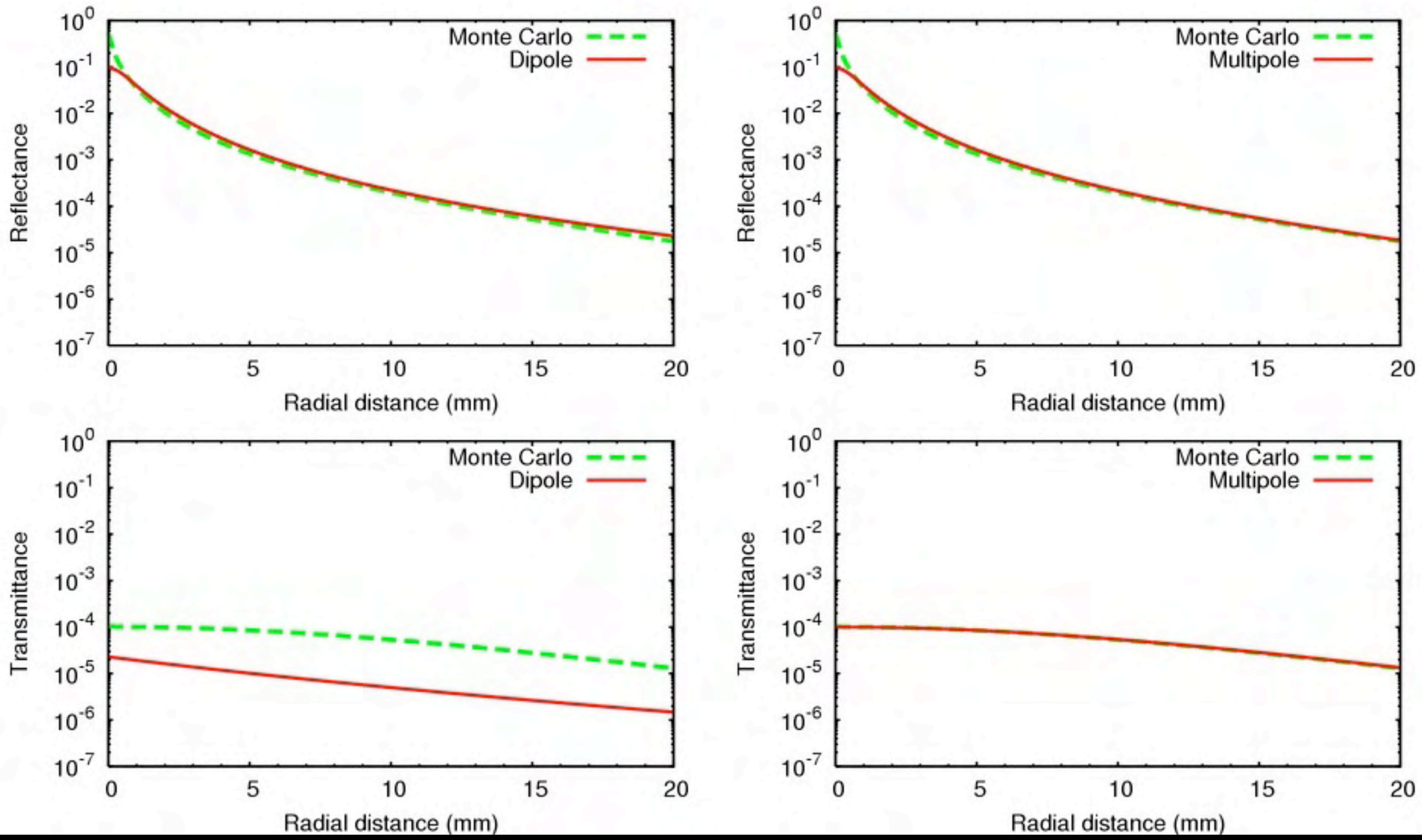

20 mean free paths

Monte Carlo

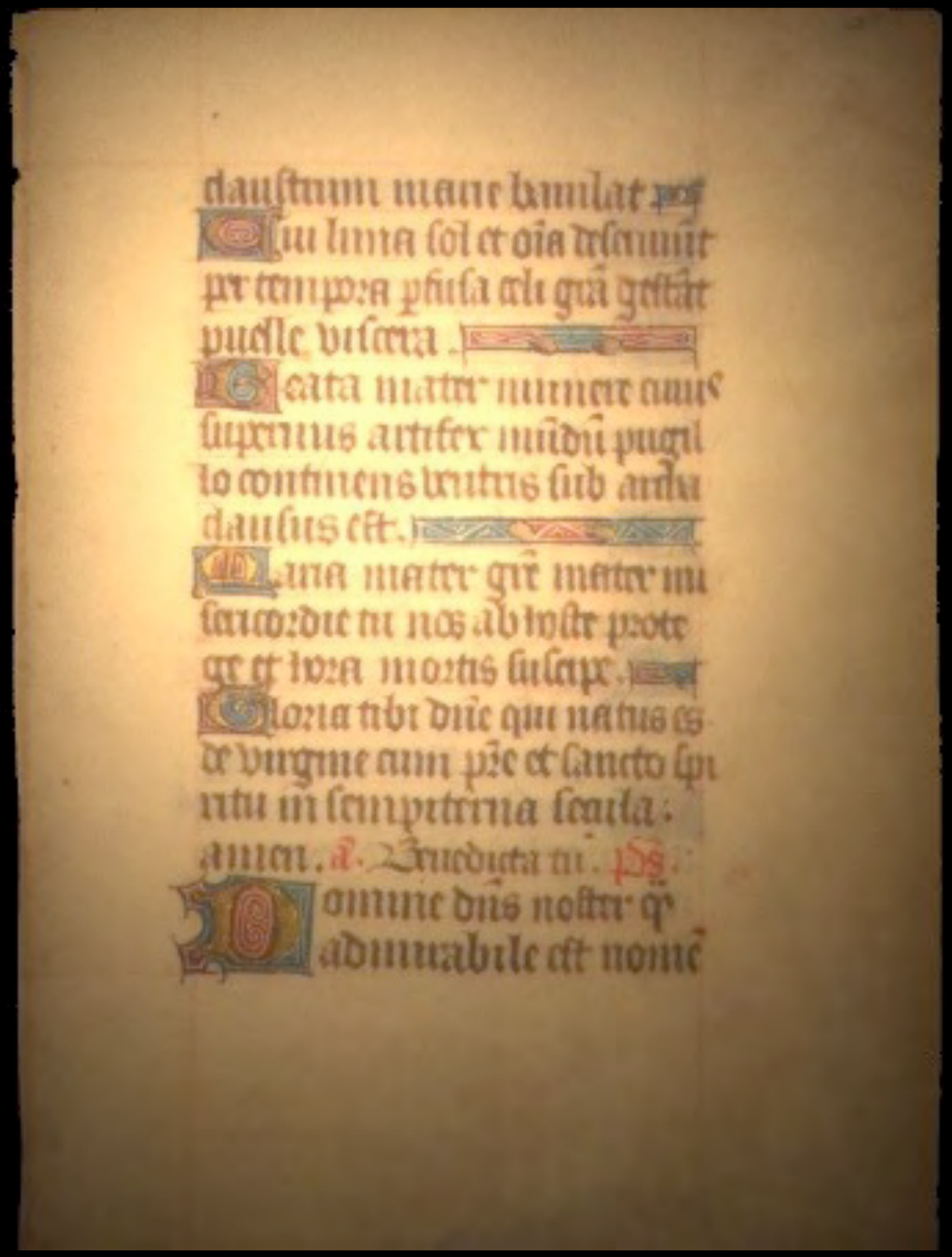

Model courtesy XYZRGB and Paul Debevec

Dipole

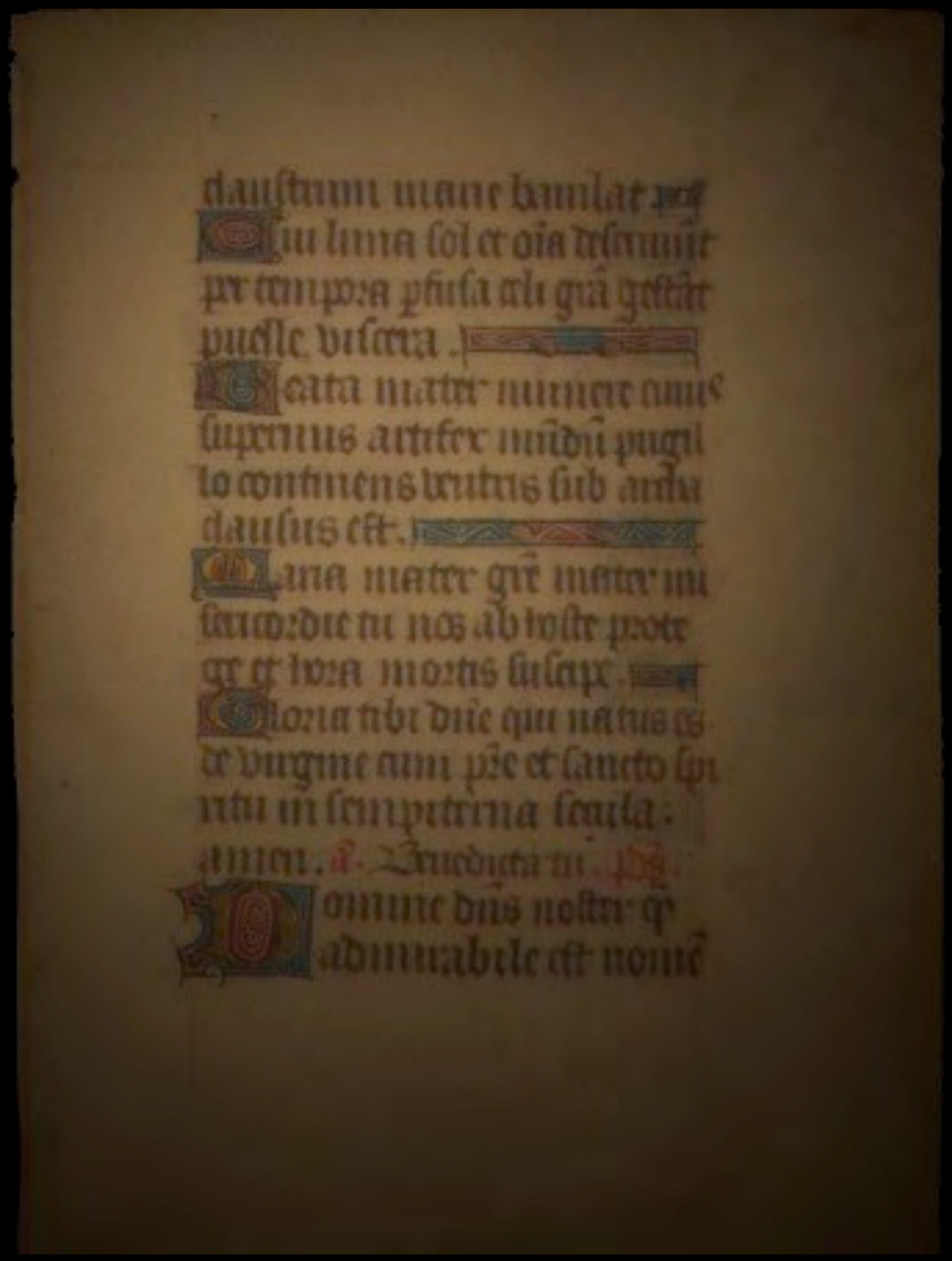

Monte Carlo

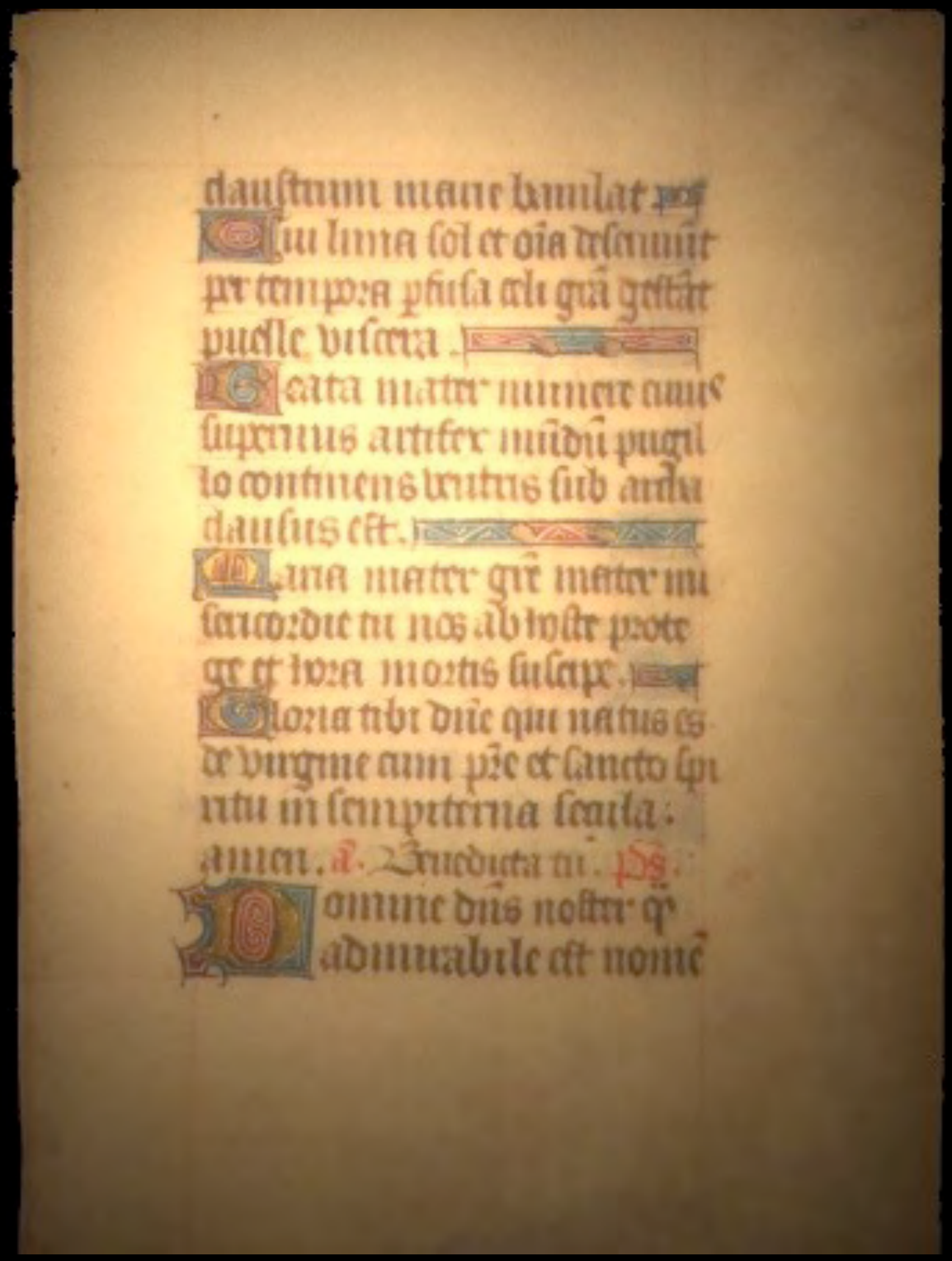

Model courtesy XYZRGB and Paul Debevec

Multipole

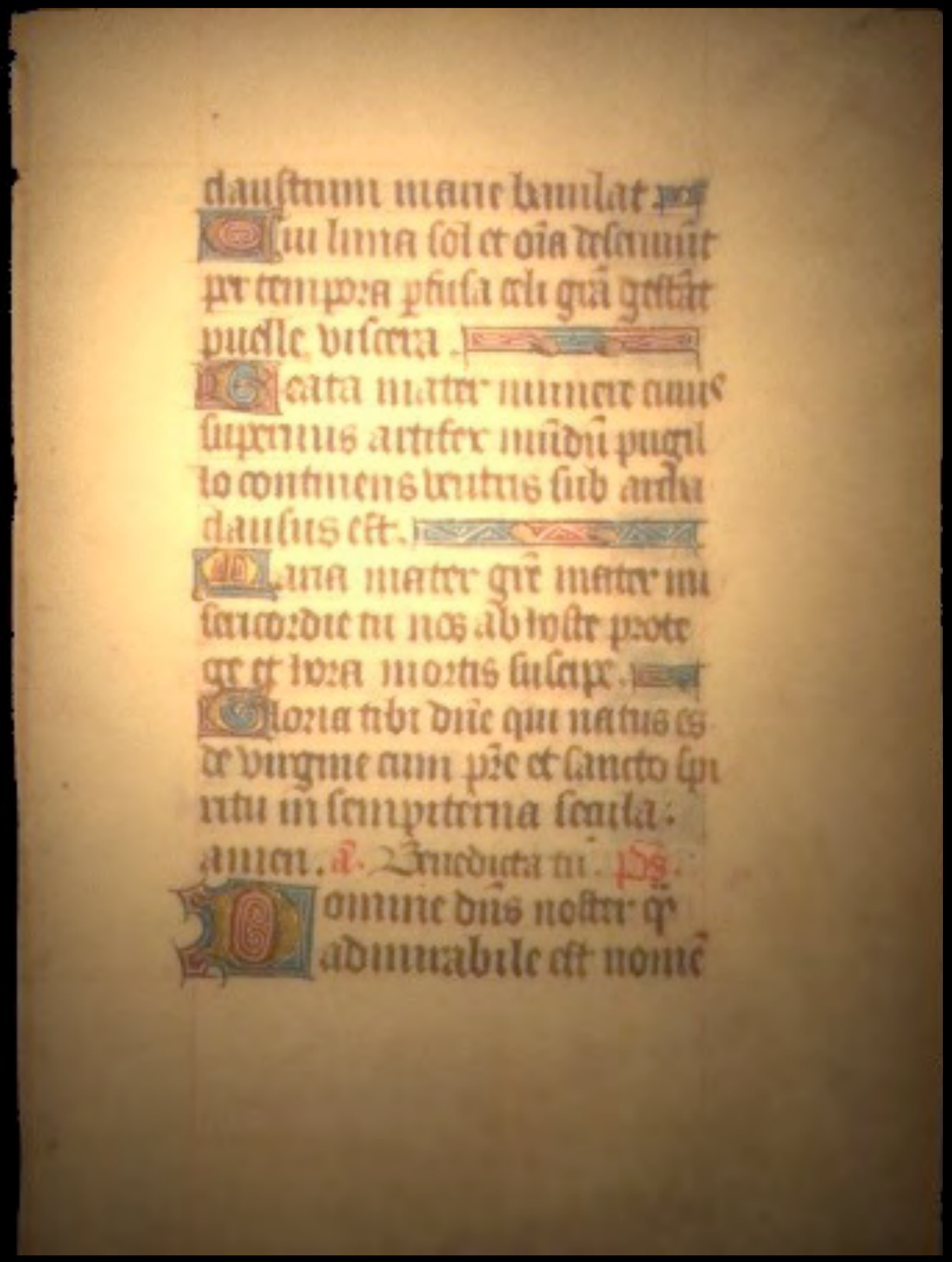

Monte Carlo

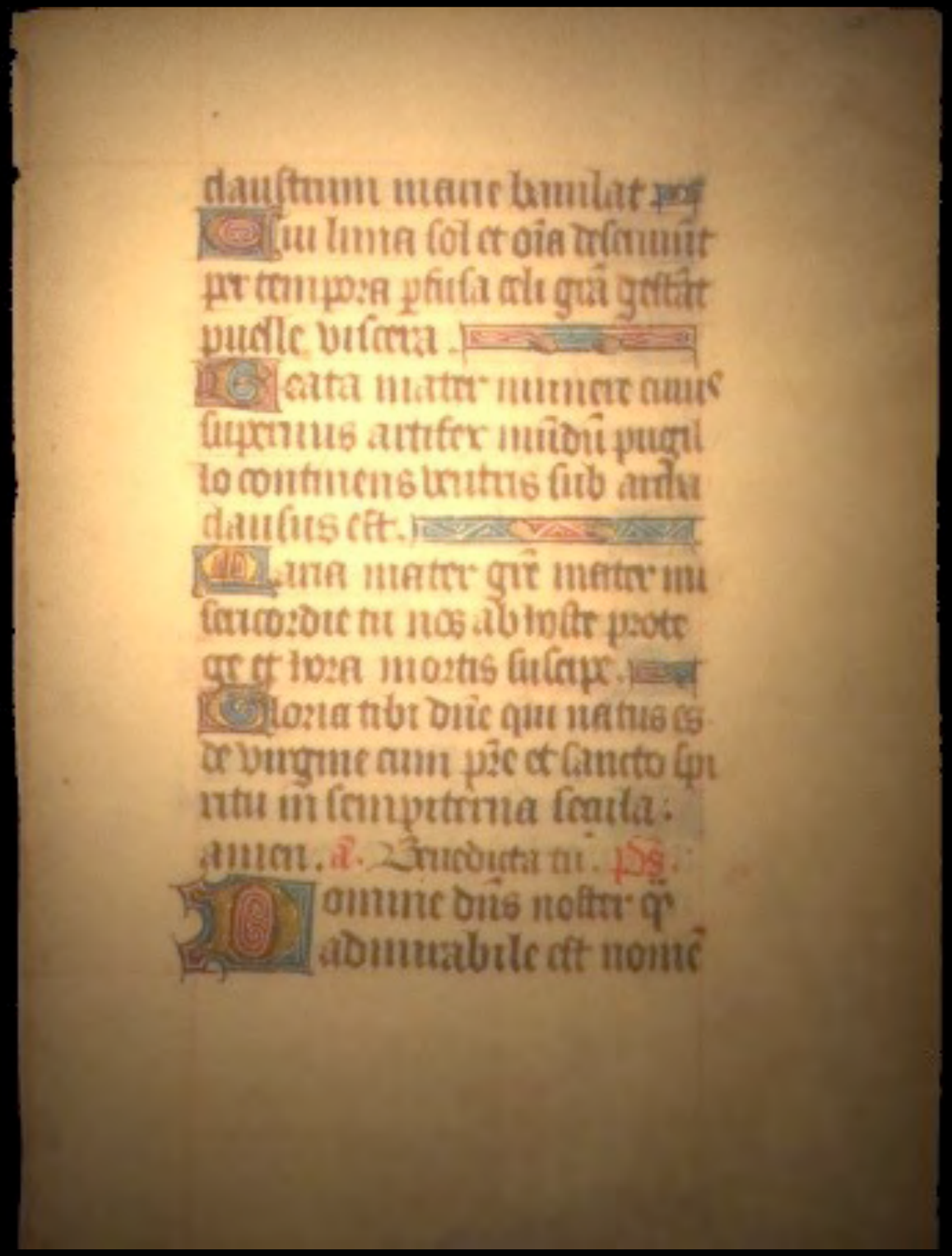

Model courtesy XYZRGB and Paul Debevec

Layered materials

Inter-layer scattering

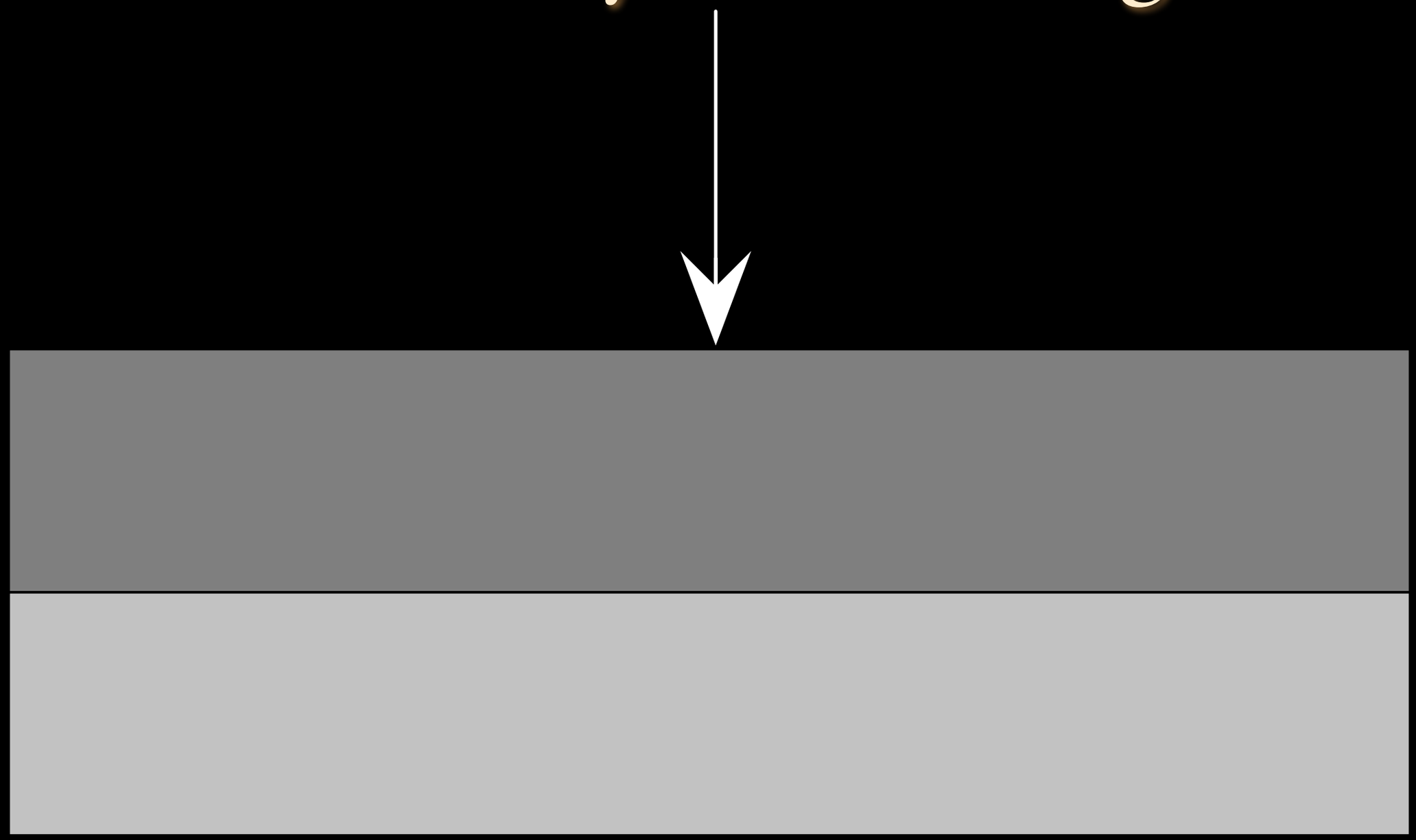

Inter-layer scattering

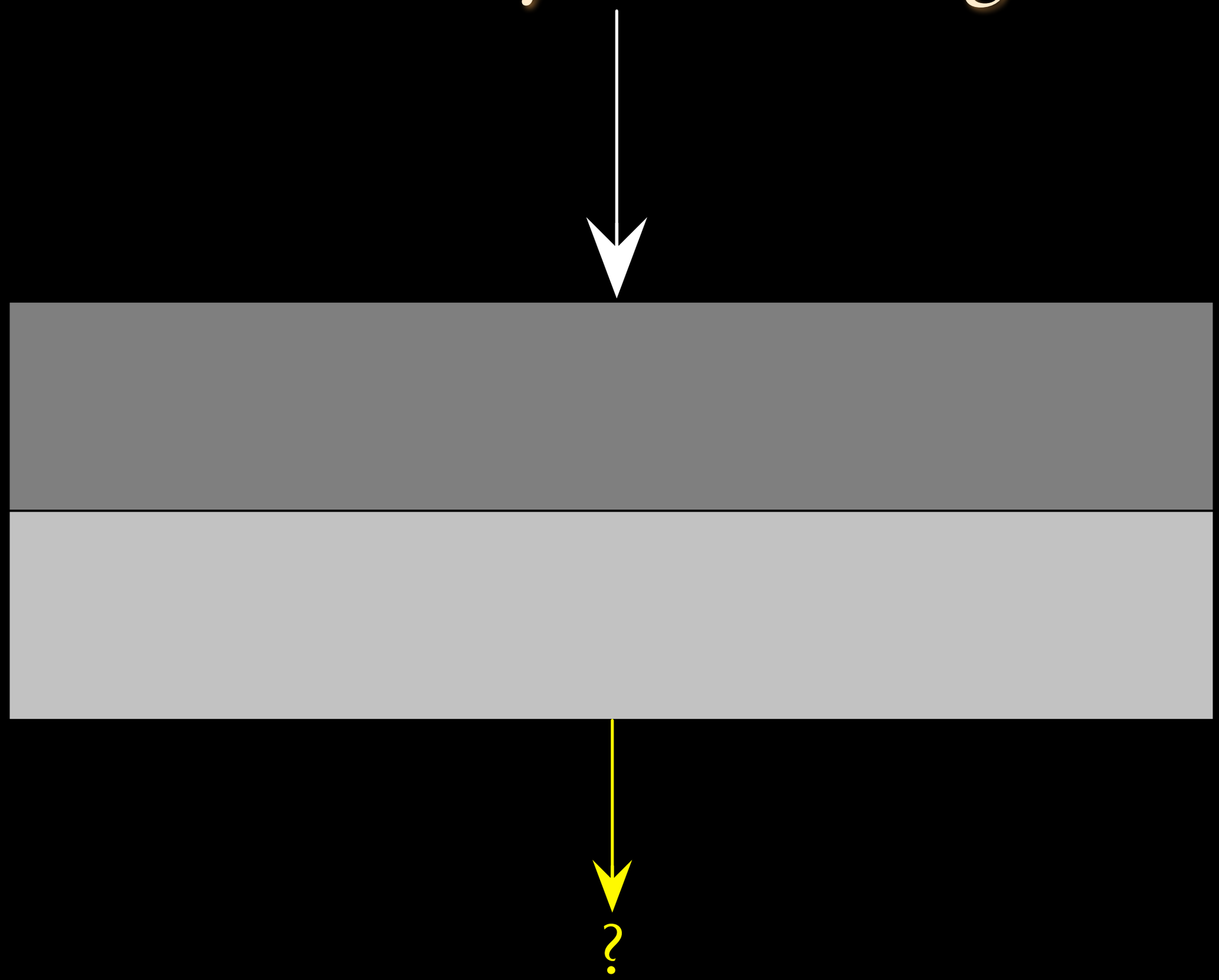

Thin slabs

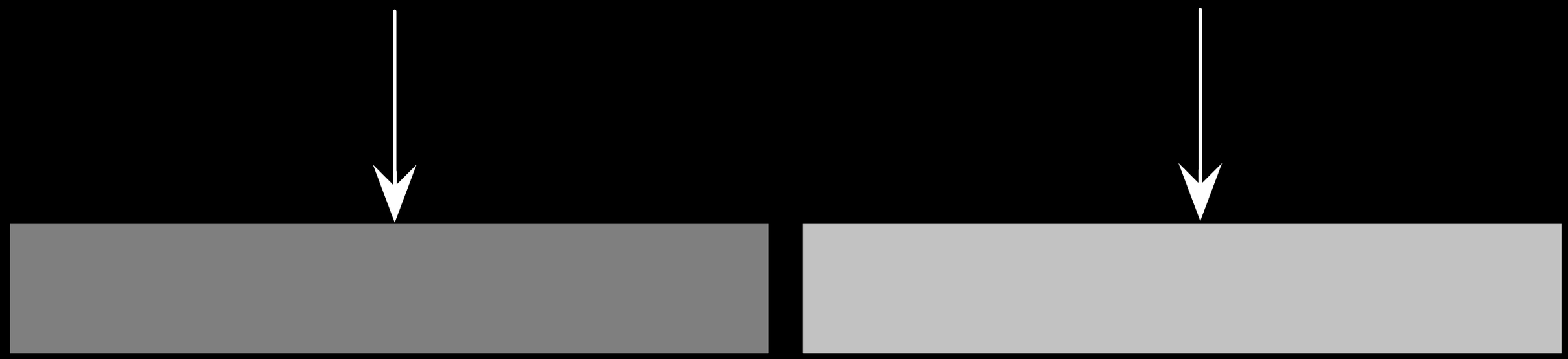

Transmittance profiles

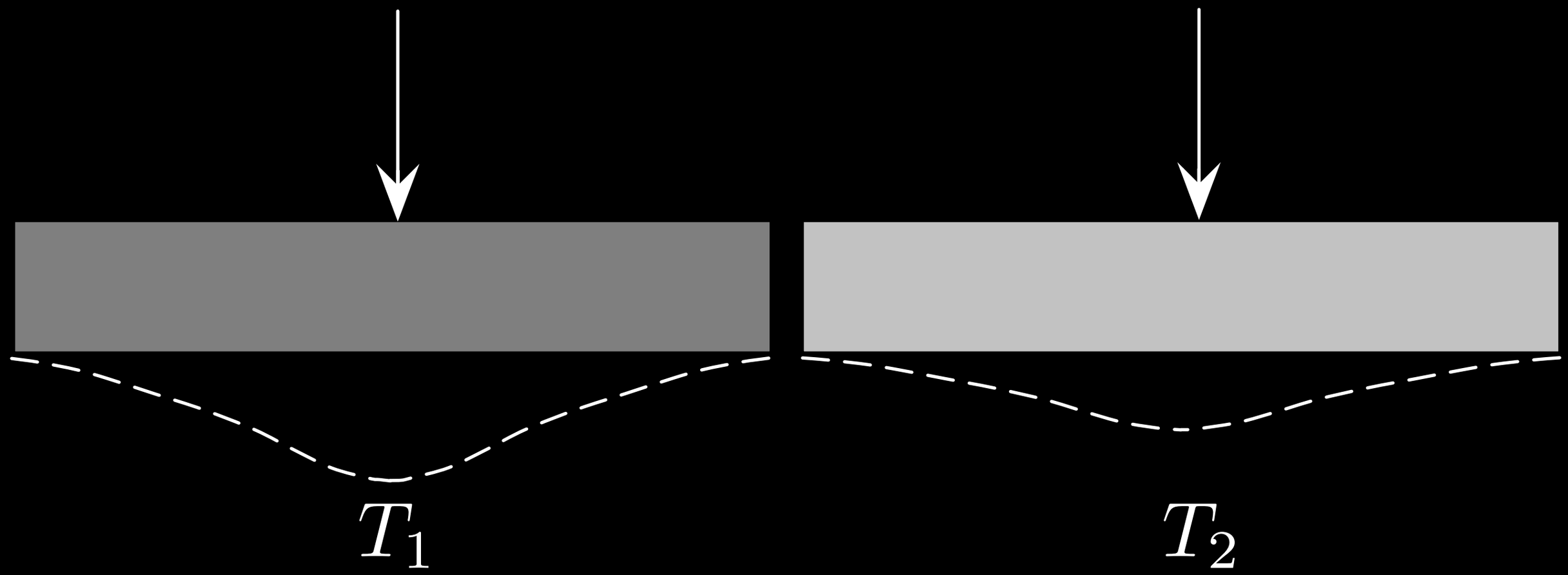

Two layers

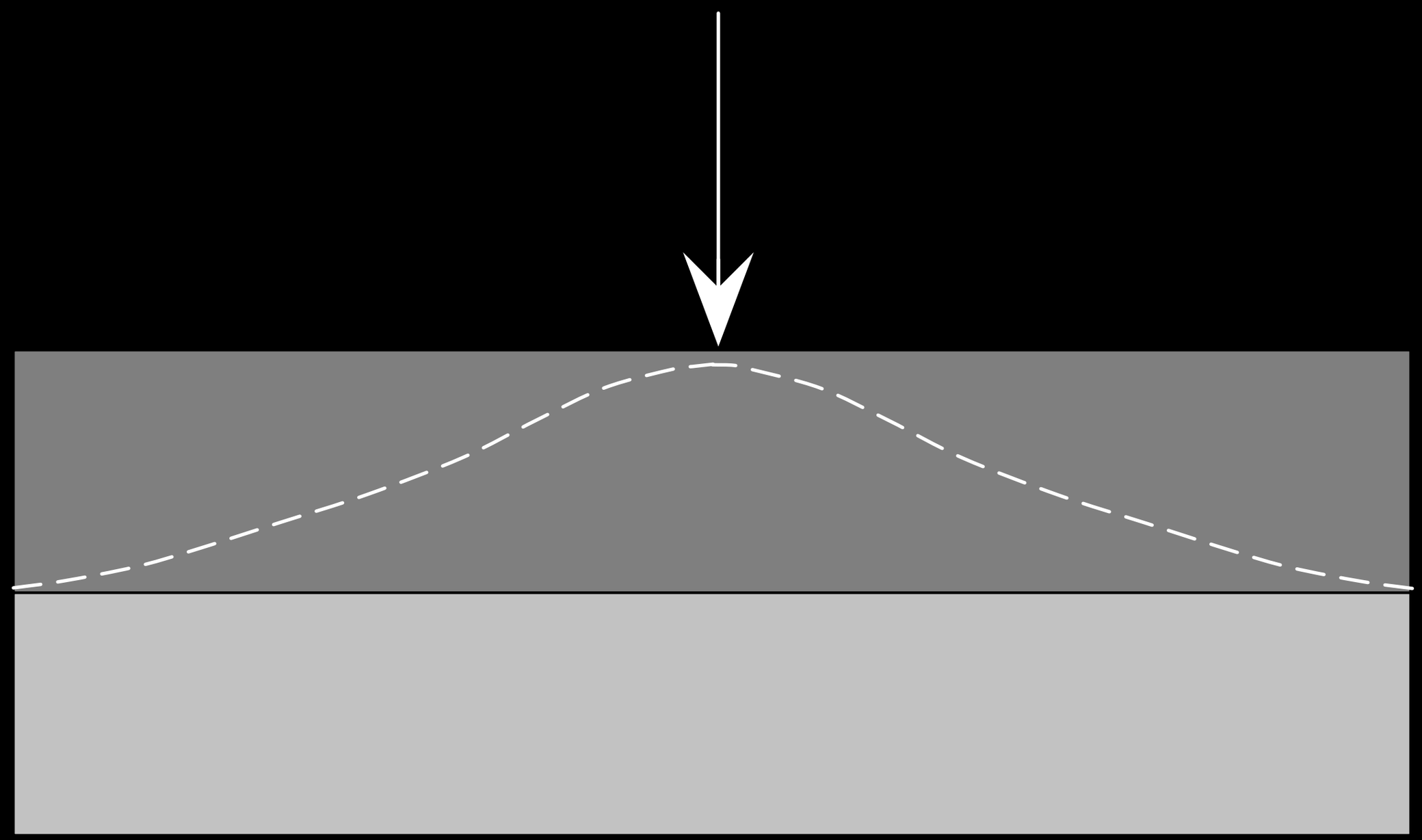

Two layers

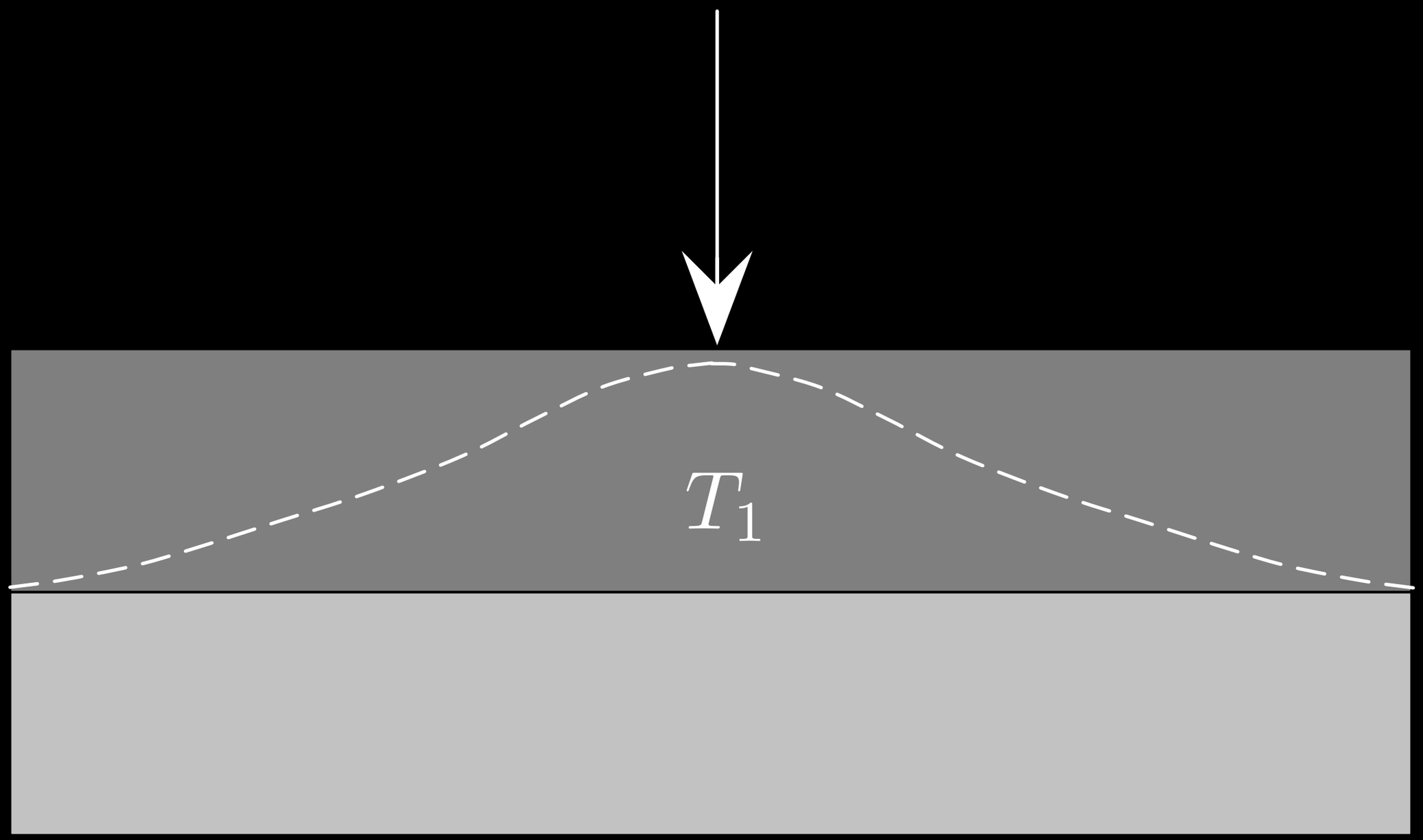

Two layers

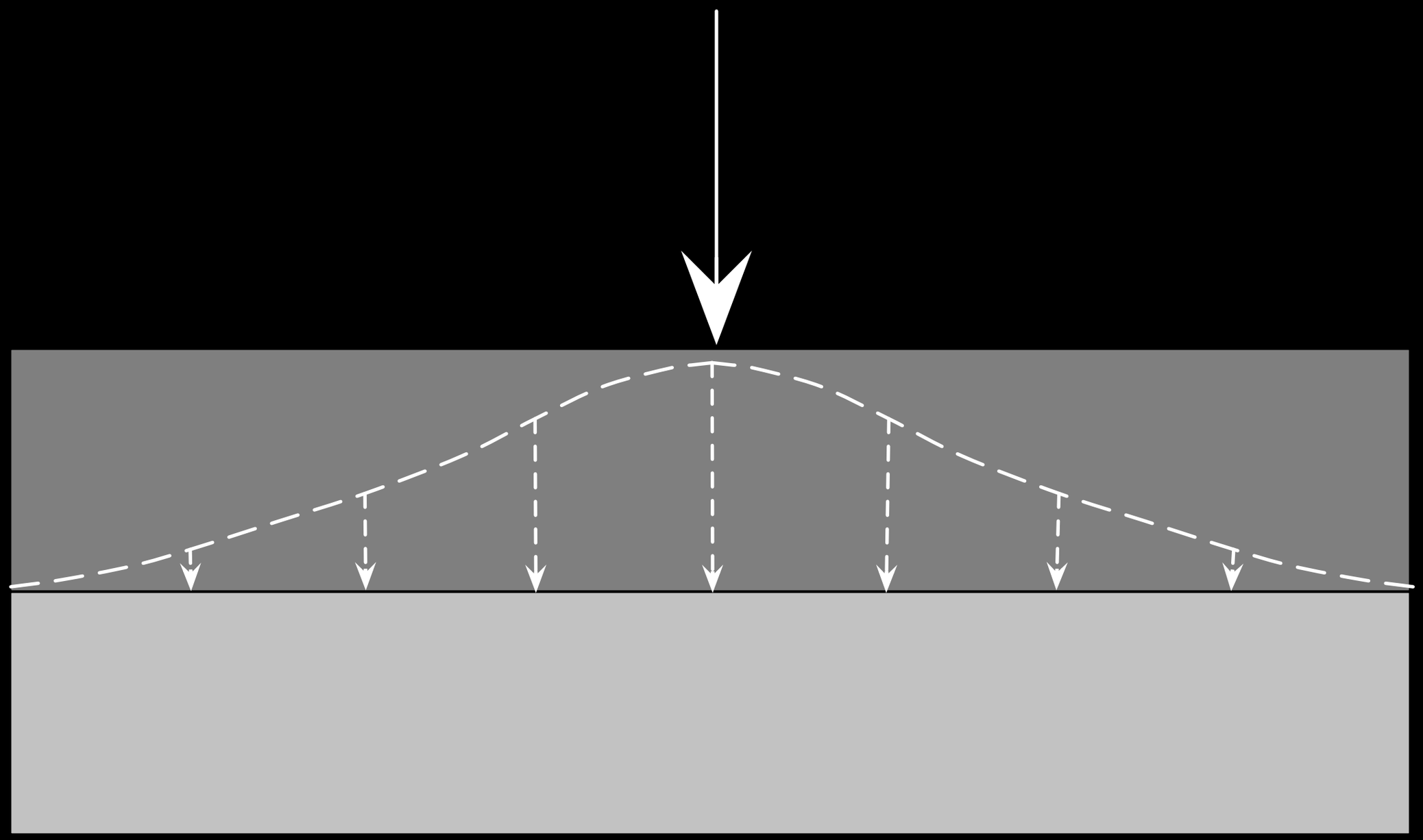

Two layers

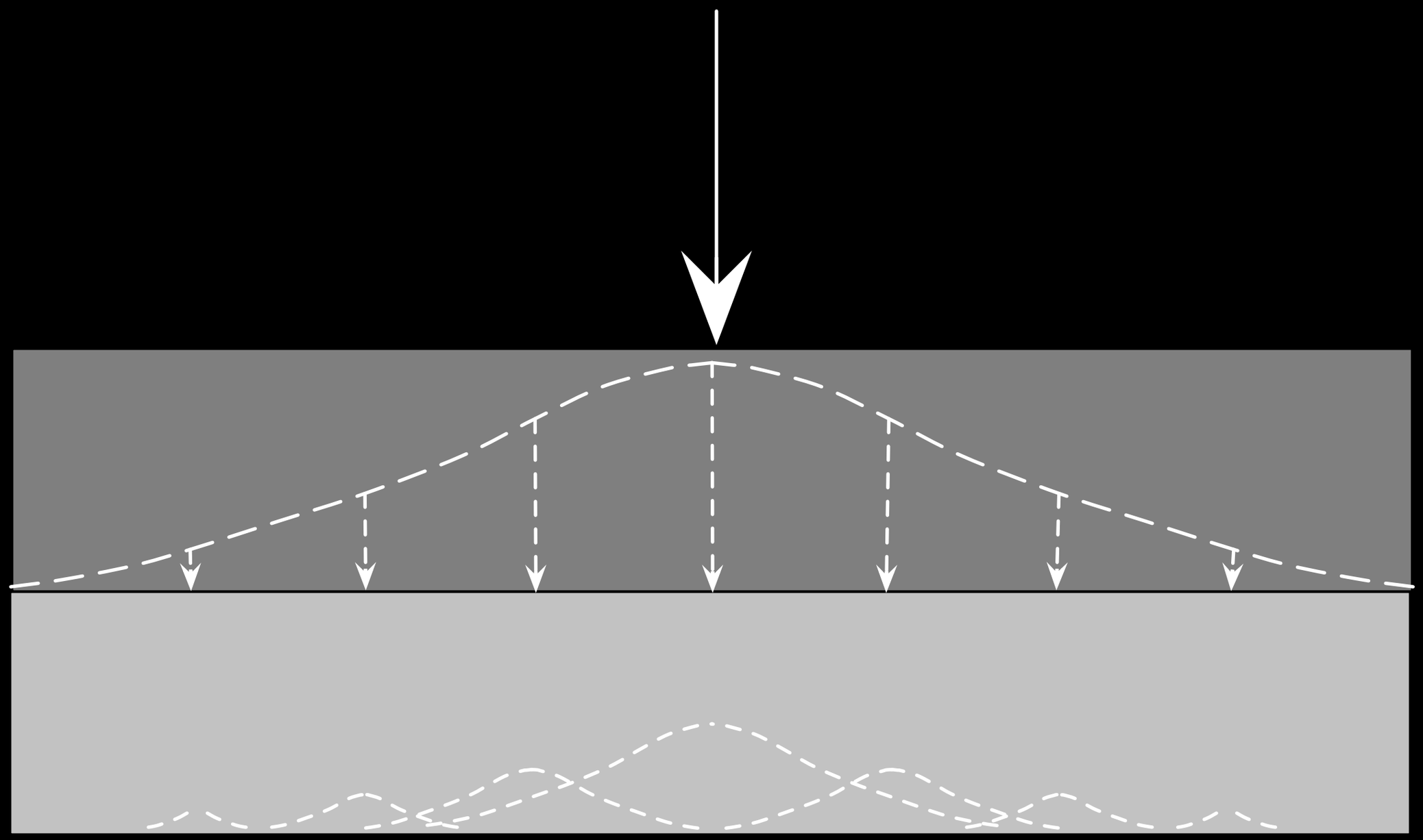

Two layers

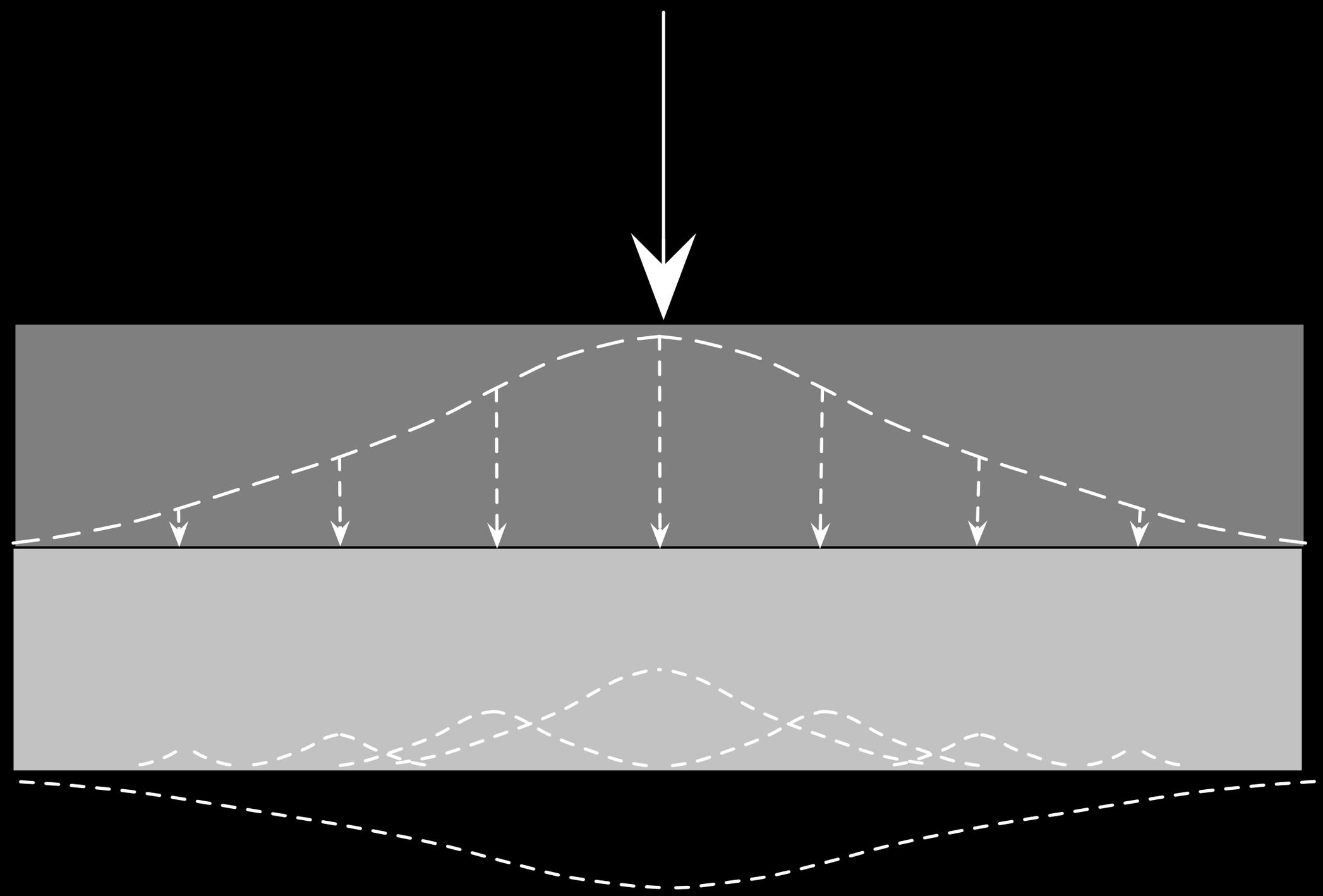

Two layers

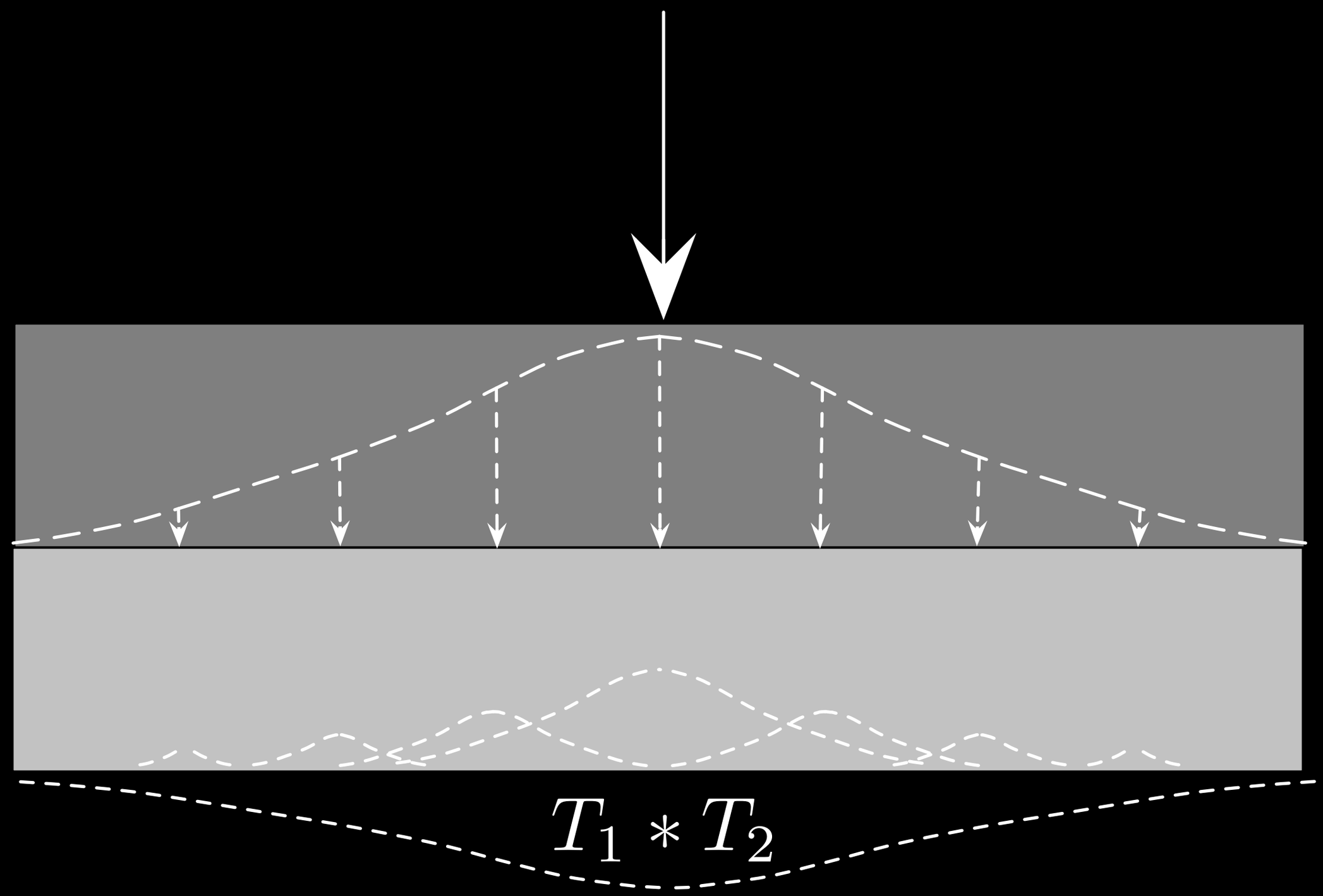

Inter-layer scattering

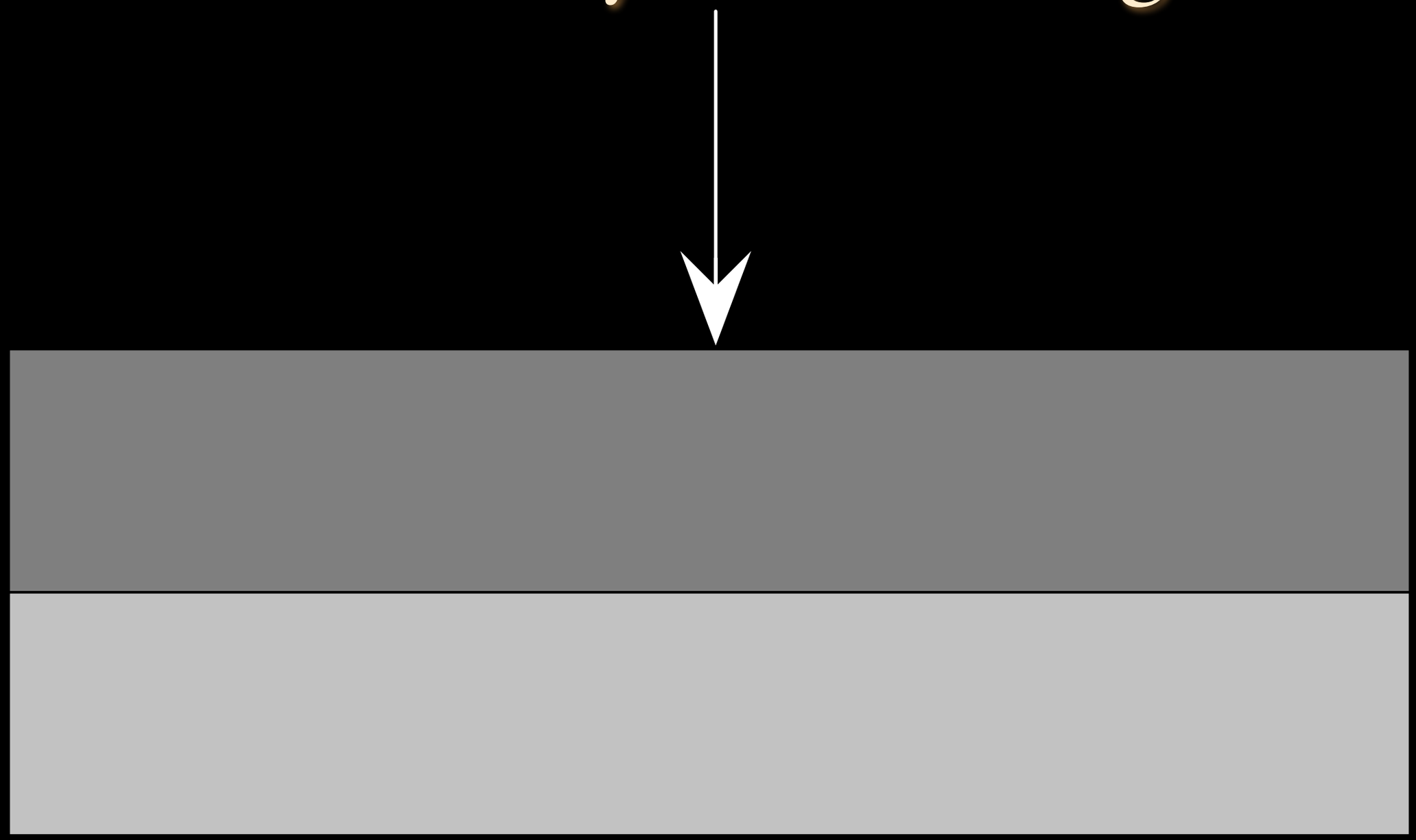

Inter-layer scattering

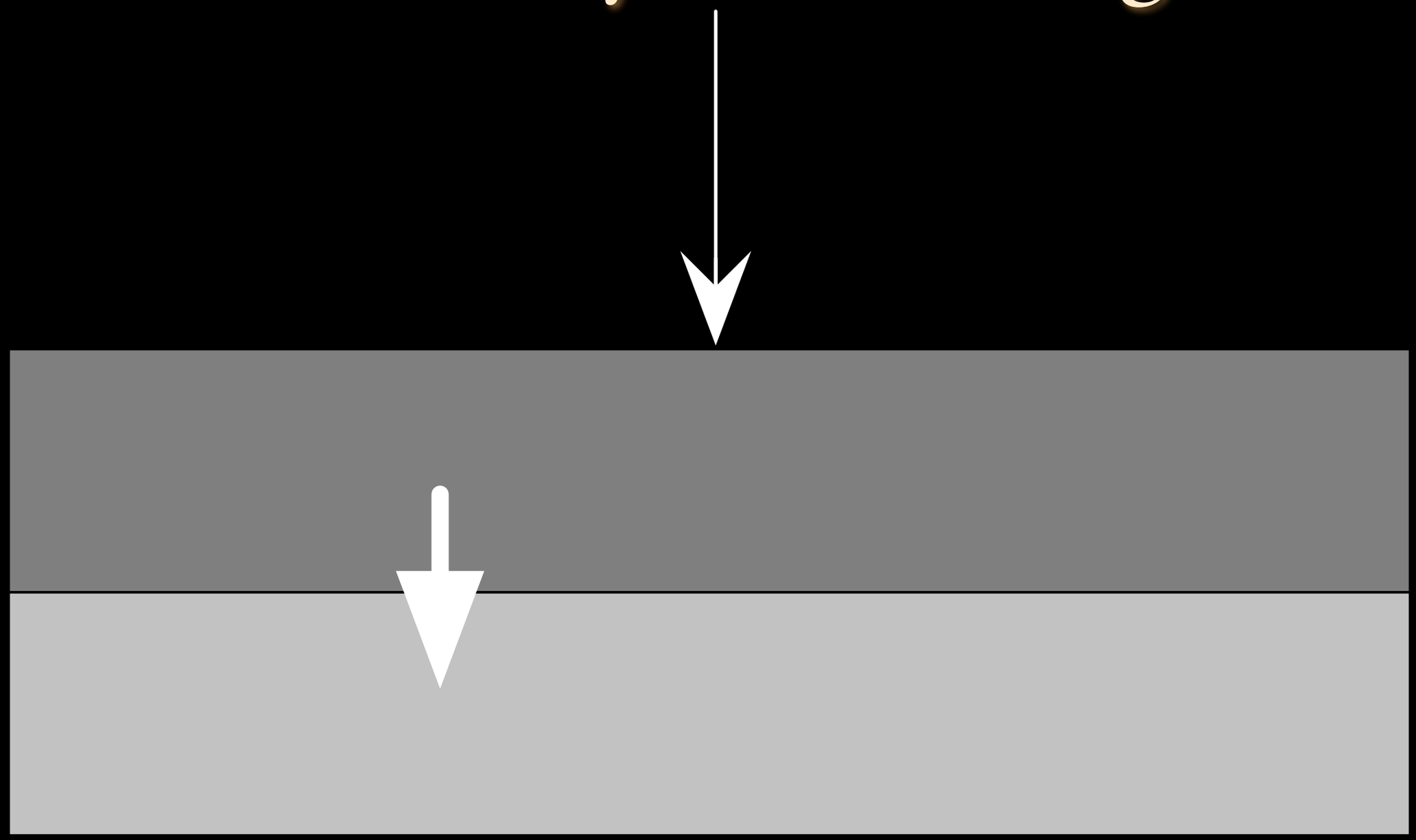

Inter-layer scattering

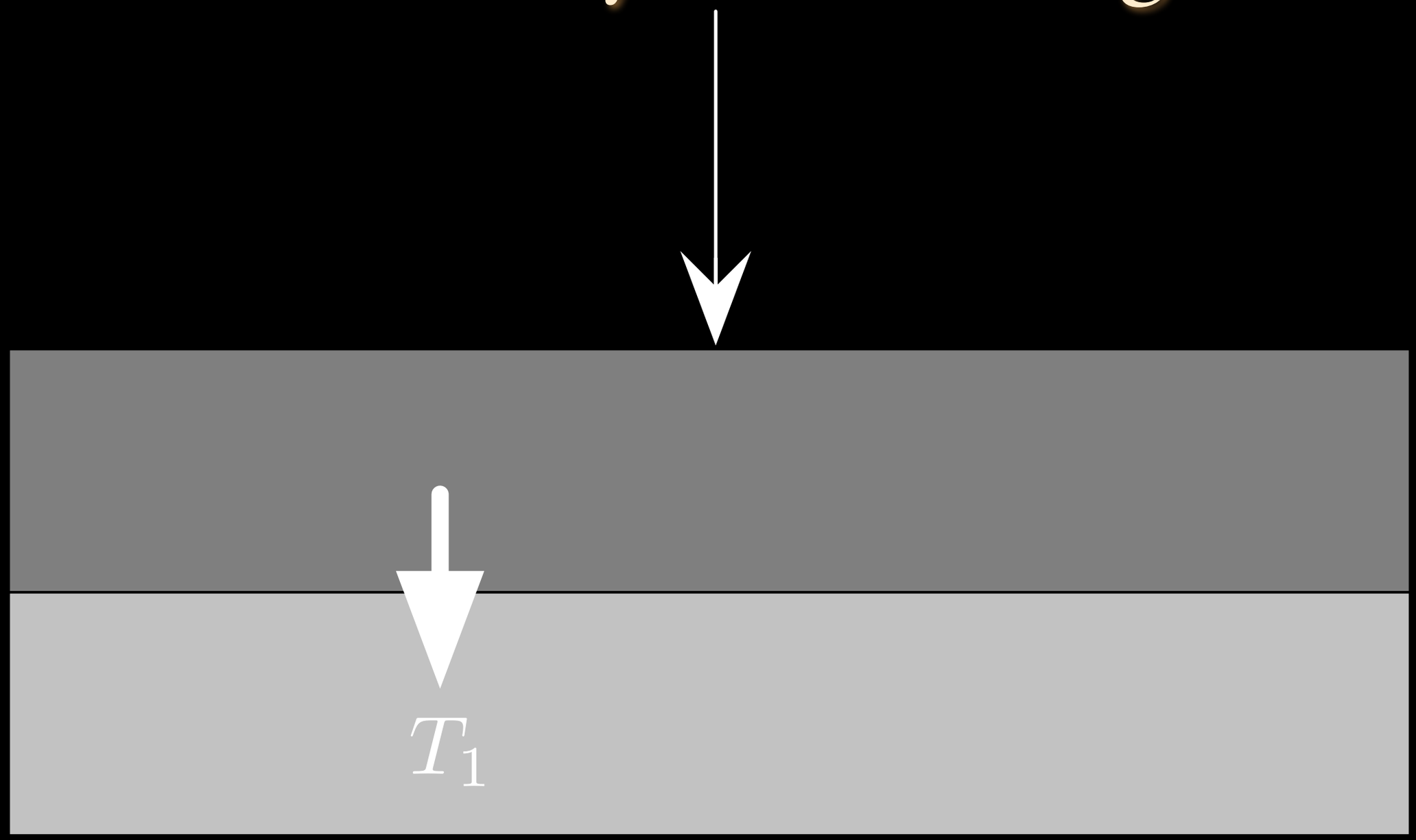

Inter-layer scattering

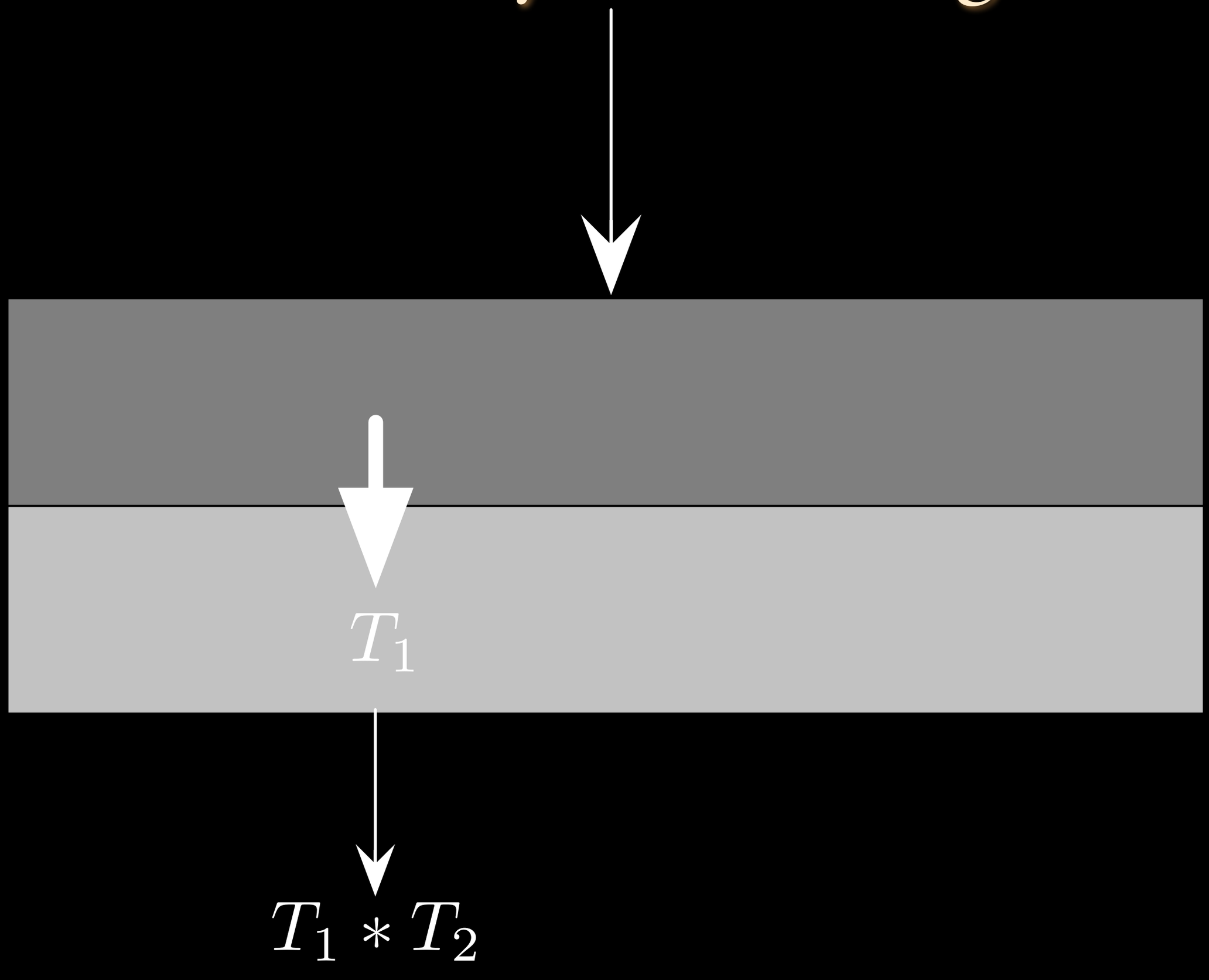

Inter-layer scattering

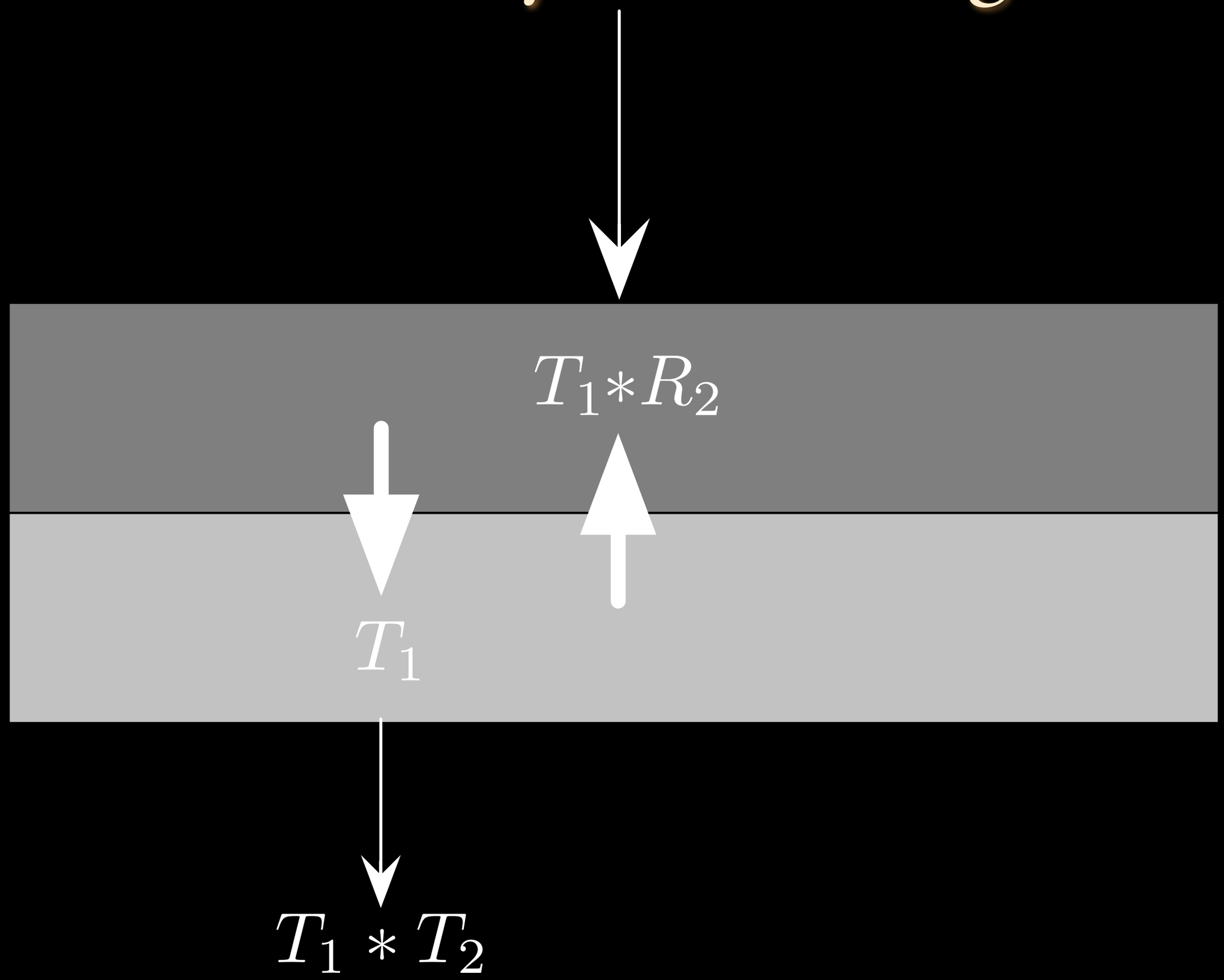

Inter-layer scattering

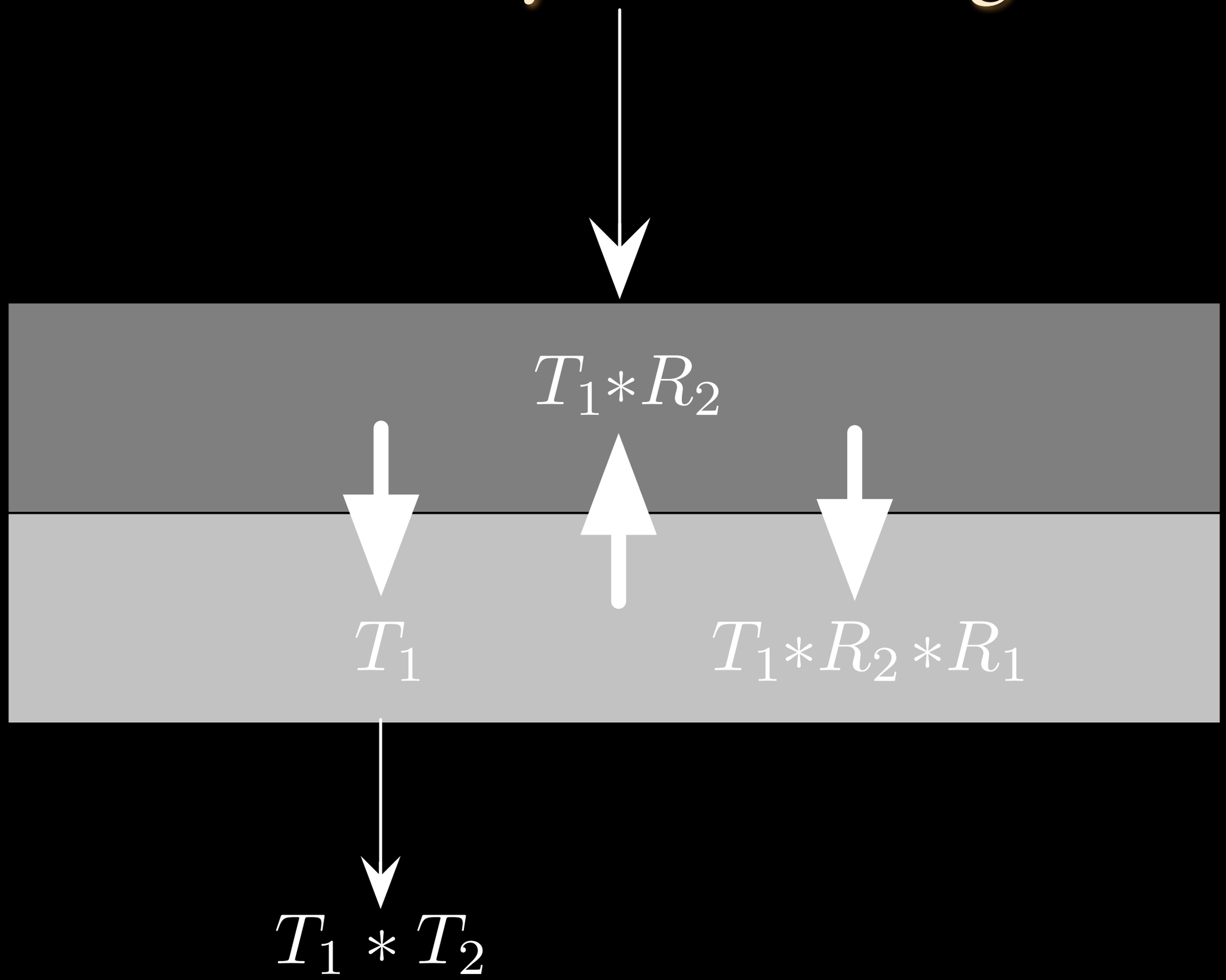

Inter-layer scattering

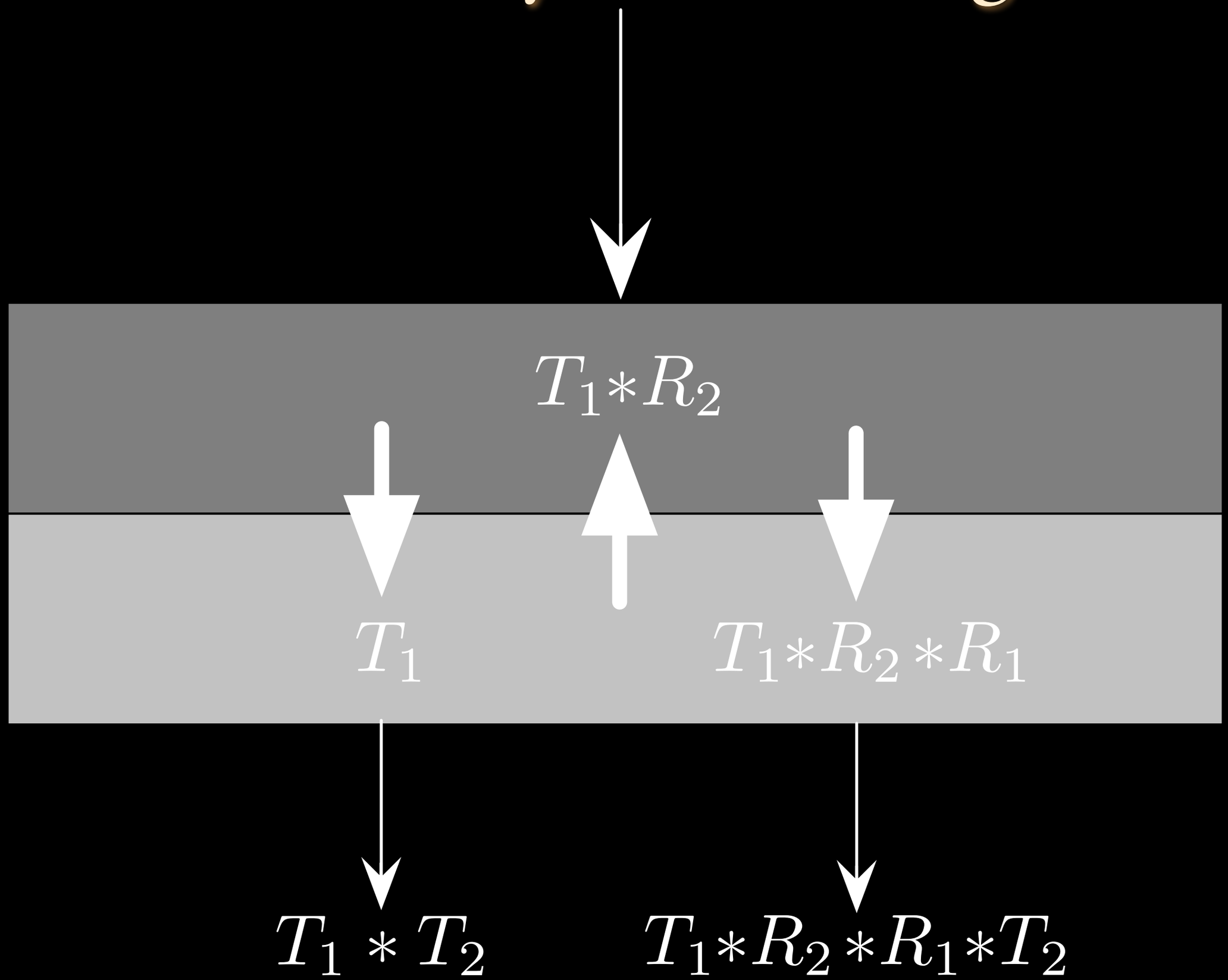

Multiple inter-layer scattering

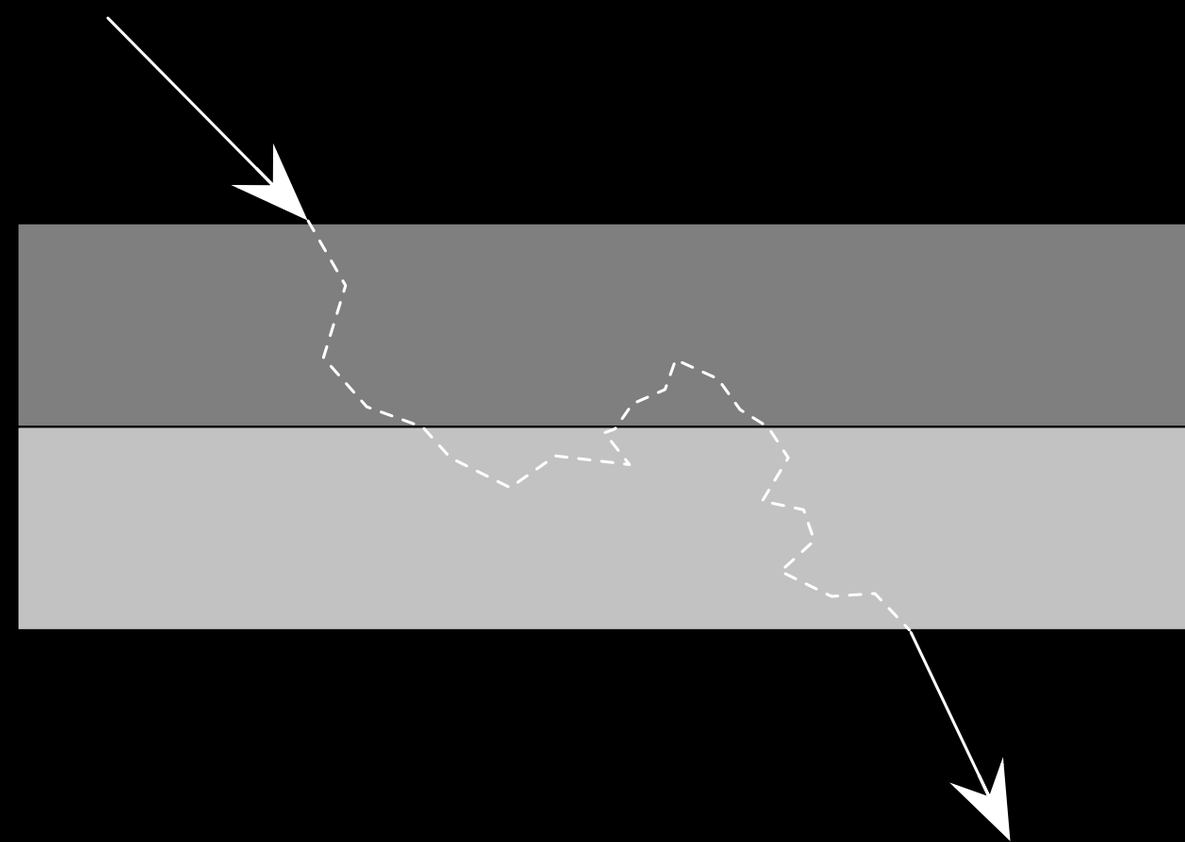

Multiple inter-layer scattering

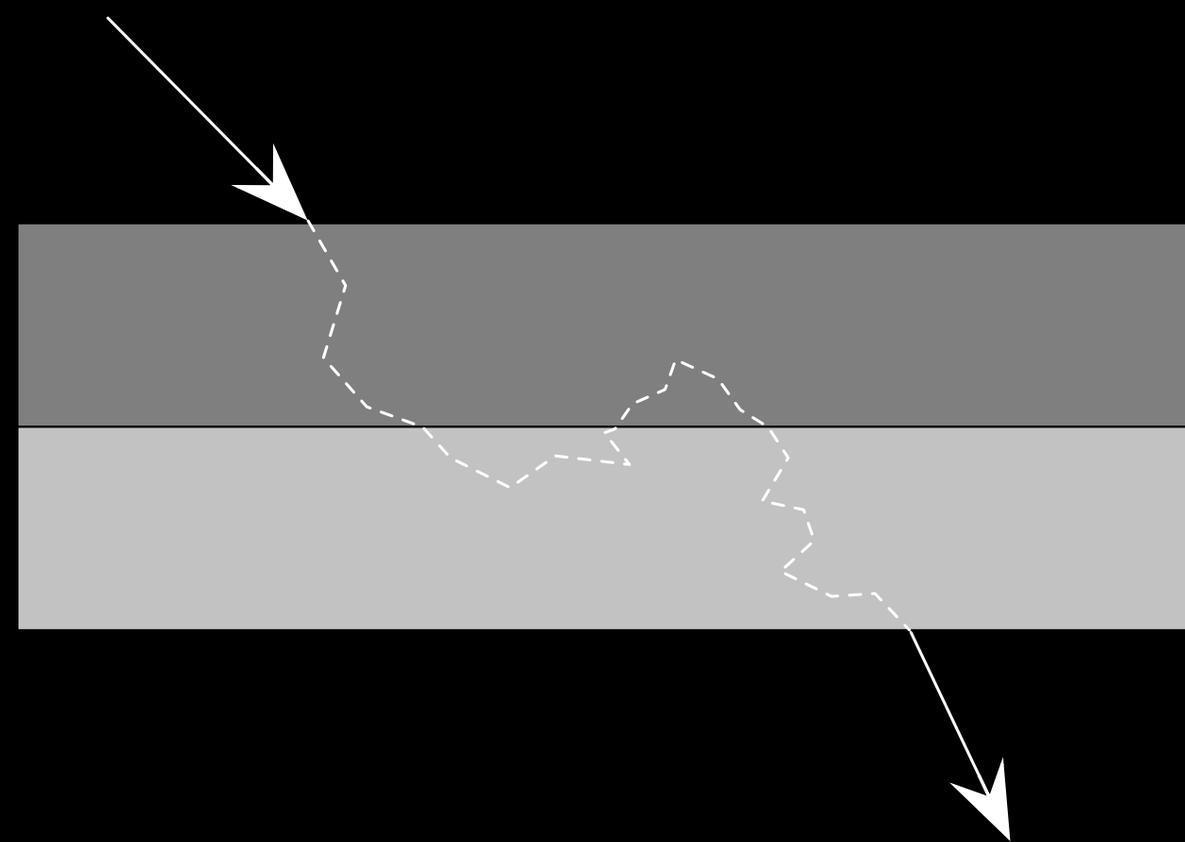

$$T_{12} = T_1 * T_2 +$$

Multiple inter-layer scattering

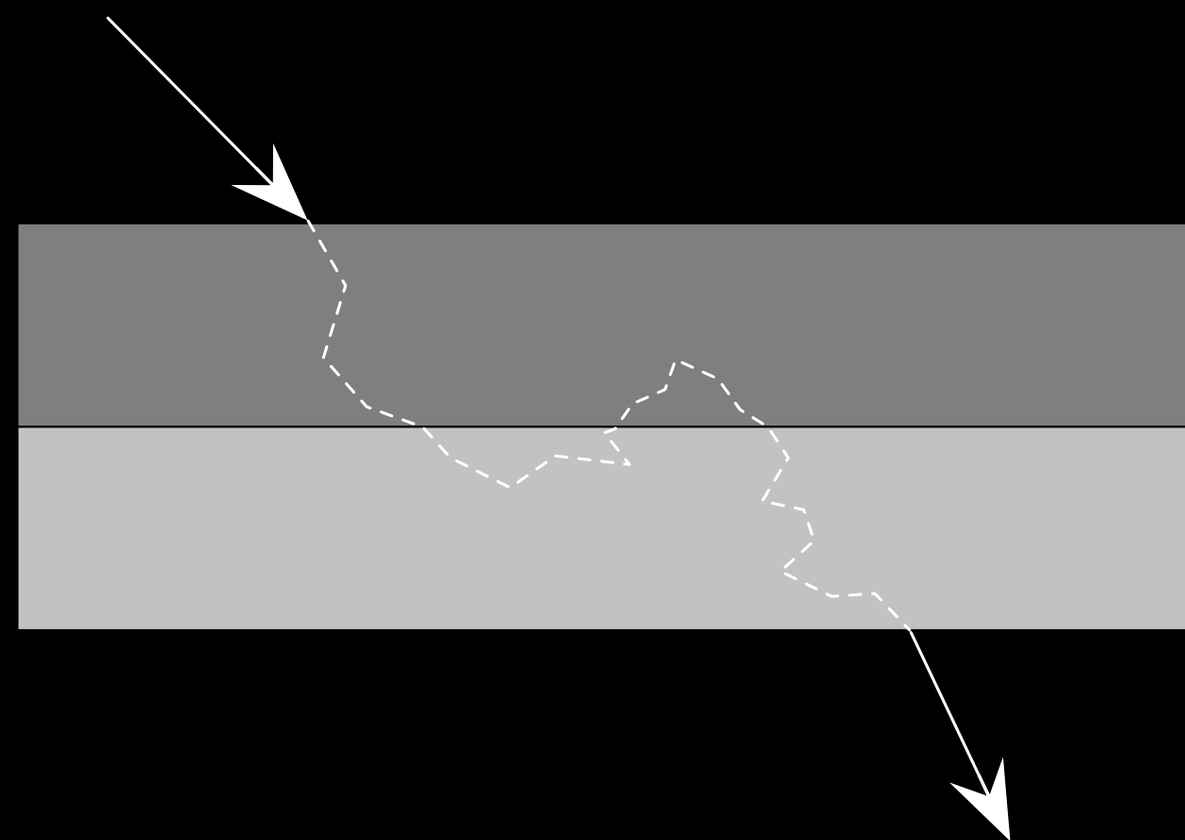

$$T_{12} = T_1 * T_2 +$$
$$T_1 * R_2 * R_1 * T_2 +$$

Multiple inter-layer scattering

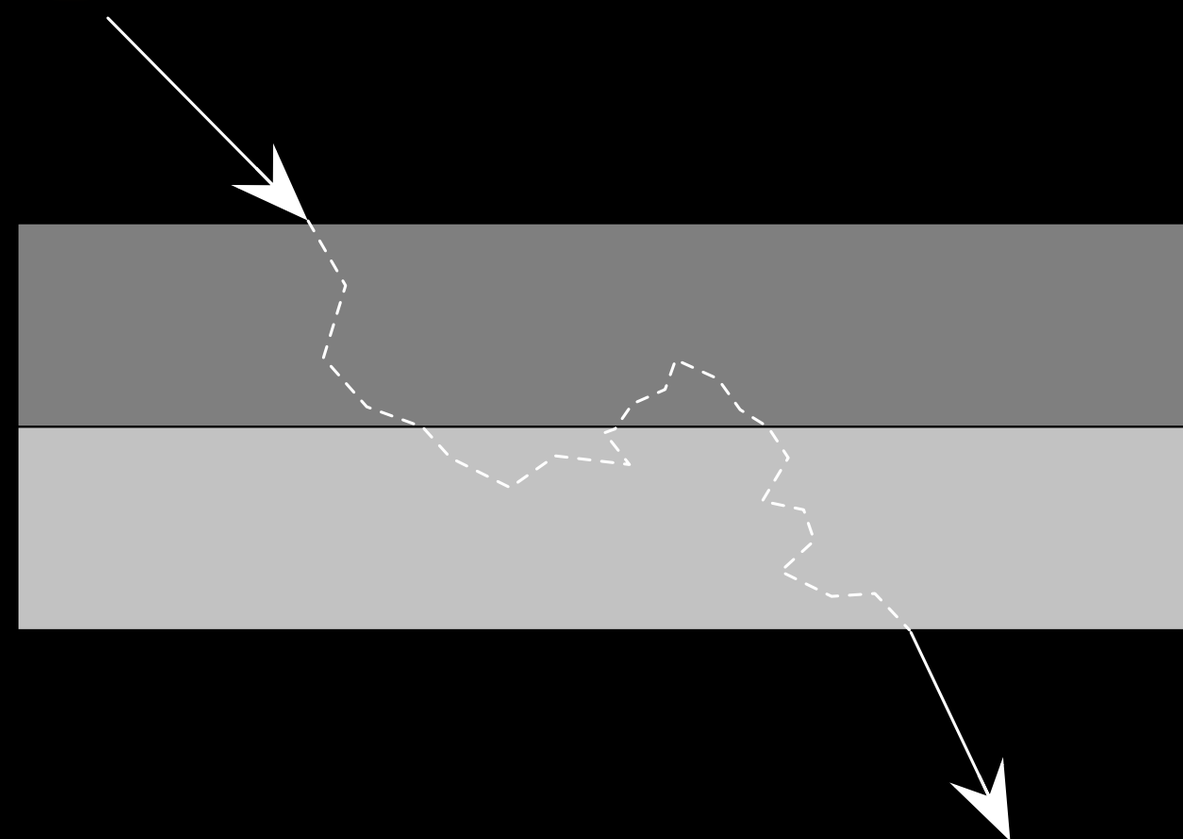

$$
\begin{aligned}
T_{12} = {} & T_1 * T_2 + \\
& T_1 * R_2 * R_1 * T_2 + \\
& T_1 * R_2 * R_1 * R_2 * R_1 * T_2 +
\end{aligned}
$$

Multiple inter-layer scattering

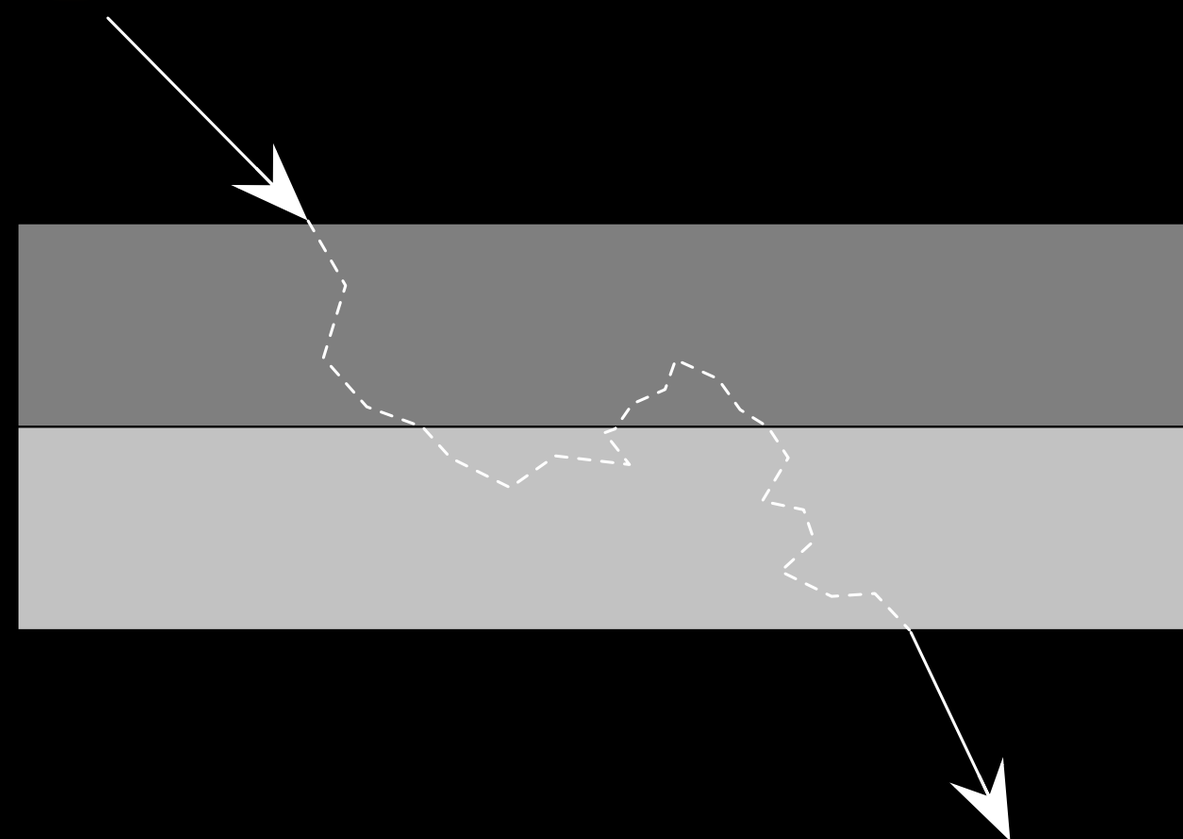

$$
\begin{aligned}
T_{12} = & T_1 * T_2 + \\
& T_1 * R_2 * R_1 * T_2 + \\
& T_1 * R_2 * R_1 * R_2 * R_1 * T_2 + \\
& \ldots
\end{aligned}
$$

Frequency response

$$\mathcal{R} = \mathbf{H}\{R\}$$

$$\mathcal{T} = \mathbf{H}\{T\}$$

$$\mathcal{T}_1\mathcal{T}_2 = \mathbf{H}\{T_1 * T_2\}$$

Frequency response

$$\mathcal{R} = \mathbf{H}\{R\}$$

$$\mathcal{T} = \mathbf{H}\{T\}$$

$$\mathcal{T}_1\mathcal{T}_2 = \mathbf{H}\{T_1 * T_2\}$$

$$\begin{aligned}
T_{12} = {} & T_1 * T_2 + \\
& T_1 * R_2 * R_1 * T_2 + \\
& T_1 * R_2 * R_1 * R_2 * R_1 * T_2 + \\
& \ldots
\end{aligned}$$

Frequency response

$$\mathcal{R} = \mathbf{H}\{R\}$$

$$\mathcal{T} = \mathbf{H}\{T\}$$

$$\mathcal{T}_1\mathcal{T}_2 = \mathbf{H}\{T_1 * T_2\}$$

$$\begin{aligned}\mathcal{T}_{12} = \mathcal{T}_1\mathcal{T}_2 &+ \\ \mathcal{T}_1\mathcal{R}_2\mathcal{R}_1\mathcal{T}_2 &+ \\ \mathcal{T}_1\mathcal{R}_2\mathcal{R}_1\mathcal{R}_2\mathcal{R}_1\mathcal{T}_2 &+ \\ \ldots\end{aligned}$$

Frequency response

$$\mathcal{R} = \mathbf{H}\{R\} \qquad \mathcal{T} = \mathbf{H}\{T\}$$

$$\mathcal{T}_1\mathcal{T}_2 = \mathbf{H}\{T_1 * T_2\}$$

$$\begin{aligned}
\mathcal{T}_{12} = \mathcal{T}_1\mathcal{T}_2 &+ \\
&\mathcal{T}_1\mathcal{R}_2\mathcal{R}_1\mathcal{T}_2 + \\
&\mathcal{T}_1\mathcal{R}_2\mathcal{R}_1\mathcal{R}_2\mathcal{R}_1\mathcal{T}_2 + \\
&\cdots \\
&= \mathcal{T}_1\mathcal{T}_2(1 + \mathcal{R}_2\mathcal{R}_1 + (\mathcal{R}_2\mathcal{R}_1)^2 + \cdots)
\end{aligned}$$

Frequency response

$$\mathcal{R} = \mathbf{H}\{R\} \qquad \mathcal{T} = \mathbf{H}\{T\}$$

$$\mathcal{T}_1\mathcal{T}_2 = \mathbf{H}\{T_1 * T_2\}$$

$$\begin{aligned}
\mathcal{T}_{12} = \mathcal{T}_1\mathcal{T}_2 &+ \\
&\mathcal{T}_1\mathcal{R}_2\mathcal{R}_1\mathcal{T}_2 + \\
&\mathcal{T}_1\mathcal{R}_2\mathcal{R}_1\mathcal{R}_2\mathcal{R}_1\mathcal{T}_2 + \\
&\dots \\
&= \mathcal{T}_1\mathcal{T}_2(1 + \mathcal{R}_2\mathcal{R}_1 + (\mathcal{R}_2\mathcal{R}_1)^2 + \cdots)
\end{aligned}$$

$$\mathcal{T}_{12} = \frac{\mathcal{T}_1\mathcal{T}_2}{1 - \mathcal{R}_2\mathcal{R}_1} \qquad \mathcal{R}_1\mathcal{R}_2 < 1$$

Model courtesy The Stanford 3D Scanning Repository

Model courtesy The Stanford 3D Scanning Repository

Model courtesy The Stanford 3D Scanning Repository

Model courtesy The Stanford 3D Scanning Repository

Model courtesy The Stanford 3D Scanning Repository

Leaf structure

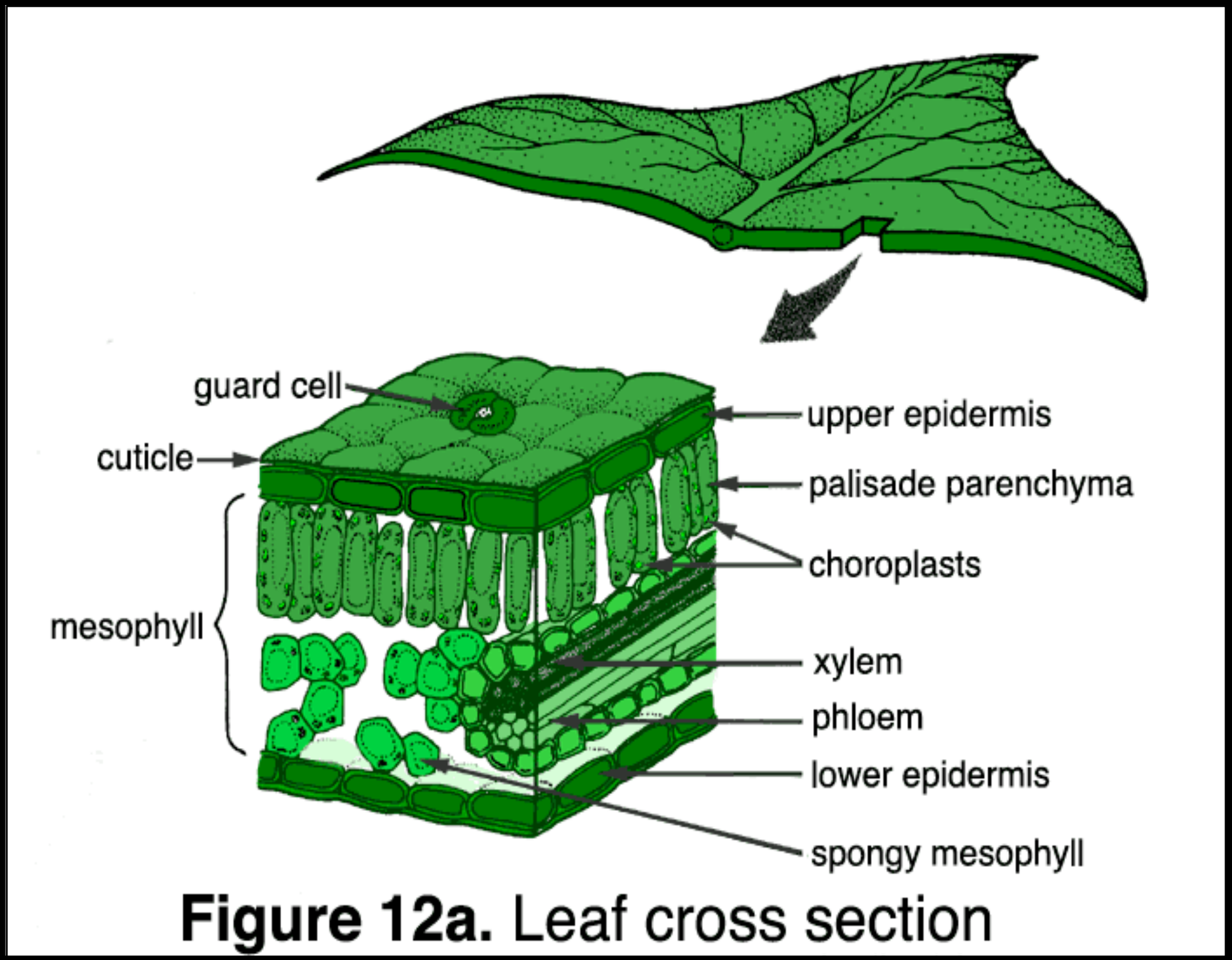

Figure 12a. Leaf cross section

From "Botany Basics," http://extension.oregonstate.edu/mg/botany/index.html

Two-layer leaf model

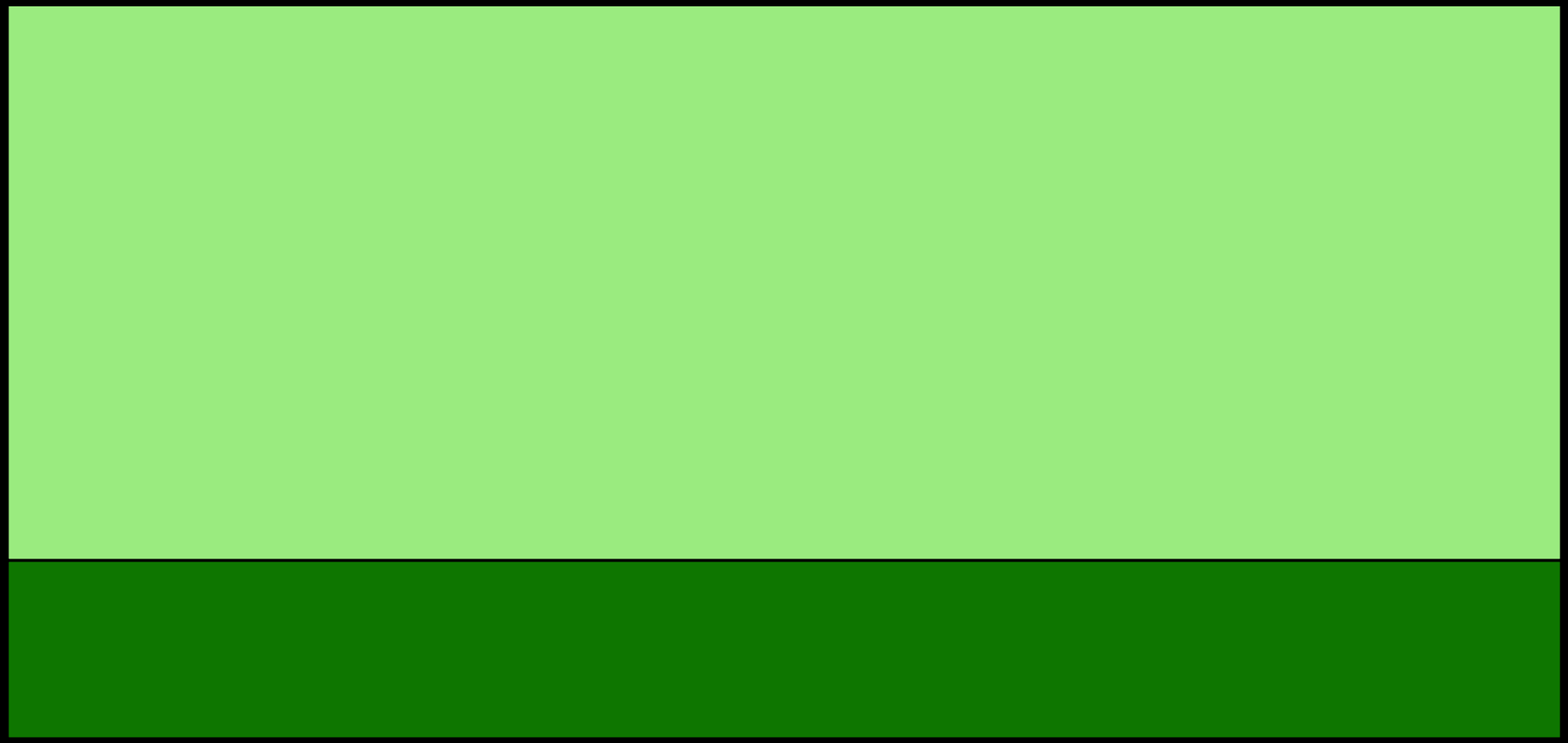

Parameters from Hemenger 1977 and Fukshansky 1993

Two-layer leaf model

Parameters from Hemenger 1977 and Fukshansky 1993

Two-layer leaf model

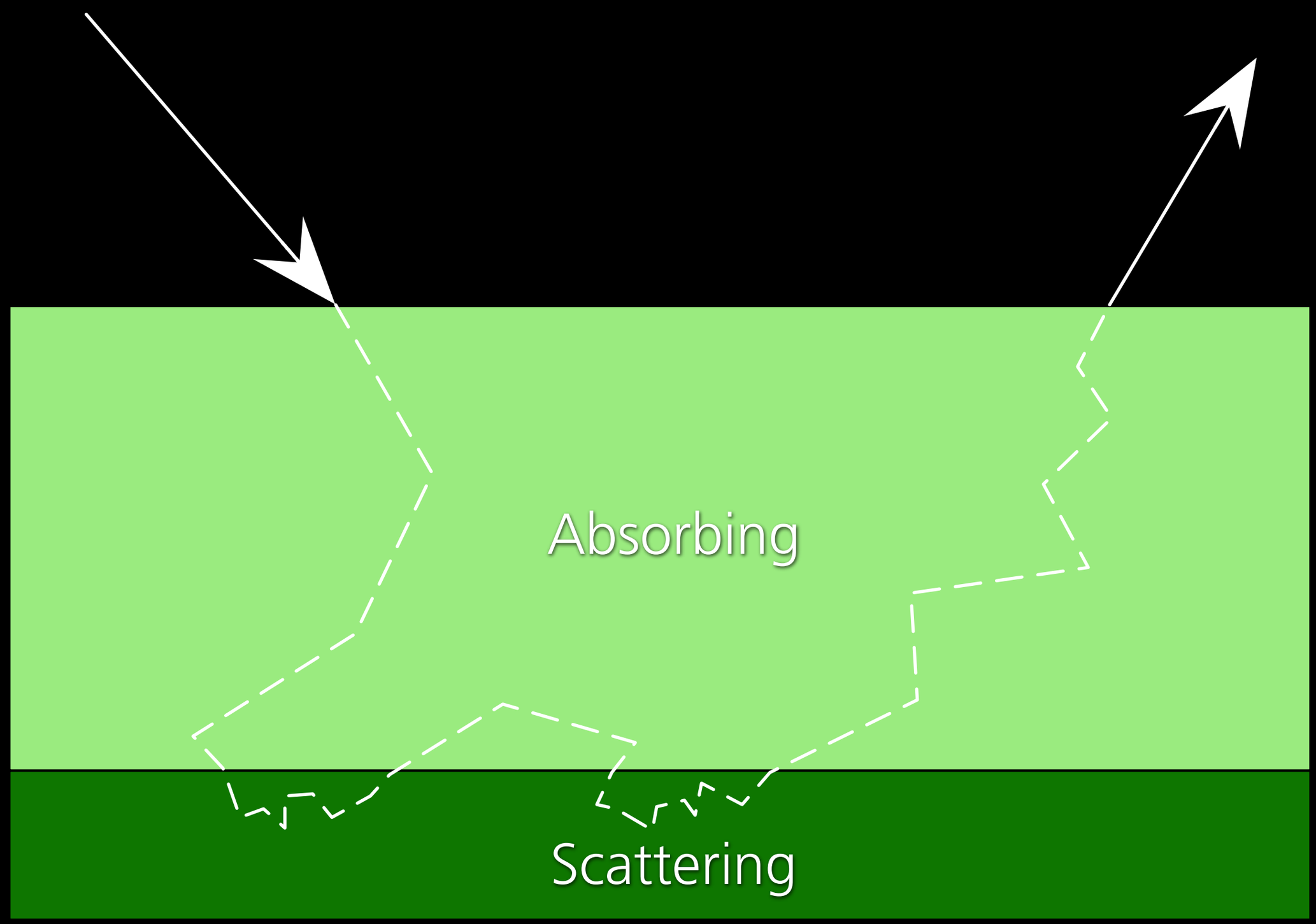

Parameters from Hemenger 1977 and Fukshansky 1993

Reflectance

Front Face

Model courtesy Arash Keshmirian
Parameters from Hemenger 1977 and Fukshansky 1993

Back Face

Reflectance

Transmittance

Front Face

Model courtesy Arash Keshmirian
Parameters from Hemenger 1977 and Fukshansky 1993

Back Face

Reflectance

No textures

Transmittance

Front Face

Model courtesy Arash Keshmirian
Parameters from Hemenger 1977 and Fukshansky 1993

Back Face

Reflectance

23.2%

46.3%

Transmittance

Front Face

Model courtesy Arash Keshmirian
Parameters from Hemenger 1977 and Fukshansky 1993

Back Face

Reflectance

23.2%

46.3%

Transmittance

9.0%

9.4%

Front Face

Model courtesy Arash Keshmirian
Parameters from Hemenger 1977 and Fukshansky 1993

Back Face

Surface Roughness

BRDF

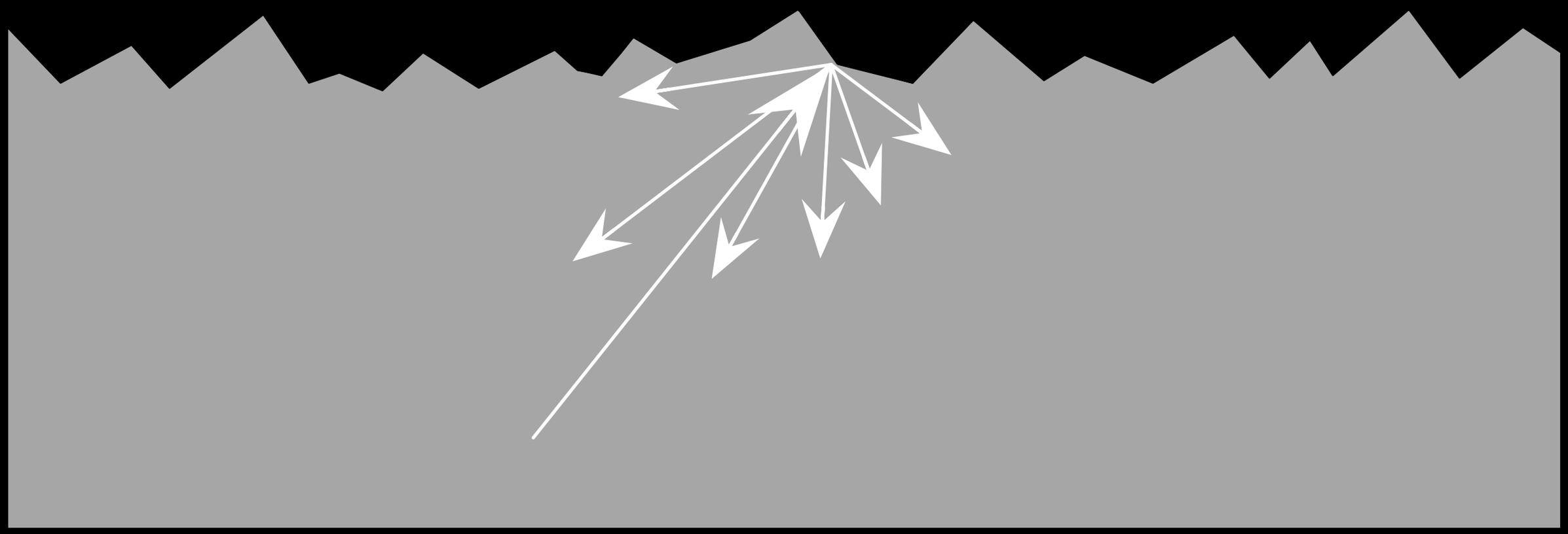

Boundary Condition

$$\int_{\Omega+} L_d(r,\vec{\omega})(-\vec{n}\cdot\vec{\omega})\ d\vec{\omega} = F_{dr}\int_{\Omega-} L_d(r,\vec{\omega})(\vec{n}\cdot\vec{\omega})\ d\vec{\omega}$$

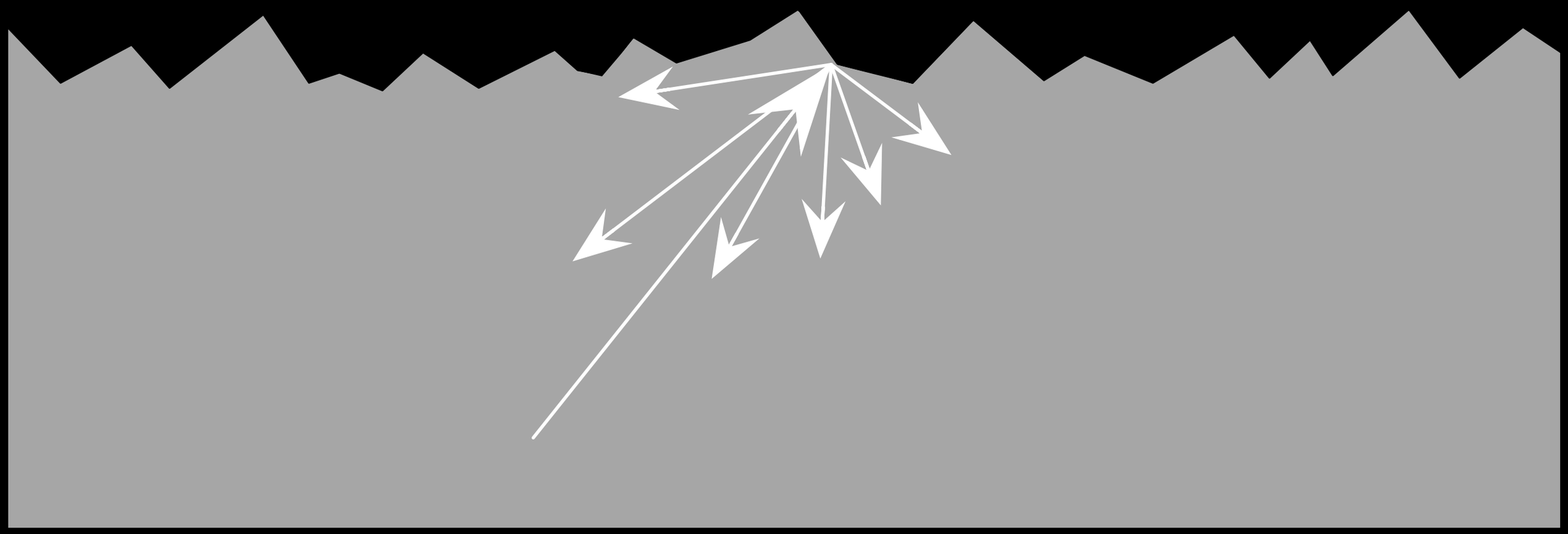

Boundary Condition

$$\int_{\Omega+} L_d(r,\vec{\omega})(-\vec{n}\cdot\vec{\omega})\ d\vec{\omega} = F_{dr}\int_{\Omega-} L_d(r,\vec{\omega})(\vec{n}\cdot\vec{\omega})\ d\vec{\omega}$$

F_{dr} = Diffuse Fresnel Reflectance

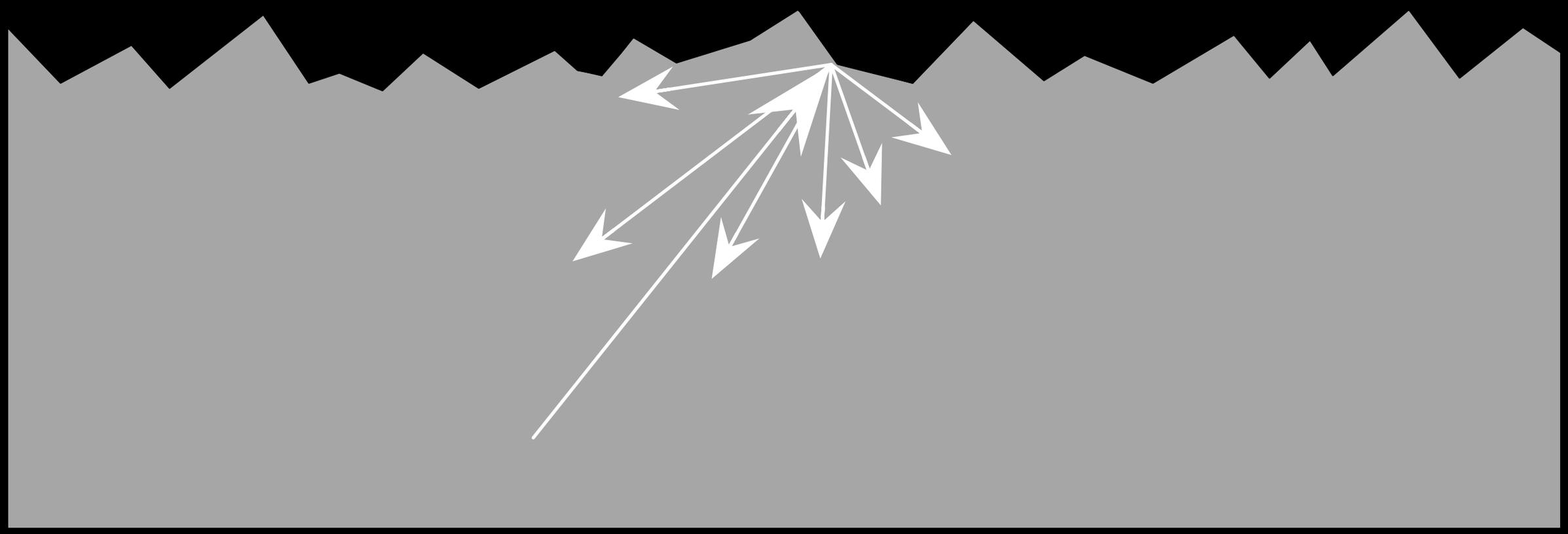

Boundary Condition

$$\int_{\Omega+} L_d(r,\vec{\omega})(-\vec{n}\cdot\vec{\omega})\ d\vec{\omega} = F_{dr}\int_{\Omega-} L_d(r,\vec{\omega})(\vec{n}\cdot\vec{\omega})\ d\vec{\omega}$$

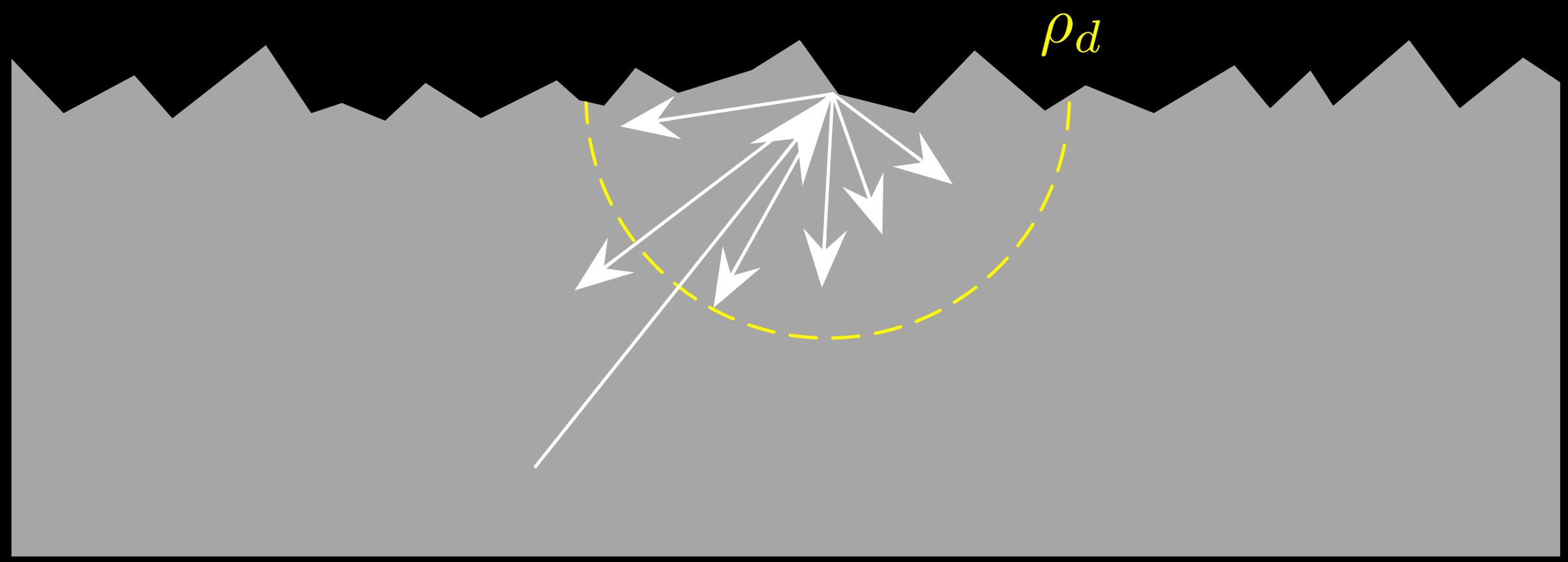

Boundary Condition

$$\int_{\Omega+} L_d(r,\vec{\omega})(-\vec{n}\cdot\vec{\omega})\ d\vec{\omega} = \rho_d \int_{\Omega-} L_d(r,\vec{\omega})(\vec{n}\cdot\vec{\omega})\ d\vec{\omega}$$

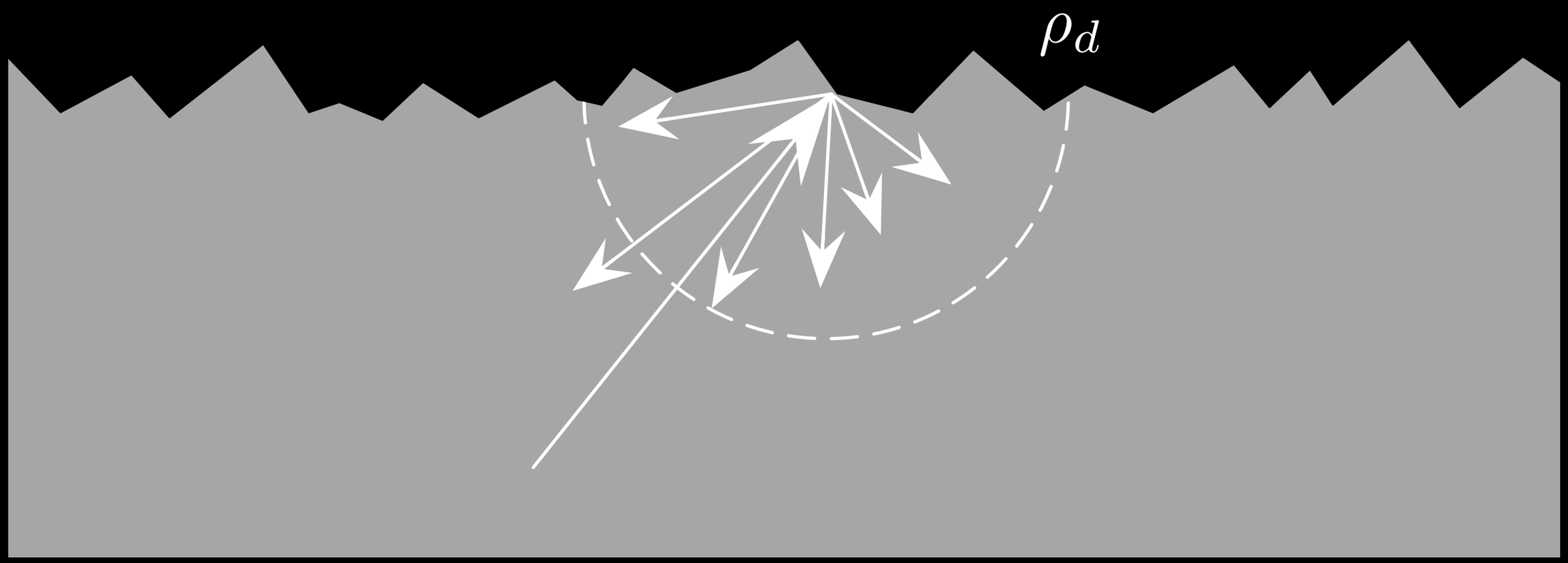

$$\sigma = 0.1$$

Model courtesy The Stanford 3D Scanning Repository

$\sigma = 0.1$

$\sigma = 0.5$

Model courtesy The Stanford 3D Scanning Repository

$\sigma = 0.1$ $\sigma = 0.5$ $\sigma = 1.0$

Model courtesy The Stanford 3D Scanning Repository

Skin model

Skin model

- High resolution head scan (~10M triangles)

Skin model

- High resolution head scan (~10M triangles)
- Three layer skin model

Skin model

- High resolution head scan (~10M triangles)
- Three layer skin model
- Parameters based on “Tissue Optics,” Tuchin 2000

Scattering

Model courtesy XYZRGB, parameters from Tuchin 2000

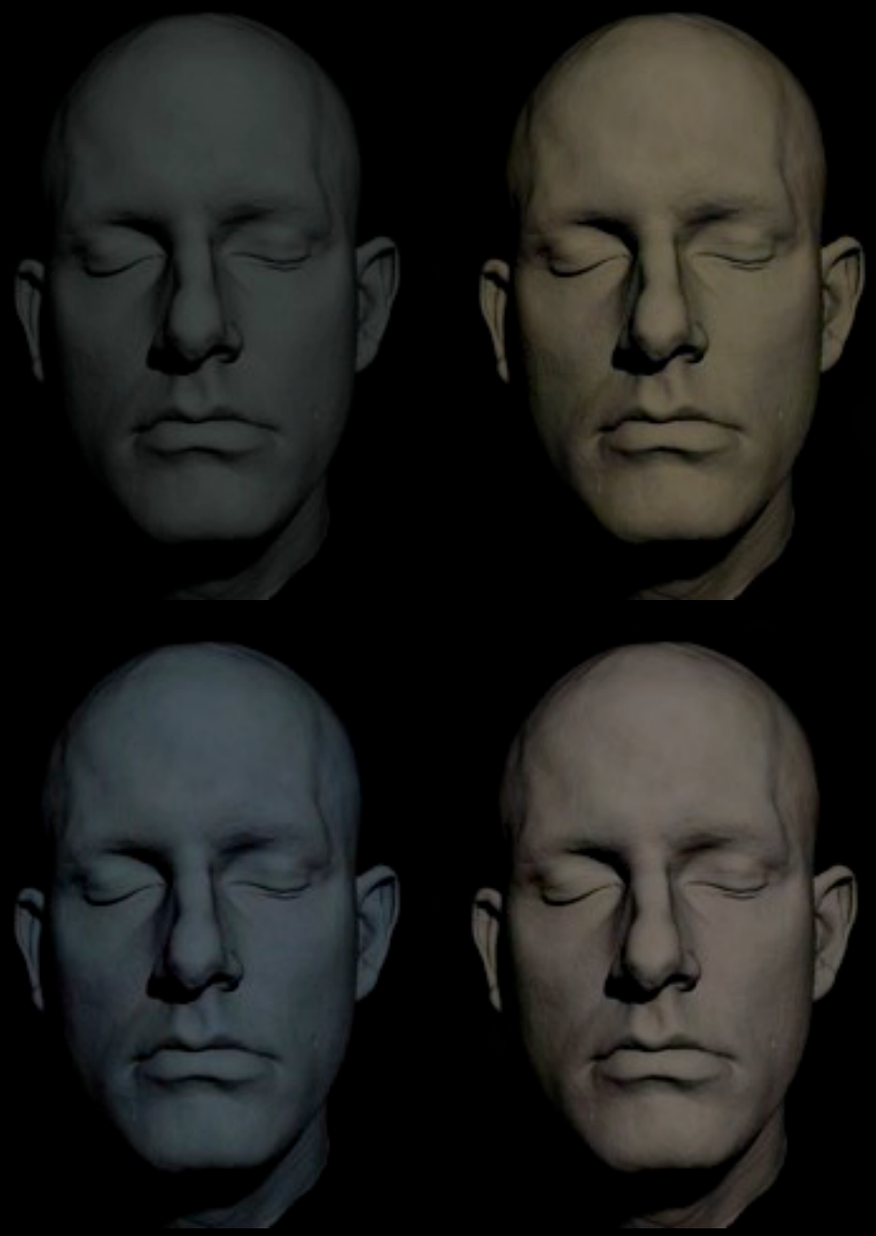

Scattering

Absorbing

Model courtesy XYZRGB, parameters from Tuchin 2000

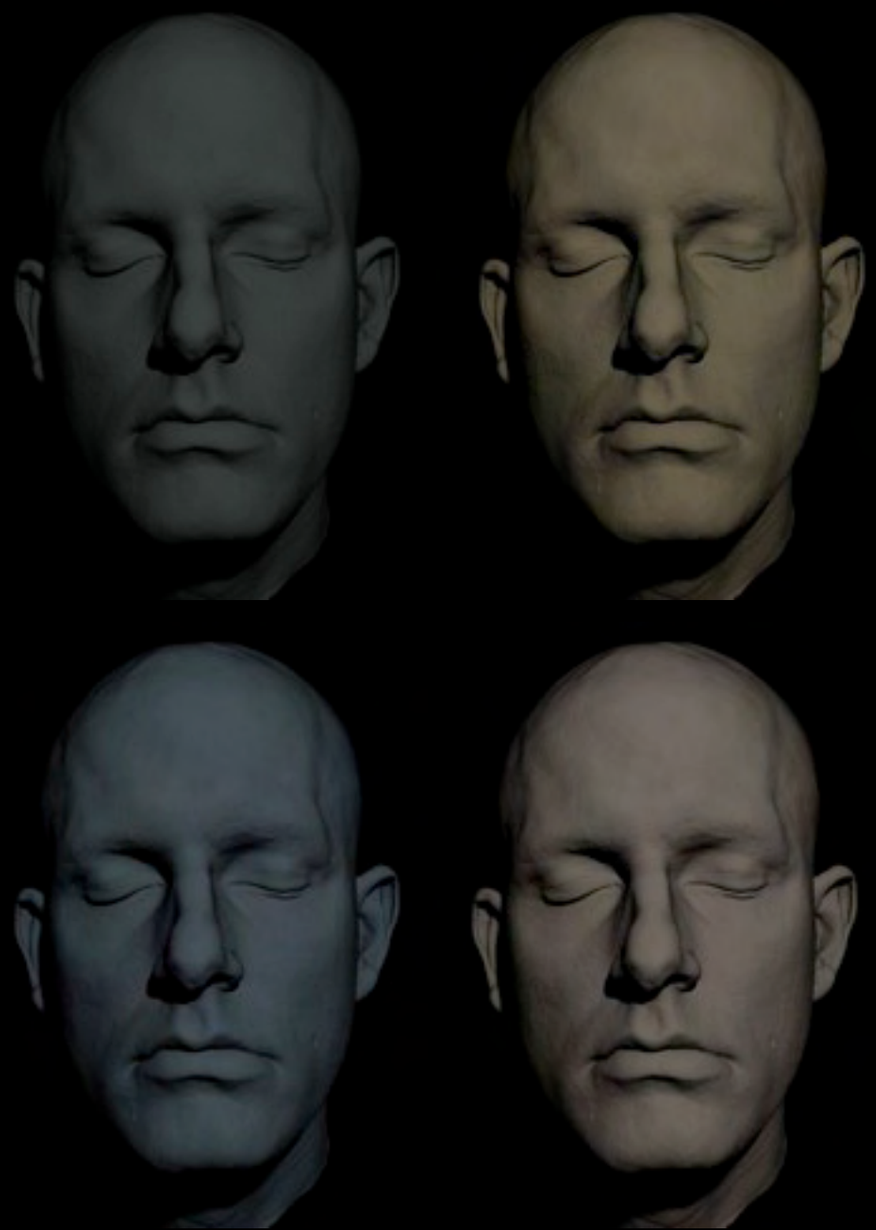

Scattering

Absorbing

Translucent

Model courtesy XYZRGB, parameters from Tuchin 2000

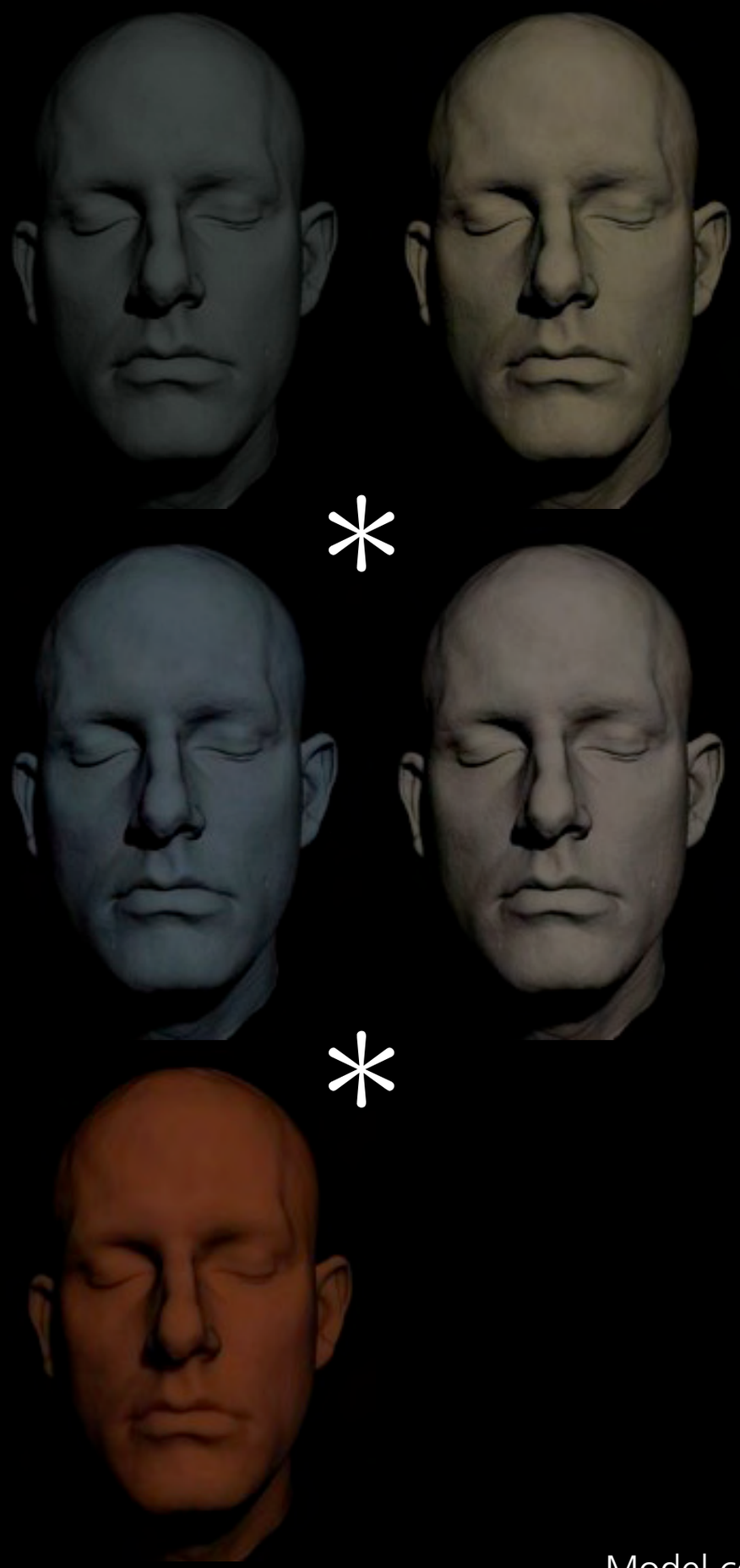

Model courtesy XYZRGB, parameters from Tuchin 2000

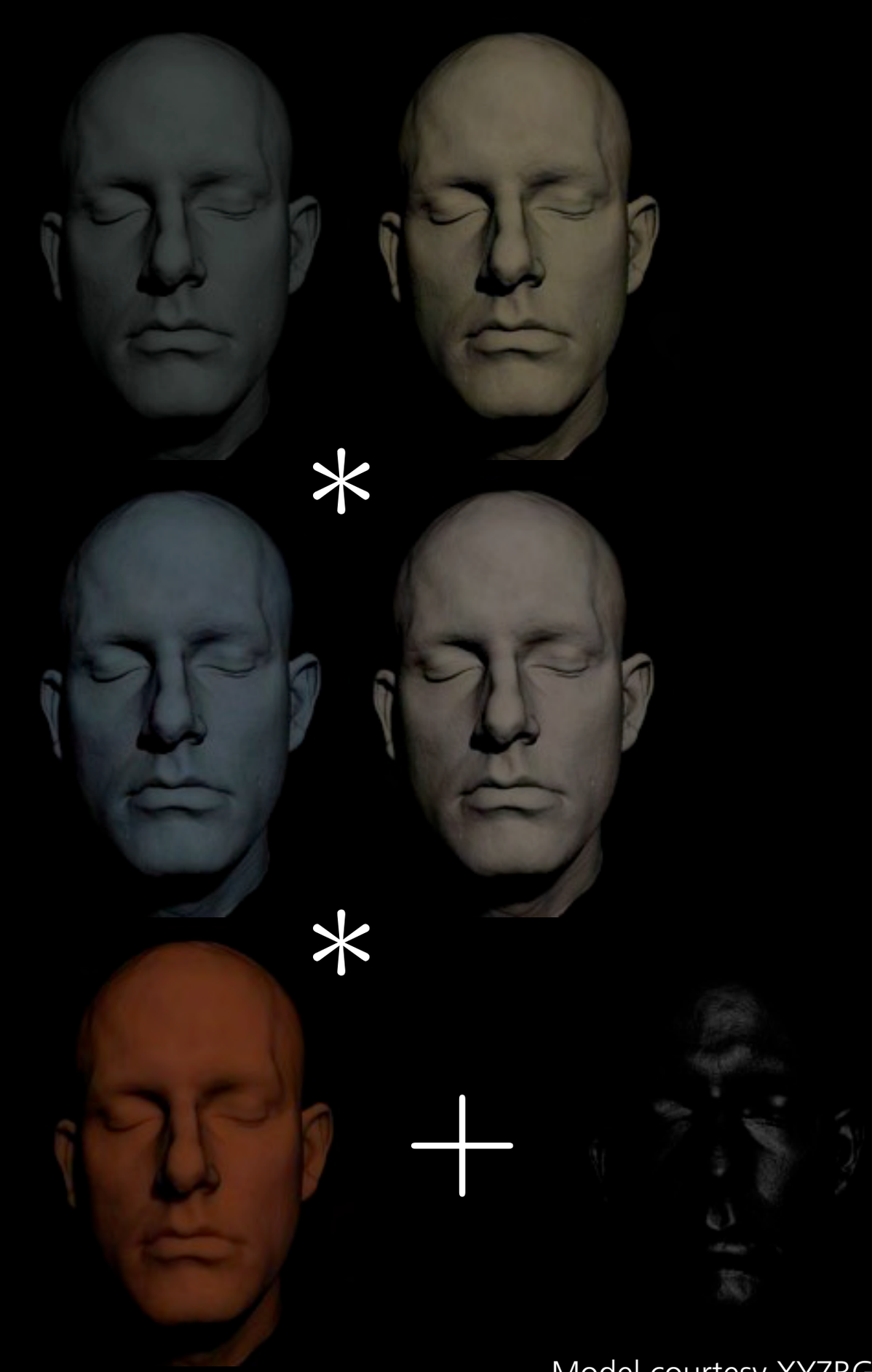

Model courtesy XYZRGB, parameters from Tuchin 2000

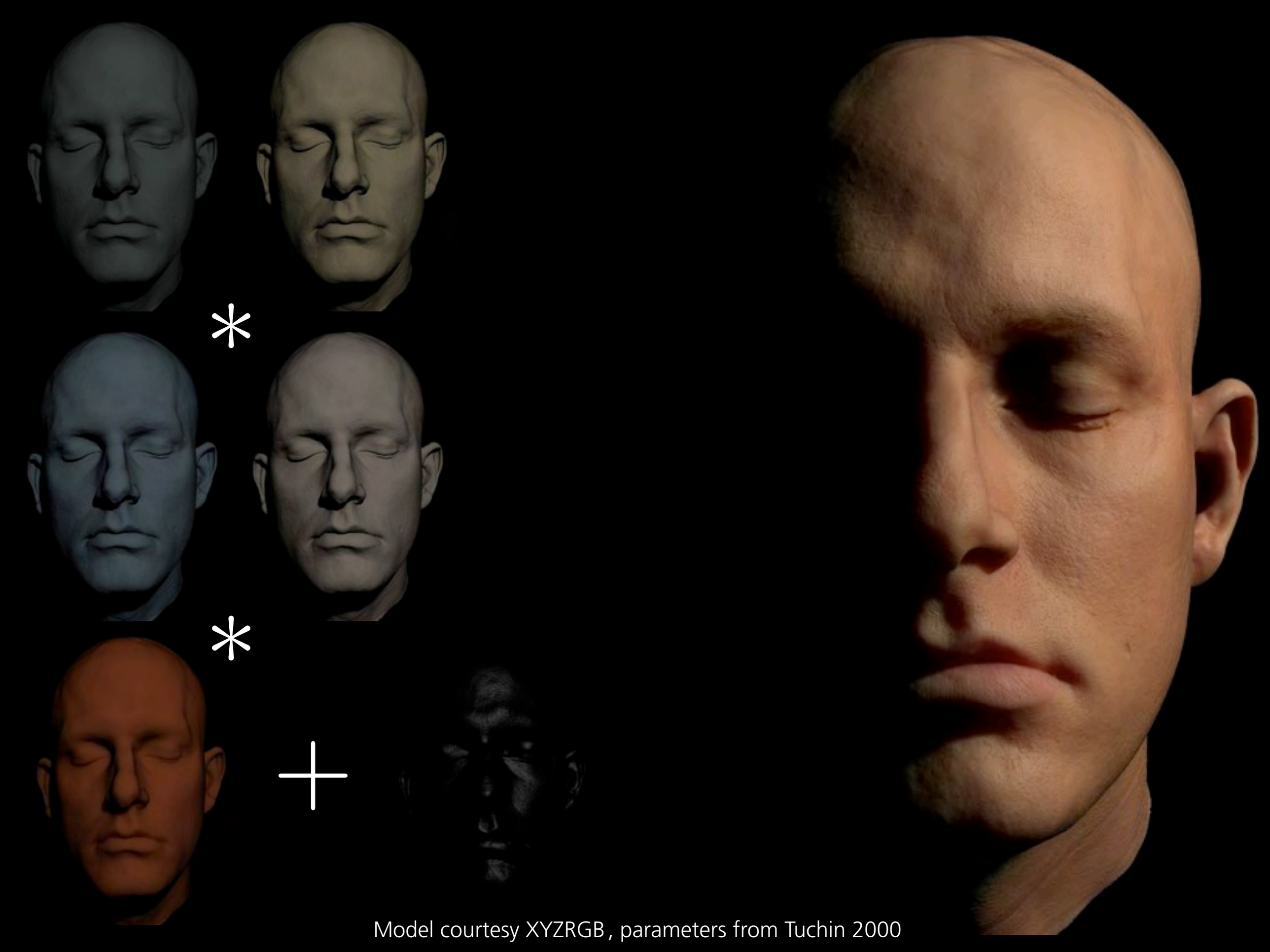

Model courtesy XYZRGB, parameters from Tuchin 2000

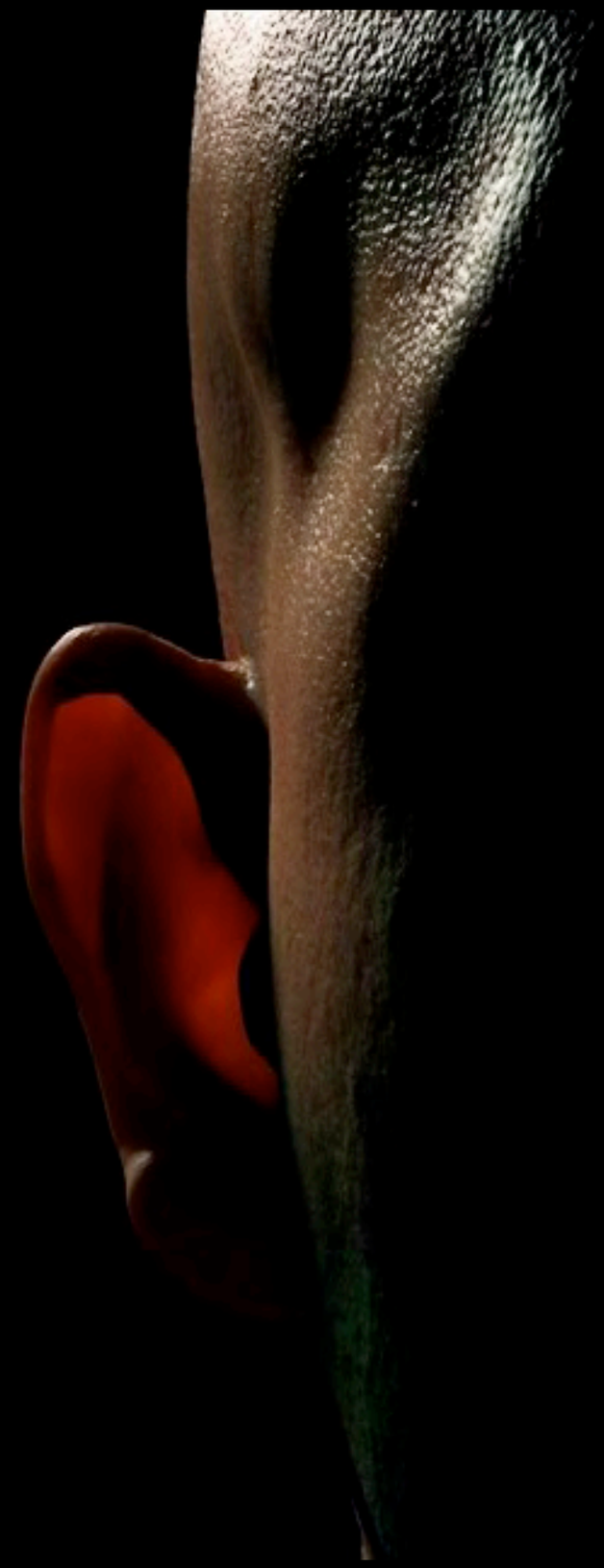

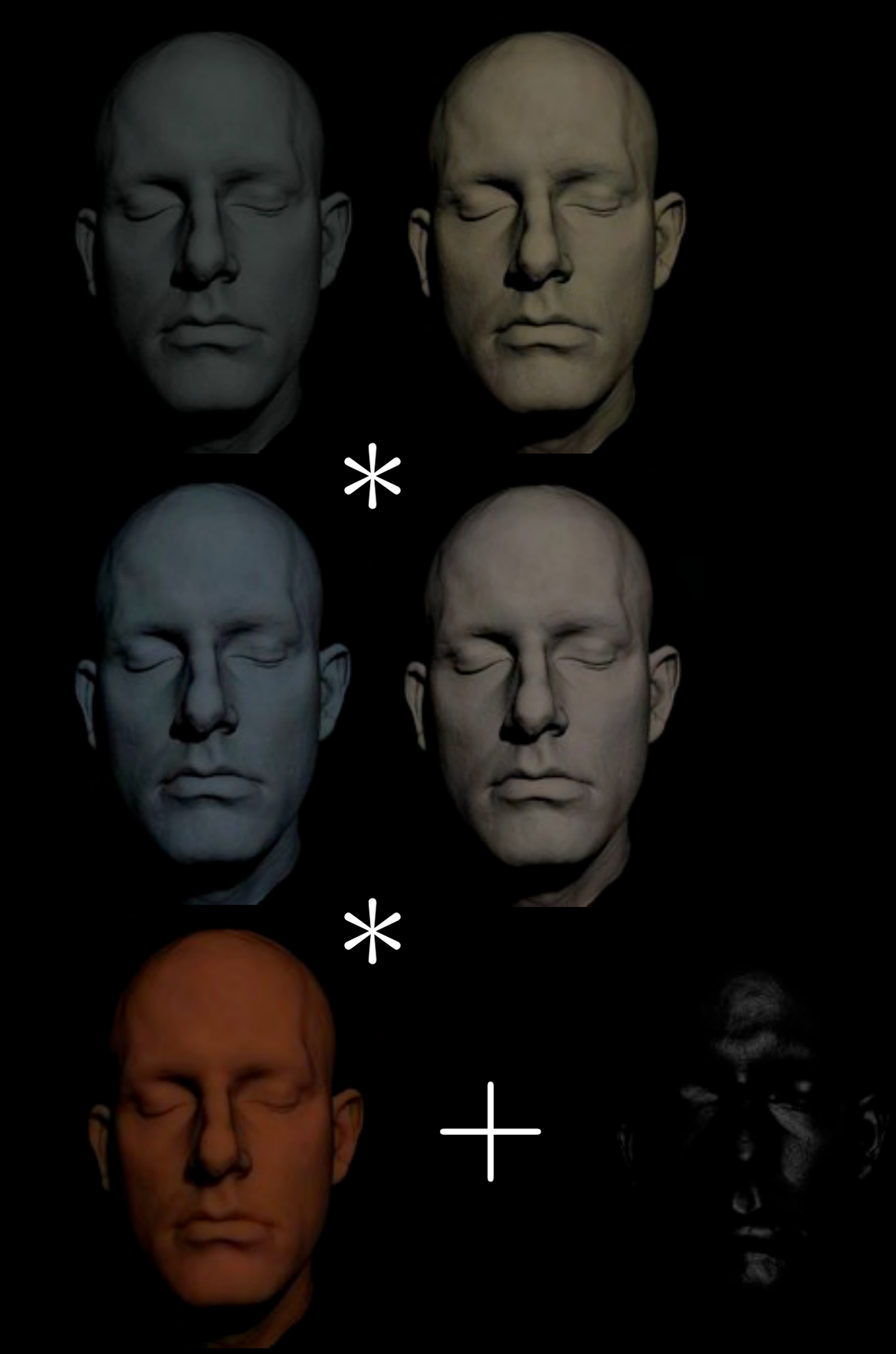

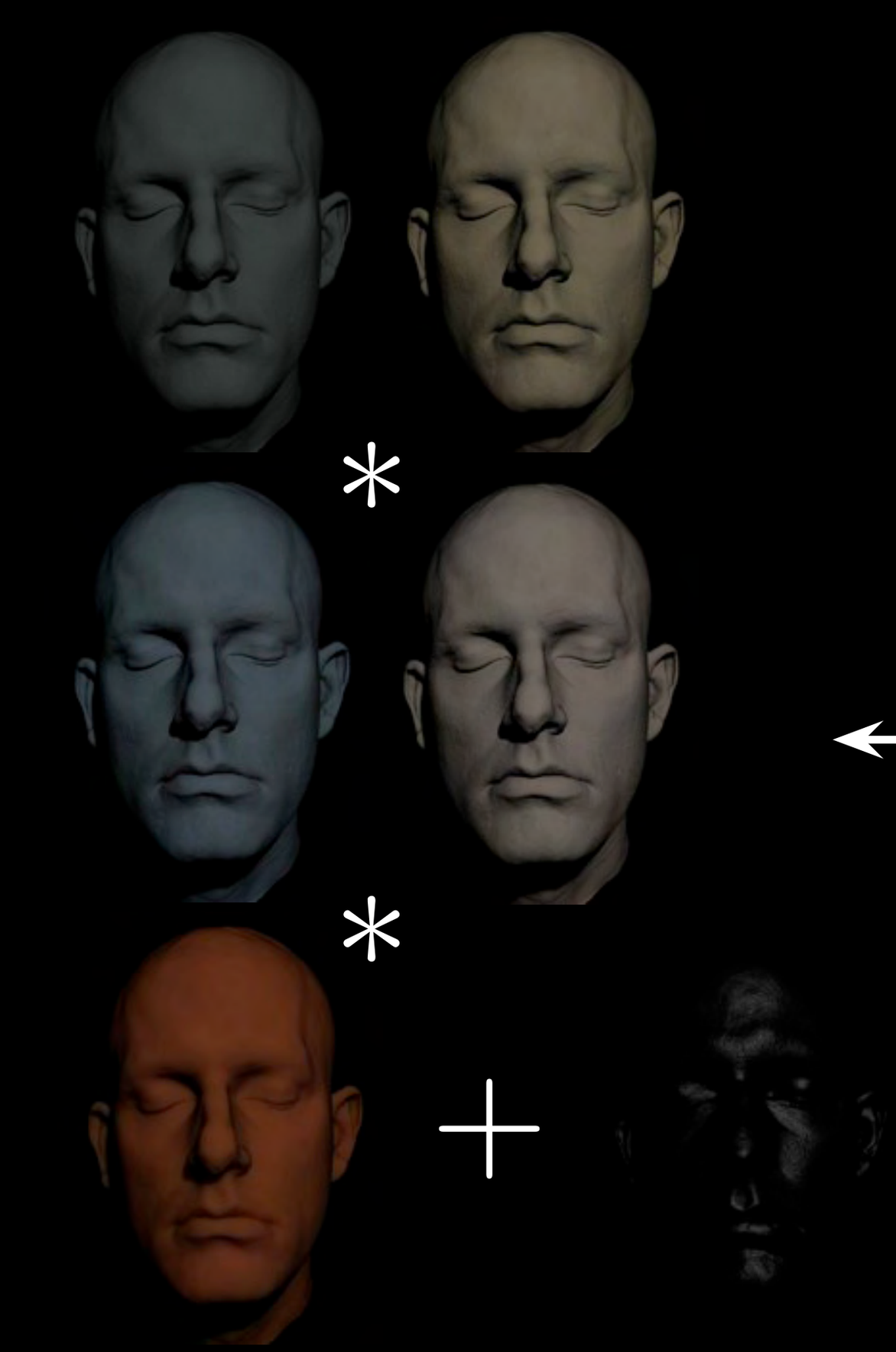

Biological properties of skin

Skin structure

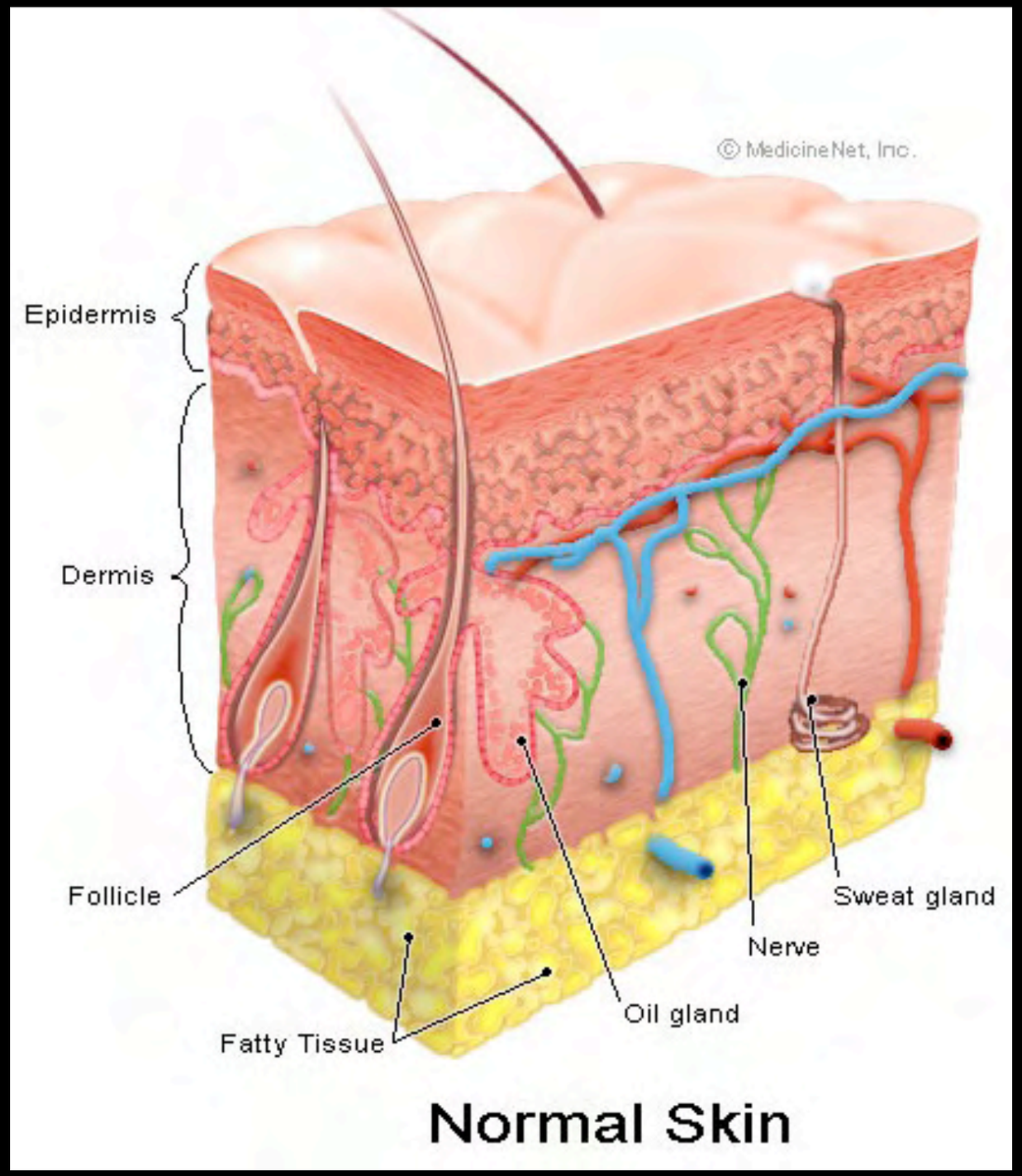

http://www.medicinenet.com

Skin absorption

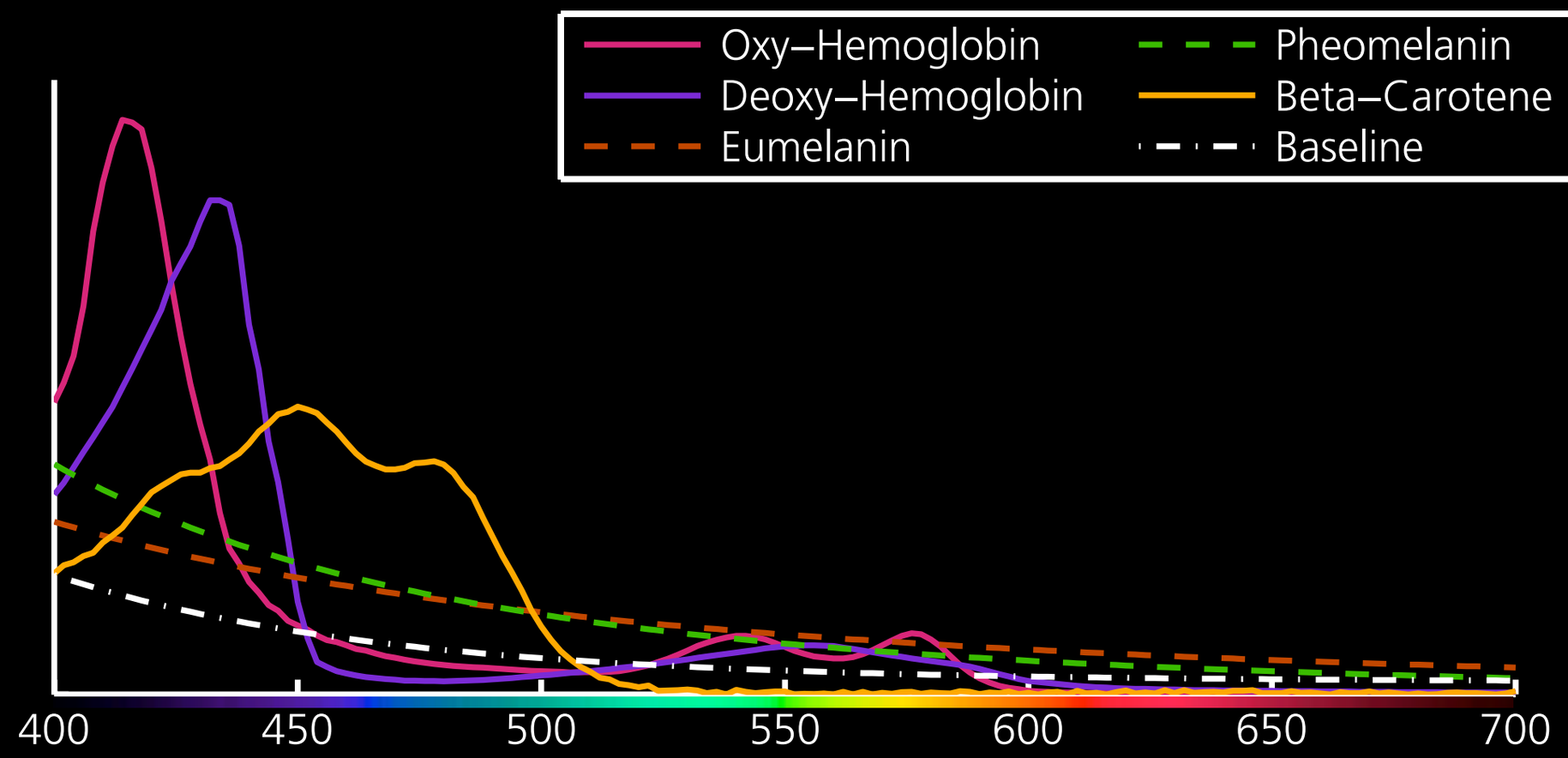

- Spectral appearance affected by
  - Chromophore absorption spectra

Skin absorption

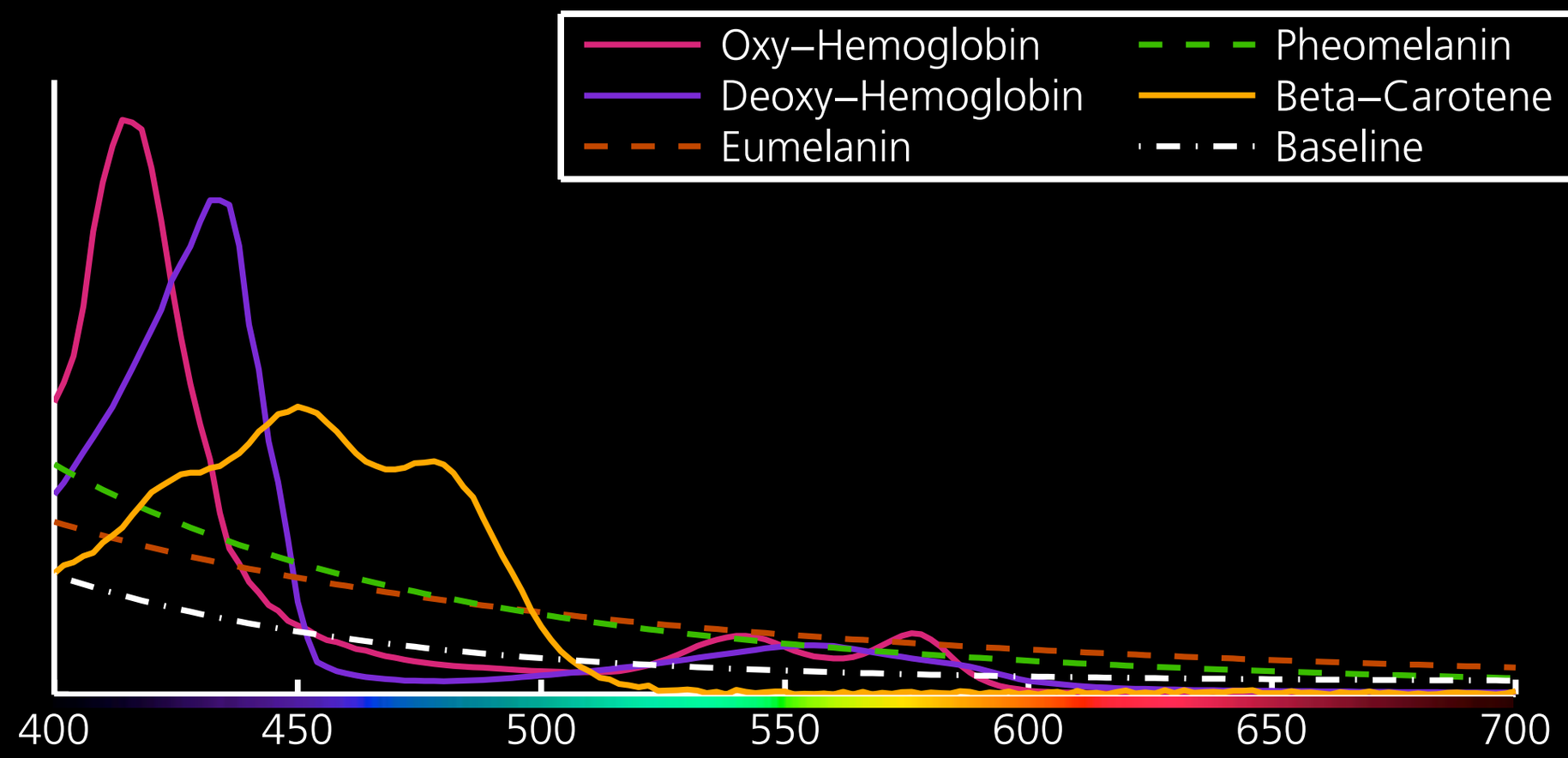

- Spectral appearance affected by
  - Chromophore absorption spectra
  - Scattering and depth of deposition

Skin structure

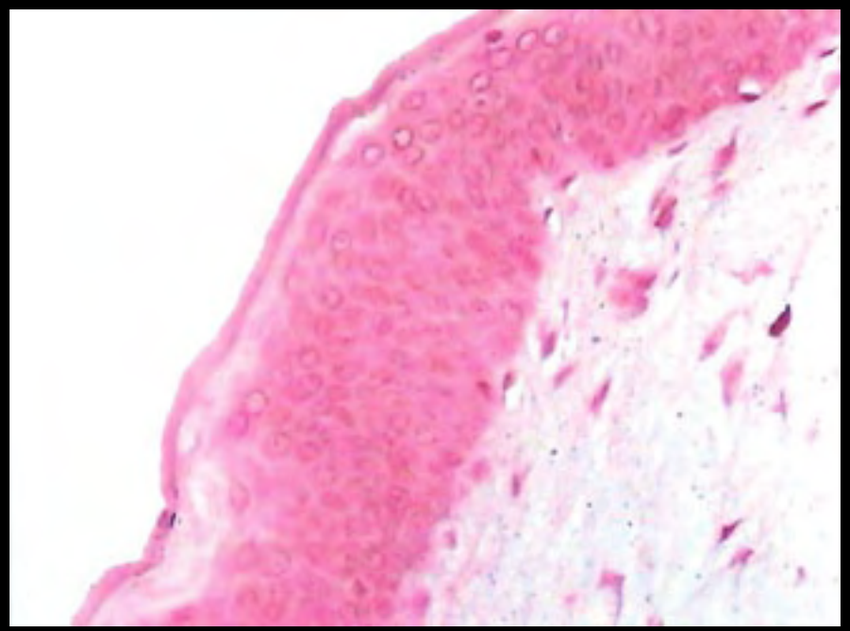

Type I (white)

Images from [Matts et al. 2007]

Skin structure

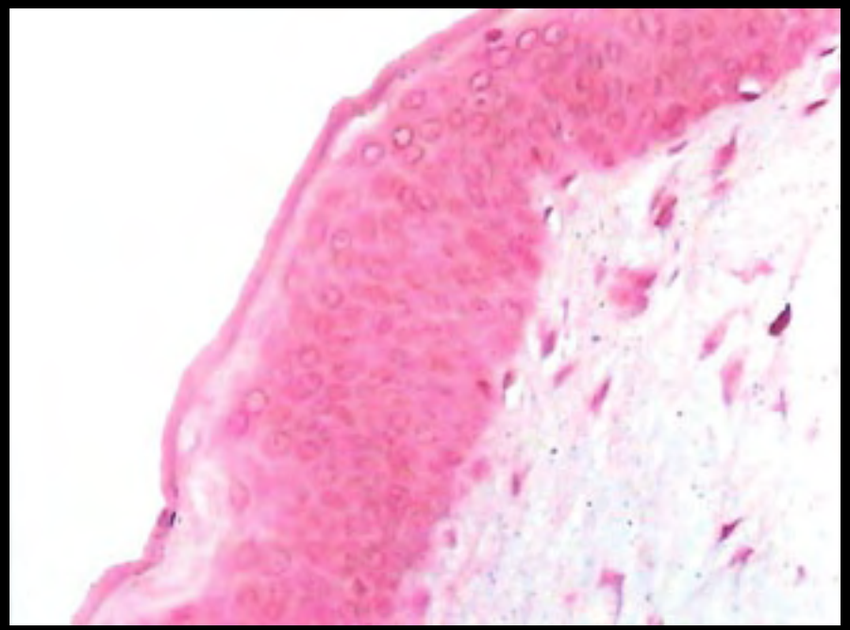

Type I (white)

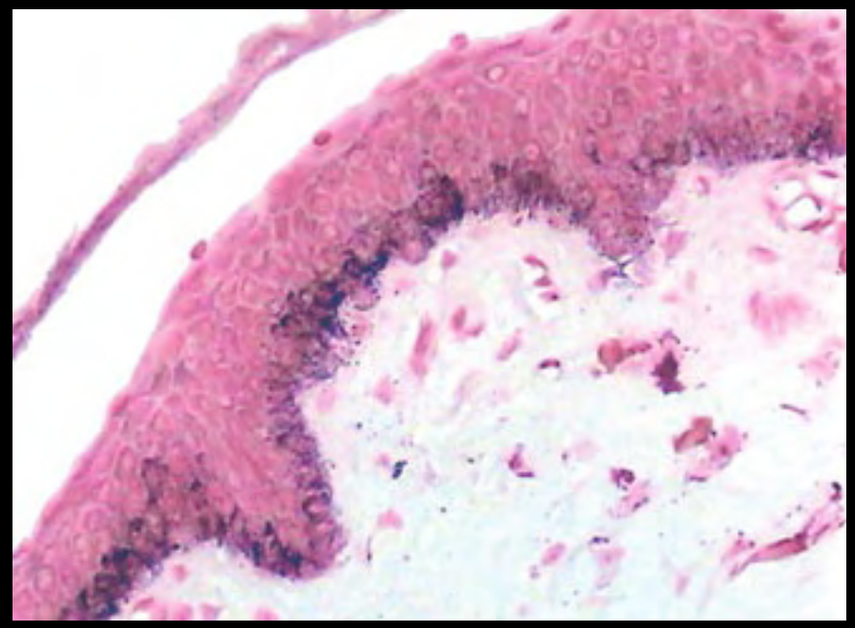

Type IV (brown)

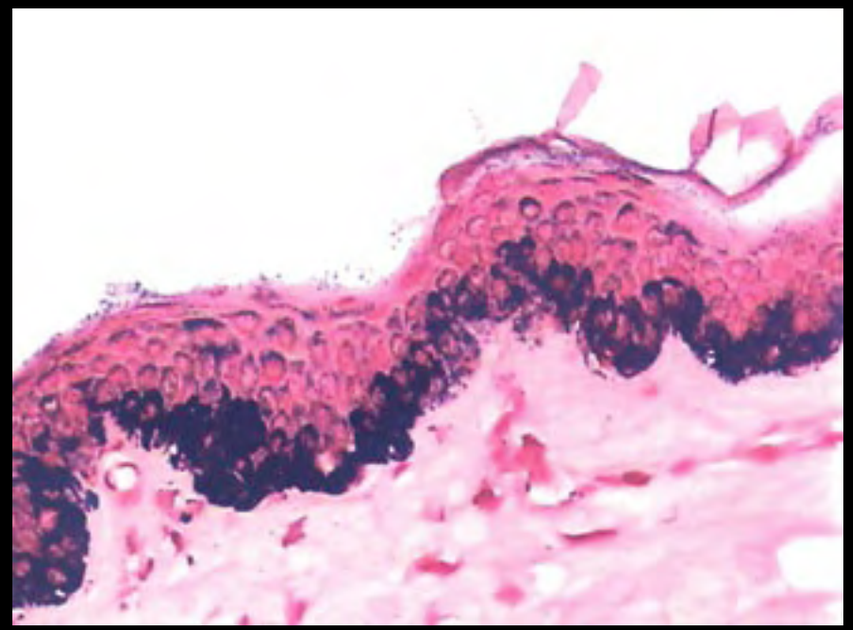

Type VI (black)

Images from [Matts et al. 2007]

Skin structure

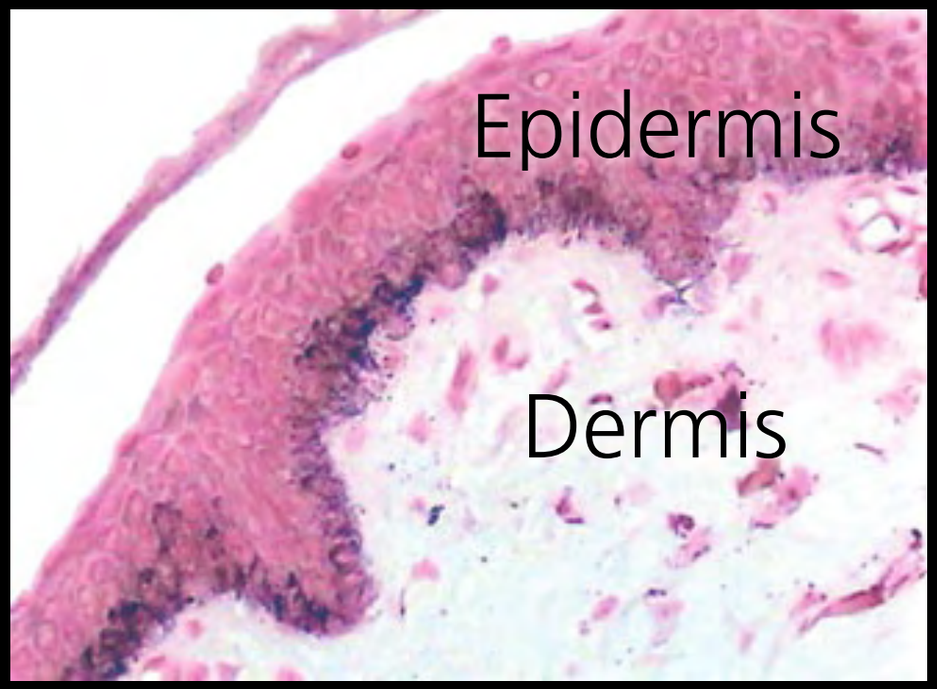

- Layered structure

Skin structure

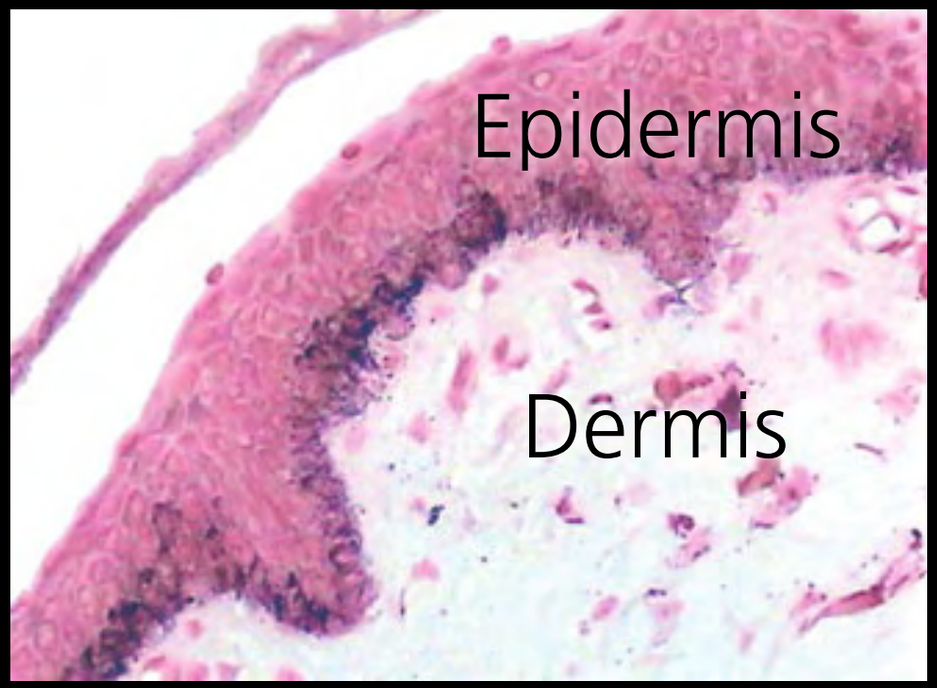

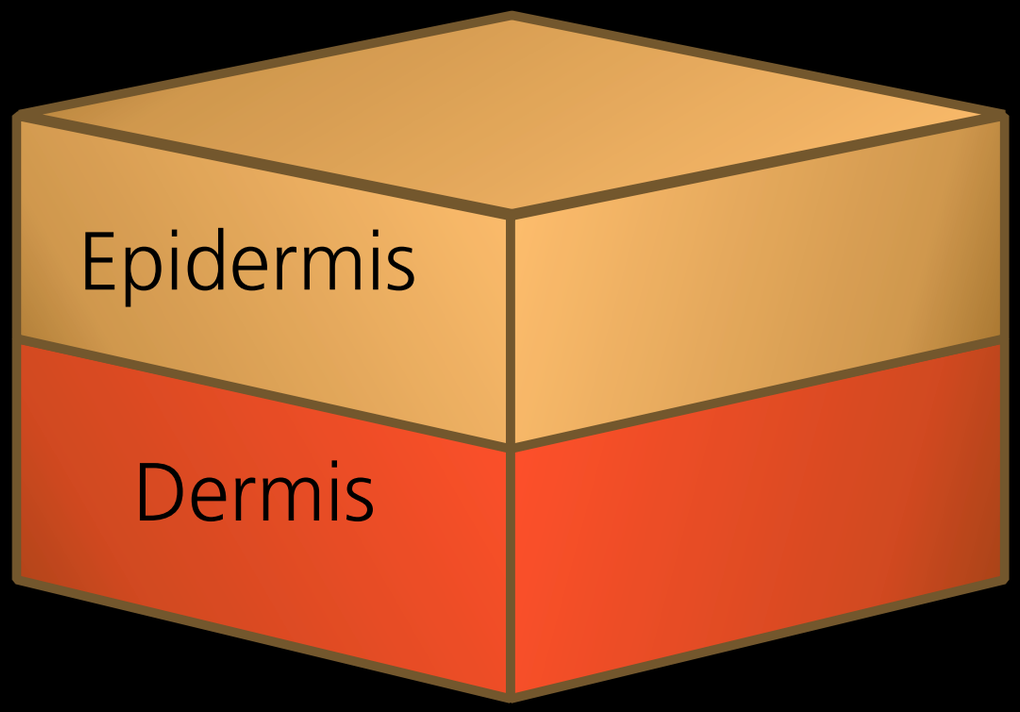

- Layered structure

Skin structure

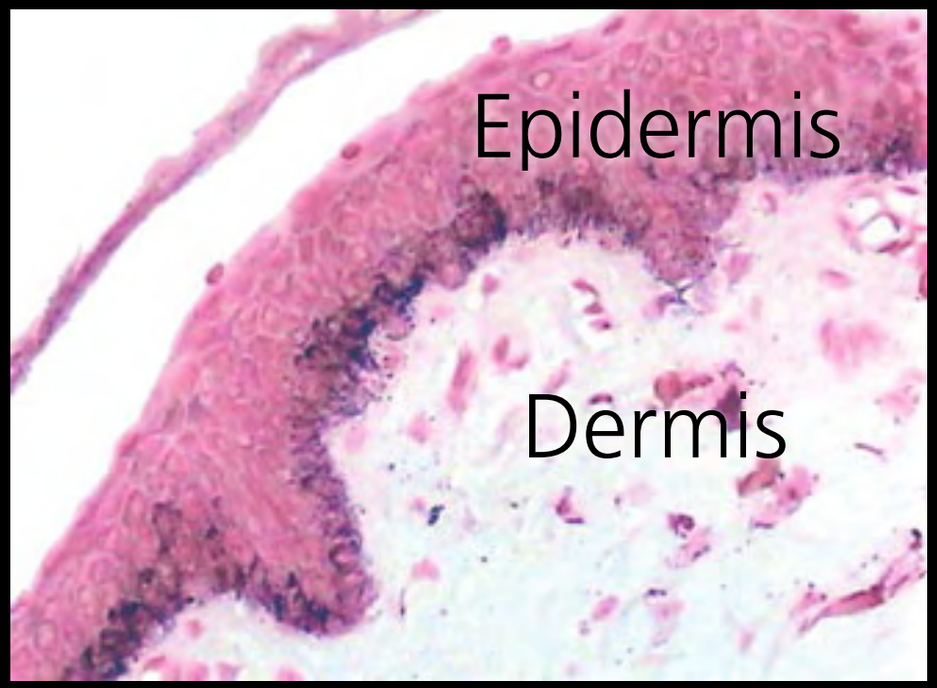

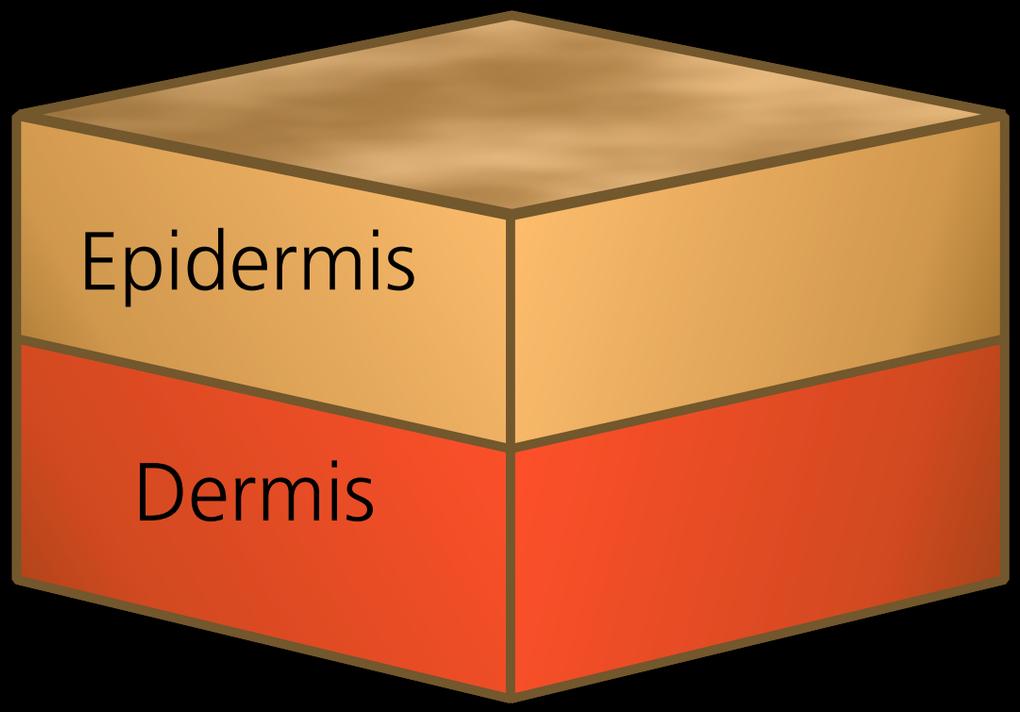

- Layered structure
- Heterogeneous medium
  - Spatial variance

Skin structure

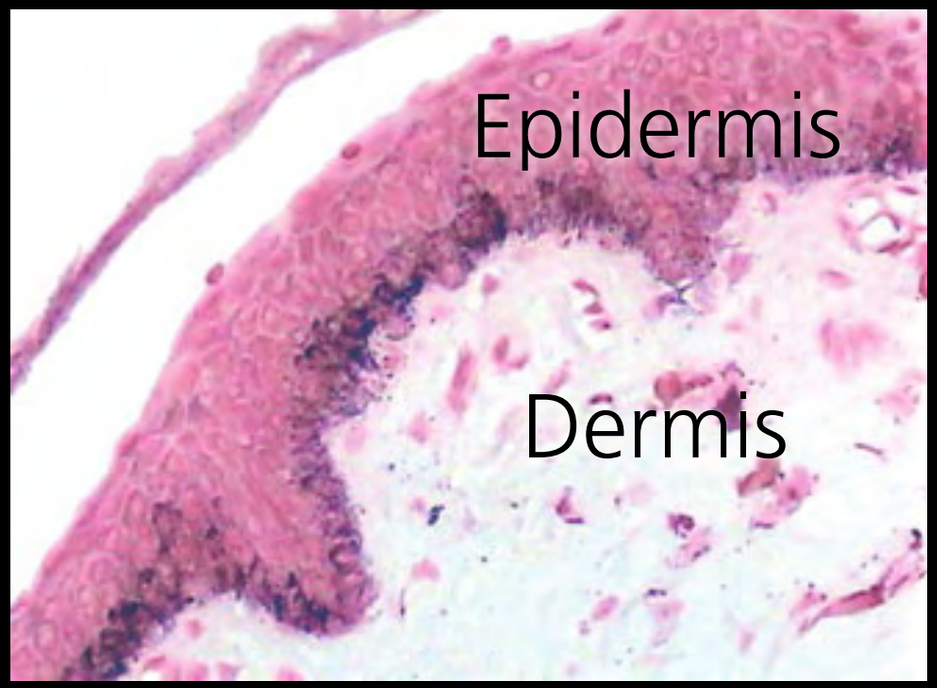

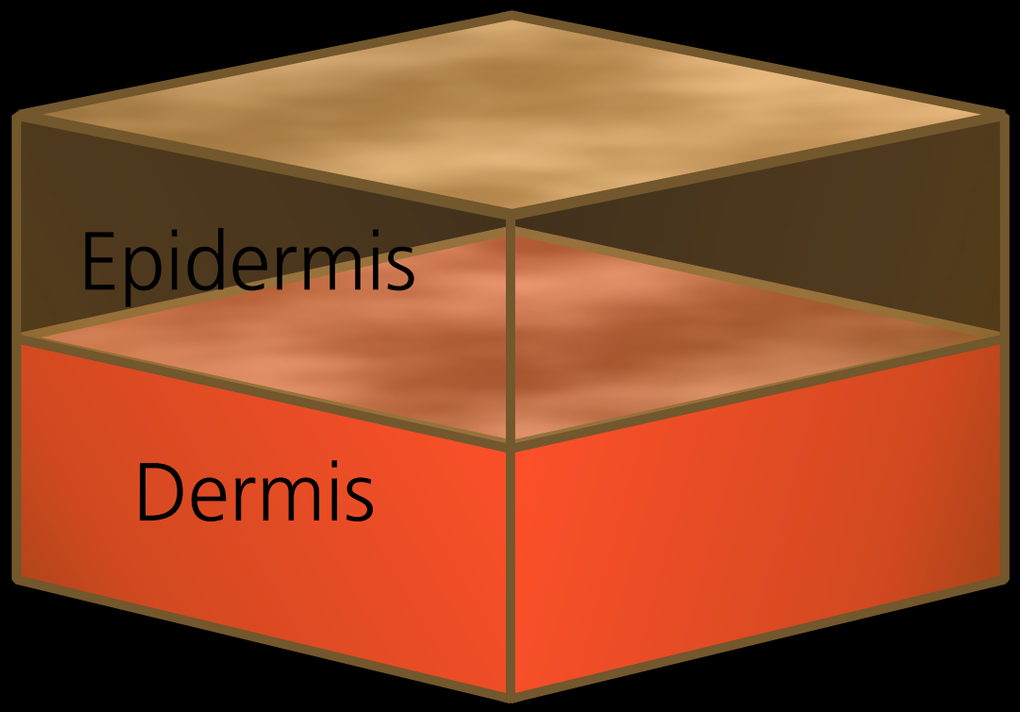

- Layered structure
- Heterogeneous medium
  - Spatial variance
  - Inter-layer absorption

Skin structure

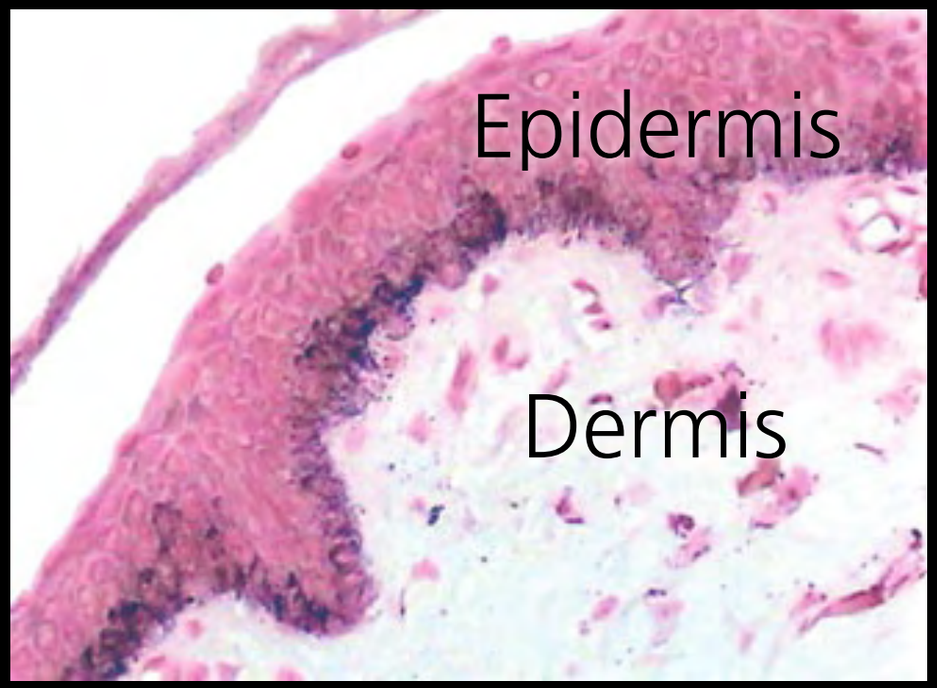

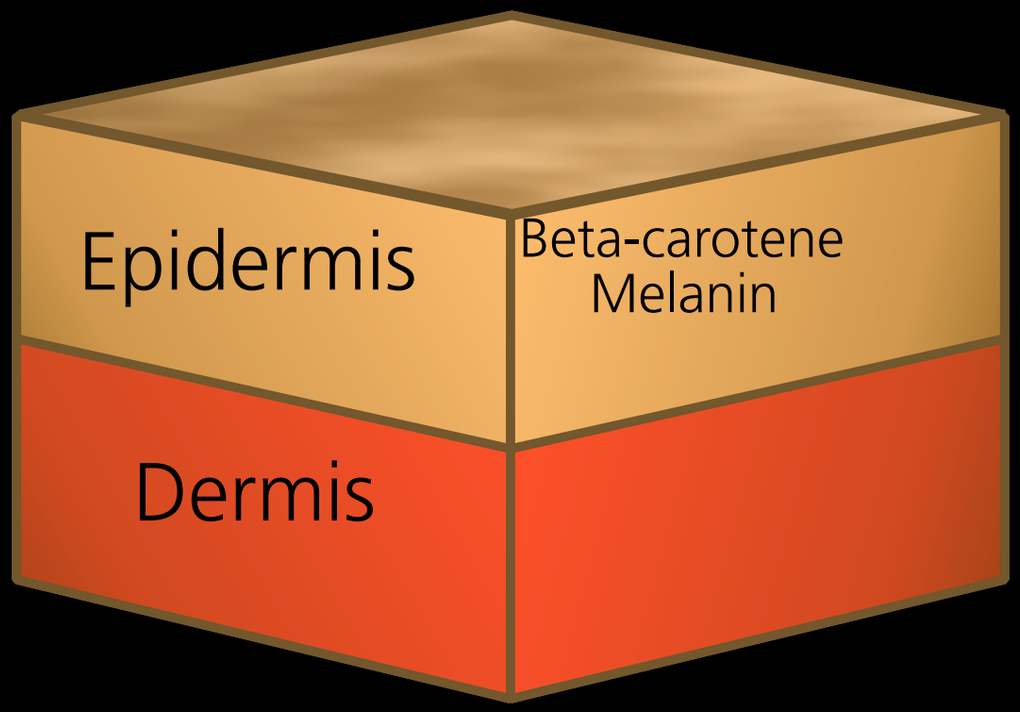

- Layered structure
- Heterogeneous medium
  - Spatial variance
  - Inter-layer absorption
- Characteristic pigment distribution

Skin structure

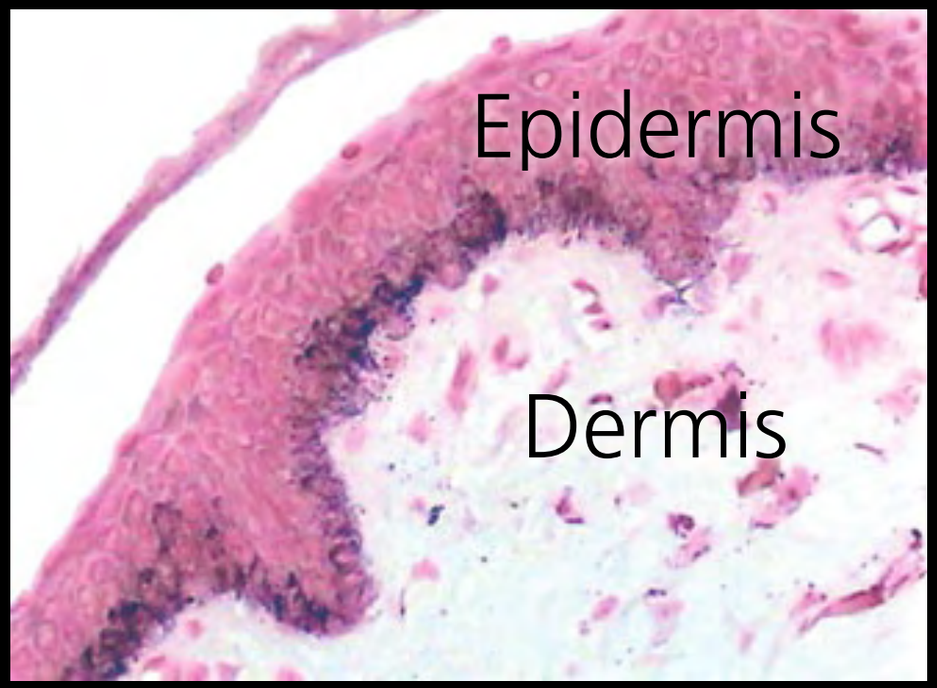

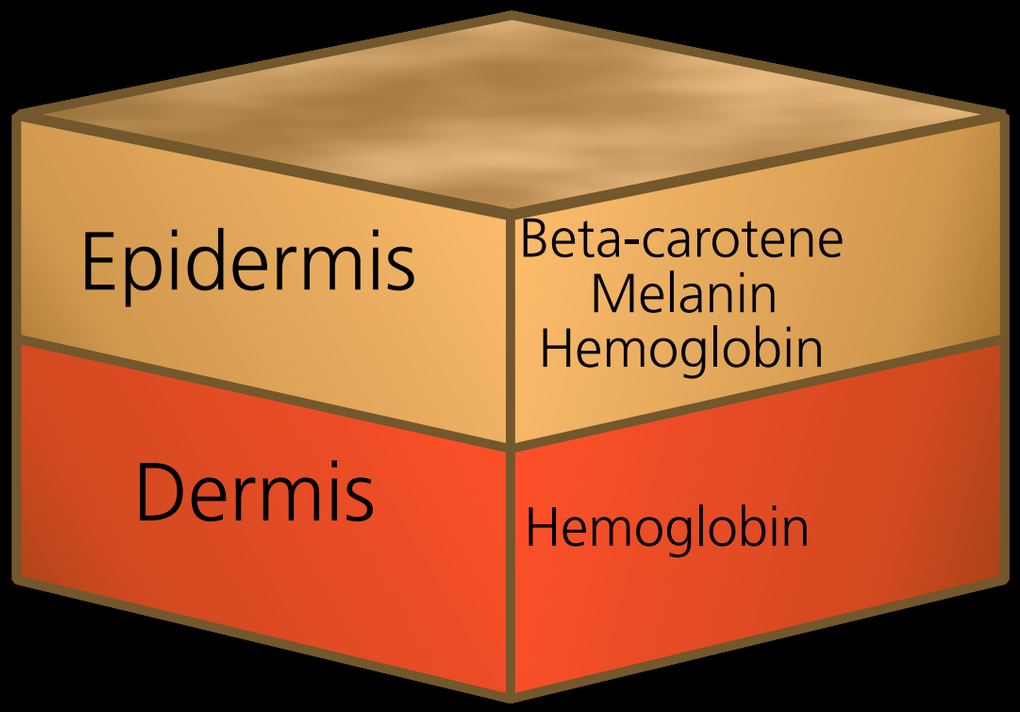

- Layered structure
- Heterogeneous medium
  - Spatial variance
  - Inter-layer absorption
- Characteristic pigment distribution

Skin structure

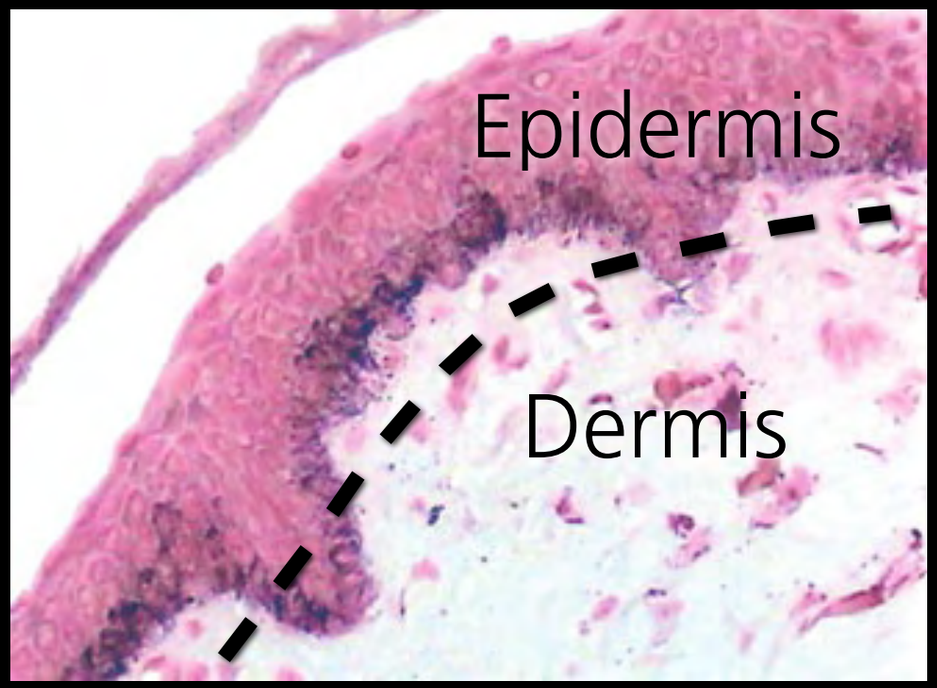

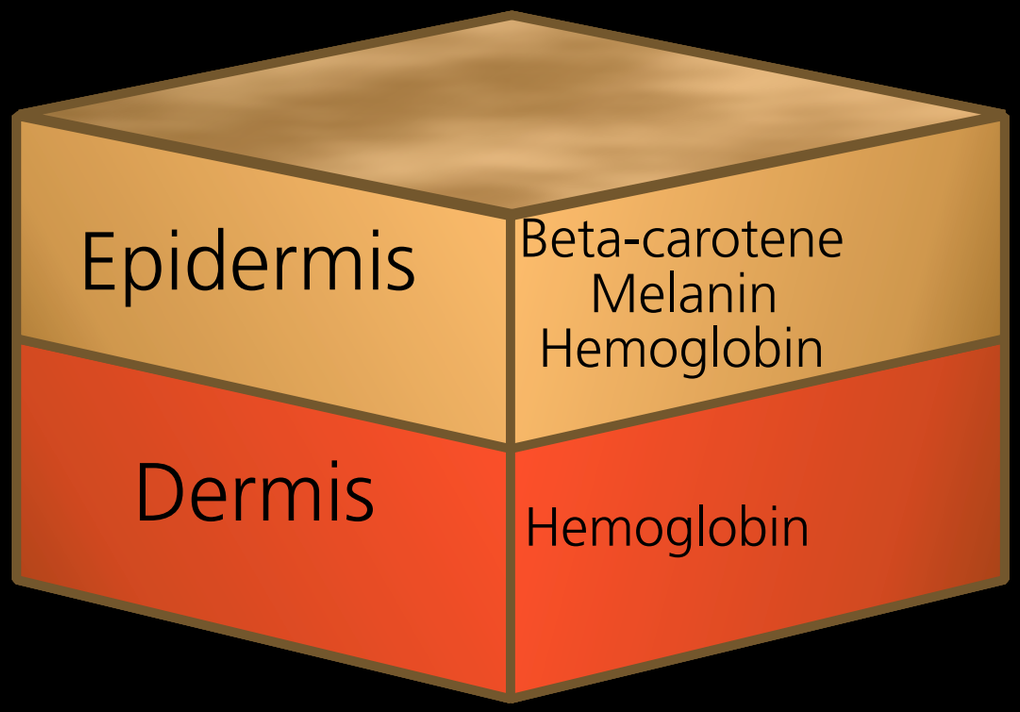

- Layered structure
- Heterogeneous medium
  - Spatial variance
  - Inter-layer absorption
- Characteristic pigment distribution

Skin model (absorption)

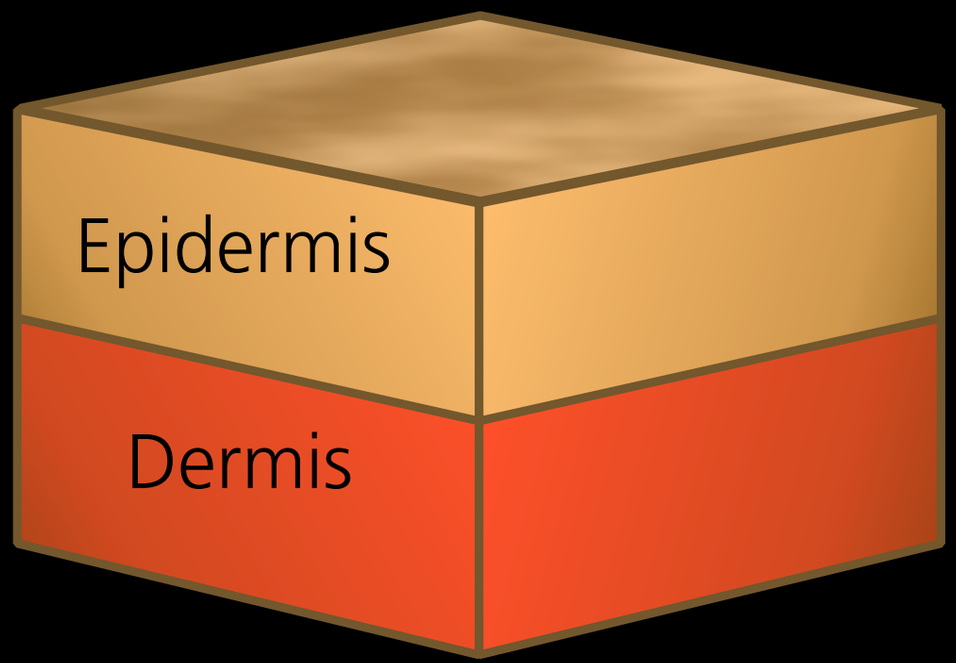

Skin model (absorption)

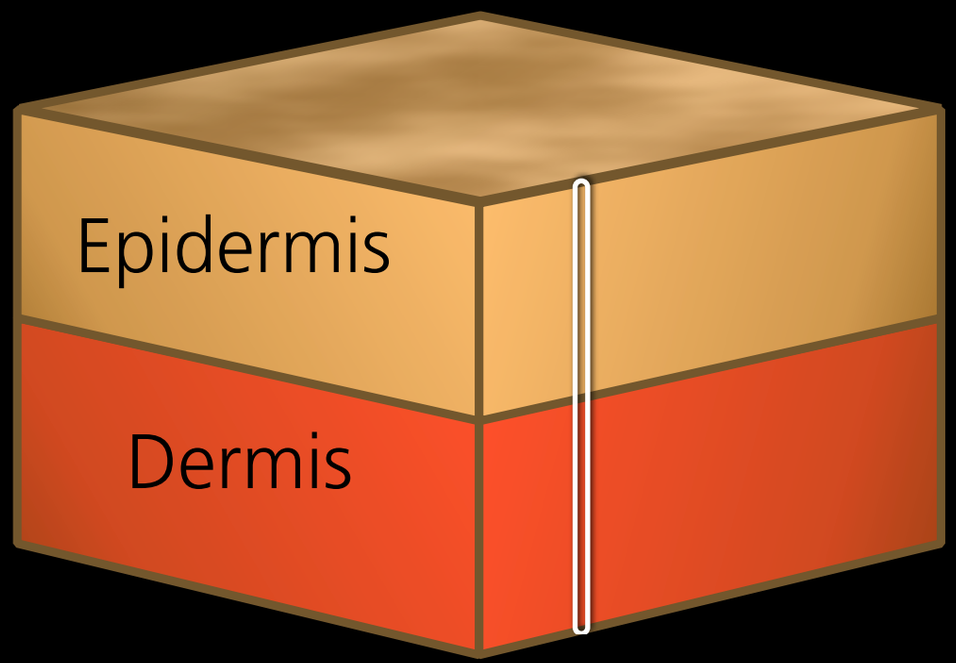

Skin model (absorption)

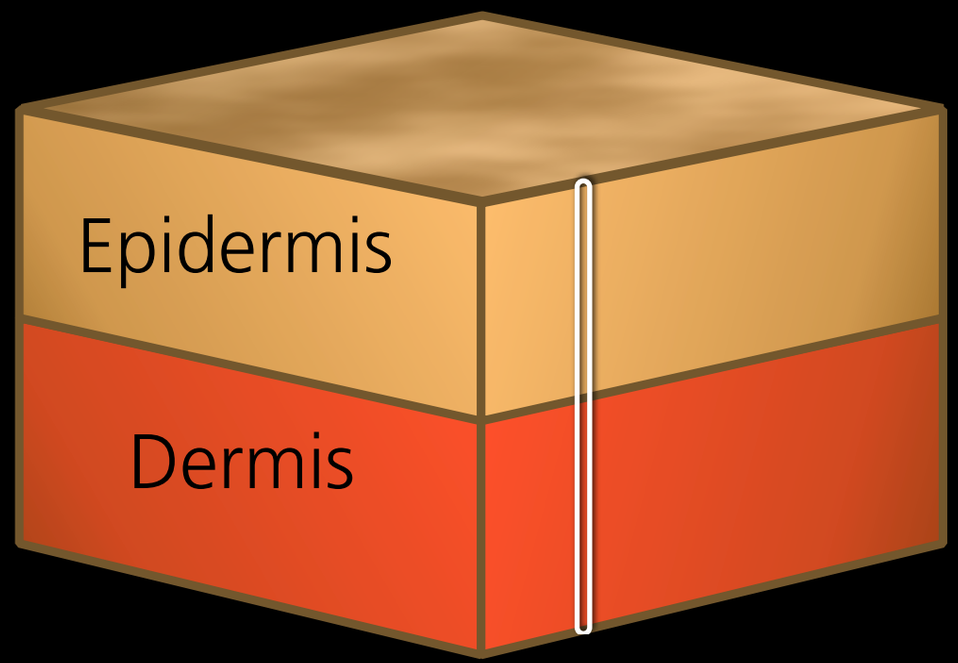

Epidermis

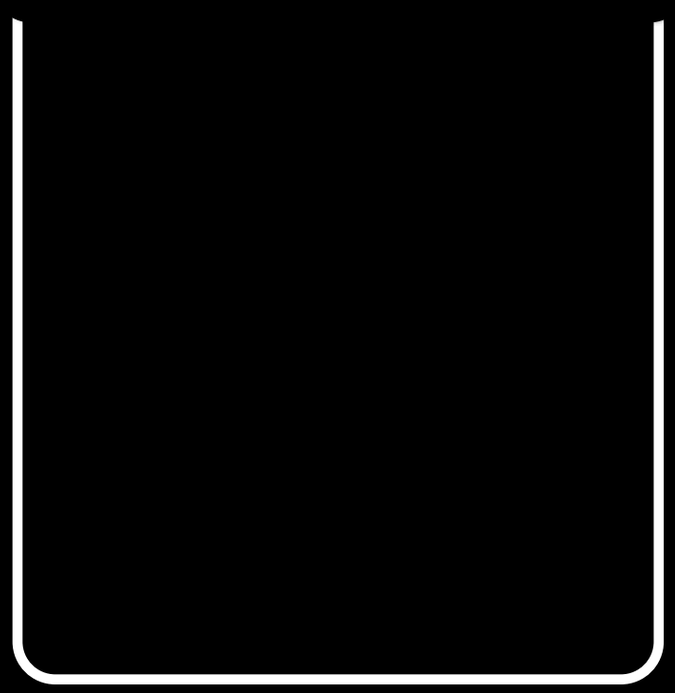

Skin model (absorption)

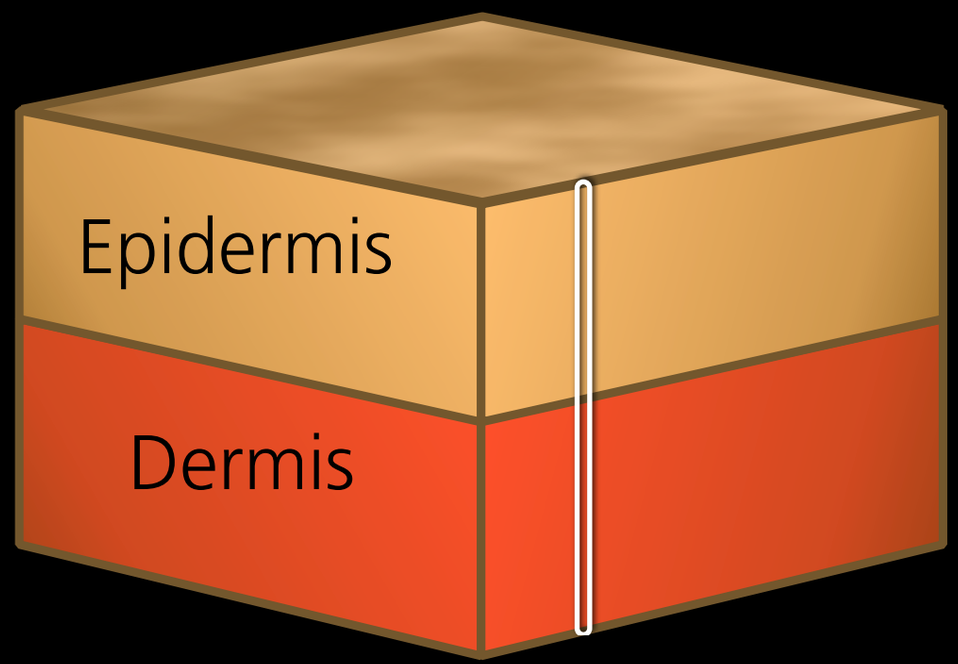

Epidermis

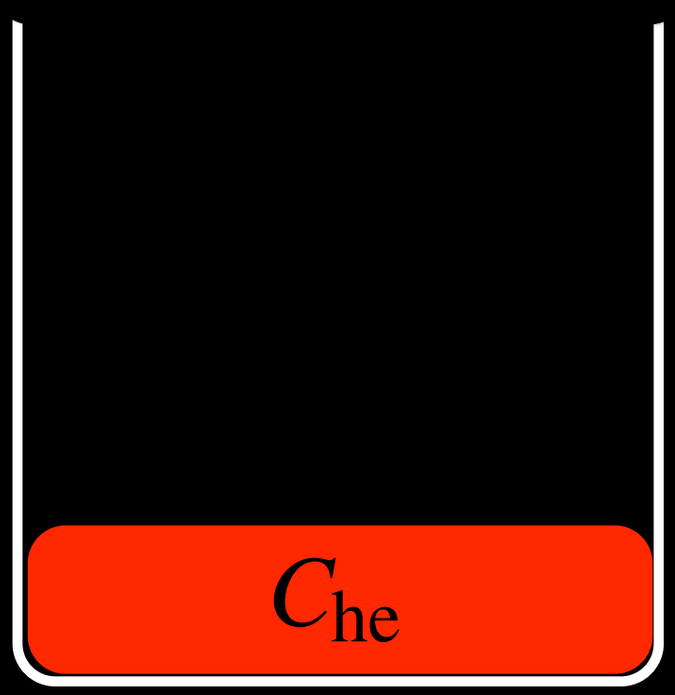

Hemoglobin

Skin model (absorption)

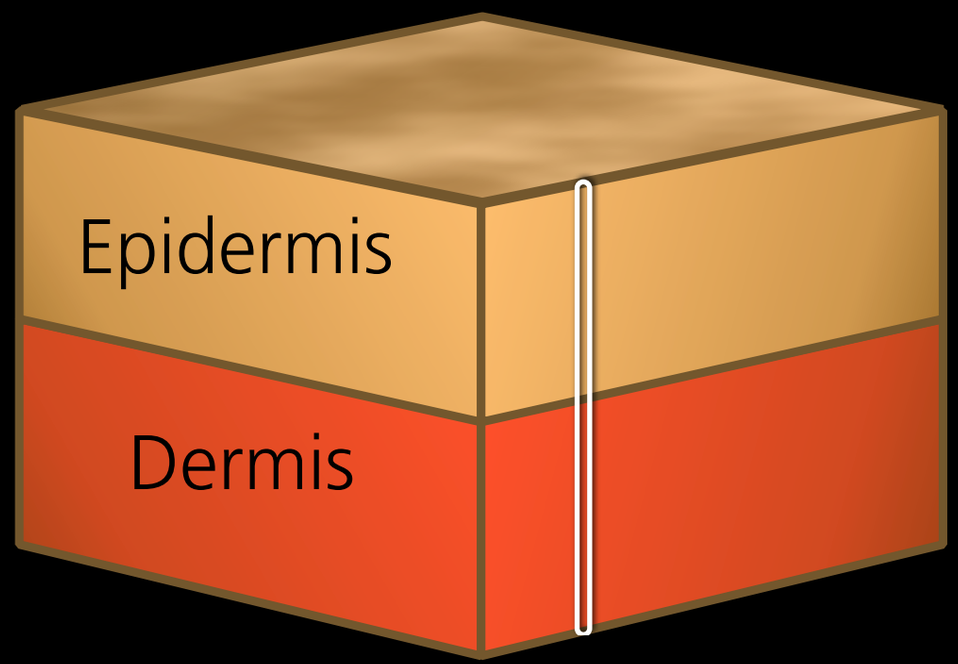

Epidermis

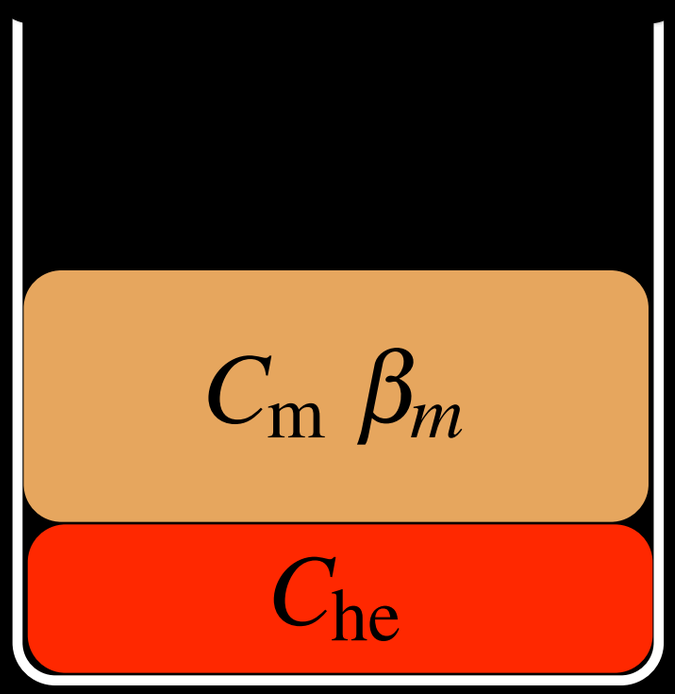

Eumelanin

Pheomelanin

Hemoglobin

Skin model (absorption)

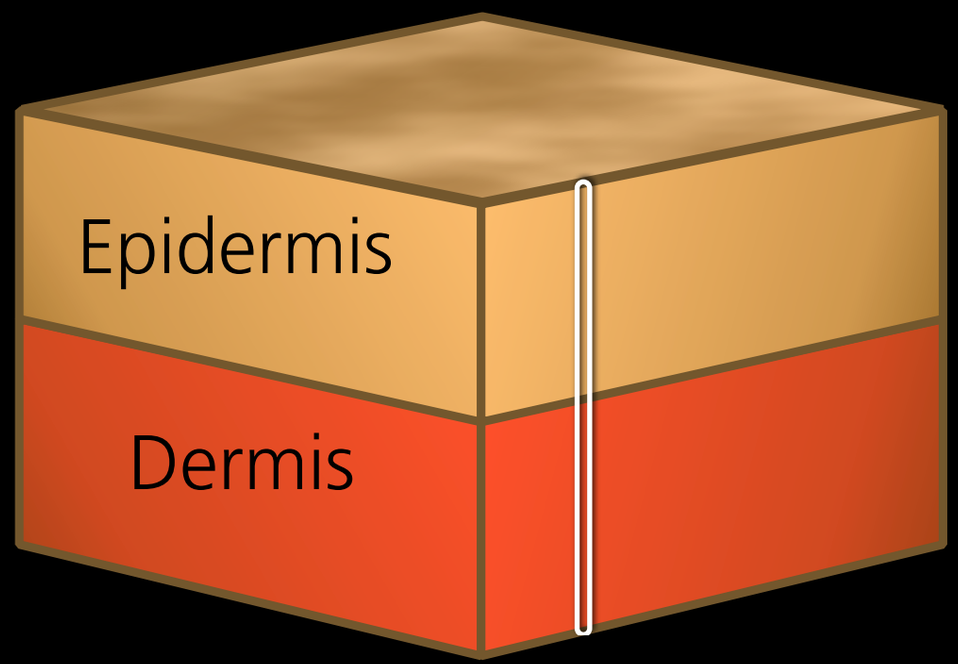

Epidermis

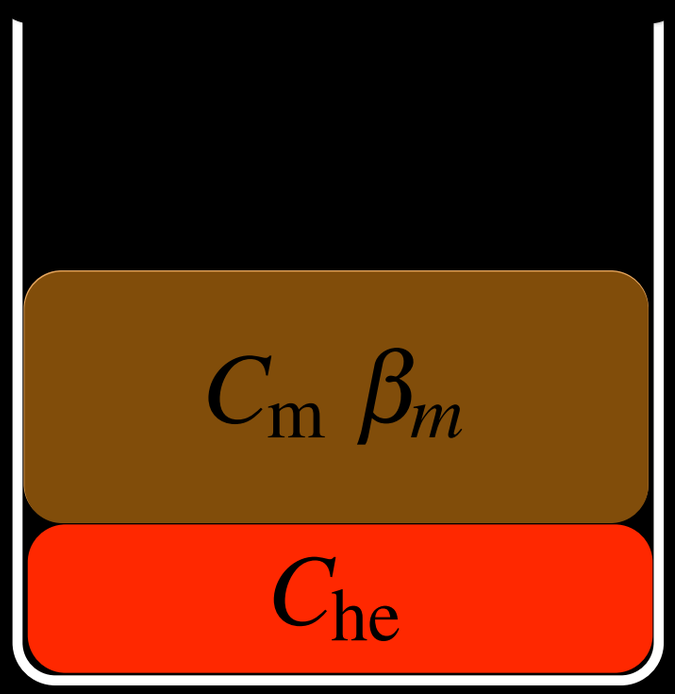

Eumelanin

Pheomelanin

Hemoglobin

Skin model (absorption)

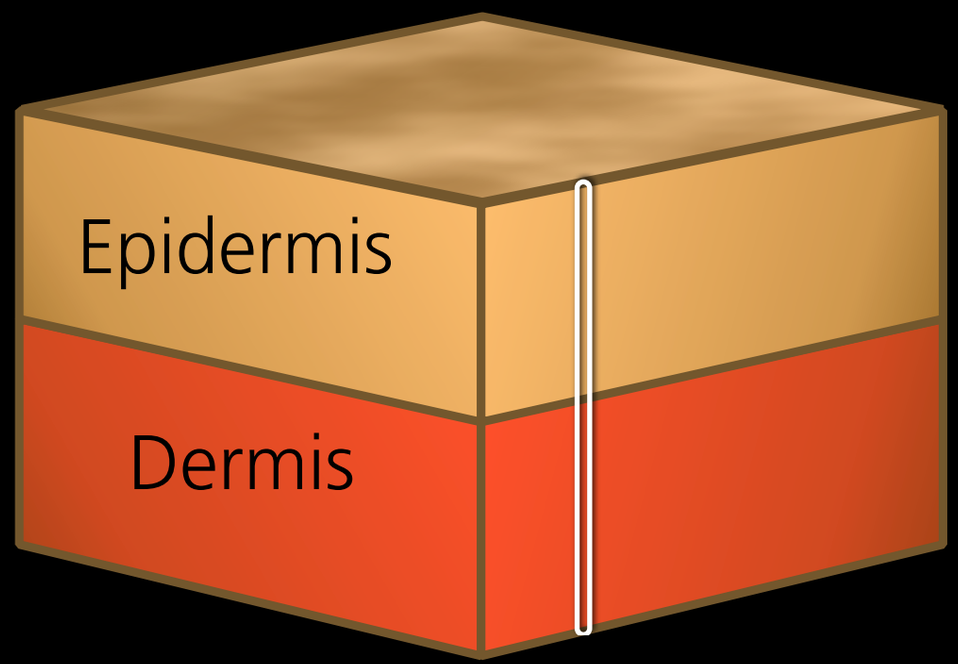

Epidermis

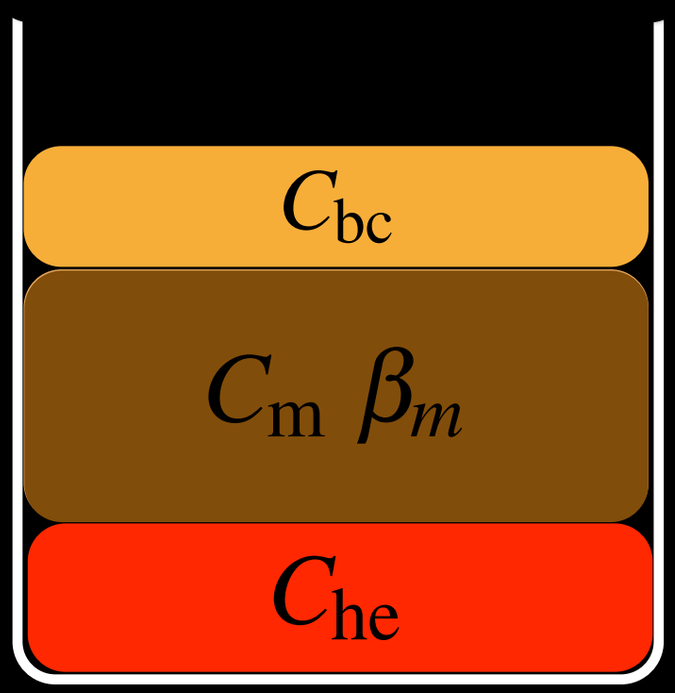

Beta-carotene

Eumelanin

Pheomelanin

Hemoglobin

Skin model (absorption)

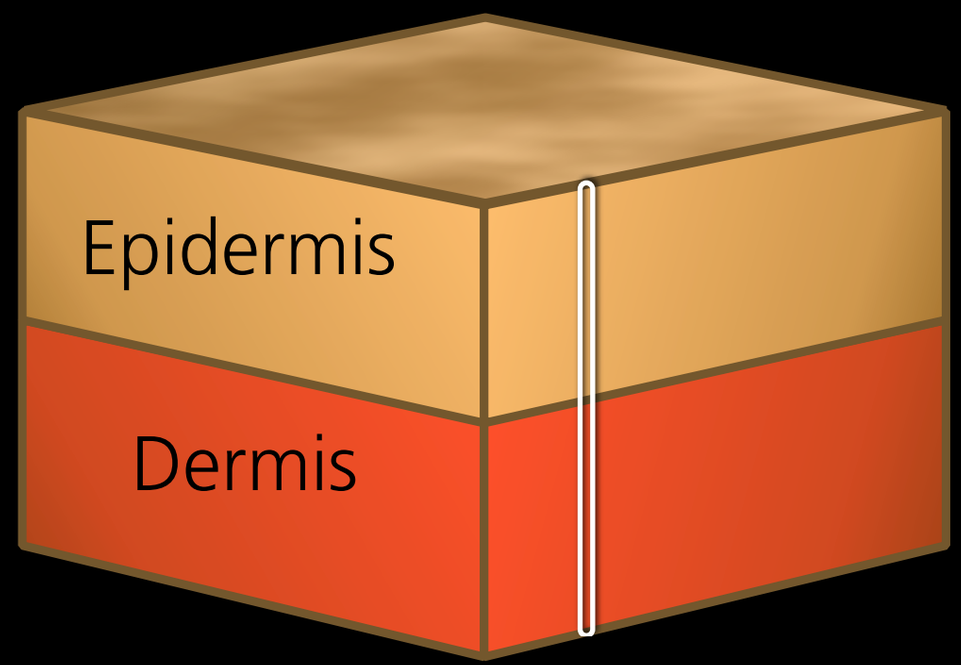

Epidermis

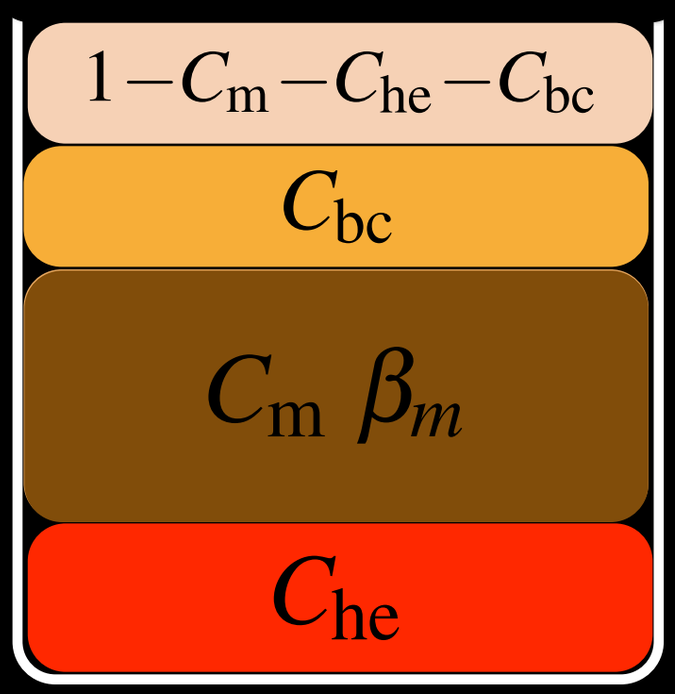

Baseline

Beta-carotene

Eumelanin

Pheomelanin

Hemoglobin

Skin model (absorption)

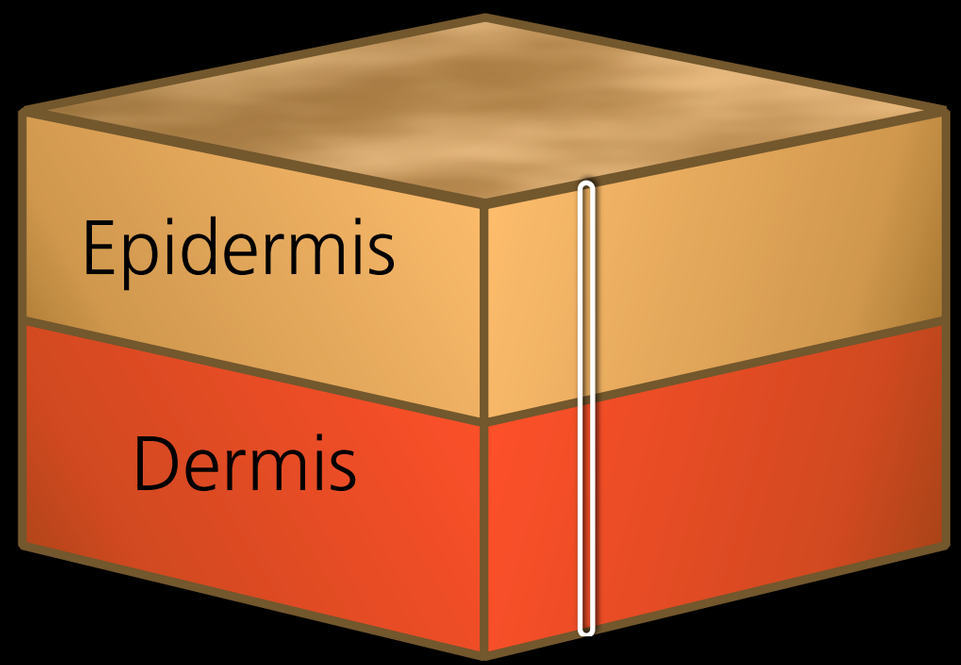

Epidermis

$1 - C_{\mathrm{m}} - C_{\mathrm{he}} - C_{\mathrm{bc}}$	Baseline
C_{bc}	Beta-carotene
$C_{\mathrm{m}}\ \beta_m$	Eumelanin Pheomelanin
C_{he}	Hemoglobin

Dermis

Skin model (absorption)

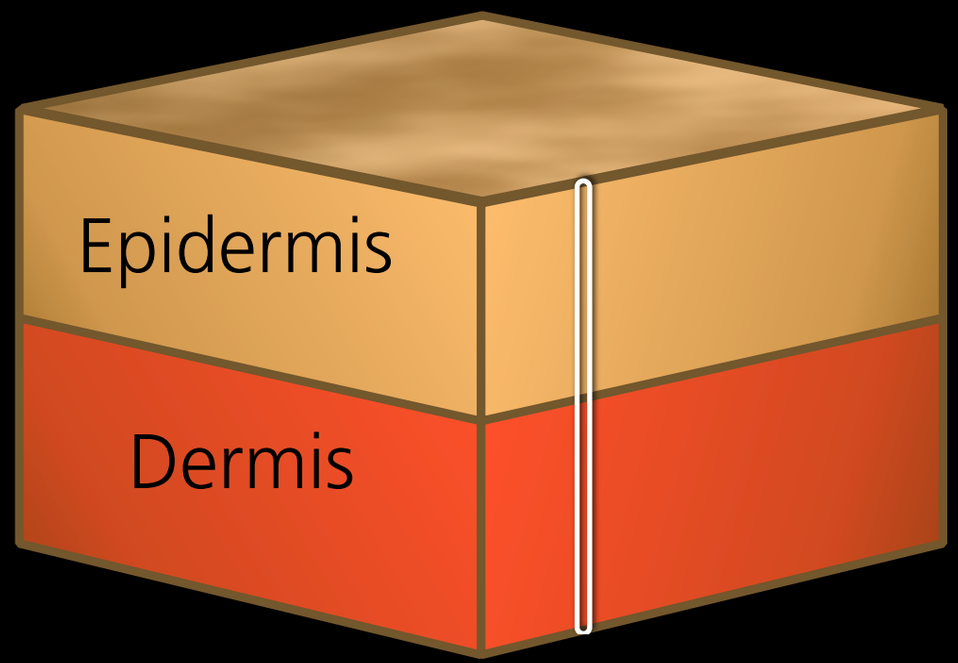

Epidermis

Dermis

$1 - C_{\mathrm{m}} - C_{\mathrm{he}} - C_{\mathrm{bc}}$ Baseline

C_{bc} Beta-carotene

$C_{\mathrm{m}}\ \beta_m$ Eumelanin

Pheomelanin

C_{he} Hemoglobin

Hemoglobin C_{hd}

Skin model (absorption)

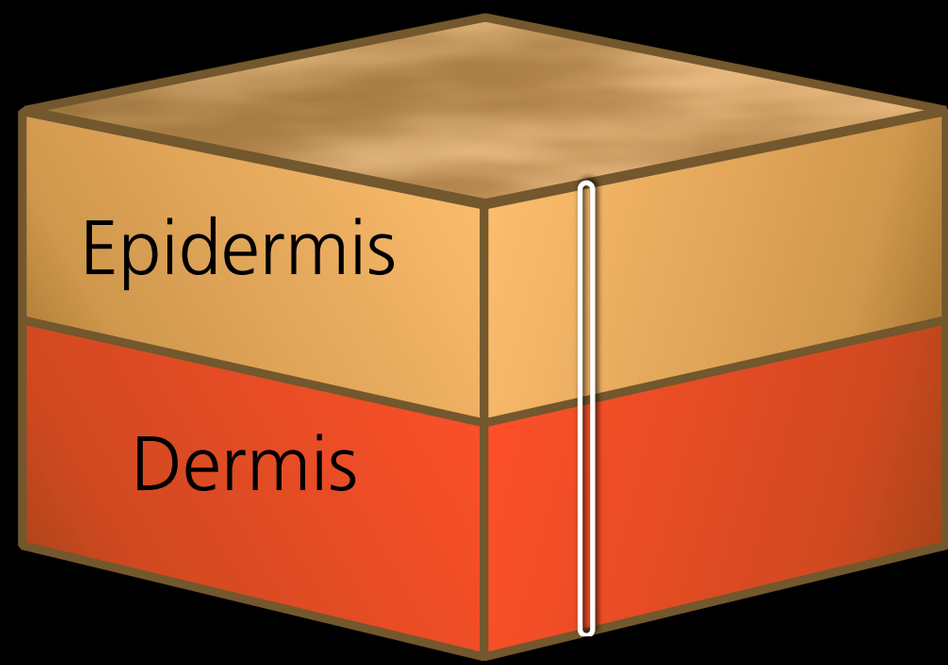

Epidermis

$1 - C_{\mathrm{m}} - C_{\mathrm{he}} - C_{\mathrm{bc}}$	Baseline
C_{bc}	Beta-carotene
$C_{\mathrm{m}}\ \beta_m$	Eumelanin Pheomelanin
C_{he}	Hemoglobin

Dermis

Baseline	$1 - C_{\mathrm{hd}}$
Hemoglobin	C_{hd}

Shading model components

Shading model components

- Surface reflectance

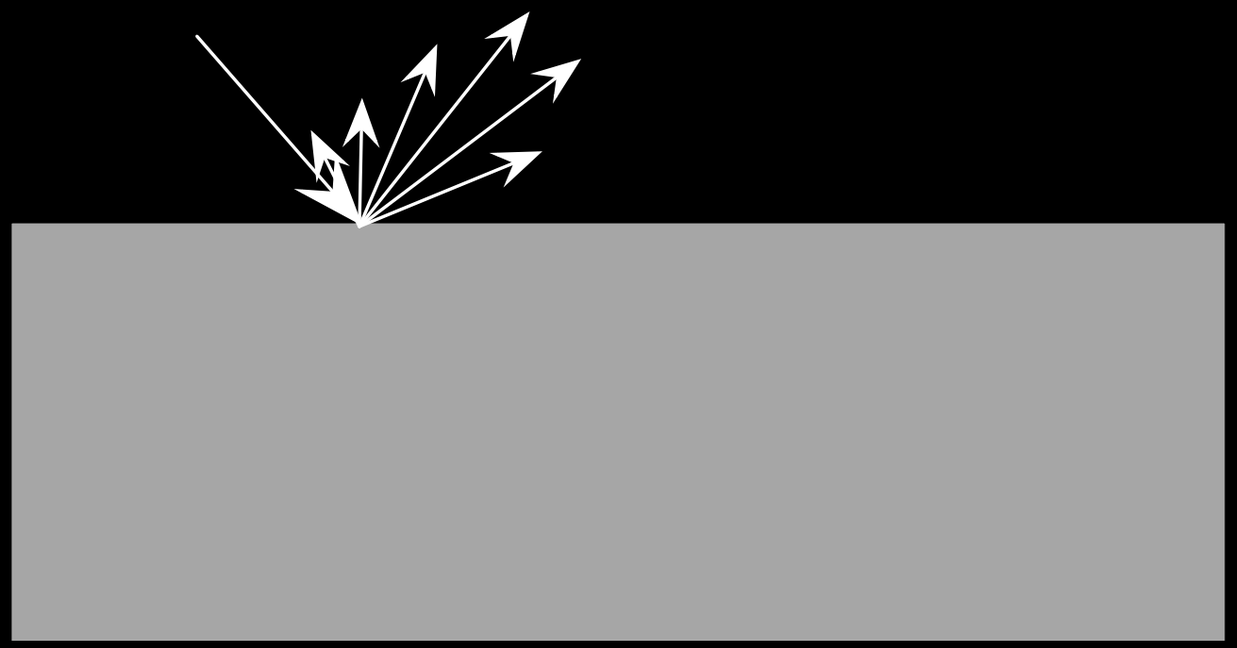

Shading model components

- Surface reflectance
- Subsurface reflectance

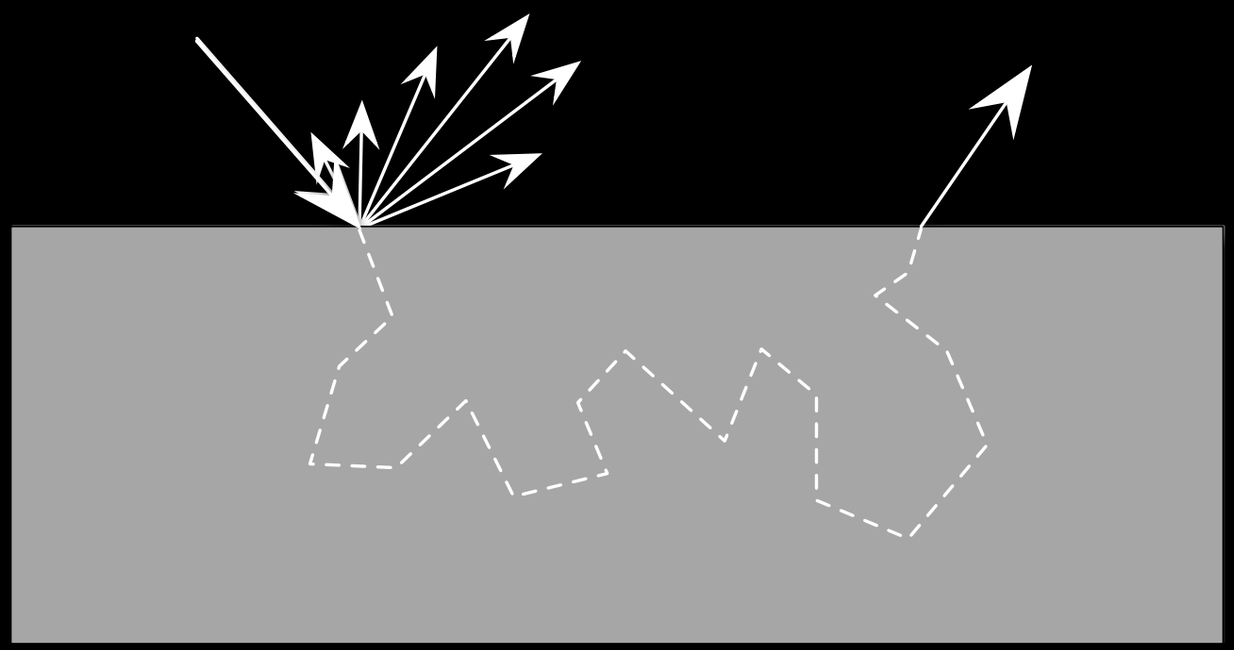

Shading model components

- Surface reflectance
- Subsurface reflectance
  - Constant thickness

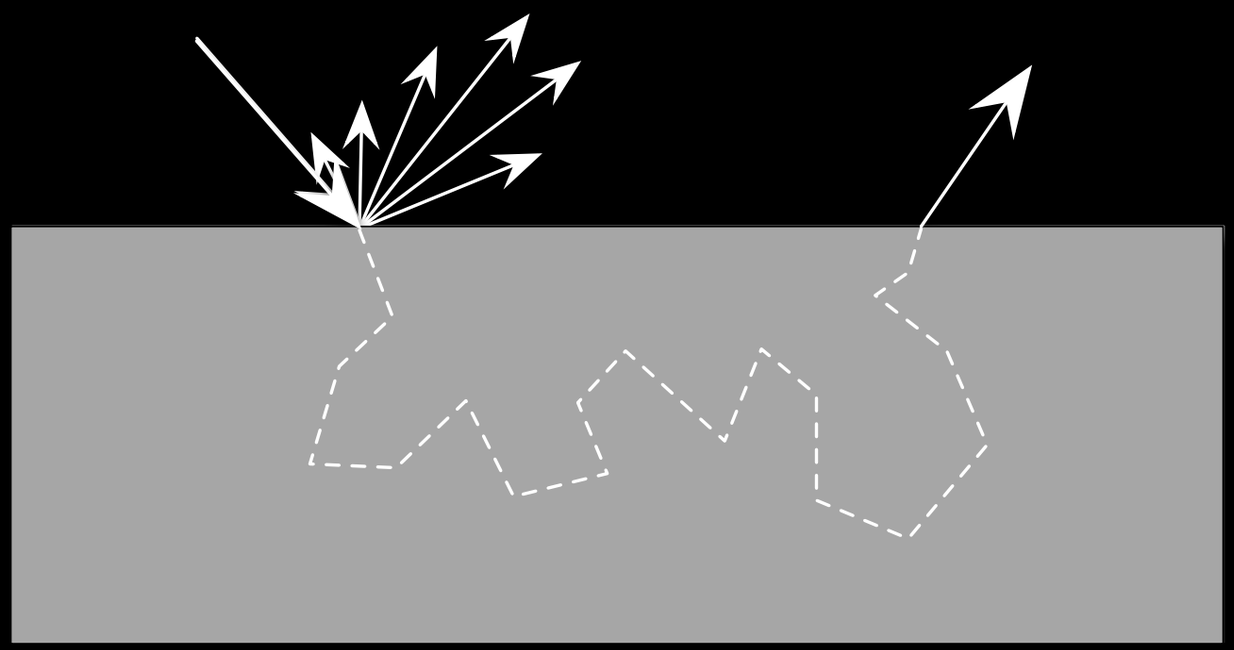

Shading model components

- Surface reflectance
- Subsurface reflectance
  - Constant thickness
  - Fixed scattering

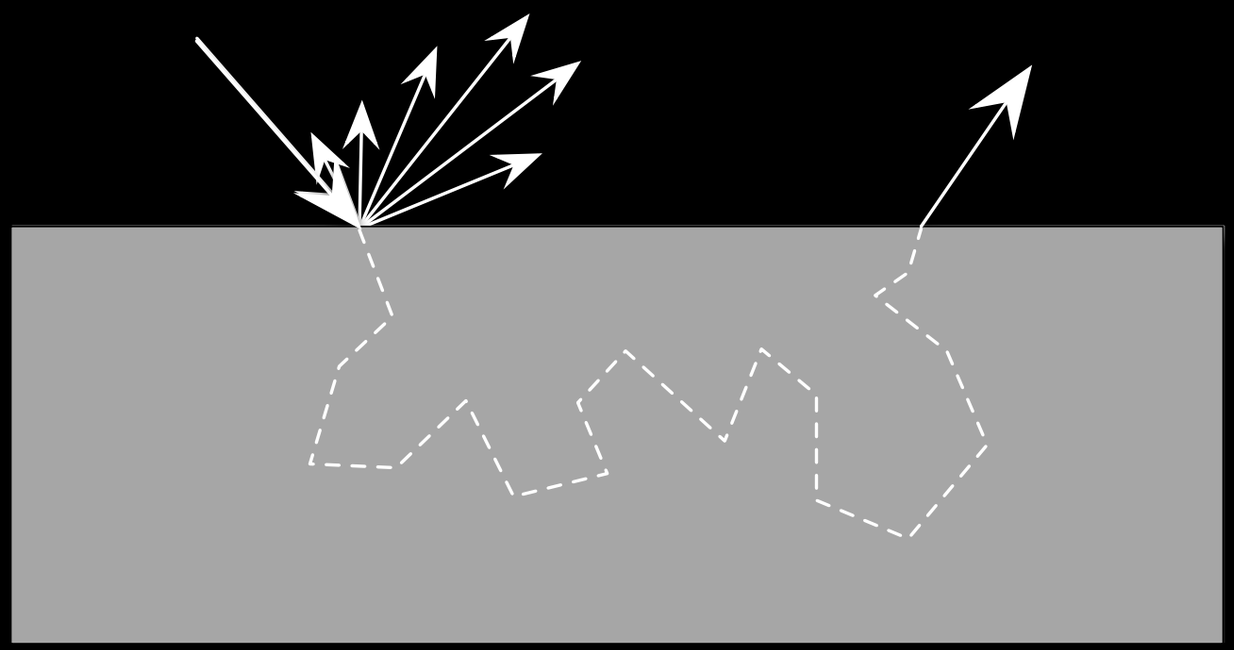

Shading model components

- Surface reflectance
- Subsurface reflectance
  - Constant thickness
  - Fixed scattering
  - Absorption from chromophores

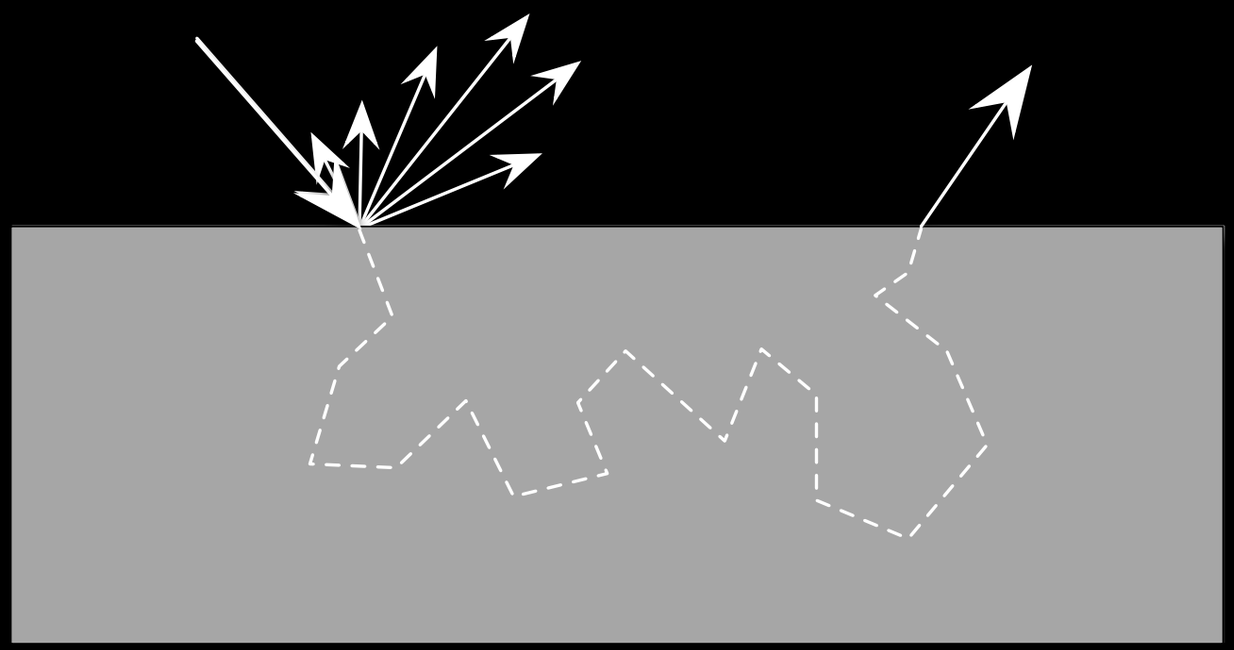

Shading model components

- Surface reflectance
- Subsurface reflectance
  - Constant thickness
  - Fixed scattering
  - Absorption from chromophores
- Multipole diffusion model

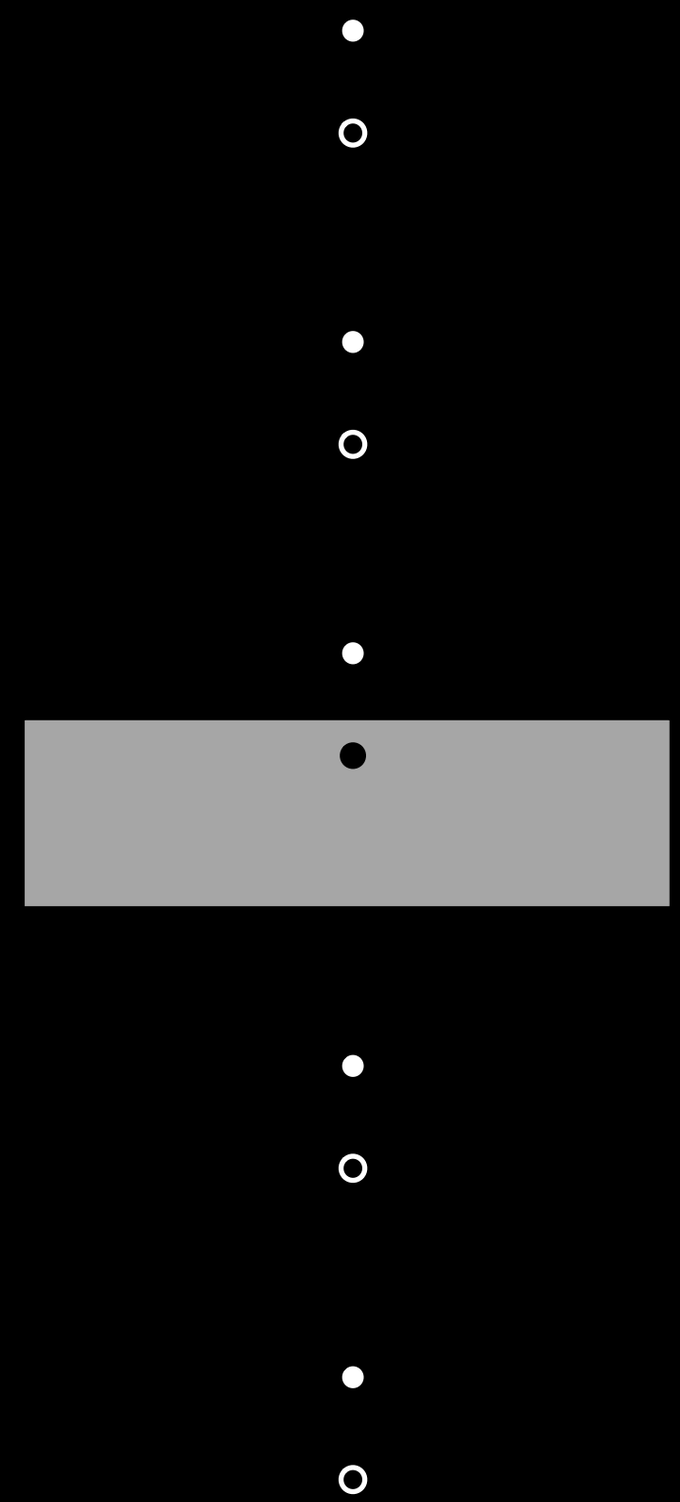

Shading model components

- Surface reflectance
- Subsurface reflectance
  - Constant thickness
  - Fixed scattering
  - Absorption from chromophores
- Multipole diffusion model

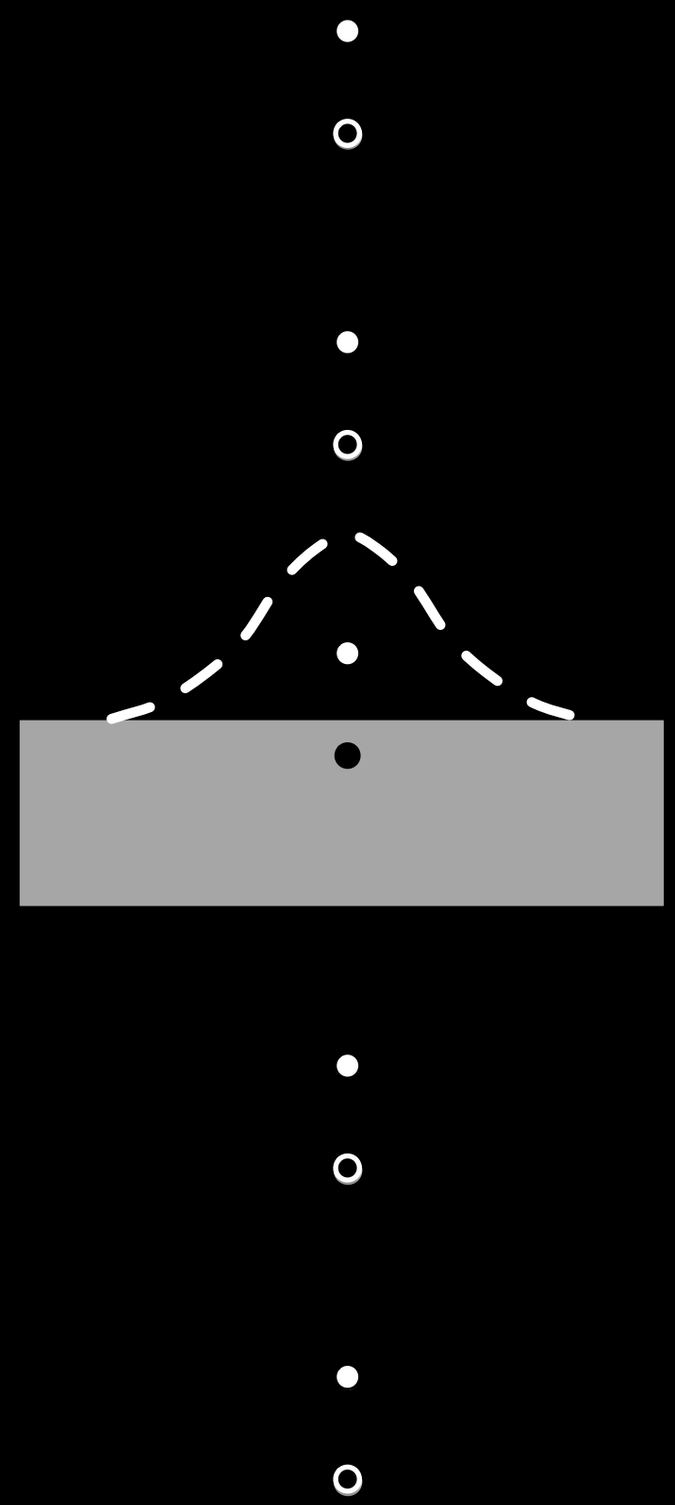

Shading model components

- Surface reflectance
- Subsurface reflectance
  - Constant thickness
  - Fixed scattering
  - Absorption from chromophores
- Multipole diffusion model

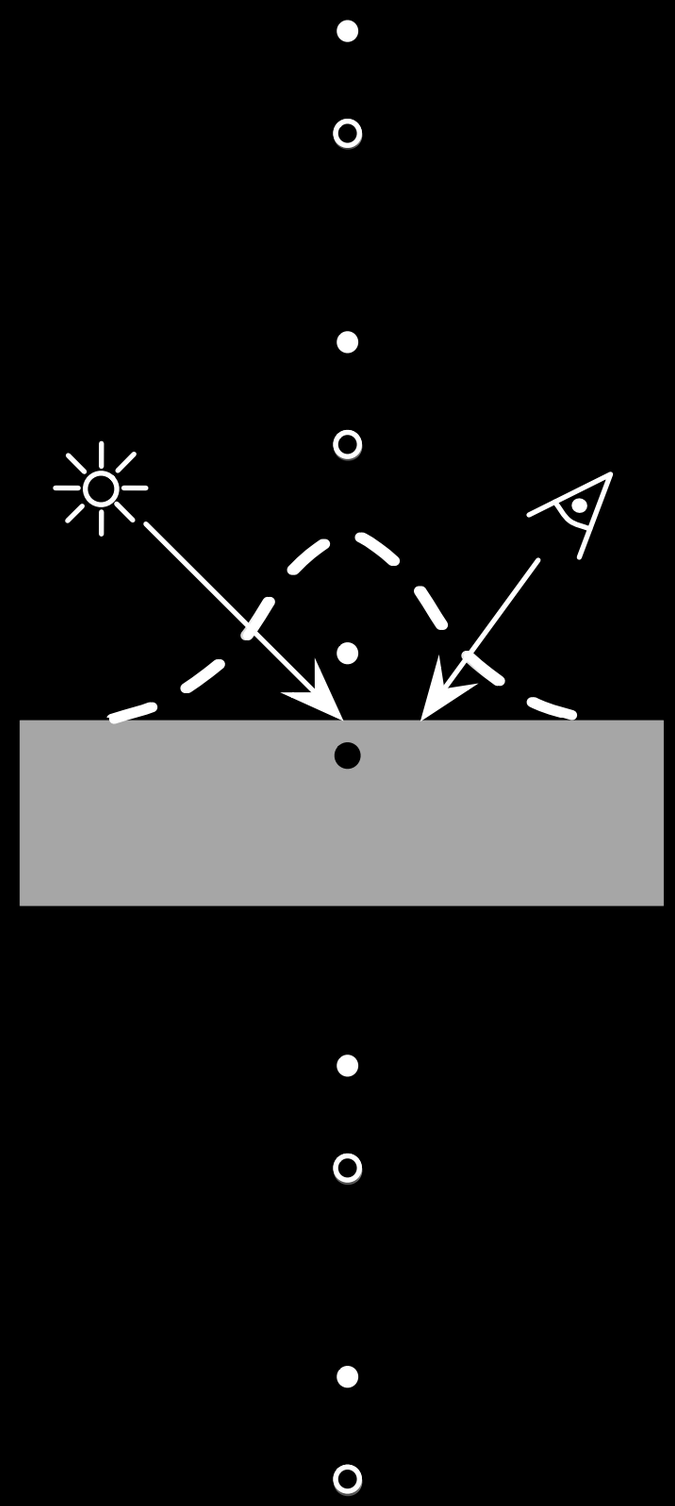

Color variation

Renderings

Photographs

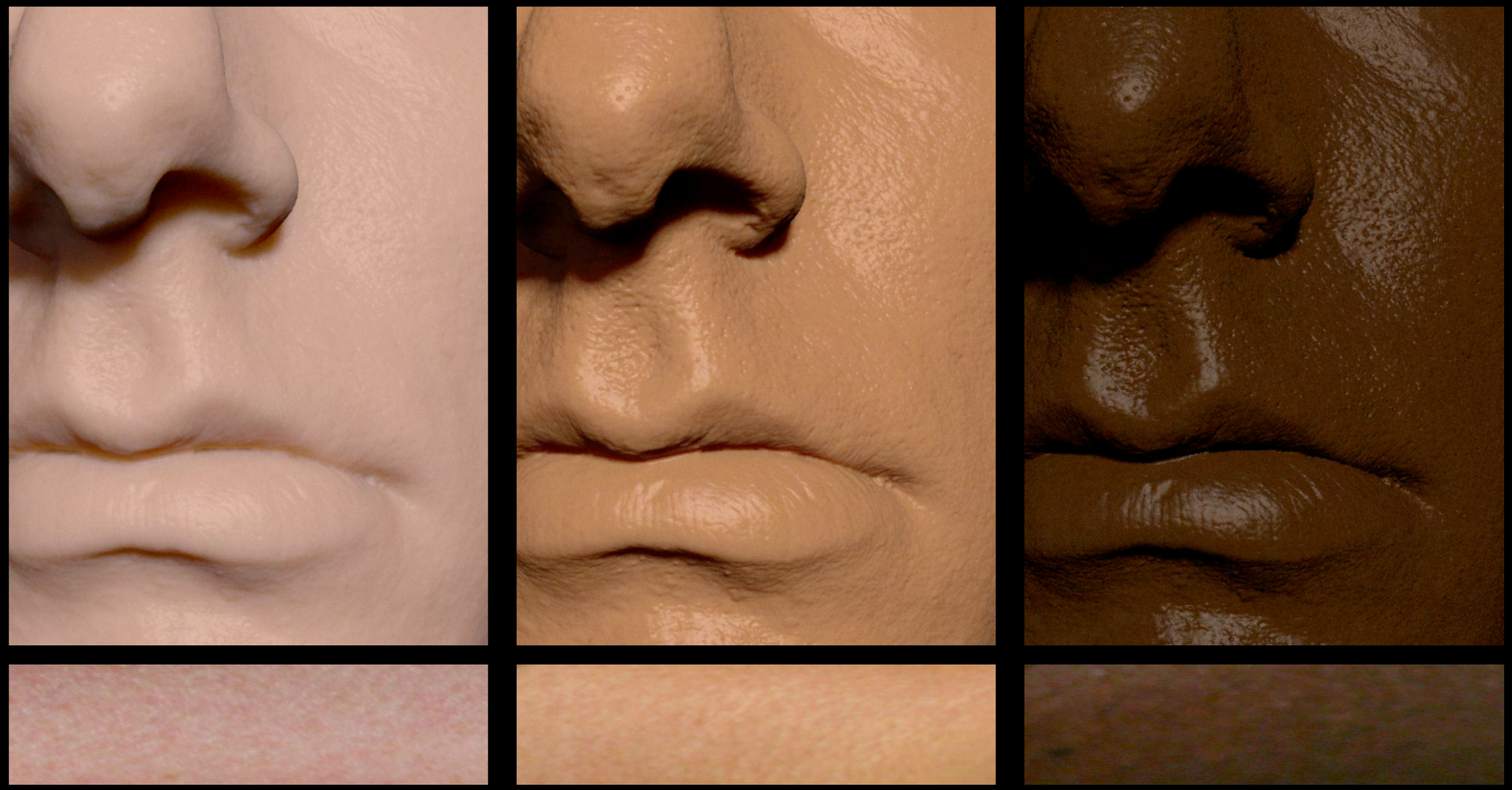

Caucasian Asian African

Matching photographs of skin

Melanin variation

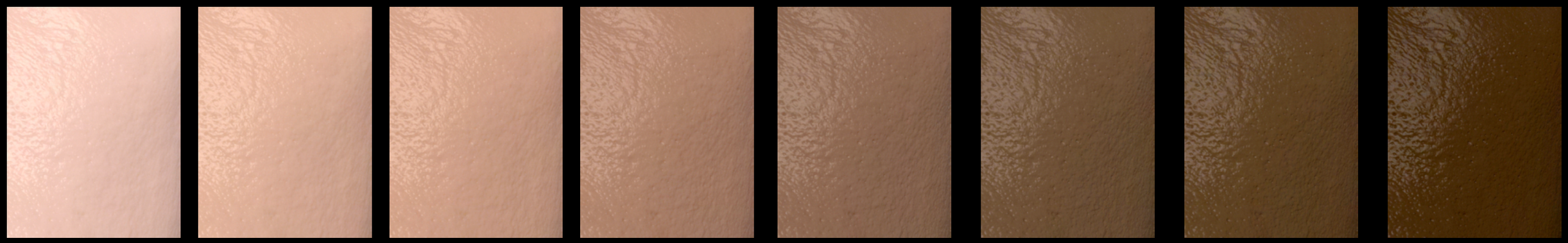

$C_m = 0.1\%$ $C_m = 1\%$ $C_m = 2\%$ $C_m = 5\%$ $C_m = 10\%$ $C_m = 20\%$ $C_m = 30\%$ $C_m = 50\%$

Total melanin volume fraction

$$\beta_m = 0.7, C_h = 0.5\%$$

Melanin variation

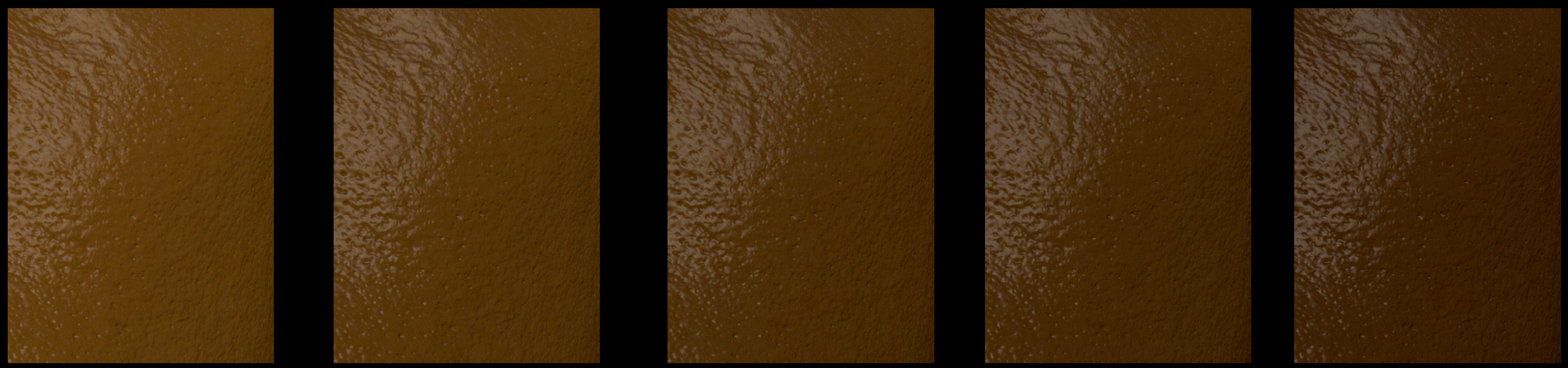

$\beta_m = 0$ $\beta_m = 0.25$ $\beta_m = 0.5$ $\beta_m = 0.7$ $\beta_m = 1$

Melanin type

$C_m = 50\%, C_h = 0.1\%$

Hemoglobin variation

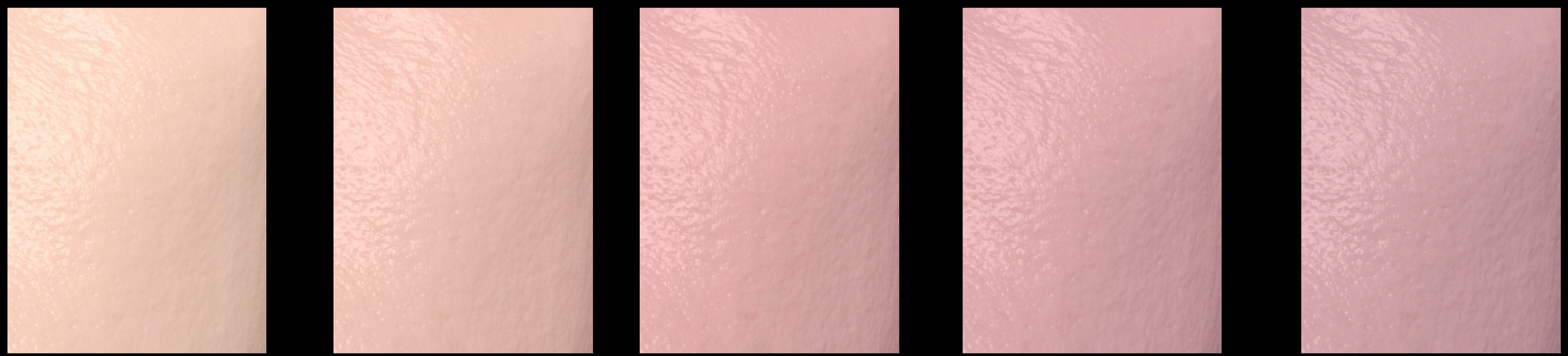

$C_h = 0.1\%$ $C_h = 1\%$ $C_h = 5\%$ $C_h = 10\%$ $C_h = 20\%$

Hemoglobin fraction

$C_m = 1\%, \beta_m = 0.5\%$

Overall variation

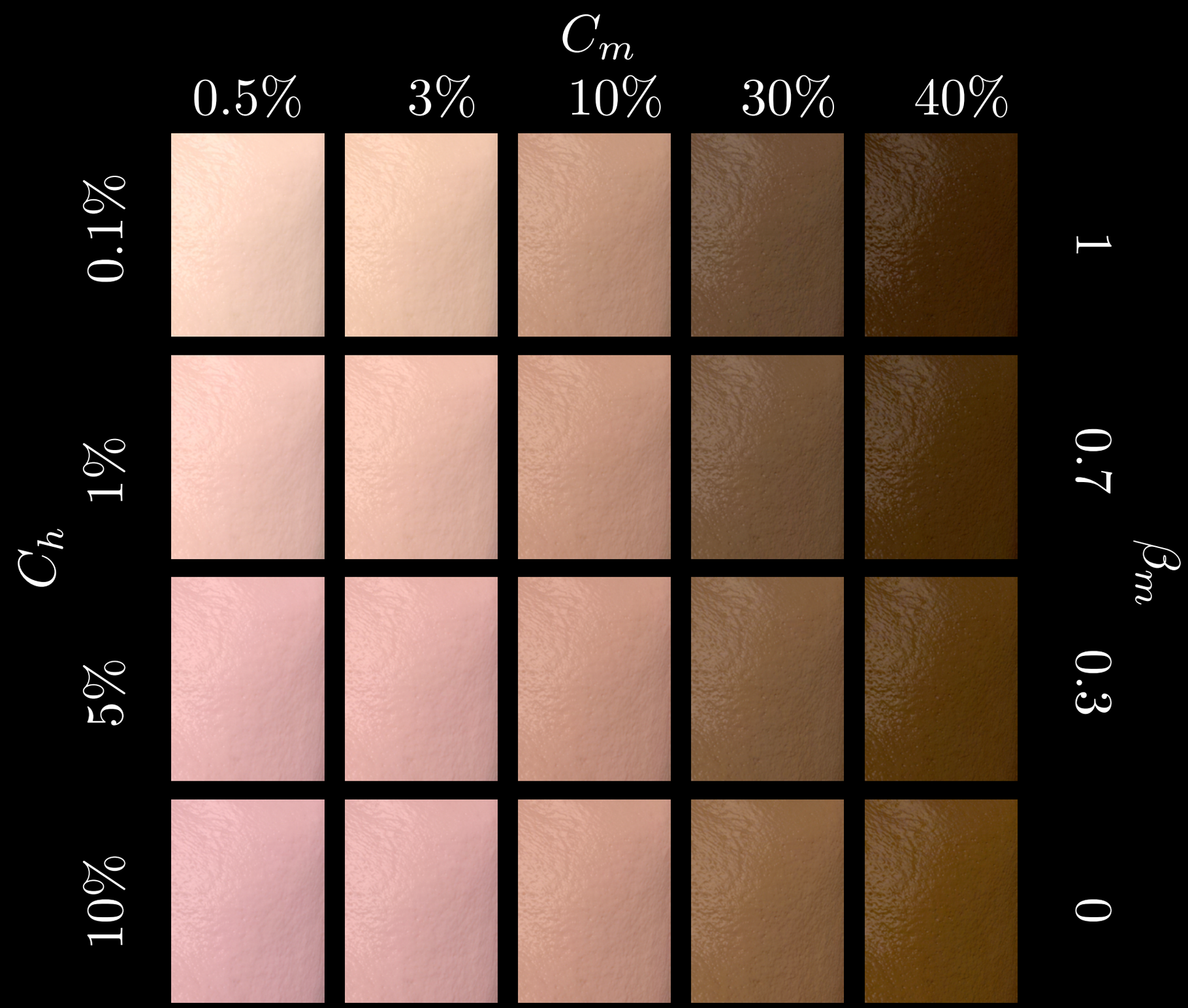

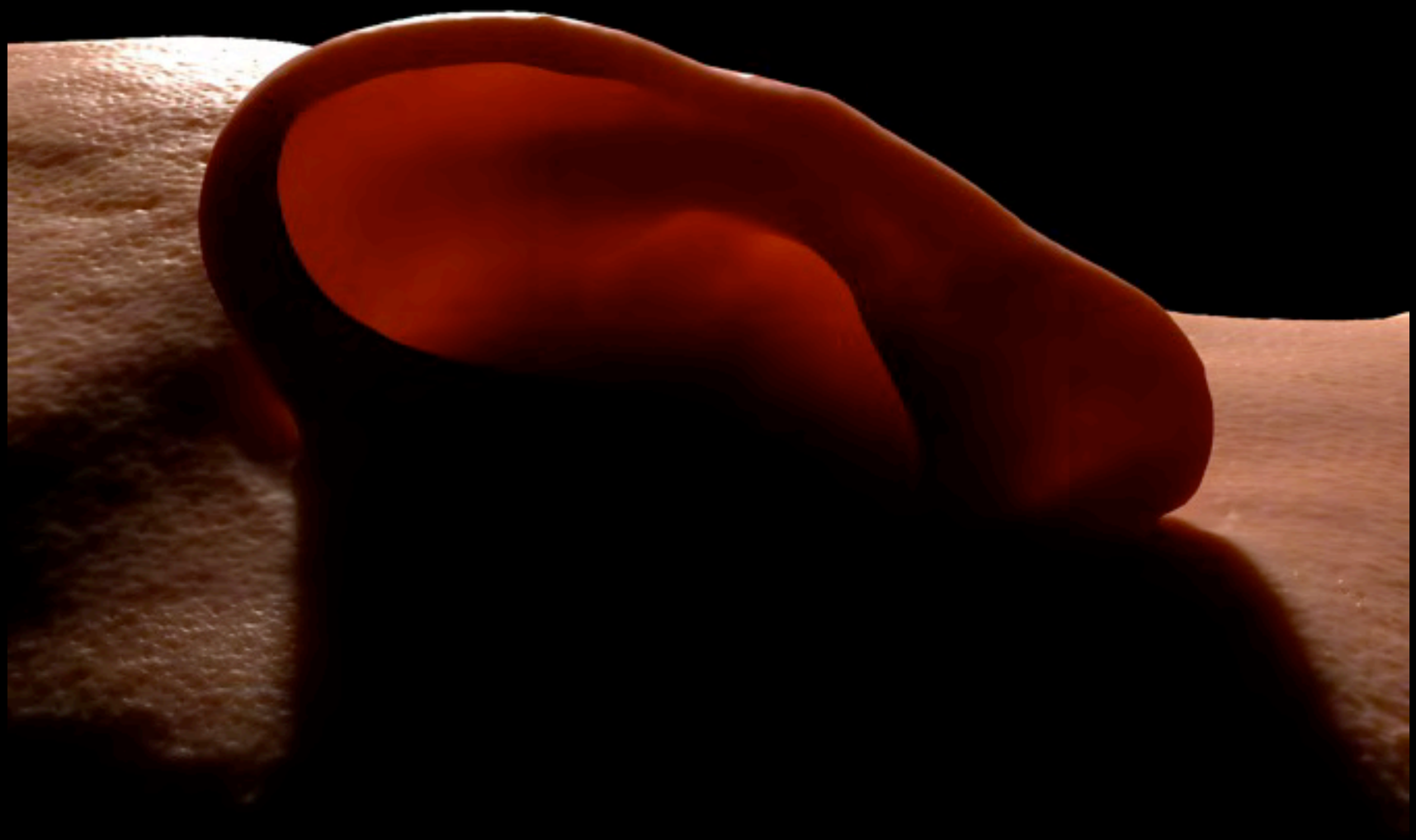

Computed spectra

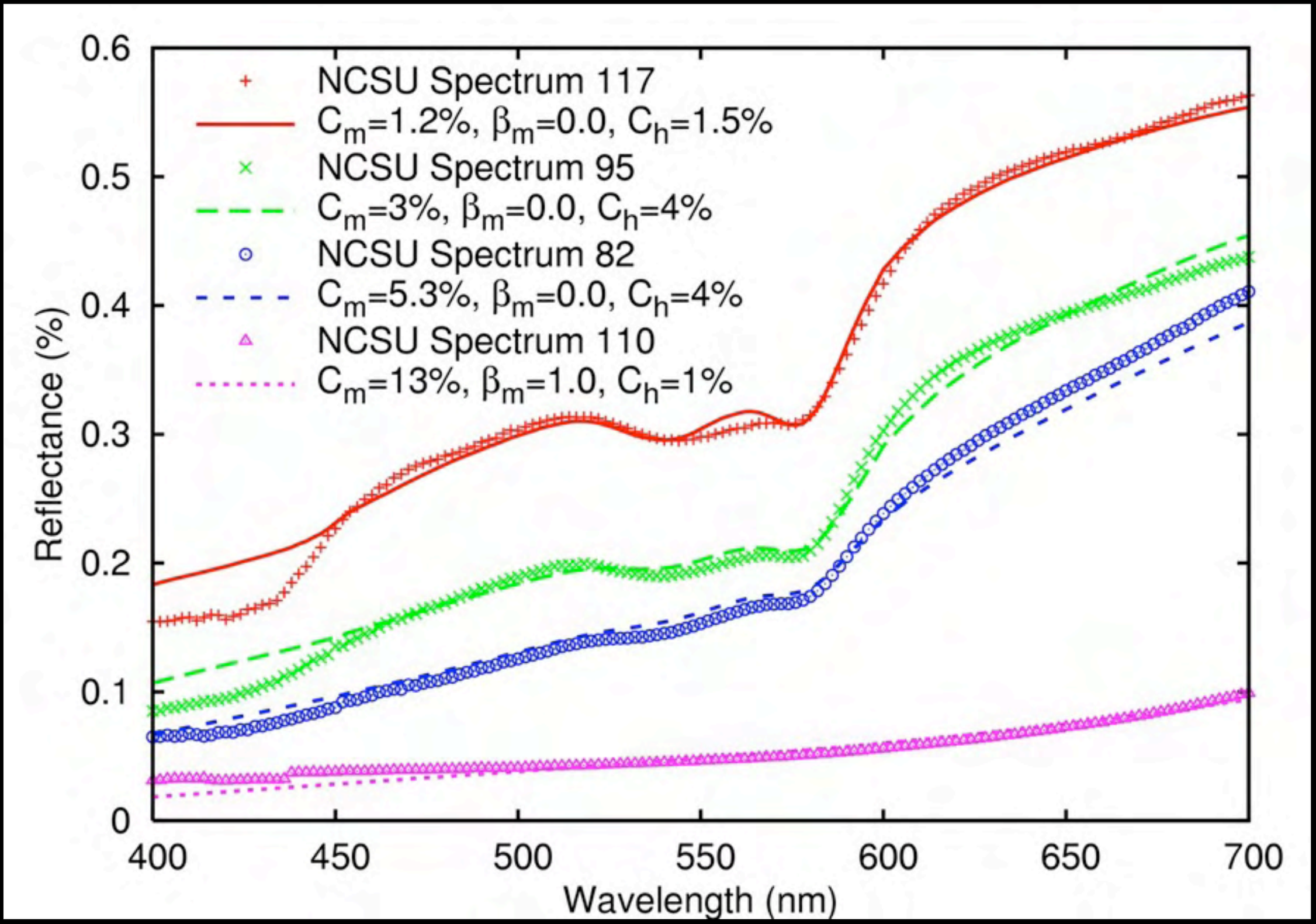


NVIDIA

Homogeneous limitations

Homogeneous limitations

- Not spatially heterogeneous

Homogeneous limitations

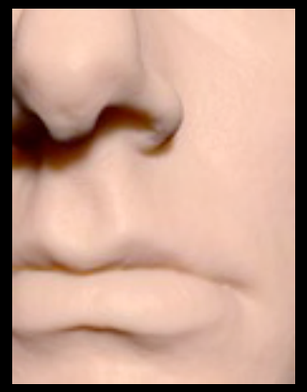

- Not spatially heterogeneous

Homogeneous limitations

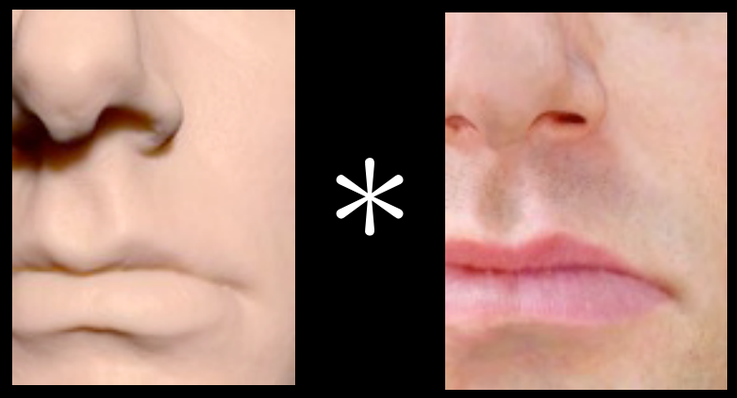

- Not spatially heterogeneous

Homogeneous limitations

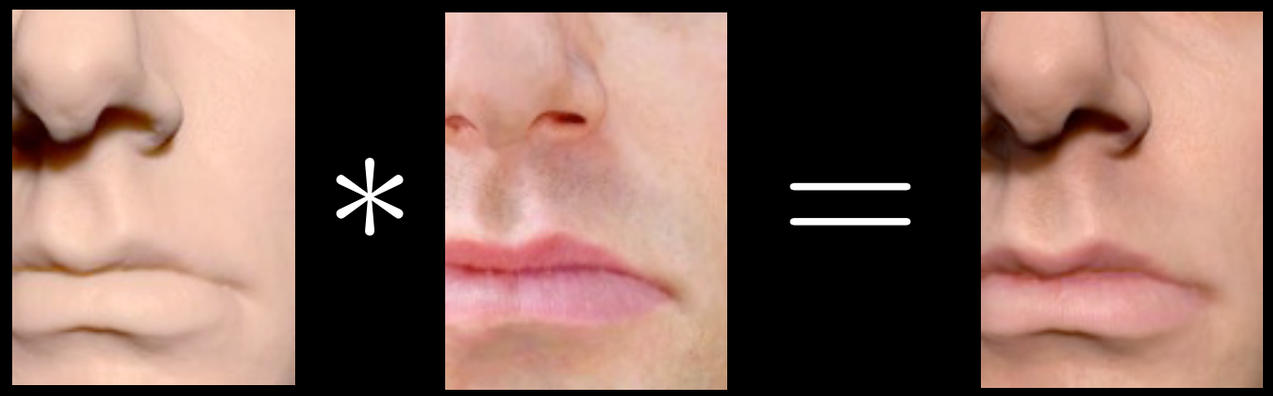

- Not spatially heterogeneous

Homogeneous limitations

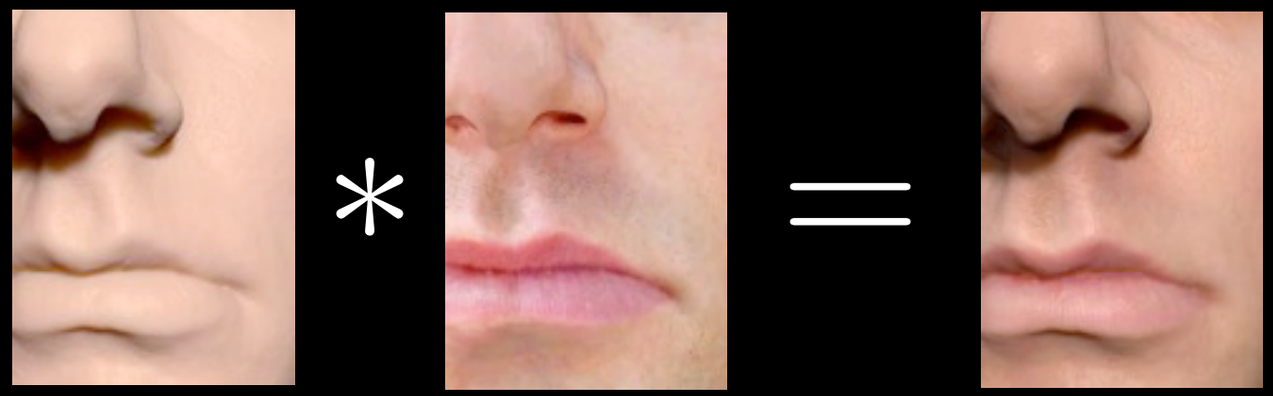

- Not spatially heterogeneous
- Measuring parameters difficult

Homogeneous limitations

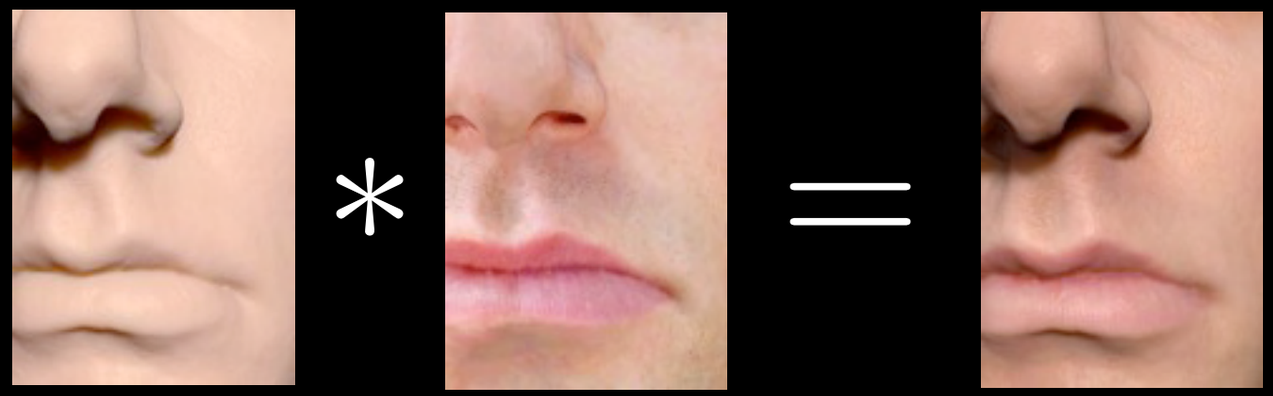

- Not spatially heterogeneous
- Measuring parameters difficult
- Artistic design difficult

Spatially-varying properties

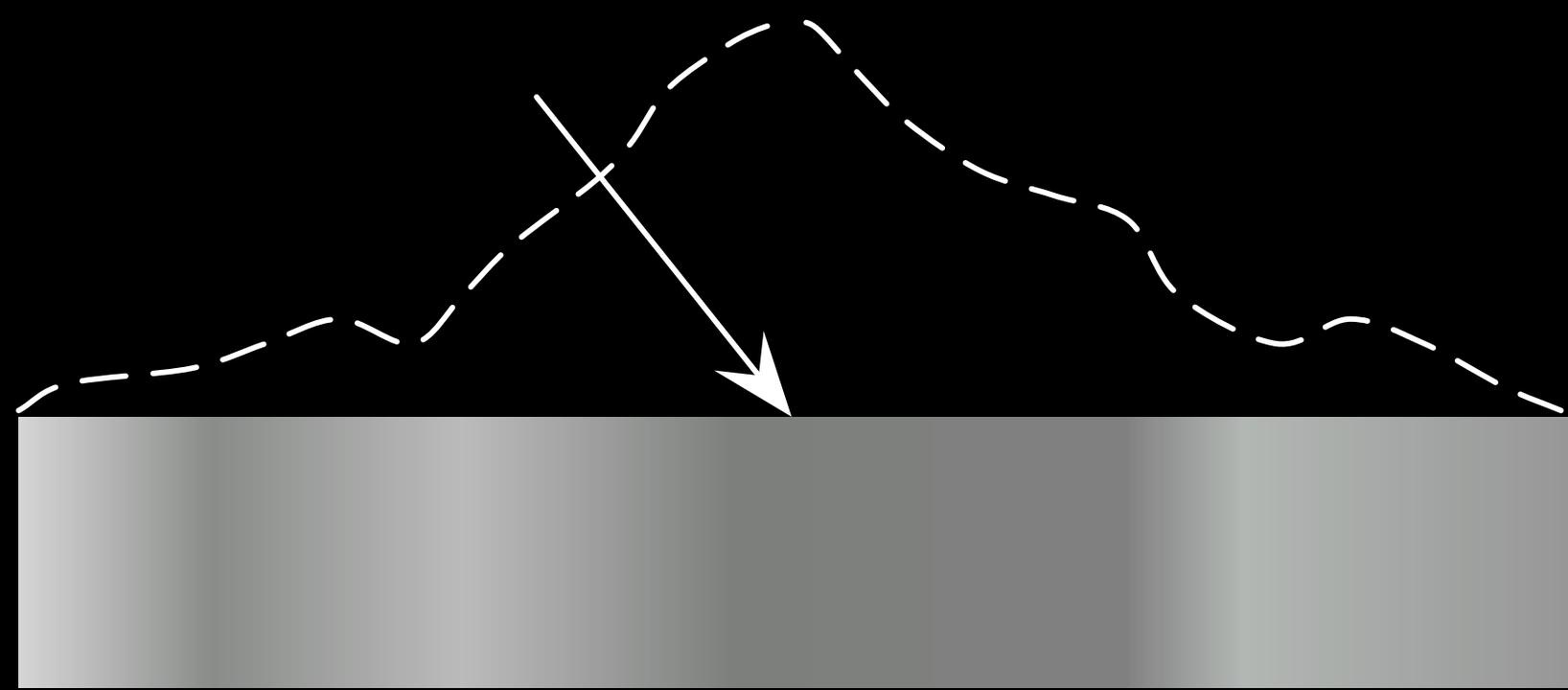

Spatially-varying properties

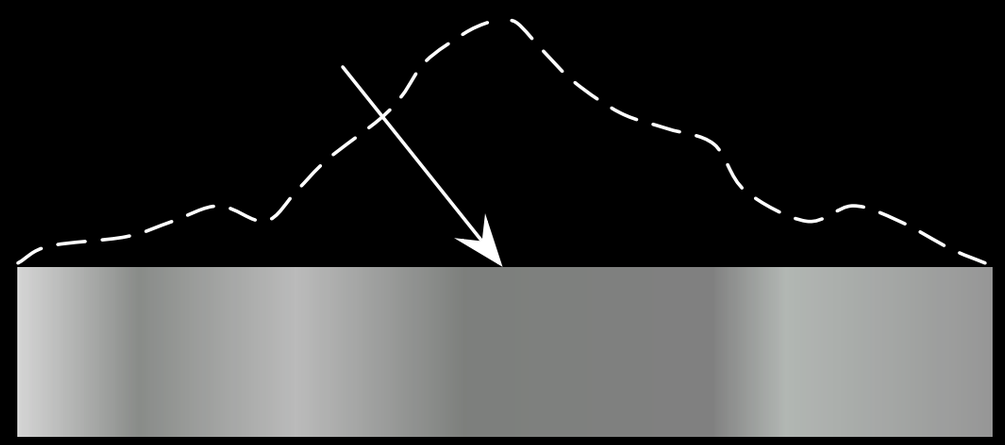

- Assumption: parameters change “slowly”

Spatially-varying properties

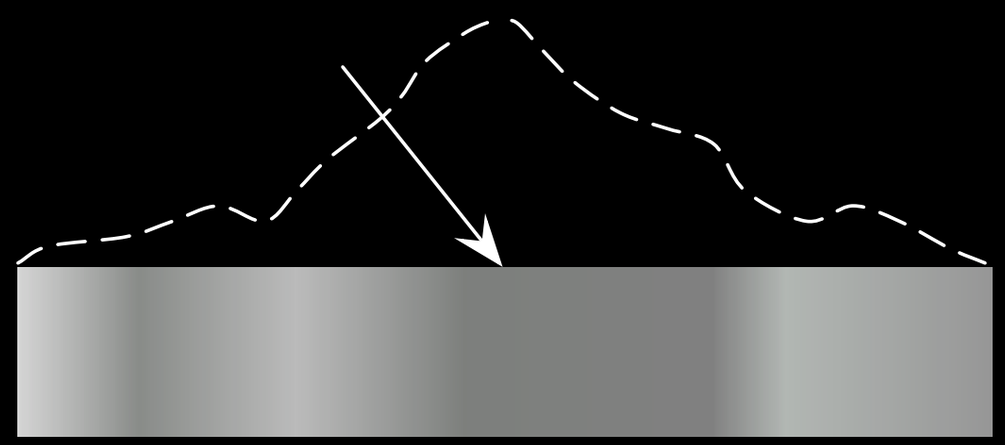

- Assumption: parameters change “slowly”
- Homogeneity between incident and exitant points

Spatially-varying properties

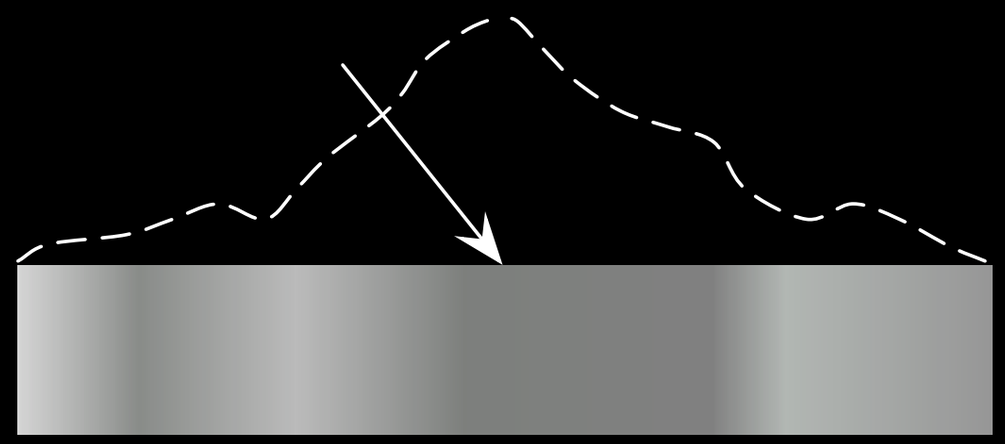

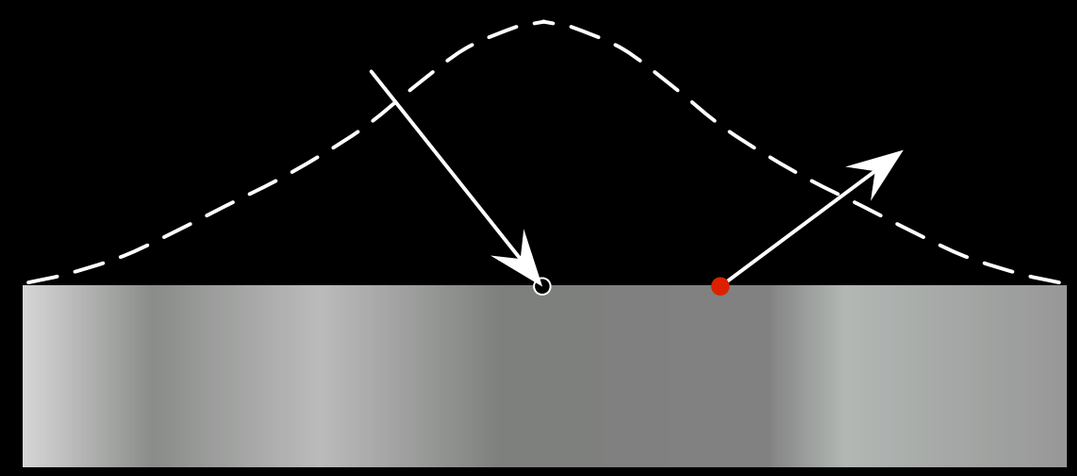

- Assumption: parameters change “slowly”
- Homogeneity between incident and exitant points

Spatially-varying properties

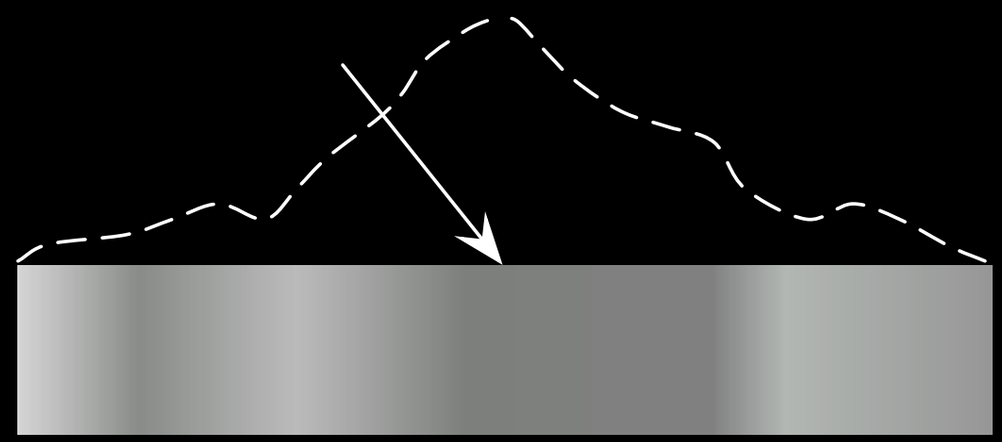

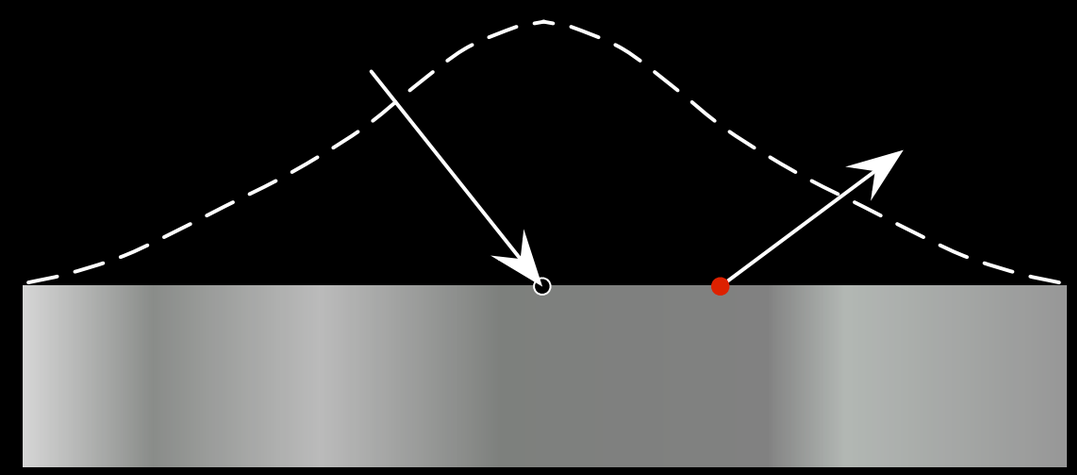

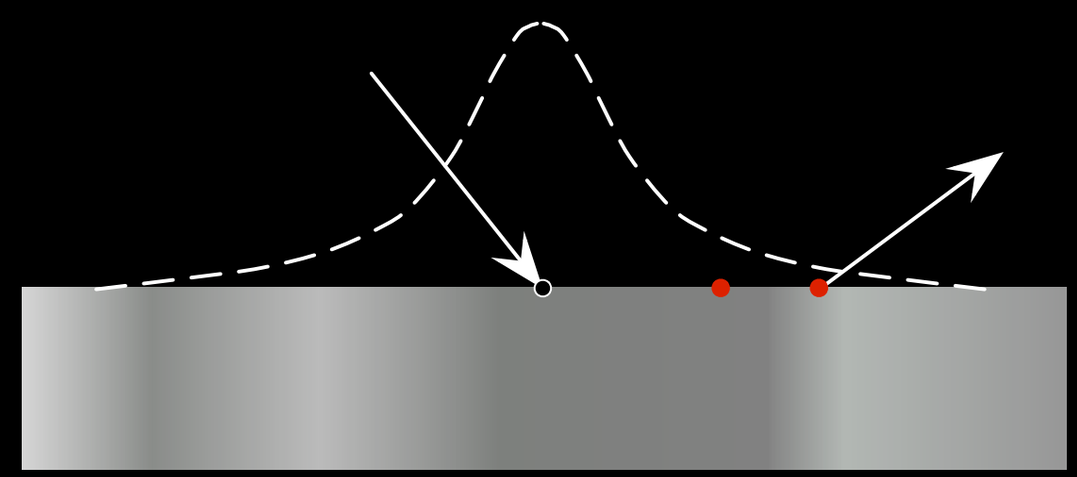

- Assumption: parameters change "slowly"
- Homogeneity between incident and exitant points

Heterogeneity through inter-scattering

Heterogeneity through inter-scattering

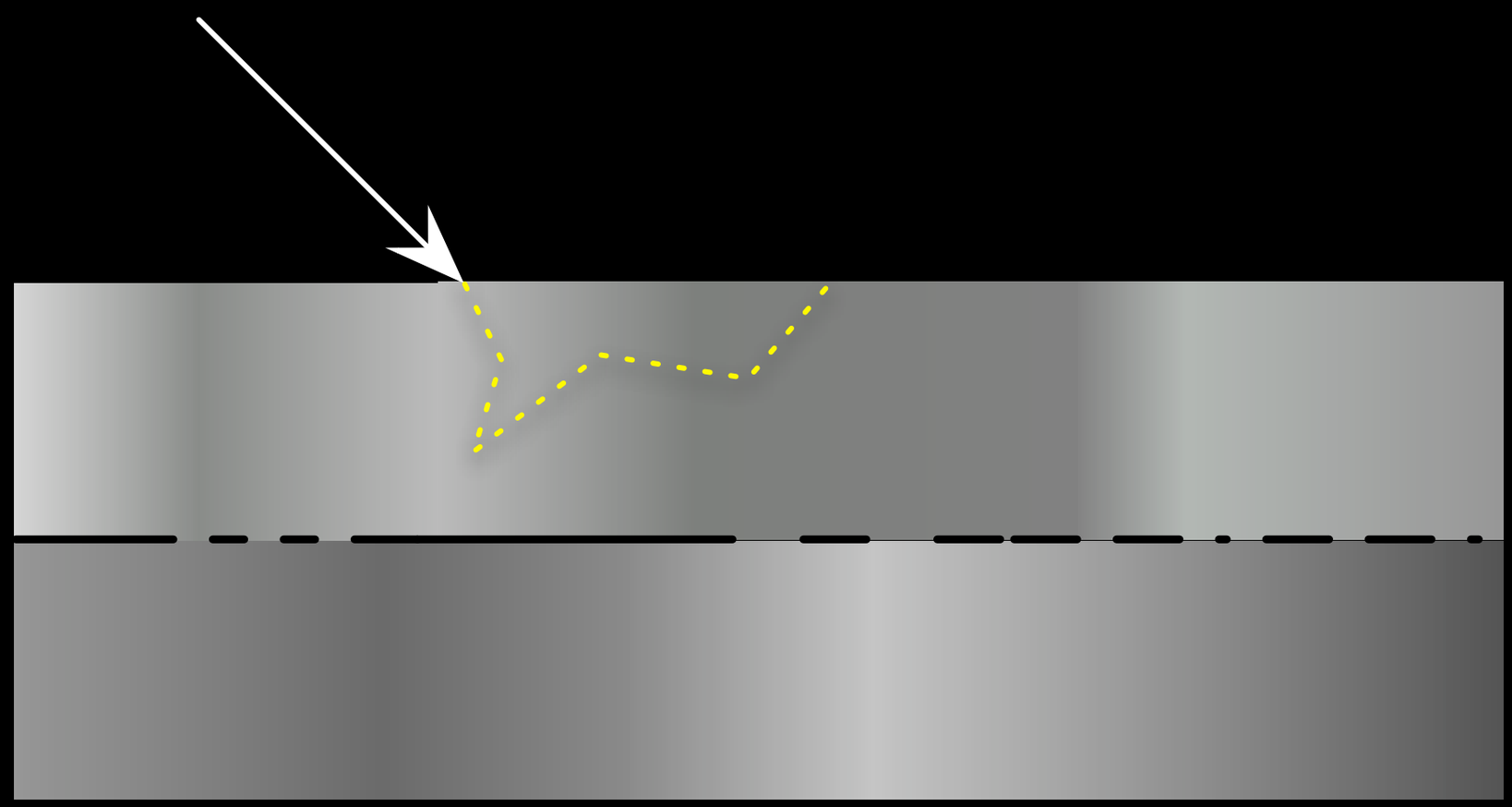

Heterogeneity through inter-scattering

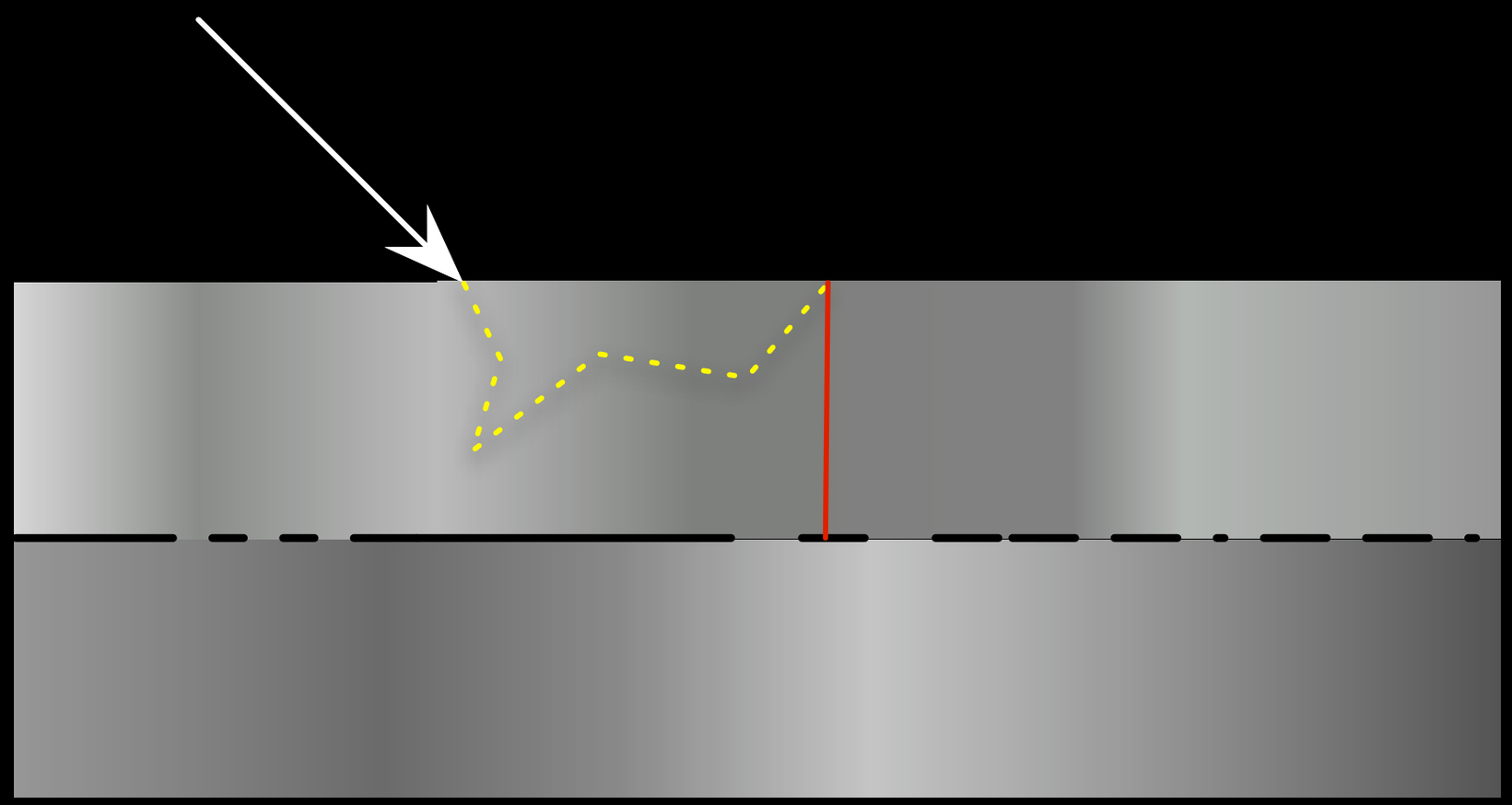

Heterogeneity through inter-scattering

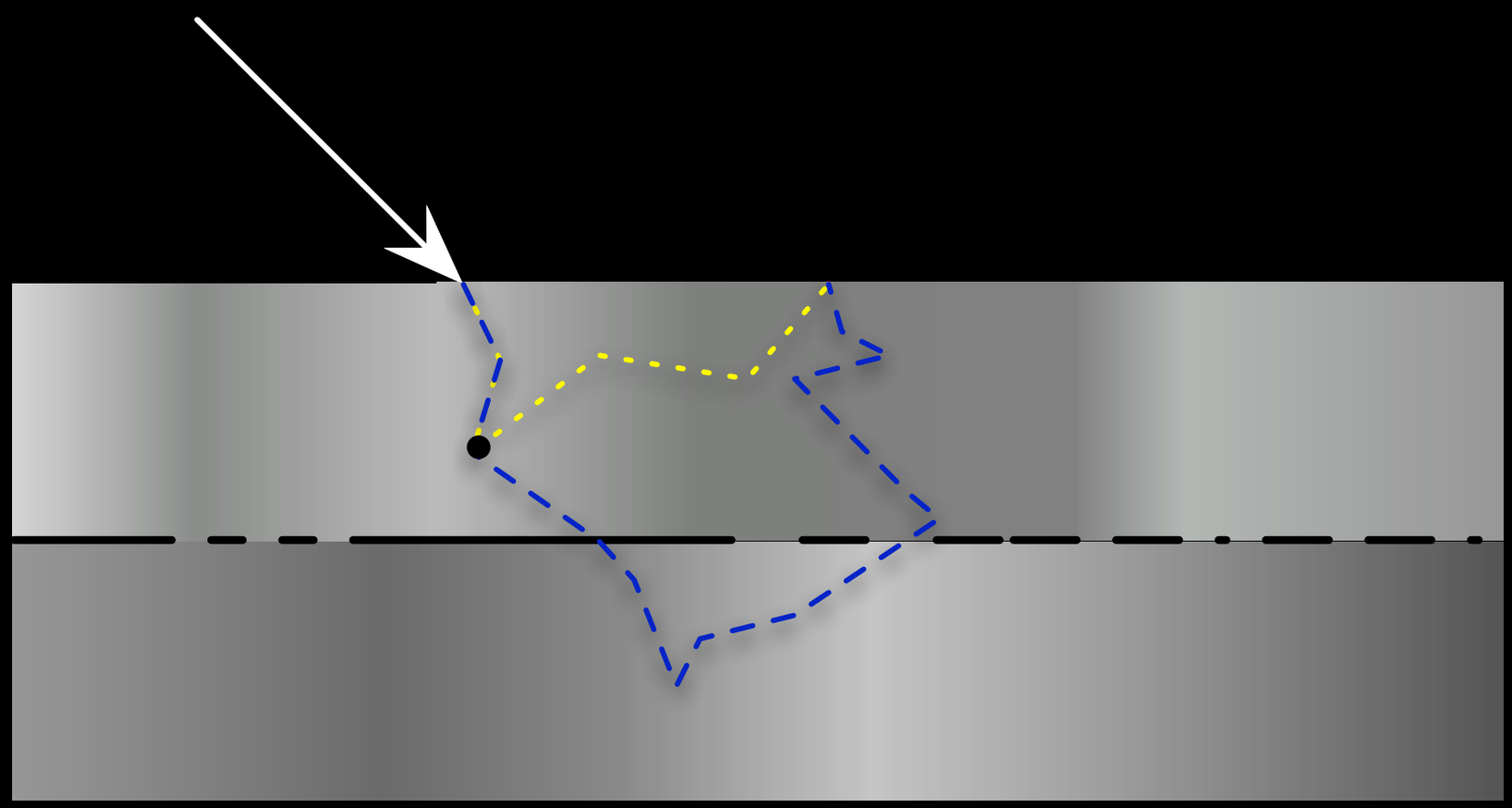

Heterogeneity through inter-scattering

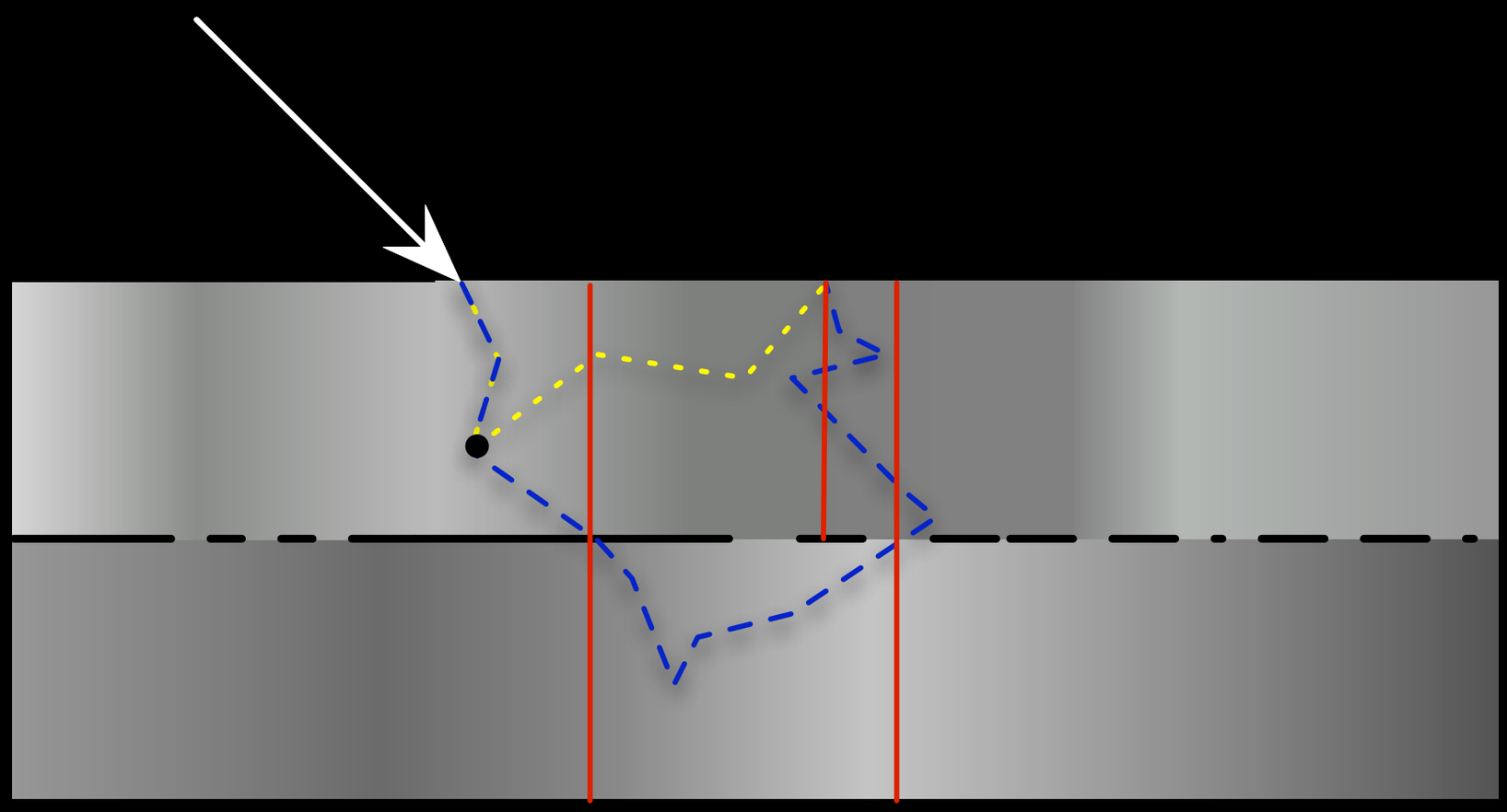

Heterogeneity through inter-scattering

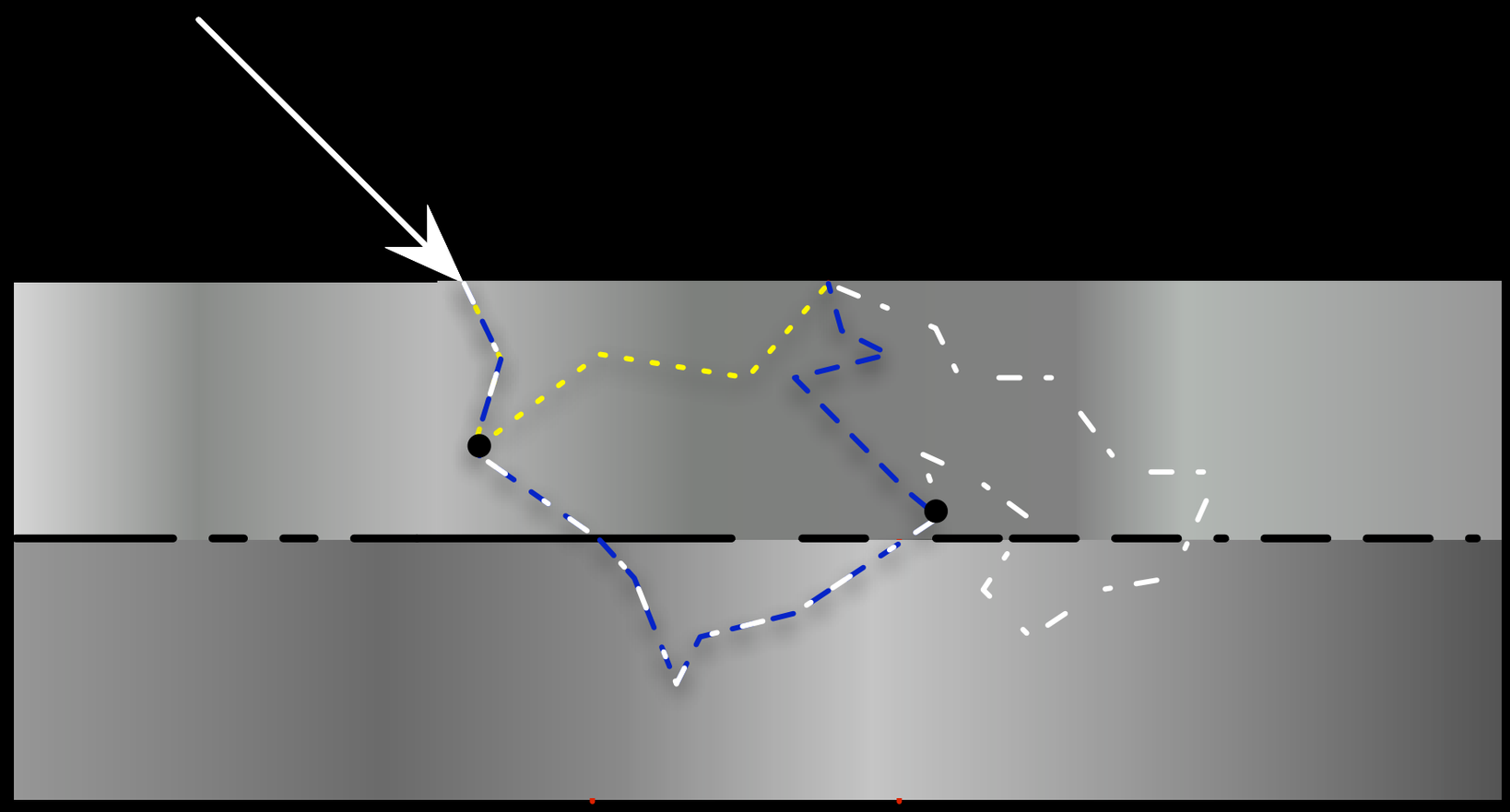

Heterogeneity through inter-scattering

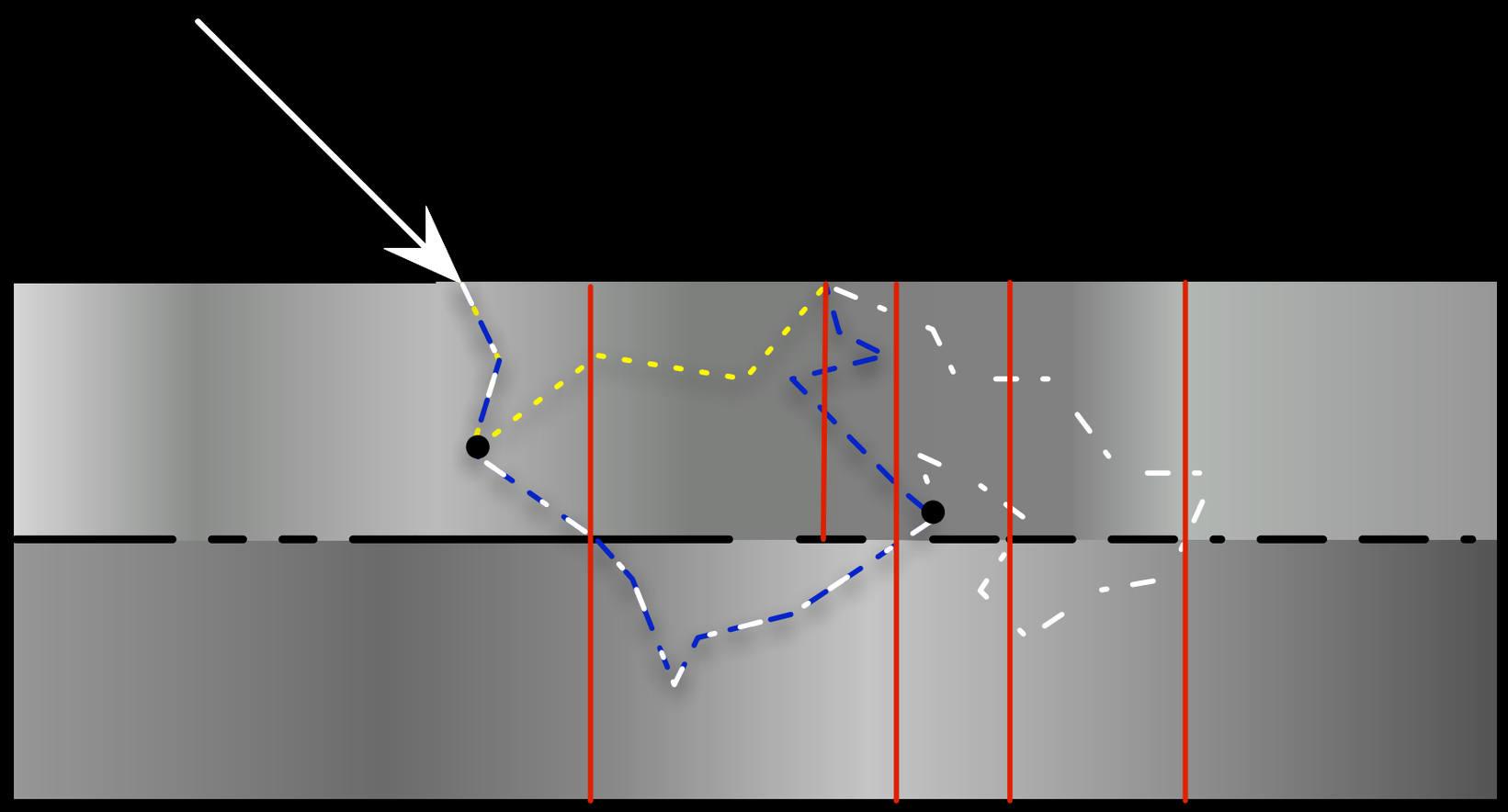

Heterogeneity through inter-scattering

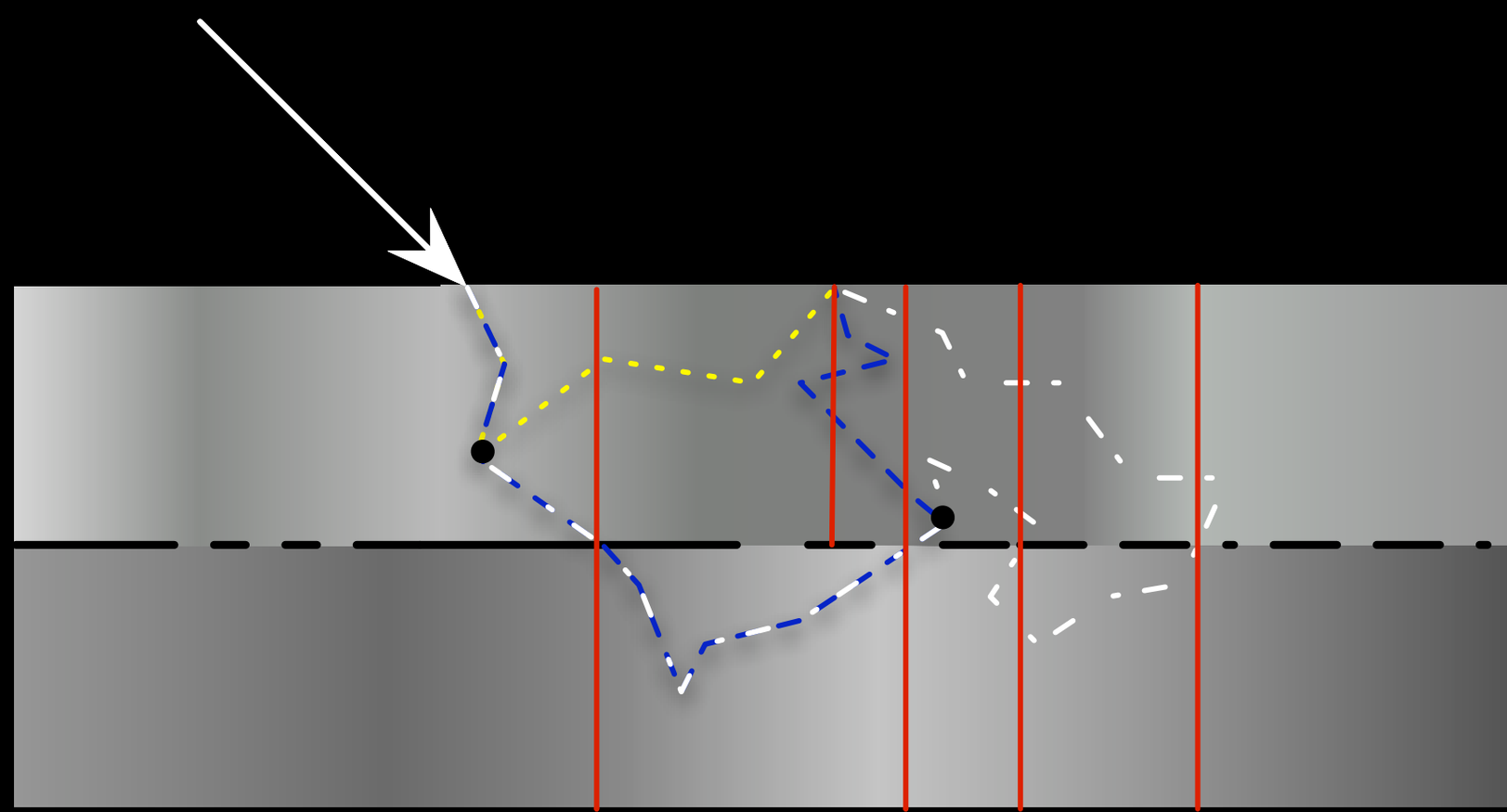

$$\Phi * R_{12}^{+} = \Phi * R_{1}^{+} + \Phi * T_{1}^{+} \mathcal{A} * R_{2}^{+} \mathcal{A} * T_{1}^{-}$$
$$+ \Phi * T_{1}^{+} \mathcal{A} * R_{2}^{+} \mathcal{A} * R_{1}^{-} \mathcal{A} * R_{2}^{+} \mathcal{A} * T_{1}^{-} + \cdots$$

Sum of 2D products of convolutions

Algorithm

Algorithm

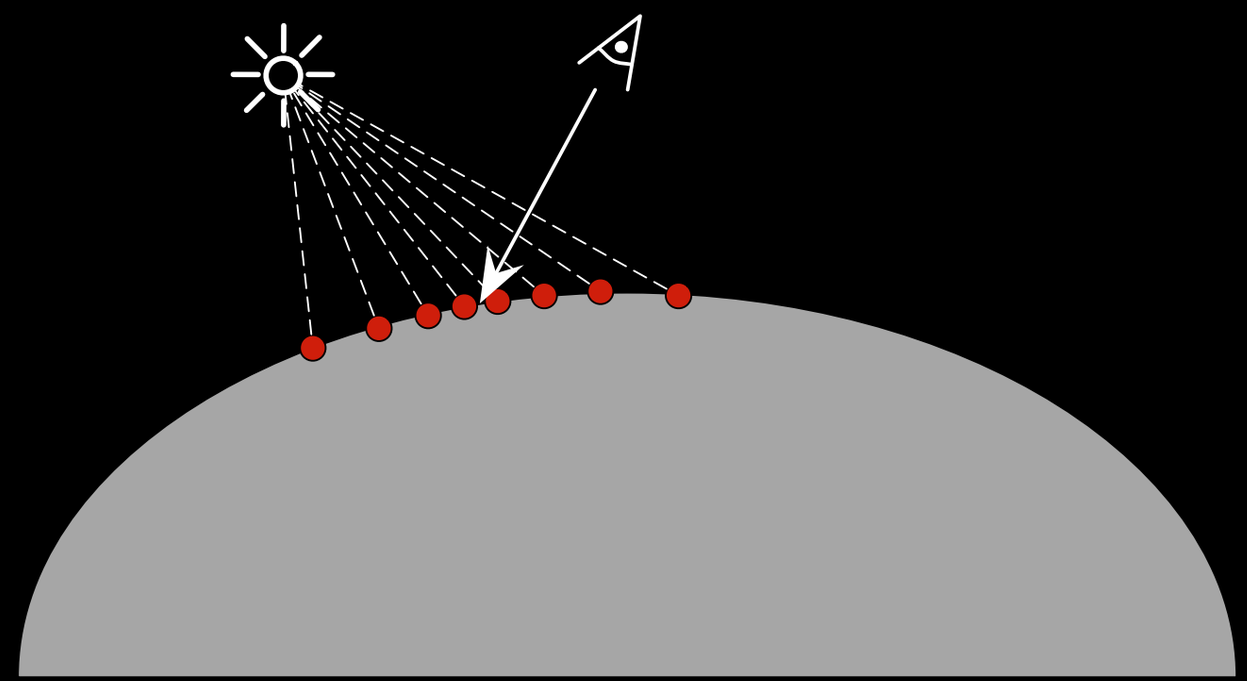

- Sample irradiance in 3D

Algorithm

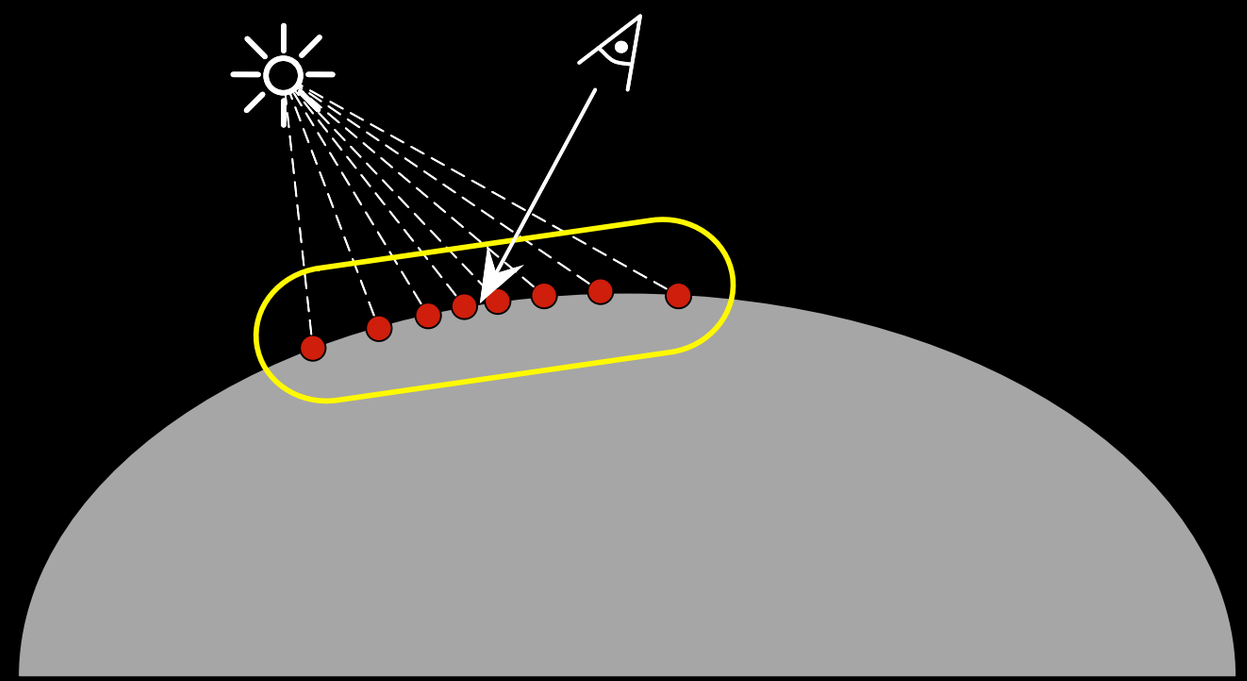

- Sample irradiance in 3D
- Project samples to UV-space

Algorithm

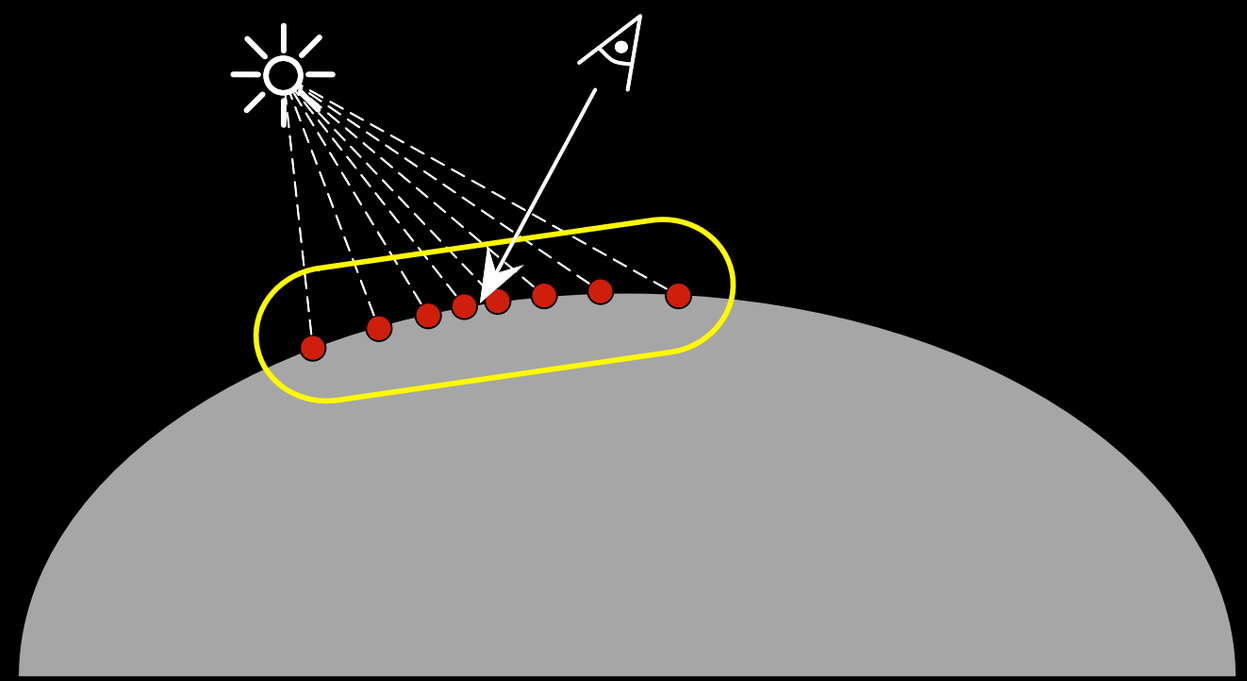

- Sample irradiance in 3D
- Project samples to UV-space
- Convolve in UV-space

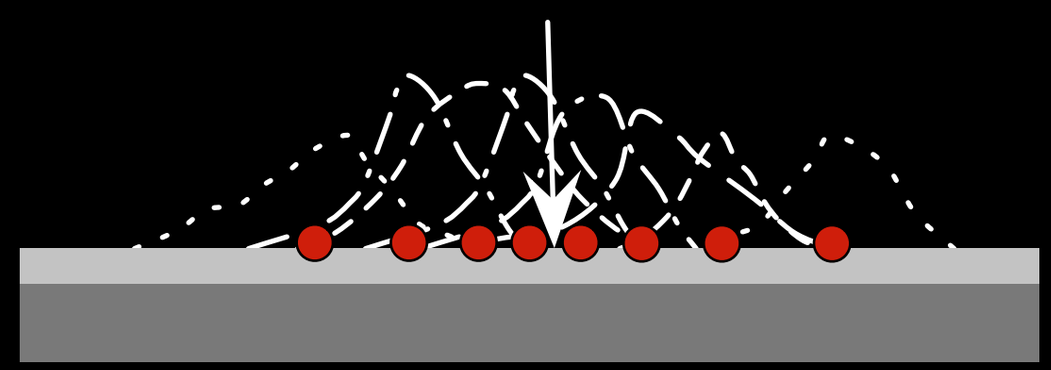

2D profiles, inter-layer absorption

Efficient Convolution

Efficient Convolution

- Sum of weighted gaussians

$$R = \sum_{i=1}^{k} w_i G(v_i)$$

Efficient Convolution

- Sum of weighted gaussians
- Separable convolution

$$R = \sum_{i=1}^{k} w_i G(v_i)$$

$$\Phi * R = \sum_{i=1}^{k} w_i G(v_i) * \Phi$$

Efficient Convolution

- Sum of weighted gaussians
- Separable convolution

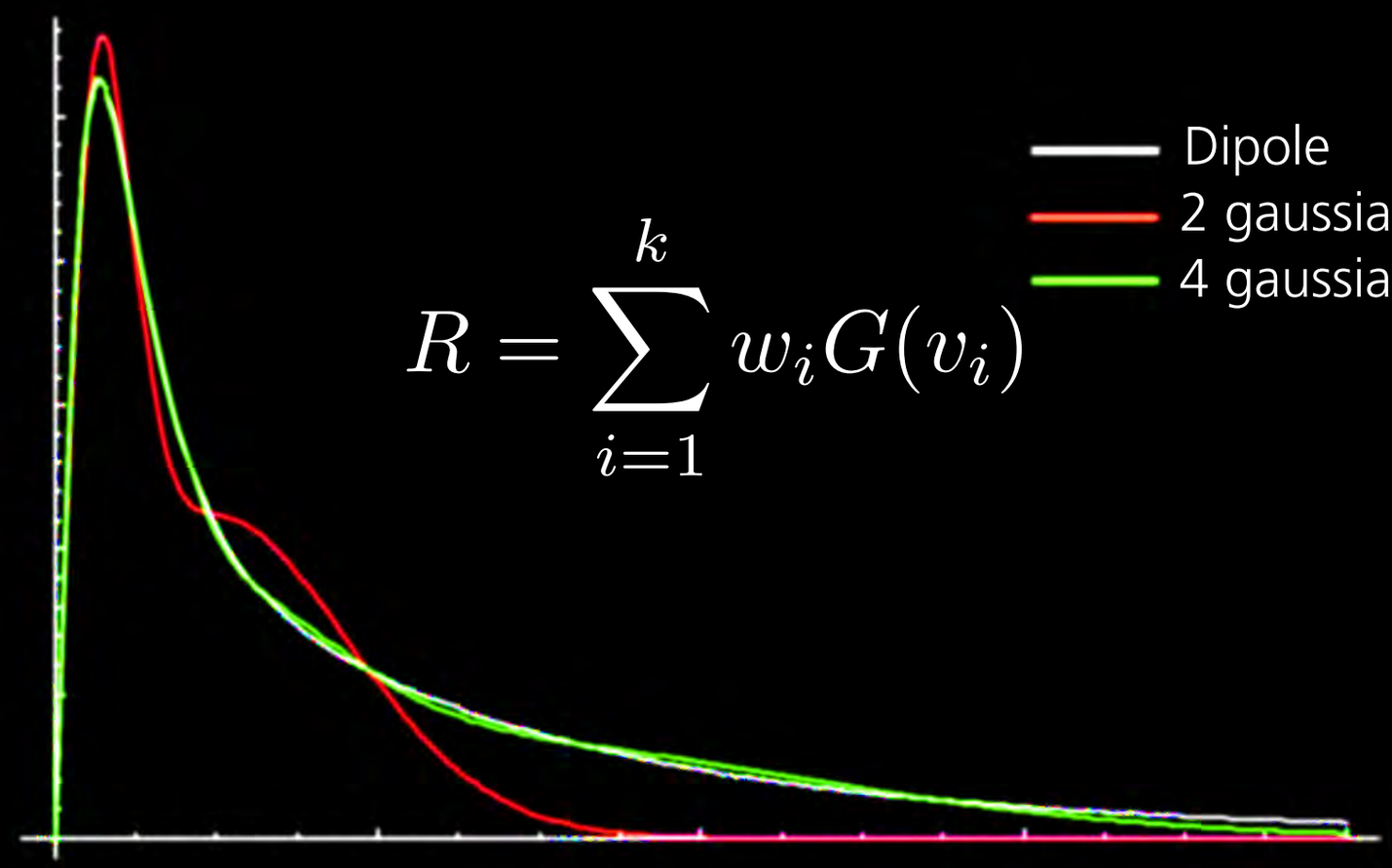

$$R = \sum_{i=1}^{k} w_i G(v_i)$$

[d'Eon et al. 2007]

$$\Phi * R = \sum_{i=1}^{k} w_i G(v_i) * \Phi$$

Efficient Convolution

- Sum of weighted gaussians
- Separable convolution
- Efficient evaluation

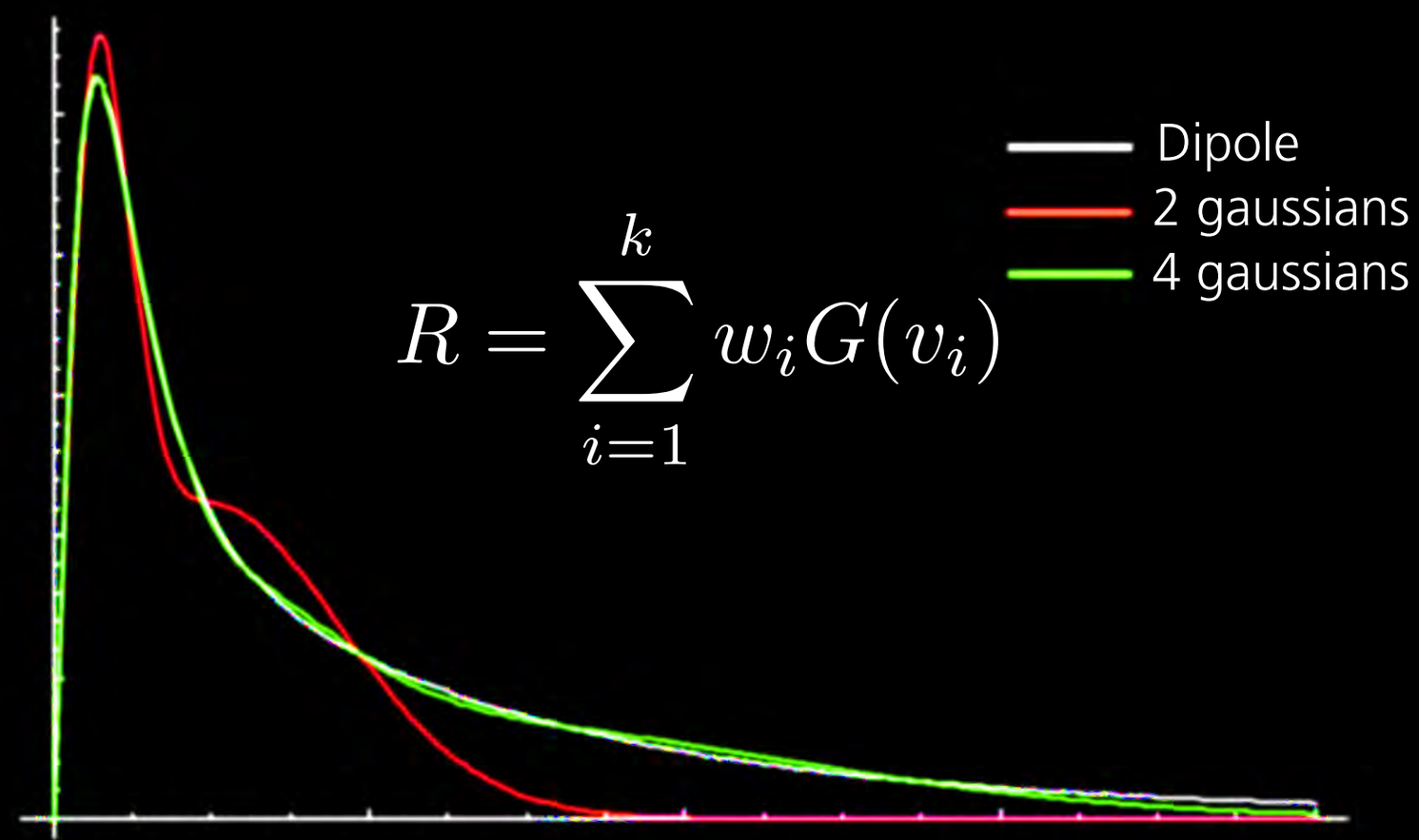

$$R = \sum_{i=1}^{k} w_i G(v_i)$$

[d'Eon et al. 2007]

$$\Phi * R = \sum_{i=1}^{k} w_i G(v_i) * \Phi$$

Efficient Convolution

- Sum of weighted gaussians
- Separable convolution
- Efficient evaluation

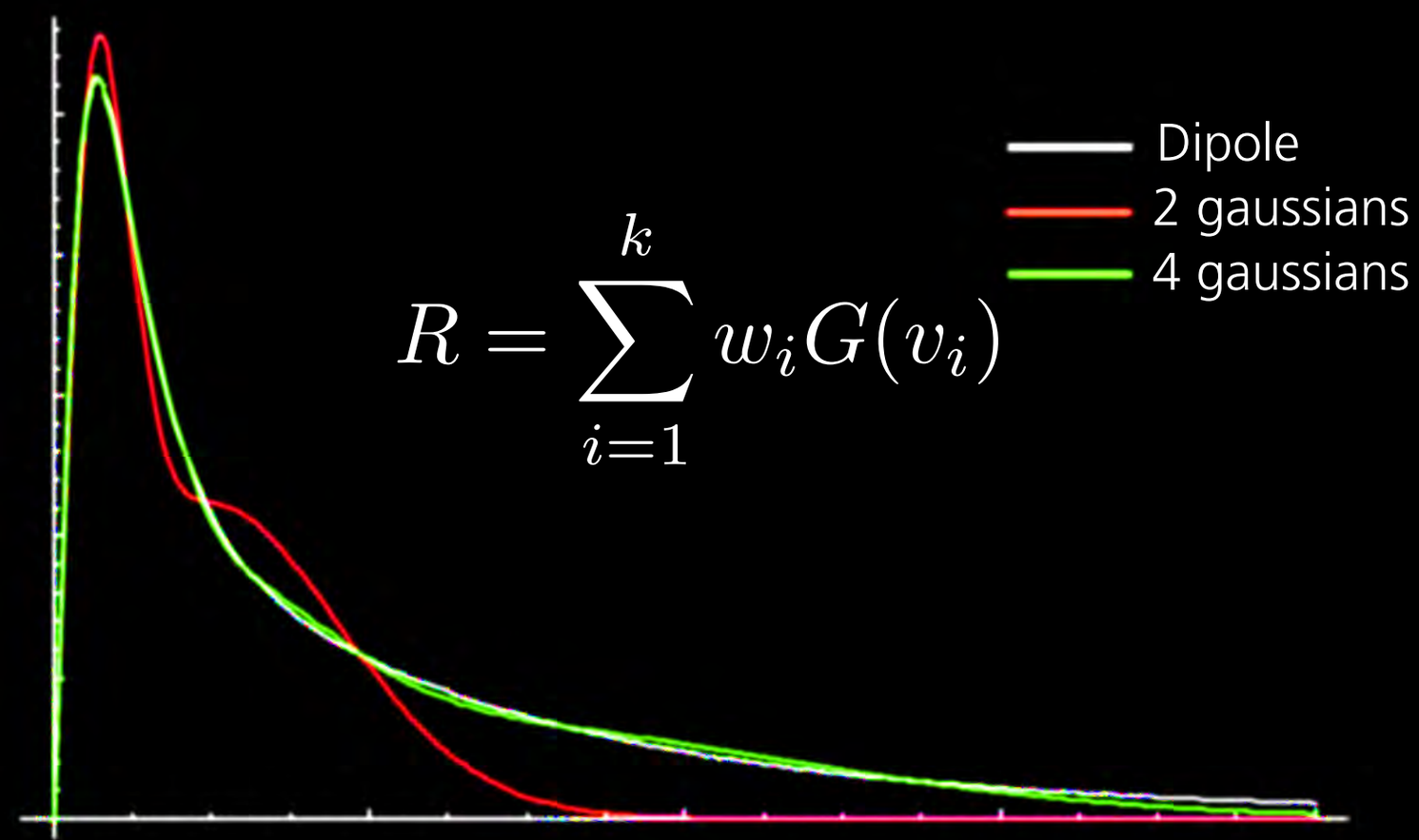

$$R = \sum_{i=1}^{k} w_i G(v_i)$$

[d'Eon et al. 2007]

Irradiance convolution

$$\Phi * R = \sum_{i=1}^{k} w_i G(v_i) * \Phi$$

Irradiance Convolution

Irradiance Convolution

- Irradiance map Φ

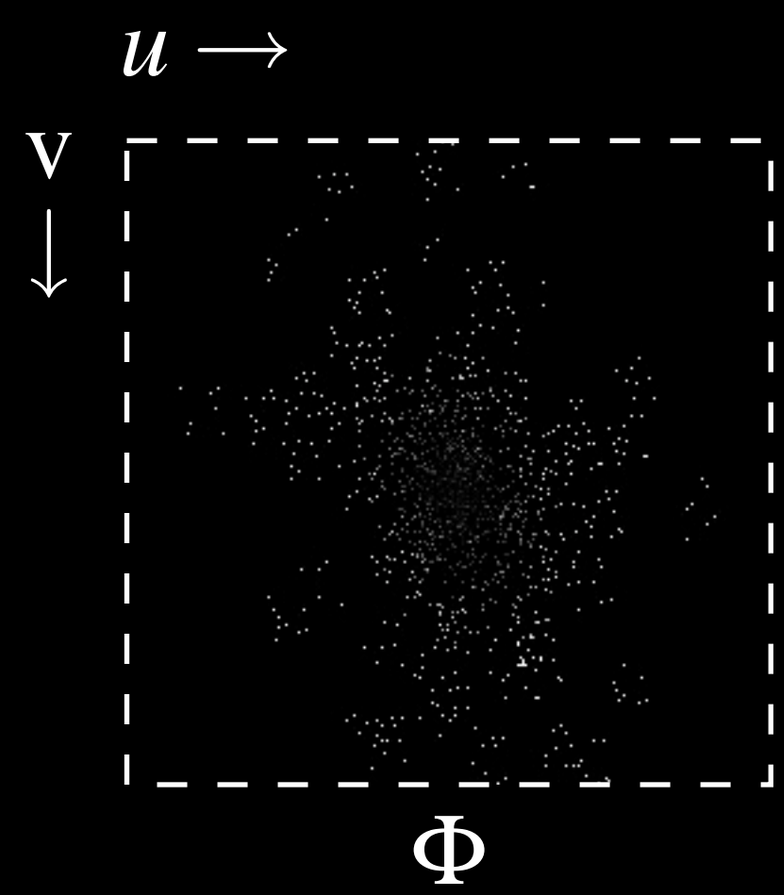

Irradiance Convolution

- Irradiance map Φ
- Blur, weight, accumulate

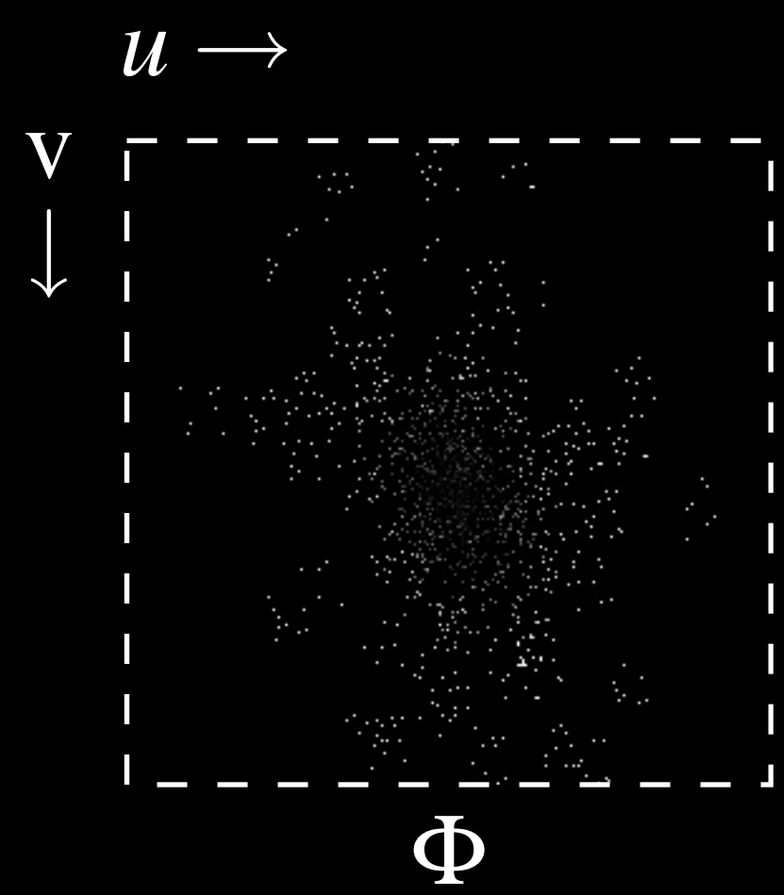

Irradiance Convolution

- Irradiance map Φ
- Blur, weight, accumulate

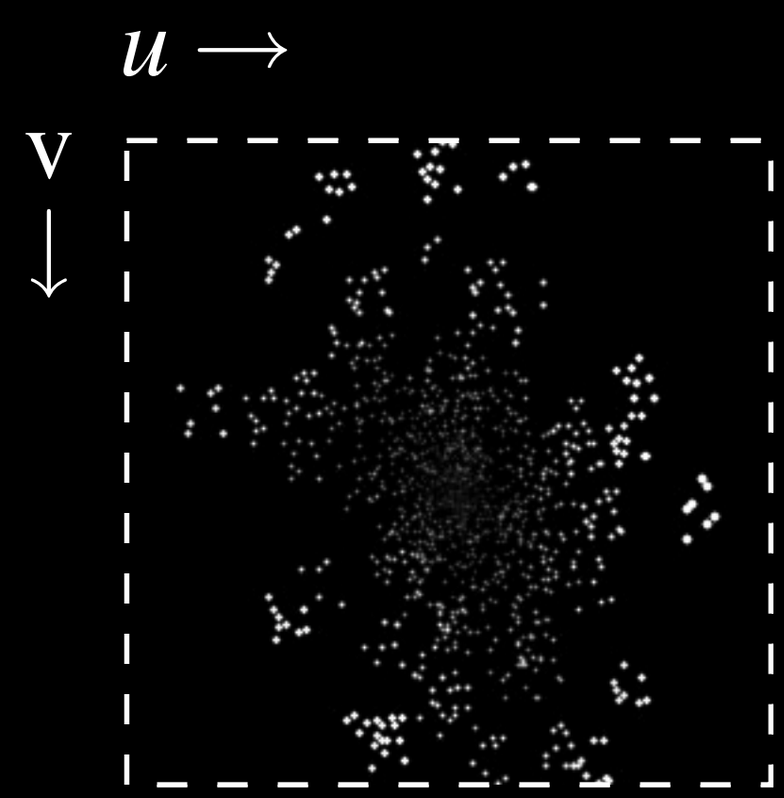

$* \; G(v_3)$

Irradiance Convolution

- Irradiance map Φ
- Blur, weight, accumulate

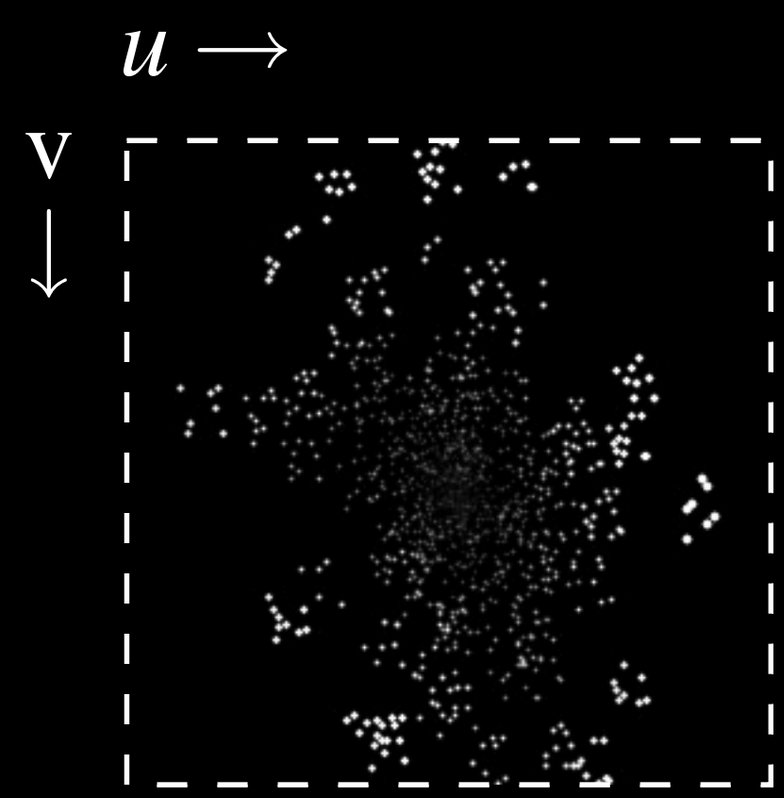

$* \; G(v_3)$

$\times \; w_3$

Irradiance Convolution

- Irradiance map Φ
- Blur, weight, accumulate

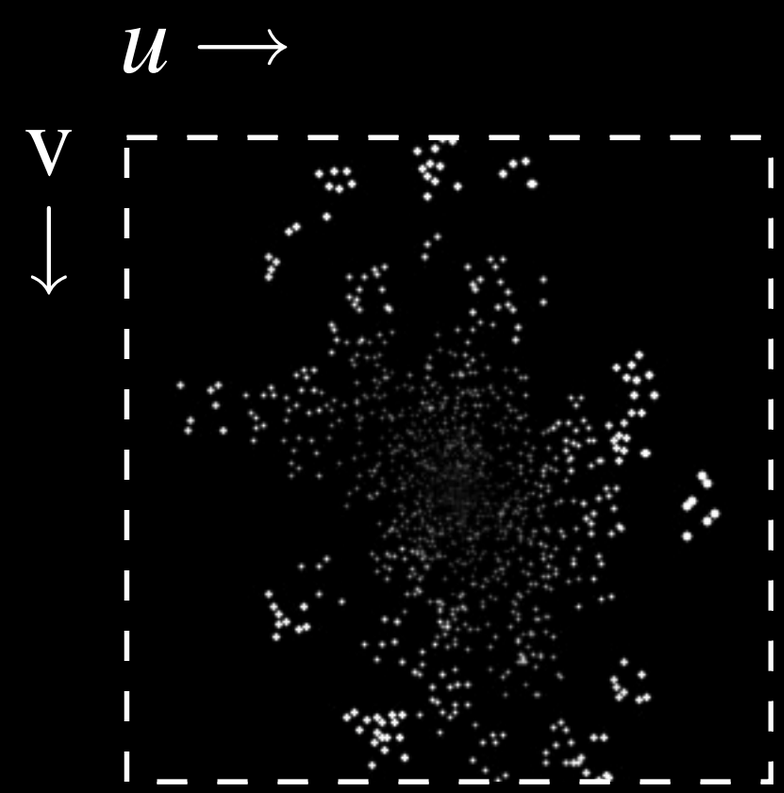

$* \; G(v_3)$

$\times \; w_3 \; \times$

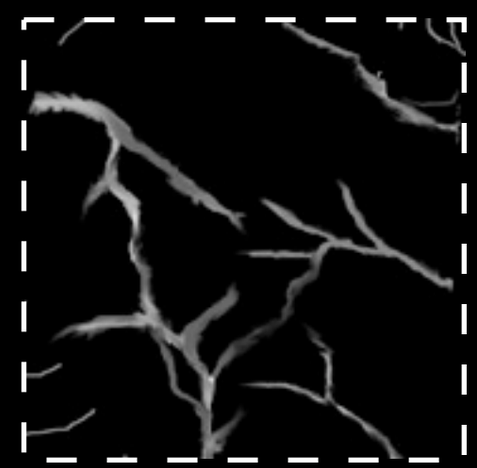

Inter-layer absorption

Irradiance Convolution

- Irradiance map Φ
- Blur, weight, accumulate

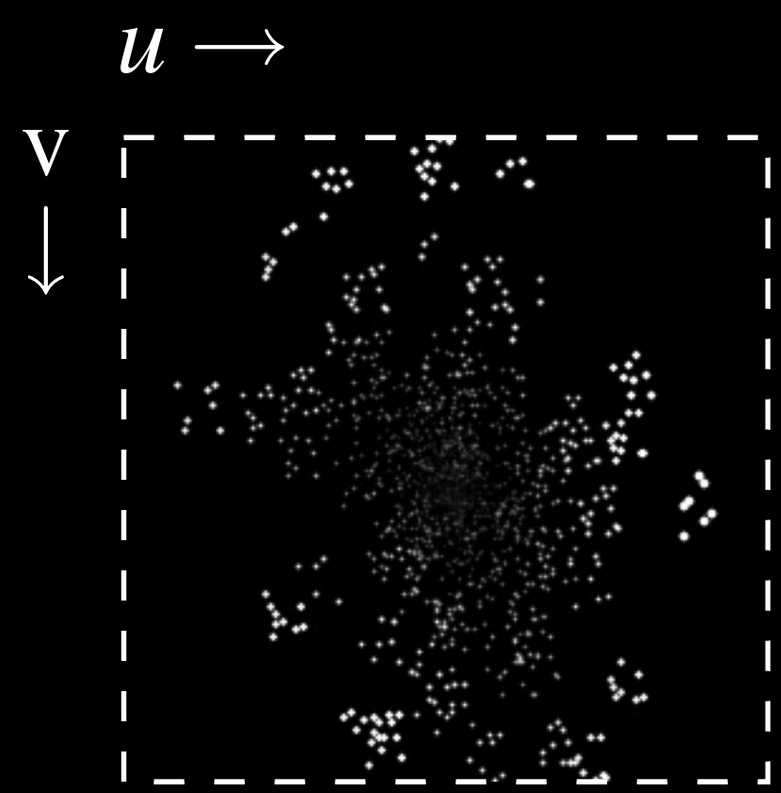

$* \; G(v_3)$

$\times \; w_3 \; \times$

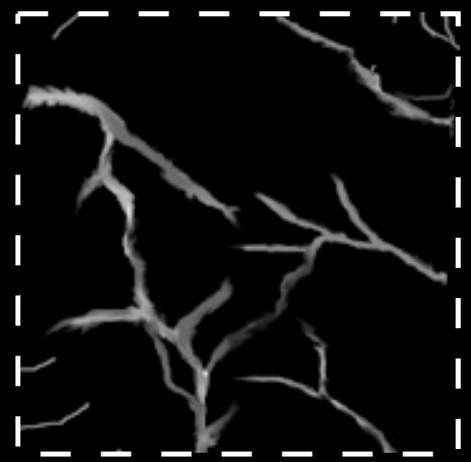

$\rightarrow$ Accumulate

Inter-layer absorption

Irradiance Convolution

- Irradiance map Φ
- Blur, weight, accumulate

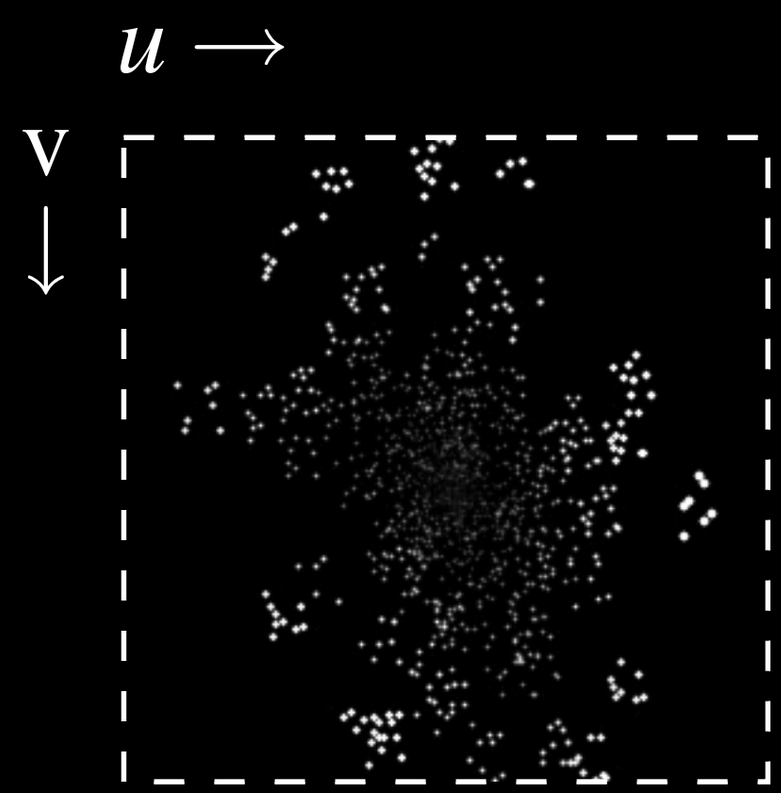

$* \; G(v_3)$

$\times \; w_3 \; \times$

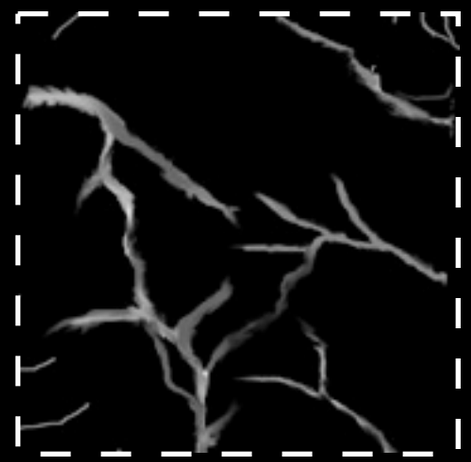

$\rightarrow$ Accumulate

Inter-layer absorption

Irradiance Convolution

- Irradiance map Φ
- Blur, weight, accumulate

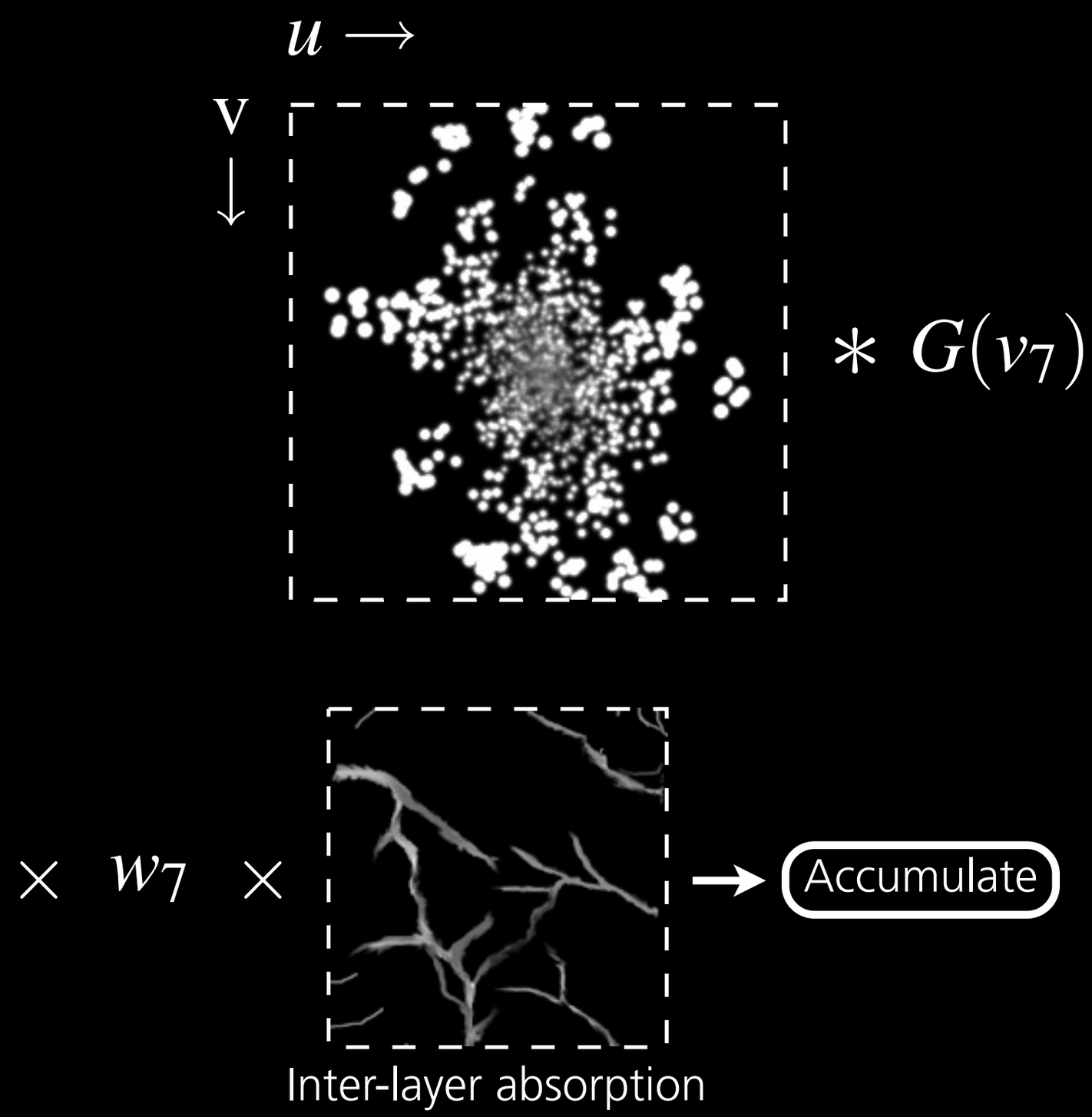

Irradiance Convolution

- Irradiance map Φ
- Blur, weight, accumulate

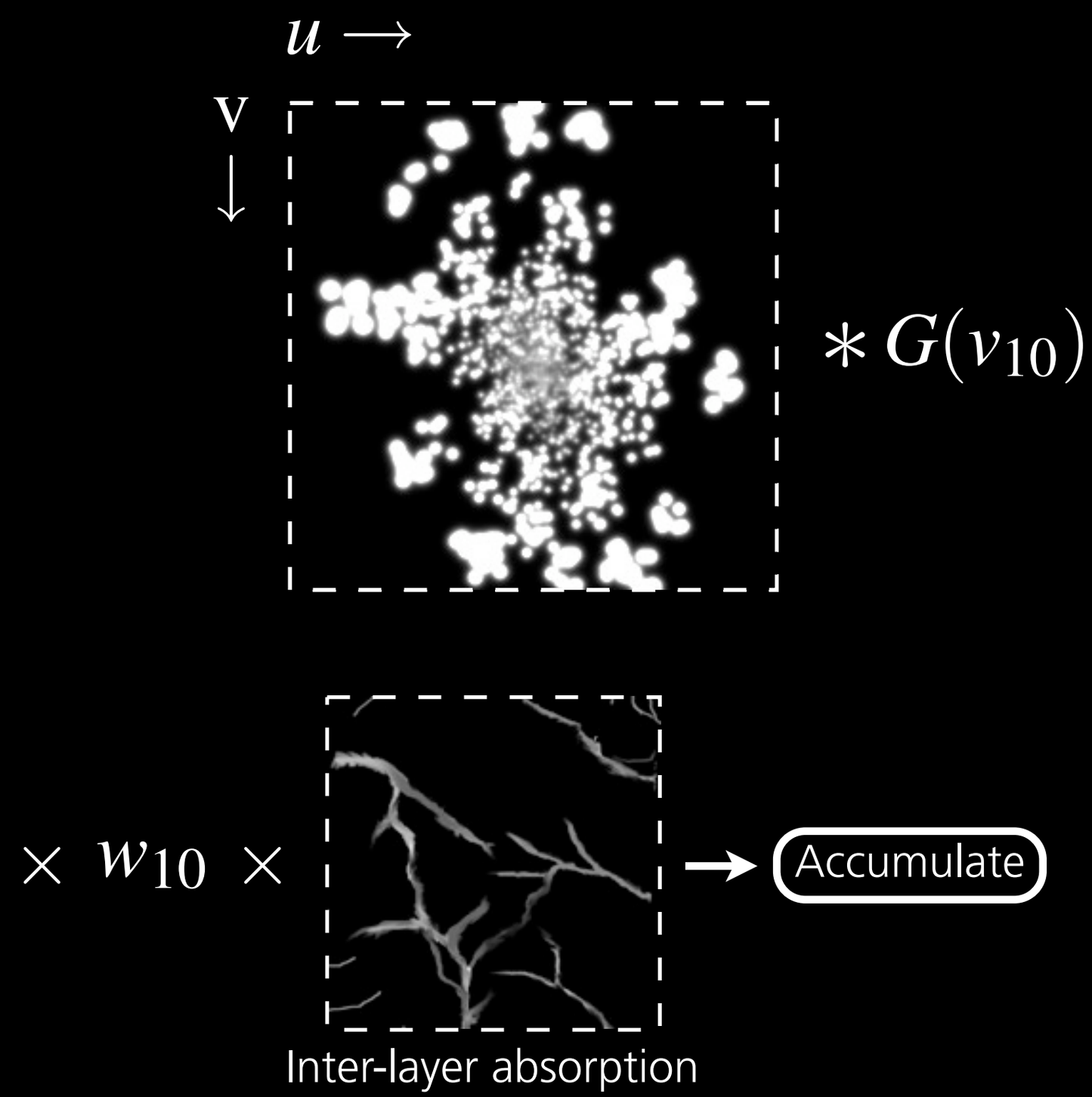

Irradiance Convolution

- Irradiance map Φ
- Blur, weight, accumulate
- Weights in LUT, indexed by σ_a

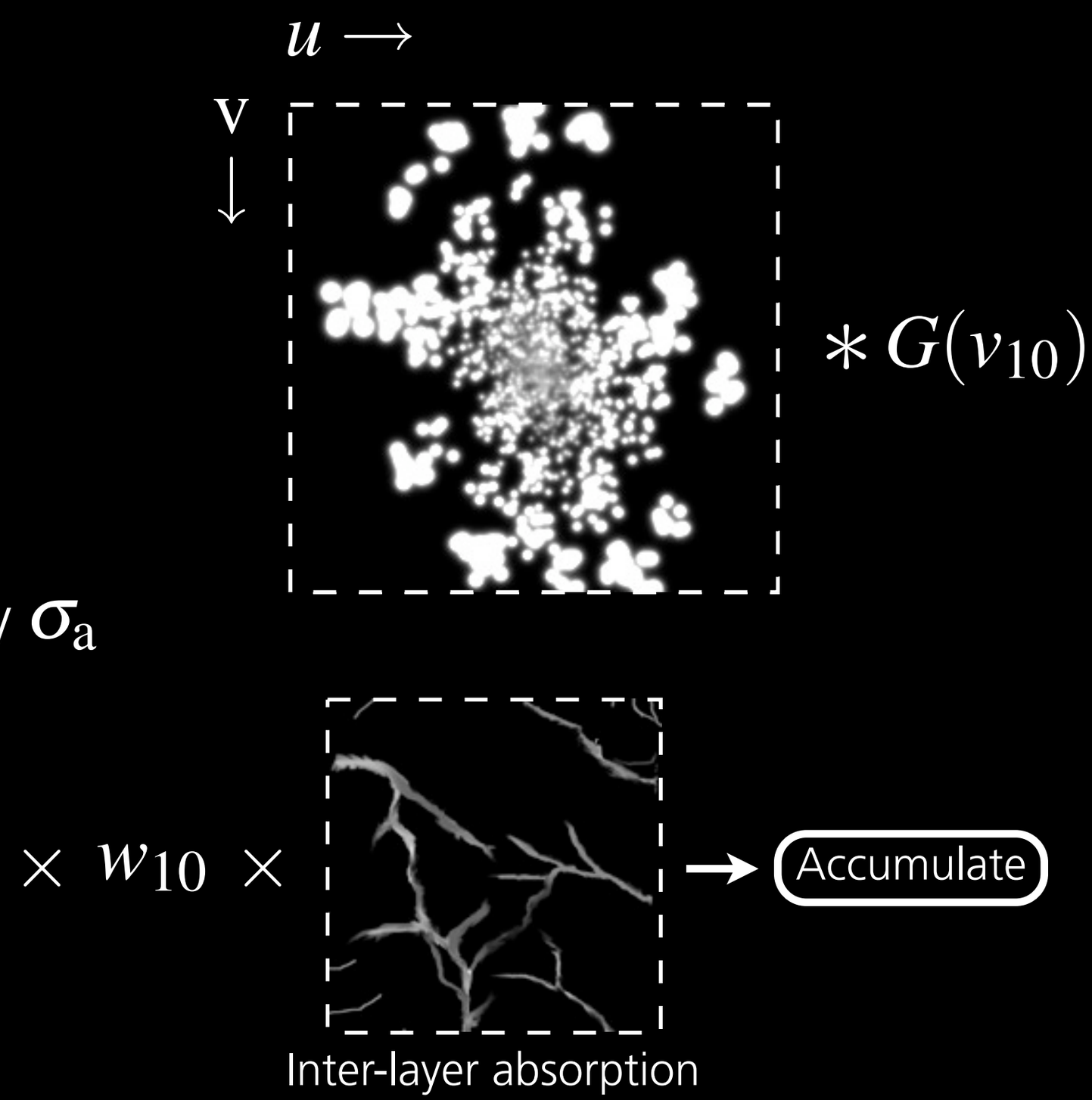

Irradiance Convolution

- Irradiance map Φ
- Blur, weight, accumulate
- Weights in LUT, indexed by σ_a
- Progressive accumulation

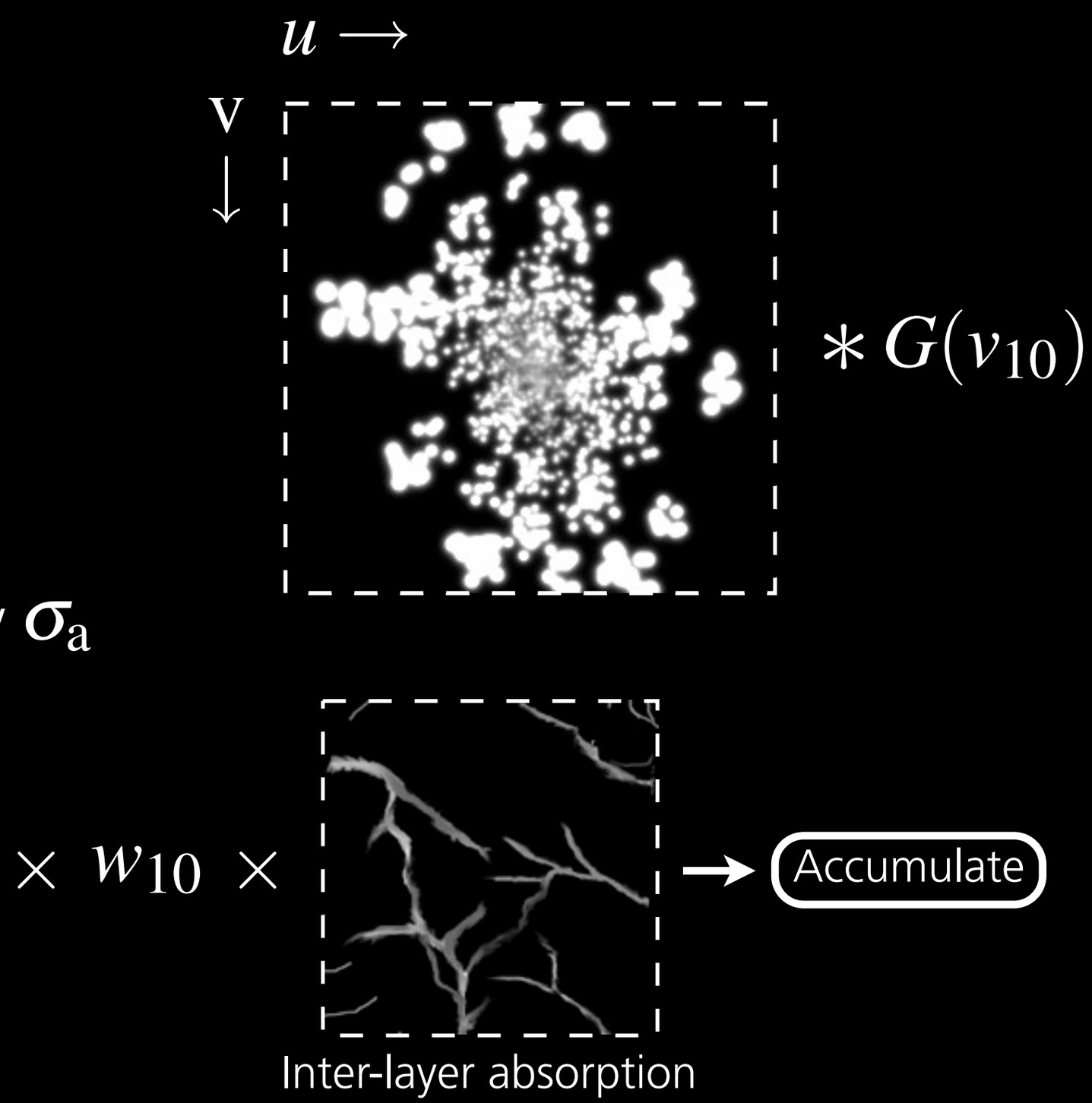

Synthetic Example

Synthetic Example

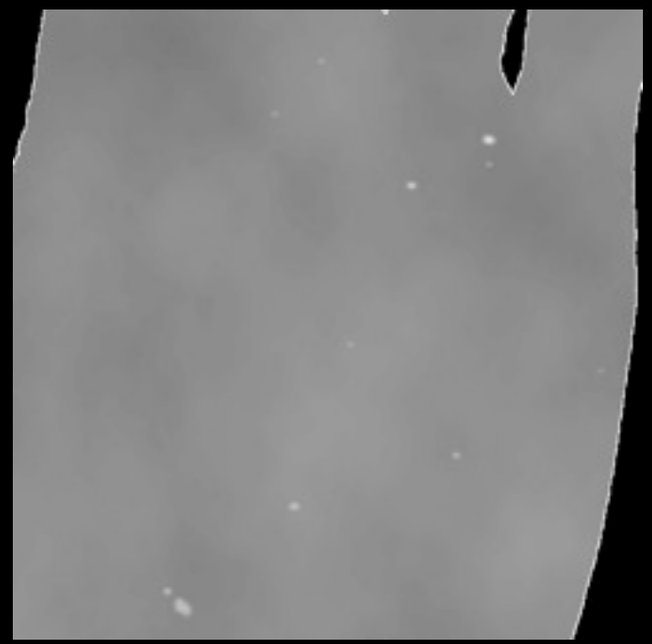

Melanin

Synthetic Example

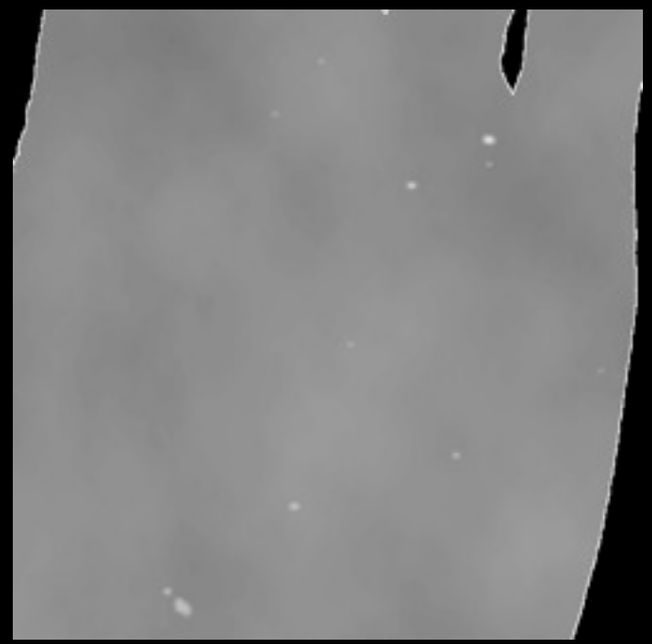

Melanin

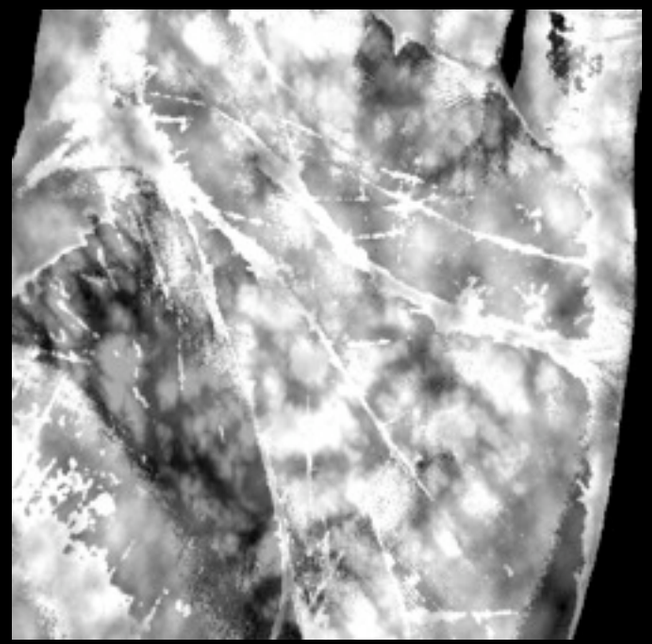

Hemoglobin

Synthetic Example

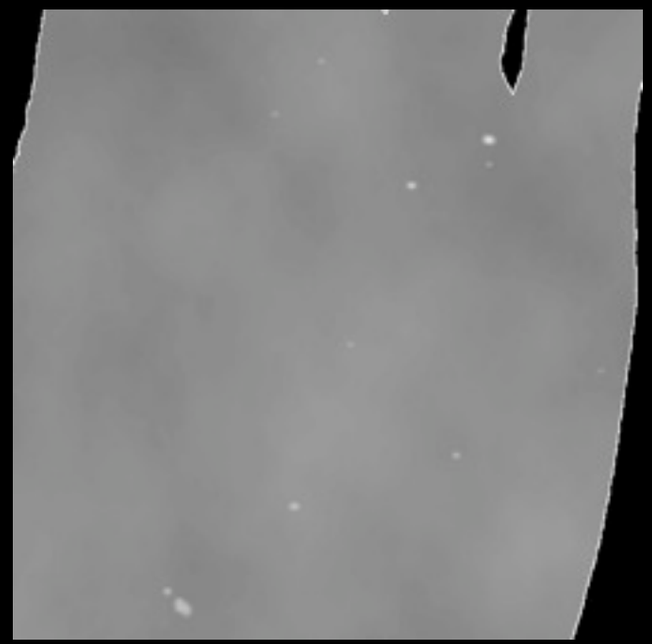

Melanin

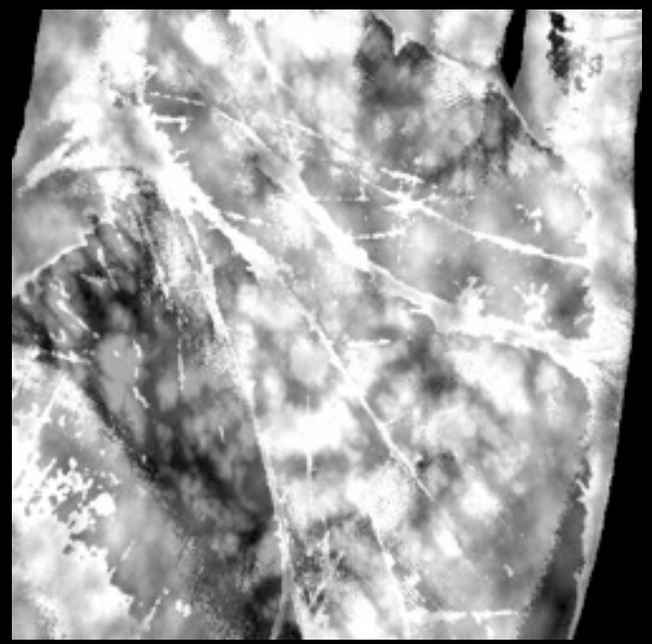

Hemoglobin

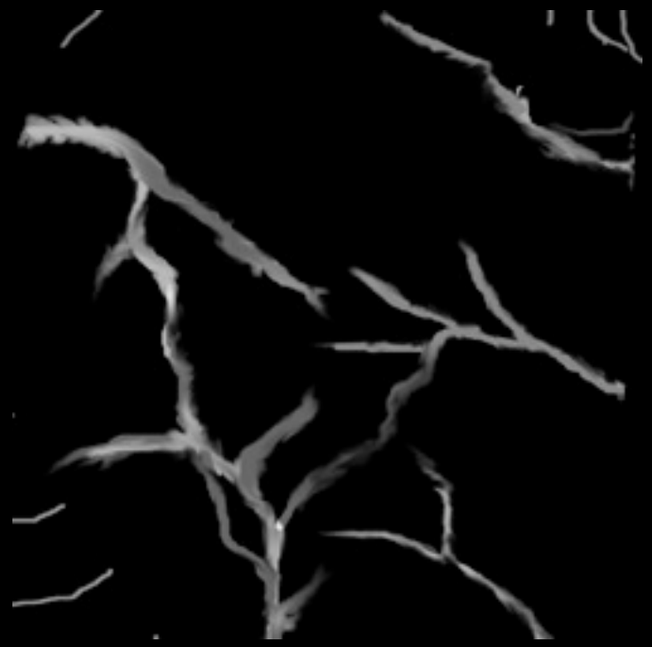

Veins (absorption)

Synthetic Example

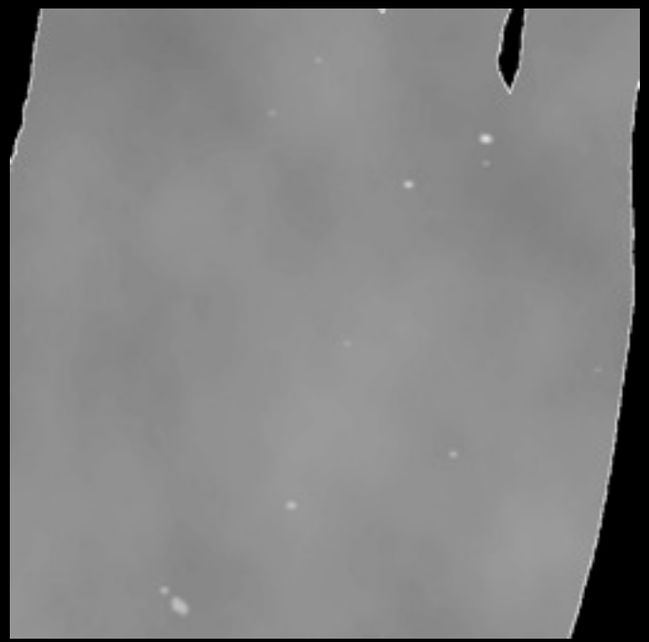

Melanin

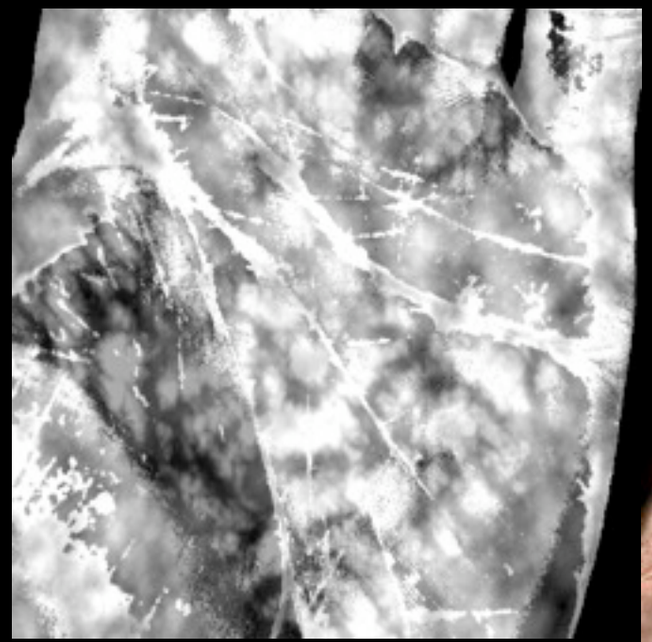

Hemoglobin

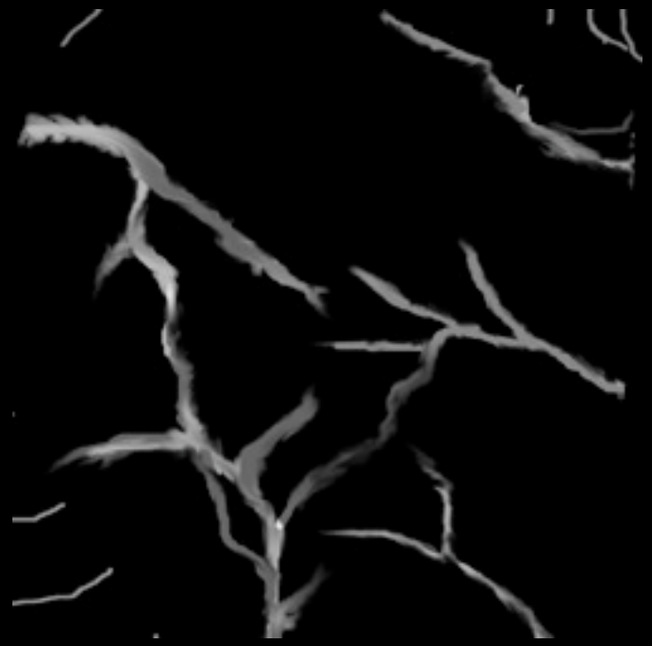

Veins (absorption)

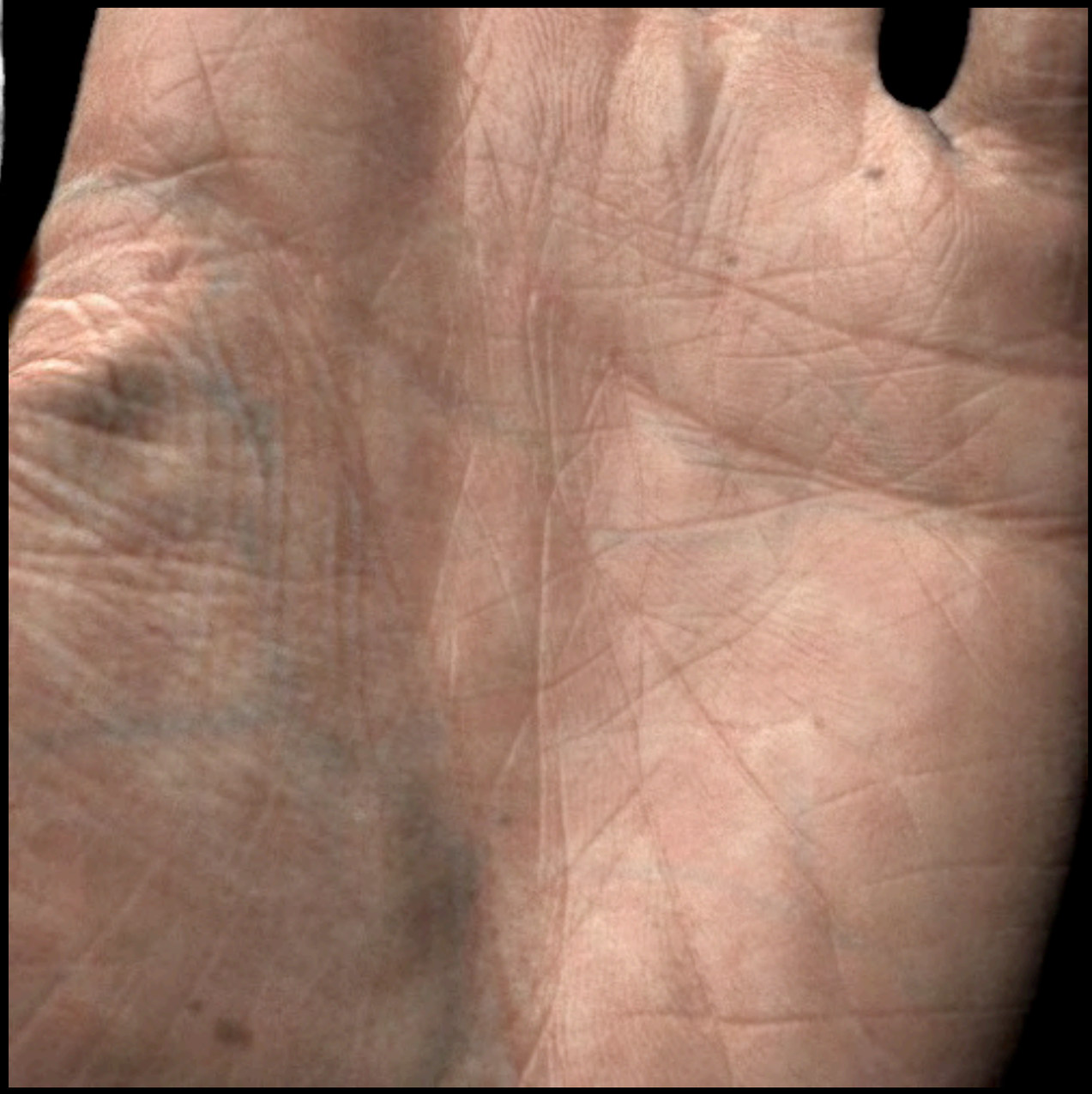

Geometry from [Ma et al. 2007]

Dynamic changes

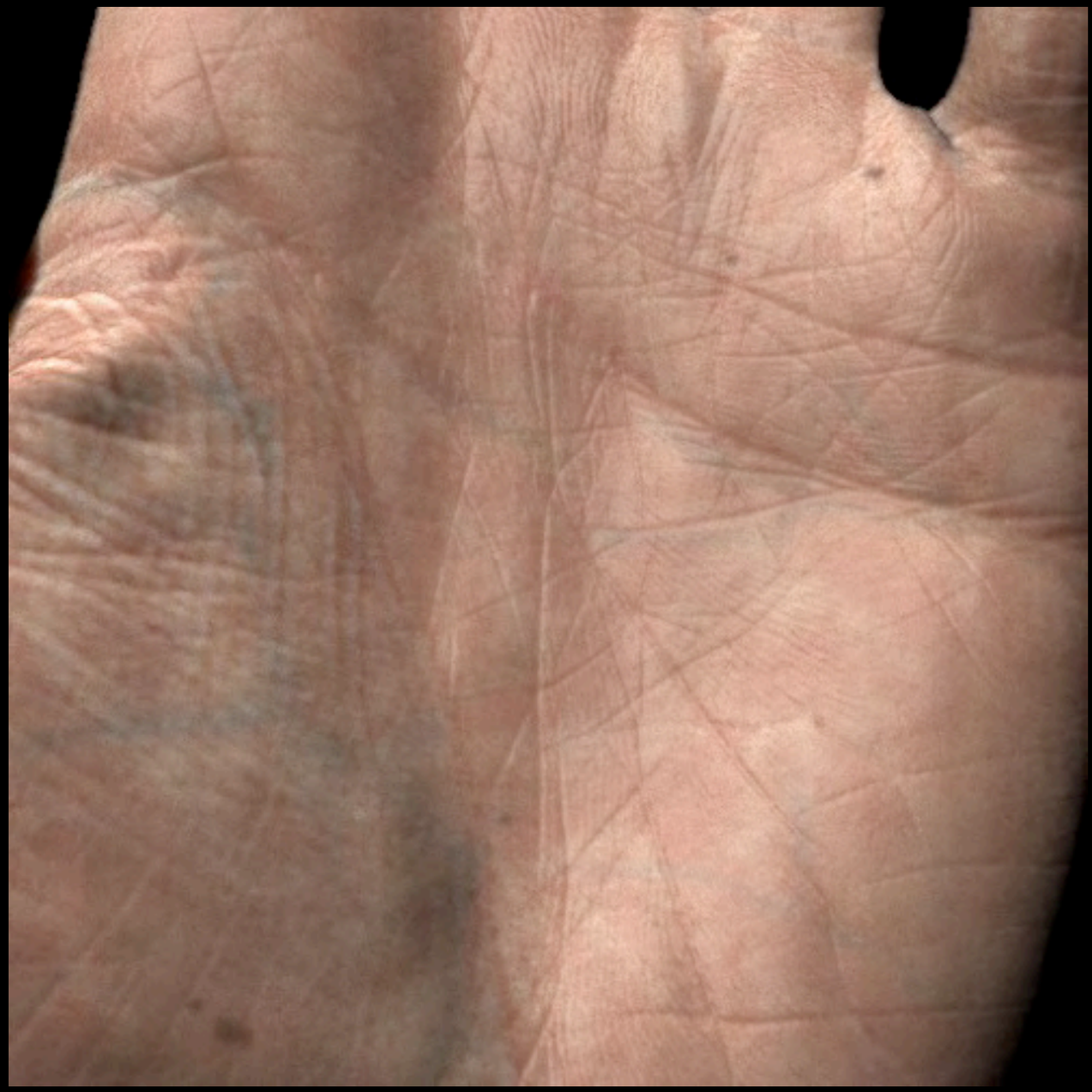

Geometry from [Ma et al. 2007]

Dynamic changes

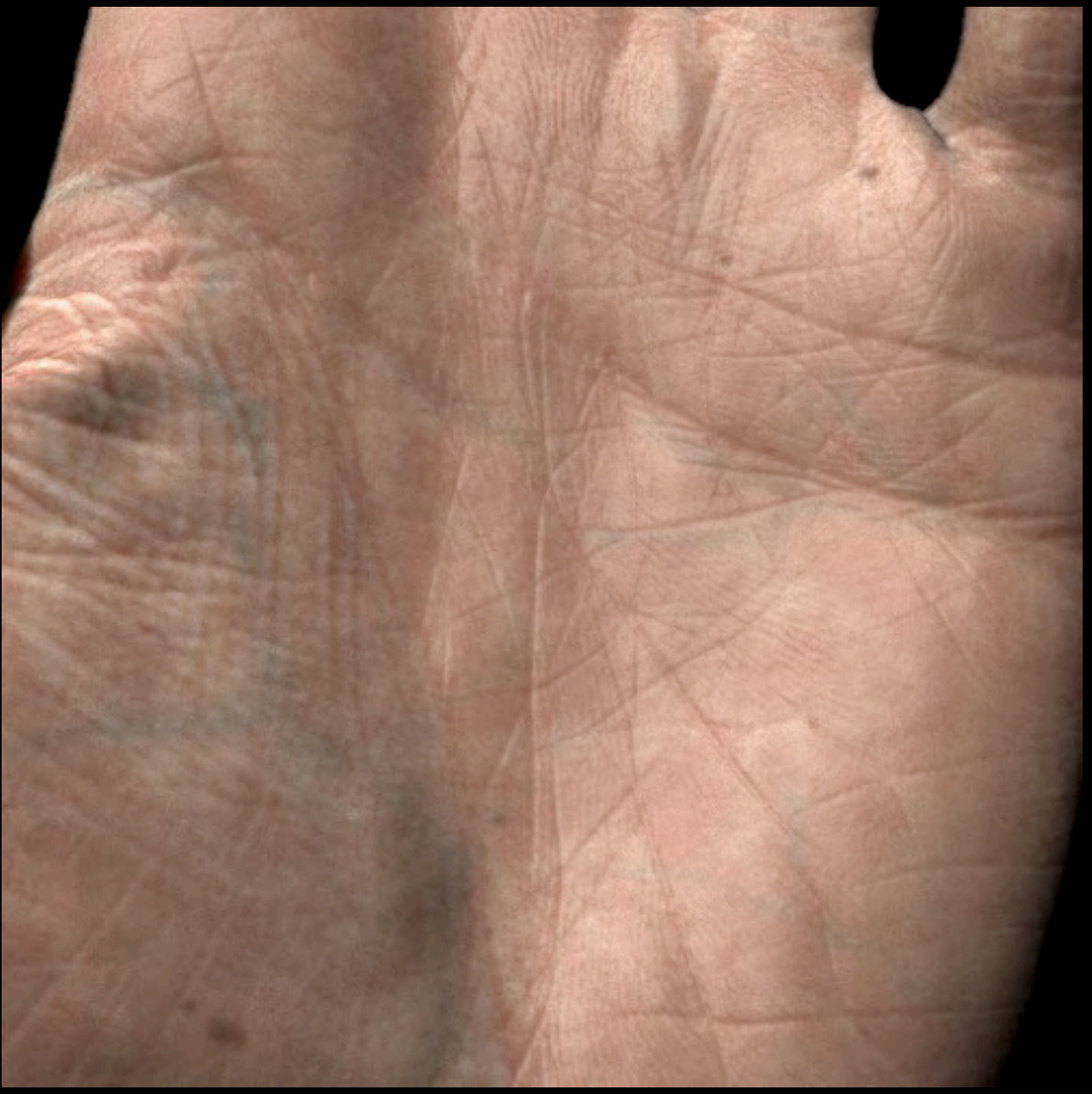

Geometry from [Ma et al. 2007]

Dynamic changes

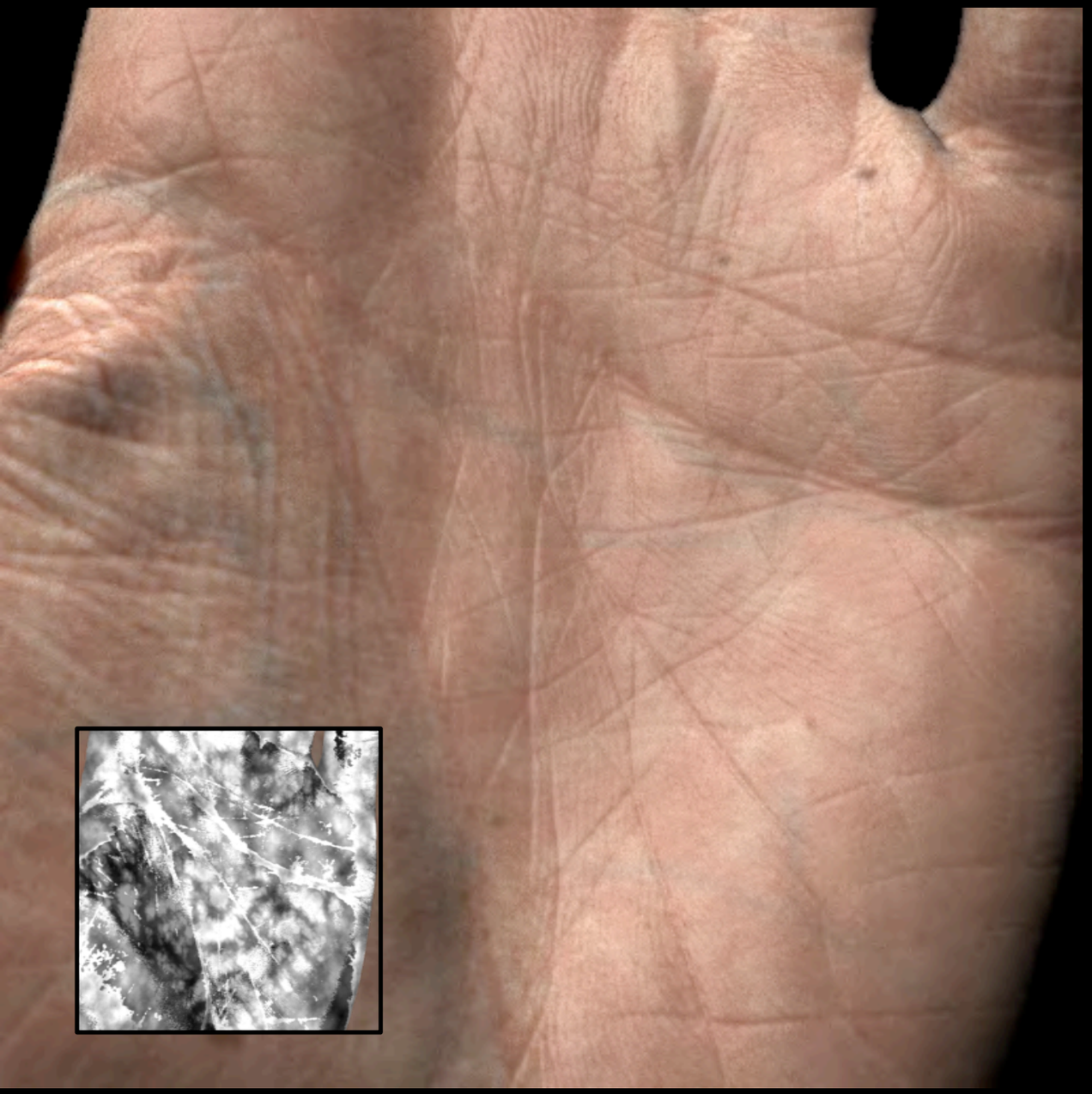

Geometry from [Ma et al. 2007]

Dynamic changes

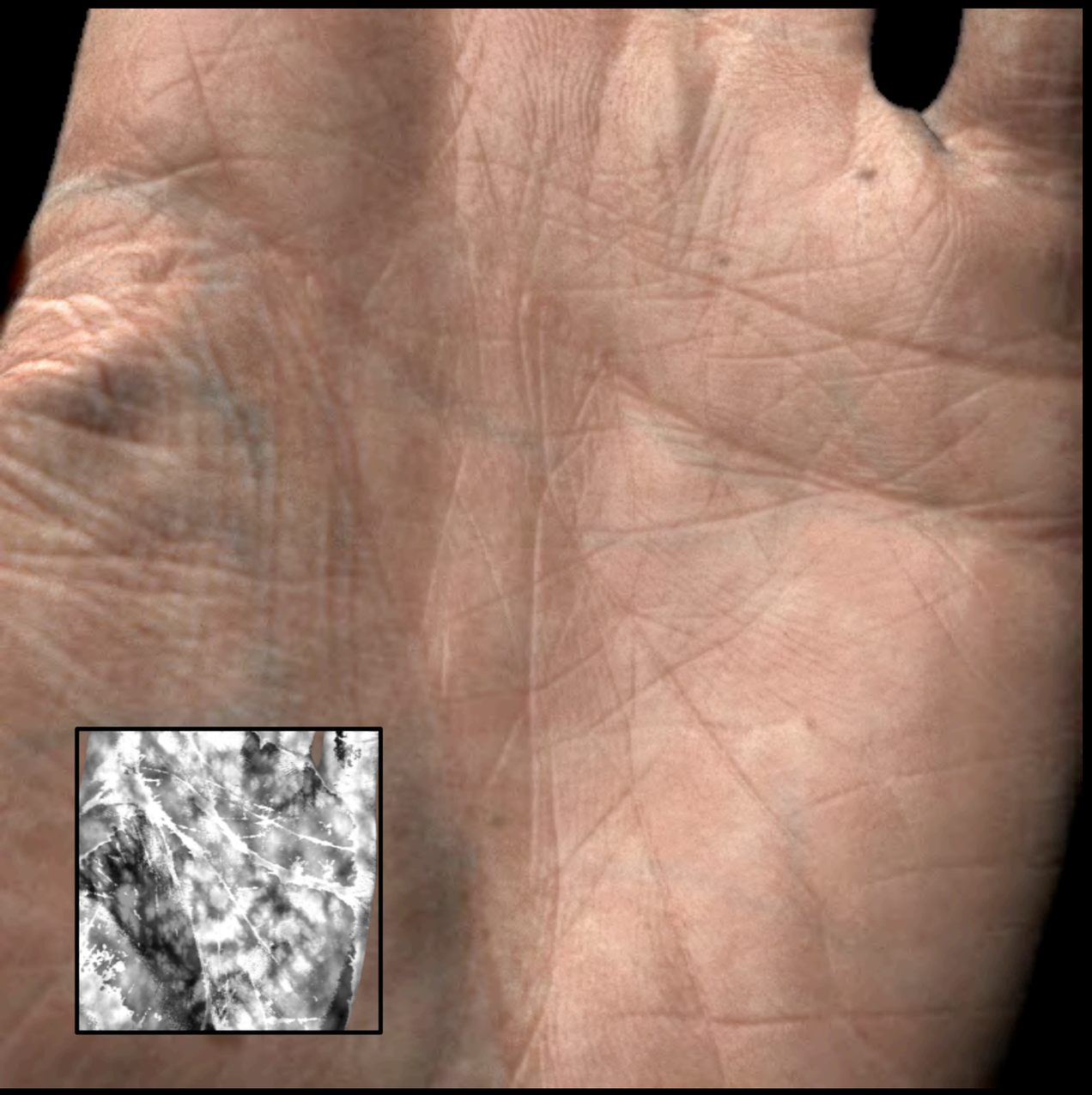

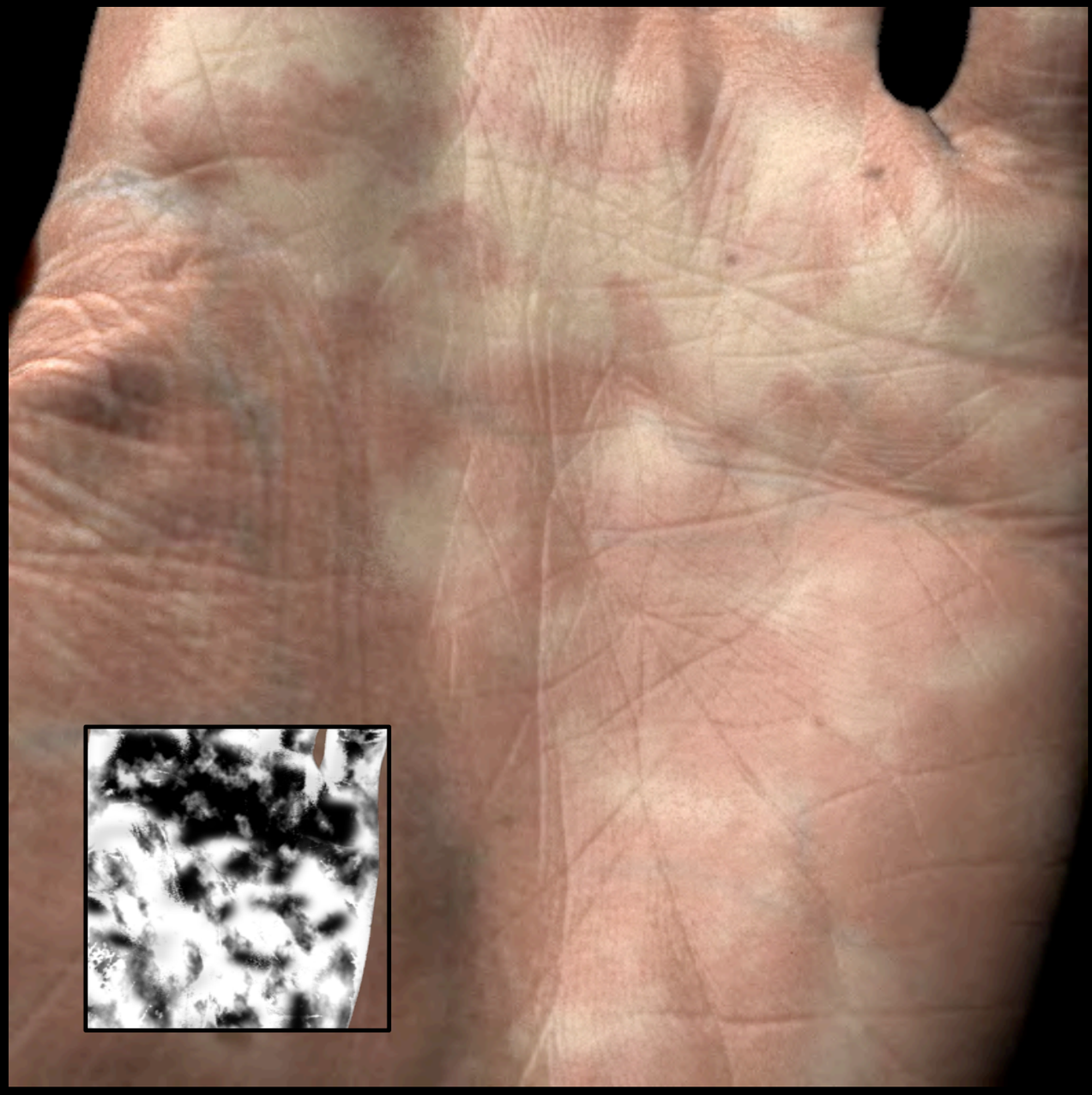

Geometry from [Ma et al. 2007]

Backlighting

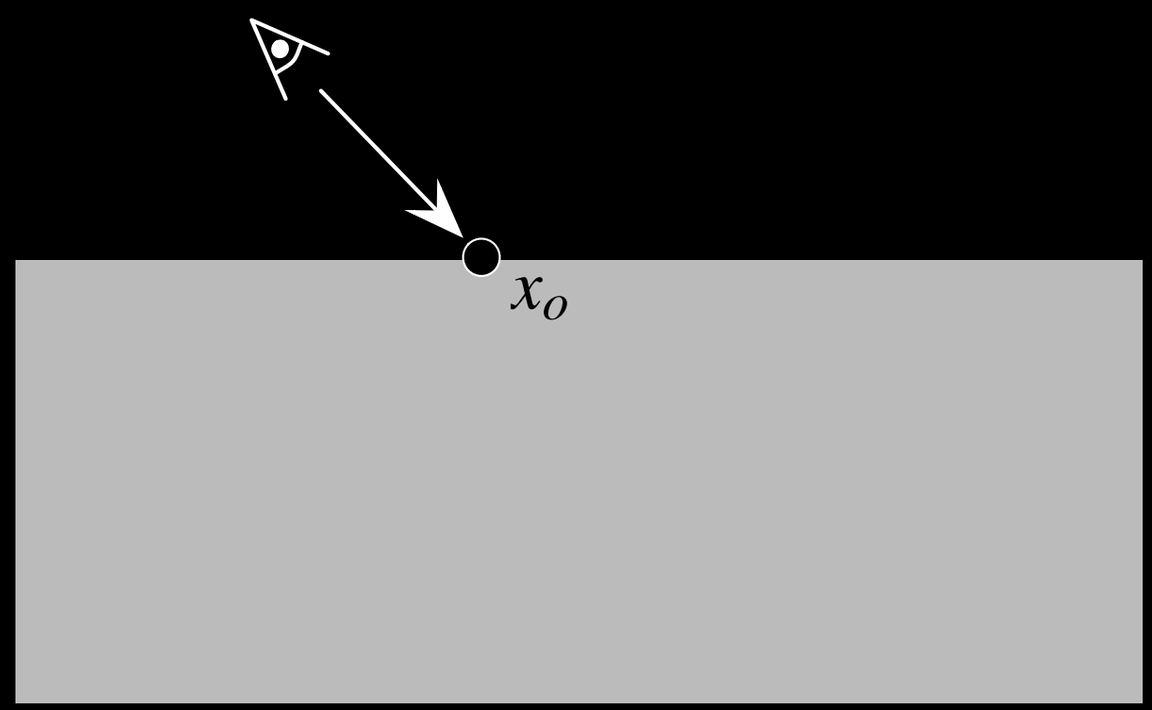

Backlighting

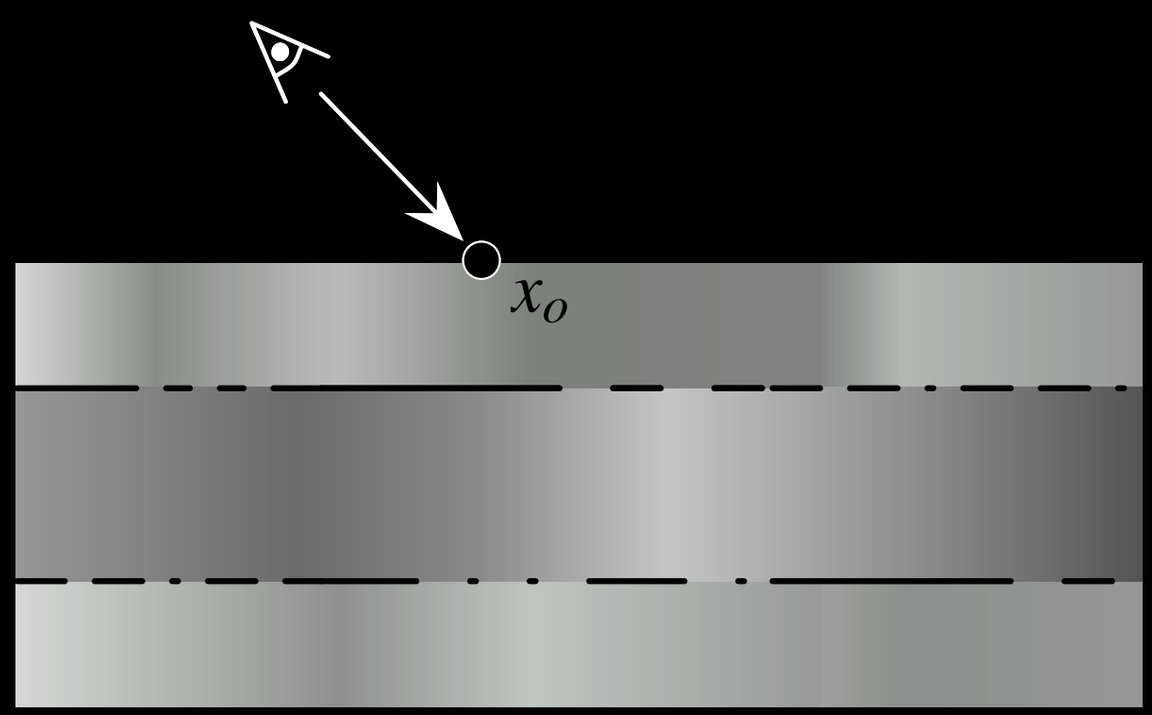

Backlighting

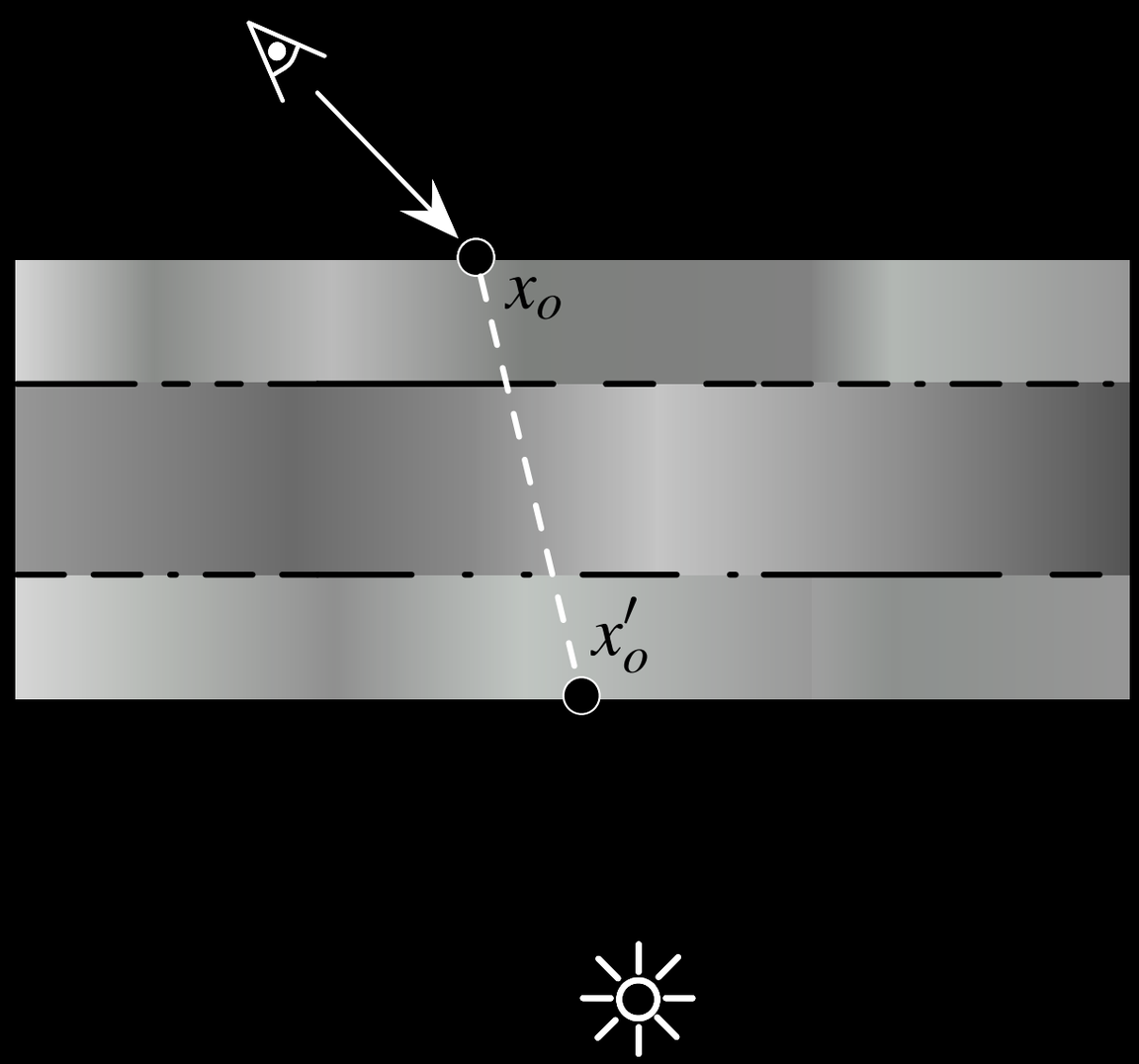

Backlighting

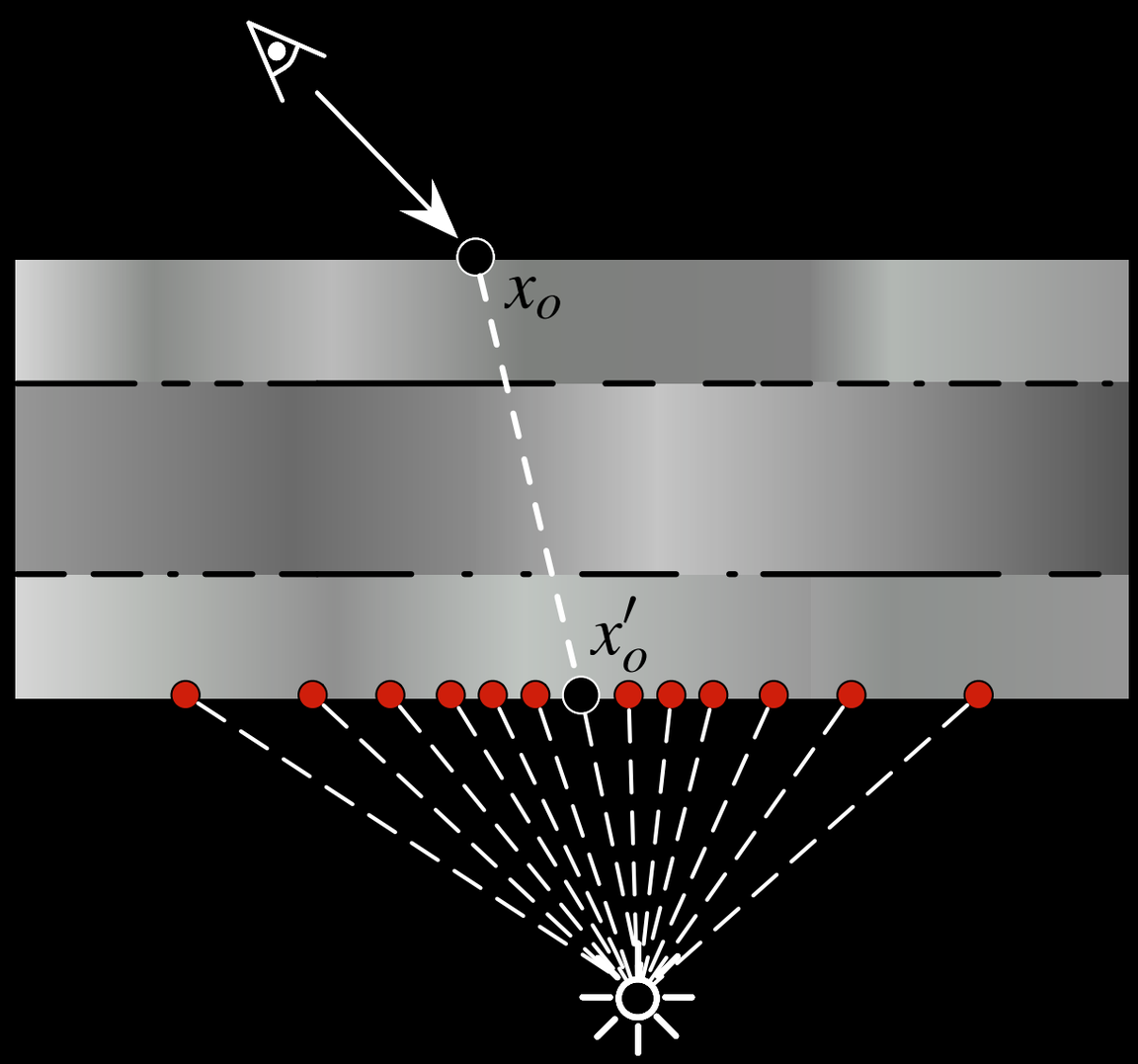

Backlighting

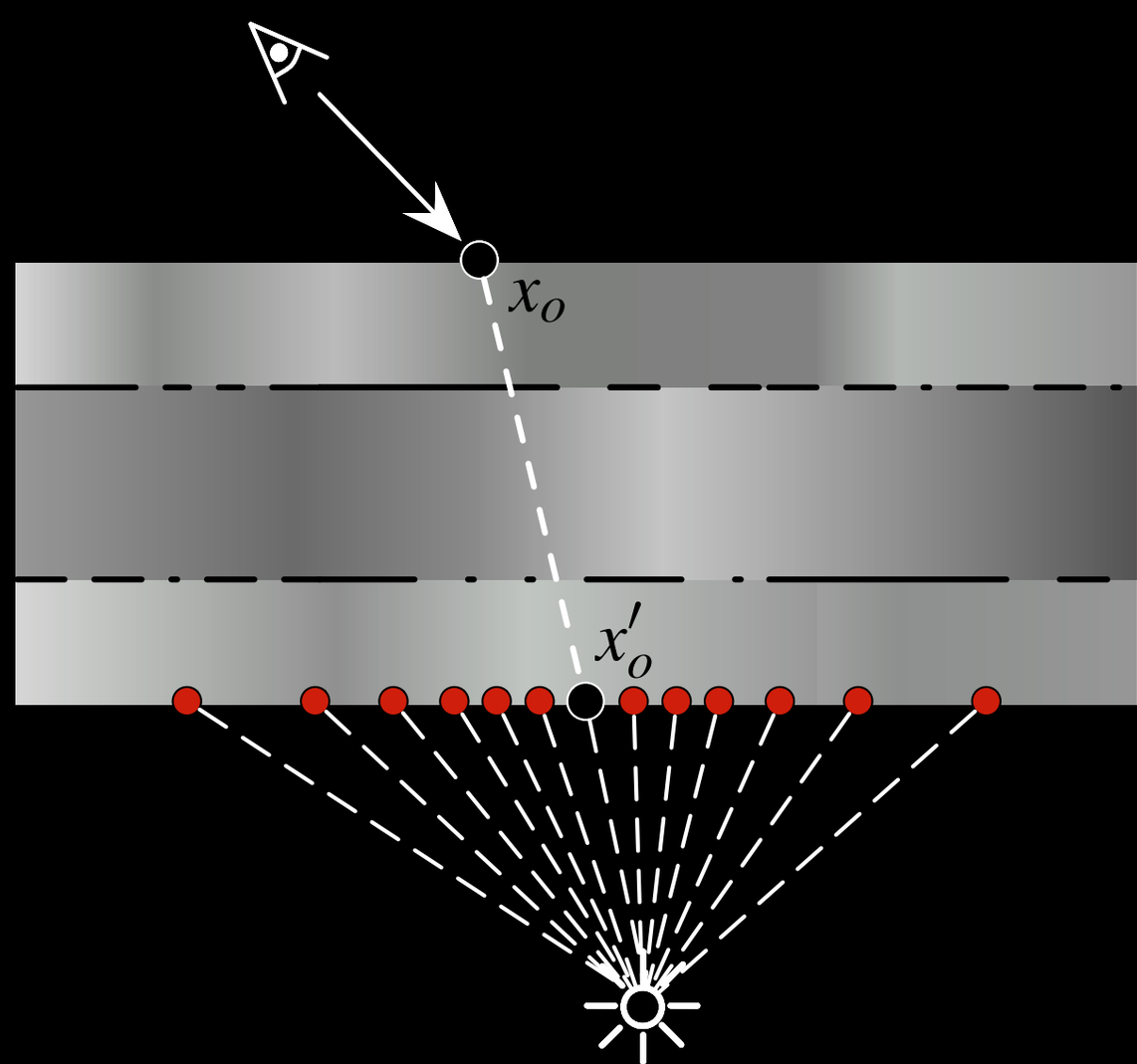

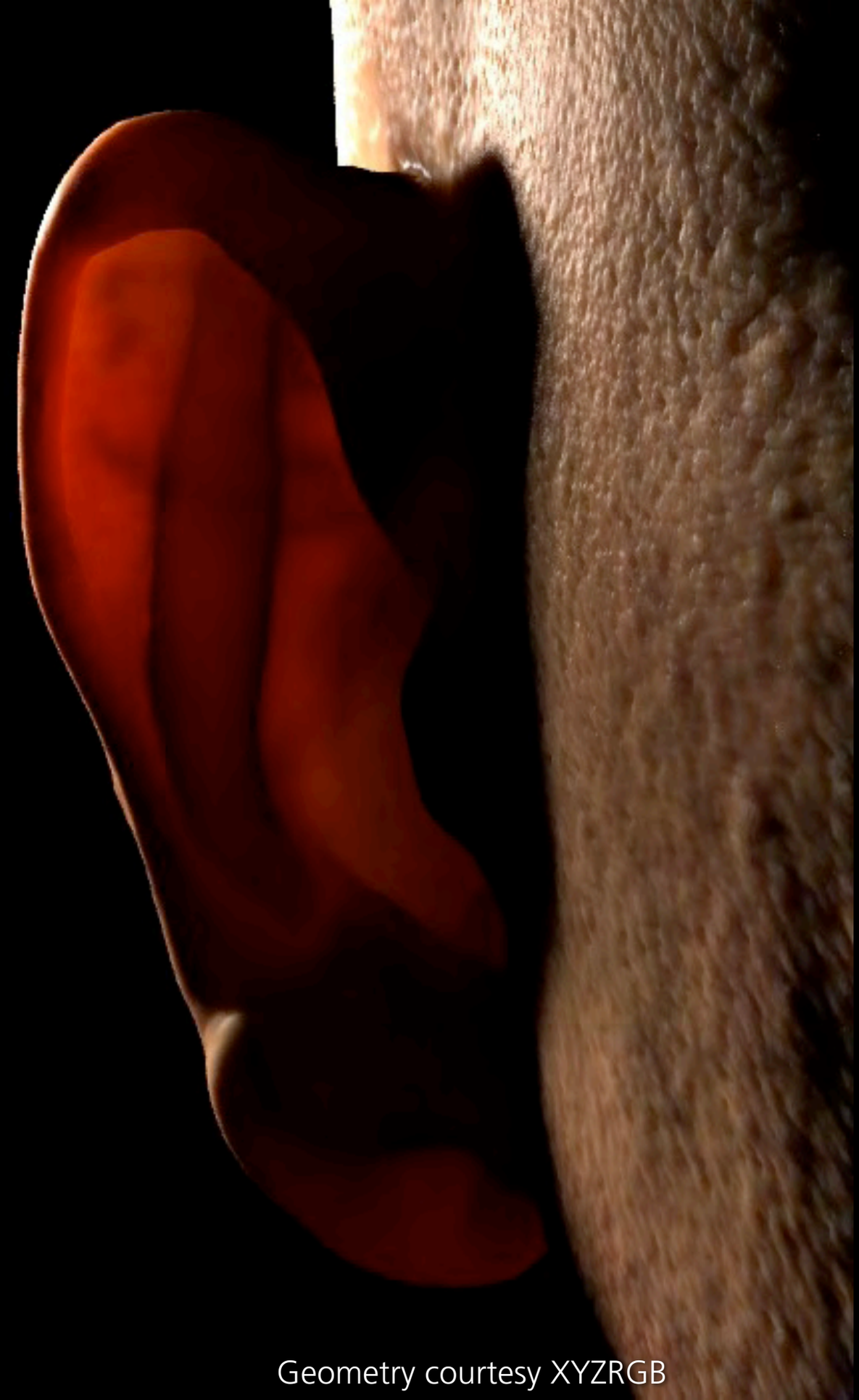

Geometry courtesy XYZRGB

Homogeneous vs. Heterogeneous

Homogeneous vs. Heterogeneous

Heterogeneous

Homogeneous vs. Heterogeneous

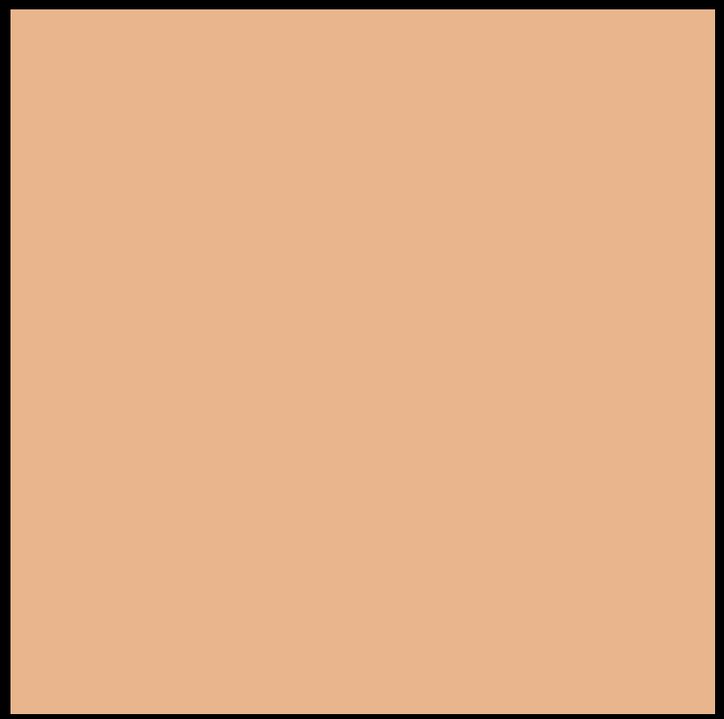

Homogeneous

Heterogeneous

Homogeneous vs. Heterogeneous

Albedo-mapped

Heterogeneous

Homogeneous vs. Heterogeneous

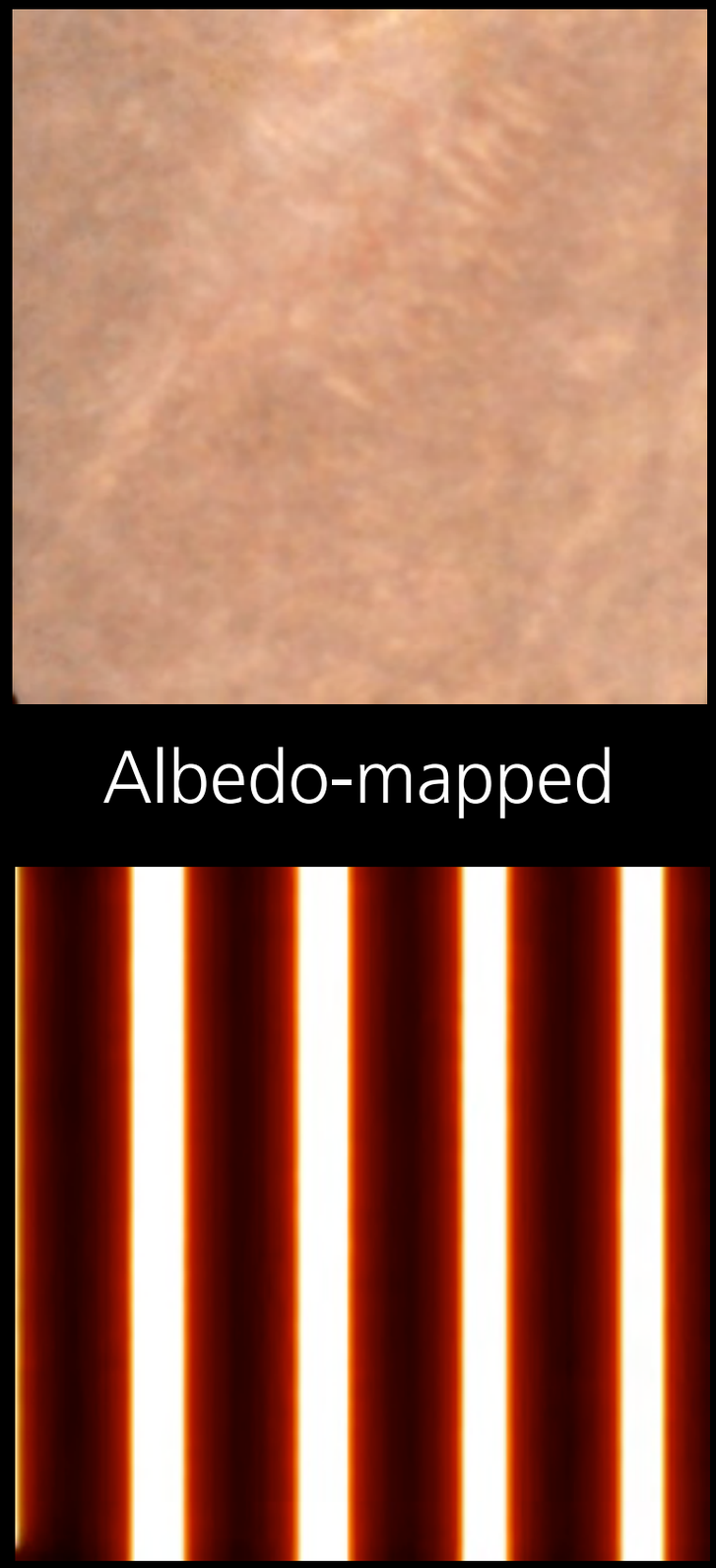

Albedo-mapped

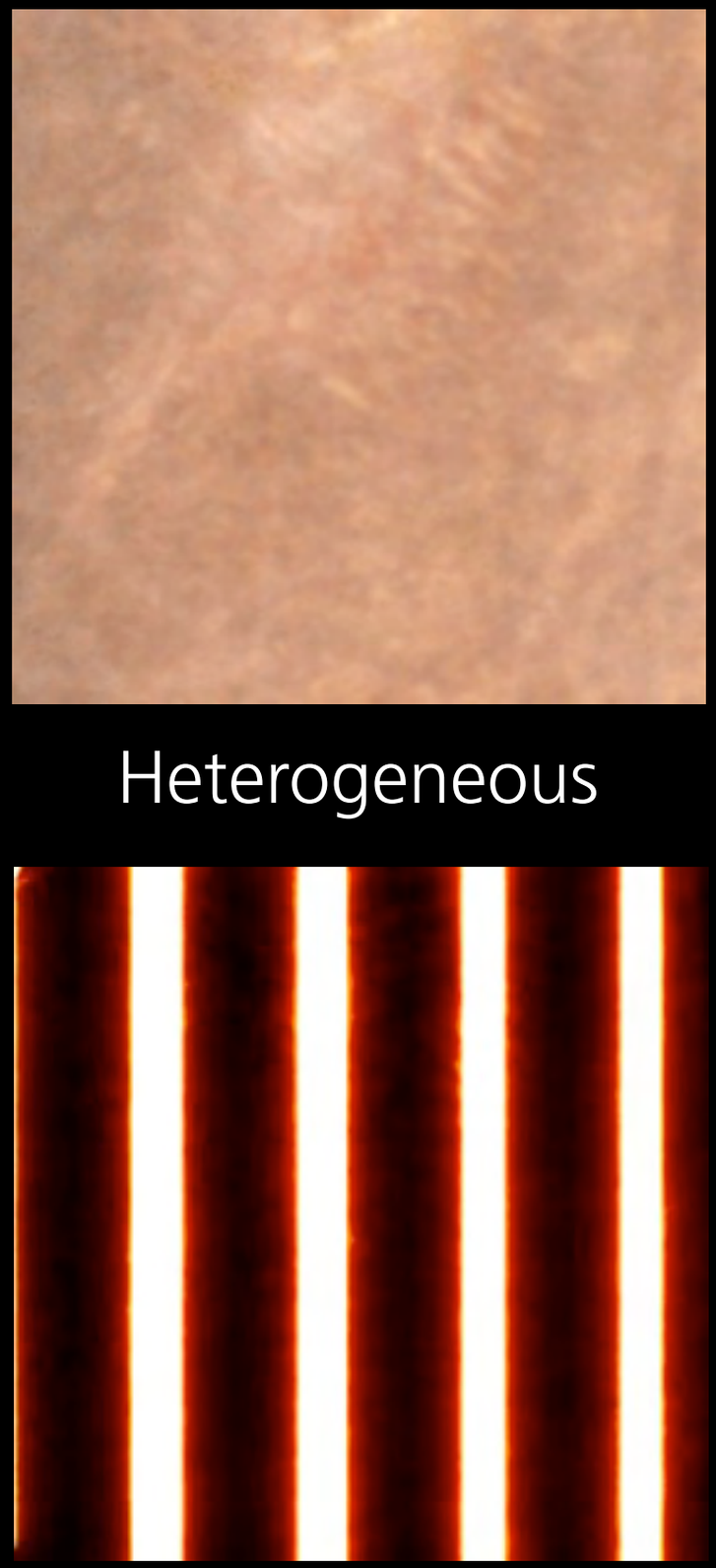

Heterogeneous

Homogeneous vs. Heterogeneous

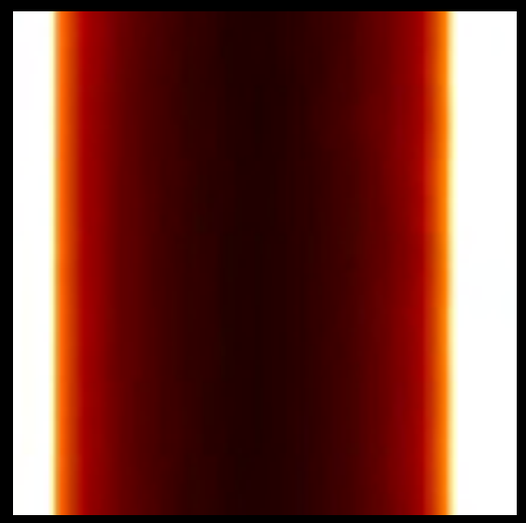

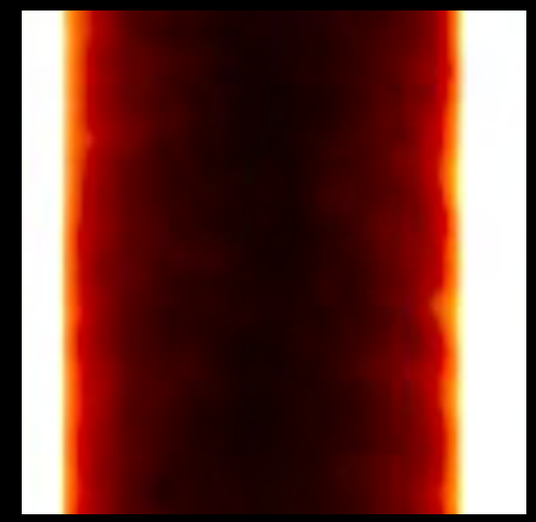

Albedo-mapped

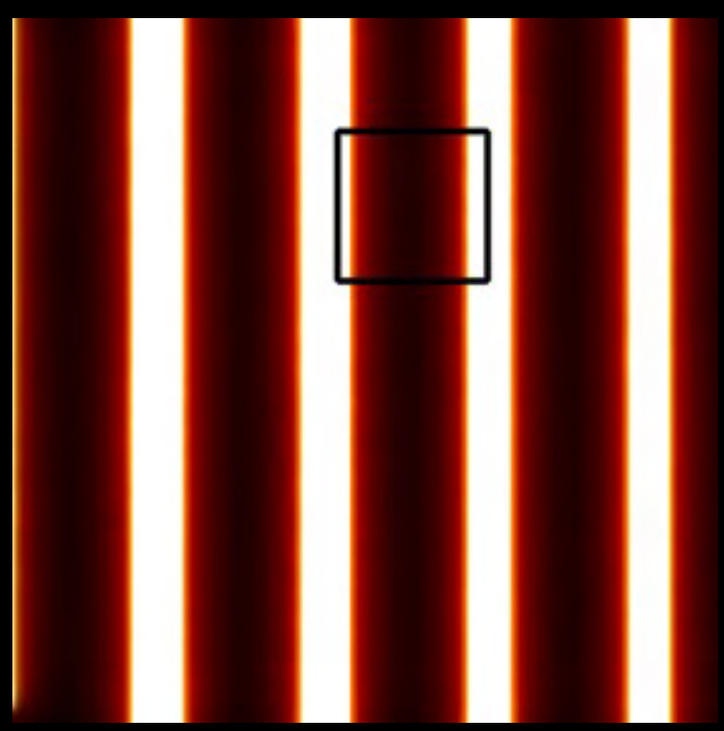

Heterogeneous

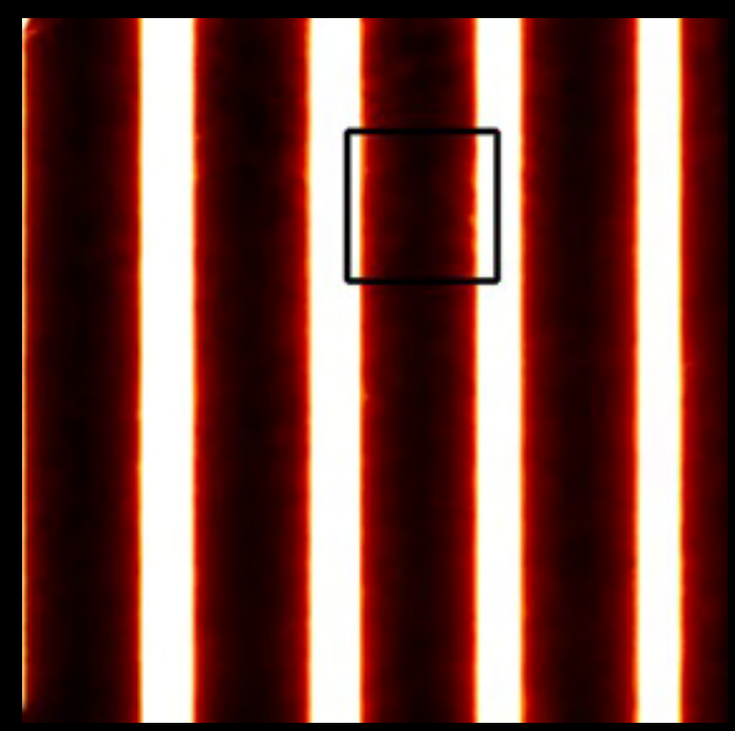

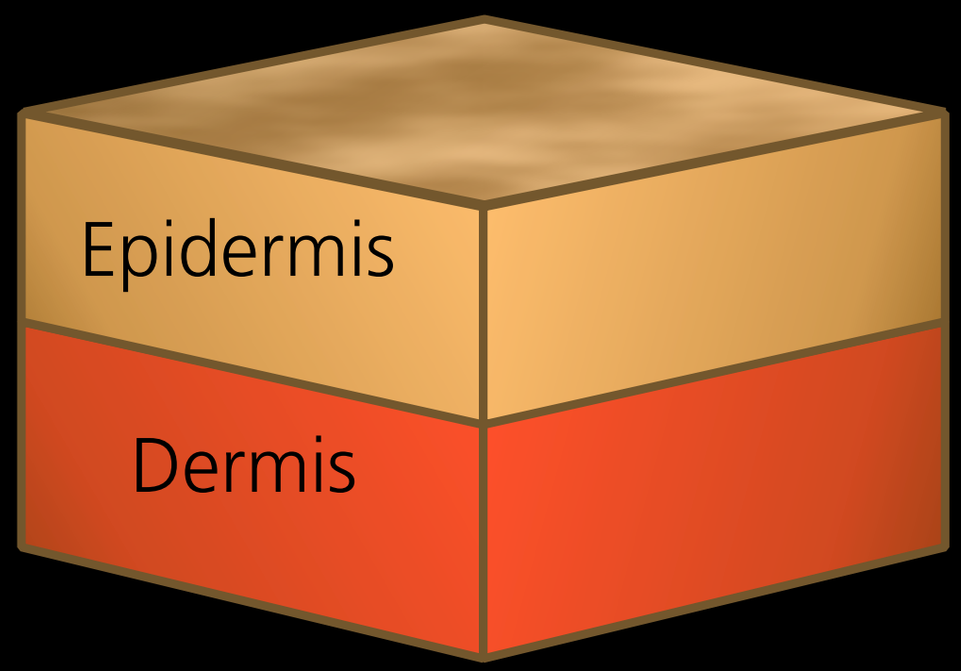

Skin specific properties

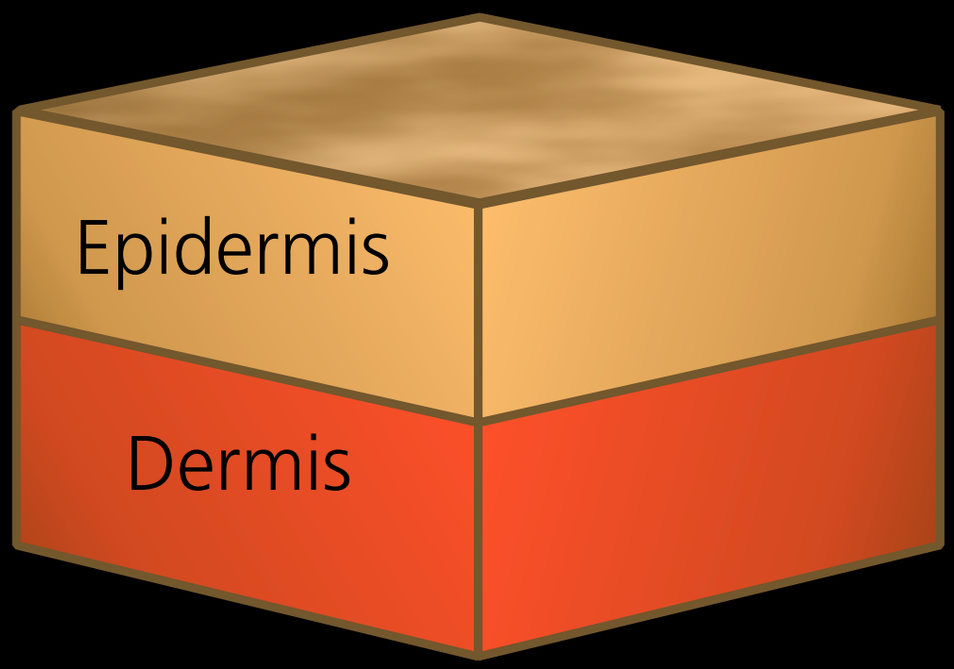

Real skin measurements

Reflectance measurements

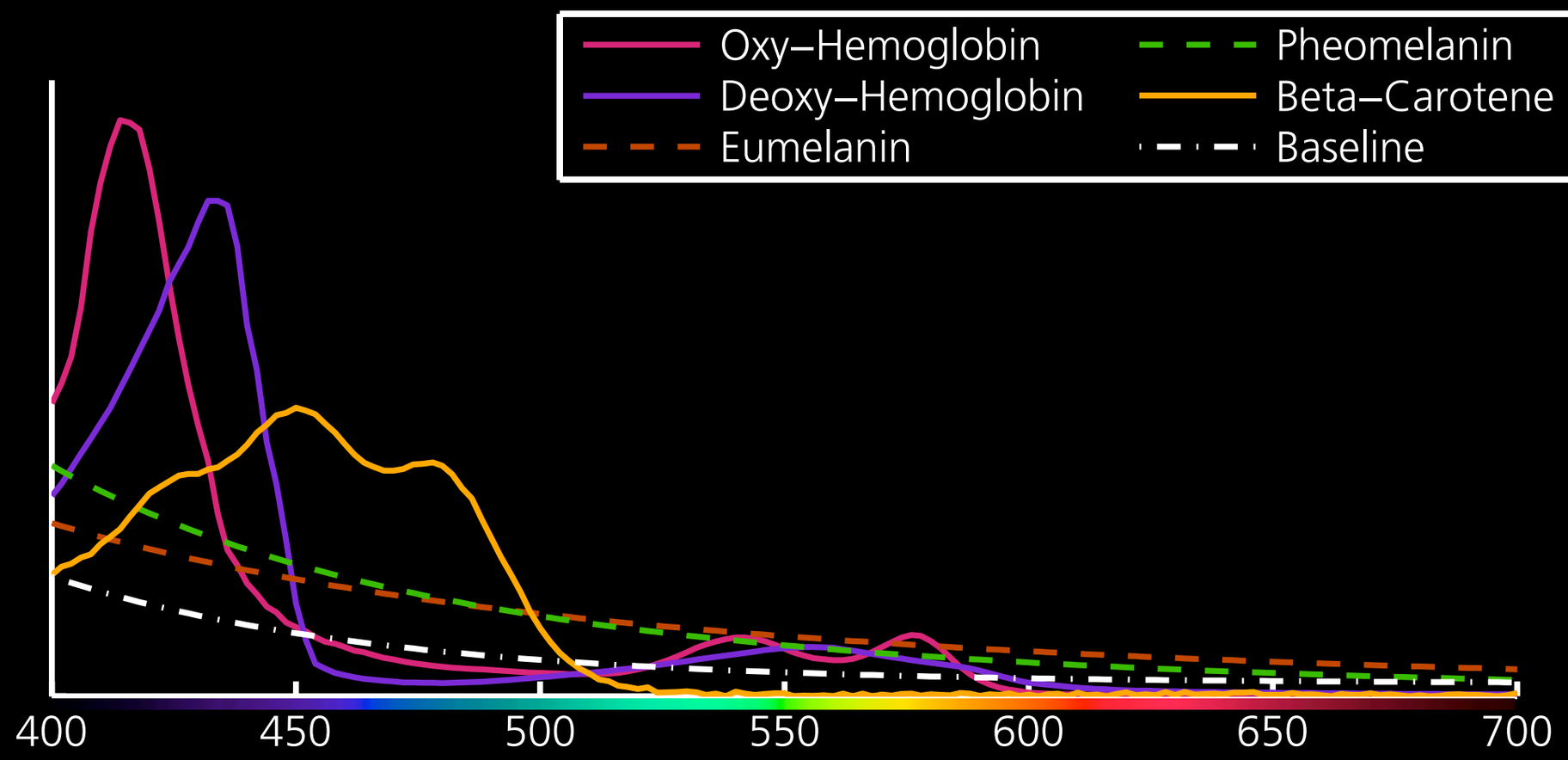

Reflectance measurements

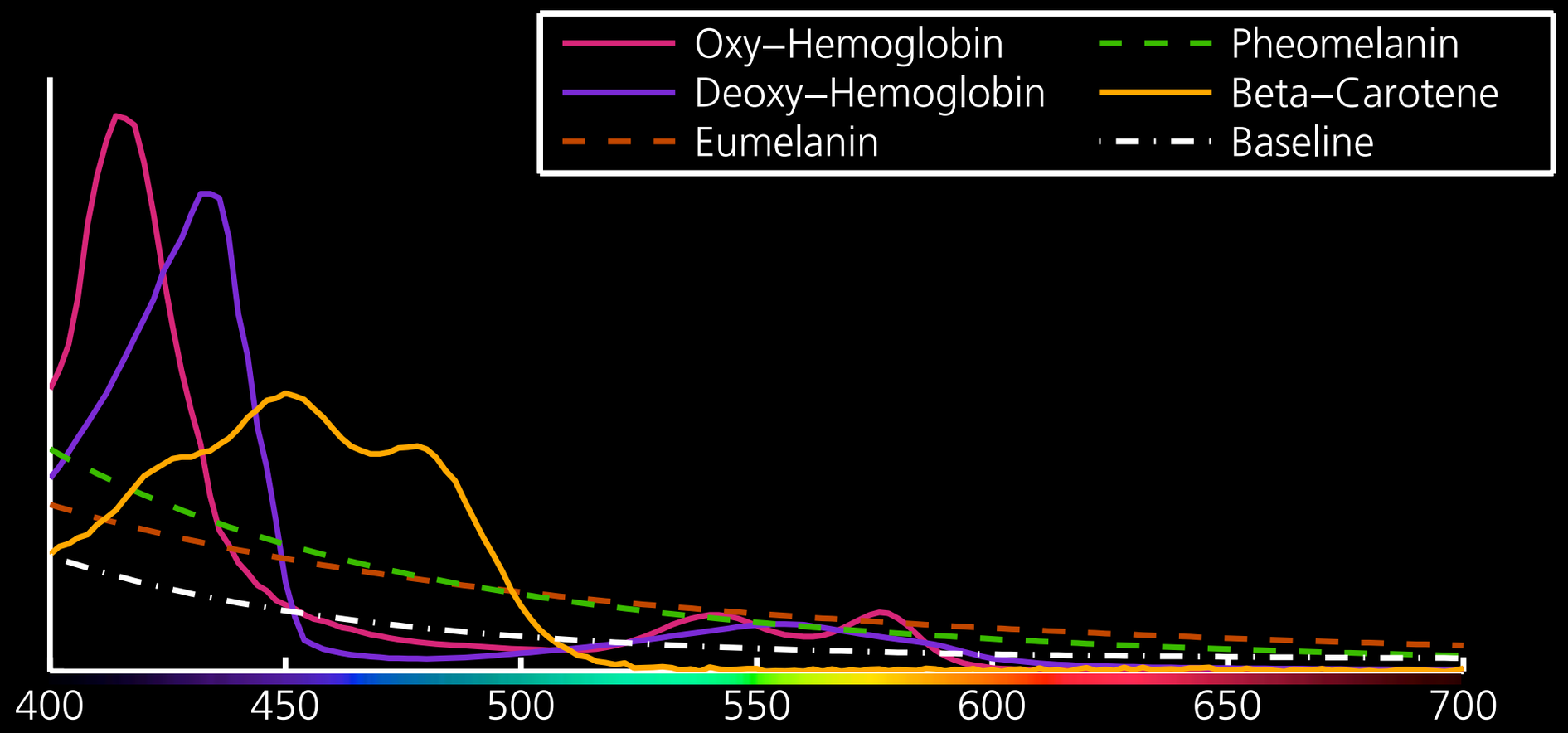

- Multi-spectral measurements

Reflectance measurements

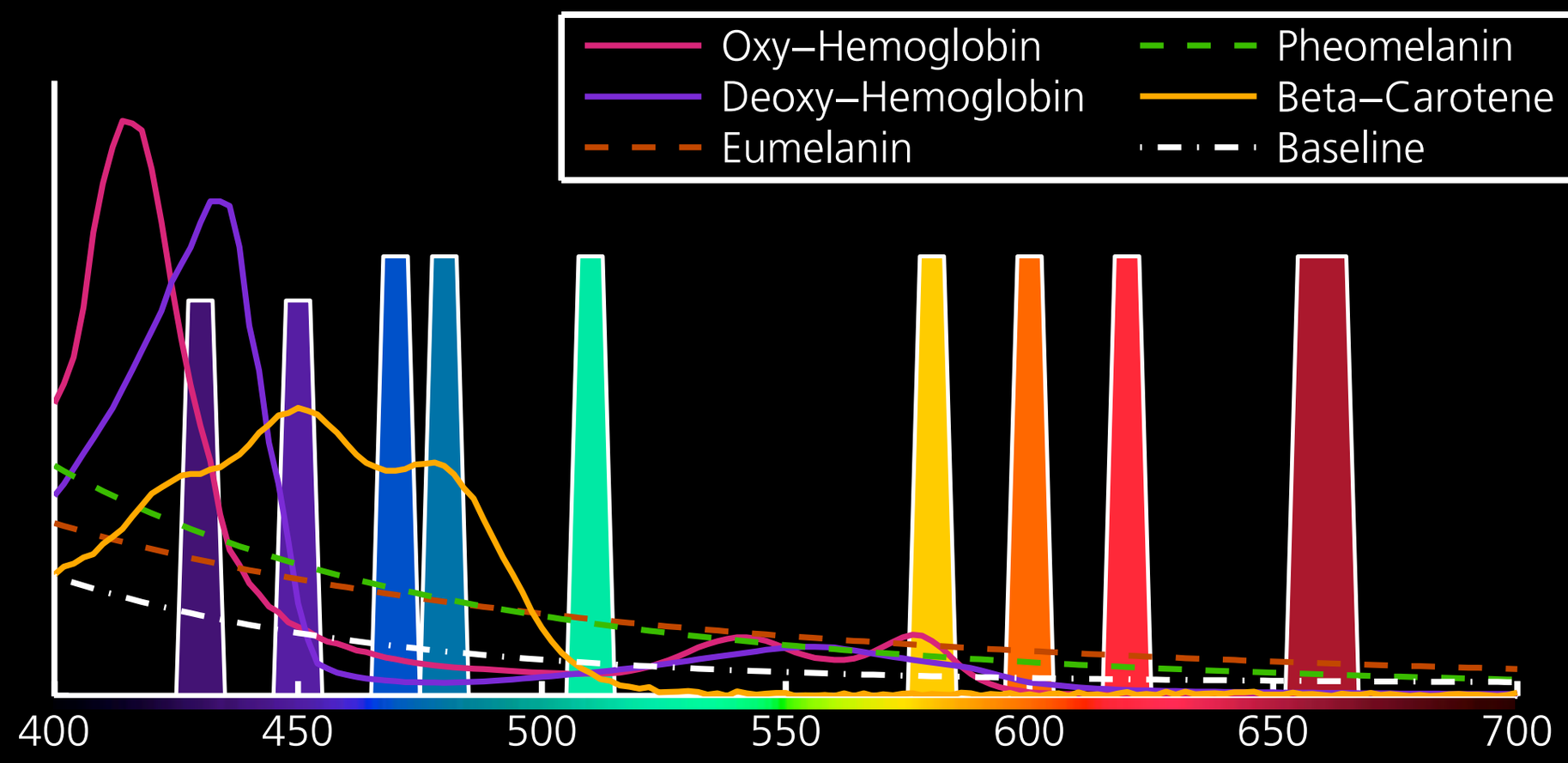

- Multi-spectral measurements
  - Nine spectral bands

Measurement setup

- Orthogonal illumination
  - Xenon flash
  - 9 band-pass filters
- Angled observation
  - Avoids back-scattering
- Cross-polarization
- Full radiometric calibration
  - Gray card captures flash variation

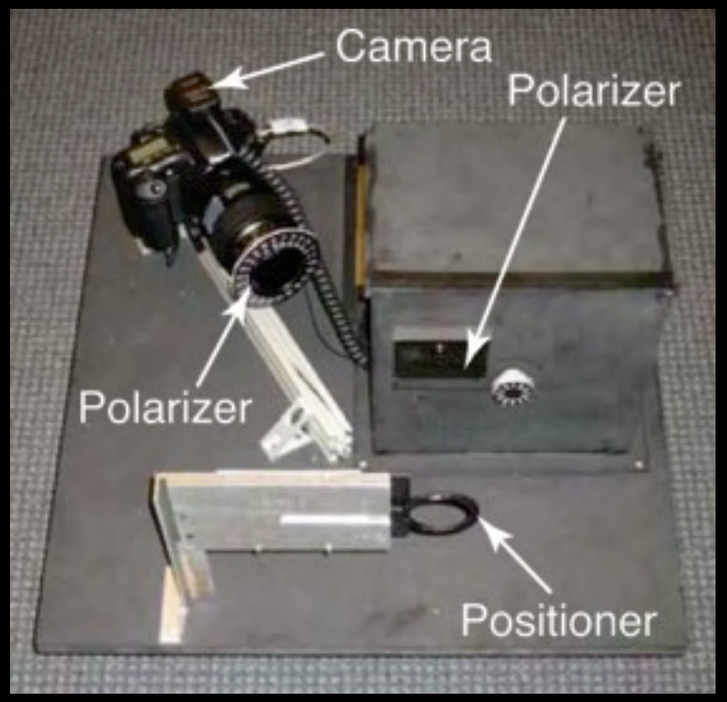

Measurement setup

- Orthogonal illumination
  - Xenon flash
  - 9 band-pass filters
- Angled observation
  - Avoids back-scattering
- Cross-polarization
- Full radiometric calibration
  - Gray card captures flash variation

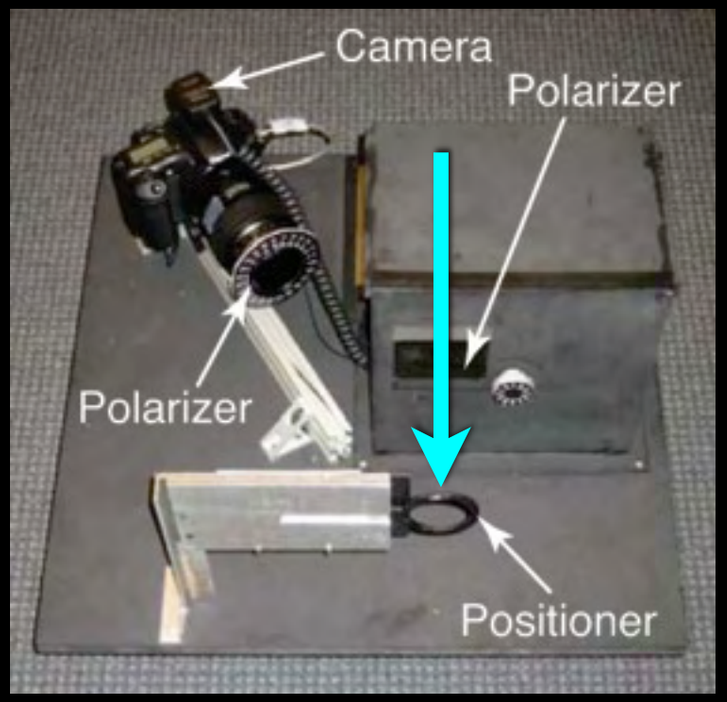

Measurement setup

- Orthogonal illumination
  - Xenon flash
  - 9 band-pass filters
- Angled observation
  - Avoids back-scattering

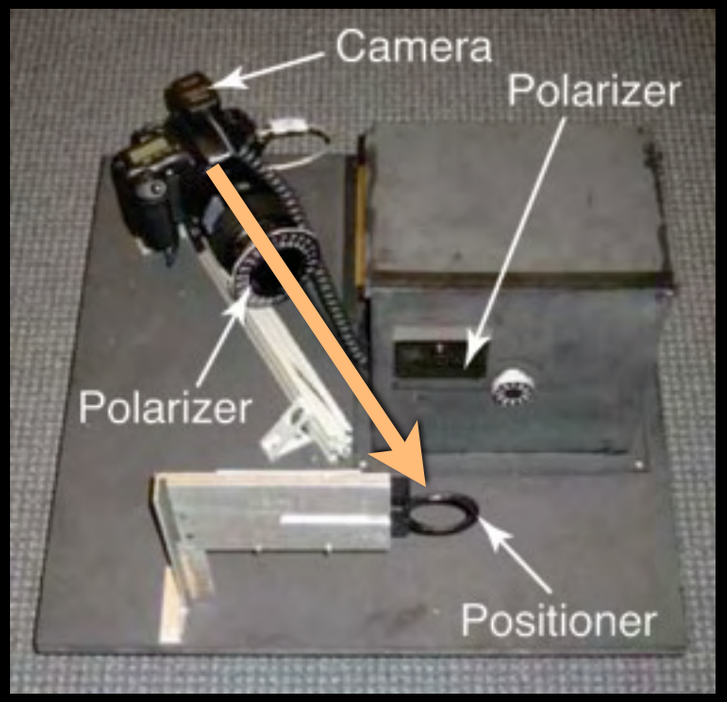

Measurement setup

- Orthogonal illumination
  - Xenon flash
  - 9 band-pass filters
- Angled observation
  - Avoids back-scattering
- Cross-polarization

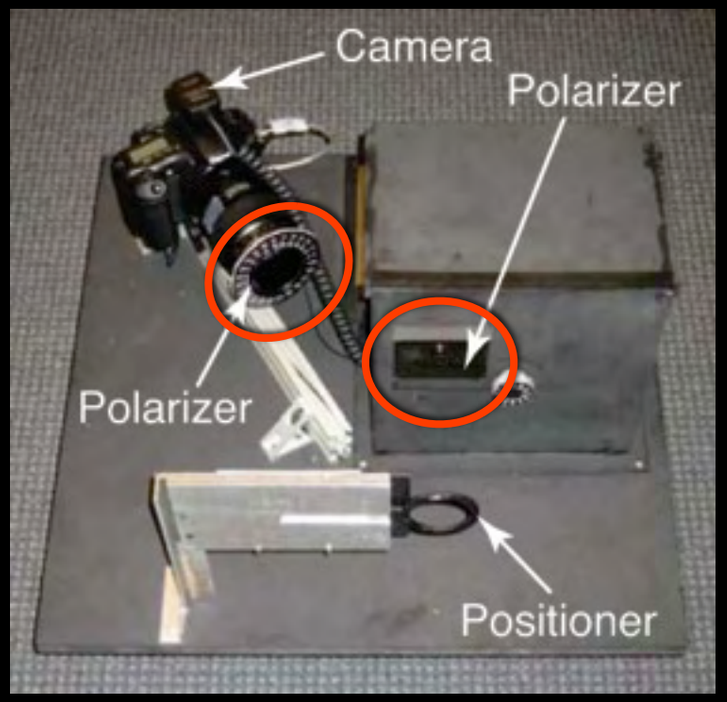

Measurement setup

- Orthogonal illumination
  - Xenon flash
  - 9 band-pass filters
- Angled observation
  - Avoids back-scattering
- Cross-polarization
- Full radiometric calibration
  - Gray card captures flash variation

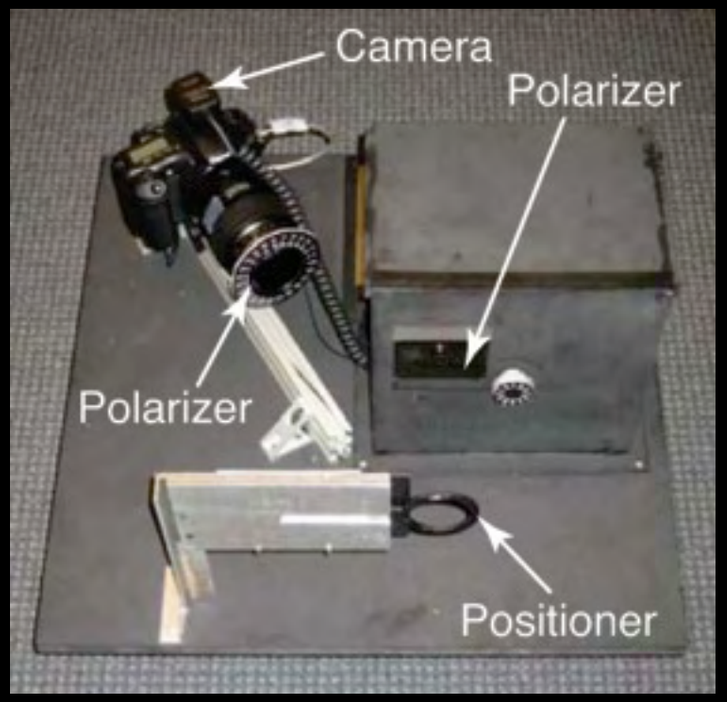

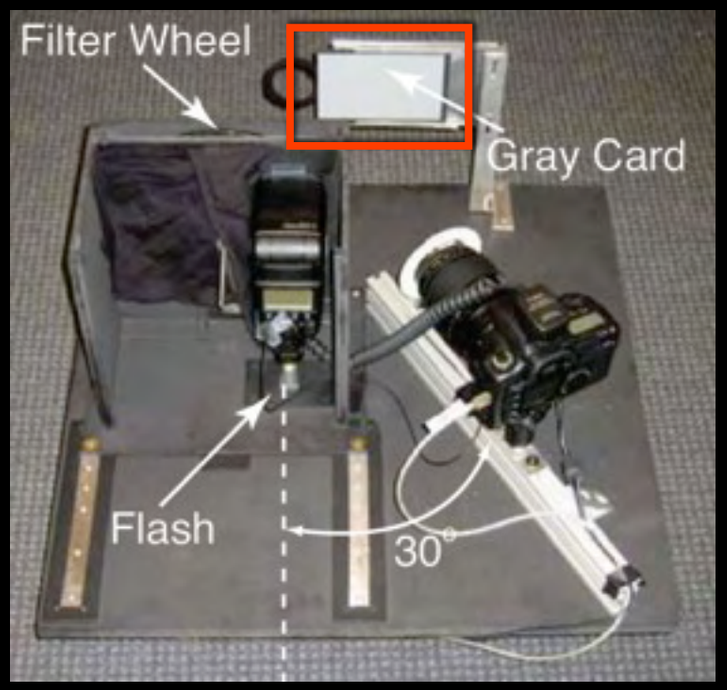

Skin preperation

Inverse rendering

Photograph

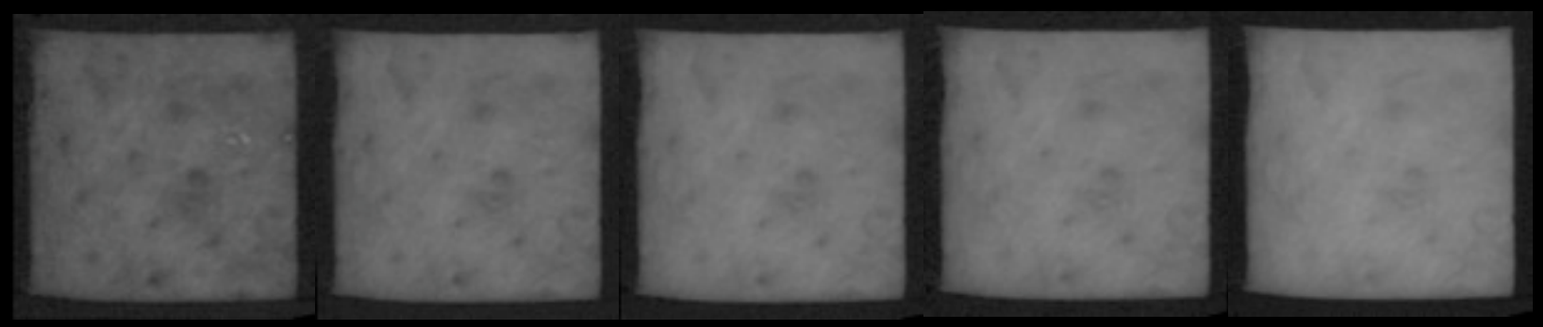

430 nm 450 nm 470 nm 480 nm 510 nm

Photograph

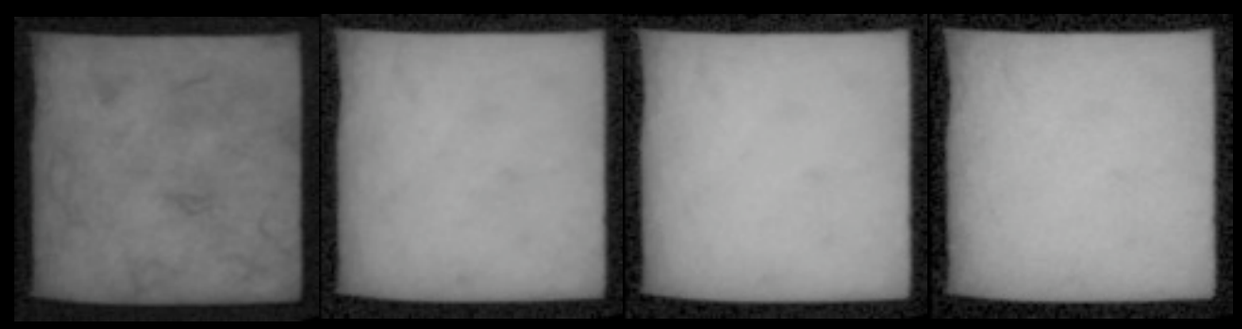

580 nm 600 nm 620 nm 660 nm

Inverse rendering

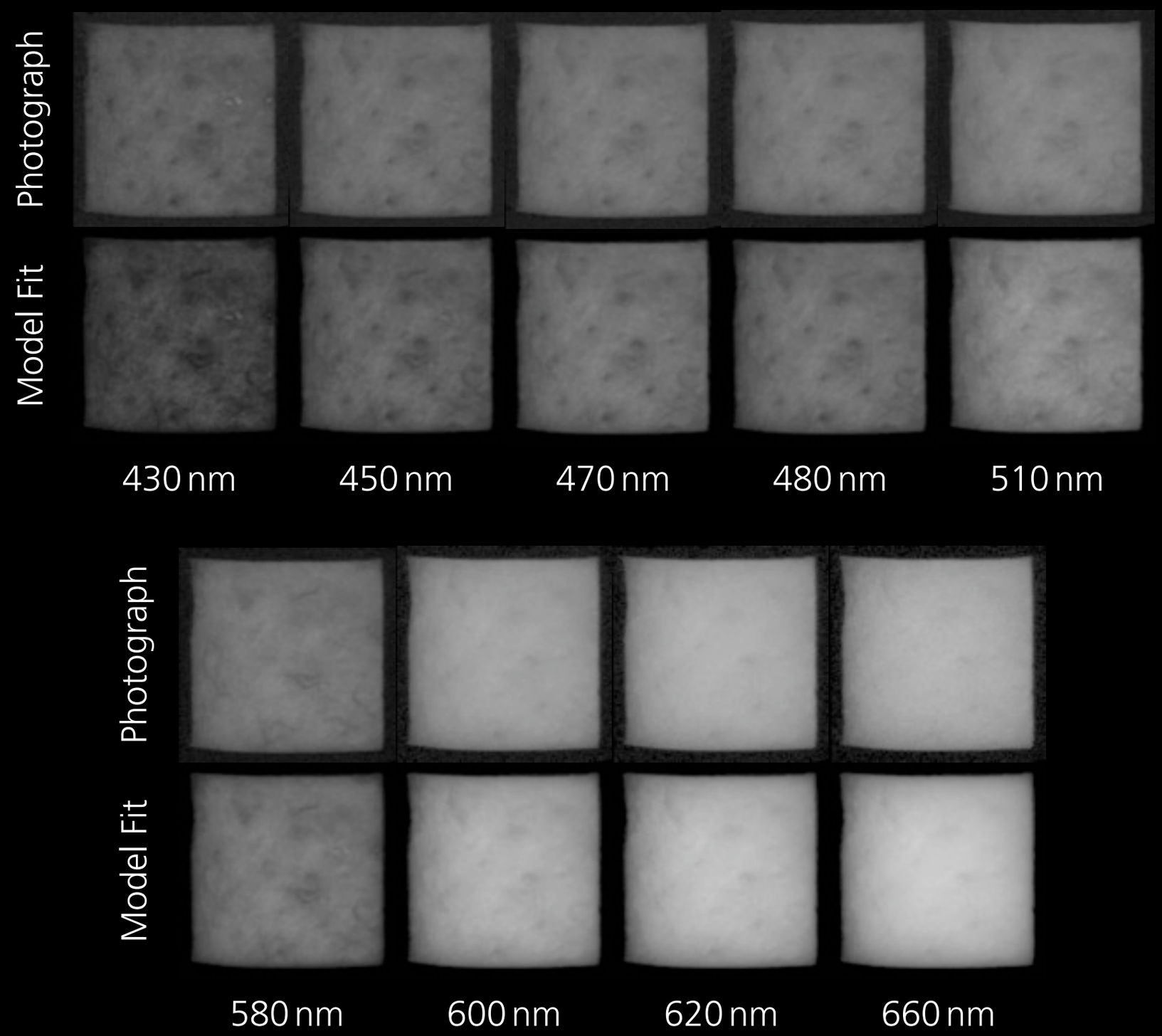

Inverse rendering

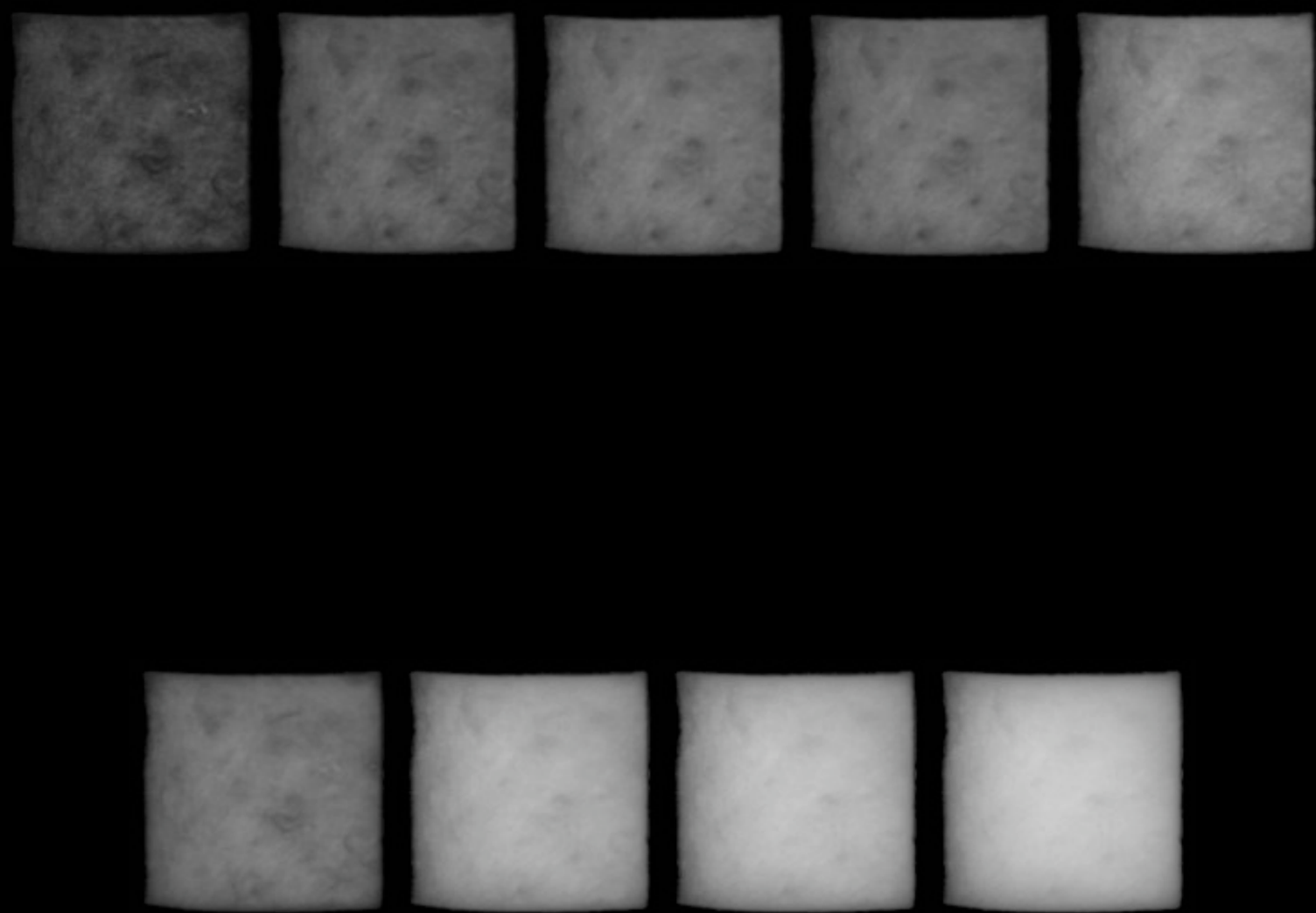

Inverse rendering

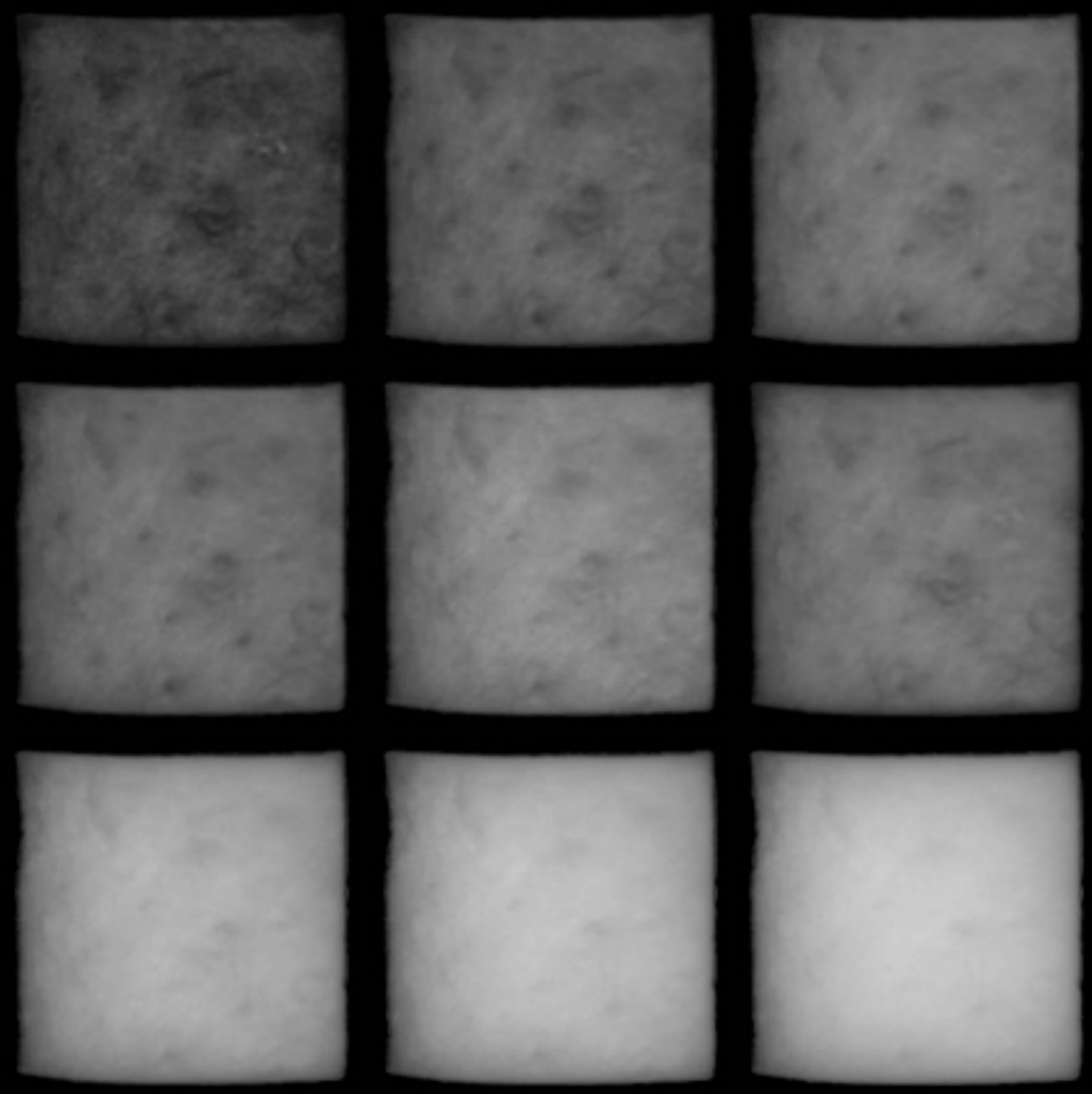

Inverse rendering

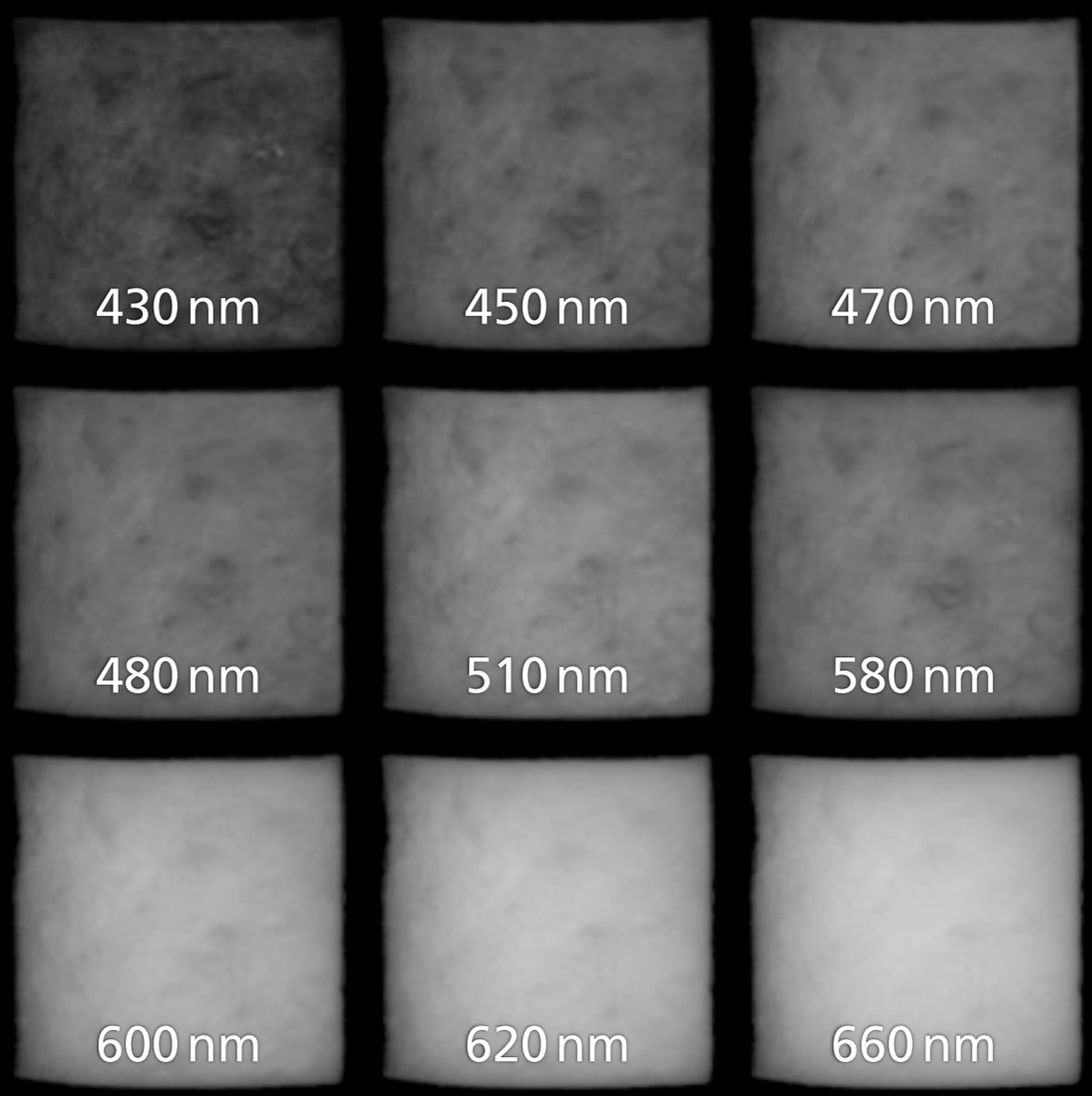

Multi-band Rendering

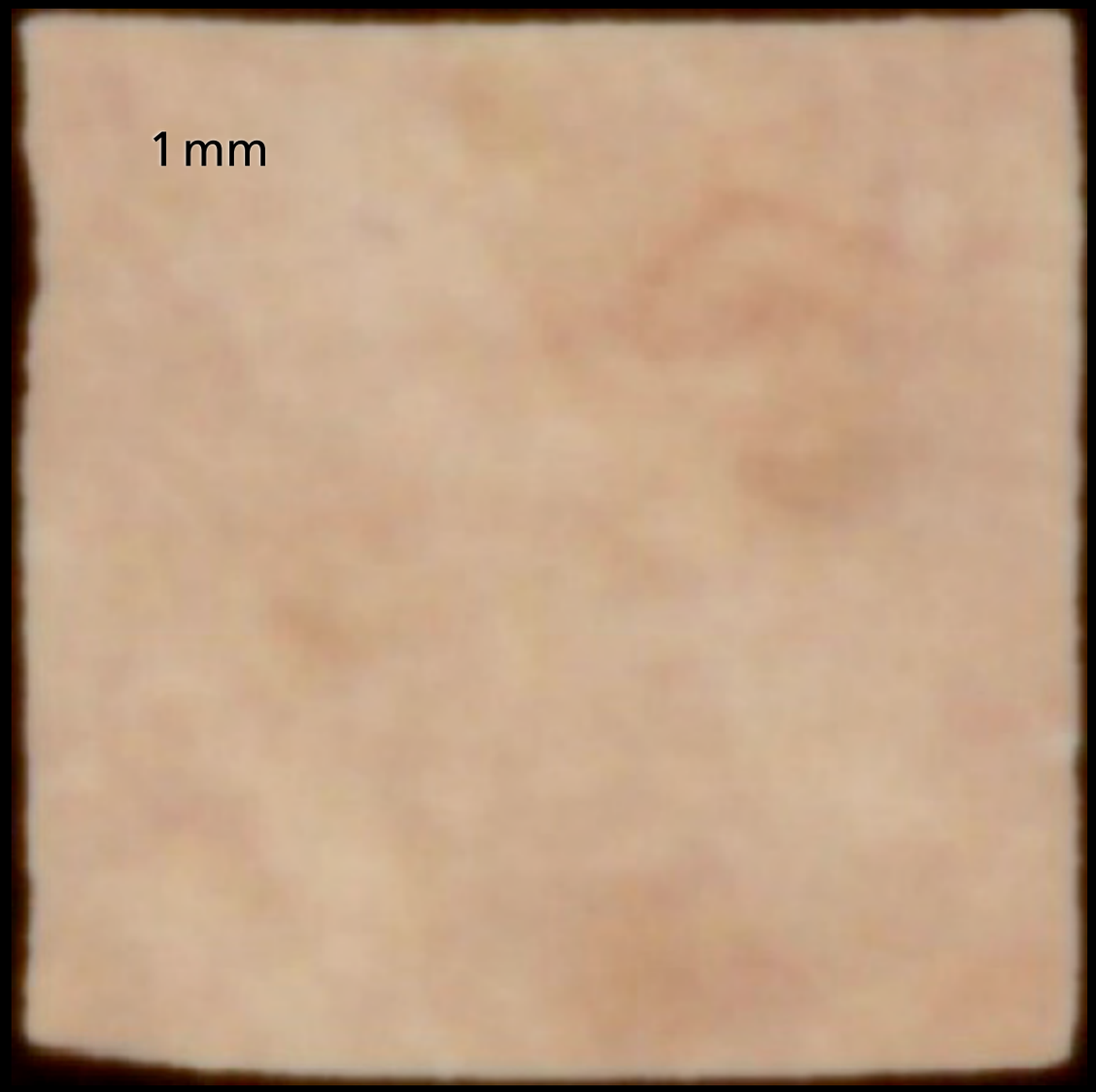

RGB Rendition

Skin measurements

- Measurements of
  - Skin types I..V

Skin measurements

- Measurements of
  - Skin types I..V

Type	*Properties*
I	white – subject to sunburn
II	tan – capable of tanning
III	dark – capable of tanning
IV	dark
V	very dark
VI	very dark

Fitzpatrick skin types

Skin measurements

Skin measurements

- Measurements of

Skin measurements

- Measurements of
  - Skin types I..V

Skin measurements

- Measurements of
  - Skin types I..V
  - Different skin regions

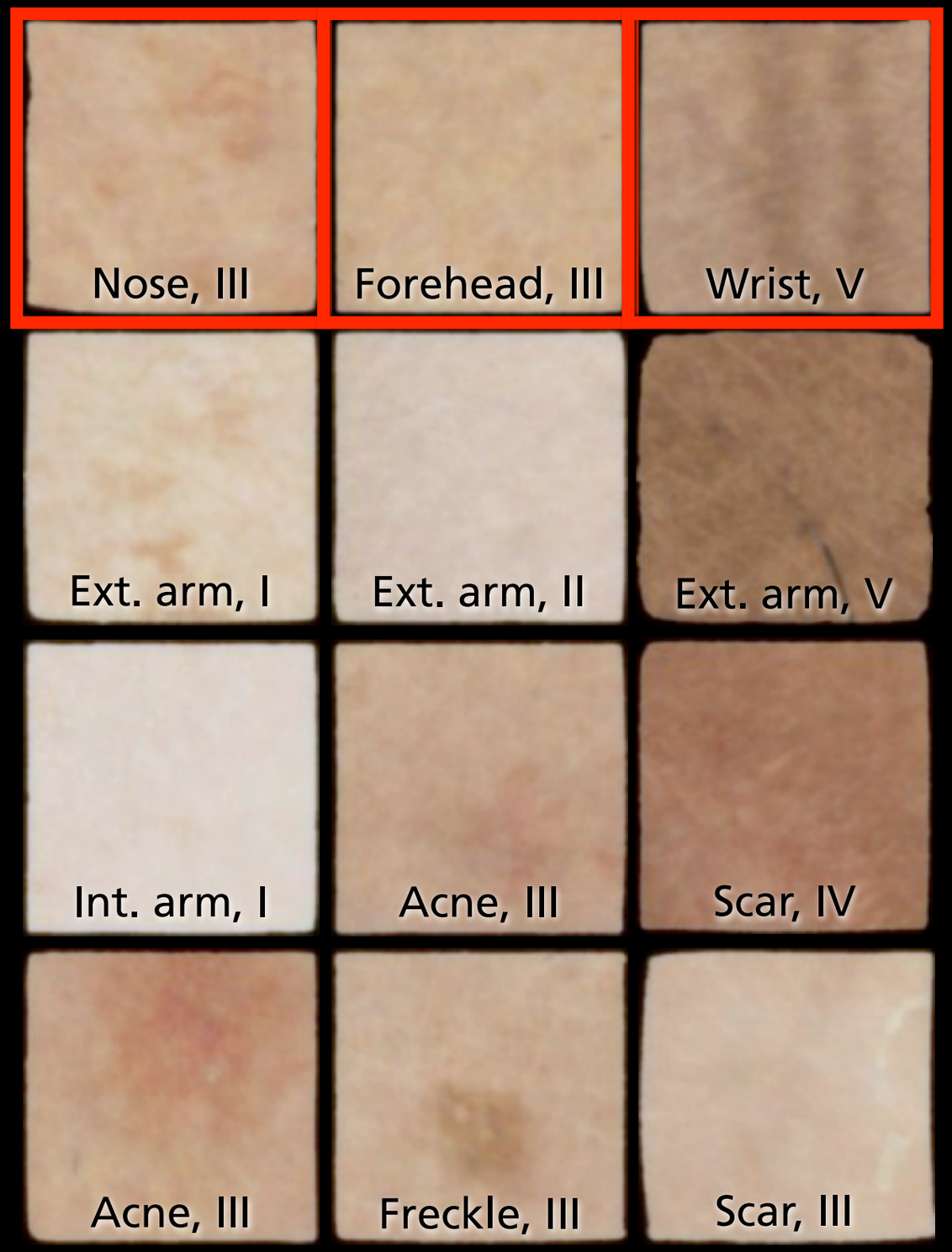

Skin measurements

- Measurements of
  - Skin types I..V
  - Different skin regions

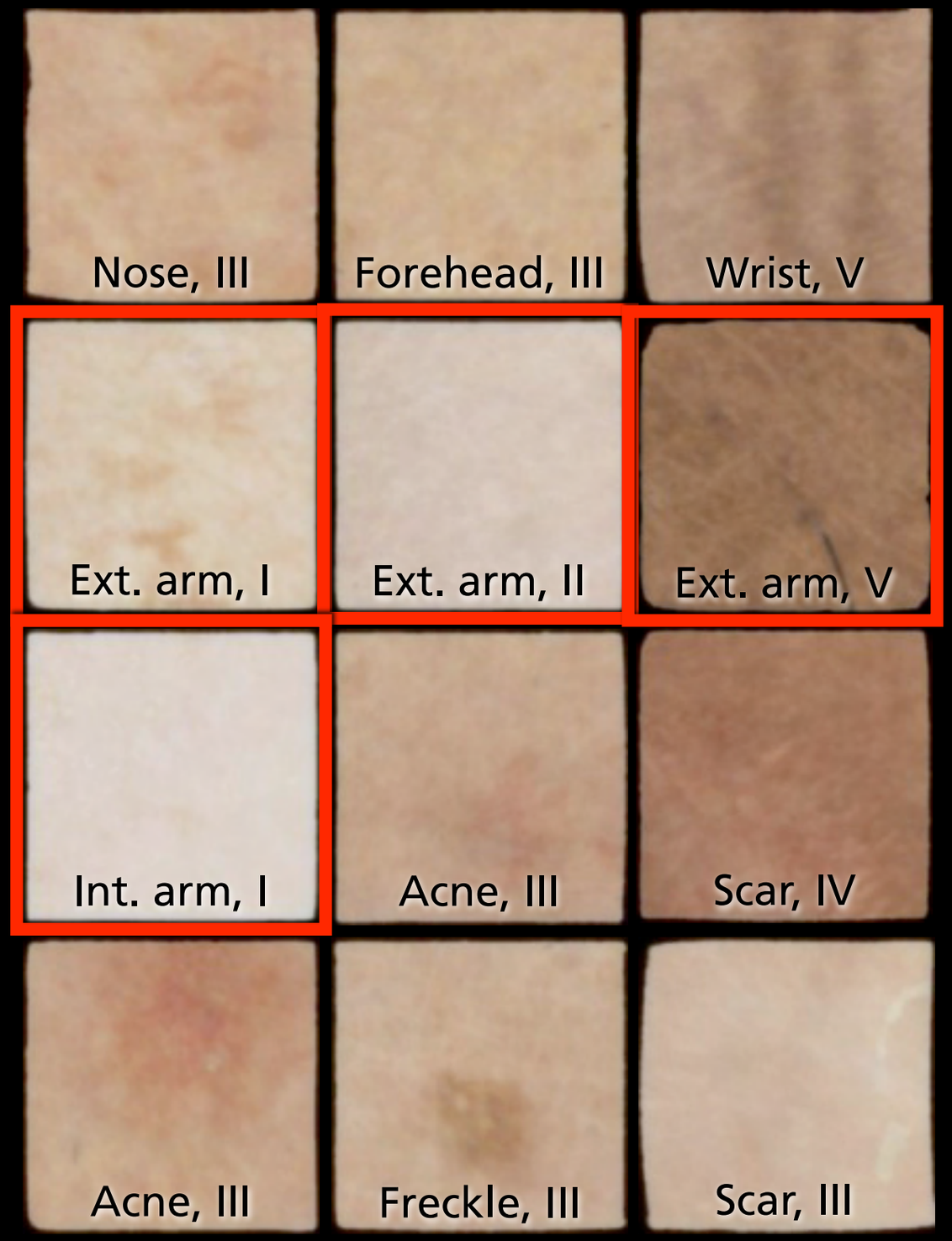

Skin measurements

- Measurements of
  - Skin types I..V
  - Different skin regions
  - Skin conditions

Skin measurements

- Measurements of
  - Skin types I..V
  - Different skin regions
  - Skin conditions

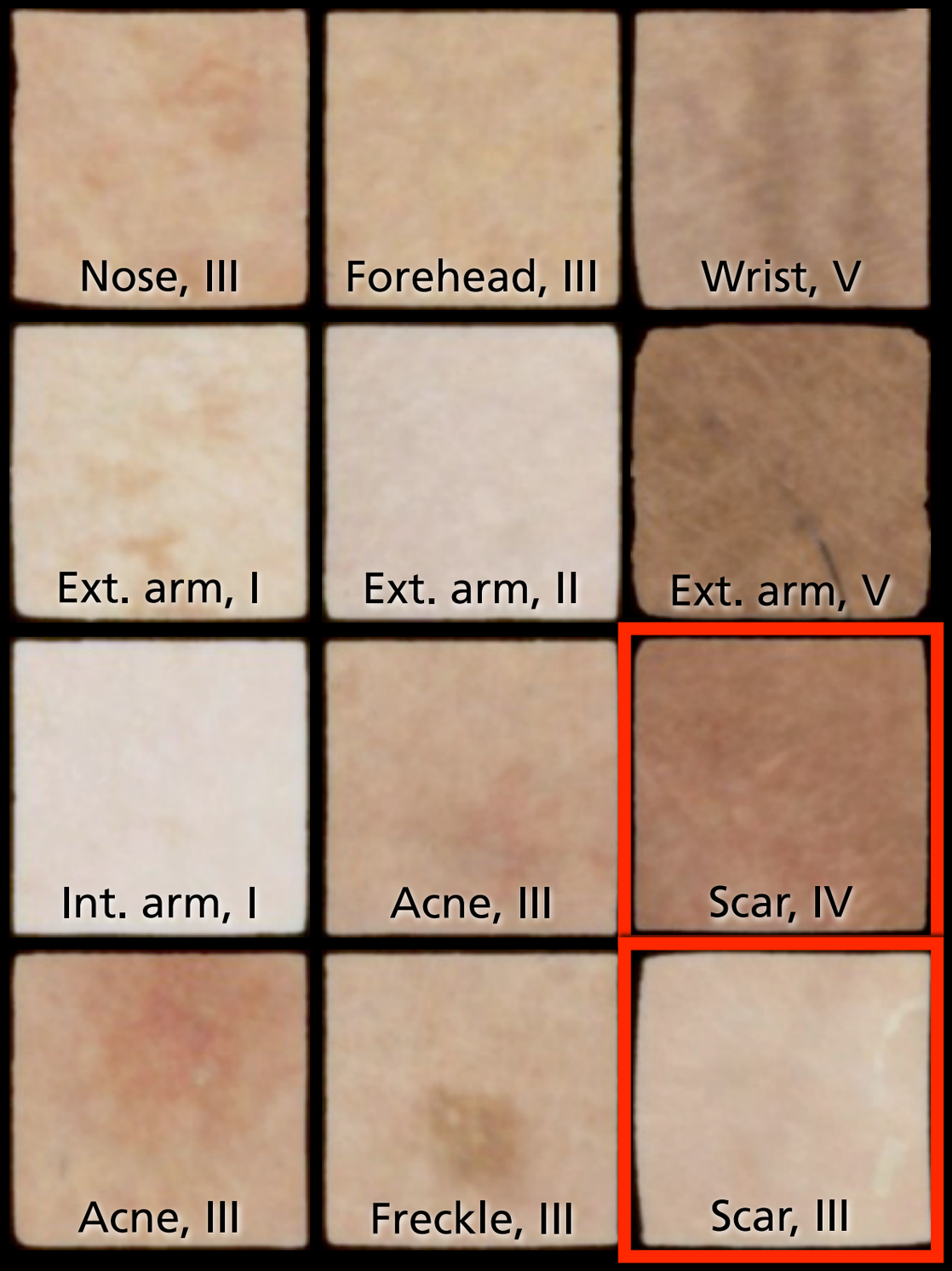

Skin measurements

- Measurements of
  - Skin types I..V
  - Different skin regions
  - Skin conditions

Chromophore distributions

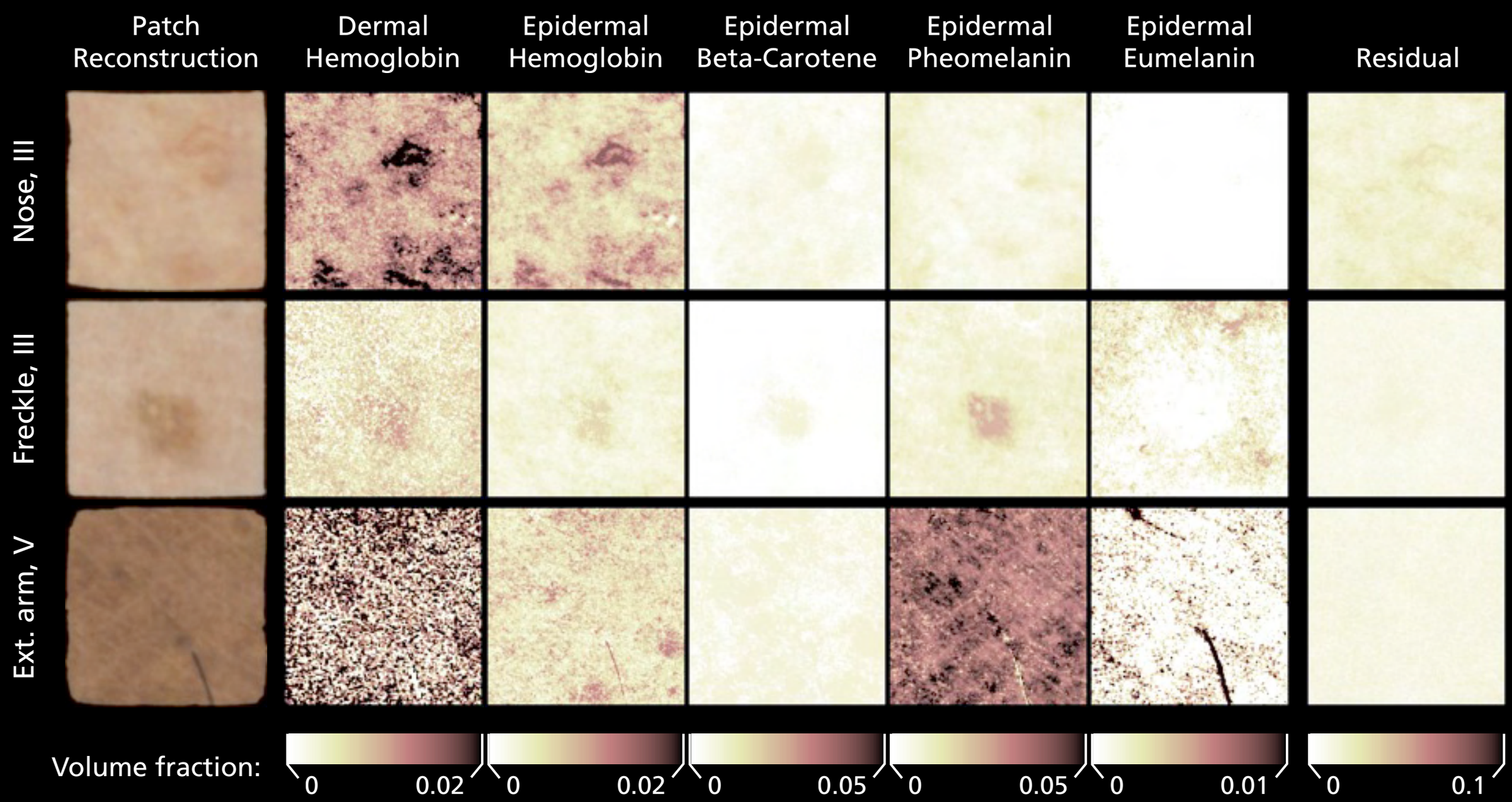

Chromophore distributions

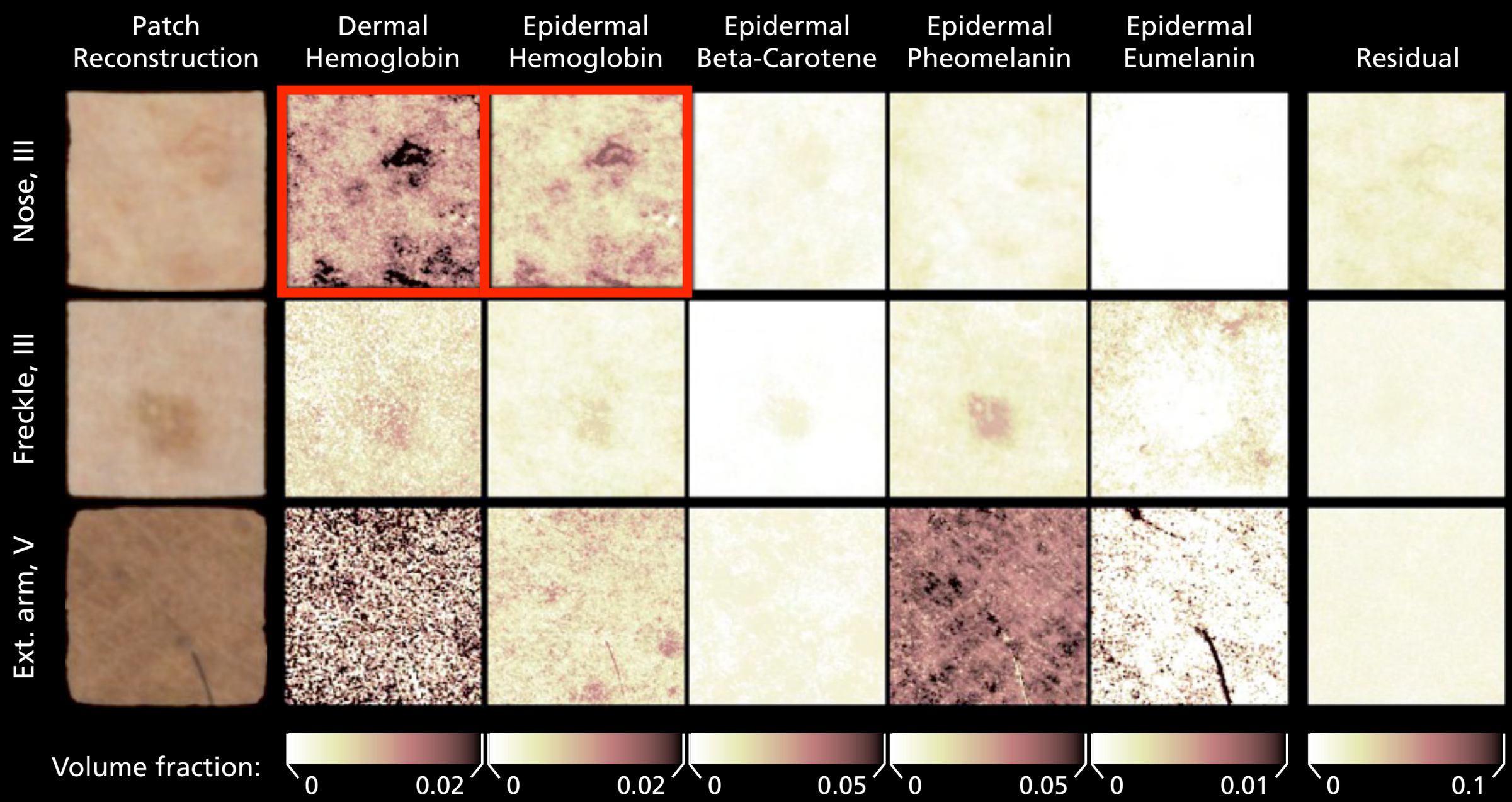

Chromophore distributions

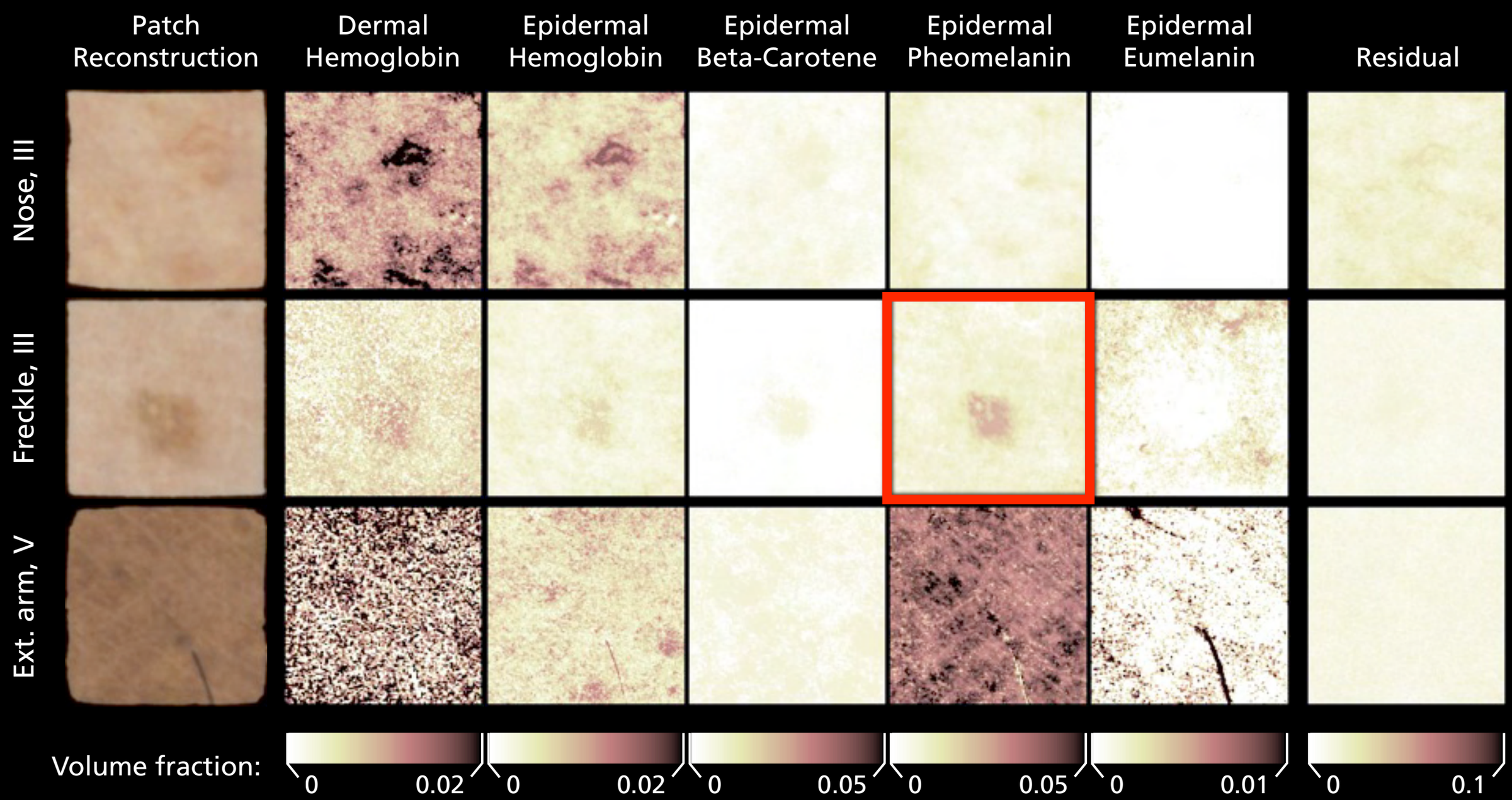

Chromophore distributions

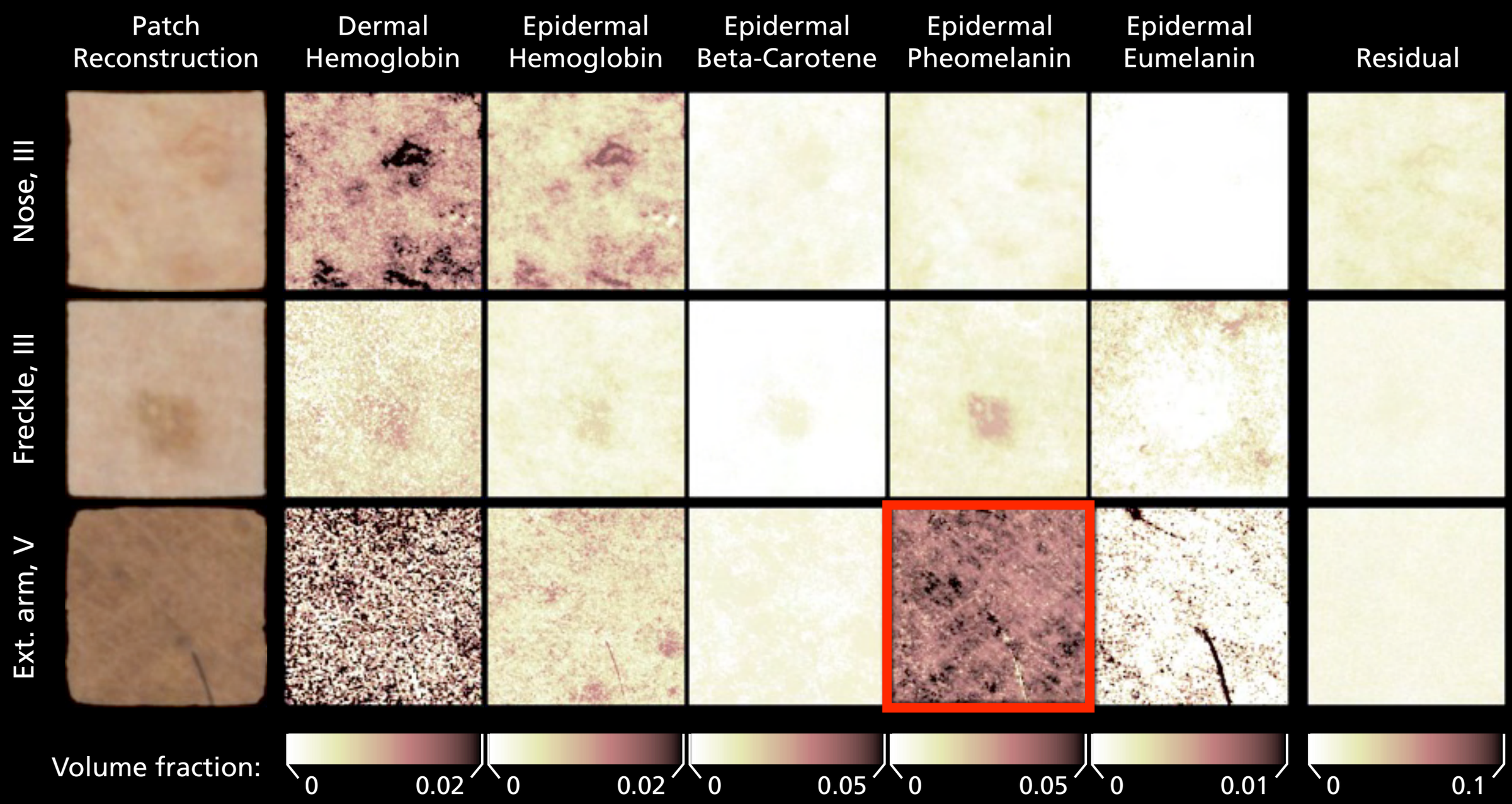

Chromophore distributions

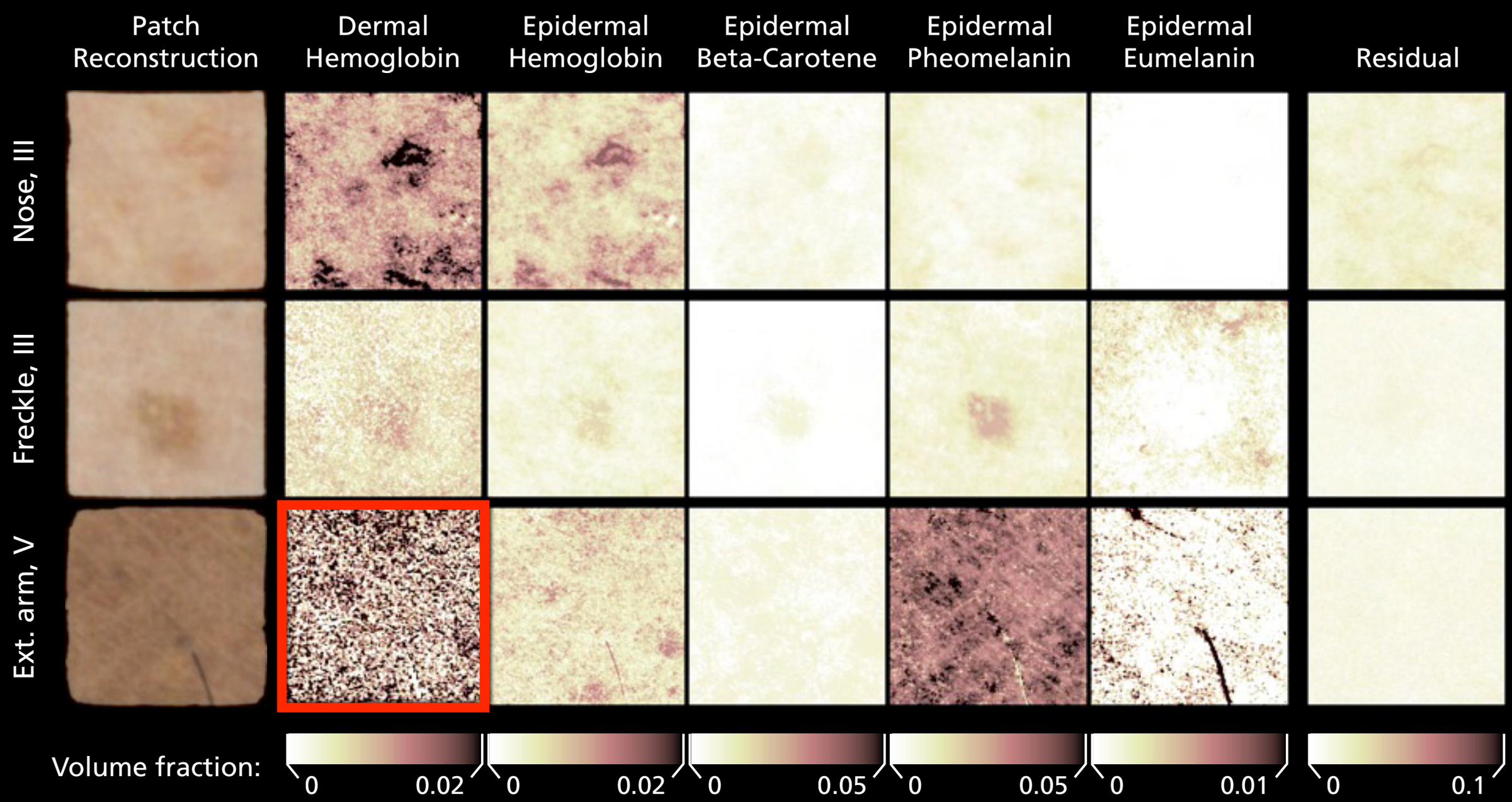

Chromophore emphasis

Scar

Chromophore emphasis

Scar

2× Hem

3× Hem

4× Hem

Chromophore emphasis

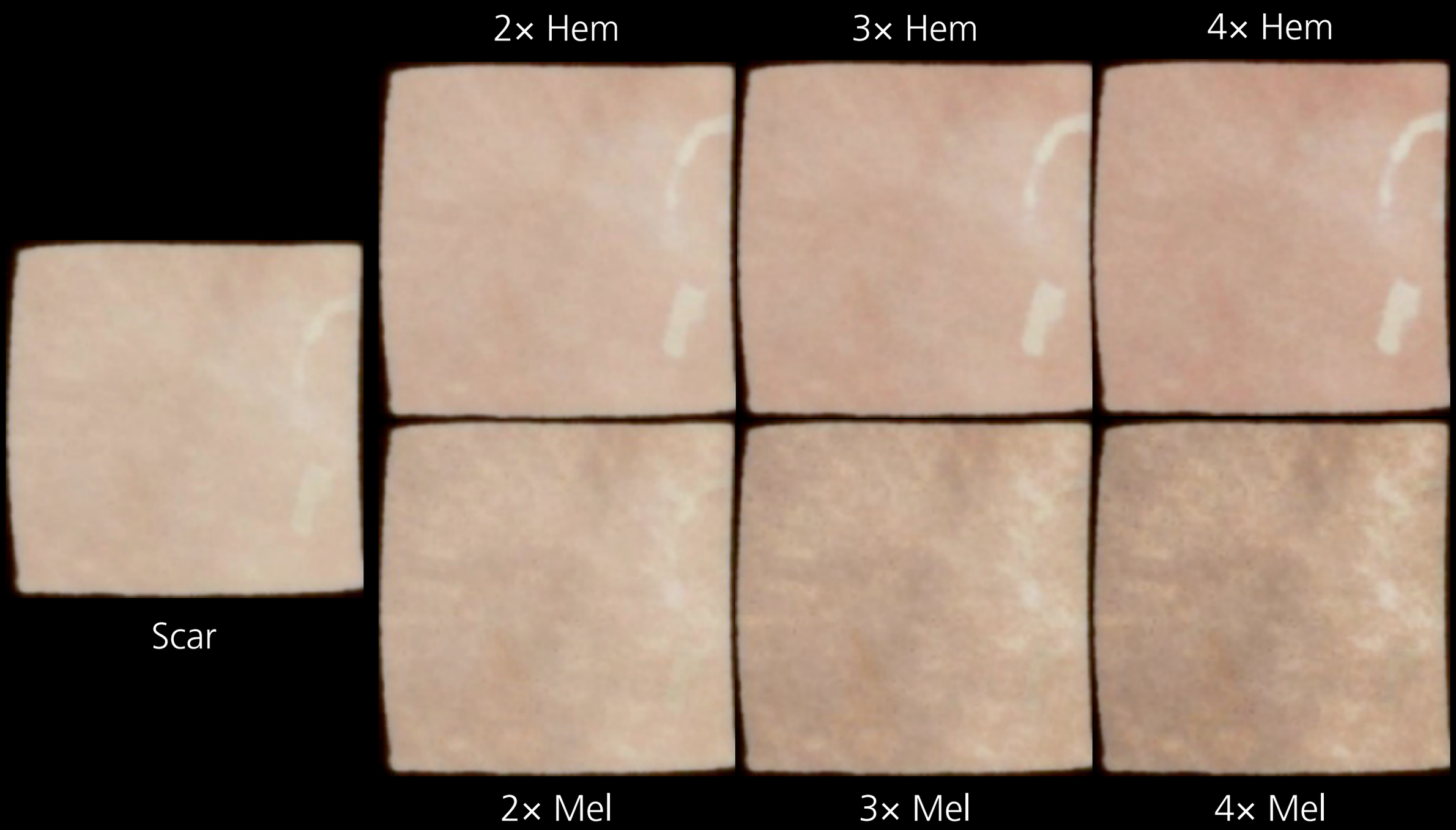

Chromophore transfer

Chromophore transfer

Chromophore transfer

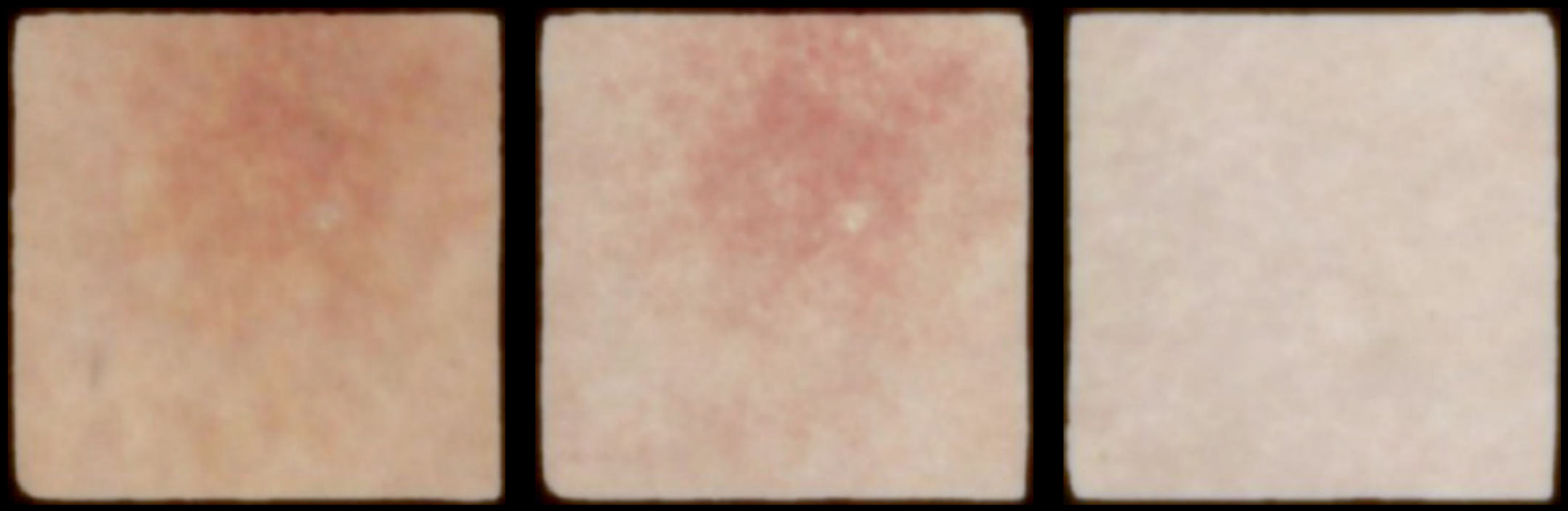

Tattoo

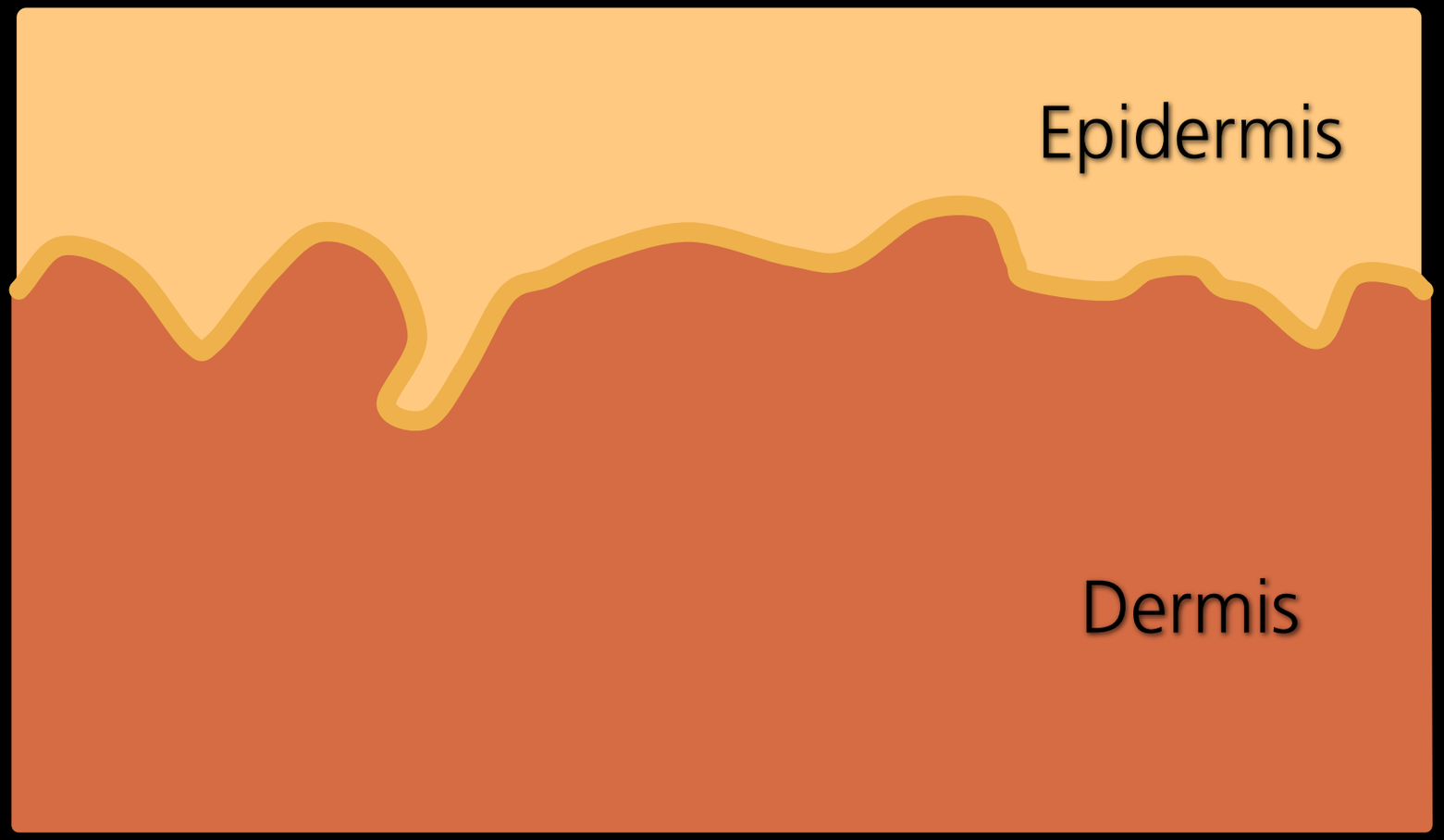

Tattoo

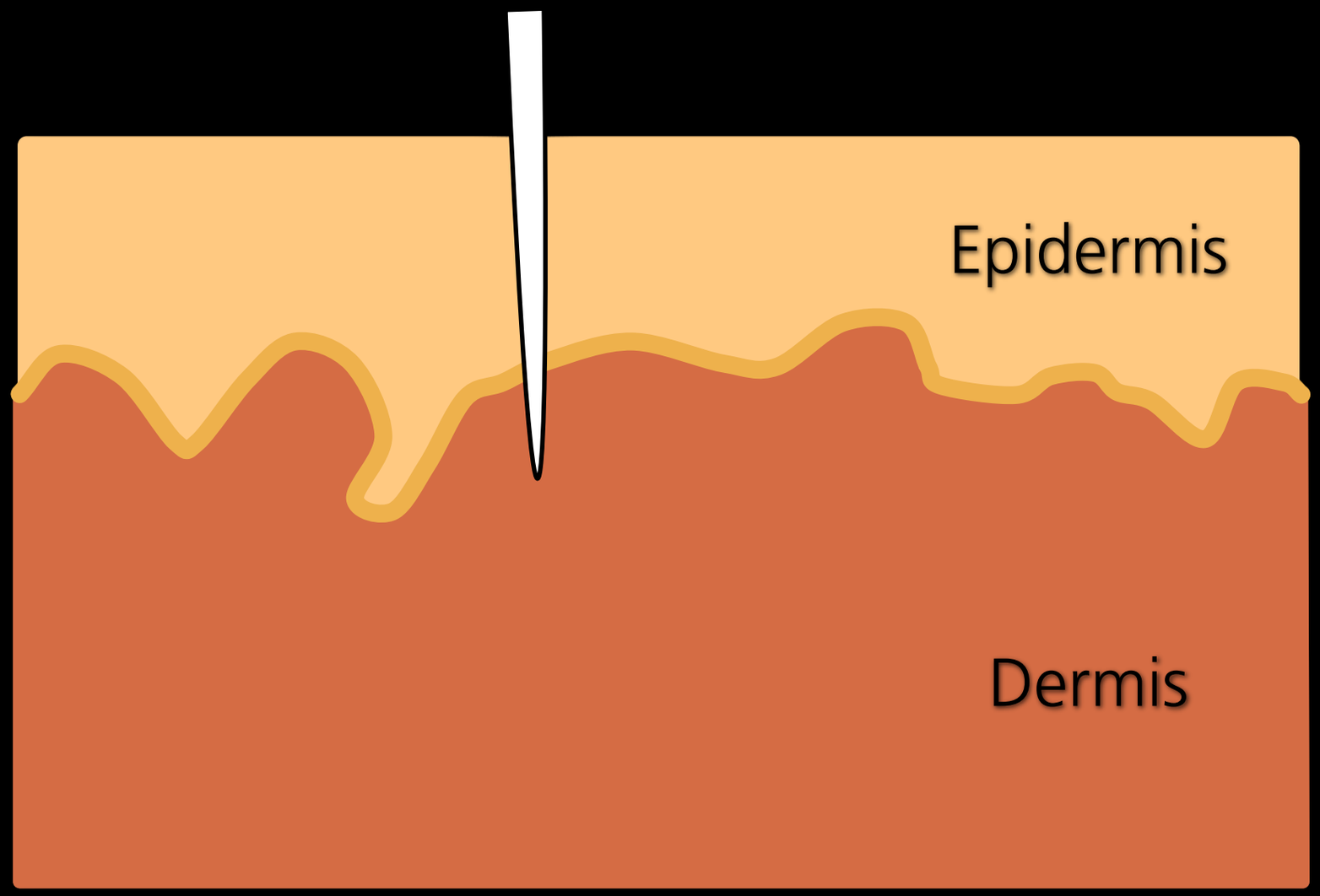

Tattoo

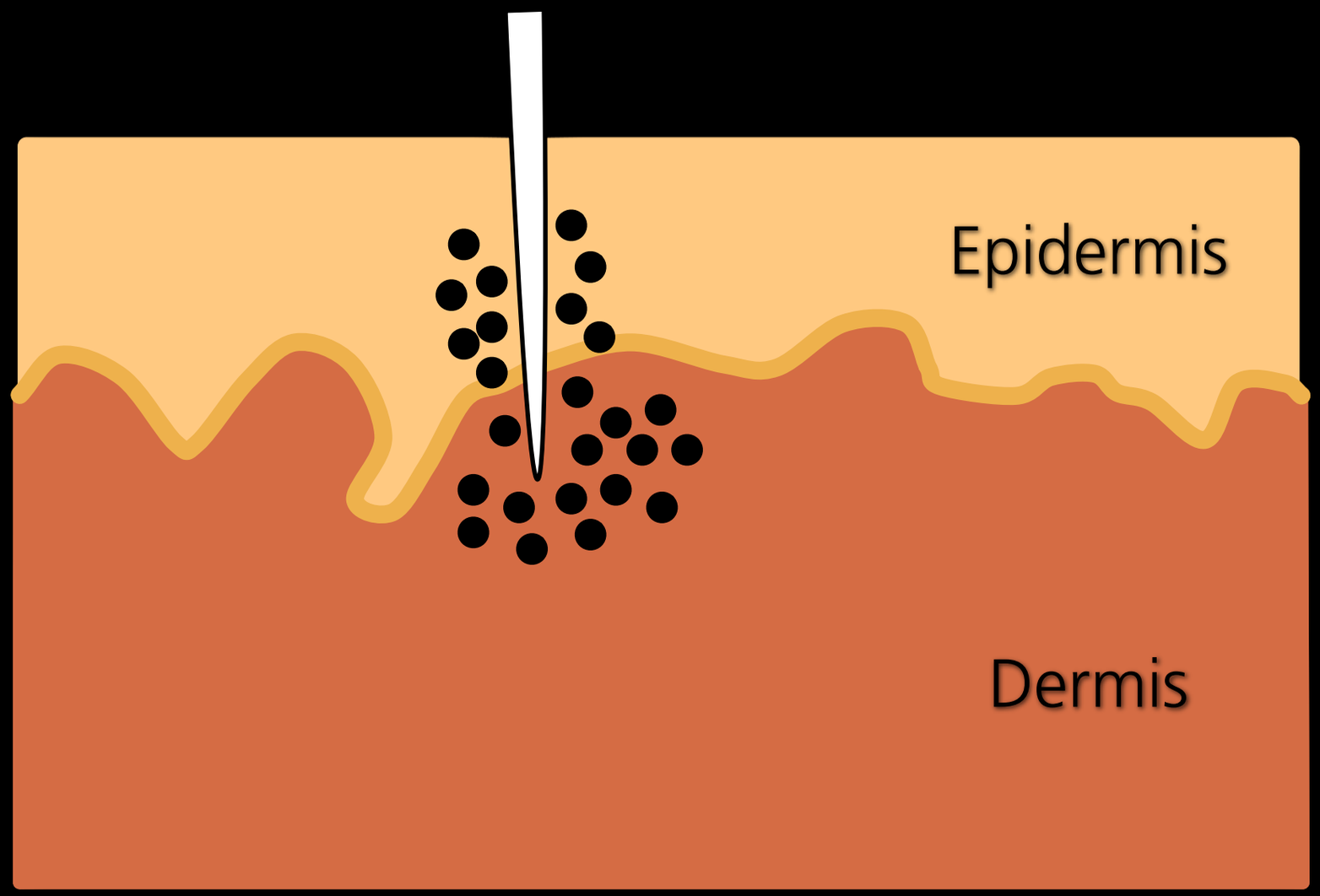

Tattoo

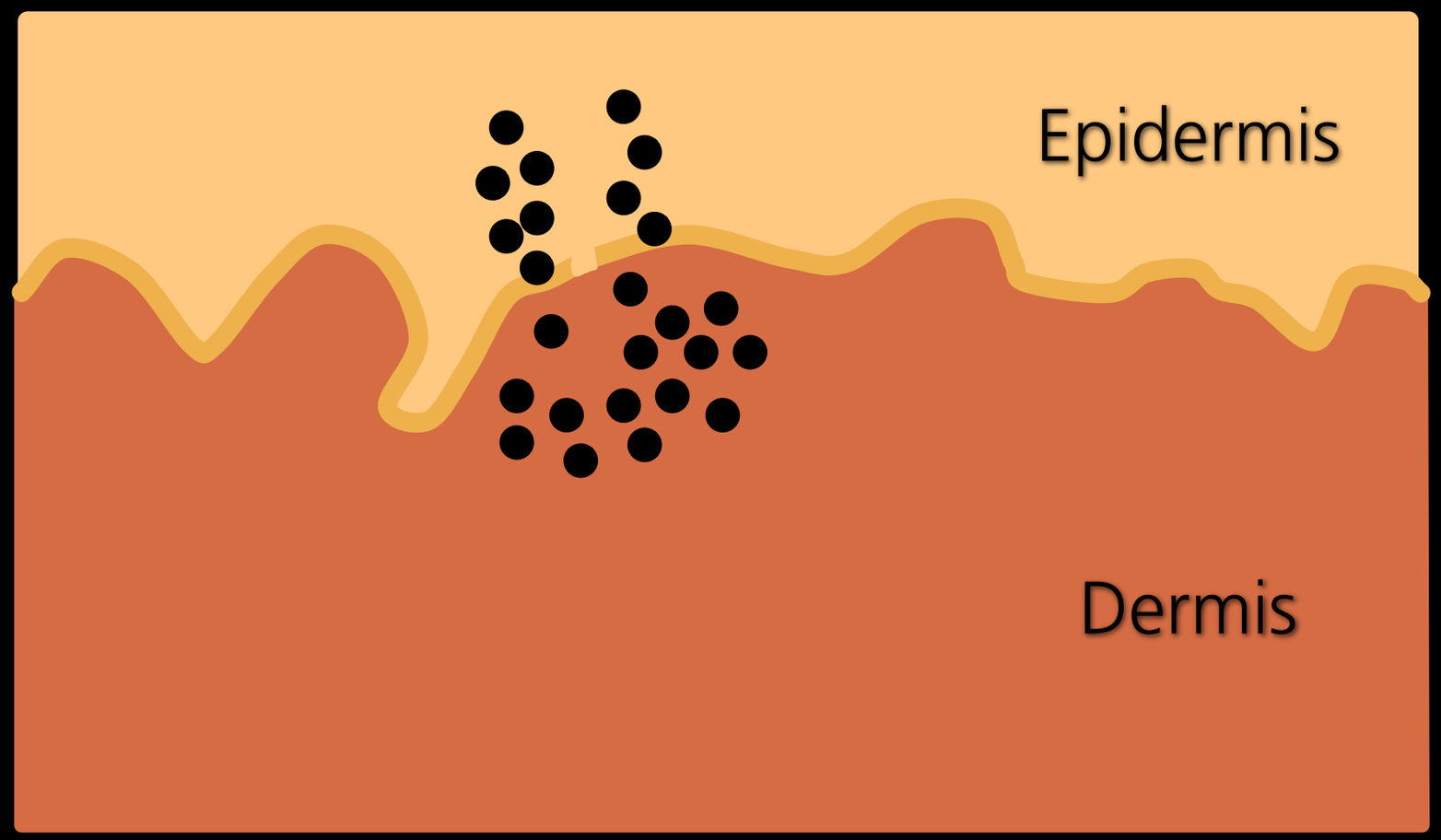

Tattoo

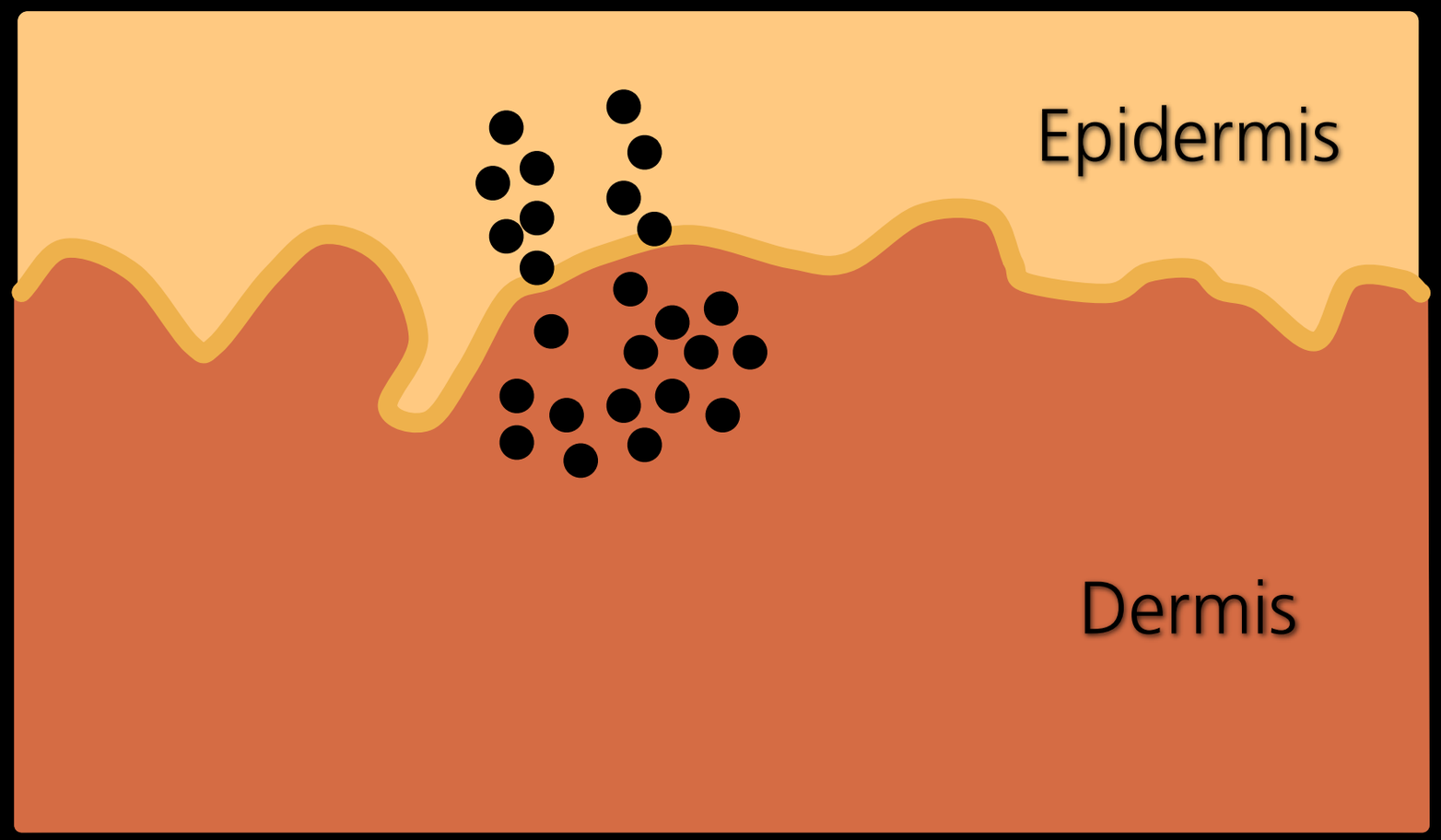

Tattoo

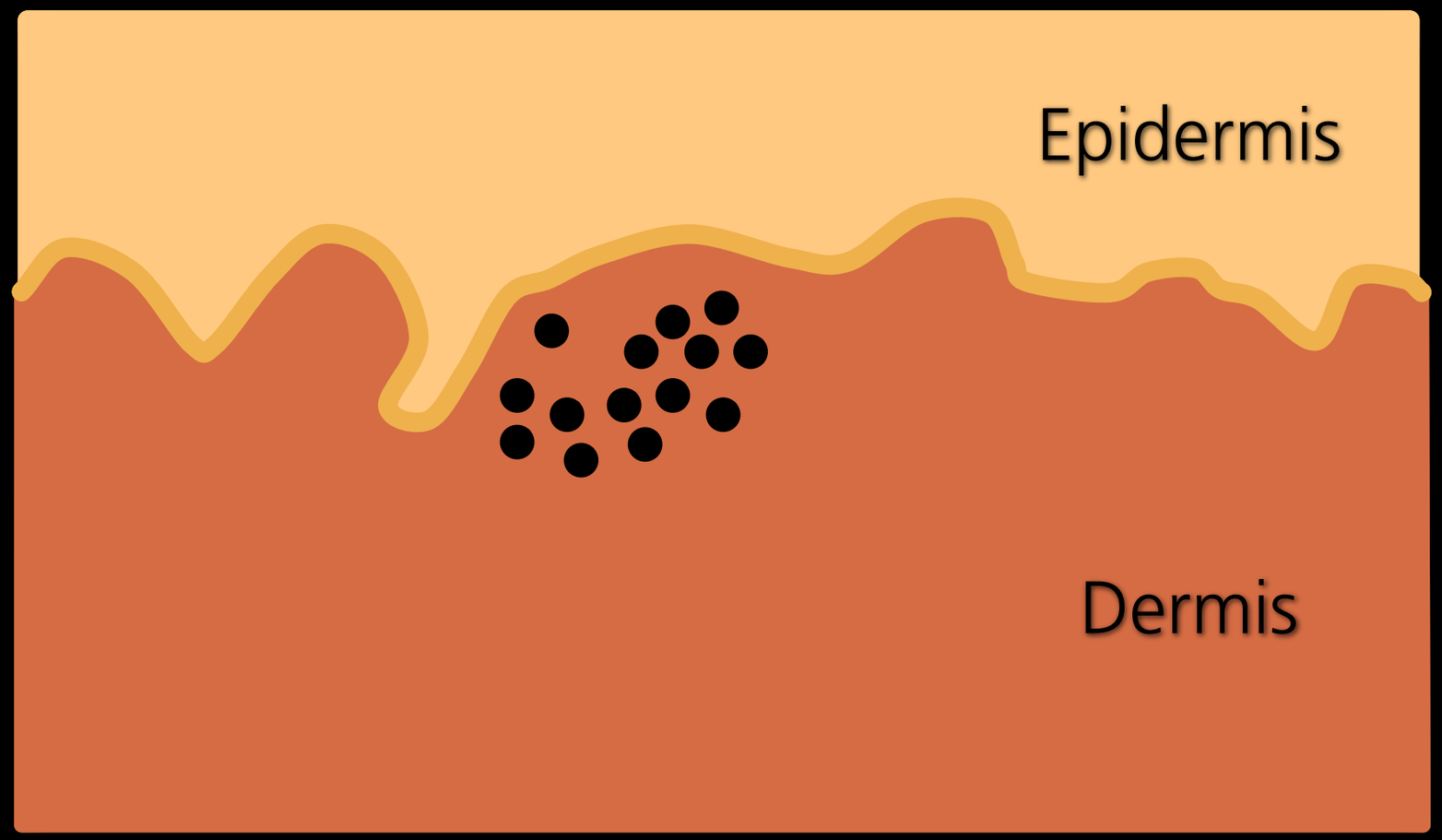

Tattoo

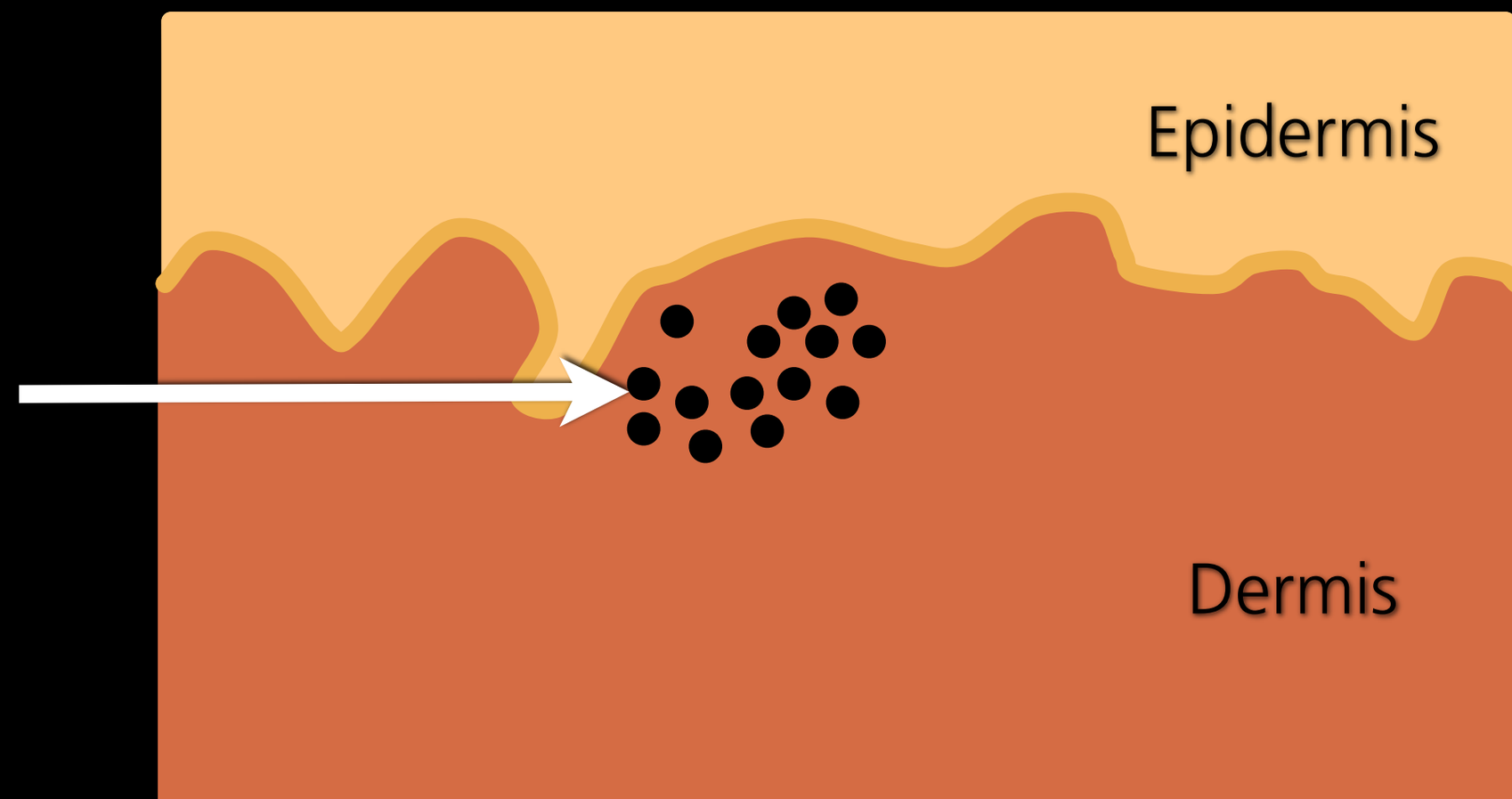

Tattoo

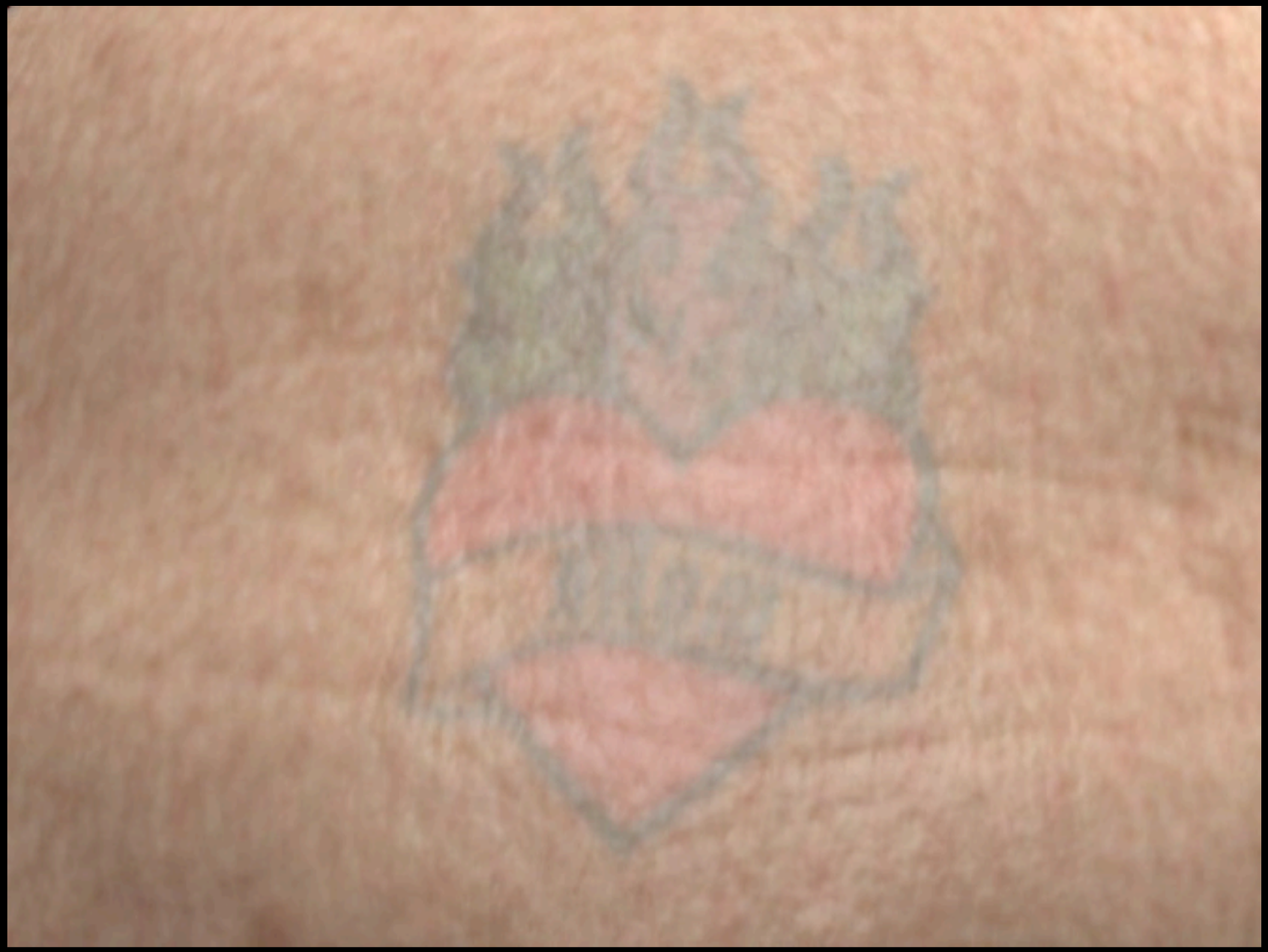

Tattoo

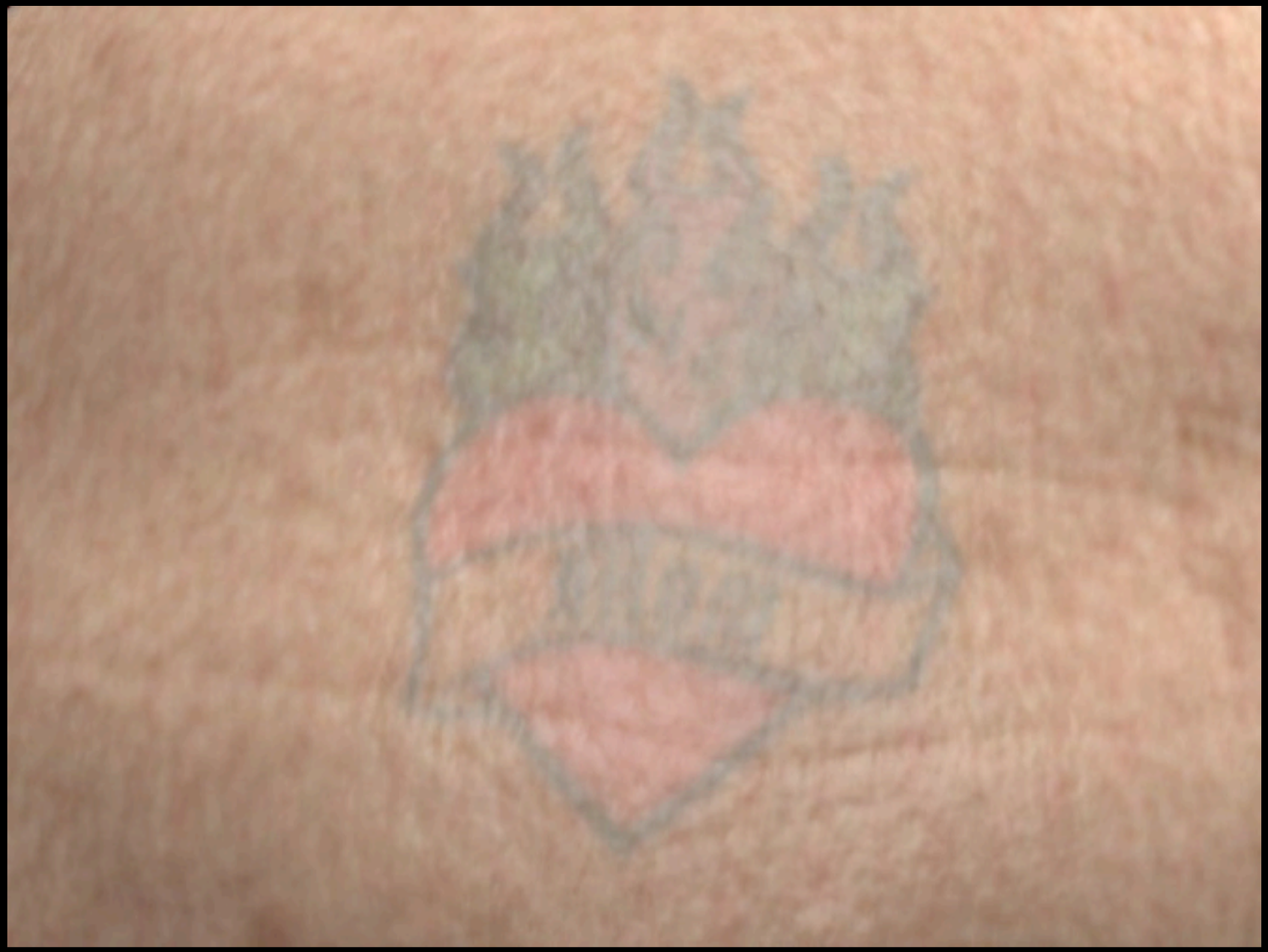

Thick measurements

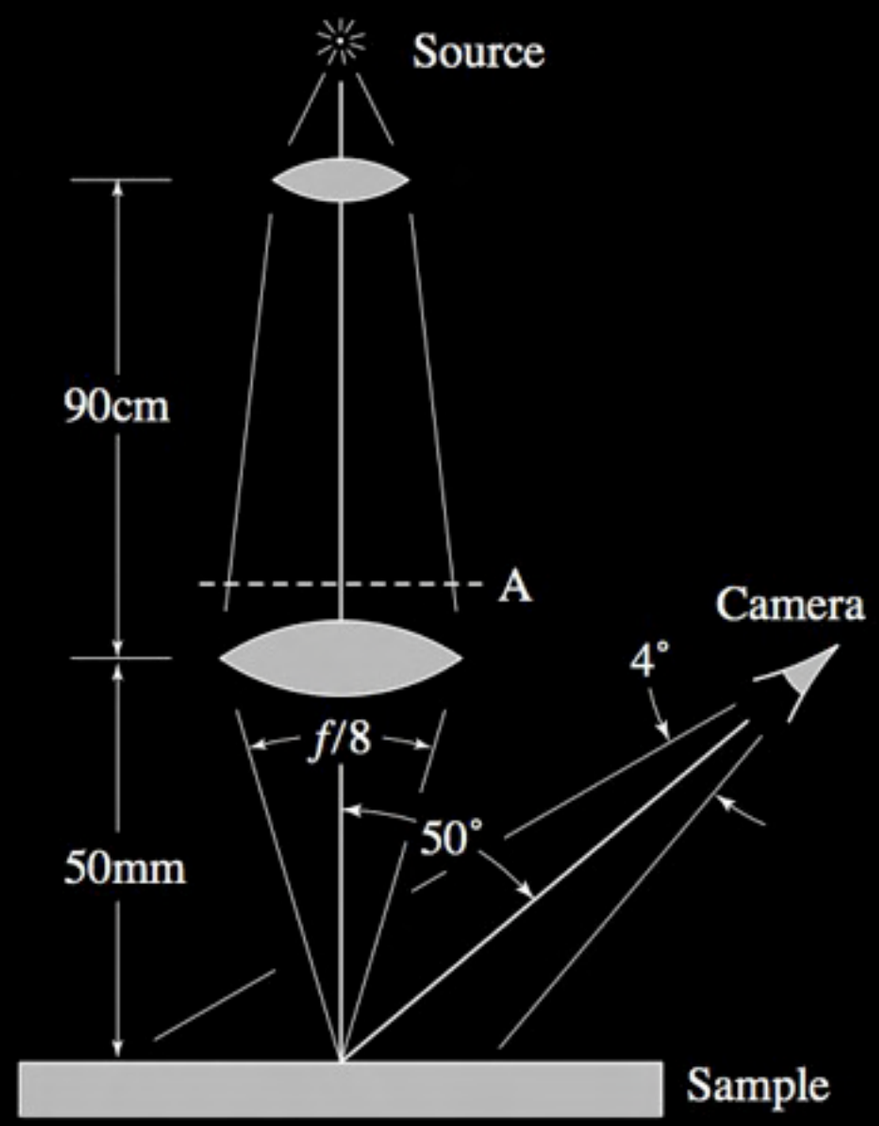

Thick measurements

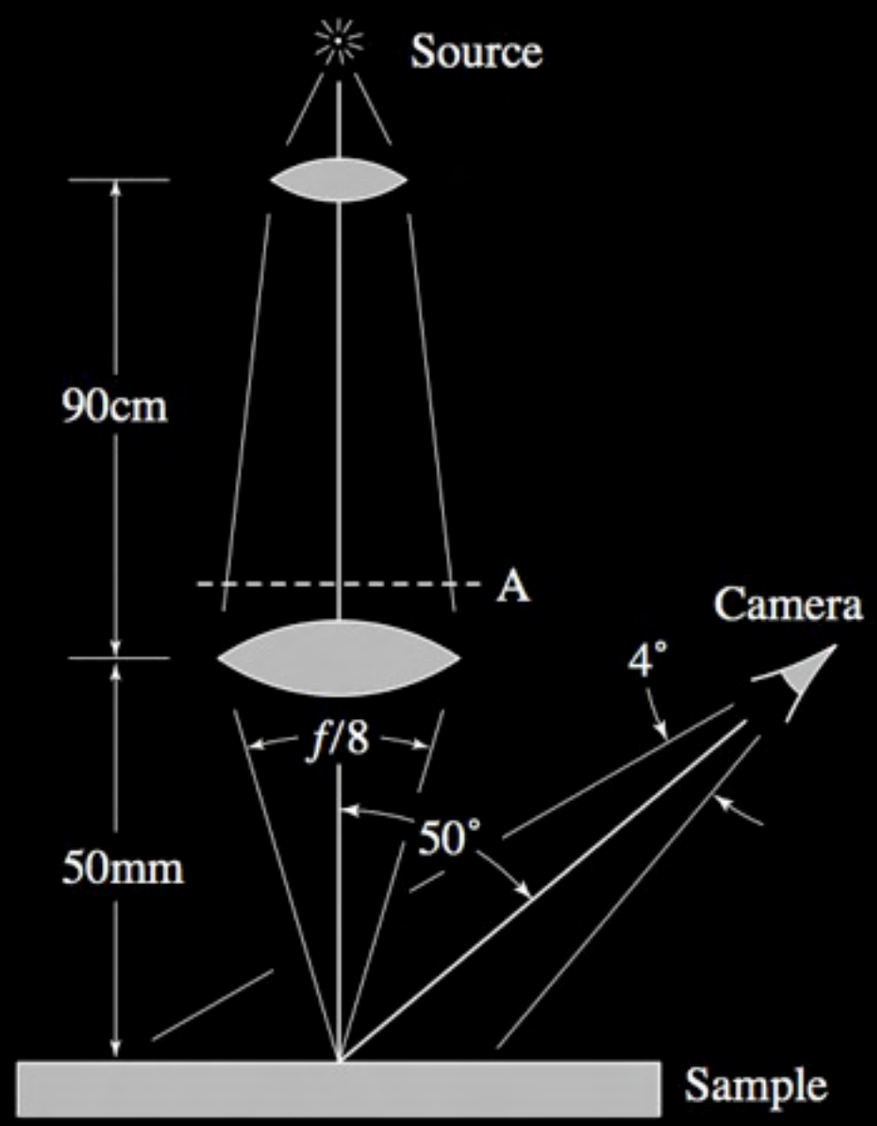

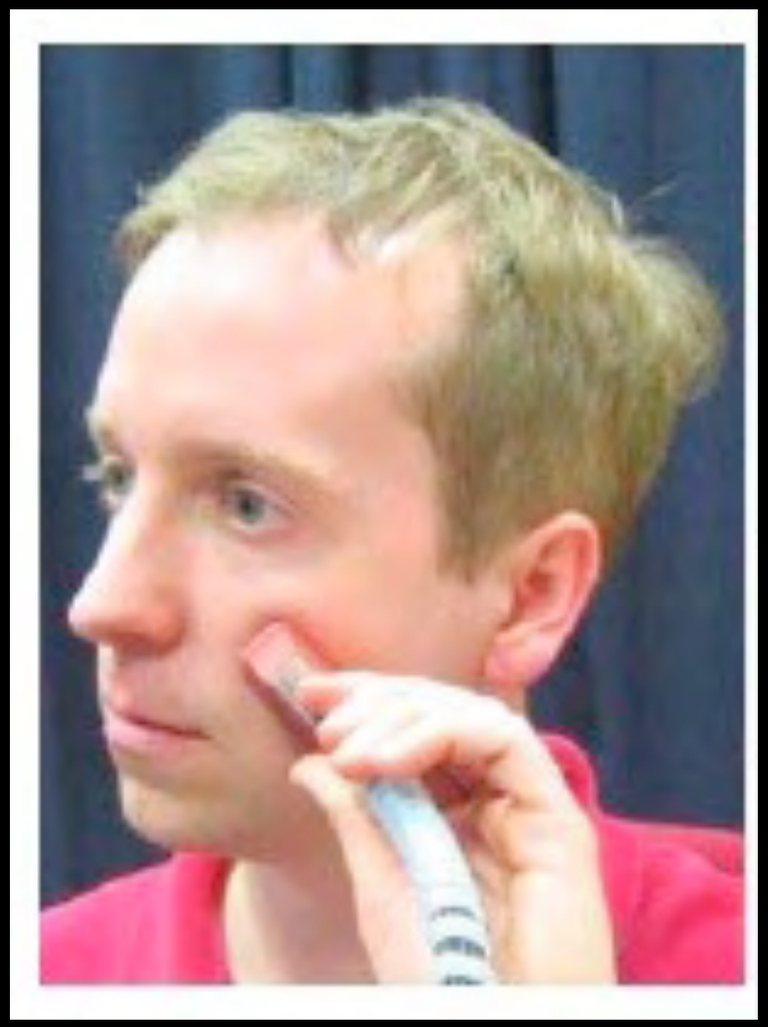

Thin materials

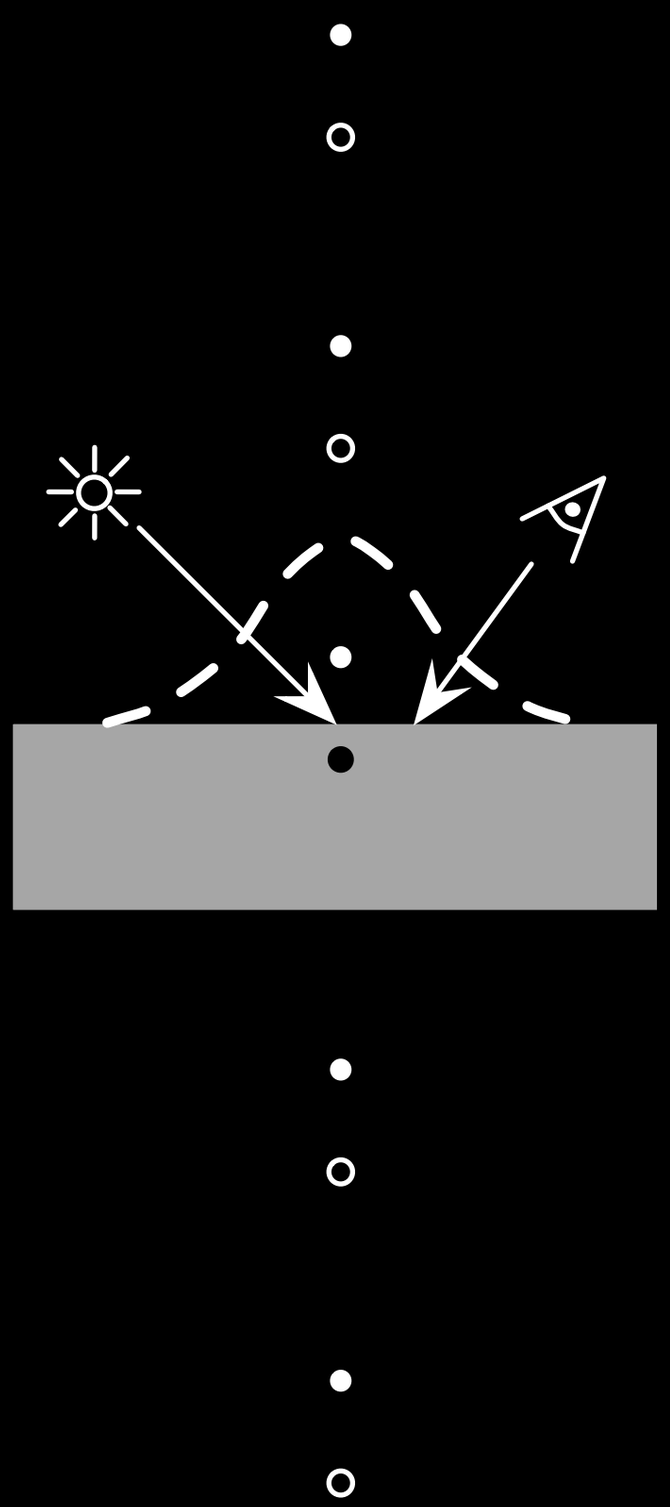

Thin materials

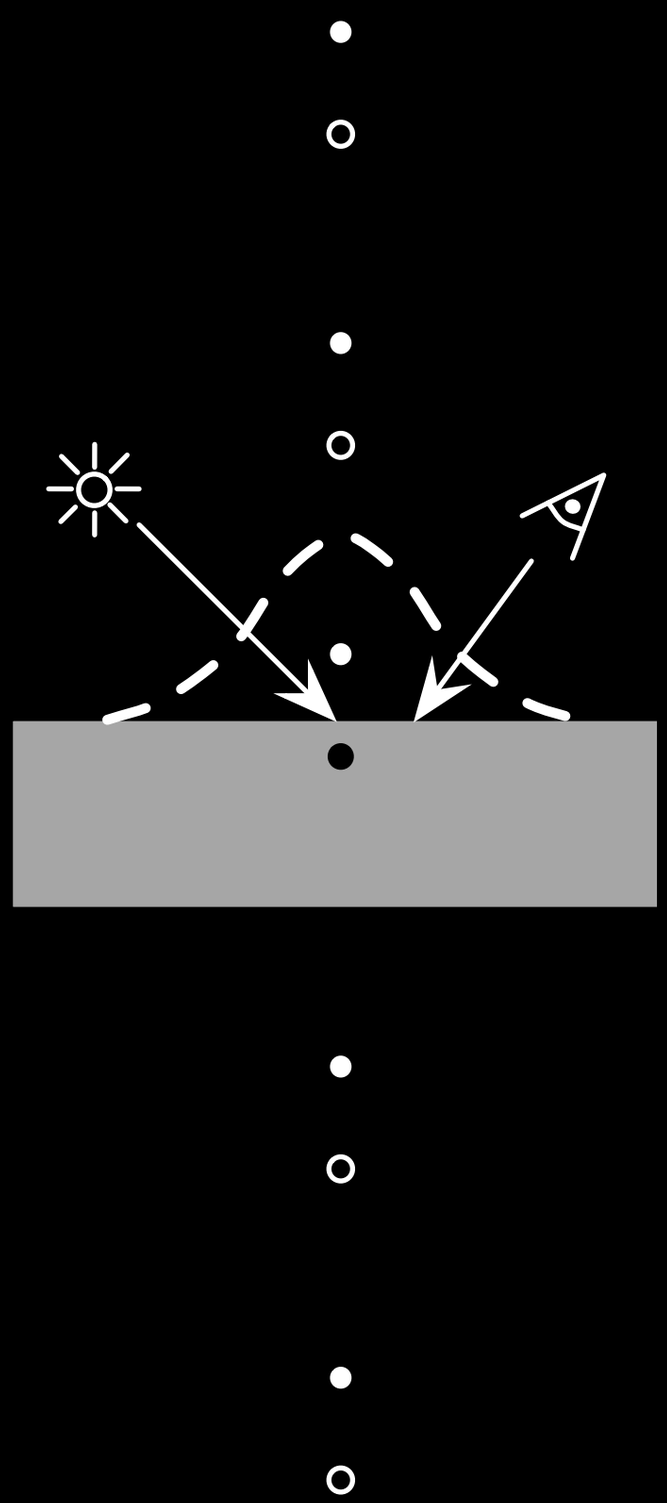

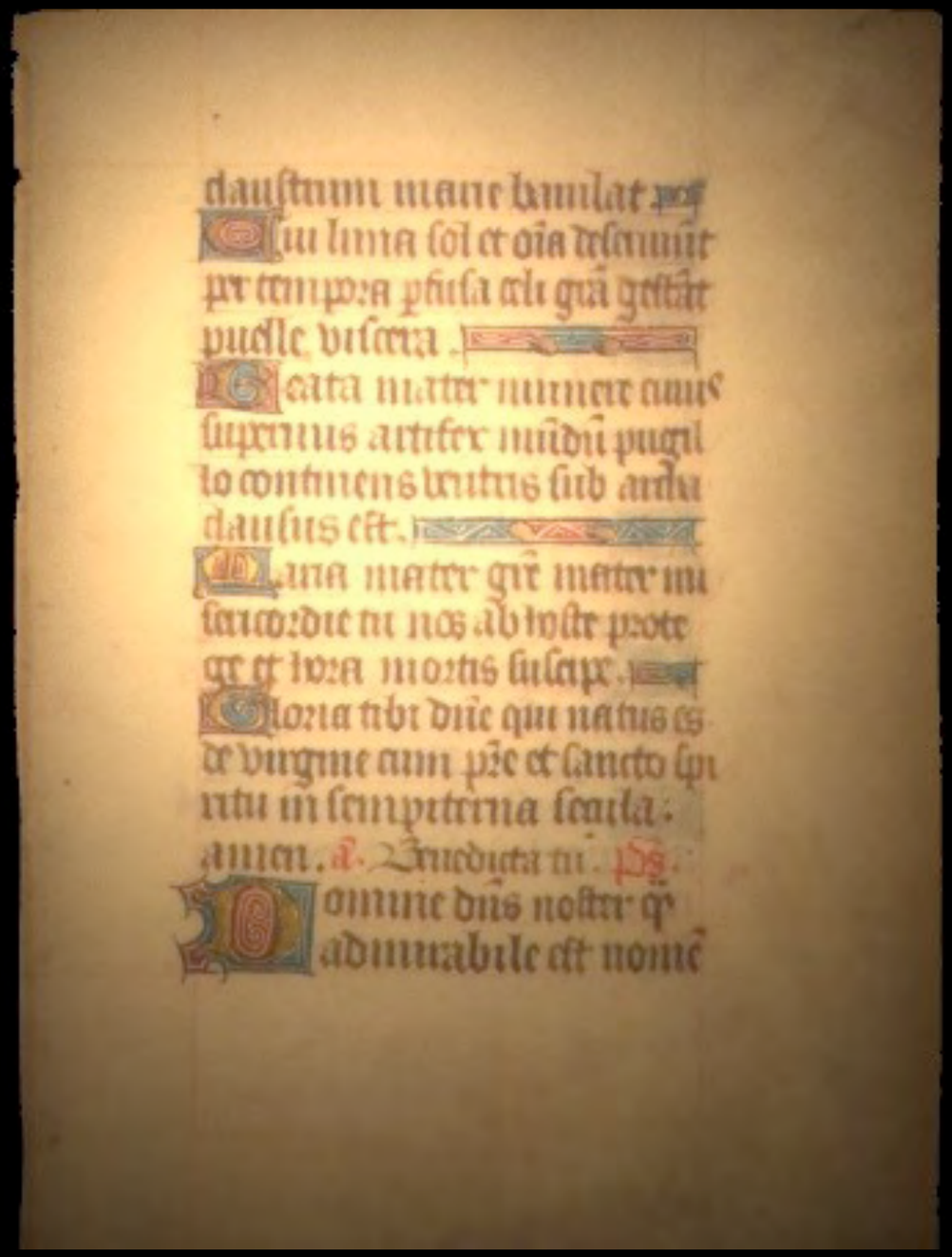

Layered materials

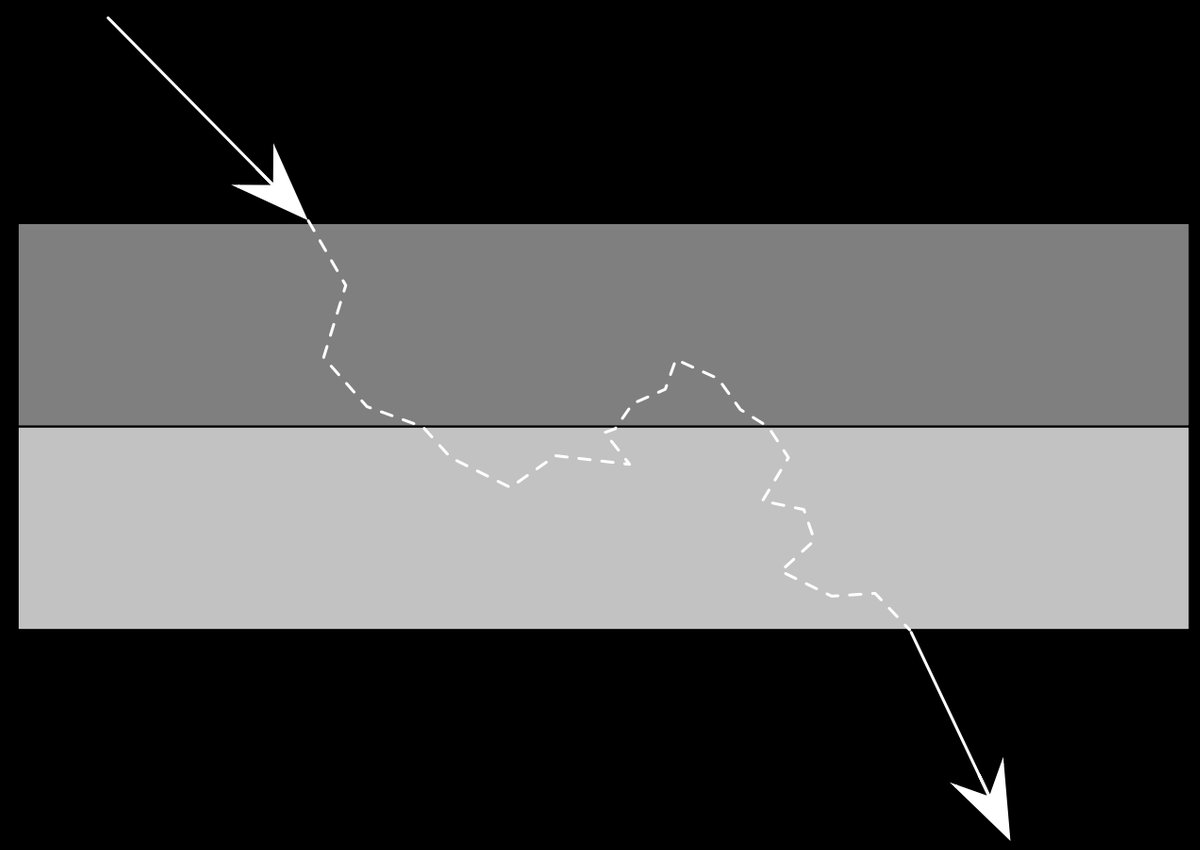

Layered materials

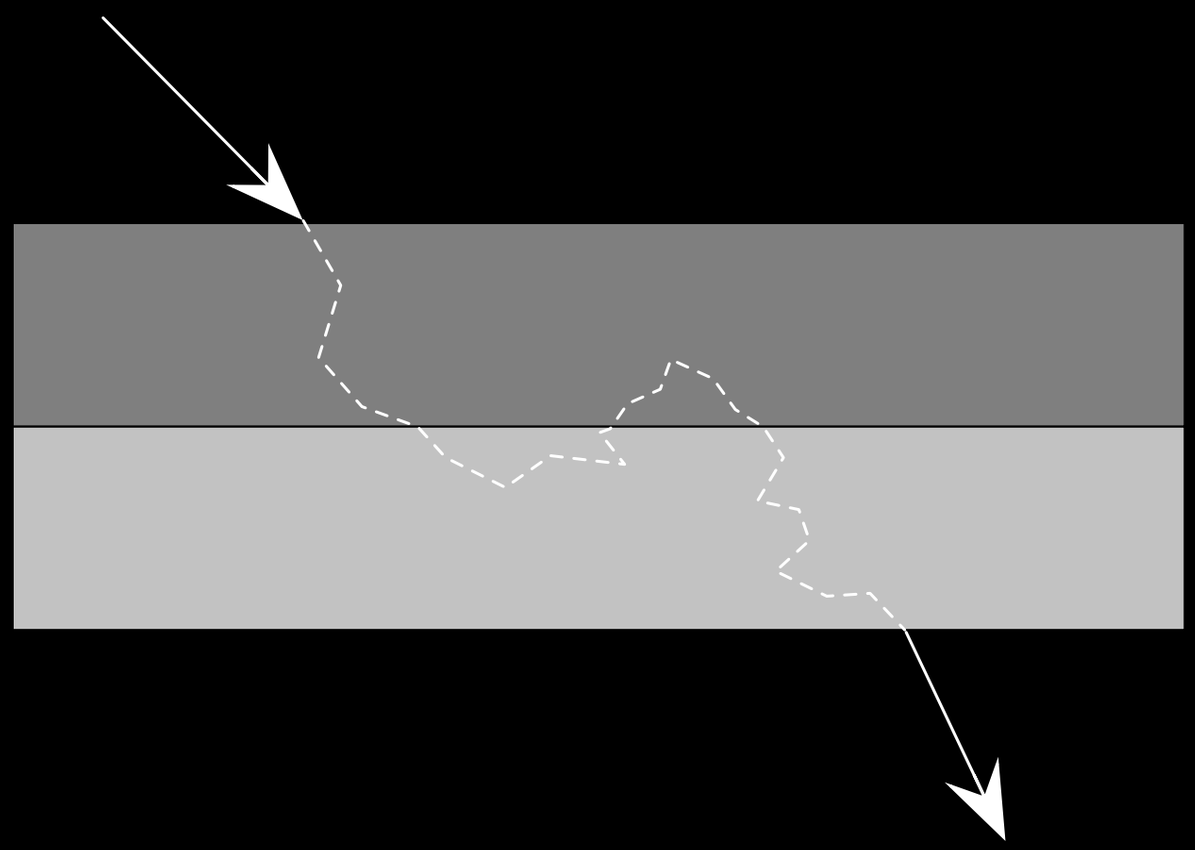

Layered materials

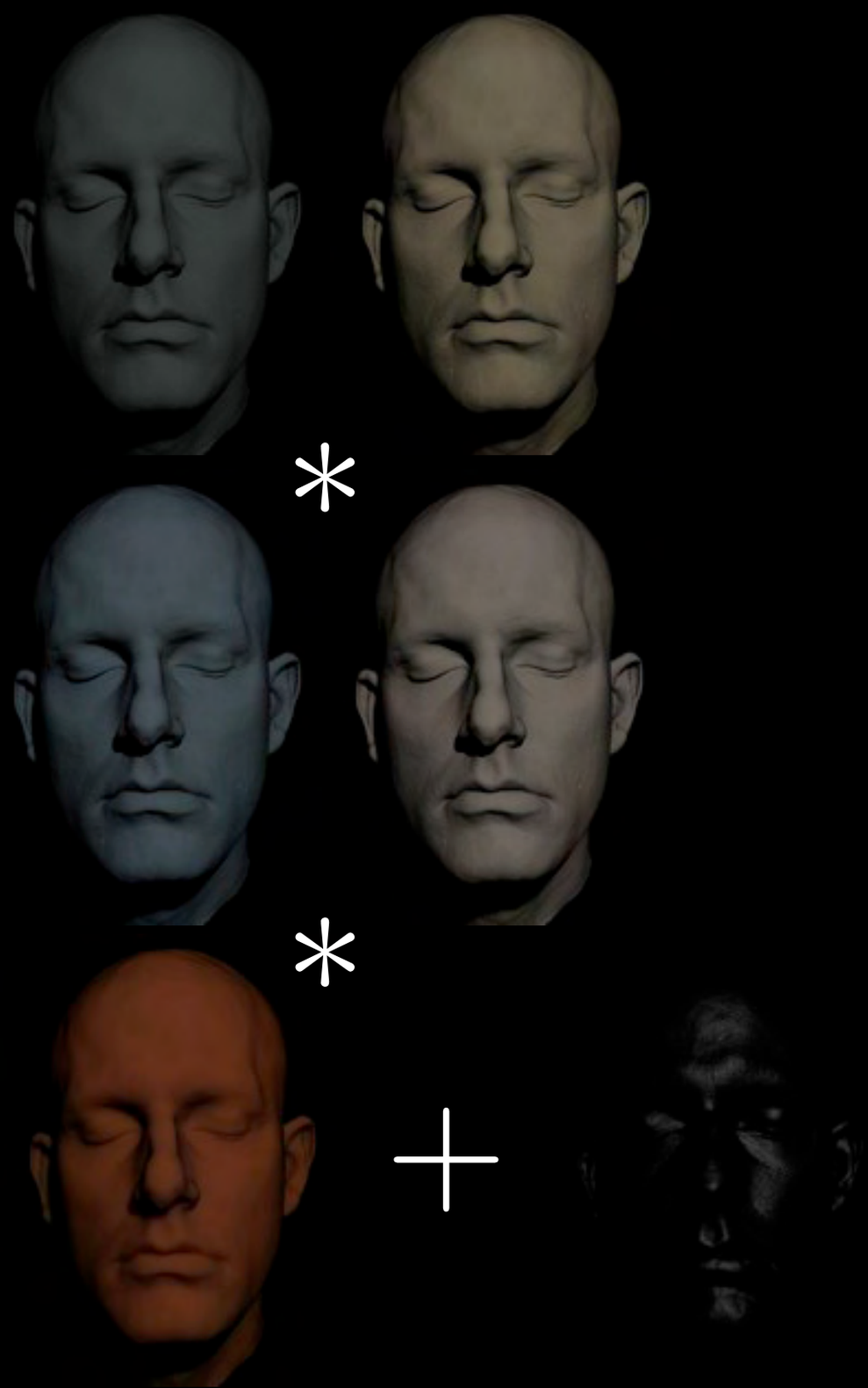

Layered materials

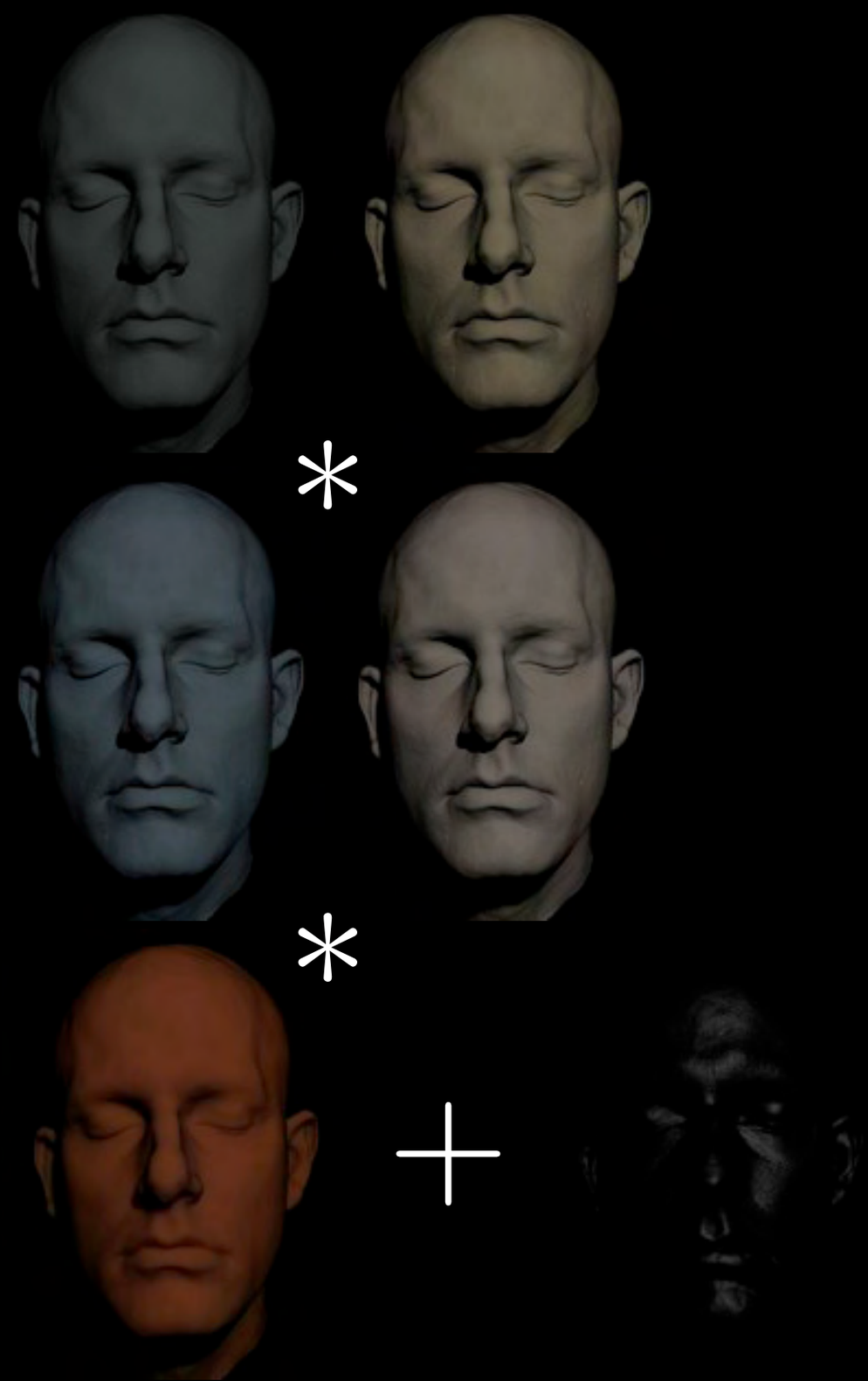

Skin appearance

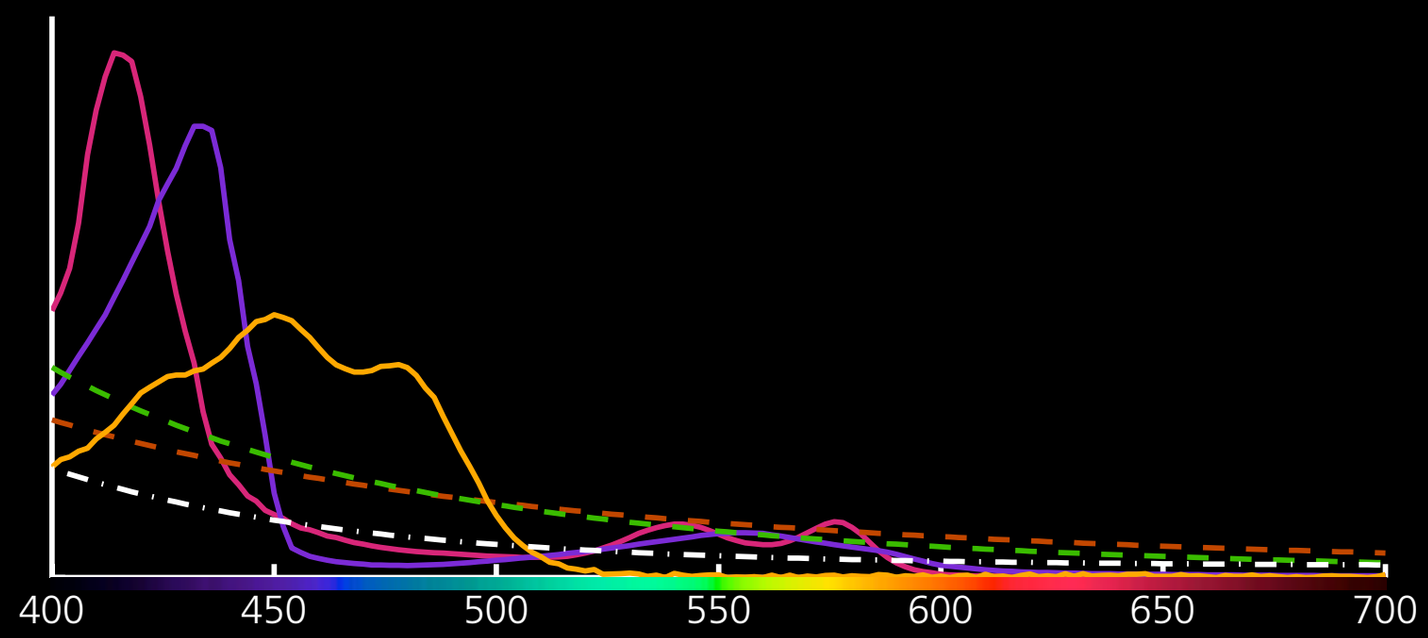

Skin appearance

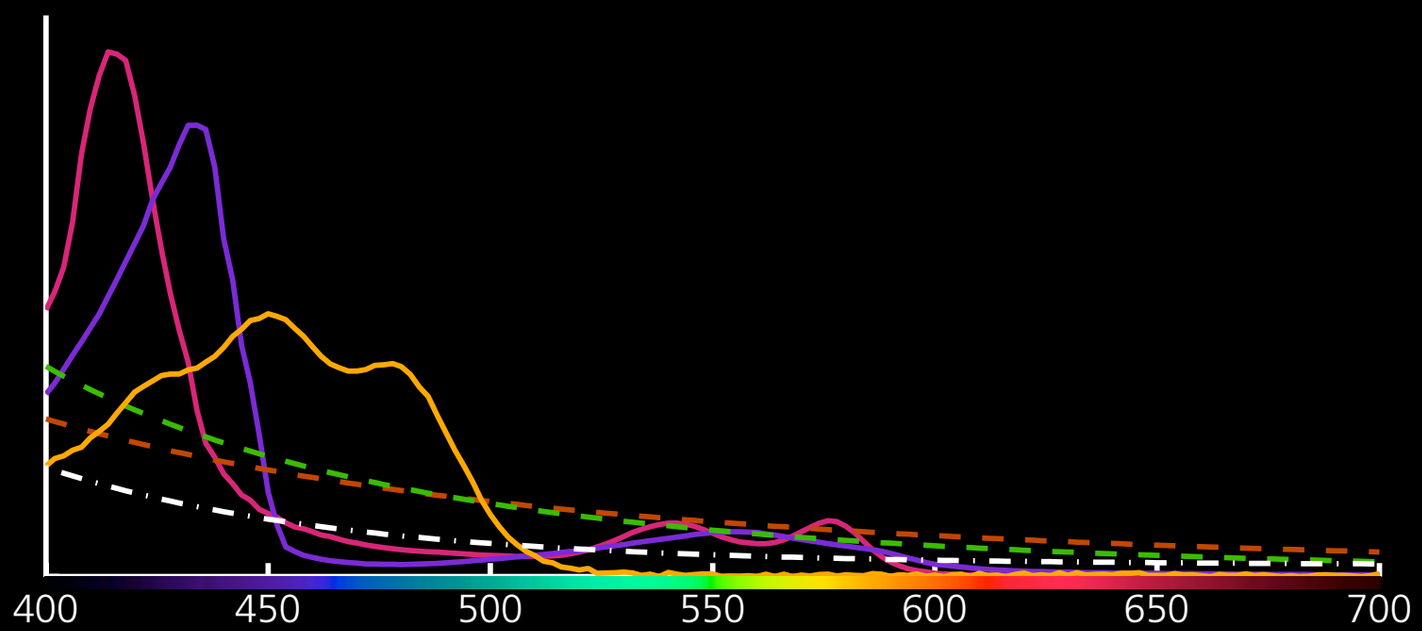

Skin acquisition

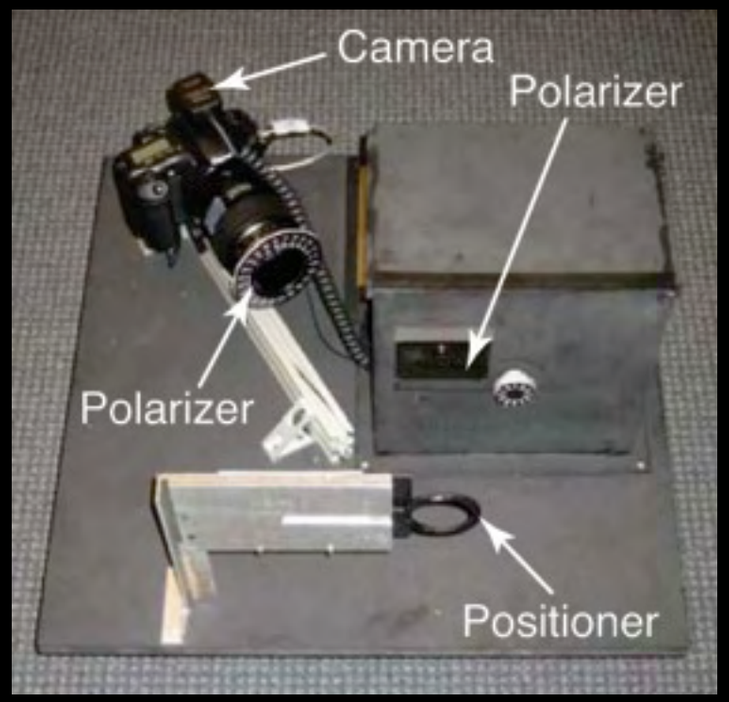

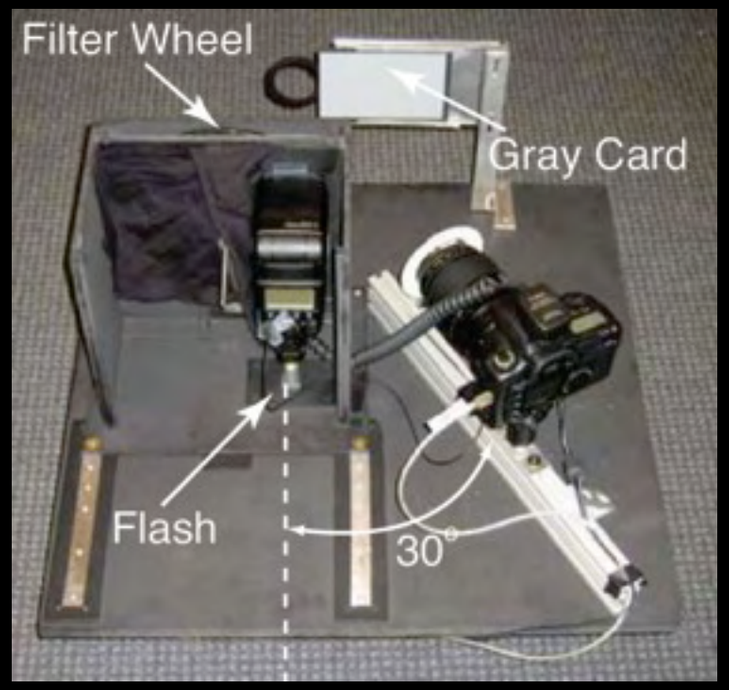

Skin acquisition

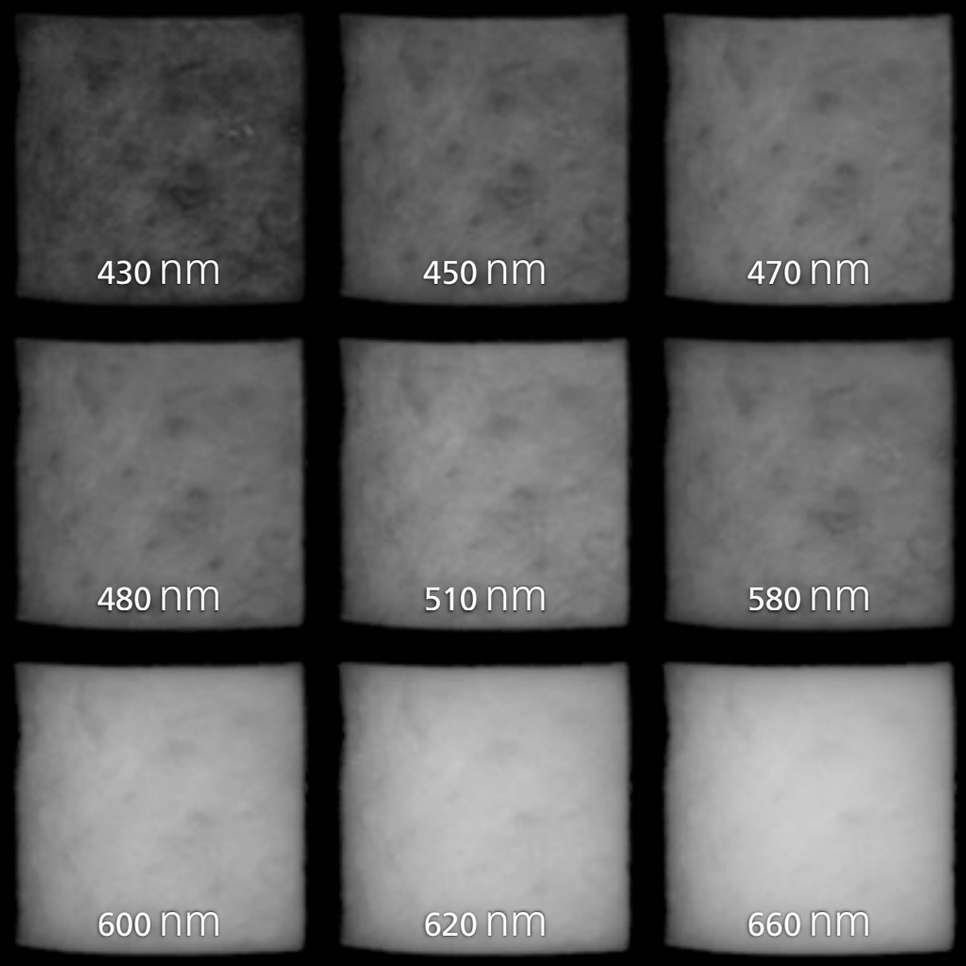

Skin acquisition

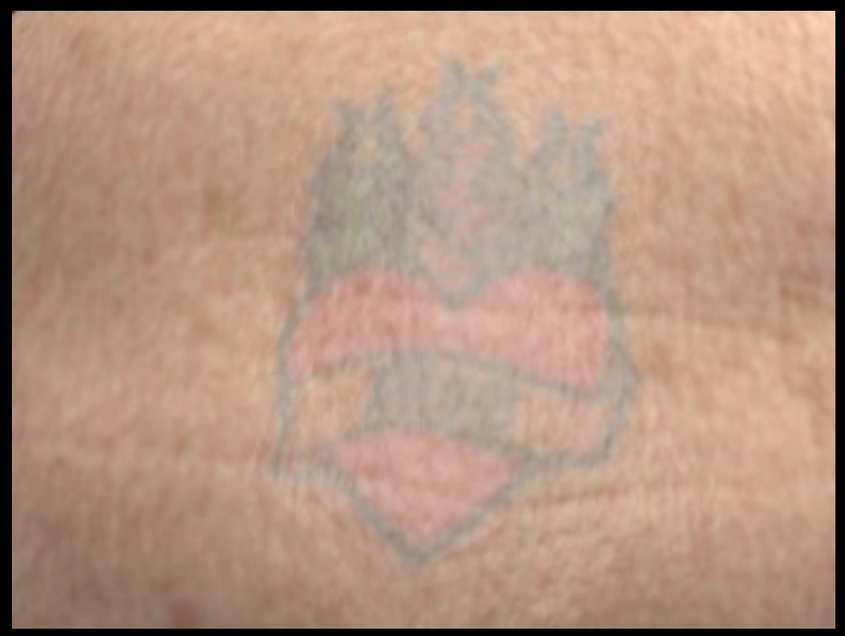

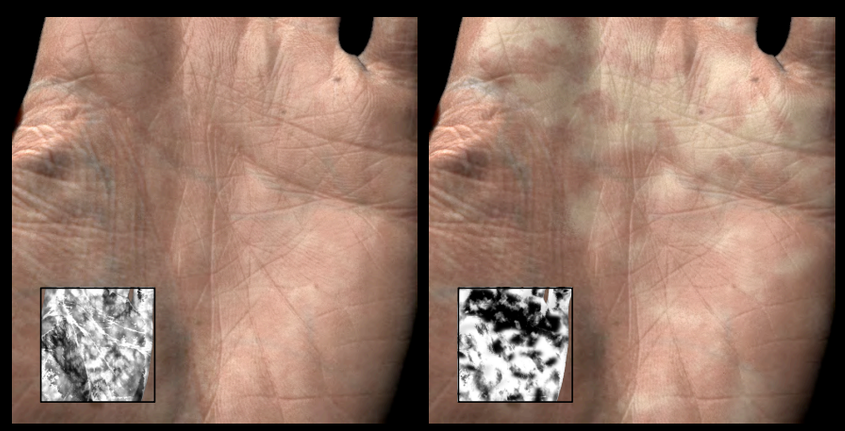

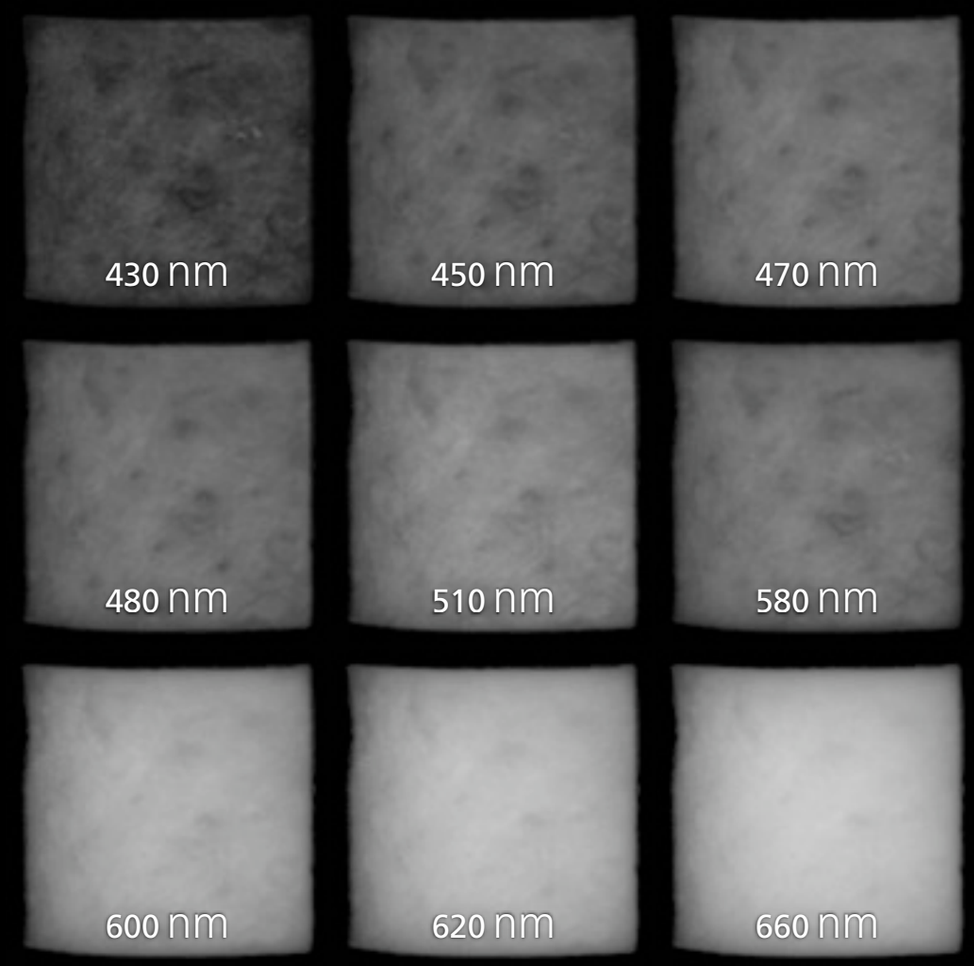

What's next?

- Very thin, curved areas
- Low-order scattering
- Deforming skin
- Clinical accuracy
- Heterogeneous translucency

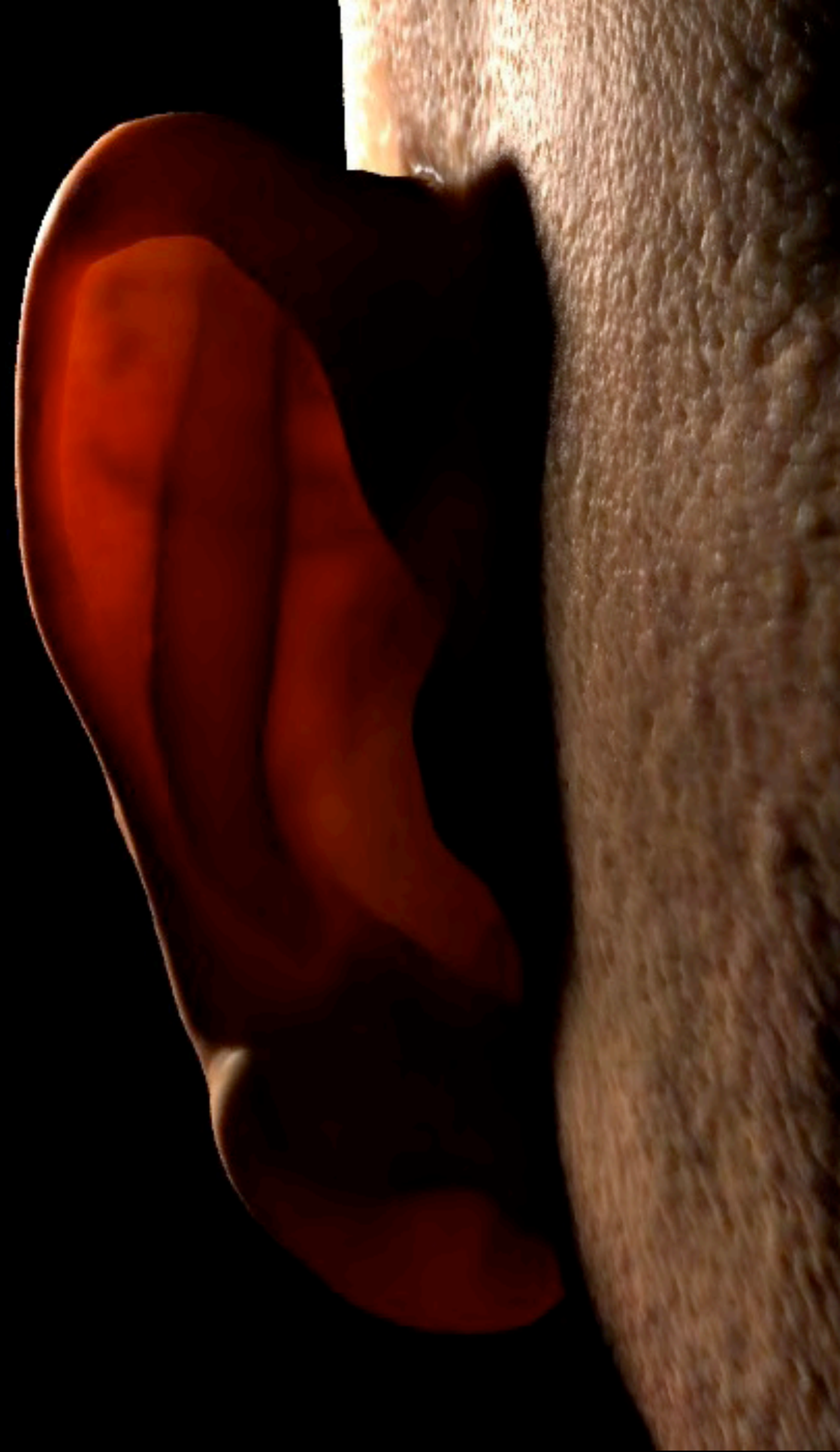

Acknowledgements

- Tim Weyrich
- Eugene d'Eon
- Neel Joshi
- Students and faculty at UCSD, Columbia and Princeton Universities
- Tiggraph and SIGGRAPH reviewers
- NVIDIA, XYZRGB
- NSF
- Sloan Foundation
- Thank you for your attention

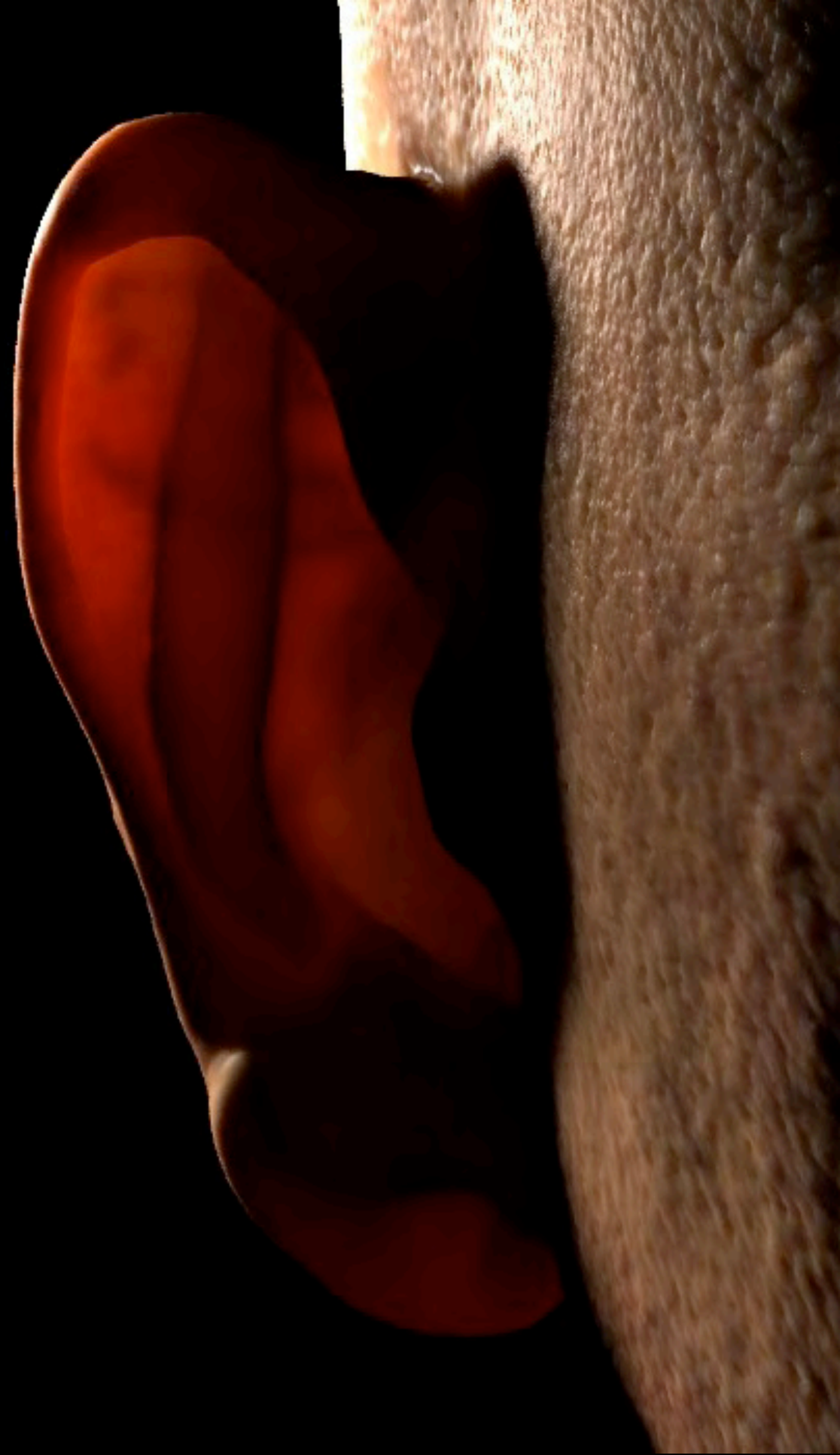

Acquiring Scattering Properties of Participating Media by Dilution

Srinivasa G. Narasimhan[1], Mohit Gupta[1], Craig Donner[2], Ravi Ramamoorthi[3], Shree K. Nayar[3], Henrik Wann Jensen[2]

[1]Carnegie Mellon University* [2]University of California, San Diego [3]Columbia University

(a) Acquired photographs (b) Rendering at low concentrations (c) Rendering at natural concentrations

Figure 1: *(a) Photographs of our simple setup consisting of a glass tank and a bulb, filled with diluted participating media (from top, MERLOT, CHARDONNAY, YUENGLING beer and milk). The colors of the bulb and the glow around it illustrate the scattering and absorption properties in these media. At low concentrations, single scattering of light is dominant while multiple scattering of light is negligible. From a single HDR photograph, we robustly estimate all the scattering properties of the medium. Once these properties are estimated, a standard volumetric Monte Carlo technique can be used to create renderings at any concentration and with multiple scattering, as shown in (b) and (c). While the colors are only slightly visible in the diluted setting in (b), notice the bright colors of the liquids - deep red and golden-yellow wines, soft white milk, and orange-red beer - in their natural concentrations. Notice, also the differences in the caustics and the strong interreflections of milk onto other liquids.*

Abstract

The visual world around us displays a rich set of volumetric effects due to participating media. The appearance of these media is governed by several physical properties such as particle densities, shapes and sizes, which must be input (directly or indirectly) to a rendering algorithm to generate realistic images. While there has been significant progress in developing rendering techniques (for instance, volumetric Monte Carlo methods and analytic approximations), there are very few methods that measure or estimate these properties for media that are of relevance to computer graphics. In this paper, we present a simple device and technique for robustly estimating the properties of a broad class of participating media that can be either (a) diluted in water such as juices, beverages, paints and cleaning supplies, or (b) dissolved in water such as powders and sugar/salt crystals, or (c) suspended in water such as impurities. The key idea is to dilute the concentrations of the media so that single scattering effects dominate and multiple scattering becomes negligible, leading to a simple and robust estimation algorithm. Furthermore, unlike previous approaches that require complicated or separate measurement setups for different types or properties of media, our method and setup can be used to measure media with a complete range of absorption and scattering properties from a single HDR photograph. Once the parameters of the diluted medium are estimated, a volumetric Monte Carlo technique may be used to create renderings of any medium concentration and with multiple scattering. We have measured the scattering parameters of forty commonly found materials, that can be immediately used by the computer graphics community. We can also create realistic images of combinations or mixtures of the original measured materials, thus giving the user a wide flexibility in making realistic images of participating media.

*e-mail:srinivas@cs.cmu.edu

1 Introduction

Very often in our daily lives, we see participating media such as fluids (juices, beverages, milks) and underwater impurities (natural ocean, river and lake waters). The propagation of light through these media results in a broad range of effects, including softer appearance of milk, coloring of wines and juices, the transformation of appearances when liquids are mixed (coffee with milk, and cocktails), the brilliant caustics from glasses containing these liquids, and low visibility in underwater situations. These effects inherently depend on several physical properties of the media such as

scattering nature, sizes, shapes, and densities of particles [Hulst 1957; Chandrasekhar 1960]. Rendering these effects accurately is critical to achieving photo-realism in computer graphics.

In the past few years, there has been a considerable effort towards developing efficient and accurate rendering algorithms for participating media, based on Monte Carlo simulation and analytic approximations. All these algorithms and models contain parameters (scattering coefficient, absorption coefficient, phase function) that directly or indirectly represent the physical properties of the medium. In order to faithfully render the effects of any participating medium, the right parameters must be input. Given the progress in developing rendering algorithms, the quality of images is now often limited by the quality of these input parameters. Since there has so far been relatively little work in measuring or estimating scattering properties of media relevant to computer graphics, the parameters are currently often set in an ad-hoc manner.

This situation is similar in some ways to that of standard surface rendering. In that case, global illumination algorithms have progressed to the point of creating almost photo-realistic images, leaving the realism limited by the quality of the reflectance models, and leading to much recent effort on measuring BRDFs. [Marschner 1998; Dana et al. 1997; Matusik et al. 2003]. However, existing methods for directly measuring physical properties for media usually require very expensive equipment, such as the particle sizing apparatus used in colloidal chemistry [Finsy and Joosten 1991; Jaeger et al. 1991], resulting in little usable data for graphics.

Earlier efforts to estimate scattering properties from images of media have often yielded ill-conditioned and non-unique results, because of the difficulties of solving the inverse light transport problem. The reasoning for the ill-conditioning of the inverse problem is mainly due to multiple scattering, which blurs the incident light field and results in significant loss of information [McCormick 1981; McCormick 1985; Antyufeev 2000]. This is analogous to the ill-conditioning of BRDF estimation under complex illumination [Ramamoorthi and Hanrahan 2001]. In this paper, we take a completely different approach. The key idea is to estimate properties of media by acquiring the data in a state where multiple scattering effects are negligible. Instead, the data is acquired when single scattering (which does not degrade the incident light significantly) is the dominant effect. This is achieved by diluting the material to low concentrations.

We present a simple and inexpensive experimental setup, along with a robust and accurate technique for measuring the scattering properties of a broad class of participating media that can be either (a) diluted in water such as juices, beverages, paints and cleaning supplies, or (b) suspended in natural waters such as impurities and organisms, or even (c) dissolved in water such as powders and sugar or salt crystals. These media collectively have a wide range of scattering and absorption properties. We first derive a simple image formation model for single scattering of light in our setup. Through extensive simulations of both our model and ground truth (with multiple scattering), we then determine the space of concentrations and scattering properties of media for which single scattering is dominant. Within this regime of valid concentrations, we conduct simulations to demonstrate that our estimation technique uniquely solves the inverse single scattering light transport problem. Finally, we present a simple experimental procedure to determine the best concentration (dilution) for any material despite no prior knowledge of its scattering properties.

We have used our approach to create a dataset of scattering parameters for **forty commonly found materials**, which can be directly used for computer graphics rendering. Once the scattering parameters have been estimated, they can be used to render realistic images of arbitrary concentrations of the material with multiple scattering, using a standard physically based volumetric rendering algorithm. Figure 1 shows two renderings of a scene with four liquids in their natural high density states and their diluted states. The scattering parameters of each material were computed using a single HDR photograph of our setup. Notice the bright saturated colors obtained despite the murky appearance of the diluted states. We can also create realistic images of mixtures of the original measured materials, thus giving the user a wide flexibility in creating realistic images of participating media.

Medium Property	Notation
Concentration or Volume Fraction	C
Scattering Coefficient (mm^{-1})	β
Absorption Coefficient (mm^{-1})	κ
Extinction Coefficient (mm^{-1})	$\sigma = \beta + \kappa$
Single Scattering Albedo	$\omega = \beta / \sigma$
Scattering Angle	θ
Henyey-Greenstein (H-G) Parameter	g
H-G Phase Function	$P(g,\theta) = \frac{1}{4\pi} \frac{1-g^2}{(1+g^2-2g\cos\theta)^{3/2}}$

Figure 2: *The different scattering properties of a participating medium and their notations used in this paper. Light transport equations are usually written in terms of three parameters σ, β and g. We estimate these parameters for participating media based on single scattering.*

2 Related Work

Figure 2 shows the most common properties of participating media including the scattering and absorption coefficients, and the phase function (angular scattering distribution represented by the Henyey-Greenstein (H-G) model [Henyey and Greenstein 1941]). The scattering and absorption coefficients are proportional to the concentration or volume fraction of the particulate medium. We will briefly review some of the representative works on the direct measurement and indirect estimation of these parameters.

Estimation based on analytic approximations to light transport. Surprisingly, little work has been done in computer graphics on the measurement of scattering properties of media. A recent work is that of [Jensen et al. 2001], on the diffusion model for subsurface scattering. They present a measurement of a number of translucent materials. However, the diffusion approximation assumes multiple scattering for optically dense media, so that only a limited amount of information on the scattering parameters can be estimated. For instance, this approximation is independent of the phase function of the medium, and therefore this important property cannot be estimated. Furthermore, the diffusion is a poor approximation when scattering is comparable to absorption [Prahl 1988]. The analytic multiple scattering model presented in [Narasimhan and Nayar 2003] has also been used to estimate properties of only purely scattering media (visibility and type of weather such as fog and mist). Our focus is somewhat different in considering fluids like juices or beverages, instead of subsurface scattering in translucent solids like marble and skin, or weather conditions such as fog. Nevertheless, our approach is valid for media with the entire range of absorbing and scattering properties, significantly extending the class of measurable media for graphics.

Most recently, Hawkins et. al., [2005] measure the extinction coefficient of optically thin smoke from the exponential attenuation of a laser beam in a tank. They also use a separate mirror setup to directly measure the phase function (see below). In contrast, our setup uses divergent beams from a simple bulb to include more light in the volume (than a single laser beam) for robust measurements, and requires only a single photograph to measure all scattering properties shown in Figure 2.

Numerical solution to inverse light transport: In cases where there are no analytic solutions to light transport, several works have taken a numerical approach to estimate scattering properties [McCormick 1996; Antyufeev 2000]. However, it is widely

known, that inverse problems in radiative transfer that take into account multiple scattering are ill-conditioned and require regularizing assumptions to obtain reliable estimates. See the reports and critiques by McCormick et al [1981; 1985]. Furthermore, the computational complexity of such inverse estimation techniques make it hard for measuring large sets of media for computer graphics or vision applications. Our focus here is on estimating scattering properties of media that can be measured in a state where multiple scattering is negligible.

The observation that single scattering is dominant for optically thin media has been made by [Hawkins et al. 2005; Sun et al. 2005]. We exploit this observation and apply the single scattering model for the first time to a large class of materials which exhibit significant multiple scattering in their natural states of existence. We also determine the exact range of optical thicknesses for which single scattering is dominant for media with arbitrary scattering properties, and propose an experimental procedure to ensure the dominance of single scattering in real data.

Goniophotometry is often used to directly measure the phase function. Here, several detectors measure radiance in different directions after being scattered by a very small volume of the medium. [Fuchs and Jaffe 2002] use thin laser light sheet microscopy for detecting and localizing microorganisms in ocean waters. [Boss and Pegau 2001; Oishi 1990] investigate the relationship of light scattering at a single angle and the extinction coefficient using specialized receivers and transmitters. However, all these techniques assume that there is no attenuation of light through the sample and require expensive devices with precise alignment of detectors and transmitters. In contrast, our setup is extremely simple (consisting of a glass tank and an off the shelf bulb), and our technique robustly estimates all properties from only a single photograph, thus making it inexpensive and easy to measure a large number of participating media.

3 Single Scattering in Dilute Media

Our approach is to measure media in a state where single scattering is dominant and multiple scattering is negligible. This is achieved by diluting the otherwise optically thick media, such as fluids, in water. The process of dilution does not usually corrupt the inherent scattering properties of media[1] since the scattering and absorption of pure water itself is negligible for very small distances (less than 50 cm) [Sullivan 1963]. We begin by presenting our acquisition setup and an image formation model for single scattered light transport within the measurement volume. We will then present extensive simulations of this model and compare with traditional Monte-Carlo approaches that include multiple scattering, to derive a valid space of scattering parameters over which single scattering is dominant. Based on this simulation, we design a simple experimental procedure to choose the best concentration for any particular medium. Later, we will describe our algorithm to estimate the scattering parameters using our image formation model.

3.1 Acquisition Setup

The measurement apparatus, shown in Figure 3, consists of a $25 \times 30 \times 30\,\text{cm}^3$ tank that is filled with the diluted scattering medium. The depth of the tank is large enough to ensure the scattering angles are adequately covered (0 to 175 degrees). The volume of the tank is designed to be large enough to dilute concentrated media such as milk. Two sides of the tank are constructed using anti-reflection glass and the other sides using diffuse black coated acrylic. A small frosted (diffuse) glass bulb fixed to a side

[1] When crystals are dissolved in water, they may exhibit different scattering properties due to ionization.

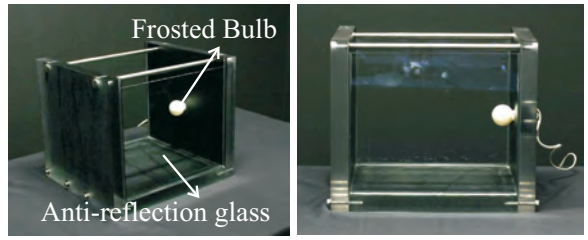

Figure 3: *Two views of the apparatus used to measure scattering properties of water-soluble media. A glass tank with rectangular cross-section is fitted with a small light bulb. The glass is anti-reflection coated. Different volumes of participating media are diluted with water in the tank, to simulate different concentrations. A camera views the front face of the tank at normal incidence to avoid refractions at the medium-glass-air boundaries.*

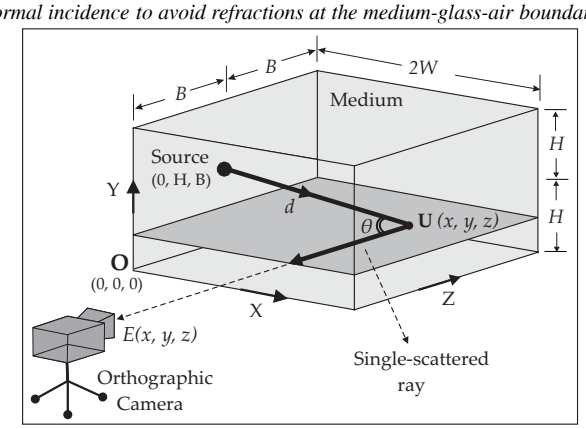

Figure 4: *A volume filled with a homogeneous participating medium and illuminated by an isotropic point light source. A camera views the front face of the volume at normal incidence. The path of one single-scattered ray as it travels from the source to the camera is shown. This ray is first attenuated in intensity over a distance d, is then scattered at an angle $\pi - \theta$, and finally, is attenuated again over a distance z, before reaching the camera. The irradiances due to all the rays that scatter into a viewing direction must be integrated to obtain the final camera irradiance.*

of the tank illuminates the medium. A Canon EOS-20D 12-bit 3504x2336 pixel digital camera with a zoom lens is placed five meters away from the tank and observes a face of the tank at normal incidence. The field of view occupied by the tank in the image is three degrees and is therefore approximately orthographic. Orthographic projection avoids the need for modeling refractions of light rays at the medium-glass-air interfaces. In all our experiments, about 25 different exposures (1/500s to 10s) were used to acquire HDR images.

3.2 Image Formation Model

Although the basic principles of single scattering are well known, the exact nature of the image formation model depends on the geometry of the volume and the locations of the source and the camera. Figure 4 illustrates the illumination and measurement geometry based on our acquisition setup. For simplicity, we will assume that the medium is illuminated by an isotropic point light source (later we extend the analysis to area sources) of intensity I_0 that is located at the coordinates $(0, B, H)$.

Consider the path of one single-scattered light ray (thick ray in Figure 4) in the medium as it travels from the source to the camera. This ray is first exponentially attenuated in intensity for a distance d. At location $\mathbf{U}\ (x, y, z)$, depending on the phase function P, a fraction of the light intensity is scattered at an angle $\pi - \theta$. Finally, the ray is attenuated again for a distance z, before it reaches the camera. Mathematically, the irradiance at the camera produced by

this ray is written as [Sun et al. 2005],

$$E(x,y,z) = \frac{I_0}{d^2} \,.\, e^{-\sigma d} \,.\, \beta P(g,\pi-\theta) \,.\, e^{-\sigma z}.$$
$$d = \sqrt{x^2+(y-H)^2+(z-B)^2} \;,\; \cos\theta = (z-B)/d \quad (1)$$

Here, $P(g,\pi-\theta)$ is the Henyey-Greenstein (H-G) phase function, and β and σ are the scattering and extinction coefficients (Figure 2). Then, the total irradiance E at pixel (x,y) in the camera is obtained by integrating intensities due to all rays that are scattered at various angles along the pixel's line of sight (Z-direction),

$$E(x,y) = \int_0^{2B} E(x,y,z)\,dz$$
$$= \beta \int_0^{2B} \frac{I_0\, e^{-\sigma(z+\sqrt{x^2+(y-H)^2+(z-B)^2})}}{x^2+(y-H)^2+(z-B)^2}\, P(g,\pi-\theta)\,dz. \quad (2)$$

The above equation relates the camera irradiances as a function of the three medium parameters, σ, β and g. Although obtaining an analytic (closed-form) solution to the above integral is hard [Sun et al. 2005], it is straightforward to evaluate it numerically.

3.3 Space of valid medium parameters

Different materials have their own natural densities and scattering properties, which are all unknown before experimentation. So, how do we know if single scattering is dominant at a particular concentration for a given material? Note that the scattering β, absorption κ and extinction σ, coefficients are proportional to the concentration (fraction of volume diluted in water) of the medium. Thus, we performed exhaustive simulations to derive the complete space of parameters for which the above image formation model is accurate[2]. For ground truth, we simulated the irradiances obtained using multiple scattering for the same set of parameter values, using a standard volumetric Monte Carlo technique. Figure 5 shows a plot of the differences between energies captured by the single scattering and multiple scattering simulations for a set of parameter values. From the RMS errors in the plot, we can define the upper bounds on the parameters κ and $\sigma = \beta + \kappa$ as those for which the energy differences between our model and the ground truth are less than five percent. For example, the valid domain where single scattering is dominant, is approximately $\sigma < 0.04$ for $\kappa < 0.004$.

3.4 How to choose the best concentration?

Based on the simulations, we present an experimental method to determine the best concentration for our measurements. Figure 6 shows images acquired of different concentrations of milk and MERLOT. Which among these images should we use to measure the scattering properties? Several heuristics may be used to decide on a particular concentration. For instance, the extent of blurring of the light source provides us a good clue to determine whether multiple scattering is significant (rightmost image in Figure 6). A better heuristic is to compute an approximation to the extinction coefficient σ from the attenuated brightness of the light source. Under single scattering, the radiance in the direction of the source (distance d) can be approximated using exponential attenuation as:

$$E(0) \approx \left(\frac{I_0}{d^2}\right) e^{-\hat{\sigma} d}, \quad (3)$$

[2]This extends the simulations in [Sun et al. 2005], where a small part of the possible parameter space (pure isotropic scattering) was considered.

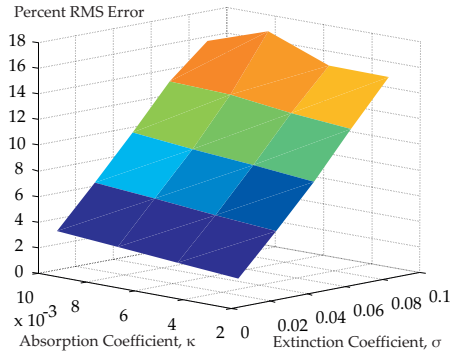

Figure 5: *Plot showing the differences between irradiances obtained by simulating single scattering and multiple scattering (ground truth) models, for a large space of parameter values σ and $\kappa = \sigma - \beta$. An upper bound on the differences of, say, 5%, can be used to define the range of parameters for which single scattering is a valid approximation. From the plot, the valid range is approximately $\sigma < 0.04$ for $\kappa < 0.004$.*

where $\hat{\sigma}$ is an estimate of the extinction coefficient σ. In the absence of multiple scattering, this estimate is closer to the true value of σ (and varies linearly with concentration), whereas, in the presence of multiple scattering, this estimate is called *diffuse or reduced attenuation coefficient* [Ishimaru 1978] and is usually much lesser than σ. Thus, we can determine whether the concentration can be used for measurement by observing the plot (Figure 7 of $\hat{\sigma}$ versus the volume fraction of the medium diluted with water). Figure 7 shows that after a certain amount of milk is added to water, the $\hat{\sigma}$ no longer remains linear with concentration (dashed line), and must not be used for measurements. For a purely absorbing liquid like wine (MERLOT), the plot is completely linear and any image that has the best signal-to-noise ratio may be used. Similarly, the plot shows that coke scatters, albeit weakly, and ESPRESSO coffee scatters light strongly. We use this simple procedure to try several concentrations and observe where the linearity in the plot fails to determine the best concentration. As a further test, we check if the estimated parameters from this concentration lie within the valid space of parameters simulated above.

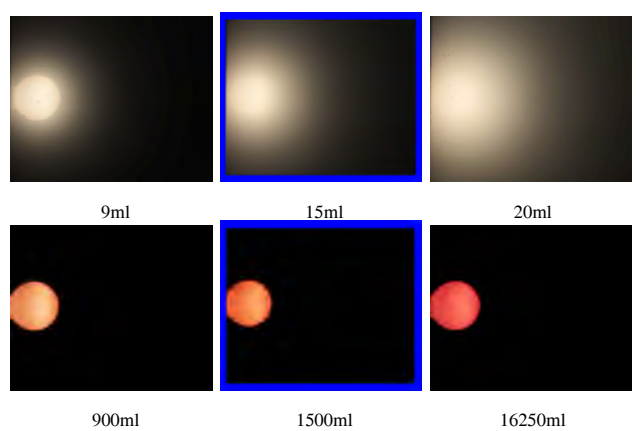

Figure 6: *Images illustrating different degrees of scattering and absorption. [Top row] Images of milk at various concentrations. Since milk is a highly scattering liquid, we observe an increase in blurring with increasing concentration. [Bottom Row] Images of red wine at various concentrations. Red wine is a highly absorbing liquid, showing only a saturation of the bulb color with increasing concentration, and no blurring. The highlighted images are chosen for estimating the parameters.*

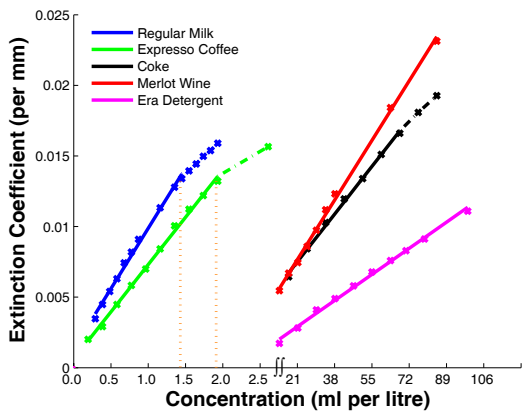

Figure 7: *Plot of extinction coefficient estimate $\hat{\sigma}$ as a function of the volume of the media diluted in water in the measurement apparatus. The plots are linear when multiple scattering is negligible and single scattering is dominant. As the concentrations of media (and hence multiple scattering) increase, the estimated $\hat{\sigma}$ is less than the true extinction coefficient σ. For a highly scattering medium such as milk, the linearity fails at very low concentrations, while for an absorbing medium such as MERLOT, the linearity is always preserved.*

4 Estimating Medium Properties based on Single Scattering

In this section, we present a non-linear minimization algorithm to estimate the properties of the medium (σ, β and g), from the measured image irradiances $E(x,y)$ (see Equation (2)). We then demonstrate the accuracy of the algorithm through extensive simulations.

4.1 Formulating the Error Function

The error at each pixel is written as the difference between the measured irradiance $E(x,y)$ and the irradiance predicted by the model in equation 2,

$$\mathscr{F}(x,y) = E(x,y) - RHS(x,y)\,. \tag{4}$$

Here $RHS(x,y)$ is the numerically evaluated right hand side integral in the model of equation 2. Then, the parameters σ, β and g can be estimated by computing the global minimum of the sum of squares of the errors of all the pixels, as,

$$\min_{\beta,\sigma,g} \sum_y \sum_x \mathscr{F}^2(x,y)\,. \tag{5}$$

The above function essentially requires a 3-parameter search. However, note that the parameter β is a global scale factor. Thus, we can eliminate β by defining a normalized error function as,

$$\mathscr{F}_{norm}(x,y) = \frac{E(x,y)}{\max\limits_{x,y} E(x,y)} - \frac{RHS(x,y)}{\max\limits_{x,y} RHS(x,y)}\,. \tag{6}$$

Now, instead of requiring a 3-parameter search, the above problem can be reduced to a 2-parameter search that minimizes the normalized objective function to estimate σ and g:

$$\min_{\sigma,g} \sum_y \sum_x \mathscr{F}^2{}_{norm}(x,y)\,. \tag{7}$$

Then, the scale factor β can be recovered using the original function $\mathscr{F}$. To compute the global minimum, we use Nelder-Meade search implemented by the Matlab^{TM} function "fminsearch".

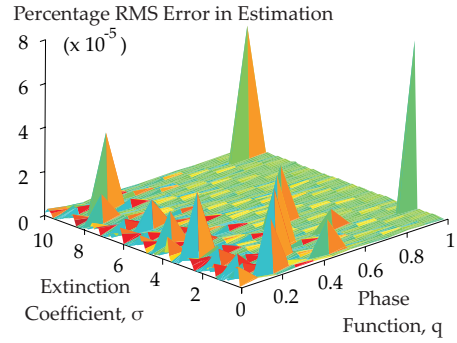

Figure 8: *Plot showing the errors in reconstruction of the single scattering parameters σ and $q = |g|$, where $-1 < g < 1$, compared to ground truth values. The low errors indicate the accuracy of our estimation technique. The maximum of the errors for positive or negative g is shown.*

4.2 Estimation Accuracy using Simulations

Fortunately, since the space of the possible parameters is small (see Section 3.3), exhaustive simulation of the above algorithm is possible. We only show the correctness of the estimated parameters σ and g, using Equation (7). The estimation of the scale factor β then follows trivially. Gaussian noise of unit standard deviation was added in all our simulations. The non-linear search was initialized randomly for both the parameters σ and g. The plot in Figure 8 shows the error in the estimated parameters as compared to ground truth values. In all the cases, the estimation errors were less than 0.0001%, and the number of iterations required for convergence was less than 100. Since the numerical evaluation of the integral is very fast, the time for convergence is usually of the order of a few minutes. This demonstrates that the inverse estimation is fast and results in unique and correct parameters.

4.3 Implementation Issues

We present two issues that need careful implementation for our algorithm to be successful on real images.

Calibrating the area source: Our method does not rely on isotropic point sources but requires only a calibrated divergent source to take advantage of the different phase angles measured in the same view and hence, any off-the-shelf bulb suffices. For our real setup, we have implemented a spherical diffuse area source. To compute the irradiance at any point P within the tank, we sample (using roughly 10x10 samples) the hemisphere of the bulb that is visible to that point P. The non-uniform directional intensities and intensity fall-off were calibrated carefully by using a light meter at discrete 3D locations within the tank. The camera also measures a pure water image (without any scattering or absorption) to give the image irradiance of each source element (sample). This irradiance along with the fall-off value and the pixel solid angle is used to determine the intensity without scattering.

Instabilities in the H-G phase function for highly absorbing media: The H-G phase function was designed for scattering media and is not defined for purely absorbing media. However, for highly absorbing media, the scattering coefficient β is very low and the average cosine $g \approx 1$ since rays only pass straight through, much like highly forward scattering media. Even though this was not a problem in simulations, the instability for $g > 0.95$ can be high in real experiments. For this special case, we simply use a truncated legendre polynomial expansion of the H-G phase function as $P(g,\theta) = \sum_i (2i+1)\, g^i\, L_i(\theta)$, and truncate to less than 100 terms. As an undesirable byproduct the fits may show some "ringing" at the tail of the phase function. However, this truncated function still fits higher brightness well and thus does not affect appearance strongly. Despite this instability, the H-G phase function is flexible enough to model the scattering behavior of all our materials.

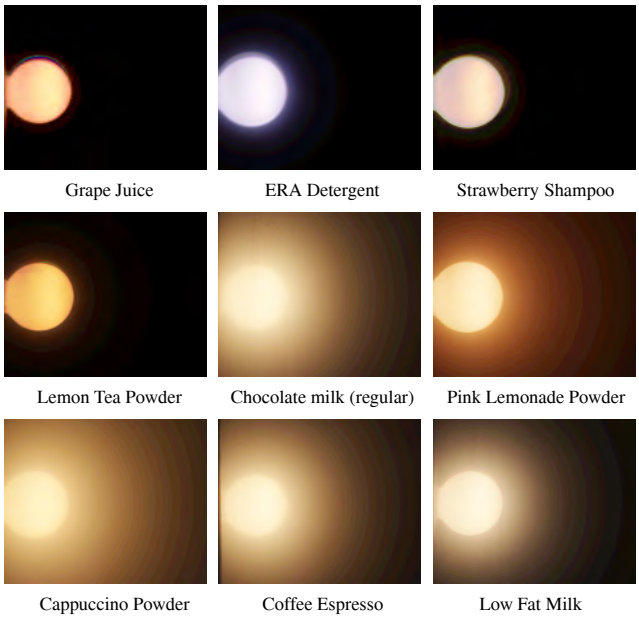

Figure 9: *Captured photographs of a variety of water-soluble media illustrating different degrees of scattering and absorption. For highly scattering media such as milk, chocolate milk and espresso, we observe a significant blur around the bulb. For highly absorbing media such as grape juice, there is very little scattering. All the images have wide dynamic range of intensities and hence, we have tone-mapped them for illustration.* **Please see supplementary material for more images.**

5 Actual Measurements and Validation

Using our approach, we have measured the scattering properties of a broad class of **forty** commonly found participating media that can be either (a) diluted in water such as juices (for example, apple, strawberry, orange), beverages (for example, coffee, soft drinks, milks, wines, beers), cleaning supplies (detergents), or (b) suspended in natural waters such as impurities and organisms, or even (c) dissolved in water such as powders and sugar, salt crystals. In addition to liquids available at the usual supermarkets, we have also collected four samples from different locations and depths in the Pacific ocean. We then present detailed validation by showing that our parameters extrapolate correctly to higher concentrations as well, where multiple scattering is prominent.

A subset of nine photographs of the diluted set of liquids contained in the glass tank is shown in Figure 9, similar to the four in Figure 1. Together, these include representative types of media such as highly scattering, highly absorbing and moderate levels of absorption and scattering. The images show a high dynamic range of brightness and are enhanced to show the scattering effects. The set of scattering parameters for all the media is shown in Table 1. The extinction (σ) and scattering (β) coefficients are given for each of the three color channels, red, green and blue. The phase function parameter g is also shown for the three color channels. Note that all the extinction and scattering coefficients are less than 0.04 in accordance with our simulations in Section 3.3. Also, as expected, in all cases, the scattering coefficient does not increase with wavelength.

5.1 Fits to Measured Brightness Profiles

We demonstrate the accuracy of our technique by reconstructing the photographs using the estimated parameters. Although we considered the brightness at all pixels in the captured photographs, for illustration purposes we show only the profile of intensity values in the direction that is radially outward from the source. Figure 10

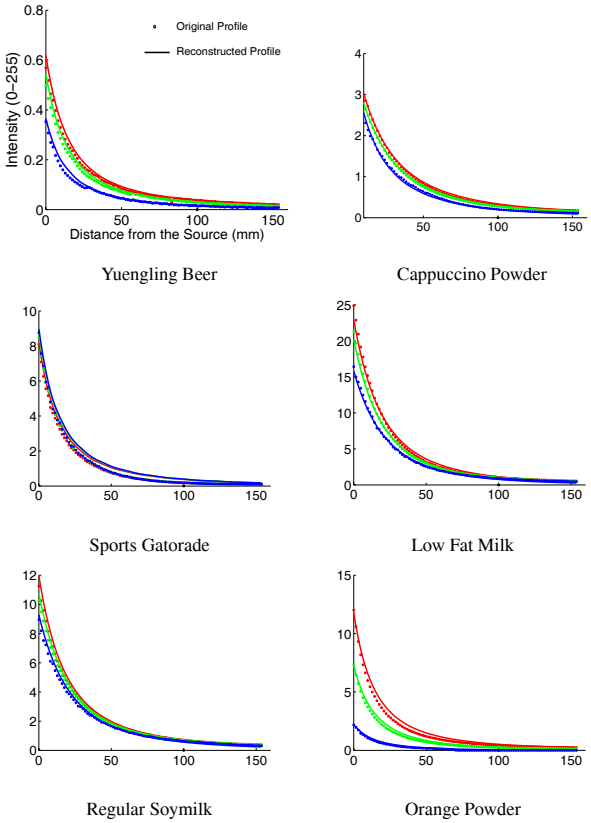

Figure 10: *Fits obtained using the estimated parameters as compared against the corresponding measured brightness profiles in the captured photographs. The brightness profile is measured radially outward from the source in the image. The red, green and blue plots correspond to the three color channels of the camera. The match between the estimated and measured data demonstrates the accuracy of the estimation technique. The fits for six (out of 40) representative materials with varying degrees of absorption and scattering are shown.* **Please see the supplementary material for more plots.**

shows the good fits obtained using the estimated parameters compared against the measured profiles for a subset of six materials of varying degrees of scattering and absorption properties (please review supplementary document for plots of other materials). When there is no scattering (pure absorption), fitting a scattering model can induce some "ringing" effect in the dark tail end of the profile. We can detect this special case and use the attenuation model to compute the absorption coefficient ($\kappa = \sigma$).

5.2 Extrapolation to higher concentrations

The extinction and scattering coefficients are proportional to the concentration of the medium. Thus, if β_1 and σ_1 are estimated at concentration c_1, then the coefficients β_2 and σ_2 at another concentration c_2 can be extrapolated using:

$$\beta_2 = \beta_1 \left(\frac{c_2}{c_1}\right) \ , \ \sigma_2 = \sigma_1 \left(\frac{c_2}{c_1}\right) . \tag{8}$$

Note, however, that g is independent of the medium concentration. While we estimate the parameters from lower concentrations, it is important to ensure that the parameters can be scaled to any concentration (where multiple scattering cannot be ignored) to produce accurate scattering effects. We show an example validation using fits obtained in comparison to the measured brightness profiles of chocolate milk at various concentrations. Figure 11 shows the fits

Material Name	Volume	Extinction Coefficient (σ) ($\times 10^{-2}$ mm^{-1})			Scattering Coefficient (β) ($\times 10^{-2}$ mm^{-1})			Average Cosine (g)			% RMS Error
		R	G	B	R	G	B	R	G	B	
Milk (lowfat)	16ml	0.9126	1.0748	1.2500	0.9124	1.0744	1.2492	0.932	0.902	0.859	0.95
Milk (reduced)	18ml	1.0750	1.2213	1.3941	1.0748	1.2209	1.3931	0.819	0.797	0.746	1.27
Milk (regular)	15ml	1.1874	1.3296	1.4602	1.1873	1.3293	1.4589	0.750	0.714	0.681	1.56
Coffee (espresso)	8ml	0.4376	0.5115	0.6048	0.2707	0.2828	0.2970	0.907	0.896	0.880	1.90
Coffee (mint mocha)	6ml	0.1900	0.2600	0.3500	0.0916	0.1081	0.1460	0.910	0.907	0.914	2.00
Soy Milk (lowfat)	16ml	0.1419	0.1625	0.2740	0.1418	0.1620	0.2715	0.850	0.853	0.842	1.75
Soymilk (regular)	12ml	0.2434	0.2719	0.4597	0.2433	0.2714	0.4563	0.873	0.858	0.832	1.68
Chocolate Milk (lowfat)	10ml	0.4282	0.5014	0.5791	0.4277	0.4998	0.5723	0.934	0.927	0.916	1.04
Chocolate Milk (regular)	16ml	0.7359	0.9172	1.0688	0.7352	0.9142	1.0588	0.862	0.838	0.806	2.19
Soda (coke)	1600ml	0.7143	1.1688	1.7169	0.0177	0.0208	0.0000	0.965	0.972	–	4.86
Soda (pepsi)	1600ml	0.6433	0.9990	1.4420	0.0058	0.0141	0.0000	0.926	0.979	–	2.92
Soda (sprite)	15000ml	0.1299	0.1283	0.1395	0.0069	0.0089	0.0089	0.943	0.953	0.952	3.22
Sports Gatorade	1500ml	0.4009	0.4185	0.4324	0.2392	0.2927	0.3745	0.933	0.933	0.935	3.42
Wine (chardonnay)	3300ml	0.1577	0.1748	0.3512	0.0030	0.0047	0.0069	0.914	0.958	0.975	5.10
Wine (white zinfandel)	3300ml	0.1763	0.2370	0.2913	0.0031	0.0048	0.0066	0.919	0.943	0.972	5.49
Wine (merlot)	1500ml	0.7639	1.6429	1.9196	0.0053	0.0000	0.0000	0.974	–	–	4.56
Beer (budweiser)	2900ml	0.1486	0.3210	0.7360	0.0037	0.0069	0.0074	0.917	0.956	0.982	5.61
Beer (coorslight)	1000ml	0.0295	0.0663	0.1521	0.0027	0.0055	0.0000	0.918	0.966	–	4.89
Beer (yuengling)	2900ml	0.1535	0.3322	0.7452	0.0495	0.0521	0.0597	0.969	0.969	0.975	4.48
Detergent (Clorox)	1200ml	0.1600	0.2500	0.3300	0.1425	0.1723	0.1928	0.912	0.905	0.892	1.99
Detergent (Era)	2300ml	0.7987	0.5746	0.2849	0.0553	0.0586	0.0906	0.949	0.950	0.971	4.17
Apple Juice	1800ml	0.1215	0.2101	0.4407	0.0201	0.0243	0.0323	0.947	0.949	0.945	4.92
Cranberry Juice	1500ml	0.2700	0.6300	0.8300	0.0128	0.0155	0.0196	0.947	0.951	0.974	4.60
Grape Juice	1200ml	0.5500	1.2500	1.5300	0.0072	0.0000	0.0000	0.961	–	–	5.19
Ruby Grapefruit Juice	240ml	0.2513	0.3517	0.4305	0.1617	0.1606	0.1669	0.929	0.929	0.931	2.68
White Grapefruit Juice	160ml	0.3609	0.3800	0.5632	0.3513	0.3669	0.5237	0.548	0.545	0.565	2.84
Shampoo (balancing)	300ml	0.0288	0.0710	0.0952	0.0104	0.0114	0.0147	0.910	0.905	0.920	4.86
Shampoo (strawberry)	300ml	0.0217	0.0788	0.1022	0.0028	0.0032	0.0033	0.927	0.935	0.994	2.47
Head & Shoulders	240ml	0.3674	0.4527	0.5211	0.2791	0.2890	0.3086	0.911	0.896	0.884	1.91
Lemon Tea Powder	5tsp	0.3400	0.5800	0.8800	0.0798	0.0898	0.1073	0.946	0.946	0.949	2.83
Orange Powder	4tbsp	0.3377	0.5573	1.0122	0.1928	0.2132	0.2259	0.919	0.918	0.922	2.25
Pink Lemonade Powder	5tbsp	0.2400	0.3700	0.4500	0.1235	0.1334	0.1305	0.902	0.902	0.904	1.02
Cappuccino Powder	0.25tsp	0.2574	0.3536	0.4840	0.0654	0.0882	0.1568	0.849	0.843	0.926	0.67
Salt Powder	1.75cup	0.7600	0.8685	0.9363	0.2485	0.2822	0.3216	0.802	0.793	0.821	1.34
Sugar Powder	5cup	0.0795	0.1759	0.2780	0.0145	0.0162	0.0202	0.921	0.919	0.931	1.80
Suisse Mocha Powder	0.5tsp	0.5098	0.6476	0.7944	0.3223	0.3583	0.4148	0.907	0.894	0.888	1.33
Mission Bay Surface Water (1-2 hours)		3.3623	3.2929	3.2193	0.2415	0.2762	0.3256	0.842	0.865	0.912	2.48
Pacific Ocean Surface Water (1 hour)		3.3645	3.3158	3.2428	0.1800	0.1834	0.2281	0.902	0.825	0.914	2.57
Mission Bay 10ft deep Water (30 min)		3.4063	3.3410	3.2810	0.0990	0.1274	0.1875	0.726	0.820	0.921	5.10
Mission Bay 10ft deep Water (8 hours)		3.3997	3.3457	3.2928	0.1018	0.1033	0.1611	0.929	0.910	0.945	5.13

Table 1: Scattering properties for 40 different water-soluble materials estimated using our technique. The second column lists the volumes V of the materials dissolved in $23-V$ litres of water to achieve the desired levels of dilution where single scattering is dominant. These parameters can be proportionately scaled to any other volume V_n, using a scale factor of V_n/V. The percentage RMS errors (obtained over all pixels) quantify the accuracy of fits achieved with the estimated parameters to the measured intensity profiles. Errors for all the highly scattering media are less than 3%. For low-scattering materials, the total intensity of profiles is relatively low, thus making the estimation more sensitive to noise. Even for such low-scattering media, the errors are less than $5-6\%$. The last four rows are the parameters for various ocean water samples at their original concentrations. The **time elapsed** between the collection of samples and the image acquisition is listed in the parentheses. Since the suspended particles in ocean water settle down with time, we observe a small decrease in scattering coefficients in the sample for which 8 hours had been elapsed as compared to the one which was imaged just 30 minutes after collection. Note that all the extinction and scattering coefficients are less than 0.04 in accordance with our simulations in Section 3.3. As expected, the scattering coefficients do not decrease with wavelength. The scattering albedos (ratio of scattering coefficients to the extinction coefficients) is much higher for the scattering media (milk, coffee, orange powder) as compared to the absorbing ones (coke, wine). For materials that have $\beta = 0$, the phase function parameter g is undefined. As seen from the values of g which are closer to 1, several media are predominantly forward scattering. The parameters for the milks match those in [Jensen et al. 2001] up to a scale factor (due to the different fat contents in the milks used), providing further support for our estimation.

in this validation experiment. First, we estimate the parameters from the photograph of only 8ml of chocolate milk diluted in water, where single scattering is dominant. In (a), we show the fit obtained compared against the measured intensity profile. However, for higher concentrations of 50ml, 100ml and 150ml, multiple scattering cannot be ignored. For these cases, we scaled the coefficients (σ and β) by factors of $\{50/8, 100/8, 150/8\}$ (see Equation 8) and use them in a standard volumetric Monte Carlo renderer that includes multiple scattering. The plots in (b) - (d) demonstrate the strong fits obtained. This demonstrates that our parameters are robust enough to be extrapolated to higher concentrations. In fact, we will show renderings of most of the liquids at their natural concentrations (Section 6) despite measuring the parameters at significantly dilute states.

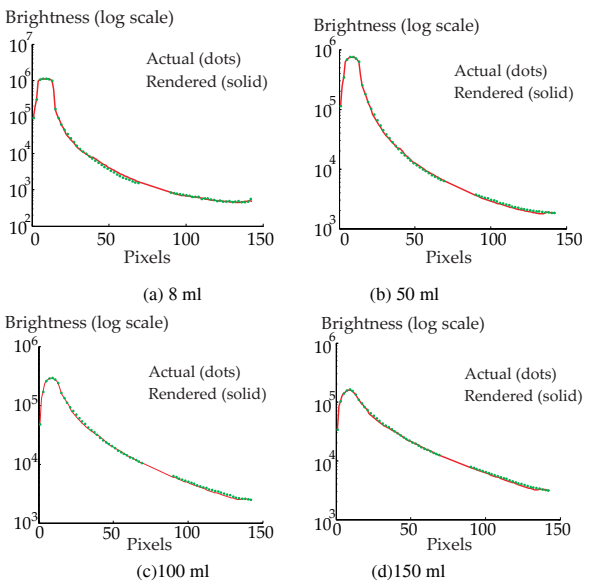

Figure 11: *Extrapolation of parameters to higher concentrations with multiple scattering. (a) 8 ml of chocolate milk is diluted in water and the parameters are estimated using the measured brightness profile. (b) - (d) The parameters estimated in (a) are scaled to higher concentrations (50ml, 100ml and 150ml) where multiple scattering cannot be ignored. Plots show a good fit between the brightness profile obtained by extrapolating our estimated parameters with a Monte Carlo renderer, and the ground truth measurements. The fits are shown in logarithmic scale.*

Figure 12: *Rendered scenes of liquids in a cognac glass under complex lighting. The KITCHEN environment map [Debevec 1998] was used for the lighting. The natural colors, shading and caustics indicate the high accuracy of our parameters.*

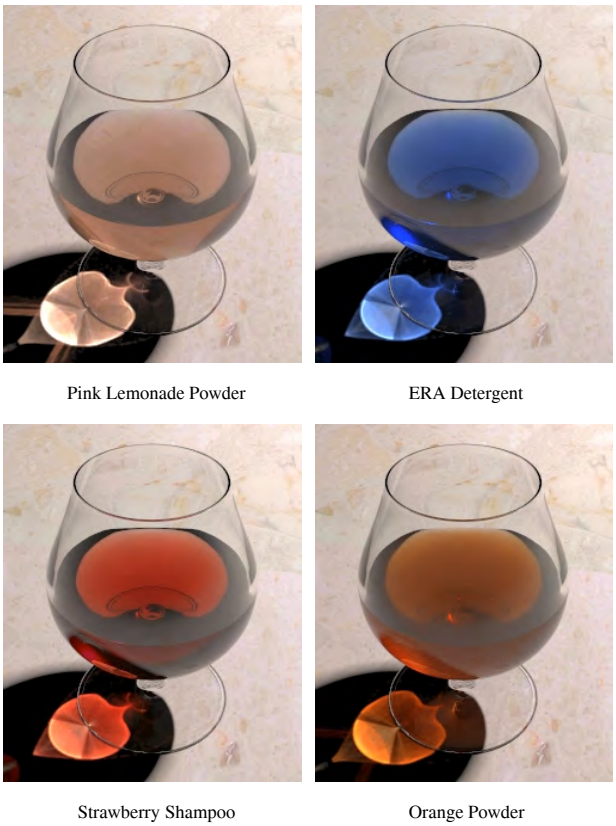

Figure 13: *Rendered scenes of liquids and powders in a cognac glass illuminated with a single directional white light source. The bright caustics show the colors transmitted through the media.*

6 Example Volumetric Renderings

The scattering properties estimated in this work can be input to any volumetric rendering algorithm to create visual effects of participating media. Here, we chose brute-force volumetric Monte-Carlo path tracing since it can be used to render arbitrary materials[3]. We use photon mapping for rendering caustics. For display purposes, we have applied a tone-mapping operator [Ward-Larson et al. 1997] to the renderings. Indices of refraction (IOR) of these media are also important for rendering. In initial experiments, we found the IOR to be between 1.33 (water) and 1.42 (milk) and varying linearly with concentrations, by using location of total internal reflection from the top of the water surface in the tank. In current renderings, we have simply used an IOR proportionate to the medium concentrations between 1.33 and 1.42, since this does not alter the visual appearance of the liquid drastically. We wish to perform thorough experiments in the future.

Figure 12 shows a mosaic of images of liquids rendered in their natural concentrations, partially filled in a cognac glass and illuminated by the "Kitchen Environment Map" [Debevec 1998]. These include two different types of wine (deep red MERLOT and golden-yellow CHARDONNAY), dark brown coffee ESPRESSO, and the golden-orange YUENGLING beer. Notice the color differences between MERLOT (no scattering) and ESPRESSO (moderate scattering) even though both of them are dark liquids. Observe that while beer and CHARDONNAY are very clear liquids, coffee is noticeably more opaque. Similarly, Figure 13 shows a mosaic of predominantly bright colored liquids such as the deep

[3]Under-sampling of path-traces can cause speckle noise seen in the renderings, and is not an artifact of our estimation.

Figure 14: *Effect of changing concentrations of a highly absorbing (MERLOT) and a highly scattering (milk) liquid. In the case of wine, notice that while the color gradually becomes deep red, the liquid remains clear, due to the lack of scattering. In the case of milk, however, we see a quick transition from a murky appearance to a soft white appearance, due to the high scattering albedo of milk.*

blue ERA detergent, the reddish strawberry shampoo, and powders dissolved in water such as the "pinkish" strawberry lemonade and orange powders. These images are illuminated only by a strong directional source to illustrate the bright caustics whose colorings are primarily due to absorption. We also present different types of novel visual effects obtained by changing or blending the parameters of different media to create realistic images of dilutions and mixtures of the original measured materials.

Effect of changing concentrations: Figure 14 illustrates the effects of changing concentrations of media in water. The top row shows a transition from pure water to MERLOT, obtained by scaling parameters of wine as in Equation 8. Notice the changes in caustics and the gradual deepening of the red color of the liquid. Note that as the transition occurs, the liquid remains clear even though the color changes; this is due to the pure absorbing nature of wine, as depicted by our parameters. The bottom row shows the effect of changing milk concentration in water. Since milk is a highly scattering medium, as expected, the appearance quickly changes from murky whitish water to soft and thick white milk. This is because the scattering albedo β/σ is high and the phase function parameter g is such that a significant amount of light diffuses into different directions.

Blending parameters for mixtures of media: For example, what are the properties of a mixture of ESPRESSO and milk, or otherwise known as *light coffee*? Consider a medium containing a mixture of two types of media, A and B. The properties of the individual media are denoted with the subscripts A and B. The scattering coefficient of the mixture is obtained by a weighted average,

$$\beta_{mix} = \frac{V_A\beta_A + V_B\beta_B}{V_A + V_B}\,. \tag{9}$$

The absorption and extinction coefficients are similarly defined. Unlike above where we just changed the scattering and absorption coefficients, here a new phase function parameter must be defined for the mixture as the weighted average [Key 2005],

$$g_{mix} = \frac{g_A\beta_A + g_B\beta_B}{\beta_{mix}}\,. \tag{10}$$

These equations can be used to render mixtures of participating media or morph from one medium into another. Figure 15 shows mixing of different proportions of milk and wine. The second example shows a more common mixing of milk and coffee. Such mixing between materials, for the first time, gives a user the flexibility to create novel renderings of participating media.

7 Conclusion

Rendering the rich visual effects of participating media, like fluids or underwater impurities, requires precise measurements of their scattering properties. In this paper, we have developed a simple device and method for accurately estimating the scattering properties of a variety of media that can be diluted in water. Our approach only requires a single high dynamic range photograph. By diluting the medium, we work in the single scattering regime, where the inverse light transport problem is well conditioned—however, we can later render at arbitrary concentrations and even mix materials. We have presented a database of scattering parameters for 40 commonly found materials. This database is the first of its kind, and enables computer graphics practitioners to accurately render a wide variety of participating media, rather than having to set parameters in an ad-hoc fashion. In the future, we would like to improve this work by investigating different phase functions and measuring indices of refraction more accurately.

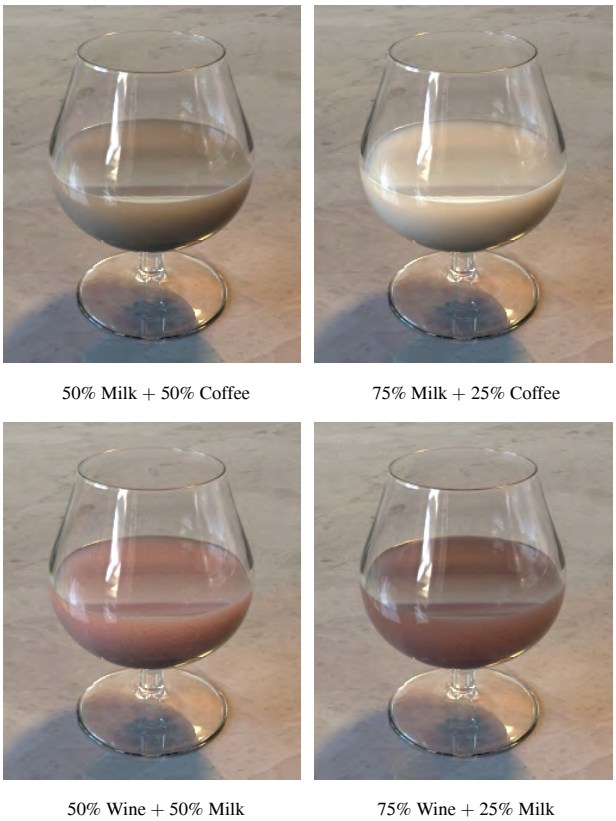

Figure 15: *Mixing two liquids - milk and coffee (top) and milk and wine (bottom), in different proportions. The wine-milk combination produces a soft pink appearance while the ESPRESSO-milk combination produces soft but brown appearance. (Minor noise due to Monte-Carlo under-sampling.)*

Acknowledgements: This work was supported by NSF Grants 0541307, 0305322, 0446916 and 0305399, and an ONR grant N00014-05-1-0188. Ramamoorthi, Jensen and Donner were supported also by Sloan Fellowships. The authors thank Terrence Boult for ocean water samples, Chao-Kuo Lin for help with experiments, and Simon Premoze for early discussions.

References

ANTYUFEEV, S. 2000. *Monte Carlo Method for Solving Inverse Problems of Radiative Transfer*. Inverse and Ill-Posed Problems Series, VSP Publishers.

BOSS, E., AND PEGAU, W. S. 2001. Relationship of light scattering at an angle in the backward direction to the backscattering coefficient. *Applied Optics 40 (30)*, 5503–5507.

CHANDRASEKHAR, S. 1960. *Radiative Transfer*. Oxford University Press.

DANA, K., NAYAR, S., VAN GINNEKEN, B., AND KOENDERINK, J. 1997. Reflectance and texture of real-world surfaces. In *Proc CVPR*, 151–157.

DEBEVEC, P. 1998. Rendering synthetic objects into real scenes: Bridging traditional and image-based graphics with global illumination and high dynamic range photography. *Proc. SIGGRAPH 98*, 189–198.

FINSY, E. G., AND JOOSTEN, J. 1991. Maximum entropy inversion of static light scattering data for the particle size distribution by number and volume. In *Advances in measurements and control of colloidal processes. Butterworth-Heineman, Ch. 30*.

FUCHS, E., AND JAFFE, J. S. 2002. Thin laser light sheet microscope for microbial oceanography. *OPTICS EXPRESS 10 (2)*, 145–154.

HAWKINS, T., EINARSSON, P., AND DEBEVEC, P. 2005. Acquisition of time-varying participating media. *ACM Trans. on Graphics (SIGGRAPH) 24*, 3, 812–815.

HENYEY, L., AND GREENSTEIN, J. 1941. Diffuse radiation in the galaxy. vol. 93, 70–83.

HULST, V. D. 1957. *Light Scattering by small Particles*. John Wiley and Sons.

ISHIMARU, A. 1978. *Wave Propagation and Scattering in Random Media. Volume 1: Single Scattering and Transport Theory*. Academic Press.

JAEGER, D., DEMEYERE, H., FINSY, R., SNEYERS, R., VANDERDEELEN, J., VAN-DER-MEEREN, P., AND VAN-LAETHEM, M. 1991. Particle sizing by photon correlation spectroscopy. part i: Monodisperse latices: influence of scattering angle and concentration of dispersed material. In *Part. Syst. Charact. 8, 179*.

JENSEN, H., MARSCHNER, S., LEVOY, M., AND HANRAHAN, P. 2001. A practical model for subsurface light transport. In *Proc. SIGGRAPH 01*, 511–518.

KEY, J. R. 2005. Streamer: User's guide. *Tech Report, NOAA/NESDIS, Madison, Wisconsin*.

MARSCHNER, S. 1998. Inverse rendering for computer graphics. *PhD Thesis, Cornell University*.

MATUSIK, W., PFISTER, H., BRAND, M., AND MCMILLAN, L. 2003. A data-driven reflectance model. *ACM Trans. on Graphics (SIGGRAPH) 22*, 3, 759–769.

MCCORMICK, N. J. 1981. A critique of inverse solutions to slab geometry transport problems. *Prog. Nucl. Energy 8*.

MCCORMICK, N. J. 1985. Sensitivity of multiple-scattering inverse transport methods to measurement errors. *JOSA A 2*.

MCCORMICK, N. J. 1996. Analytical transport theory applications in optical oceanography. *Annals of Nuclear Energy 23*, 381–395.

NARASIMHAN, S. G., AND NAYAR, S. K. 2003. Shedding light on the weather. In *CVPR 03*, 665–672.

OISHI, T. 1990. Significant relationship between the backward scattering coefficient of sea water and the scatterance at 120 degrees. *Applied Optics 29 (31)*, 4658–4665.

PRAHL, S. A. 1988. Light transport in tissue. *PhD Thesis, University of Texas at Austin*.

RAMAMOORTHI, R., AND HANRAHAN, P. 2001. A signal processing framework for inverse rendering. *Proc. SIGGRAPH 01*, 117–128.

SULLIVAN, S. A. 1963. Experimental study of the absorption in distilled water, artificial sea water, and heavy water in the visible region of the spectrum. *JOSA 53*.

SUN, B., RAMAMOORTHI, R., NARASIMHAN, S. G., AND NAYAR, S. K. 2005. A practical analytic single scattering model for real time rendering. *ACM Trans. on Graphics (SIGGRAPH) 24*, 3, 1040–1049.

WARD-LARSON, RUSHMEIER, H., AND PIATKO. 1997. A visibility matching tone reproduction operator for high dynamic range scenes. *IEEE Trans. on Visualization and Computer Graphics 3*, 4, 291–306.

Eurographics Symposium on Rendering (2005)
Kavita Bala, Philip Dutré (Editors)

Non-Linear Volume Photon Mapping

Diego Gutierrez†, Adolfo Munoz, Oscar Anson and Francisco J. Seron

GIGA, Universidad de Zaragoza, Spain

Abstract

This paper describes a novel extension of the photon mapping algorithm, capable of handling both volume multiple inelastic scattering and curved light paths simultaneously. The extension is based on the Full Radiative Transfer Equation (FRTE) and Fermat's law, and yields physically accurate, high-dynamic data than can be used for image generation or for other simulation purposes, such as driving simulators, underwater vision or lighting studies in architecture. Photons are traced into the participating medium with a varying index of refraction, and their curved trajectories followed (curved paths are the cause of certain atmospheric effects such as mirages or rippling desert images). Every time a photon is absorbed, a Russian roulette algorithm based on the quantum efficiency of the medium determines whether the inelastic scattering event takes place (causing volume fluorescence). The simulation of both underwater and atmospheric effects is shown, providing a global illumination solution without the restrictions of previous approaches.

Categories and Subject Descriptors (according to ACM CCS): I.3.7 [Computer Graphics]: Three-Dimensional Graphics and Realism

1. Introduction

Simulation of nature has always been one of the loftiest goals of computer graphics, providing a rich range of visual phenomena. Most of the times, the effect to be reproduced can be faked using a top-down approach, where the final desired result guides the implementation. This usually turns out relatively fast, ad-hoc methods that yield more than acceptable results. However, a physically correct simulation is necessary in certain fields where accuracy is a must. Underwater vision, driving simulators, the military, architectural lighting design etc. are fields where it is not enough to render an image which resembles reality. Predictive algorithms must be developed instead, where the image is the final visualization of the physically correct data generated. A bottom-up approach is then necessary: first, the basic laws of physics that govern the phenomenon need to be described and fed to the rendering system; the phenomenon itself will just be the logical, inevitable output. This approach sacrifices rendering speed in exchange for reliable, physically accurate numerical data that can be used for purposes beyond image generation.

Two of the greatest sources of visually appealing phenomena in nature are participating media and a varying index of refraction. Participating media are the cause of such well-known effects such as fog, clouds or blurry underwater vision, whereas a varying index of refraction yields mirages, rippling images, twinkling stars or some spectacular sunsets. Sources of inelastic scattering in ocean waters can greatly affect visibility and alter its color, whereas distortions caused by temperature differences can further alter the perception of things in such environment. Simulating underwater rescue missions, laying submarine data cables or even the correct interpretation of ancient World Heritage sites can benefit from an accurate description of light that includes an ampler range of phenomena.

We present in this paper a physically-based spectral simulation of light, solving the Full Radiative Transfer Equation (FRTE) and applying Fermat's law, which includes multiple inelastic scattering as well as an accurate description of the non-linear paths followed by the light rays in media with a varying index of refraction. It is based on an extension of the volume photon map algorithm presented by Wann Jensen and Christensen [JC98]. The main contributions are a full global illumination solution which supports non-linear light

† e-mail: diegog@unizar.es

paths and is free of the restrictions of previous works, and the physically-correct simulation of volume fluorescence in participating media, caused by inelastic scattering, including efficient computation of caustics. Atmospheric effects and underwater imagery are simulated as case studies to demonstrate the algorithm. To our knowledge, there is no previous research in computer graphics literature that models together physically-based inelastic scattering in participating, inhomogeneous media where the index of refraction varies continuously. Related previous works therefore span two different categories: inelastic scattering in participating media and non-linear light propagation.

Rendering participating media is not a new field in computer graphics, and an exhaustive review can be found in [PPS97]. There are two types of scattering events in a participating medium: *elastic* scattering, where no transfer of energy occurs between wavelengths, and *inelastic* scattering, where such energy transfers do occur, from shorter to longer wavelengths. Spectral global illumination algorithms that handle participating media only take into account elastic scattering, with the strategy consisting on decoupling the solutions for each sampled wavelength, then adding them to obtain the final image. No interaction between wavelengths is computed. To the authors' knowledge, the only previous work that simulates volume inelastic scattering in participating media is owed to Cerezo and Seron [CS03], using a discrete ordinate method. Unfortunately their method requires both rectangular meshing of the geometry, as well as an angular and spatial discretization which imposes high memory requirements, thus limiting the complexity of the scenes that can be reproduced (the problem is aggravated when simulating highly anisotropic scattering). They also cannot provide a full solution, failing to render caustics. Surface inelastic scattering works include [Gla95b] or [WTP01], but their methods are not extensible to participating media.

With respect to non-linear ray tracing, the first method to deal with non-straight light paths is owed to Berger et al. [BTL90], refracting the ray according to Snell's law in each of a series of flat homogeneous layers, thus achieving a piece-wise linear approximation of a curved path. This was challenged by Musgrave [Mus90], who develops a purely reflective model where rays follow a parabolic path, following the Kuhlar/Fabri physical model [FFLV82]. A more general approach to non-linear ray tracing is proposed by Gröller [Grö95], although the work does not study the influence of the index of refraction in the curvature of the rays, visualizing mathematical and physical systems instead. In the paper by Stam and Languenou [SL96], the authors use geometrical optics to describe how light bends if the index of refraction of the medium varies continuously. They nevertheless fail to provide a physically-based analytical expression for the index of refraction as a function of temperature and wavelength, and solve the equations only for two specific cases, thus losing generality. Seron et al. [SGGC05] implement a method of curved ray tracing capable of simulating the inferior mirage and some sunset effects, although they do not attempt to calculate any lighting, deforming pre-lit textures instead. In [HW01] gravitational light bending is visualized according to the theory of general relativity, whereas other relativity- and physics-related papers include the bending caused by neutron stars or black holes [Nem93], so they cannot (nor pretend to) simulate the phenomena described in this paper. Yngve et al. [YOH00] describe a simple method to simulate the bending of light by interpolating a density field, but they need to exaggerate the variation of the index of refraction tenfold for the effect to be visible.

The paper is organized as follows: section 2 provides the physically-based background, with an overview of inelastic scattering, the FRTE and the Fermat's law. In section 3 we describe our extension of the volume photon map algorithm to include inelastic scattering and curved light paths, with sections 4 and 5 providing case studies of underwater imagery and atmospheric effects respectively. The discussion of the results and some additional images are presented in section 6, to finish the paper in section 7 with the conclusions and future work.

2. Physically-based Framework

We now present the physical framework of our work, by first introducing what inelastic scattering is, then deriving the FRTE that needs to be solved to account for it. In order to be able to compute non-linear light paths, we will use Fermat's law to obtain the correct trajectories.

2.1. Inelastic scattering

Inelastic scattering implies an energy transfer from wavelength λ' to λ, with $\lambda' < \lambda$ within the visible spectrum, and gives rise to fluorescence and phosphorescence phenomena. Fluorescence occurs when a molecule absorbs a photon of wavelength λ' (called excitation wavelength), and re-emits it at a longer wavelength λ according to a *fluorescence efficiency function* $P_f(\lambda)$. The time lapse between the two events is 10^{-11} to 10^{-8} seconds, so for computer graphics it can be taken as an instantaneous process. For pure substances, re-emission is isotropic and the wavelength of the re-emitted photons is independent of the different excitation wavelengths, although the intensity of the re-emission does depend on them. Phosphorescence is a similar process, governed by the *phosphorescence efficiency function*, with the main difference being that the re-emitted energy declines with time according to a function $d(t)$.

2.2. Full Radiative Transfer Equation

Usually, participating media algorithms solve the integro-differential Radiative Transfer Equation (RTE), which takes into account emission, absorption and elastic scattering, but

does not yield a solution for inelastic scattering events. Following the notation in [JC98], and reformulating to include wavelength dependencies, the RTE can be written as:

$$\frac{\partial L_\lambda(x,\overrightarrow{w})}{\partial x} = \alpha_\lambda(x)L_{e,\lambda}(x,\overrightarrow{w}) + \sigma_\lambda(x)L_{i,\lambda}(x,\overrightarrow{w}) - \alpha_\lambda(x)L_\lambda(x,\overrightarrow{w}) - \sigma_\lambda(x)L_\lambda(x,\overrightarrow{w}) \quad (1)$$

where $\frac{\partial L(x,\overrightarrow{w})}{\partial_x}$ represents the variation of radiance L at a point x in the direction $\overrightarrow{w}$, α and σ are the absorption and scattering coefficients, L_e is the emitted radiance and L_i is the in-scattered radiance. Defining the extinction coefficient as $\kappa_\lambda(x) = \alpha_\lambda(x) + \sigma_\lambda(x)$ and integrating $L_{i,\lambda}$ over the sphere Ω we get:

$$\frac{\partial L_\lambda(x,\overrightarrow{w})}{\partial x} = \alpha_\lambda(x)L_{e,\lambda}(x,\overrightarrow{w}) + \sigma_\lambda(x)\int_\Omega p_\lambda(x,\overrightarrow{w}',\overrightarrow{w})L_\lambda(x,\overrightarrow{w}')d\overrightarrow{w}' - \kappa_\lambda(x)L_\lambda(x,\overrightarrow{w}) \quad (2)$$

which is the integro-differential, wavelength-dependent RTE governing the transport of light in participating media, with $p_\lambda(x,\overrightarrow{w}',\overrightarrow{w})$ being the phase function that defines the re-emission direction. However, this equation does not account for energy transfers between wavelengths, the phenomenon known as inelastic scattering. To be able to compute these inelastic scattering events, we need to develop the RTE equation further, by adding a term that accounts for such energy transfers. This term can be expressed as a double integral over the domains of the solid angle and wavelength:

$$\int_\Omega \int_\lambda \alpha_{\lambda_i}(x) f(x,\lambda_i \to \lambda) L_{\lambda_i}(x,\overrightarrow{w}') \frac{p_\lambda(x,\overrightarrow{w}'_i,w)}{4\pi} d\overrightarrow{w}_i d\lambda_i \quad (3)$$

where α_{λ_i} is the absorption coefficient for wavelength λ_i (remember there is no inelastic scattering without previous absorption), $f(x,\lambda_i \to \lambda)$ is the function that governs the efficiency of the energy transfer between wavelengths, defined as the probability of a photon of λ_i being re-emitted at λ. For fluorescence and phosphorescence, this phase function is isotropic [Mob94]. Adding this term to the RTE (equation 2) we obtain the FRTE:

$$\frac{\partial L_\lambda(x,\overrightarrow{w})}{\partial x} = \alpha_\lambda(x)L_{e,\lambda}(x,\overrightarrow{w}) + \sigma_\lambda(x)\int_\Omega p_\lambda(x,\overrightarrow{w}',\overrightarrow{w})L_\lambda(x,\overrightarrow{w}')d\overrightarrow{w}' - \kappa_\lambda(x)L_\lambda(x,\overrightarrow{w}) + \int_\Omega \int_\lambda \alpha_{\lambda_i}(x) f(x,\lambda_i \to \lambda) L_{\lambda_i}(x,\overrightarrow{w}') \frac{p_\lambda(x,\overrightarrow{w}'_i,w)}{4\pi} d\overrightarrow{w}_i d\lambda_i \quad (4)$$

which is the equation that must be solved to take into account multiple inelastic scattering in participating media, thus being able to render volume fluorescence effects.

2.3. Varying index of refraction in inhomogeneous media

A varying index of refraction n_λ defines an inhomogeneous medium where light travels in curved paths. These curved paths result in a distorted image, with the mirages being probably the best known manifestation of the effect. To be able to simulate this type of inhomogeneous medium, we therefore need to obtain the curved trajectory of light as it traverses it. The direction $\overrightarrow{w}$ in equation 4 therefore needs to be recomputed at each differential step, accounting for the changes in n_λ. We obtain this corrected direction at each step by solving Fermat's law, which defines how light traverses one given medium.

The following derivation of Fermat's law uses the work of Gutierrez et al. [GSMA04] and is not meant to be exhaustive. As stated in [Gla95a], *a ray of light, when travelling from one point to another, follows a path that corresponds to a stationary value of the optical path length* (OPL). The OPL is defined as the index of refraction times the travelled path (or the distance the light would have travelled in a vacuum during the flight time through the material), and in its differential form it can be formulated as $d(OPL) = ndl$, where l is the path travelled by the light ray. The equation shows how light gets bent towards the areas with a greater index of refraction, as Snell's law also predicts for the boundary of two homogeneous media. A stationary value corresponds to a maximum or a minimum in the function, thus the derivative equals zero. We can therefore write:

$$\delta(OPL) = \delta\int_A^B ndl = \int_A^B \delta ndl + \int_A^B n\delta(dl) = \int_A^B \frac{\delta n}{\delta x_i}\delta x_i dl + \int_A^B n\delta(dl) = 0 \quad (5)$$

where x_i are the vector components of l. Considering dx_i as variables and taking increments we get $\delta(dl) = \frac{dx_i}{dl}\delta(dx_i)$. Since light trajectories start and end at the stationary points A and B, we get $\delta x_i(A) = 0$ and $\delta x_i(B) = 0$. Equation 5 then results:

$$\delta L = \int_A^B \left[\frac{\partial n}{\partial x_i} - \frac{d}{dl}\left(n\frac{dx_i}{dl}\right)\right]\delta x_i dl = 0 \quad (6)$$

Since this equation must hold for any value of δx_i, the integrand must equal zero, so we finally come up with the equation that must be solved to obtain the path followed by light while traversing any medium, as a function of the index of refraction at each point:

$$\frac{d}{dl}\left(n\frac{d\overrightarrow{r}}{dl}\right) - \nabla n = 0 \Leftrightarrow \frac{d}{dl}\left(n\frac{dx_j}{dl}\right) - \frac{\partial n}{\partial x_j} = 0\,(j = 1,2,3) \quad (7)$$

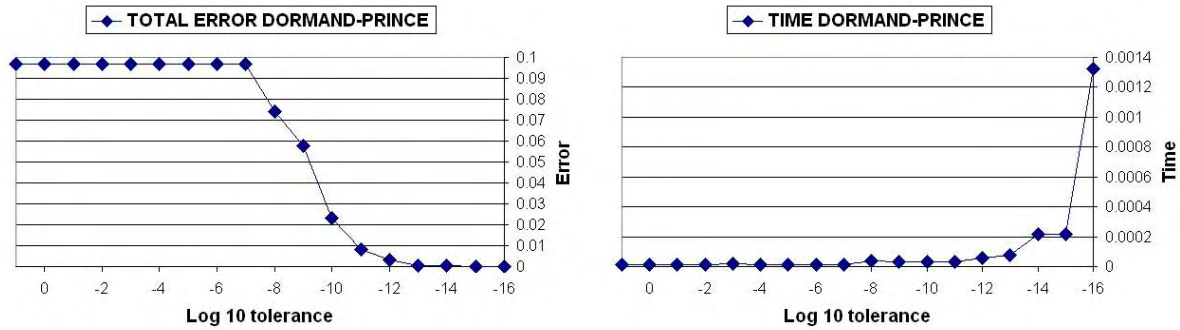

Figure 1: *Error and rendering time (secs.) as functions of the error tolerance in the Dormand-Prince RK5(4)7M method for a test scene.*

where $\vec{r} = x_j$ are the coordinates (x, y, z) of each point. This equation cannot be solved analytically, and thus we must apply a numerical method. We now need to rewrite equation 7 in order to solve it in a more efficient way than the Euler method presented in [GSMA04]:

$$\frac{d^2 x_j}{dl^2} = \frac{1}{n}\left(\frac{\partial n}{\partial x_j} - \frac{dn}{dl}\frac{dx_j}{dl}\right) \tag{8}$$

Doing the change of variable $y_j = \frac{dx_j}{dl}$ we obtain:

$$y_j' = \frac{1}{n}\left(\frac{\partial n}{\partial x_j} - \frac{dn}{dl} y_j\right) \tag{9}$$

where $\frac{dn}{dl} = \frac{dn}{dx_j}\frac{dx_j}{dl}$. The change of variable can also be written as:

$$x_j' = y_j \tag{10}$$

Equations 9 and 10 define a system where x_j represents the position and y_j the velocity at a given point in the trajectory, which can be written in matrix form as:

$$\begin{pmatrix} x_j \\ y_j \end{pmatrix}' = \begin{pmatrix} y_j \\ \frac{1}{n}\left(\frac{\partial n}{\partial x_j} - \frac{dn}{dl} y_j\right) \end{pmatrix} \tag{11}$$

This equation 11 has the form $Y' = f(l, Y)$, which defines an Initial Value Problem with $Y(0) = \alpha$. We solve this problem by applying the embedded Runge-Kutta method RK5(4)7M from the Dormand-Prince family. A detailed description of the method and the error tolerance can be found in [DP80].

We have tested the implementation in a simple scene where the index of refraction varies according to the equation $n = 1 + ky$, with y representing height, and k varying from -0.1 to 0.1. This distribution of n can be solved analytically, so we can measure the numerical error against the exact solution. Figure 1 shows the error of the Dormand-Prince RK5(4)7M method as the tolerance is reduced, along with the time it takes to reach the solution. As it can be seen, error tolerances in the range of 10^{-8} to 10^{-12} yield good results without much of a time penalty. Error tolerances beyond 10^{-14} start increasing rendering times considerably.

3. Extension of the Volume Photon Mapping Algorithm

Ray tracing techniques involve shooting rays into the scene from the camera and following them to detect hits with the geometry, then shooting shadow rays to the lights to find out direct illumination. With curved light paths this turns out to be highly impractical, though, since finding the ray with the physically-correct curvature which goes from the intersection point to the light is computationally very expensive (or the solution might not even exist). Groeller [Grö95] proposes three solutions: considering shadow rays to follow straight paths, retrieving all lighting information straight from the textures, and finally voxelizing the space and prestoring the approximated incident directions of light sources for each voxel, by launching rays from the light sources into the scene prior to the render pass. The first two are clearly not physically-based, while the third only approximates the solution with a preprocessing step.

In order to obtain a physically-based solution for multiple inelastic scattering in inhomogeneous media with a varying index of refraction n, we have extended the volume photon mapping algorithm [JC98] to account both for volume fluorescence and the distortions caused by the changing n.

For inelastic scattering, we need to model the possibility of an absorbed photon being re-emitted at a different wavelength. Equation 4 includes a term $f(x, \lambda_i \rightarrow \lambda)$ known as *wavelength redistribution function*, which represents the ef-

ficiency of the energy transfer between wavelengths. It is defined as the quotient between the energy of the emitted wavelength and the energy of the absorbed excitation wavelength, per wavelength unit. Reformulating in terms of photons instead of energy we have the *spectral quantum efficiency function* $\eta(x, \lambda_i \rightarrow \lambda)$, defined as the number of photons emitted at λ per wavelength unit, divided by the number of absorbed photons at λ_i. Both functions are dimensional (nm^{-1}), and are related as follows:

$$f(x, \lambda_i \rightarrow \lambda) = \eta(x, \lambda_i \rightarrow \lambda)\frac{\lambda_i}{\lambda} \tag{12}$$

A related dimensionless function that describes inelastic scattering is the *quantum efficiency* Γ, defined as the total number of photons emitted at all wavelengths divided by the number of photons absorbed at excitation wavelength λ_i. It is related to the spectral quantum efficiency function by the equation:

$$\Gamma(\lambda_i) = \int_{\lambda} \eta(x, \lambda_i \rightarrow \lambda) d\lambda \tag{13}$$

Our extension to the volume photon mapping algorithm includes a) solving Fermat's law to obtain the curved trajectory of each photon if the index of refraction varies (and also for the eye rays shot during the radiance estimate phase), thus being able to overcome the shadow ray problem presented above and to obtain a full solution including effects such as color bleeding and caustics; and b) the inclusion of the quantum efficiency Γ to govern the probability of an inelastic scattering event. As shown in figure 2, once the albedo-based Russian roulette determines that a certain photon has been absorbed by the medium, a second Russian roulette based on the quantum efficiency determines whether an inelastic scattering event takes place, and therefore the photon has to be re-emitted at a different wavelength. This is done by generating a random number $\xi_{in}[0,1]$ so that:

$$\xi_{in}[0,1] \rightarrow \begin{cases} \xi_{in} \leq \Gamma & \text{Photon is re-emitted} \\ \xi_{in} > \Gamma & \text{Photon remains absorbed} \end{cases} \tag{14}$$

If re-emitted, the new wavelength must be obtained, for which we must sample the spectral quantum efficiency function $\eta(x, \lambda_i \rightarrow \lambda)$ for the excitation wavelength λ_i. This can be simply done by rejection sampling the function, but to increase efficiency we perform importance sampling using the inverse of its cumulative distribution function (cdf). A random number $\psi[0,1]$ therefore yields the new wavelength for the re-emitted photon. Steeper areas of the cdf increase the probability of a photon being re-emitted at the corresponding wavelengths.

Figure 2 shows the basic scheme of the algorithm. The sequence of events in the original volume photon mapping by [JC98] is represented inside the grey area.

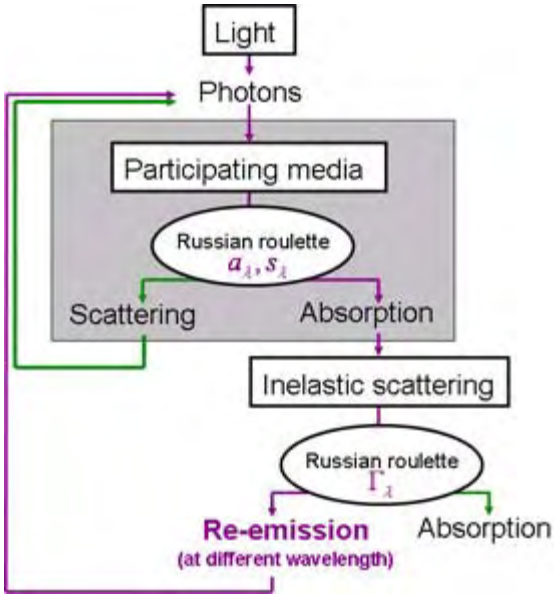

Figure 2: *Our extended volume photon mapping algorithm.*

4. Case Study: Underwater Imagery

We chose deep ocean waters as our first case study, given its rich range of elastic and inelastic scattering phenomena and the fact that it is a medium well studied by oceanographers. Pure seawater absorbs most wavelengths except for blue: the absorption coefficient peaks at 760 nanometers, and reaches a minimum at 430 nm. The phase function p is modelled as the phase function in pure sea water plus the phase function of the scattering by suspended particles, as proposed in [Mob94] ($p = p_w + p_p$). For pure water we use a phase function similar to Rayleigh's:

$$p_w(\theta) = 0.06225(1 + 0.835cos^2\theta) \tag{15}$$

while the scattering caused by particles is modelled using a Henyey-Greenstein phase function with $g = 0.924$:

$$p_p(\theta, g) = \frac{1 - g^2}{(1 + g^2 - 2gcos\theta)^{3/2}} \tag{16}$$

It is very common in ocean waters to see a color shift ranging from greenish to very bright green, or even yellowish. These hue shifts are due to the variation in the concentration and type of the suspended microorganisms, mainly phytoplankton, which presents a maximum absorption at 350 nm. rapidly decreasing to almost zero beyond 500 nm. The

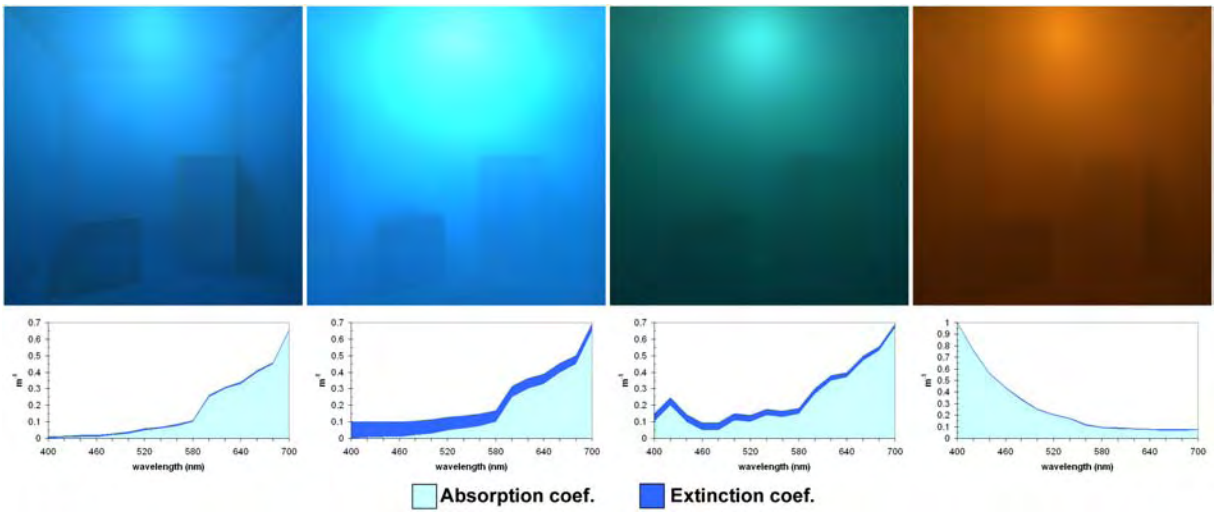

Figure 3: *Fluorescent ocean water in Cornell rooms. (a), (b) and (c) show varying concentrations of chlorophyll* ($0.05mg/m^3$, $0.1mg/m^3$ *and* $5mg/m^3$ *respectively). (d) High concentration of yellow matter* ($5mg/m^3$).

most important element in the phytoplankton is chlorophyll, which presents spectral absorption peaks in the blue and red ends of the spectrum and is the most important source of volume fluorescence in the waters. For chlorophyll, $\Gamma^c(\lambda_i)$ is wavelength-independent, with values ranging from 0.01 to 0.1 (we use the superscript c for chlorophyll). As with most inelastic scattering event, the re-emission phase function is isotropic.

Another important source of fluorescence is the Color Dissolved Organic Matter (CDOM), also called yellow matter, present in shallow ocean waters and harbors. $\Gamma^y(\lambda_i)$ is also wavelength-independent, with values between 0.005 and 0.025, and re-emission is also isotropic [Haw92].

All the images in the paper have been rendered on a Beowulf system composed of six nodes, each one being a Pentium 4 @ 2.8 GHz. with 1 Gb. of RAM. Figure 3 shows different colorations of ocean water, according to varying chlorophyll and yellow matter concentrations which trigger inelastic scattering events with different probabilities. The images were rendered with 250,000 photons stored in the volume photon map and 200 photons used for the radiance estimate. This high numbers are needed to obtain accurate results, since we use the volume photon map to compute both direct and indirect illumination. Direct illumination in participating media with a varying index of refraction cannot be efficiently computed using ray tracing techniques, as explained at the beginning of section 3. The spectrum was sampled at nine intervals. Below each picture, the resulting absorption and extinction curves (functions of the different concentrations of chlorophyll in the modelled waters) are shown for each case. Image (a) shows little fluorescence (low chlorophyll concentration of $0.05mg/m^3$), and the waters are relatively clear. When chlorophyll concentration increases, fluorescence events become more prominent and the image first gets a milky aspect (b), losing visibility and reaching a characteristic green hue when chlorophyll reaches $5mg/m^3$. Image (d) shows fluorescence owed to yellow matter. The absorption function in this case has been modelled after [Mob94]: $a_y(\lambda) = a_y(440)^{-0.014(\lambda-440)}$ where $a_y(440)$ is the empirical absorption at 440 nm. Rendering times for the images were six minutes.

5. Case Study: Atmospheric Phenomena

The images in this section illustrate some of the most relevant effects in nature owed to curved light paths. To achieve physically correct results we have modelled the Earth as a sphere with a radius of 6371 units (one unit equals one kilometer); the atmosphere is another concentric sphere with a thickness of 40 kilometers. Taking the 1976 *USA Standard Atmosphere* (USA76) [USG76], we first obtain a standard temperature and pressure profile of the whole 40 kilometers, with temperature decreasing at an approximate rate of 0.6°C per 100 meters. In order to curve light correctly according to Fermat's law, we need to obtain the wavelength-dependent index of refraction as a function of both the temperature and pressure given by the USA76. To do so, we follow the method described in [GSMA04], by first obtaining density as a function of temperature $T(h)$ and pressure $P(h)$ using the Perfect Gas law $\rho(h) = \frac{P(h)M}{RT(h)}$, where M and R are constants of values $28.93 \cdot 10^{-3}\, kg/mol$ and $8.3145\, J/mol \cdot K$ respectively. The Gladstone-Dale law [GD58] relates $n(\lambda, h)$ as a function of both $\rho(h)$ and $n(\lambda)$, given by the expression:

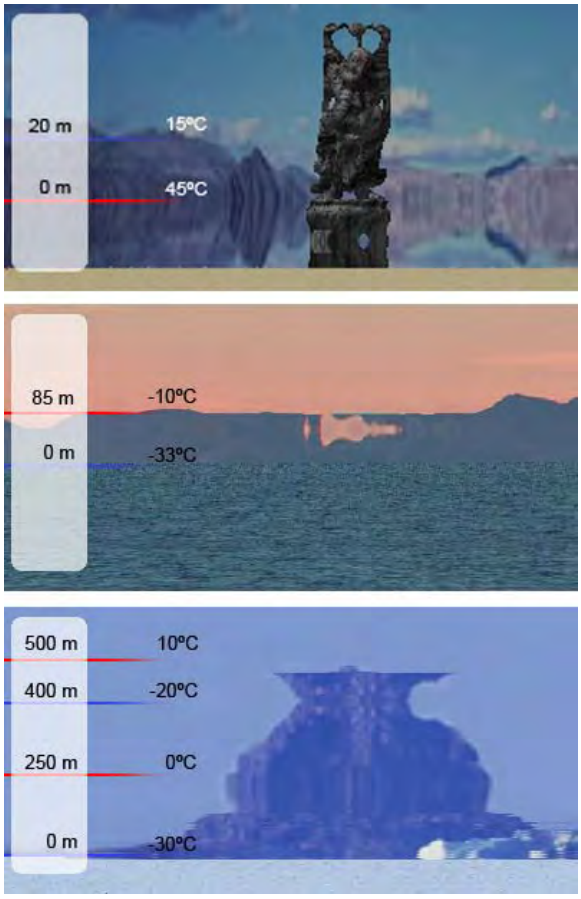

Figure 4: *Simulation of several atmospheric phenomena. Top: inferior mirage. Middle: superior mirage. Bottom: Fata Morgana.*

$$n(h,\lambda) = \rho(h) \cdot (n(\lambda) - 1) + 1 \tag{17}$$

The only missing function is now $n(\lambda)$, which we obtain from Cauchy's analytical formula [BW02]:

$$n(\lambda) = a \cdot \left(1 + \frac{b}{\lambda^2}\right) + 1 \tag{18}$$

where a and b depend on the medium considered (for air, their values are $a = 29.79 \cdot 10^{-5}$ and $b = 5.67 \cdot 10^{-5}$). Sellmeier [BW02] provides a slightly more elaborated formula, but we have chosen Cauchy's for efficiency reasons.

Combining equations 17 and 18 we finally obtain our profile for $n(\lambda, h)$, which we can alter at will to obtain the desired effects. To interpolate the complete, altered profiles for the whole 40 km. we use Fermi's distribution, as proposed in [VDWGL00].

The camera in the scenes is placed far from the mirages at a specific height for each effect to be seen (they can only appear if the observer's line of vision forms an angle less than one degree with the horizon). The error tolerance in the Dormand-Prince RK5(4)7M method has been set to 10^{-9}, and the spectrum has been sampled in three wavelengths. Figure 4 (top) shows our simulation of an inferior mirage, which occurs when the ground is very hot and heats up the air layers right above it, thus creating a steep temperature gradient (30°C in 20 meters). As a consequence, light rays get bent upwards, and an inverted image of the Happy Buddha and the background appears on the ground. The camera is placed 10 meters above the ground. The image took 14 minutes to render.

Inversion layers are caused by an increase of air temperature with height, reversing the standard behavior where temperature decreases as a function of height. This happens most commonly above cold sea waters, and the light rays get bent downward, giving rise to the superior mirage. Figure 4 (middle) shows our simulation, modelling an inversion layer with a temperature gradient of 23°C. The apparent hole in the mountains is actually formed by the superior inverted image of the real mountains. The camera is placed also 10 meters above the ground, and the image took four minutes and 32 seconds to render. The great decrease in rendering time compared to the inferior mirage is owed to the simpler geometry of the scene, since the far away mountains are textured low-resolution objects.

Maybe less known than the two previous examples, the Fata Morgana occurs as a concatenation of both superior and inferior mirages, and is a much rarer phenomenon. Figure 4 (bottom) shows our simulation with two inversion layers with steep temperature gradients. There is an inferior mirage image across the middle of the mountain plus a superior mirage with the inverted image on top. The shape of the mountain gets greatly distorted; the Fata Morgana has historically tricked arctic expeditions, making them believe they were seeing huge mountains that were just a complicated pattern of upright and inverted images of the real, much lower hill (*Fata Morgana* is in fact the name of a fairly enchantress skilled in the art of changing shape, which she learnt from Merlin the Magician). The camera is placed at 300 meters (for the Fata to be visible it needs to be between the inversion layers), and the rendering time was five minutes.

6. Discussion

The method described has been implemented in Lucifer, our in-house global illumination renderer. It can handle multiple inelastic scattering in inhomogeneous participating media with a varying index of refraction, thus rendering effects such as mirages or fluorescence in ocean waters with full lighting computation. It deals well with strong anisotropy in the phase functions and the effects of backscattering, since no discretizations of the scene must be performed,

and thus the shortcoming of the only previous work on volume fluorescence [CS03] is overcome. It also supports real light sources, with photometric data input specified in the standard CIBSE TM14 format [CIB88]. This is a must for predictive rendering and for generating physically accurate data. The real light sources are sampled so that photons are emitted proportionally to the distribution of the light, given by its photometry.

Spectral images are calculated in high dynamic range, in order to obtain accurate data from the simulations. For tone reproduction purposes we map luminances to the display based on the work by Ward et al. [LRP97] and Pattanaik et al. [PTYG00]. To increase realism during the visualization of the images, an additional operator has been added which simulates the effects of chromatic adaptation in the human eye. This operator is specially important in the realistic depiction of underwater imagery, where the cones in the human eye might undergo a loss of spectral sensitivity after having been exposed to the same wavelength for a long period of time (underwater imagery being usually blue or green mostly). The complete description of such operator can be found in [GSMA04].

As stated in the introduction, the algorithm implemented is general and physically-based. This allows us to use the radiometric and photometric data obtained from the simulations for any purpose other than rendering, such as professional architectural lighting or accurate simulations of deep underwater vision, given the exact description of the luminaire to be used and the water conditions. This accuracy obviously increases rendering times compared to faked, ad-hoc solutions. To improve efficiency, we impose an early light path termination and an adaptive integration step while solving Fermat's law. Choosing the Dormand-Prince RK5(4)7M numerical method over the more standard Euler method has produced speedups of up to 106.4. We have also used a parallel implementation on a six-PC Beowulf system of our non-linear photon mapping algorithm, achieving additional speedups between 4.2 and 4.8.

The non-linear photon mapping implementation allows us to extend several sunset effects similar to the ones simulated in [GSMA04], by including a thin layer of fog between the observer and the sun. The solar disk gets distorted into different shapes, while light is scattered through the layer of fog, thus achieving a "winter sunset" look (figure 5, left and middle). Figure 5 right shows volume caustics generated by a crystal sphere in a fluorescent medium.

Figure 6 shows several renders obtained with Lucifer. All of them are lit by a Philips SW-type© luminaire, specified according to the CIBSE TM14 format. The only light source is immersed in the medium, so no caustics from the interaction of sunlight with the surface appear. The medium modelled does not emit light, although adding that to the model is straightforward and would allow us to simulate effects such as bioluminiscence in the water. Fluorescence

Figure 5: *Sunset effects through a layer of fog. Left: flattened sun. Middle: split sun. Right: Volume caustics in a fluorescent medium.*

owed to inelastic scattering is computed according to the varying concentrations of chlorophyll in each image (between 0.01 and $0.1 mg/m^3$). The volume photon map in all the images contains 500.000 photons, and the radiance estimate used 250. Again, these high numbers are needed since we compute direct lighting with the photon map. The top two images represent a sunken boat along a Happy Buddha in clear, shallow waters (left) or deep underwater with a chlorophyll concentration of $0.05 mg/m^3$(right). For the bottom-left image, we have added a volume temperature field that simulates a heat source outside the image as explained in [SGGC05], deriving the index of refraction using the formula $n = 1 + \frac{T_o}{T}(n_o - 1)$ as proposed by Stam and Languenou [SL96]. The distortions caused by the varying index of refraction are visible, similar to the characteristic rippling in a real desert scene. The bottom-middle image uses a smoke-like medium, modelled as a 3D turbulence function, whereas the last to the right shows the effects of a highly anisotropic medium. The images are 400 pixels wide and took between 30 and 40 minutes to render, without any penalty imposed by the anisotropy in the last image.

7. Conclusion and Future Work

We proposed a novel extension of the widely used photon mapping technique, which accounts for multiple inelastic scattering and can provide a full global illumination solution in inhomogeneous media with a varying index of refraction, where light paths are bent. No pre-lit textures are needed in this case, since both direct and indirect lighting is calculated from the photon map. The method is physically-based and yields accurate high-dynamic results that can either be output as an image to a display device (via tone mapping), or used in other fields as raw data. Inelastic scattering is calculated during the photon tracing stage, so the extra cost required is just a second Russian roulette per absorption. The accompanying video shows the feasibility of the approach for animations.

Practically all inelastic scattering effects in the visible range of the spectrum mean a transfer of energy from shorter to longer wavelengths. Nevertheless, the algorithm presented in this work can handle rarer inelastic scattering events where energy gets transferred from longer to shorter wave-

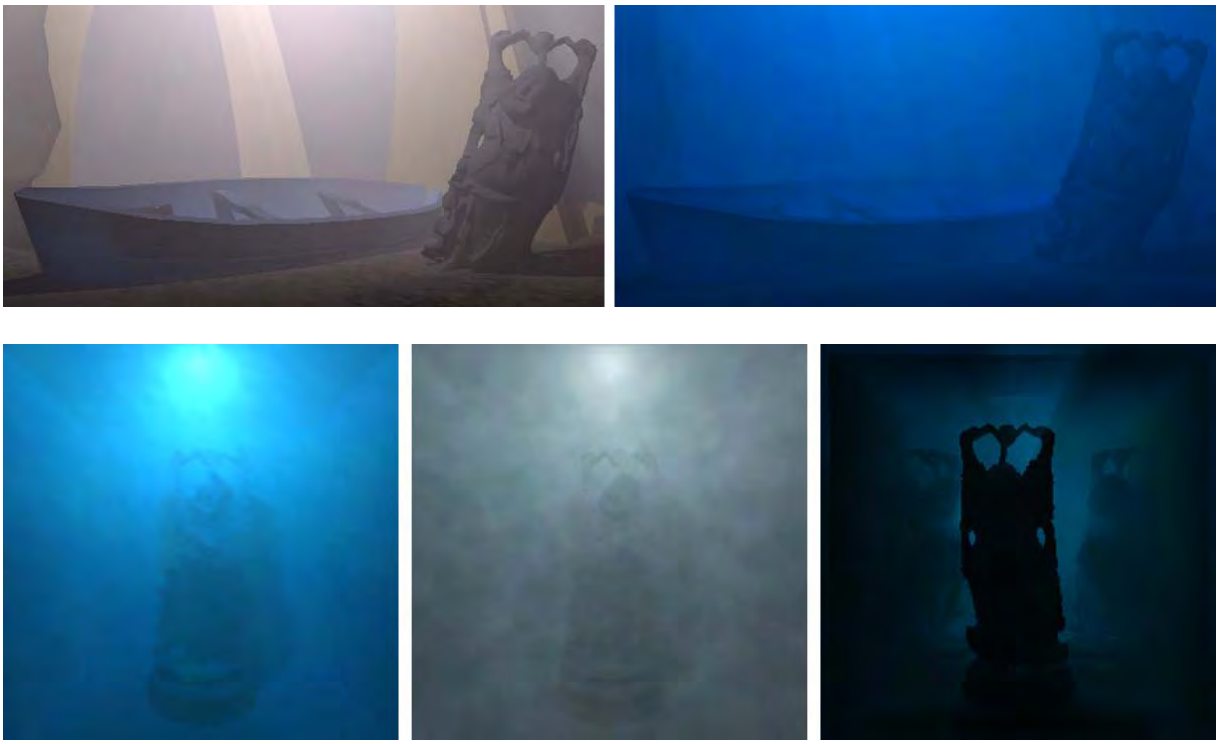

Figure 6: *Different images with inelastic scattering in participating media. Top left: very low chlorophyll concentration. Top right: higher concentration yields more inelastic scattering events. Bottom left: distortions caused by a 3D temperature field. Bottom middle: 3D turbulence field simulating smoke. Bottom right: highly anisotropic medium.*

lengths (such as a fraction of the Raman scattering that occurs naturally in several solids, liquids and gases [Mob94]), since it does not follow a cascade, one-way scheme from the blue end to the red end of the spectrum. The application of these type of inelastic scattering to computer graphics is probably just marginal, but the data generated can be very useful to physicists or oceanographers. Adding phosphorescence effects could make use of the work by Cammarano and Wann Jensen [CJ02], although a more straightforward approach would be to use the decay function $d(t)$ in each frame. Any number of light sources can be used in the scene, even with different photometric descriptions.

The bottleneck of the algorithm is solving the paths for each photon and eye-ray using Fermat's law. Although the use of a Dormand-Prince method has drastically reduced rendering times by two orders of magnitude, additional work needs to be done to achieve near real-time frame rates. Importance maps could be used for this purpose, although two other promising fields of research lay ahead: the first one is the implementation of the algorithm on GPUs, as proposed by Purcell et al. [PDC*03]. The second would try to take advantage of temporal coherence of light distribution, as presented by Myszkowski et al. [MTAS01].

8. Acknowledgements

This research was partly done under the sponsorship of the Spanish Ministry of Education and Research through the project TIN2004-07672-C03-03. The authors would also like to thank Eduardo Jiménez for his initial contribution to this work.

References

[BTL90] BERGER M., TROUT T., LEVIT N.: Ray tracing mirages. *IEEE Computer Graphics and Applications 10*, 3 (May 1990), 36–41.

[BW02] BORN M., WOLF E.: *Principles of Optics: Electromagnetic Theory of Propagation, Interference and Diffraction of Light*. Cambridge University Press, 2002.

[CIB88] CIBSE: *Standard File Format for Transfer of Luminaire Photometric Data*. The Chartered Institution of Building Services Engineers, 1988.

[CJ02] CAMMARANO M., JENSEN H. W.: Time dependent photon mapping. In *Proceedings of the 13th Eurographics workshop on Rendering* (2002), Eurographics Association, pp. 135–144.

[CS03] CEREZO E., SERON F.: Inelastic scattering in participating media. application to the ocean. In *Proceedings of the Annual Conference of the European Association for Computer Graphics, Eurographics 2003* (2003), pp. CD–ROM.

[DP80] DORMAND J., PRINCE P.: A family of embeded runge-kutta formulae. *Journal of Computational and Applied Mathematics 6(1)* (1980), 19–26.

[FFLV82] FABRI E., FIORZO G., LAZZERI F., VIOLINO P.: Mirage in the laboratory. *Am. J. Physics 50(6)* (1982), 517–521.

[GD58] GLADSTONE J. H., DALE J.: On the influence of temperature on the refraction of light. *Phil. Trans. 148* (1858), 887.

[Gla95a] GLASSNER A.: *Principles of Digital Image Synthesis*. Morgan Kaufmann, San Francisco, California, 1995.

[Gla95b] GLASSNER A. S.: A model for fluorescence and phosphorescence. In *Photorealistic Rendering Techniques* (1995), Sakas P. S. G., Müller S., (Eds.), Eurographics, Springer-Verlag Berlin Heidelberg New York, pp. 60–70.

[Grö95] GRÖLLER E.: Nonlinear ray tracing: visualizing strange worlds. *The Visual Computer 11*, 5 (1995), 263–276.

[GSMA04] GUTIERREZ D., SERON F., MUNOZ A., ANSON O.: Chasing the green flash: a global illumination solution for inhomogeneous media. In *Spring Conference on Computer Graphics* (2004), (in cooperation with ACM SIGGRAPH A. P., Eurographics), (Eds.), pp. 95–103.

[Haw92] HAWES S.: *Quantum Fluorescence Efficiencies of Marine Fulvic and Humid Acids*. PhD thesis, Dept. of Marince Science, Univ. of South Florida, 1992.

[HW01] HANSON A. J., WEISKOPF D.: Visualizing relativity. siggraph 2001 course 15, 2001.

[JC98] JENSEN H. W., CHRISTENSEN P. H.: Efficient simulation of light transport in scenes with participating media using photon maps. In *SIGGRAPH 98 Conference Proceedings* (jul 1998), Cohen M., (Ed.), Annual Conference Series, ACM SIGGRAPH, Addison Wesley, pp. 311–320. ISBN 0-89791-999-8.

[LRP97] LARSON G. W., RUSHMEIER H., PIATKO C.: A visibility matching tone reproduction operator for high dynamic range scenes. *IEEE Transactions on Visualization and Computer Graphics 3*, 4 (Oct. 1997), 291–306.

[Mob94] MOBLEY C.: *Light and Water. Radiative Transfer in Natural Waters*. Academic Press, Inc., 1994.

[MTAS01] MYSZKOWKSI K., TAWARA T., AKAMINE A., SEIDEL H. P.: Perception-guided global illumination solution for animation. In *Computer Graphics Proceedings, Annual Conference Series, 2001 (ACM SIGGRAPH 2001 Proceedings)* (Aug. 2001), pp. 221–230.

[Mus90] MUSGRAVE F. K.: A note on ray tracing mirages. *IEEE Computer Graphics and Applications 10*, 6 (Nov. 1990), 10–12.

[Nem93] NEMIROFF R. J.: Visual distortions near a neutron star and black hole. *American Journal of Physics 61(7)* (1993), 619–632.

[PDC*03] PURCELL T. J., DONNER C., CAMMARANO M., JENSEN J., HANRAHAN P.: Photon mapping on programmable graphics hardware. In *SIGGRAPH/Eurographics Workshop on Graphics Hardware* (2003), Eurographics Association, pp. 041–050.

[PPS97] PEREZ F., PUEYO X., SILLION F.: Global illumination techniques for the simulation of participating media. In *Proc. of the Eigth Eurographics Workshop on Rendering* (1997), pp. 16–18.

[PTYG00] PATTANAIK S., TUMBLIN J. E., YEE H., GREENBERG. D. P.: Time-dependent visual adaptation for realistic image display. In *SIGGRAPH 2000, Computer Graphics Proceedings* (2000), Akeley K., (Ed.), Annual Conference Series, ACM Press / ACM SIGGRAPH / Addison Wesley Longman, pp. 47–54.

[SGGC05] SERON F., GUTIERREZ D., GUTIERREZ G., CEREZO E.: Implementation of a method of curved ray tracing for inhomogeneous atmospheres. *Computers and Graphics 29(1)* (2005).

[SL96] STAM J., LANGUÉNOU E.: Ray tracing in non-constant media. In *Eurographics Rendering Workshop 1996* (New York City, NY, June 1996), Pueyo X., Schröder P., (Eds.), Eurographics, Springer Wien, pp. 225–234. ISBN 3-211-82883-4.

[USG76] USGPC: *U.S. Standard Atmosphere*. United State Government Printing Office, Washington, D.C., 1976.

[VDWGL00] VAN DER WERF S., GUNTHER G., LEHN W.: Novaya zemlya effects and sunsets. *Applied Optics 42*, 3 (2000).

[WTP01] WILKIE A., TOBLER R., PURGATHOFER W.: Combined rendering of polarization and fluorescence effects. In *Rendering Techniques '01 (Proc. Eurographics Workshop on Rendering 2001)* (2001), Gortler S.J. M. K. e., (Ed.), Eurographics, Springer-Verlag, pp. 197–204.

[YOH00] YNGVE G. D., O'BRIEN J. F., HODGINS H.: Animating explosions. In *Proceedings of the Computer Graphics Conference 2000 (SIGGRAPH-00)* (New York, July 23–28 2000), Hoffmeyer S., (Ed.), ACMPress, pp. 29–36.

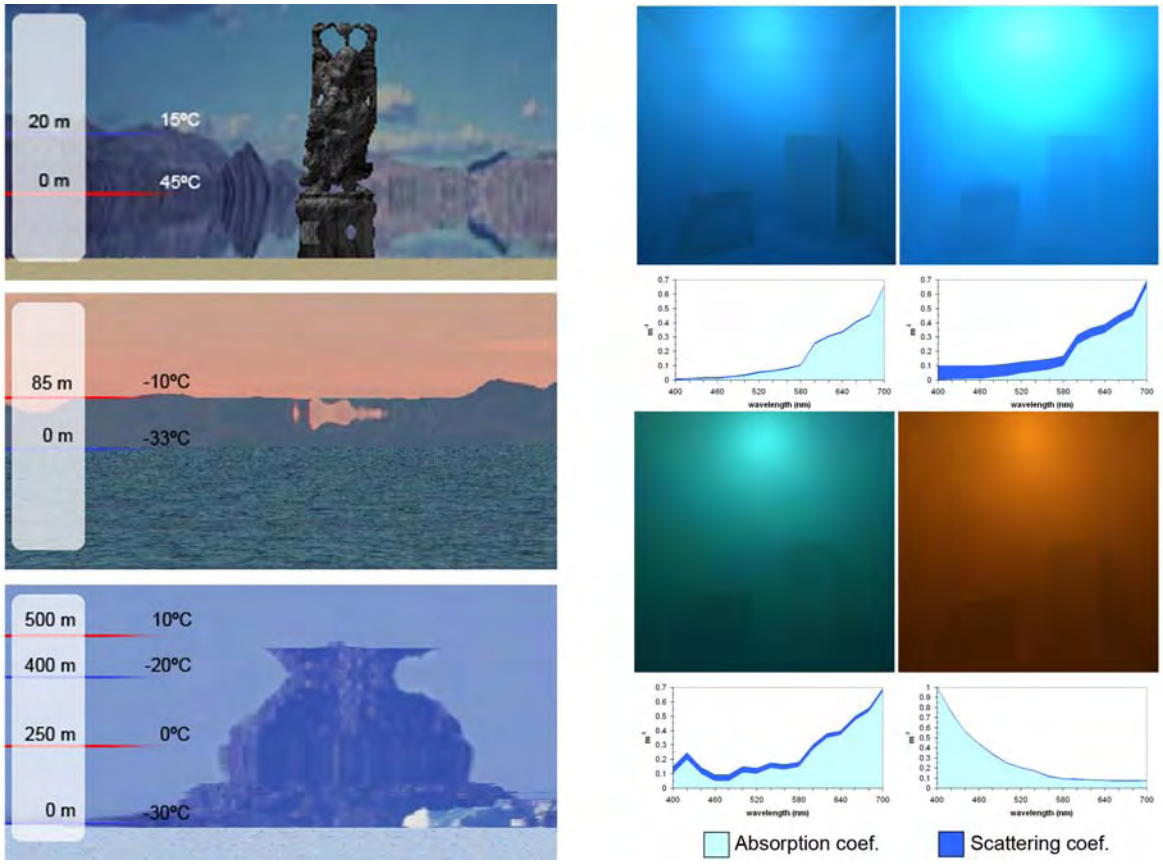

EUROGRAPHICS 2008 / G. Drettakis and R. Scopigno
(Guest Editors)

Volume 27 (2008), Number 2

Visualizing Underwater Ocean Optics

Diego Gutierrez, Francisco J. Seron, Adolfo Munoz and Oscar Anson

University of Zaragoza, Spain

Abstract

Simulating the in-water ocean light field is a daunting task. Ocean waters are one of the richest participating media, where light interacts not only with water molecules, but with suspended particles and organic matter as well. The concentration of each constituent greatly affects these interactions, resulting in very different hues. Inelastic scattering events such as fluorescence or Raman scattering imply energy transfers that are usually neglected in the simulations. Our contributions in this paper are a bio-optical model of ocean waters suitable for computer graphics simulations, along with an improved method to obtain an accurate solution of the in-water light field based on radiative transfer theory. The method provides a link between the inherent optical properties *that define the medium and its* apparent optical properties*, which describe how it looks. The bio-optical model of the ocean uses published data from oceanography studies. For inelastic scattering we compute all frequency changes at higher and lower energy values, based on the spectral quantum efficiency function of the medium. The results shown prove the usability of the system as a predictive rendering algorithm. Areas of application for this research span from underwater imagery to remote sensing; the resolution method is general enough to be usable in any type of participating medium simulation.*

Categories and Subject Descriptors (according to ACM CCS): I.3.7 [Computer Graphics]: Three-Dimensional Graphics and Realism

1. Introduction

Ocean water is arguably the richest participating medium in terms of optical thickness and the number and type of interactions that occur in it. This paper deals with the physically-based rendering of underwater scenes by simulating the in-water light field, based on a compact bio-optical model that takes into account the *dissolved* and *particulate* matter, optically influential constituents of the water. To ensure accuracy, we use published data obtained from a wide range of literature in the field of oceanography. Our model is not restricted to just the visible spectrum and can be adapted to any type of known ocean water in particular, or to any kind of participating medium in general.

Scattering in water is caused by interactions of light at molecular level and with particles [Mob94]. It can be classified in two broad categories: *elastic* or *inelastic* scattering, depending on whether the scattered photon maintains or changes its energy in the process. The inelastic scattering events can be further subclassified according to the nature of the energy transfer: *Stokes* scattering, when a molecule of the medium absorbs the photon and re-emits it with a lower energy, and *anti-Stokes* scattering, when the re-emitted photon has a higher energy. Both cases are covered by our model. The process implies an energy transfer from wavelength λ' to λ, with λ' being the excitation wavelength and λ the re-emitted wavelength. The former case implies a shift towards longer wavelengths, whereas in the latter the scattered photon has a shorter wavelength. Major forms of elastic events in water include Einstein-Smoluchowski scattering (see Section 3.2), whereas for inelastic events, *Raman* scattering and *fluorescence* are the two most prominent (see Section 3.3).

The presence and concentrations of the constituents in the water determine its optical properties. These optical properties are divided in two classes: *inherent* and *apparent*. The *inherent optical properties* (IOP) only depend on the constituents of the water, whereas the *apparent optical properties* (AOP) are not properties of the aquatic medium itself, although they do depend on its characteristics. Typical IOP are the absorption coefficient, the scattering coefficient or the scattering phase function. Some of the AOP include irradiance reflectance, attenuation coefficients or the average cosines [Pre76]. To obtain the in-water light field,

we rely on the physically based theory of *radiative transfer* [Cha60], which relates the IOP and AOP. More precisely, the link is provided through the Radiative Transfer Equation (RTE) [SCP94], which takes into account emission, absorption and elastic scattering. Unfortunately this equation can not account for the phenomenon known as *inelastic scattering* described previously, which is of significant importance in ocean waters. We consequently expand the RTE by adding an extra term, thus obtaining the Full Radiative Transfer Equation (FRTE) [Gla95] and solving it by using an extended version of the method presented by Gutierrez et al. [GMAS05]:

$$\begin{aligned}\frac{\partial L(\lambda,\vec{\omega}_o)}{\partial x} &= \alpha(\lambda)\,L_e(\lambda,\vec{\omega}_o) - \kappa(\lambda)\,L(\lambda,\vec{\omega}_o)\\ &\quad + \sigma(\lambda)\int_{\Omega} p(\lambda,\vec{\omega}_i,\vec{\omega}_o)\,L(\lambda,\vec{\omega}_i)\,d\vec{\omega}_i\\ &+ \int_{\Omega}\int_{W}\left\{\sigma(\lambda',\lambda)\,p(\lambda',\lambda,\vec{\omega}_i,\vec{\omega}_o)\,L(\lambda',\vec{\omega}_i)\right\}d\lambda'\,d\vec{\omega}_i \qquad (1)\end{aligned}$$

where L is the radiance and $\vec{\omega}_i$ and $\vec{\omega}_o$ are, respectively, the incoming and outgoing directions of that radiance. α, σ and κ are the absorption, scattering and extinction coefficients respectively. We assume $L_e(\lambda,\vec{\omega}_o)$ to be zero, thus making the medium non-emissive. Note that the last term models the inelastic scattering events and is expressed as a double integral over the domains of the solid angle Ω and wavelength W. Here $p(\lambda',\lambda,\vec{\omega}_i,\vec{\omega}_o)$ is the phase function for inelastic events and $\sigma(\lambda',\lambda)$ is the inelastic scattering function for the energy exchange between λ' and λ. For simplicity, when considering elastic interactions ($\lambda = \lambda'$) parameters λ,λ' are simplified to a single parameter λ. For processes such as fluorescence, where the photons are inelastic scattered to longer wavelengths, the function $\sigma(\lambda',\lambda)$ is usually expressed as:

$$\sigma(\lambda',\lambda) = \alpha(\lambda')\,f(\lambda',\lambda) \qquad (2)$$

where $\alpha(\lambda')$ is the inelastic absorption coefficient and $f(\lambda',\lambda)$ is the *wavelength redistribution function*, which governs the efficiency of the energy transfer between wavelengths. It is defined as the probability of a photon of λ' that inelastically scatters being re-emitted at λ. Therefore, (2) expresses the inelastic scattering as a percentage of the inelastic absorption coefficient. Section 3.3 gives more details on how to model this redistribution function $f(\lambda',\lambda)$.

Our research on water simulation encompasses the fields of both computer graphics and oceanography, and it is free from the restrictions of previous works. The main contributions of this paper are:

- A compact, parameterized bio-optical model of ocean waters which can be used in computer graphics applications.
- A resolution method based on the theory of radiative transfer, which solves the FRTE by handling *all* kinds of inelastic scattering events and modeling both absorption and elastic scattering accurately. This method is based on photon mapping [Jen01].
- A link between the IOP of water and the resulting light field, which in turn defines its AOP, based on radiative transfer theory.

The remainder of this paper is organized as follows: Section 2 presents previous work on the simulation of light transport in water bodies. In Section 3 a comprehensive bio-optical model is developed, whilst section 4 presents our simulation method. The paper ends with the results and conclusions.

2. Related work

The simulation of light transport in participating media usually either relies on Monte-Carlo techniques for ray tracing (Rushmeier and Torrance [RT87]; Nakamae et al. [NKON90]; Tadamura and Nakamae [TN95]) or attempts to solve the RTE, such as the method proposed by Kaneda et al. [KYNN91]. Nishita et al. [NSTN93] display water from outer space modifying this method, but both works only take into account single scattering. In the work of Premoze and Ashikhmin [PA01], no radiance due to scattering is calculated at all, using empirical equations based on experimental data instead. Mobley [Mob94] developed a method to solve the RTE analytically, but it cannot be extended to take into account inelastic scattering. Recently, the Lorenz-Mie theory has been generalized and applied to rendering natural waters by Frisvad, Christensen and Jensen [FCJ07], also neglecting the effects of inelastic scattering. Cerezo and Seron [CS04] also develop a bio-optical model. Whilst the goal of their work is closely related to ours, we overcome here significant shortcomings:

- They use a discrete ordinate method, which requires an angular and spatial discretization of the volume to be rendered. This imposes high memory requirements which seriously limit the complexity of the scenes that can be reproduced.
- In their work, inelastic scattering simulations are limited to fixed re-emissions in the 680 *nm*. wavelength..
- They cannot provide a full solution to the light transport problem.

Gutierrez et al. [GMAS05] present a method that deals with participating media in which the index of refraction is not homogeneous, while also taking into account the simulation of some inelastic scattering events. They apply their method to the simulation of underwater imagery using a simplified, four-parameter model of ocean waters. In this regard, our paper offers improvement in the following ways:

- Our bio-optical model of ocean waters is more complete, thus making the simulations more accurate.
- They also fail to develop a complete description for the complex inelastic scattering events that occur underwater, and the method is limited to re-emissions at lower energy levels and at fixed wavelengths. In this paper *all* inelastic scattering events can be modeled, including *Anti Stokes* scattering events like *Raman scattering* (see Section 3.3).

- We additionally offer simulations using real data from different seas as a means of visual validation.

3. The Bio-Optical Model

The various constituents of ocean water have a great influence in its optical properties. In order to solve the forward problem in ocean optics, the IOP have to be modeled and used in the FRTE. The values of these IOP can be obtained as the sum of the contributions of pure water and the dissolved particles and particulate matter present in the water, as proposed in [Mob94]. Optically pure water is devoid of any dissolved or suspended matter, and thus there is no scattering or absorption owed to particles or organic material [Mor74]. For *saline* pure water the salt concentration (35 to 39 parts per thousand) does influence the scattering and absorption functions. In particular it absorbs most wavelengths except for blue, with the absorption coefficient peaking at 760 *nm*, and reaching a minimum at 430 *nm*.

We develop our bio-optical model from three main IOP, with others like the extinction coefficient or the albedo derived from those three. These IOP are the absorption coefficient (3), the scattering coefficient (4) and the phase function (5), which for the elastic case can be written as (see Table 4 for a more detailed description of the functions used, including both the elastic and inelastic cases):

$$\alpha(\lambda) = \alpha_w(\lambda) + \sum_i \alpha_i(\lambda) \tag{3}$$

$$\sigma(\lambda) = \sigma_w(\lambda) + \sum_i \sigma_i(\lambda) \tag{4}$$

$$p(\lambda,\theta) = \frac{\sigma_w(\lambda)}{\sigma(\lambda)} p_w(\lambda,\theta) + \sum_i \frac{\sigma_i(\lambda)}{\sigma(\lambda)} p_i(\lambda,\theta) \tag{5}$$

where θ is the angle between the incoming $\vec{\omega}_i$ and outgoing $\vec{\omega}_o$ directions, the subscript w stands for the contribution of the pure water (fresh or salty) and the subscript i stands for the constituents in the water body such as biological particles or dissolved substances. We include three types of such constituents in our model, namely CDOM (Colored Dissolved Organic Matter, also know as yellow matter, present mainly in shallow ocean waters and harbors), phytoplankton (microscopic plants rich in chlorophyll) and minerals and organic detritus. The rest of this section will characterize the three main IOP (with elastic and inelastic scattering treated separately) for pure water and the three constituents. The next section will show how radiative transfer theory is applied to simulate the light field (which define the AOP) and render the final images.

3.1. Modeling Absorption

For the spectral absorption function of pure water $\alpha_w(\lambda)$ we rely on the work of Smith and Baker [SB81], whose tabulated values are well known in oceanography studies (shown in Table 1). Following further studies by Pope and Fry [PF97], we use those values as an upper bound, to account for the fact that the true absorption can be, in fact, lower. The function shows that absorption is more prominent both in the UV and red ends of the spectrum. [PF97] also shows that absorption by salt in oceanic water is negligible. Based on the data by Bricaud, Morel and Prieur [BMP81], we model absorption by CDOM by fitting an exponential curve of the form:

$$\alpha_y(\lambda) = \alpha_y(\lambda_0)\, e^{-S_y(\lambda-\lambda_0)} \tag{6}$$

where the subscript y denotes the constituent CDOM. λ_0 is a reference wavelength, often chosen to be 440 *nm* for yellow matter, and S_y is the slope of the semilogarithmic absorption curve [Kir94]. S_y is usually taken to be constant, with a value of 0.014 nm^{-1}, but has been found to vary both geographically and temporally, and is also dependent on the wavelength range over which it is calculated [BMP81]. The values of absorption $\alpha_y(\lambda_0)$ at reference wavelengths also vary in a range between 0.01 m^{-1} to 20 m^{-1}, as a function of turbidity [Kir94].

Phytoplankton absorbs a great amount of visible light, due to its chlorophyll pigment. The absorption function for chlorophyll peaks strongly at 430 *nm* and 670 *nm*, being very weak in the mid range of the visible spectrum (thus the more phytoplankton the greener the hue of the water). The concentration of the chlorophyll in the water usually ranges from 0.01 mg/m^3 for open waters to 100 mg/m^3. The spectral absorption coefficient of the phytoplankton is usually expressed as a function of this concentration C as:

$$\alpha_p(\lambda) = C\,\alpha_p^*(\lambda) \tag{7}$$

where C can be defined as the concentration of the main pigment chlorophyll-a (Chl_a) or as the sum of the concentrations of Chl_a and its degradation products, the pheopigments. α_p^* is the *specific spectral absorption coefficient* (the absorption per unit of concentration) for a particular species of phytoplankton, given in m^2/mg. Typical values for specific absorptions of different species of phytoplankton can be found in the work of Sathyendranath, Lazzara and Prieur [SLP87] (see Table 1). A rough correspondence between chlorophyll concentrations and several oceanic water types is given by Morel [Mor88]. The absorption owed to organic detritus and minerals can be approximated by an exponential function, according to Roesler, Perry and Carder [RPC89]:

$$\alpha_d(\lambda) = \alpha_d(\lambda_0)\, e^{-S_d(\lambda-\lambda_0)} \tag{8}$$

Here the reference wavelength 400 *nm* is selected for λ_0 and typical values for the exponent coefficient S_d will be in the range between 0.006 nm^{-1} to 0.014 nm^{-1}, although 0.011 nm^{-1} is the most common value [RPC89]. Further studies confirm that the absorption spectra of minerals and detritus is well described by an exponential function with an average slope S_d of 0.0123 nm^{-1}, with slightly lower values than predicted at wavelengths below 440 *nm* [BSF*03].

Table 1: *Absorption coefficient for a clear water body α_w (after Smith and Baker [SB81]) and specific absorption coefficient for phytoplankton α_p^* (after Sathyendranath, Lazzara and Prieur [SLP87]).*

λ	$[nm]$	380	440	500	550	610	670	720	780
α_w	$[cm^{-1}]$	0.00022	0.000145	0.000257	0.000638	0.00289	0.0043	0.01169	0.0236
α_p^*	$[m^2 \cdot mg^{-1}]$	0.025	0.035	0.02	0.01	0.007	0.015	0.001	0.0001

3.2. Modeling Elastic Scattering

For the pure water term we use the volume scattering function defined by the Einstein-Smoluchowski theory [Maz02], which models scattering at molecular level as small-scale fluctuations. Whilst usually Rayleigh's scattering is used instead, Einstein-Smoluchowski provides more accurate results, is well defined and imposes no overheads in the simulations. Its scattering coefficient and phase function are given by:

$$\sigma_w(\lambda) = 16.06\,\beta_w(\lambda_0, 90^\circ)\left(\frac{\lambda_0}{\lambda}\right)^{4.32} \tag{9}$$

$$p_w(\theta) = 0.06225\left(1 + 0.835\cos^2\theta\right) \tag{10}$$

Typical values for $\beta_w(\lambda_0, 90^\circ)$ for both fresh and saline pure water are given in [Mor74]. These values range from $14.1 \cdot 10^{-4}\ m^{-1}$ to $134.5 \cdot 10^{-4}\ m^{-1}$. All the scattering produced by CDOM has inelastic nature and thus will be described in next section.

Gordon and Morel [GM83] found that phytoplankton, even in small concentrations, also contribute to the total elastic scattering in the water. Its contribution is given by:

$$\sigma_p(\lambda) = \left(\frac{550}{\lambda}\right) 0.30\,C^{0.62} \tag{11}$$

where the constant 0.30 is selected to fit the data collected from many types of waters. The actual upper bound for this constant has a value of 0.45 [GM83]. The phase function due to phytoplankton is given by an isotropic function ($p_p = 1/\pi$).

The elastic scattering caused by organic detritus and minerals can be modeled based on Mie theory [GSO03]. The Henyey-Greenstein phase function models forward scattering fairly well but fails to reproduce backscattering with the same precision. We found that we can achieve a better fit by using a Two-Terms Henyey-Greenstein phase function (TTHG) [HG41]:

$$p_d(\theta, \zeta, g_f, g_b) = \zeta\, p_{HG}(\theta, g_f) + (1-\zeta)\, p_{HG}(\theta, g_b) \tag{12}$$

where ζ is a weighting function between zero and one. This common way of utilizing this combination defines a forward scattering lobe (first term), plus a backscattering lobe (second term), with $g_f \in [0..1]$ and $g_b \in [-1..0]$. p_{HG} represents a simple Henyey-Greenstein phase function (HG):

$$p_{HG}(\theta, g) = \frac{1-g^2}{(1+g^2-2g\cos\theta)^{3/2}} \tag{13}$$

The TTHG function not only models backscattering more precisely, but it can describe more complex particle scattering models, improving the fit at large and small angles as well. The shape of each of the two HG functions can be approximated by an ellipsoid, avoiding the relatively expensive exponent in its evaluation. The observation was first introduced by Schlick [BLSS93]. Due to the great variety of particulate matter, the scattering coefficient σ_d can adopt a wide range of values. Table 2 shows typical values of this function (data after Stramski et al. [SBM01]).

3.3. Modeling Inelastic Scattering

For inelastic scattering, we need to model the possibility of an absorbed photon being re-emitted at a different wavelength. (2) includes a term $f(\lambda', \lambda)$ known as *wavelength redistribution function*, which represents the efficiency of the energy transfer between wavelengths. It is defined as the quotient between the energy of the emitted wavelength and the energy of the absorbed excitation wavelength, per wavelength unit. Reformulating in terms of photons instead of energy we have the *spectral quantum efficiency function* $\eta(\lambda', \lambda)$, defined as the ratio between the number of photons emitted at λ per wavelength unit, and the number of absorbed photons at λ'. Both functions are dimensional (nm^{-1}), and are related as follows:

$$f(\lambda', \lambda) = \eta(\lambda', \lambda)\,\frac{\lambda'}{\lambda} \tag{14}$$

The wavelength redistribution function f, and therefore its associated spectral quantum efficiency function η, can be seen as a re-radiation matrix. A related dimensionless function that describes inelastic scattering is the *quantum yield* $\Gamma(\lambda')$, defined as the total number of photons emitted at all wavelengths divided by the number of photons absorbed at excitation wavelength λ'. It is related to the spectral quantum efficiency function by:

$$\Gamma(\lambda') = \int_W \eta(\lambda', \lambda)\, d\lambda \tag{15}$$

The three functions $\Gamma(\lambda')$, $f(\lambda', \lambda)$ and $\eta(\lambda', \lambda)$, depend on both the medium and the type of inelastic event. The two inelastic events with more influence in the in-water light field are fluorescence and Raman scattering. Phytoplankton and CDOM are important fluorescence sources, whilst Raman scattering is produced by pure water; minerals and detritus, on the other hand, do not produce any inelastic event.

Table 2: *Scattering coefficient for detritus σ_{dt} and minerals σ_m (After Stramski et al. [SBM01]).*

	λ	$[nm]$	380	440	500	550	610	670	720	780
detritus	σ_{dt}	$[m^{-1}]$	0.045	0.0375	0.0325	0.03	0.0285	0.0275	0.027	0.027
minerals	σ_m	$[m^{-1}]$	0.0675	0.0525	0.05	0.045	0.04	0.036	0.034	0.032
total	σ_d	$[m^{-1}]$	0.1125	0.09	0.0825	0.075	0.0685	0.0635	0.061	0.059

3.3.1. Fluorescence

Fluorescence occurs when a molecule absorbs a photon of wavelength λ', and re-emits it at a longer wavelength λ according to the *fluorescence efficiency function* $\eta_F(\lambda',\lambda)$. For the two main sources of fluorescence (phytoplankton and CDOM), re-emission follows an isotropic phase function. For phytoplankton, the wavelength of the re-emitted photons is independent of the excitation wavelength, although the intensity does show wavelength dependency [Mob94].

It is very common in ocean waters to see a color shift ranging from greenish to very bright green, or even yellowish. These hue shifts are mainly due to the variation in the concentration and type of the suspended microorganisms, specially phytoplankton and its related chlorophyll concentration, which presents an absorption function peaking at 350 *nm* and rapidly decaying to almost zero beyond 500 *nm*. Only wavelengths between 370 and 690 *nm* can trigger fluorescence due to phytoplankton. This can be modeled as a dimensionless function $g_p(\lambda')$ so that:

$$g_p(\lambda') \equiv \begin{cases} 1 & \text{if } 370 \leq \lambda' \leq 690 \text{ nm} \\ 0 & \text{otherwise} \end{cases} \tag{16}$$

The wavelength-independent quantum yield for phytoplankton $\Gamma_p(\lambda')$ ranges from 0.01 to 0.1. Using (14) and (16), the relationship between the wavelength redistribution function $f_p(\lambda',\lambda)$ and the spectral quantum efficiency function $\eta_p(\lambda',\lambda)$ is:

$$f_p(\lambda',\lambda) = \eta_p(\lambda',\lambda)\frac{\lambda'}{\lambda} \equiv \Gamma_p\, g_p(\lambda')\, h_p(\lambda)\, \frac{\lambda'}{\lambda} \tag{17}$$

where $h_p(\lambda)$ is the *fluorescence emission function* per unit wavelength, and can be approximated by a gaussian [Mob94]:

$$h_p(\lambda) = \frac{1}{\sqrt{2\pi}\lambda_\sigma} \exp\left\{-\frac{(\lambda-\lambda_0)^2}{2(\lambda_\sigma)^2}\right\} \tag{18}$$

$\lambda_0 = 685\,nm$ is the wavelength of maximum emission and $\lambda_\sigma = 10.6\,nm$ represents the standard deviation. Using (7) and (17) we can now compute the inelastic scattering coefficient owed to phytoplankton $\sigma_p(\lambda',\lambda)$ following (2).

The other important source of fluorescence in water is CDOM. For relatively high concentrations of CDOM, its quantum yield $\Gamma_y(\lambda')$ varies between 0.005 and 0.025. Following the work of Hawes [Haw92] we use the following formula to describe its spectral fluorescence quantum efficiency function:

Table 3: *Water constituents and interactions*

Constituent	Absorption	Elastic Scat.	Inelastic Scat.
Pure water (w)	Yes	Yes	Raman Scattering
Minerals, detritus (d)	Yes	Yes	No
Phytoplankton (p)	Yes	Yes	Fluorescence
CDOM (y)	Yes	No	Fluorescence

$$f_y(\lambda',\lambda) = A_0(\lambda')\exp\left\{-\left(\frac{\frac{1}{\lambda}-\frac{A_1}{\lambda'}-B_1}{0.6\left(\frac{A_2}{\lambda'}+B_2\right)}\right)^2\right\}\frac{\lambda'}{\lambda} \tag{19}$$

where A_0, A_1, A_2, B_1 and B_2 are empirical parameters whose values depend on the specific composition of the CDOM and can be found in [Mob94] (see Table 5). A_1 and A_2 are dimensionless, whereas the rest are given in nm^{-1}. Like fluorescence due to phytoplankton, we can use (6) and (19) to compute the inelastic scattering coefficient $\sigma_y(\lambda',\lambda)$ following (2).

Our model can be easily extended to account for phosphorescence phenomena, which are intrinsically similar to fluorescence and are governed by the *phosphorescence efficiency function*. The only difference is that the re-emitted energy declines with time according to a function $d(t)$.

3.3.2. Raman scattering

Raman scattering influences the in-water light field, specially at great depths where sun irradiance becomes zero and only Raman radiance remains. It occurs when vibration and rotation in water molecules exchange energy with incoming photons, re-emitting them with approximately the same wavelength, but allowing for small shifts towards longer or shorter wavelengths. It can also be considered a spontaneous process. To isolate Raman inelastic events from fluorescence and other scattering events, it is usually studied in pure water, filtered several times, so that the second term in (4) becomes zero.

The Raman wavelength redistribution function $f_w(\lambda',\lambda)$ is usually described in terms of a sum of four Gaussian functions [Mob94]:

$$f_w(\lambda',\lambda) = \frac{10^7}{\lambda'^2}\frac{\sum_{j=1}^{4} A_i \frac{1}{\Delta\tilde{\nu}_i}\exp\left\{-\frac{\left[10^7\left(\frac{1}{\lambda'}-\frac{1}{\lambda}\right)-\tilde{\nu}_i\right]^2}{\Delta\tilde{\nu}_i{}^2}\right\}}{\sqrt{\frac{\pi}{4\ln 2}}\sum_{j=1}^{4} A_j} \tag{20}$$

where $\tilde{\nu}$ is the wavenumber ($\tilde{\nu} = 10^7/\lambda$) given in cm^{-1}. Typical parameter values A_i, $\tilde{\nu}_i$ and $\Delta\tilde{\nu}_i$ for the Raman redistribution function are given by Walrafen [Wal69] and are

shown in Table 5. The inelastic scattering coefficient can now be obtained using α_w and f_w in (2).

4. The simulation method

Having so far developed our bio-optical model, we can now formalize it into a set of parameters and equations to fully simulate the in-water light field. To summarize, the four constituents of the model and their interactions with light are given in Table 3. Table 4 shows how the main functions that define the model are derived from IOP and related functions at constituent level.

Table 4: *The main functions of the model*

Equations	
$\alpha(\lambda)$	$= \alpha_d(\lambda)+\alpha_p(\lambda)+\alpha_w(\lambda)+\alpha_y(\lambda)$
$\sigma(\lambda)$	$= \sigma_w(\lambda)+\sigma_d(\lambda)+\sigma_p(\lambda)$
$p(\lambda,\theta)$	$= \frac{\sigma_w(\lambda)p_w(\lambda,\theta)+\sigma_d(\lambda)p_d(\lambda,\theta)+\sigma_p(\lambda)p_p(\lambda,\theta)}{\sigma(\lambda)}$
$\kappa(\lambda)$	$= \alpha(\lambda)+\sigma(\lambda)$
$\alpha_I(\lambda')$	$= \alpha_p(\lambda')+\alpha_w(\lambda')+\alpha_y(\lambda')$
$p_I(\lambda',\lambda,\theta)$	$= \frac{\alpha_p(\lambda')p_p(\lambda',\lambda,\theta)+\alpha_w(\lambda')p_w(\lambda',\lambda,\theta)+\alpha_y(\lambda')p_y(\lambda',\lambda,\theta)}{\alpha_I(\lambda')}$
$f_I(\lambda',\lambda)$	$= \frac{\alpha_p(\lambda')f_p(\lambda',\lambda)+\alpha_w(\lambda')f_w(\lambda',\lambda)+\alpha_y(\lambda')f_y(\lambda',\lambda)}{\alpha_I(\lambda')}$

Table 5: *Parameters of the model*

Parameter	Equations	Simulated values	Units
C	(7) (11)	$[0..1.0]$	$\frac{mg}{m^3}$
$\alpha_d(400)$	(8)	$[0..0.1]$	m^{-1}
$\alpha_y(440)$	(6)	$[0..0.1]$	m^{-1}
S_y	(6)	0.014	nm^{-1}
S_d	(8)	0.011	nm^{-1}
A_0	(19)	$\frac{150}{700}$	nm^{-1}
A_1	(19)	4	-
A_2	(19)	4	-
B_0	(19)	$\frac{1}{450\cdot 10^{-7}}$	nm^{-1}
B_1	(19)	$\frac{1}{650\cdot 10^{-7}}$	nm^{-1}
Γ_p	(17)	0.1	-
Γ_y	(19)	0.025	-
A_i, $i = 1..4$	(20)	$0.41, 0.39, 0.10, 0.10$	-
$\widetilde{\nu}_i$, $i = 1..4$	(20)	$3250, 3425, 3530, 3625$	-
$\Delta\widetilde{\nu}_i$, $i = 1..4$	(20)	$210, 175, 140, 140$	-

The model allows for easy adjusting of its parameters to simulate different types of water and thus obtain different in-water light fields. As well as minerals and detritus, other particulate components of water can be added from oceanographic studies (although minerals and detritus have the greatest influence in the final appearance of water). Mie theory can again be used to model the scattering by these new particles, and the phase function can be approximated by using a Two Terms Henyey-Greenstein phase function (12). An overview of the most significant parameters of the model, the equations in which they can be found and the corresponding values used for the simulations in this paper can be found in Table 5. Note that for simplicity we have not included the values that are already specified throughout the text during the explanation of the bio-optical model (more specifically, those included in tables 1 and 2). The first three correspond to the parameters analyzed in Figure 2.

Once we have formalized the model into a set of equations, we rely on radiative transfer theory to obtain a solution for the in-water light field. We solve the Full Radiative Transfer Equation (1) by extending the traditional photon mapping algorithm [Jen01] by taking into account all ten different events specified in Table 3, while allowing for both Stokes or anti-Stokes inelastic scattering. This enhancement is done in both stages: photon tracing and radiance estimation.

During the photon tracing stage in the original photon mapping method [Jen01], a Russian roulette algorithm is triggered at each interaction with the medium, deciding whether the photon is scattered or absorbed. In [GMAS05] the authors add a second Russian roulette which separates absorption from inelastic scattering; in the latter case, a new photon is generated at a different wavelength, but the algorithm considers just a single type of inelastic event with Stokes behavior. No anti-Stokes events are simulated. In contrast, our method uses just a single Russian roulette to choose between ten different kinds of interactions (including three types of inelastic events where the photons may gain or lose energy), and can be easily extended to handle an arbitrary number of different interactions. Finally, we improve the radiance estimation stage over previous methods by adding a term to take into account the contributions from the inelastic scattering events. The next subsections present the algorithm in more detail.

4.1. Stage 1: Photon tracing

We shoot photons from the light sources and let them interact with the geometry and the medium according to its optical distance, which is a function of the extinction coefficient (as in the original photon mapping method). We statistically decide at each interaction which type of event occurs (refer to Table 3) with just a single Russian roulette. At the interactions, photons are stored in a kd-tree as in traditional photon mapping.

The wavelength spectrum is box sampled into N_λ samples, so absorption ($\alpha(\lambda)$) and scattering coefficients ($\sigma(\lambda)$) are implemented as N_λ-dimensional arrays while wavelength redistribution functions ($f(\lambda',\lambda)$) are implemented as $N_\lambda \times N_\lambda$ square matrices. Each of the photons carries information about a portion of flux ($\Delta\Phi$) at a certain sampled wavelength (λ'). Importance sampling is used for computing the optical distance, so $\Delta\Phi$ does not change along the photon tracing stage, while λ' changes for inelastic scattering events.

In order to apply the Russian roulette algorithm, we will define an albedo $\Lambda_j(\lambda)$ for each interaction j as follows:

- If interaction j represents an elastic scattering event, then $\Lambda_j(\lambda) = \frac{\sigma_j(\lambda)}{\kappa(\lambda)}$
- If j represents an absorption interaction that does not

show inelastic scattering (detritus and minerals, basically), then $\Lambda_j(\lambda) = \frac{\alpha_j(\lambda)}{\kappa(\lambda)}$

- For each absorption interaction that could generate inelastic scattering (pure water, phytoplankton and CDOM) we define its *inelastic probability* (χ_j), the probability that an absorption event generates an inelastic scattering event:

$$\chi_j(\lambda') = \int_{\lambda_a}^{\lambda_b} f_I(\lambda',\lambda)d\lambda \approx \sum_{i=1}^{N_\lambda} f_I(\lambda',\lambda_i) \qquad (21)$$

where λ_a and λ_b are the lower and upper limits of the simulated wavelengths, and $i \in [1..N_\lambda]$ refer to samples in wavelength domain:

  - If interaction j represents the effective inelastic scattering event within the absorption interaction: $\Lambda_j(\lambda) = \frac{\alpha_j(\lambda)}{\kappa(\lambda)}\chi_j(\lambda)$
  - If interaction j represents the pure absorption event (no inelastic scattering happening at all): $\Lambda_j(\lambda) = \frac{\alpha_j(\lambda)}{\kappa(\lambda)}(1-\chi_j(\lambda))$

Thus, at each interaction a random number ξ between 0 and 1 is generated resulting in (between parenthesis, example values of Λ_j at $\lambda = 500nm$ that determine the size of the corresponding interval are included):

- $\xi\varepsilon[0,\xi_1) \rightarrow$ absorption by pure water ($2.51 \cdot 10^{-1}$).
- $\xi\varepsilon[\xi_1,\xi_2) \rightarrow$ Raman scattering, inelastic scattering by pure water ($1.21 \cdot 10^{-9}$).
- $\xi\varepsilon[\xi_2,\xi_3) \rightarrow$ absorption by minerals and detritus ($7.12 \cdot 10^{-2}$).
- $\xi\varepsilon[\xi_3,\xi_4) \rightarrow$ absorption by phytoplankton ($4.90 \cdot 10^{-3}$).
- $\xi\varepsilon[\xi_4,\xi_5) \rightarrow$ inelastic scattering by phytoplankton ($2.18 \cdot 10^{-3}$).
- $\xi\varepsilon[\xi_5,\xi_6) \rightarrow$ absorption by CDOM ($7.83 \cdot 10^{-2}$).
- $\xi\varepsilon[\xi_6,\xi_7) \rightarrow$ inelastic scattering by CDOM ($1.21 \cdot 10^{-2}$).
- $\xi\varepsilon[\xi_7,\xi_8) \rightarrow$ elastic scattering by pure water ($7.44 \cdot 10^{-3}$)
- $\xi\varepsilon[\xi_8,\xi_9) \rightarrow$ elastic scattering by minerals and detritus ($2.94 \cdot 10^{-1}$).
- $\xi\varepsilon[\xi_9,1] \rightarrow$ elastic scattering by phytoplankton ($2.79 \cdot 10^{-1}$).

where $\xi_i(\lambda)$ is given by $\xi_i(\lambda) = \sum_{j=1}^{i}\Lambda_j(\lambda)$

To compute the new re-emitted wavelength after a inelastic scattering event i, the normalized wavelength redistribution function $\frac{f_i(\lambda',\lambda)}{\chi_i(\lambda')}$ is treated as a probability distribution function (PDF) given the excitation wavelength λ'. To sample it efficiently we first build its normalized cumulative distribution function (CDF) and then inverse importance sample this CDF. Greater values of the PDF for a given wavelength will translate to steeper areas of the CDF, thus increasing the probability of a re-emission at such wavelength. Note that the definition of $f_i(\lambda',\lambda)$ is not limited to the visible spectrum, which might result in re-emissions happening at wavelengths beyond the visible spectrum. However, as $\chi_i(\lambda')$ is limited to the simulated (visible) spectrum, only inelastic interactions within this spectrum are considered. It could happen that a photon inelastically scattered at such wavelengths suffers a second inelastic scattering event that brings it back to the visible light range. Given the low probability of this chain of events and our computer graphics approach, we assume that a photon beyond the visible spectrum is definitely absorbed. Figure 1 shows a global overview of the algorithm during the photon tracing stage.

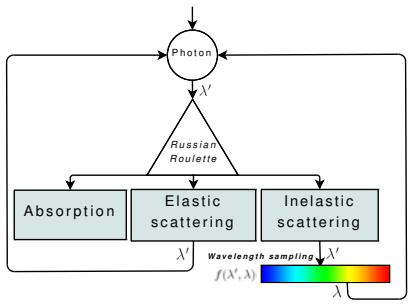

Figure 1: *Photon tracing algorithm. Inelastic scattering events generate a photon with a different associated wavelength according to the wavelength redistribution function.*

4.2. Stage 2: radiance estimate

To estimate radiance we adopt a tradeoff between speed and memory requirements similar to the proposed by Jensen and Christensen [JC98]: we only store photons in the photon map if they have been reflected or transmitted from surfaces, or if they have already been scattered at least once. Thus, we can compute single scattering more efficiently by ray marching through the medium and sampling the light sources by casting shadow rays. Taking into account the wavelength redistribution function for inelastic scattering, a new addend will be added at each step of the ray marching process:

$$\sum_{l=1}^{N}\sum_{i=1}^{N_\lambda}\left\{L_l\left(\lambda_i',\vec{w}_l\right)p_I\left(\lambda_i',\lambda,\vec{w}_l,\vec{w}_o\right)\alpha_I\left(\lambda_i'\right)f_I\left(\lambda_i',\lambda\right)\Delta x\right\} \qquad (22)$$

where $i \in [1..N_\lambda]$ and $l \in [1..N]$ refer to samples in the wavelength and light source domain respectively, $\vec{w}_l$ is the direction to the light with an incoming radiance L_l and Δx represent the ray marching steps.

Multiple scattering will be computed from the photon map, finding in the kd-tree the n photons which are closest to the estimation point by using the typical nearest neighbours algorithm. To account for multiple *inelastic* scattering we modify the radiance estimate expression of [JC98] by including a new term:

$$\sum_{k=1}^{n}\left\{p_I\left(\lambda_k',\lambda,\vec{w}_k,\vec{w}_o\right)f_I\left(\lambda_k',\lambda\right)\frac{\Delta\Phi_k}{\frac{4}{3}\pi r^2}\right\} \qquad (23)$$

where r is the radius of the sphere that contains the n closest photons, and k represents each of the stored photons.

5. Results

We have used the values from Table 5 for our simulations. In the images produced we only vary the chlorophyll concentration C, minerals and detritus turbidity $\alpha_d(400)$ and

(a) $C = 0, \alpha_d = 0, \alpha_y = 0$ (b) $C = 0.01, \alpha_d = 0, \alpha_y = 0$ (c) $C = 0.1, \alpha_d = 0, \alpha_y = 0$ (d) $C = 1, \alpha_d = 0, \alpha_y = 0$

(e) $C = 0, \alpha_d = 0.1, \alpha_y = 0$ (f) $C = 0.01, \alpha_d = 0.1, \alpha_y = 0$ (g) $C = 0.1, \alpha_d = 0.1, \alpha_y = 0$ (h) $C = 1, \alpha_d = 0.1, \alpha_y = 0$

(i) $C = 0, \alpha_d = 0, \alpha_y = 0.1$ (j) $C = 0.01, \alpha_d = 0, \alpha_y = 0.1$ (k) $C = 0.1, \alpha_d = 0, \alpha_y = 0.1$ (l) $C = 1, \alpha_d = 0, \alpha_y = 0.1$

Figure 2: *Resulting pictures varying the chlorophyll concentration C, the minerals and detritus turbidity α_d at 400nm and the CDOM turbidity α_y at 440nm.*

CDOM turbidity $\alpha_y(440)$. The choice of those three parameters to reduce the dimensionality of the model was based on their greater overall influence on the resulting light field. The photon map contains 400000 photons, with 250 used in the estimation of radiance. Ray-marching depth is set at 200 steps. Each of the images has been rendered in a Dual Xeon Pentium 4 at 2.8GHz with 2GB RAM at 512×384 resolution, casting one ray per pixel, and took approximately 20 minutes to render. This time is roughly independent of the number of parameters of the bio-optical model. In order to reduce these computation times, several optimization techniques could be adopted, like using adaptive ray-marching or radiance caching strategies [JDZJ08]. Additionally, perceptual issues could be taken into account, using just an approximate solution in areas of the image where the error is known to be perceptually negligible [SGA*07].

Energy balances show that on average almost 99% of the energy emitted by the light sources is absorbed after just a few interactions of the photons, with very incremental variation after the fourth interaction and negligible contribution after the fifth. This relatively fast convergence is due to the strong absorption in water. We have therefore limited the number of interactions per photon to five, in order to speed up the simulations. Variations of the parameters C, $\alpha_d(400)$ and $\alpha_y(440)$ yield different probabilities for absorption, elastic and inelastic scattering events, which in turn affect the in-water light field. The results can be seen in Figure 2, with each of the varying parameters influencing the final light field as follows:

- Chlorophyll concentration (C) affects mainly both elastic and inelastic scattering. The effects of inelastic scattering are mostly masked by the more predominant elastic scattering and absorption, which increases slowly. The third column in Figure 2 shows brighter images than the previous two due to in-scattering. For higher values (fourth column), out-scattering prevails and the images become darker.
- Minerals and detritus turbidity $(\alpha_d(400))$ increases absorption at lower wavelengths, thus reducing the brightness of the scene and the overall blue hue. Scattering is also increased, making the images appear murkier. Figure 2 shows variations of the minerals and detritus turbidity between the first and second rows for direct comparison.
- CDOM turbidity $(\alpha_y(440))$ slightly increases absorption (darker images) and introduces inelastic scattering (change in hue). This can be seen by comparing the first and third rows in Figure 2.

We have undergone a visual validation of our model by rendering different natural waters. Figure 3 shows the resulting underwater images for Atlantic, Mediterranean, Baltic, North Sea and shallow coastal waters rich in CDOM respectively. All the images have been simulated at the same depth

Figure 3: *Rendered images of different waters. From left to right: Atlantic, Mediterranean, Baltic, North Sea and shallow coastal waters rich in CDOM. Smaller patches below for comparison purposes by Frisvad et al. [FCJ07] (used with permission).*

and are illuminated by the same isotropic point light source. The changes in color are clearly noticeable, from a darker blue in the case of Atlantic water, to the greener hue in the image of the North Sea. The smaller patches below the first four images correspond to the simulations by Frisvad et al. [FCJ07] for the same types of water, and are shown for comparison purposes. Our simulations based on radiative transfer approximately match their simulations based on Lorenz-Mie theory. The differences are mainly owed to two factors: on the one hand, the overall darker tone in our images is due to in-water absorption, whereas [FCJ07] renders the *surface* of the water body; on the other hand, the absence of inelastic scattering effects in [FCJ07] can have a visible influence the final appearance of water, as shown in Figure 4 for the Baltic case. The properties of the water have been adjusted according to measurements found in [BSF*03] [Mob94] for our bio-optical model and [BSF*03] in the model by Frisvad et al. In both cases, it is only the changes in the constituents of the waters which yield the different colors. We have additionally performed a numerical analysis of the in-water radiance field, to quantify the influence of each constituent. The results can be seen in Figure 5.

6. Conclusion

We have presented a complete bio-optical model of ocean water based on parameterizing its intrinsic optical properties. Relying on radiative transfer theory, we obtain the resulting in-water light field by extending the rendering algorithm presented in [GMAS05]. The extension can now handle more complex interactions between light and water, including inelastic scattering with anti-Stokes behavior, where the scattered photon absorbs energy from the medium and is re-emitted at *higher* energies. We have additionally studied the influence of the parameters in the apparent optical properties of water in the scene, which are defined by the light field obtained. We have performed an energy-balance analysis, and visual validation of the method has been provided by direct comparison with images by Frisvad et al. [FCJ07], rendering different types of waters based on published constituent data.

We have included Raman scattering by pure water and fluorescence by phytoplankton and CDOM as inelastic scattering events with energy transfers. Even though their combined quantitative contribution to the overall radiance field is usually less than 2% (see Figure 5), this relatively small percentage does have a clear influence on the apparent optical properties, as Figure 4 shows. We thus argue that these events, usually overlooked in computer graphics literature, are qualitatively important for underwater imagery and should be included in a complete simulation. Other types of inelastic scattering such as *Compton*, *Bragg* or *Brillouin* could also be added, although their influence is more incremental. Other particulate elements could be easily added as well just by including their corresponding absorption and scattering coefficients in the model; however, the three constituents treated here (phytoplankton, minerals and detritus and CDOM) have the most influence in the final radiance field.

The results show how the model developed can easily be used for physically-based simulations of underwater imagery. We believe this work can be of interest not only in the computer graphics community, but in remote sense or oceanographic studies as well.

Figure 4: *The influence of inelastic scattering in the apparent optical properties of water (Baltic sea): Left, no inelastic scattering. Center, just chlorophyll inelastic scattering (as in [GMAS05]). Right, all inelastic scattering events included in the simulation.*

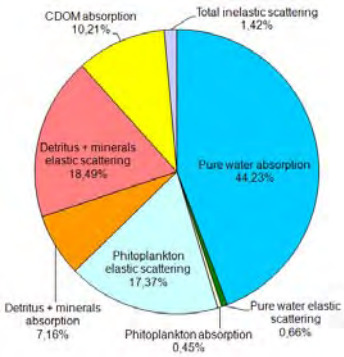

Figure 5: *Radiance distribution of the resulting in-water light field per type of event (Baltic Sea).*

Acknowledgments

We thank the anonymous reviewers for their valuable comments. This research was partly done under the sponsorship of the Spanish Ministry of Education and Research through the projects TIN2004-07672-C03-03 and TIN2007-63025.

References

[BLSS93] BLASI P., LE SAEC B., SCHLICK C.: A rendering algorithm for discrete volume density objects. *Computer Graphics Forum (Eurographics 93) 12*, 3 (1993), 201–210. 4

[BMP81] BRICAUD A., MOREL A., PRIEUR L.: Absorption by dissolved organic matter of the sea (yellow substance) in the uv and visible domains. *Limnol. Oceanogr. 26*, 1 (1981), 43–53. 3

[BSF*03] BABIN M., STRAMSKI D., FERRARI G. M., CLAUSTRE H., BRICAUD A., OBOLENSKY G., HOEPFFNER N.: Variations in the light absorption coefficients of phytoplankton, nonalgal particles, and dissolved organic matter in coastal waters around europe. *J. Geophys. Res. 108(C7)*, 3211 (2003). 3, 9

[Cha60] CHANDRASEKHAR S.: *Radiative Transfer*. Dover Publications, Inc., 1960. 2

[CS04] CEREZO E., SERON F. J.: Rendering natural waters taking fluorescence into account: Research articles. *Comput. Animat. Virtual Worlds 15*, 5 (2004), 471–484. 2

[FCJ07] FRISVAD J. R., CHRISTENSEN N. J., JENSEN H. W.: Computing the scattering properties of participating media using Lorenz-Mie theory. *ACM Trans. Graph. 26*, 3 (2007), 60. 2, 9

[Gla95] GLASSNER A. S.: *Principles of Digital Image Synthesis*. Morgan Kaufmann Publishers Inc., San Francisco, CA, USA, 1995. 2

[GM83] GORDON H. R., MOREL A.: *Remote Assessment of Ocean Color for Interpretation of Satellite Visible Imagery: A Review*, vol. 4 of *Lecture Notes on Coastal and Estuarine Studies*. Springer-Verlag, New York, 1983. 4

[GMAS05] GUTIERREZ D., MUNOZ A., ANSON O., SERÓN F. J.: Non-linear volume photon mapping. In *Proc. of the Eurographics Symposium on Rendering Techniques, Konstanz, Germany, June 29 - July 1, 2005* (2005), pp. 291–300. 2, 6, 9

[GSO03] GREEN R. E., SOSIK H. M., OLSON R. J.: Contributions of phytoplankton and other particles to inherent optical properties in new england continental shelf waters. *Limnol. Oceanogr. 48*, 6 (2003), 2377–2391. 4

[Haw92] HAWES S.: *Quantum fluorescence efficiencies of marine fulvic and humid acids*. PhD thesis, Dept. of Marince Science, Univ. of South Florida, 1992. 5

[HG41] HENYEY L., GREENSTEIN J.: Diffuse radiation in the galaxy. *Astrophysics Journal 93* (1941), 70–83. 4

[JC98] JENSEN H. W., CHRISTENSEN P. H.: Efficient simulation of light transport in scenes with participating media using photon maps. In *SIGGRAPH 98 Conference Proceedings* (jul 1998), Cohen M., (Ed.), Annual Conference Series, ACM SIGGRAPH, Addison Wesley, pp. 311–320. 7

[JDZJ08] JAROSZ W., DONNER C., ZWICKER M., JENSEN H. W.: Radiance caching for participating media. *To appear in ACM Transactions on Graphics* (2008). 8

[Jen01] JENSEN H. W.: *Realistic image synthesis using photon mapping*. A.K. Peters, Natick, Massachussets, 2001. 2, 6

[Kir94] KIRK J. T.: *Light and photosynthesis in aquatic ecosystems*. Cambridge University Press, New York, 1994. 3

[KYNN91] KANEDA K., YUAN G., NAKAMAE E., NISHITA T.: Realistic visual simulation of water surfaces taking into account radiative transfer. In *Proc. of CAD/Graphics 91* (1991), pp. 25–30. 2

[Maz02] MAZO R. M.: *Brownian Motion: Fluctuations, Dynamics and Applications*, vol. 112 of *International Series of Monographs on Physics*. Oxford University Press Inc., Great Clarendon Street, Oxford, 2002, ch. Einstein-Smoluchowski Theory, pp. 46–62. 4

[Mob94] MOBLEY C. D.: *Light and Water: Radiative Transfer in Natural Waters*. Academic Press, Inc., San Diego, 1994. 1, 2, 3, 5, 9

[Mor74] MOREL A.: *Optical Aspects of Oceanography*. Academic Press, New York, 1974. 3, 4

[Mor88] MOREL A.: Optical modeling of the upper ocean in relation to its biogenous matter content (case i waters). *Journal of Geophysical Research 93*, C9 (1988), 10749–10768. 3

[NKON90] NAKAMAE E., KANEDA K., OKAMOTO T., NISHITA T.: A lighting model aiming at drive simulators. *Computer Graphics 24*, 4 (Aug. 1990), 395–404. 2

[NSTN93] NISHITA T., SHIRAI T., TADAMURA K., NAKAMAE E.: Display of the earth taking into account atmosphere scattering. In *Computer Graphics (SIGGRAPH '93 Proceedings)* (1993), vol. 24, pp. 175–182. 2

[PA01] PREMOZE S., ASHIKHMIN M.: Rendering natural waters. *Comput. Graph. Forum 20*, 4 (2001), 189–199. 2

[PF97] POPE R. M., FRY E. S.: Absorption spectrum (380–700 nm) of pure water. ii. integrating cavity measurements. *Applied Optics 36*, 33 (1997), 8710–8723. 3

[Pre76] PREISENDORFER R. W.: *Introduction*, vol. 1 of *Hydrologic Optics*. National Technical Information Service, Springfield, IL, 1976. 1

[RPC89] ROESLER C. S., PERRY M. J., CARDER K. L.: Modeling in situ phytoplankton absorption from total absorption spectra in productive inland marine waters. *Limnol. Oceanogr. 34*, 8 (1989), 1510–1523. 3

[RT87] RUSHMEIER H. E., TORRANCE K. E.: The zonal method for calculating light intensities in the presence of a participating medium. *Computer Graphics 21*, 4 (July 1987), 293–302. 2

[SB81] SMITH R. C., BAKER K. S.: Optical properties of the clearest natural waters (200–800 nm). *Appl. Opt. 20* (1981), 177–184. 3, 4

[SBM01] STRAMSKI D., BRICAUD A., MOREL A.: Modeling the inherent optical properties of the ocean based on the detailed composition of planktonic community. *Applied Optics 40* (2001), 2929–2945. 4, 5

[SCP94] SPINRAD R. W., CARDER K. L., PERRY M. J. (Eds.): *Ocean Optics*. No. 25 in Oxford Monographs on Geology and Geophysics. Oxford University Press, 1994. 2

[SGA*07] SUNDSTEDT V., GUTIERREZ D., ANSON O., BANTERLE F., CHALMERS A.: Perceptual rendering of participating media. *ACM Transactions of Applied Perception 4*, 3 (2007). 8

[SLP87] SATHYENDRANATH S., LAZZARA L., PRIEUR L.: Variations in the spectral values of specific absorption of phytoplankton. *Limnol. Oceanogr. 32*, 2 (1987), 403–415. 3, 4

[TN95] TADAMURA K., NAKAMAE E.: *Computer Graphics: Developments in Virtual Environments*. Academic Press, 1995, ch. Modeling the colour of Water in Lightning Design, pp. 97–114. 2

[Wal69] WALRAFEN G. E.: Continuum model of water–an erroneous interpretation. *Journal of Chemical Physics 50*, 1 (January 1969), 567–569. 5